energies

Volume II
Mining Innovation

Edited by
Krzysztof Skrzypkowski

Printed Edition of the Special Issue Published in *Energies*

MDPI

Volume II: Mining Innovation

Volume II: Mining Innovation

Editor

Krzysztof Skrzypkowski

This is a reprint of articles from the Special Issue published online in the open access journal *Energies* (ISSN 1996-1073) (available at: https://www.mdpi.com/journal/energies/special_issues/Volume_II_Mining_Innovation).

For citation purposes, cite each article independently as indicated on the article page online and as indicated below:

LastName, A.A.; LastName, B.B.; LastName, C.C. Article Title. *Journal Name* **Year**, *Volume Number*, Page Range.

Contents

About the Editor

Krzysztof Skrzypkowski

Krzysztof Skrzypkowski is a Professor of Mining Engineering at the AGH University of Science and Technology, Faculty of Civil Engineering and Resource Management in Krakow, Poland. Professor Skrzypkowski obtained his PhD (doctorate) and DSc (habilitation) degrees in AGH in 2014 and 2021, respectively. His scientific research concerns the stability of underground mine workings, particularly the selection of support for room and roadway excavations. In addition, his research interests focus on computer-aided design and the determination of geotechnical parameters of backfill materials. As the head of the rock bolting laboratory, he performs model, numerical and industrial tests on various mechanisms of cooperation between the mining support and the rock mass. He is the author of over 120 scientific publications and several patents and a utility model regarding the monitoring and yielding of the rock bolt and steel arch support. As an academic lecturer, he works closely with scientific institutes, industry and universities involved in the exploitation of mineral raw materials.

Preface to "Volume II: Mining Innovation"

This Special Issue, "Volume II: Mining Innovation", includes seventeen articles concerning numerical, laboratory, analytical, artificial intelligence and industrial research into underground mining.

The issues discussed in the articles include the selection of an arch yielding support for preparatory workings in a hard coal seam with particular emphasis on the fault zone; assessing the performance of yielding rockbolts, which can be served as a promising tool to improve and optimize the design of rock supporting in burst-prone ground; sill pillar recovery schemes, loss in the stopes and assessing the feasibility of recovering two sill pillars in a hard rock mine; a method for determining effective geomechanical parameters for technological and residual pillars with the application of measurement data, excavation convergence measurements and statistical methods; impact of rock mass geomechanical parameters on the stability of preparatory headings driven in two rock mass types with different strength and deformation parameters and their influence on the safety of mining in underground copper ore mines located within the Legnica-Glogow Copper District; the stress evolution of the working face through an abandoned roadway in a coal mine. Furthermore, hydraulic fracturing technology combined with floor grouting and hydraulic support for the abandoned roadway was proposed to stabilise the working face for safe mining; and modified long short-term memory was used to detect the formation of explosive methane–air mixtures in the longwall face and to identify possible explosive gas accumulations prior to them becoming hazards. A review of reliability and fault analysis methods for heavy equipment and their components used in mining and the advantages and limitations of the algorithm are discussed, and the efficiency of new machine learning methods was compared to the traditional methods. A description of a system for the automatic determination of rock-breaking target poses for impact hammers used in underground mines is available. A model of the manipulator for supporting assembly works in mining excavations with a description of its basic functions was constructed, using kinematics and stability. A simplified calculation method in a flood discharge system for a tailing pond was conceived of; measurements of impact and friction sensitivity were made, measurements of the detonation velocity in blastholes were considered and, the determination of brisance via a Hess test and analysis of rock fragmentation was achieved. When researching the various properties of waste rock to select the appropriate cutting methods and tools, attention was paid to the abrasive properties, i.e., the rock's abrasiveness. It was found that the affinity of coal for water and methanol is related to the content of oxygen in the coal rather than the rank of the coal. Furthermore, the modified active carbons were found to be suitable for applications in hydrogen storage systems. For the new challenges facing mining, it was noted that, with reference to the SARS-CoV-2 virus, recommendations, guidelines and decisions were presented which were established after the appearance of the first wave of cases in Poland. Moreover, human resources in the field of education and the stimulation of innovation in the aspect of energy transition were presented.

The exploitation of raw mineral and rock materials and the accompanying processes are carried out in complex geological and mining conditions for which the presented innovations may be helpful not only at the design stage but also during their implementation.

Krzysztof Skrzypkowski
Editor

Choice of the Arch Yielding Support for the Preparatory Roadway Located near the Fault

Krzysztof Skrzypkowski [1,*], Krzysztof Zagórski [2], Anna Zagórska [3], Derek B. Apel [4], Jun Wang [4], Huawei Xu [4] and Lijie Guo [5,6]

[1] Faculty of Civil Engineering and Resource Management, AGH University of Science and Technology, Mickiewicza 30 Av., 30-059 Kraków, Poland

[2] Faculty of Mechanical Engineering and Robotics, AGH University of Science and Technology, Mickiewicza 30 Av., 30-059 Kraków, Poland; zagkrzys@agh.edu.pl

[3] Research Centre in Kraków, Institute of Geological Sciences, Polish Academy of Science, Senacka 1, 31-002 Kraków, Poland; ndzagors@cyf-kr.edu.pl

[4] School of Mining and Petroleum Engineering, University of Alberta, Edmonton, AB T6G 2R3, Canada; dapel@ualberta.ca (D.B.A.); jun8@ualberta.ca (J.W.); hx1@ualberta.ca (H.X.)

[5] BGRIMM Technology Group, No. 22, Beixing Road, Daxing District, Beijing 102628, China; guolijie@bgrimm.com

[6] National Centre for International Research on Green Metal Mining, Beijing 100160, China

* Correspondence: skrzypko@agh.edu.pl

Abstract: The article presents a method of selecting an arch yielding support for preparatory workings driven in a hard coal seam. Particular attention was paid to discontinuous deformation in the form of a fault, which significantly contributes to the change of the excavation protection schemes. On the basis of the geometry of the machines and devices in the designed excavation, the support was selected, which was then checked for the ventilation criterion. In the next stage, analytical calculations were carried out using the determined spacing of the steel support in the fault zone and the area outside of it. Additionally, using the RS3 numerical software based on the finite element method, a rock mass model with a fault was built, through which the preparatory excavation passes. The aim of the research was to determine the total displacements occurring in the fault crossing zone for the excavation without support and with the use of steel arch yielding and with additional reinforcement in the form of straight segments. In conclusion, it was found that the variants of the excavation reinforcement can be modeled and selected in advance, which allows for the fastest possible execution of the driving and the maintenance of the minimum movement dimensions while passing through the fault.

Keywords: arch yielding support; fault; minimal section method; RS3

1. Introduction

Underground mining of hard coal deposits requires the construction and maintenance of many preparatory workings, which are driven by a certain time advance in relation to the exploitation of the deposit. Such a technological process makes it necessary to ensure the stability of workings in the long term. These issues are of particular importance in relation to preparatory workings, the useful life of which is often related to the life of longwalls. Preparatory workings are located in an environment with many geological factors, such as continuous and discontinuous deformations, high stresses and natural hazards [1], including the impact of remains and operating edges [2] that contribute to additional loads on mining supports. Both the roadways and inclined drifts are supported by an independent arch yielding support [3]; rock bolt and cable support [4–6], including steel arch and bolts [7,8]; and shotcrete [9,10], or new solutions are sought with the use of a hydraulic support [11]. The previously used steel sets support is often exposed to the influence of saline mine waters [12]. First of all, leaks occur in different places and

periods of the excavation's existence, depending on the degree of fracture and crushed rocks in the fault area [13,14]. Driven preparatory excavations in the immediate vicinity of the fault are secured with a support, the main task of which is to ensure the stability of the excavation throughout its lifetime and the dimensions of its cross-section, as well as to protect people, machines and devices against rock fragments moving from the roof or side walls [15]. In conditions of additional loads caused by the immediate vicinity of the fault, the arch yielding support should be characterized by a defined load capacity resulting from the strength parameters of its individual elements and the ability to deform under control [16]. The occurrence of changes in the geometry of the support without damaging its structural elements is ensured by the appropriate flexibility of the support as well as its spacing. The individual arches of the steel support, set at specific intervals, are connected with each other by means of struts that keep the distance between them and prevent them from twisting in the event of uneven loading. The length of the struts is usually adjusted to the spacing of the arches with a pitch of at least 0.1 m. Most often, this pitch is 0.25 m, which translates into the distance between the frames: 0.5, 0.75, 1.0, 1.25, 1.5 m [17]. The flexibility of the support provides the possibility of displacement of the support structural elements in relation to each other as a result of the impact of specific load values. The selection of the arch yielding support of the preparatory workings is made with the assumption of the safety coefficients [18]. The basic factor determining the stability of the excavation is the correct selection of the parameters of the support, both in terms of geometry and strength. This selection is based on the assumption that the designed excavation is made in rocks with specific strength, deformation and structural parameters. The mutual relation of these values determines the processes taking place in the vicinity of the excavation exposed to the fault and directly determines the spacing of the support. Important factors influencing the load-bearing capacity of the arch yielding support include the physical and mechanical parameters of the steel used to make individual elements of the support of mining excavations [19]. Currently, the most commonly used steel grades are 25G2, 34GJ, 31Mn4, S480W, G480V, S550W and HŁ CORR, which are characterized by their yield point and minimum tensile strength of 340 MPa and 550 MPa, respectively [20]. The need to verify theoretical solutions has led to the creation and development of laboratory stands in research and development units, the task of which is to better understand the behavior of the structure [21] and the cooperation of the support with the rock mass [22]. Yang et al. [23] pointed out top and bottom arch strengthening for a new steel sets designed for underground roadways. Lv et al. [24] conducted laboratory test of square steel confined concrete in a geometric scale 1:1 and indicated the possible places of damage. Wu et al. [25] simulated the surrounding rock stress by means of the model tests. As a result of the recognition of the impact of various physicomechanical factors, it is possible to make a practical assessment of the application of the steel sets in natural conditions. Research on physical models, which reflect the impact of the fault on the stability of the excavation, is of particular importance. Wang et al. [26] stated that the presence of fault increases the risk of dynamic phenomena. Wang et al. [27] pointed out that in the immediate vicinity of the fault, there is a great risk of sudden rock fall into the excavation. A common method of reinforcing the excavation while passing through the fault is the use of an additional bolt and cable support [28]. Adoko et al. [29] used RS2 software to model drift with and without supports. According to their calculations, the use of rock bolting and concrete contributed to a more than two-fold reduction in the value of stresses around the excavation. Xiong et al. [30] found and proved on the basis of numerical modeling that the combination of several types of support contributes to an effective and significant reduction in roadway deformation, thanks to which the excavation retains its functionality for longer. The irregularities in the deposits of hard coal can be divided into primary and secondary. The primary irregularities arose simultaneously with seam formation and secondary irregularities after the seam formation. For the selection of the casing and operation, the greatest challenge includes faults (Figure 1a), which are the shifts of the layers in relation to each other with a simultaneous interruption of their continuity. The shifts occur along the cracks in the

rock mass. In the case of a normal fault, the fault plane is inclined towards the dropped wing. On the other hand, for an inverted fault, the layer overlap occurs in such a way that the older layers lie partially over the younger ones. Depending on the direction of the fault plane in relation to the seam strike, longitudinal faults (Figure 1b) and transverse faults (Figure 1c) are distinguished. The fault is longitudinal when the contours of the step plane run parallel to the extent of the seam, transverse when the contours run perpendicular to the extent. In addition, there are also oblique faults where the contours of the fault plane form a right angle with the length of the deck. The gap along which the layers have shifted is called the fault gap. Fault fissures are often water-bearing and constitute one of the sources of water inflow to underground mine's workings. In hard coal seams, faults are sometimes reservoirs of gases, such as carbon dioxide or methane. Sometimes, the disturbed layers adhere tightly to each other in a plane smoothly polished by rock friction while moving. The wider fault gaps are filled with rock crumbs, sand and clay.

(**a**)

(**b**)

Figure 1. *Cont.*

(**c**)
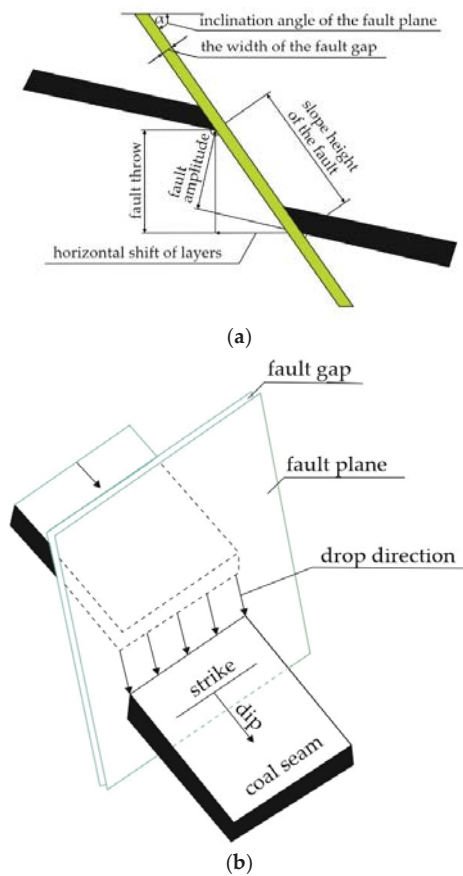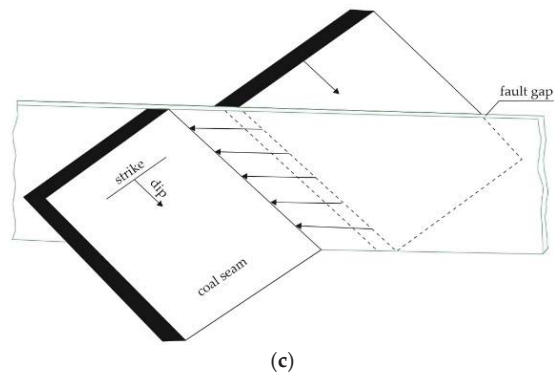
Figure 1. Fault: (**a**) basic parameters; (**b**) longitudinal; (**c**) transverse.

Despite significant progress in the selection of the arch yielding support for underground preparatory workings and numerous laboratory, numerical and industrial tests, there is still a gap in the calculation algorithm in taking into account the selection of forehead equipment, ventilation criterion and geomechanical calculations. The article presents a method of selecting the arch yielding support for the preparatory excavation, which was driven in the fault zone. Based on analytical calculations, the support spacing in the immediate fault zone as well as outside of it was calculated. Using the spatial numerical software based on the finite element method, three variants of the excavation performance were modeled: without support; with the use of steel arch yielding; and with additional reinforcement in the form of straight segments. The results of the numerical simulations were the total displacement distributions around the driven preparatory roadway.

2. Mining and Geological Conditions of the Driven Excavation

Rock lumps of hard coal, claystone and sandstone were collected from the 800 m level roadway in one of the mines of the Upper Silesian Coal Basin in Poland. The forehead is driven mechanically with the R-130 roadheader (Figure 2), while the excavated material from the face is loaded with the machine loader onto the belt feeder. The extent of geological layers in the area of the planned works generally runs along NNW–SEZ. The collapse of the layers does not exceed 3°, generally NE. The excavation is driven in the layer of coal seam 207 with a thickness of about 4 m. Directly at the roof and the floor of the excavation, there is a layer of claystone over which there is a several dozen meter layer of sandstone (Figure 3).

Figure 2. Forehead, place of sampling.
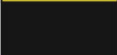
Column	Description	Range of thickness variations, (m)
	sandstone	10–30
	coal seam 206	1.3–2.8
	claystone	0.4–2.0
	coal seam 206	0.1–0.5
	claystone	0.1–4.5
	sandstone	19–28
	claystone	0.1–0.9
	coal seam 207	2.5–4.1
	claystone	0.1–2.8
	sandstone	13–57

Figure 3. Lithological profile of the coal seam.

The roadway is driven in a rock mass where there is no methane hazard, and above all, it is made outside the area that is subject to rock bursts and gas and rock outbursts. The excavation is classified as "A" class of coal dust explosion hazard, which means that in the driven coal seam or its part, there is mine dust protected in a natural way. In addition, mine dust contains at least 80% of non-flammable solids of natural origin, the amount of hazardous coal dust is less than 10 g/m^3 of the excavation and the mass of coal dust without non-flammable solids, settling on a given surface at a given time hereinafter referred to as dust settling intensity, is less than 0.15 g/m^2 per day [31]. Coal seam no. 207 was classified into the fifth most dangerous group of self-igniting. The incubation period of endogenous fire is 32 days, while the activation energy A is 46.5 kJ/mol, and the self-igniting index Sza is 137 °C/min [32]. In the vicinity of the designed excavation, the temperature of rocks is about 20 °C. The conducted measurements and their results as well as the practice acquired during the exploitation of the coal seam no. 207 indicate that, during driving, the substitute climate temperature should not exceed 26 °C for workplaces. In the event of a water hazard, the excavation area was classified as the weakest in a three-point scale. Water to the preparatory roadway can flow mainly from the depletion of carboniferous aquifers associated with sandstones lying between seams 206 and 207 in the form of condensation and roof leakages. In the area of the excavation, there is a geological disturbance in the form of faults with a throw size from 1.8 m to 2.5 m, which occurred along the north–eastern side of the side (Figure 4).

Figure 4. The area of the roadway with marked faults.

Laboratory Tests of Rocks from Driven Excavation

In the laboratory of the Department of Mining Engineering and Occupational Safety of AGH in Krakow, cylindrical samples with a diameter of 50 mm and a height of 100 mm were cut using a core drill (Figure 5a,b). The samples prepared in this way were tested (Figure 5c–e) on a testing machine, which was equipped with three strain gauges and a cable encoder to measure the displacement, while the horizontal strains were measured with three electronic dial gauges (Figure 5c). The load rate was 0.5 kN/s. The results are summarized in Table 1. The main objective of the laboratory tests was to determine the deformation and strength parameters of three types of rocks, coal, sandstone and clay slate, which surround the hard coal seam. In the laboratory tests, no rheological tests of hard coal related to creep and relaxation were performed, because the hard coal showed the characteristics of an elastic-brittle material. The test results were used in numerical modeling to estimate the total displacement for different variants of roadway II protection. All types of rock were taken from the forehead of the roadway II. There was no visible stratification in the rocks from which samples of both coal, sandstone and clay slate had been cut.

Table 1. Summary of the results of strength and deformation tests for rocks in the area of the designed excavation.

Type of Rock	Density (kg/m^3)	Compressive Strength (MPa)	Tensile Strength (MPa)	Young's Modulus (GPa)
Coal	1296	15.45	1.37	2.3
Claystone	2440	16.5	1.55	10.3
Sandstone	2560	47	3.62	5.4

Figure 5. Preparation of samples for testing: (**a**) testing machine equipped with sensors; (**b**) cutting samples in a block of coal with a trepan drill; (**c**) a lump of clay slate with samples cut out; (**d**) electronic sensors of horizontal deformation; (**e**) Brazilian tensile strength test; (**f**) compression of sandstone samples.

3. Choice of the Arch Yielding Support

3.1. Minimum Section Method

In order to determine the dimensions of the cross-section of roadway II, the method of minimum sections was first used, which consists in determining the minimum width and minimum height of the excavation. In order to determine the minimum width S_{min}, all widths of devices in the excavation and the minimum movement distances between the devices and the excavation support were added [33]. The minimum height H_{min} is

calculated as the minimum height, but the dimensions are summed up in the largest cross-section. The sum of the width and height together with the movement distances should be multiplied by 1.1 due to the possibility of clamping the excavation, thus reducing the excavation cross-section. The individual widths and heights of machines and devices along with the minimum movement distances are presented in Table 2.

Table 2. Dimensions of machines and devices with minimum movement distances.

Type of Machine or Device	Width (mm)	Height (mm)
Suspended monorail: BIZON 120-X	1200	1500
Belt conveyor: GWAREK-1000	1350	1000
Fire pipeline	315	
Drainage pipeline	315	
Compressed air pipeline	250	
Duct diameter	1000	
Passage for miners	700	1800
Rail of suspended monorail	155	
Movement intervals		
From	**To**	**Minimum distance (mm)**
Belt conveyor	Arch yielding support	250
Suspended monorail	Belt conveyor	400
Duct	Belt conveyor	600
Floor	Suspended monorail	300
Rail of suspended monorail	Roof arch	500

The minimum width S_{min} and the height H_{min} of the excavation were determined according to Equations (1) and (2):

$$S_{min} = \left(\sum x_a + \sum x_b\right) \cdot 1.1 \text{ (mm)}, \tag{1}$$

where

x_a—the width of the device (mm);
x_b—minimum movement distance between individual devices and the support (mm);

$$H_{min} = \left(\sum y_a + \sum y_b\right) \cdot 1.1 \text{ (mm)}, \tag{2}$$

where

y_a—height of the device in a given cross-section (mm);
y_b—minimum movement distance between the device and the support (mm).

Taking into account the dimensions of machines and devices and the movement distances (Table 2), the minimum width and height were calculated according to Equations (3) and (4).

$$S_{min} = [(1350 + 1200 + 700 + 315) + (250 + 400)] \cdot 1.1 = 4640 \text{ mm} \tag{3}$$

$$H_{min} = [(155 + 1500 + 500) + (300)] \cdot 1.1 = 2700 \text{ mm} \tag{4}$$

Then, based on the calculated values of S_{min} and H_{min}, the ŁP8/V29/A three-part support was selected [34] (Table 3), which should meet the conditions of Equations (5) and (6).

$$S_{catalogue} \geq S_{min} \tag{5}$$

$$H_{catalogue} \geq H_{min} \tag{6}$$

Table 3. Basic dimensions of the support arches ŁP8.

Type of Support	Height, $H_{catalogue}$ (mm)	Width, $S_{catalogue}$ (mm)	Cross-Section (m²)
ŁP7/V29/A	3100	4200	11.08
ŁP8/V29/A	3300	4700	13.07
ŁP9/V29/A	3500	5000	14.76

The three types of supports are presented in the Table 3 in order to show the optimal arch yielding support selection. The first type, ŁP7/V29/A, was not selected because it did not meet the S_{min} condition. However, the third type, ŁP9/V29/A, was also not selected due to the too high costs of roadway support; therefore, type ŁP8/V29/A was selected. Thus, the condition was met because 4700 mm $\geq$ 4640 mm and 3300 mm $\geq$ 2700 mm. The arrangement of machines and devices with spaces is shown in Figure 6.
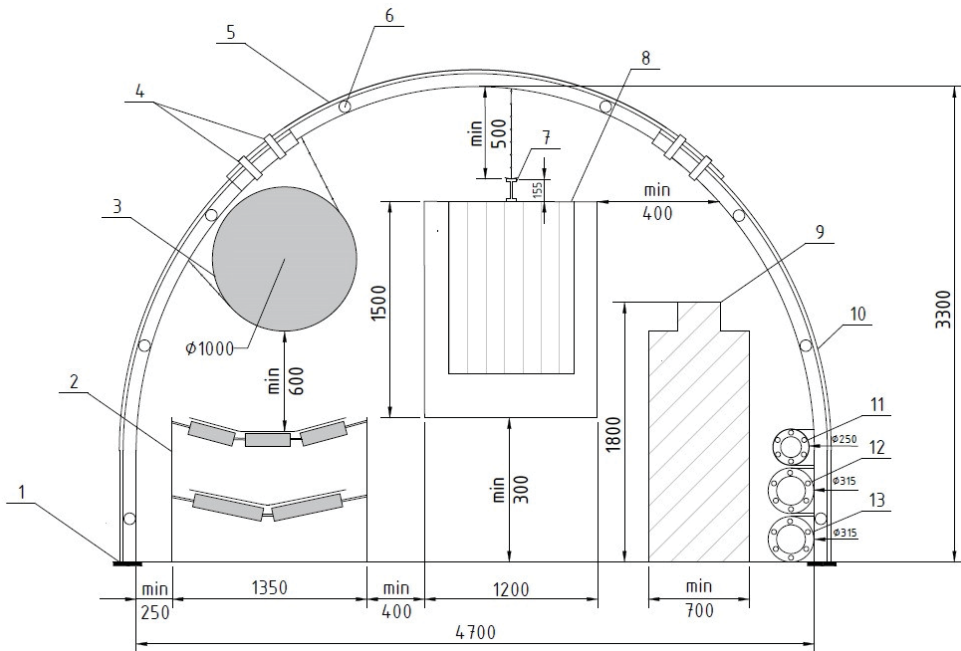
Figure 6. Cross-section of the roadway II: 1—support foot; 2—belt conveyor GWAREK-1000; 3—duct; 4—double yoke stirrups; 5—roof arch of the yielding support ŁP8/V29/A; 6—multi-element strut; 7—rail of suspended monorail; 8—BIZON 120-X suspended monorail; 9—passage for miners; 10—sidewall arch; 11—compressed air pipeline; 12—drainage pipeline; 13—fire pipeline.

The arch yielding support was made of steel elements with a "V" profile. As it is a preparatory excavation not exposed to the effects of longwall exploitation, no convergence was observed at the driving stage. The expected course of the slide of the steel sets elements at the longwall exploitation stage is estimated at the level of 0.3 mm/m. In order to define the dimensions of the roadway II cross-section in the breakout, 300 mm was added to the catalogue height and width. Therefore, the height H_w and width S_w of the excavation cross-section in the breakout were calculated according to Equations (7) and (8):

$$H_w = H_{kat} + 300 = 3600 \text{ mm,} \qquad (7)$$

where
H_w—height of the cross-section of the excavation in the breakout (mm);
H_{kat}—catalogue height of the ŁP8 support arches ($H_{catalogue}$ = 3300 mm);

$$S_w = S_{kat} + 300 = 5000 \text{ mm,} \tag{8}$$

where:

S_w—width of the cross-section of the excavation in the breakout (mm);

S_{kat}—catalogue width of the ŁP8 support arches $\left(S_{catalogue} = 4700 \text{ mm}\right)$.

3.2. Ventilation Criterion

The selected dimensions of the arch yielding support must meet the ventilation requirements for preparatory workings [35]. For this purpose, the actual velocity V_{rz} of the flowing air in the excavation was determined, and then the value was compared with the calculated values of the minimum V_{min} and maximum V_{max} velocity. For the designed roadway excavation, there must be the following relationship (9):

$$V_{min} \leq V_{rz} \leq V_{max} \left(\frac{m}{s}\right), \tag{9}$$

where

V_{rz}—actual air flow velocity (m/s);
V_{max}—permissible maximum air velocity in the excavation (m/s);
V_{min}—the minimum permissible air velocity in the excavation (m/s).

The actual air flow velocity V_{rz} in the excavation was calculated according to Equation (10):

$$V_{rz} = \frac{Q_a}{F}, \left(\frac{m}{s}\right), \tag{10}$$

where

Q_a—the required air flow rate at the outlet from the duct (m^3/s) was calculated according to Equation (11) [36];
F—usable cross-section of the excavation (m^2), assumed F = 13.07 m^2 (Table 3);

$$Q_a = \frac{Q_b}{P_q}, \left(\frac{m^3}{s}\right), \tag{11}$$

where

Q_b—fan flow, m^3/s (for Axial Flow Fan—Type ES 9-500/80, Q_b = 10.2 m^3/s) [37];
P_q—the expenditure reserve ratio (dimensionless) is given by Equation (12):

$$P_q = 0.77 \cdot \exp \cdot \left(L \cdot \sqrt[3]{\frac{k^2}{2}} \cdot r\right) + 0.23 \cdot \exp \cdot \left(-2 \cdot L \cdot \sqrt[3]{\frac{k^2}{2}} \cdot r\right) \tag{12}$$

where

L—length of the duct, m (L = 80);
k—leakage rate of the duct, m^3/(sN$^{1/2}$) (k = 0.003);
r—unit resistance, flow rate of the duct, Ns^2/m^9 (r = 0.003590).

The actual air flow velocity V_{rz} was 4.87 m/s.

The minimum air velocity in excavation V_{min} is associated with the indication of whether the designed excavation is subject to the methane hazard. The air velocity in the excavation, which is ventilated by a duct in non-methane fields or in methane fields of I category methane hazard, cannot be less than 0.15 m/s, and in methane fields II, III and IV of the methane hazard category, it cannot be less than 0.3 m/s [35]. Roadway II is not covered by the methane hazard, so V_{min} = 0.15 m/s. The maximum air velocity in the excavation V_{max} for the exploitation excavations cannot exceed 5 m/s, for the preparatory excavations 8 m/s, and in shafts and small shafts, it cannot exceed 12 m/s [35]. Due to the fact that roadway II is a preparatory excavation, V_{max} = 8 m/s. After specifying the value

of the actual, minimum and maximum velocities, they were inserted into Equation (9), which shows that the ventilation criterion for the driven excavation was met because $0.15 \leq 4.87 \leq 8$ m/s.

3.3. Arch Yielding Support Calculation

The arch yielding support for roadway II was selected according to the method of Professor Rułka [38]. It is one of the three methods commonly used in Polish underground hard coal mining. This method can be used if the weighted average value of the compressive strength of the indicated roof rock package is not less than 10 MPa; the weighted average water permeability value of the indicated roof and floor rock packages is at least 0.5; the energy of probable tremors in the vicinity of the designed excavation is not greater than 5×10^5 J; the angle of the transverse inclination of the rock layers is not more than 30°; the angle of the excavation is not more than 35°. In addition, the designed excavation is located at a depth of 300–1200 m and the width of the cross-section of the excavation in the breakout is a maximum of 8 m. In order to determine the geomechanical properties of rocks in the area of the designed excavation, the range of the Z_{roof} and Z_{floor} rocks should be determined according to Equations (13) and (14):

$$Z_{roof} = 1.0 \cdot H_c \tag{13}$$

$$Z_{floor} = 0.5 \cdot H_c \tag{14}$$

where

H_c—height of the cross-section of roadway II in the breakout (m).

Figure 7 shows the lithological profile of the rock range, which was taken into account when selecting the support for roadway II.
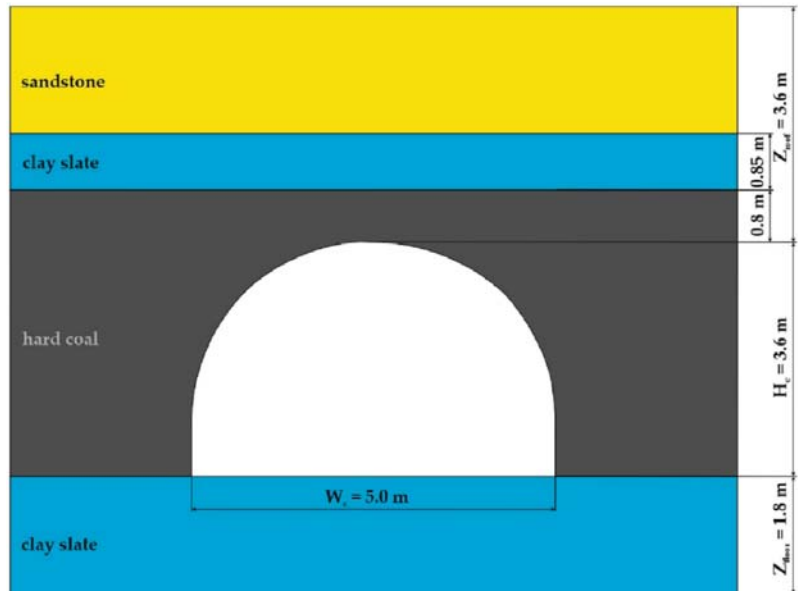
Figure 7. Lithological profile for roadway II.

The selection of the arch yielding support was calculated according to Equation (15):

$$d \leq \frac{W_{N_c}}{q_0} \tag{15}$$

where

d—arch yielding support spacing, m;
W_{N_c}—computational index of load capacity of support arches, MN/m;
q_0—computational load, MPa.

The support load index W_{N_c} = 0.0905 MPa was calculated according to Equation (16):

$$W_{N_c} = 0.5544 \cdot W_N \cdot 0.8 \cdot k_l \tag{16}$$

where

W_N—load capacity index of support arches, MN/m (for section V29 made of steel S480W, W_N = 0.255) [39];
k_l—lining coefficient (in the designed excavation a tight lining will be used; therefore k_l = 0.8; for mechanical, loose and non-loose lining, the coefficient is, respectively: 1.0, 0.6 and 0.4);
0.5544—constant value related to the factor of utilization of the maximum load capacity of arches;
0.8—constant value related to the load unevenness factor.

The computational load q_0 = 0.0357 MPa is calculated according to Equation (17):

$$q_0 = k_g \cdot k_u \cdot k_\alpha \cdot k_\beta \cdot k_e \cdot k_s \cdot q_N + q_d, \text{ MPa,} \tag{17}$$

where

k_g—the rock mass weakening coefficient in the determined rock packet (Figure 7), which ranges from 0.79 to 3.64, k_g = 1.881, was calculated according to Equation (18):

$$k_g = 1.7391 \cdot (1.1 - 0.007 \cdot RQD) \cdot (2.8 - 1.8 \cdot R_s) \cdot (1.07 - 0.0002 \cdot H), \tag{18}$$

where

H—depth of roadway II, H = 800 m;
RQD—rock quality designation, RQD = 40%;
R_s—coefficient of the influence of rock moisture on their strength, R_s = 0.75;
k_u—fault action coefficient for excavations that are located in the fault zone k_u = 1.2;
k_α—coefficient of the influence of the transverse inclination of the rock layers, for $\alpha \leq 15°$; k_α = 1.0, while for $15° \leq \alpha \leq 35°$ k_α = 1.15;
k_β—coefficient of the longitudinal inclination of the excavation impact, for $\beta \leq 15°$ k_α = 1.0, while for $15° \leq \beta \leq 25°$ k_β = 1.15 and for $25° \leq \beta \leq 35°$ k_β = 1.20;
k_e—exploitation edge influence factor (roadway II is outside the impact range and a distance of more than 120 m from the edge, therefore k_e = 1);
k_s—the impact factor of the adjacent excavation (roadway II is driven parallel to roadway I at a distance of about 225 m) according to Formula (19), k_s = 1.0:

$$k_s = 1 + \frac{1}{\left(1 + \frac{x_s}{W_c}\right)^2} \tag{19}$$

where

W_c—width of the excavation in the breakout, W_c = 5 m (Figure 7);
x_s—distance between roadways, x_s = 225 m (Figure 4);
q_N—the characteristic value of the vertical static loads of the supportg, q_N = 0.0446, was calculated according to Equation (20):

$$q_N = q_w \cdot \frac{W_{ca}}{W_c}, \text{ MPa,} \tag{20}$$

where

W_{ca}—computational width, W_{ca} = 7.1798, which is calculated according to Equation (21):

$$W_{ca} = W_c + H_c \cdot k_0, \text{ m,} \tag{21}$$

W_c—width of the excavation in the breakout, W_c = 5 m (Figure 7);

H_c—height of the excavation in the breakout, H_c = 3.6 m (Figure 7);

k_0—coefficient of the influence of the angle of internal friction of rocks in the sidewall (compressive strength of coal = 15.45 MPa (Table 1), k_0 = 0.6055);

q_w—conditional pressure. Taking into account the effect of depth, coal compression strength and design width), q_w = 0.0311 MPa, was calculated according to Equation (22):

$$q_w = 0.001 \cdot (0.357 \cdot W_{ca} + 21.425) \cdot (0.0019 \cdot H + 0.4187) \cdot (1.145 - 0.0145 \cdot C_{sroof}), \text{ MPa,} \quad (22)$$

where

W_{ca}—computational width, m;

H—depth of roadway II, H = 800 m;

C_{sroof}—weighted average compressive strength of rocks in roof rocks (Table 1 and Figure 7), C_{sroof} = 32.7 MPa;

Q_d—dynamic unit load was determined on the basis of Figure 8, q_d = 0.015 (roadway II is located 50 m below the shock layer, and the expected shock energy is 1×10^5 J).
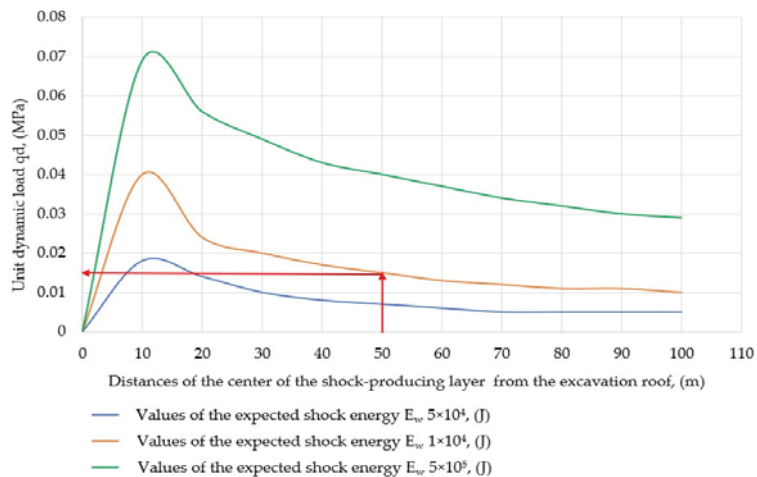
Figure 8. Dependence of the unit dynamic load q_d on the value of the expected shock energy E_w and the distance of the center of the shock-producing layer from the excavation roof.

After selecting all the coefficients, the support spacing was calculated according to Formula (15). The calculations were made for the part of the excavation without the fault (23) and with its impact (24).

$$d_{without\ fault} \leq \frac{W_{N_c}}{q_0} = \frac{0.0905}{0.098} = 0.92 \text{ m} \quad (23)$$

$$d_{with\ fault} \leq \frac{W_{N_c}}{q_0} = \frac{0.0905}{0.1156} = 0.78 \text{ m} \quad (24)$$

The calculations show that, for the part of the excavation without the fault, the support spacing should be less than 0.92 m. However, the impact contributes to the reduction in spacing to 0.78 m. Due to the geometry of the struts used to stabilize the support arches, it can be assumed that, in the fault zone, support spacing should be 0.75 m and 0.9 m outside of it.

4. Discussion

Driving preparatory workings is a fundamental goal for the exploitation of a deposit with a longwall panel. For this reason, the optimization and continuous improvement

of the efficiency of driving and securing workings in the vicinity of faults are important issues. A thorough analysis of the geological conditions, taking into account the experience gained during the previous works in similar conditions, is the basis for making a decision on the possibility and method of securing the excavation while passing through the fault. While driving the preparatory workings, headgate and tailgate, their performance may be suspended as a result of discontinuous deformations. A special case is the situation when the excavation of the excavation does not reveal any significant geological disturbances that could affect production capacities and, in the course of further progress, one encounters obstacles such as thickness reduction and faults that prevent effective driving. This is an obvious financial loss of underground mining plants related to the expenditure on the construction of such workings. Due to the fact that, in Poland, the basic type of support for preparatory excavations is the arch yielding support, and only in two underground coal mines ("Bogdanka" and Budryk") a separate rock bolt support was used in the research roadway, the article attempts to present the advantages of an independent bolt support, which can be an alternative to currently used security methods. Taking into account the rising prices of steel, limiting its consumption by introducing the bolt support can bring significant savings for the mining plant. Cost elements are closely related to labor, materials, equipment and transportation. One solution contributing to the reduction in overall costs may be to replace the arch yielding support with rock bolts, of course if the geological conditions allow the use of this type of support. In accordance with Polish mining regulations [35], the use of a separate rock bolt support in coal mining plants is allowed for preparatory and room workings with a cross-sectional area not exceeding 30 m^2 and a working width not exceeding 7 m. In addition, the roof rocks have an average-weighted uniaxial compressive strength, tested for a rock packet with a thickness of 3 m, that is not less than 15 MPa for layers with a plate structure and rock quality designation not less than 20% or 10 MPa for layers with a massive structure, and quality designation of not less than 40%. In addition, the rock mass is dry or non-sagging, and the water permeability coefficient is not less than 0.8. Currently, the rock bolt support is embedded in the carbon rock mass only by means of the resin cartridges and a cement binder. Expansion or friction bolts are not used. A threaded rod with a length of up to 2.7 m is made of a steel ribbed bar, while longer bolts are made as a cables or strings up to 15 m long. The calculation of the economic effects due to the use of a stand-alone rock bolt support consists in comparing the costs incurred for making the excavation in the bolted support with the costs incurred for making the same excavation in the arch yielding support (Table 4).

Table 4. Cost structure for arch yielding and rock bolt supports.

Cost	Arch Yielding Support with a Cross-Section of 13 m^2	Rock Bolt Support in Length 2.5 m
Labour, %	19.51	37.78
Material, %	71.81	51.11
Equipment, %	3.25	6.67
Transport, %	5.42	4.44
Total cost of 1 m, PLN	3690	2250

The largest issue, accounting for more than half of the total cost of a stand-alone rock bolt support, is the materials. The costs of material, equipment and transport per meter of the excavation are relatively constant over a certain period of time, while the labor costs change with the increase in productivity, which in turn is conditioned by the increase in experience acquired by the mining crew and the use of highly efficient and failure-free equipment. Due to the compressive strength of coal, which in the area of the designed excavation is only 0.45 MPa higher (Table 1) above the minimum value, a decision was made not to use a separate bolt support. In order to determine the impact of the fault on the

change in the total displacement around the roadway, a spatial numerical model was built in the RS3 software [40] based on the finite element method. The main goal of numerical simulations was to determine the difference in changing the total displacement distribution for an excavation without support and that is secured by means of steel arch yielding without and with steel segments. The rock mass model was cubic with a side length of 60 m (Figure 9a–c). In the coal layer, an excavation 5 m wide and 3.6 high was designed.

(**a**)

(**b**)

Figure 9. *Cont.*

(c)
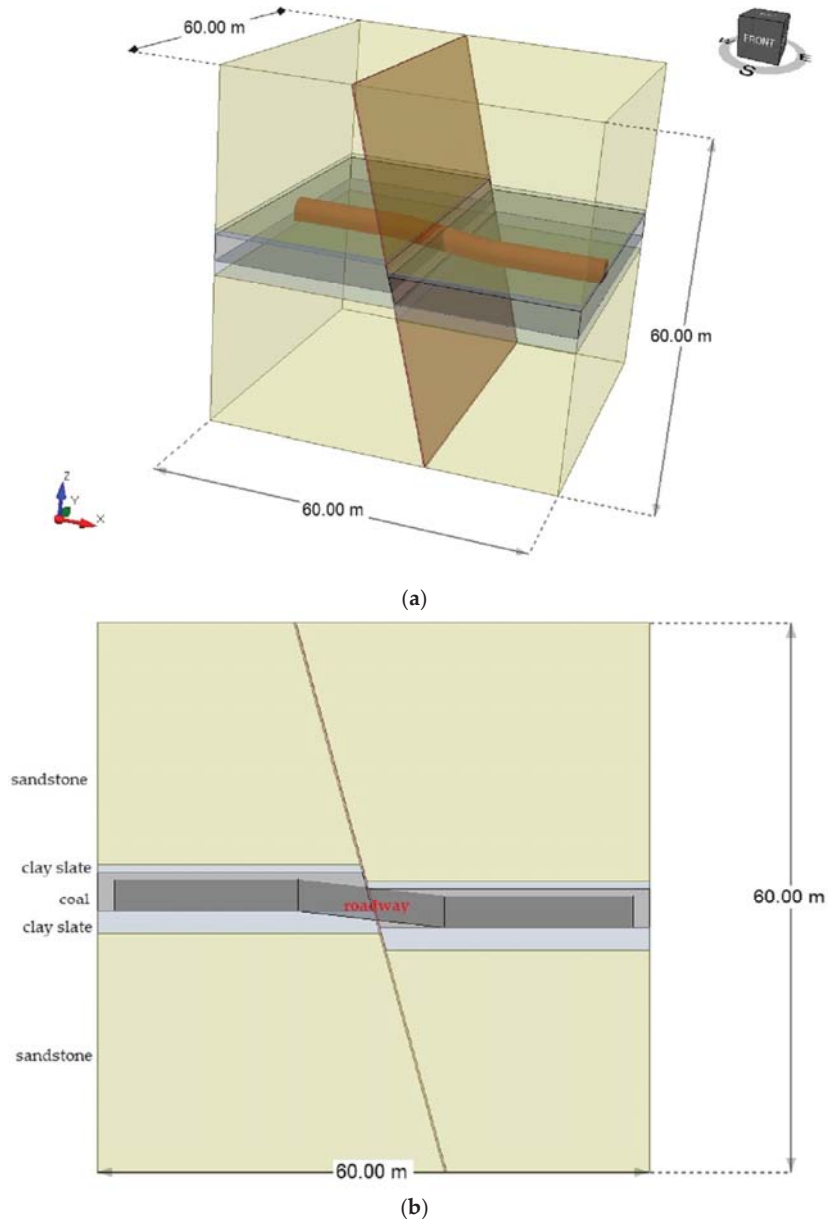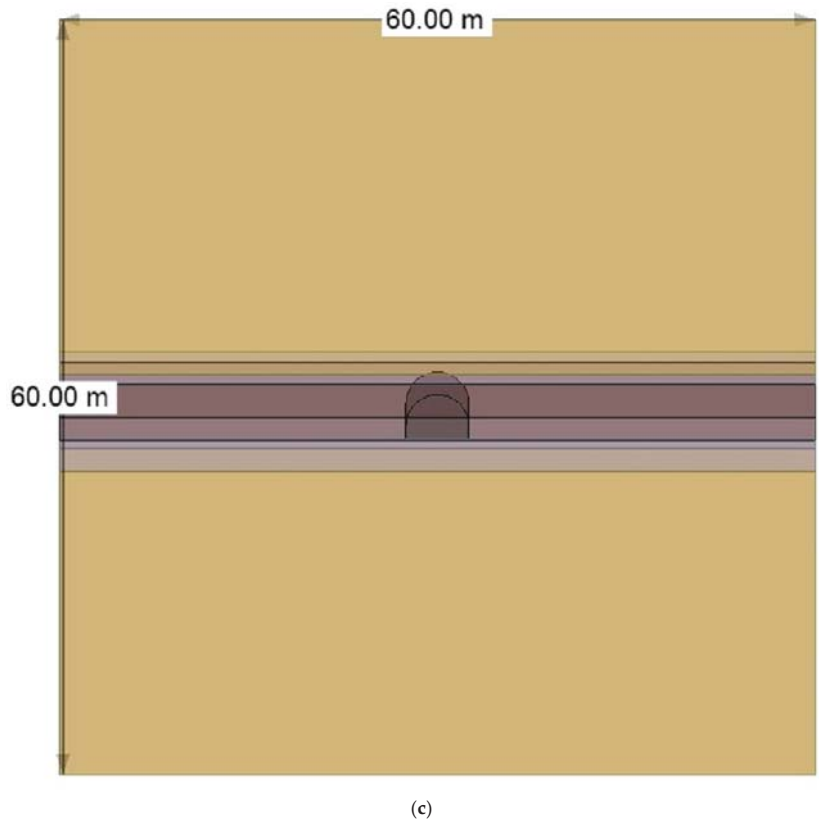
Figure 9. Rock mass model: (**a**) spatial view; (**b**) side view; (**c**) front view.

The horizontal extent of the zone of increased impact of the rock mass on the support due to the fault on both sides of the fault plane was determined according to Equation (25) [38]:

$$L_u = \frac{2.5 \cdot \sqrt{h_u}}{\sin \delta} \qquad (25)$$

where

L_u—fault action zone (m);
h_u—the height of the fault throw (m);
δ—the angle of the fault plane (°).

For a fault with the throw size h = 1.8 m and the inclination angle of the fault plane $\delta = 75°$, $L_u = 3.47$ m. Moreover, when the fault crosses the excavation (Figure 4), the fault zone of the fault L_u should be double. Therefore, in the numerical model, both in front of and behind the fault, the compaction zone of the arch yielding support was at least 7 m. Out of several dozen possibilities of failure criteria offered by the RS3 numerical program, the Generalized Hoek–Brown criterion was selected, which belongs to the elastic/plastic group. The material constants were adopted from RocData software [41]. The strength, deformation and structural parameters for the individual layers and for the fault are presented in Table 5. In the model, it was assumed that the width of the fault gap was 0.2 m and that it was filled with crushed rocks. The arch yielding support and steel straight segments were modeled as beam elements, for which the minimum tensile strength for the S480W steel grade is 480 MPa. The support spacing in the fault zone and outside

this zone was 0.75 m and 0.9 m, respectively. The results of the calculations are shown in Figure 10a–c.

Table 5. Geomechanical parameters adopted in the numerical models.

Type of Rock	Unit Weight (MN/m³)	Compressive Strength (MPa)	Young's Modulus (MPa)	Poisson Ratio	Geological Strength Index	m_b	s	a
Coal	0.0127	15.45	2300	0.3	65	0.756	0.009	0.502
Claystone	0.0239	16.5	10,300	0.23	70	1.678	0.018	0.501
Sandstone	0.0251	47	5400	0.25	75	5.169	0.036	0.501
Fault	0.0127	12.36	2000	0.3	50	0.185	0.001	0.506

The maximum value of total displacement around the roadway without support was 0.02 m. This value occurs in the roof of the hanging part in the immediate vicinity of the fault. Securing the excavation with the arch yielding support at a spacing of 0.9 m and 0.75 m in the fault impact zone reduces the value of total displacements by 10%. On the other hand, the additional reinforcement of the support with steel segments causes the value of total displacements to drop to 0.016 m, which is 80% of the value for the excavation without the support.

(**a**)

Figure 10. *Cont.*

(**b**)

(**c**)
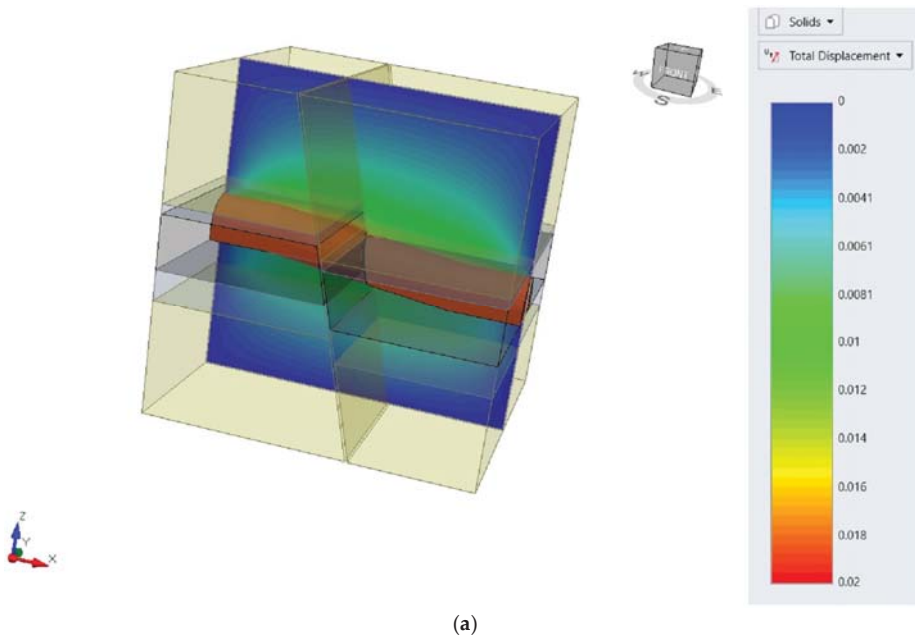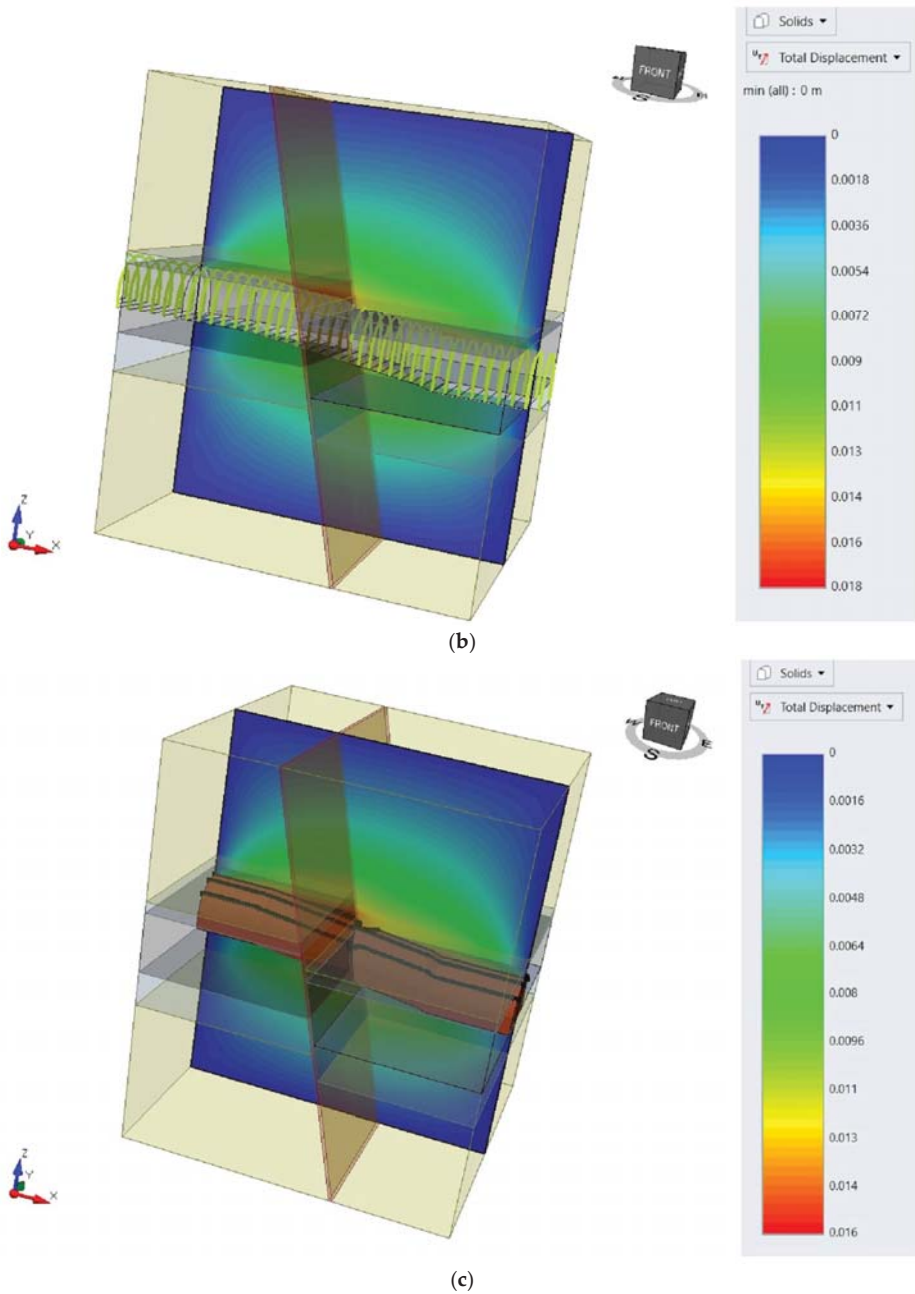
Figure 10. Total displacement distribution around the roadway: (**a**) without support; (**b**) with the arch yielding support; (**c**) with arch yielding and steel straight segments support.

5. Conclusions

In order to ensure the stability of the preparatory excavation, all possible negative factors affecting the mining and geological conditions of the excavation area should be

taken into account. As a result of the application of the minimum contours method, the ventilation criterion and geomechanical calculations, the ŁP8/V29 arch yielding supports with a spacing of 0.9 m were selected. If the excavation passes through a fault, the spacing was reduced to 0.75 m. The fault zone, both in front of and behind the fault, was calculated at 7 m. Based on numerical calculations, the following was found:

1. The projected total displacement around the roadway without support, which crosses the fault, was 0.02 m, while the use of the arch yielding support at a distance of 0.9 m outside the fault and 0.75 m in the fault zone reduces the total displacement value by 10%;
2. Additional reinforcement of the support in the form of steel straight segments contributes to a reduction in the value of total displacement by 11% and 20% compared to the excavation with and without the support.

The selection of driving roadways and mining supports in the fault conditions is associated with the necessity to use additional reinforcement and increasingly durable mining supports. In the case of support arches made of flexible arches, increasingly larger sizes of sections are used, which can be additionally made of steel with increased strength parameters. Due to the implementation of more and more modern mechanization of both transport and driving processes, the support of preparatory workings has increasingly larger cross-sectional dimensions. It is connected with the necessity to provide more and more working space for machines and devices, as well as for miners. Correctly selected support for preparatory workings is one of the most important issues when performing works in accordance with mining technology, because it plays a key role in ensuring the safety of the crew and continuity of production. The difficulty of designing the support increases with the deteriorating mining and geological conditions, such as the state of increased stress or discontinuous deformation of the rock mass. Although the method of securing workings in hard coal mines has not changed for several years, because preparatory workings mainly use the arch yielding support, all time activities are based on research and previous experience aimed at the most optimal selection of the support along with its strengthening in the given conditions of the rock mass. Strengthening the support of roadways in hard coal mines is a commonly used practice. The need to increase the load-bearing capacity of the used support occurs both at the stage of driving the excavation in the event of worse geological conditions, e.g., a fault, and during the operation of the excavation associated with an additional dynamic load. The experience and practice in the use of the support so far shows that, in most cases, the possible variants of increasing the load-bearing capacity of the support are not planned in advance, but their ad hoc methods are used, which have worked well in the given conditions earlier not necessarily taking into account the fact of whether the selected reinforcement variant for a given case is an optimal variant. However, the continuous possibility of modifying the load-bearing capacity of the casing is its undoubted advantage and the fact that it permits the obtainment of the expected effect, which is the smallest possible deformation of the support, allowing for the safety and full functionality of the excavation in accordance with the assumptions.

Institutional Review Board Statement: Not applicable.

Informed Consent Statement: Not applicable.

Data Availability Statement: The data presented in this study are new and have not been previously published.

Conflicts of Interest: The authors declare no conflict of interest.

References

1. Cheng, G.; Li, L.; Zhu, W.; Yang, T.; Tang, C.; Zheng, Y.; Wang, Y. Microseismic investigation of mining-induced brittle fault activation in a Chinese coal mine. *Int. J. Rock Mech. Min. Sci.* **2019**, *123*, 104096. [CrossRef]
2. Burtan, Z.; Zorychta, A.; Cieślik, J.; Chlebowski, D. Influence of mining operating conditions on fault behavior. *Arch. Min. Sci.* **2014**, *59*, 691–704. Available online: https://journals.pan.pl/Content/93633/PDF/10267-Volume59_Issue3-08_paper.pdf?handler=pdf (accessed on 20 November 2014). [CrossRef]
3. Li, Q.; Li, J.; Zhang, J.; Wang, C.; Fang, K.; Liu, L.; Wang, W. Numerical Simulation Analysis of New Steel Sets Used for Roadway Support in Coal Mines. *Metals* **2019**, *9*, 606. [CrossRef]
4. Xie, Z.; Zhang, N.; Wei, Q.; Wang, J.; Sharifzadeh, M. Study on Mechanical Properties and Application of a New Flexible Bolt. *Appl. Sci.* **2021**, *11*, 924. [CrossRef]
5. Wang, P.; Zhang, N.; Kan, J.; Wang, B.; Xu, X. Stabilization of Rock Roadway under Obliquely Straddle Working Face. *Energies* **2021**, *14*, 5759. [CrossRef]
6. Wang, J.; Apel, D.B.; Xu, H.; Wei, C.; Skrzypkowski, K. Evaluation of the Effects of Yielding Rockbolts on Controlling Self-Initiated Strainbursts: A Numerical Study. *Energies* **2022**, *15*, 2574. [CrossRef]
7. Šňupárek, R.; Konečný, P. Stability of roadways in coalmines alias rock mechanics in practice. *J. Rock Mech. Geotech. Eng.* **2010**, *2*, 281–288. [CrossRef]
8. Shan, R.; Li, Z.; Wang, C.; Wei, Y.; Bai, Y.; Zhao, Y.; Tong, X. Research on the mechanism of asymmetric deformation and stability control of near-fault roadway under the influence of mining. *Eng. Fail. Anal.* **2021**, *127*, 105492. [CrossRef]
9. Mei, Y.; Li, W.; Yang, N.; Wang, G.; Li, T.; Sun, T. Failure Mechanism and Optimization of Arch-Bolt Composite Support for Underground Mining Tunnel. *Adv. Civ. Eng.* **2020**, *2020*, 5809385. [CrossRef]
10. Kang, H.; Jiang, P.; Wu, Y.; Gao, F. A combined "ground support-rock modification-destressing" strategy for 1000-m deep roadways in extreme squeezing ground condition. *Int. J. Rock Mech. Min. Sci.* **2021**, *142*, 104746. [CrossRef]
11. Liu, H.; Jiang, Z.; Chen, W.; Chen, F.; Ma, F.; Li, D.; Liu, Z.; Gao, H. A Simulation Experimental Study on the Advance Support Mechanism of a Roadway Used with the Longwall Coal Mining Method. *Energies* **2022**, *15*, 1366. [CrossRef]
12. Horst, R.; Modrzik, M.; Ficek, P.; Rotkegel, M.; Pytlik, A. Corroded steel support friction joint load capacity studies as found in Piast-Ziemowit coal mine. *Min. Inform. Autom. Electr. Eng.* **2018**, *1*, 81–94. [CrossRef]
13. Zhou, Q.; Herrera-Herbert, J.; Hidalgo, A. Predicting the Risk of Fault-Induced Water Inrush Using the Adaptive Neuro-Fuzzy Inference System. *Minerals* **2017**, *7*, 55. [CrossRef]
14. Cao, Z.; Gu, Q.; Huang, Z.; Fu, J. Risk assessment of fault water inrush during deep mining. *Int. J. Min. Sci. Technol.* **2022**, *32*, 423–434. [CrossRef]
15. Chen, J.; Dai, X.; Zhang, J. Analytical Study of the Confining Medium Diameter Impact on Load-Carrying Capacity of Rock Bolts. *Math. Probl. Eng.* **2021**, *2021*, 6680886. [CrossRef]
16. Qian, D.; Zhang, N.; Pan, D.; Xie, Z.; Shimada, H.; Wang, Y.; Zhang, C.; Zhang, N. Stability of Deep Underground Openings through Large Fault Zones in Argillaceous Rock. *Sustainability* **2017**, *9*, 2153. [CrossRef]
17. Kalmet. Available online: https://www.kalmet.com.pl/pl/oferta/elementy_obudow_gorniczych.html (accessed on 19 February 2022).
18. Pytlik, A. Experimental studies of static and dynamic steel arch support load capacity and sliding joint temperature parameters during yielding. *Arch. Min. Sci.* **2020**, *65*, 469–491. [CrossRef]
19. Grodzicki, M.; Rotkegel, M. The concept of modification and analysis of the strength of steel roadway supports for coal mines in the Soma Basin in Turkey. *Studia Geotech. Mech.* **2018**, *40*, 38–45. [CrossRef]
20. Hutalab. Available online: http://www.hutalab.com.pl (accessed on 22 February 2022).
21. Rotkegel, M. ŁPw Steel Arch Support–Designing and Test Results. *J. Sustain. Min.* **2013**, *12*, 34–40. [CrossRef]
22. Li, W.; Liu, J.; Chen, L.; Zhong, Z.; Liu, Y. Roadway Support in Deep "Three-Soft" Coal Seam: A Case Study in Yili Mining Area, China. *Shock Vib.* **2021**, *2021*, 8851057. [CrossRef]
23. Yang, R.; Li, Q.; Li, Q.; Zhu, X. Assessment of Bearing Capacity and Stiffness in New Steel Sets Used for Roadway Support in Coal Mines. *Energies* **2017**, *10*, 1581. [CrossRef]
24. Lv, Z.; Qin, Q.; Jiang, B.; Luan, Y.; Yu, H. Comparative study on the mechanical mechanism of confined concrete supporting arches in underground engineering. *PLoS ONE* **2018**, *13*, e0191935. [CrossRef] [PubMed]
25. Wu, H.; Jia, Q.; Wang, W.; Zhang, N.; Zhao, Y. Experimental Test on Nonuniform Deformation in the Tilted Strata of a Deep Coal Mine. *Sustainability* **2021**, *13*, 13280. [CrossRef]
26. Wang, H.; Jiang, Y.; Xue, S.; Mao, L.; Lin, Z.; Deng, D.; Zhang, D. Influence of fault slip on mining-induced pressure and optimization of roadway support design in fault-influenced zone. *J. Rock Mech. Geotech. Eng.* **2016**, *8*, 660–671. [CrossRef]
27. Wang, H.; Shi, R.; Lu, C.; Jiang, Y.; Deng, D.; Zhang, D. Investigation of sudden faults instability induced by coal mining. *Saf. Sci.* **2019**, *115*, 256–264. [CrossRef]

28. Lu, Y.; Wei, W.; Zhiyu, T. Study on Mechanical Mechanism and Stability of Surrounding Rock in Fault Structure Roadway. *ResearchSquare* **2021**, *2*, 1–22. [CrossRef]
29. Adoko, A.C.; Yakubov, K.; Kaunda, R. Reliability Analysis of Rock Supports in Underground Mine Drifts: A Case Study. *Geotech. Geol. Eng.* **2021**, *11*, 2101–2116. [CrossRef]
30. Xiong, Y.; Kong, D.; Cheng, Z.; Wen, Z.; Ma, Z.; Wu, G.; Liu, Y. Instability Control of Roadway Surrounding Rock in Close-Distance Coal Seam Groups under Repeated Mining. *Energies* **2021**, *14*, 5193. [CrossRef]
31. Regulation of the Minister of the Environment of January 29, 2013 on Natural Hazards in Mining Plants. Natural Hazards in Mining Plants. Available online: https://www.prawo.pl/akty/dz-u-2021-1617-t-j,17955795.html (accessed on 10 February 2022). (In Polish).
32. Polish Standard: PN-93/G-04558. Hard Coal. Determination of Spontaneous Ignition Indexes. Polish Committee for Standardization: Warszawa, Poland, 1993. (In Polish)
33. Polish Standard: PN-G/06009. Horizontal and Inclined Underground Roadways in Mine Enterprises–Movement Clearances and Dimensions of Man Passages. Polish Committee for Standardization: Warszawa, Poland, 1997. (In Polish)
34. Polish Standard: PN-93/G-15000/02. Roadway Support with Susceptible Timber Frames Made of Special Sections. Arch Susceptible Frames ŁP of Sections Type V, Series A. Dimensions. Polish Committee for Standardization: Warszawa, Poland, 1993. (In Polish)
35. Tchórzewski, K. Regulation of the Minister of Energy on detailed requirements for the operation of underground mining plants of 23 November 2016. *J. Laws* **2017**, *1118*, 18. (In Polish)
36. Wacławik, J. *Mine Ventilation*; AGH Publishing House: Kraków, Poland, 2010; Volume I, p. 391. (In Polish)
37. CST. Available online: https://cst-germany.com/pl/product/axial-flow-fan-type-es9-500-80-pu-stage-id184 (accessed on 24 February 2022).
38. Rułka, K.; Mateja, J.; Kowalski, E.; Skrzyński, K.; Stałęga, S.; Wojtusiak, A.; Schinohl, J. *Simplified Rules for the Selection of Frame Support for Roadway Workings in Hard Coal Mining Plants*; Central Mining Institute Publishing House: Katowice, Poland, 2001; pp. 1–30. (In Polish)
39. Polish Standard: PN-H-93441-1:2013-12. Hot Rolled Steel Sections for Mining-Part 1: General Requirements and Research. Polish Committee for Standardization: Warszawa, Poland, 2013. (In Polish)
40. RocScience. Available online: https://www.rocscience.com/software/rs3 (accessed on 10 March 2022).
41. RocData. Available online: https://www.rocscience.com/support/rocdata/release-notes (accessed on 12 March 2022).

Article

Evaluation of the Effects of Yielding Rockbolts on Controlling Self-Initiated Strainbursts: A Numerical Study

Jun Wang [1], Derek B. Apel [1,*], Huawei Xu [1], Chong Wei [1] and Krzysztof Skrzypkowski [2,*]

[1] School of Mining and Petroleum Engineering, University of Alberta, Edmonton, AB T6G 2R3, Canada; jun8@ualberta.ca (J.W.); hx1@ualberta.ca (H.X.); cwei4@ualberta.ca (C.W.)

[2] Faculty of Civil Engineering and Resource Management, AGH University of Science and Technology, 30-059 Kraków, Poland

[*] Correspondence: dapel@ualberta.ca (D.B.A.); skrzypko@agh.edu.pl (K.S.)

Abstract: In this paper, a 2D distinct element method (DEM) model of a deep tunnel in an underground coal mine is built to thoroughly evaluate the effects of yielding (D-bolt and Roofex) and the traditional rockbolt (fully resin-grouted rebar) on controlling self-initiated strainbursts. The occurrence of self-initiated strainbursts is judged based on the stiffness difference between the loading system and rock masses for the first time. The results suggest that the total deformations of the tunnel supported with Roofex and resin-grouted rebar are 1.53 and 2.09 times that of D-bolts (1411 mm). The average velocities of detached rock blocks in the tunnel supported with Roofex and resin-grouted rebar are 3.22 and 3.97 m/s, respectively, which are much higher than that of D-bolts (0.34 m/s). 13 resin-grouted rebar bolts are broken during the strainburst, while D-bolts and Roofex survive. Compared with Roofex (295.16 kJ) and resin-grouted rebar (125.19 kJ), the D-bolt can reduce the most kinetic energy (469.30 kJ). D-bolt and resin-grouted rebar can maintain high axial force levels (214.87 and 151.05 kN) during strainbursts. Both Roofex and resin-grouted rebar fail to control strainbursts. The bolt number significantly influences the control effects of yielding rockbolts on strainbursts. 9 and 12 D-bolts cannot control the strainburst, while 15 and 18 D-bolts can make the tunnel stable. In addition, the detachment and ejection of rocks between rockbolts can be well restrained using surface retain elements, e.g., steel arch. This study highlights the usage of numerical modeling methods in assessing the performance of yielding rockbolts, which can be served as a promising tool to improve and optimize the design of rock supporting in burst-prone grounds.

Keywords: strainburst; local mine stiffness; yielding rockbolt; numerical modeling; distinct element method; underground mining

1. Introduction

Strainburst is an unstable rock failure phenomenon at excavation boundaries of deep tunnels in mining and civil engineering projects. It is characterized by the sudden and violent ejection of rock materials. Strainburst is the most common type of rockbursts in all underground excavations [1]. It can damage equipment and facilities, which will further delay production and cause tremendous economic loss [2]. Worse still, strainburst can also result in many injuries and fatalities [3]. Hence, much work needs to be conducted to control and mitigate strainburst damage.

Generally, strainburst can be classified into two types: self-initiated and remotely triggered [4]. The self-initiated strainburst occurs due to the concentration of excavation-induced tangential stress and the existence of a relatively "soft" loading environment in the rock mass surrounding the fracturing rock [5]. There is not a remote seismic event involved in self-initiated strainbursts. The remotely triggered strainburst is caused by the combination of a remote seismic event triggered by large-scale mining activities and high static stress [6,7]. Self-initiated strainburst is a more frequently encountered type

of strainbursts, because it happens in both mining and civil engineering projects while remotely triggered strainburst usually occurs only in mining environments [7]. This study specifically focuses on the investigation of the control of self-initiated strainbursts.

To date, many measures and strategies have been proposed to control and mitigate strainburst damage. For instance, distress drilling and blasting are two standard measures to reduce strainburst risks by transferring concentrated stresses to rock masses in-depth. Another common tactic is using yielding rockbolts. This type of rockbolts allows yielding to absorb more kinetic energy and have higher displacement capacities than conventional rockbolts (e.g., expansion-shell bolt and rebar bolt). Hence, yielding rockbolts can resist the dynamic loads and accommodate large deformation caused by rock fracturing, dilation, and ejection during strainbursts [7]. In the last several decades, many different types of yielding rockbolts have been developed to control rockbursts, e.g., Cone bolt [8], Roofex [9,10], Garford bolt [11], D-Bolt [12,13], Yield-Lok [14], and He-bolt [15].

A critical task is to evaluate the effects (e.g., control of rock damage and the capacity of energy-absorption) of yielding rockbolts on controlling strainbursts before being widely used. The methodologies to study rockbolt performance mainly include field tests [16–18], laboratory test, and numerical modeling. The field test method can obtain real-time data and assess the in situ performance of rockbolts, but they are usually time-consuming, expensive, and dangerous, especially in burst-prone grounds. Compared with field tests, the experimental methods have the advantages of repeatability, safety, and flexibility [19]. At present, the evaluation of the rockbolt performance in strainburst conditions is conducted mainly using the drop test [10–12,20–22]. The research has achieved many positive outcomes, providing excellent references for understanding the behavior of different types of yielding rockbolts under dynamic impacts. However, the drop test is straightforward and is only a crude simulation of rockburst loading. The complex interaction between seismic waves, rockbolts, and reinforced rock masses is not considered. For instance, Bosman et al. [23] stated that the dynamic capacity of a rockbolt is not a constant value, and the loading mode of a rockbolt will affect its dynamic capacity. Therefore, the impact loading from conventional drop tests might not represent rockburst loading. Wu et al. [18] also pointed out that the impact load in drop tests cannot represent the impact of ground pressure load, and the existing test system generally cannot reproduce the complex ground support/rock mass interaction that exists in an underground environment. Besides, original rock stress is not considered in tests.

With the rapid development of information technology (IT) and computer equipment, various numerical methods and codes have been developed and employed to simulate complex physical phenomena in rock mechanics and rock engineering [24–27]. The numerical simulation methods have been acknowledged as effective research and engineering design tools as it can represent the realistic mechanical behavior of rock masses and support elements with rational input data (e.g., excavation size and shape, material properties, and boundary conditions) and calibration procedures [28]. Nie et al. [29] developed rockbolt models using DDA to investigate the failure mechanism of an expansion-shell bolt, fully grouted rebar, split set, and D-bolt in simulated pull-out and drop tests. Marambio et al. [30] modeled a laboratory-scale test via FLAC3D to study the performance of threadbar in dynamic loading. The simulation results matched well with laboratory observations. Yokota et al. [31] assessed a self-developed deformation-controlled rockbolt (DC-bolt)'s behavior in tunnel supporting via DDA simulation. Zhang and Nordlund [19] employed the UDEC program to investigate the differences of dynamic performances of a fully grouted rebar between the simulated drop tests and seismic loading in the configuration where two slightly separated rock bars were used. Zhao et al. [32] studied the influence of structure element position on the anchoring effect of energy-absorption bolts via simulating pull-out tests in FLAC3D.

In summary, most current work focuses on evaluating the performance of traditional rockbolts under dynamic loading, while some researchers try to simulate the dynamic behavior of yielding rockbolts by reproducing drop tests. Few numerical studies have been

reported to assess the performance of yielding rockbolts during self-initiated strainbursts with actual seismic loading. As mentioned above, the impact loading in drop tests might not represent rockburst loading, and the rock stress is also absent. Hence, the complex interaction between seismic waves, rockbolts, and reinforced rock masses during self-initiated strainbursts with explicit rock detachment and ejection (requiring the distinct element method (DEM) or DEM-related hybrid methods) needs to be further numerically investigated.

This study aims to evaluate the effects of yielding rockbolts on controlling self-initiated strainbursts using DEM modeling. The rationality and capability of DEM software UDEC in modeling self-initiated strainbursts are first validated through comparison with laboratory tests. Then, two types of yielding rockbolts (Roofex and D-bolt) and the traditional rockbolt (fully resin-grouted rebar, for comparison) are modeled via the "rockbolt" element in UDEC after an exact calibration procedure. Instead of conventional drop tests, a 2D model of a deep tunnel in an underground coal mine is built to fully evaluate the performance (e.g., the dynamic capacity of energy absorption and control of rock damage) of yielding and traditional rockbolts during simulated strainbursts. The occurrence of self-initiated strainbursts is judged based on the stiffness difference between the loading system and rock masses for the first time.

2. Validation of UDEC in Modeling Self-Initiated Strainbursts

2.1. Brief Introduction of the True Triaxial Experiments of Self-Initiated Strainbursts

Considering that the self-initiated strainburst is a structural failure of rock masses near the excavation boundary, Su et al. [33,34] conducted a series of true triaxial tests of rock samples by reproducing strainbursts in a self-developed true triaxial testing facility (see Figure 1a,b). In tests, rock samples with the dimension of 100 mm (length) × 100 mm (width) × 200 mm (height) were used to simulate the burst volume of a representative rock element (RRE) (Figure 1c,d). The cracking and ejecting processes of rock samples during strainbursts were monitored by an acoustic emission (AE) system and two high-speed cameras. The tangential stress concentration and radial stress distribution of near-boundary rock masses were simulated by a loading path that keeps one face free and loads on the other faces (Figure 1c). The detailed test procedures are as follows: (1) maintain one face of the rock sample free (y-direction) and apply loads to the other five faces simultaneously to a pre-defined initial stress state; (2) maintain stresses in x and y directions, and increase the stress in z-direction until the strainburst occurs.
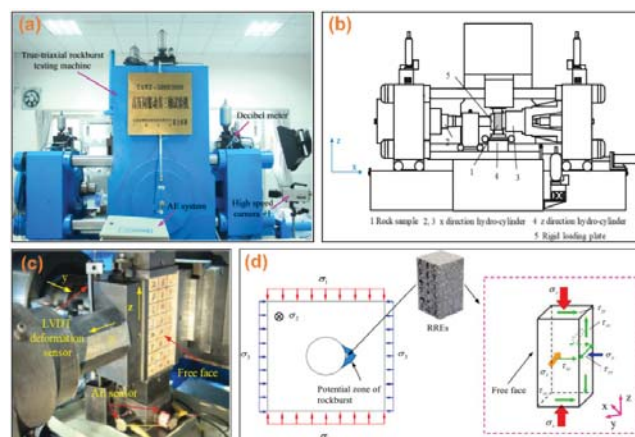
Figure 1. A true triaxial strainburst testing facility: (**a**,**b**) are the loading configuration; (**c**) is the stressed rock sample; (**d**) shows the boundary conditions and stress state of the rock sample ((**a**) is from Su et al. [34]; (**b**–**d**) are from Hu et al. [35]).

2.2. Validation of UDEC Simulation

In order to validate the reliability and accuracy of the 2D distinct element code UDEC in modeling self-initiated strainbursts, numerical simulation results were compared with the laboratory test results from Hu et al. [35]. The model configuration, including the model dimension, block shape and size, material properties, constitutive models, and loading mode, are the same as those used by Hu et al. [36,37]. The only difference is that the 3D distinct element code 3DEC rather than UDEC was employed in their studies.

A Trigon approach developed by Gao et al. [38] was used to generate blocks in the model (Figure 2a), as this approach is capable of reproducing the realistic fracturing processes (e.g., crack initiation, propagation, and coalescence) of rocks without adopting complicated constitutive models [39–41]. In the Trigon approach, a rock or rock mass is represented as an assembly of triangular blocks bonded together by contacts [38]. The fracturing process can be exhibited either by the sliding or opening of contacts. In the simulation, the blocks have an average edge length of 6 mm, which was sufficiently fine to simulate the failure behavior of rocks [36,37]. The material properties of blocks and contacts are listed in Table 1. In order to trigger a strainburst (unstable failure), the top platen has a lower stiffness (4 GN/m) than the post-peak characteristic stiffness of the rock sample (4.51 GN/m), which represents a soft loading system. Accordingly, Young's modulus and length of the top platen are 40 GPa and 100 mm, respectively. The stiffness of lateral and bottom platens are 1372 GN/m and 686 GN/m, respectively, representing much stiff loading systems, and thus the loading system stiffness (LSS) effect can be ignored [42].
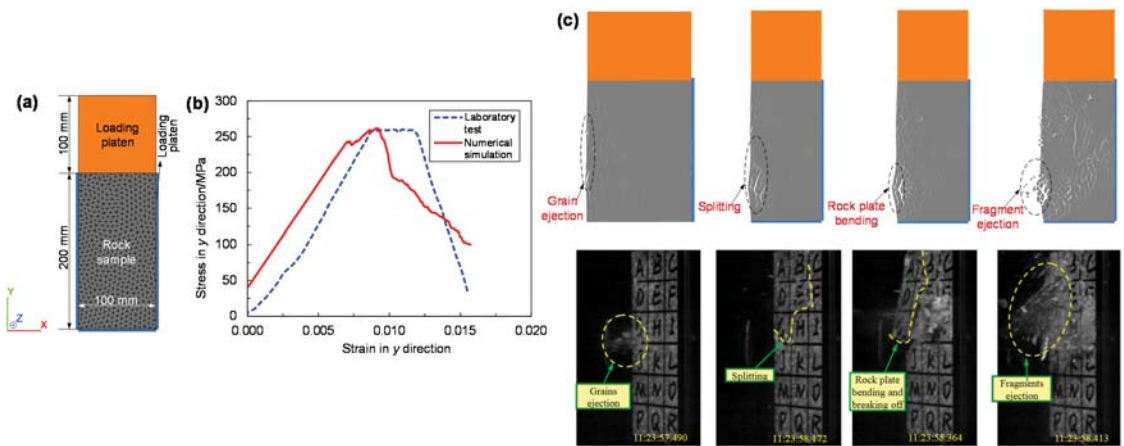
Figure 2. A numerical model for simulating self-initiated strainbursts and the comparison between the simulation and experimental results: (**a**) numerical model; (**b**) stress-strain curves obtained by the simulation and laboratory test [35]; (**c**) comparison between simulated failure stages and modes and experimental observations [35].

Table 1. Material properties used in the model [36,37].

Items	Block Properties			Contact Properties							
	ρ (kg/m³)	K (GPa)	G (GPa)	k_n (GPa/m)	k_s (GPa/m)	σ^t (MPa)	c_r^j (MPa)	φ^j (°)	φ_r^j (°)	σ_t^j (MPa)	σ_{tr}^j (MPa)
Granodiorite	2650	21.22	12.12	210,000	83,370	52	0	61.5	22	13	0
Top platen	7700	33.33	15.38				-				
Other platens	7700	171.67	79.23				-				
Interface between platens and rock sample		-		210,000	83,370	0	0	14.57	0	0	0

Note: ρ, K, and G are the bulk density, bulk modulus, and shear modulus of blocks. k_n and k_s are the normal and shear stiffness of contacts. c^j, φ^j, and σ_t^j are the cohesion force, internal friction angle, and tensile strength of contacts. c_r^j, φ_r^j, and σ_{tr}^j are the residual values of cohesion forces, internal friction angle, and tensile strength of contacts.

The simulation was implemented as following procedures: (1) A pre-defined initial stress state (σ_x = 5 MPa, σ_y = 45 MPa, and σ_z = 30 MPa) was applied to the model, and the "geostatic equilibrium" was achieved after sufficient calculation steps [36,37]. The model boundaries were initially fixed to simulate the in situ state. (2) One lateral platen and its boundary conditions in *x*-direction were removed, while other boundary conditions remained unchanged. A constant velocity of 0.1 m/s was applied to the surface of the top platen until the peak strength (*y*-direction) was reached. (3) The dynamic mode in UDEC was activated. The local damping ratio was set at 0.05 after a trial-and-error process. The boundary conditions (e.g., fixed boundary) used in the static stage can cause the reflection of outward propagating waves back into the model and do not allow the necessary energy radiation. Thus, the viscous boundary developed by Lysmer and Kuhlemeyer [43] was used in the dynamic calculation.

The comparison between the simulated results and laboratory test results is shown in Figure 2b,c. It can be seen that the stress-strain curve, failure stages, and failure modes including grain ejection, splitting and bending of rock plates, and fragment ejection during the strainburst test, can be realistically captured by numerical modeling. Hence, the capability and accuracy of UDEC in modeling the self-initiated strainburst are validated. In Hu et al. [36,37], they needed to compare simulation results with laboratory test results of cuboid rock samples and investigate the influence of intermediate stress on indoor strainburst failure. Thus, the 3D program 3DEC was used in their research. As mentioned above, strainbursts usually occur at the excavation boundary of a tunnel in a high geo-stress environment. Therefore, if there are no nearby excavations, the plane strain assumption of a 2D model would be rational. The accuracy of UDEC in modeling the self-initiated strainburst has also been verified with experimental results in this study. Besides, the employment of UDEC can significantly reduce the calculation cost compared with 3DEC. Figure 3 shows an example that the run time of 3DEC is around 90 times that of UDEC when dealing with the same problem, indicating that UDEC is more productive than 3DEC. Therefore, UDEC is adopted considering both reliability and efficiency.
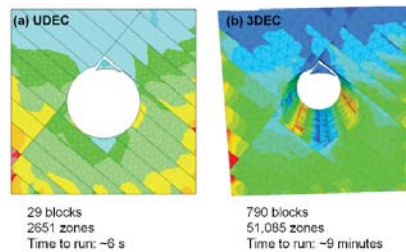
Figure 3. An example about the comparison of the run time between UDEC and 3DEC [44].

3. Numerical Modeling

3.1. Model Setup

3.1.1. Model Dimensions and Boundary Conditions

The simulation of the self-initiated strainburst at a laboratory scale is helpful to understand its detailed damage mechanisms (e.g., fracturing process and failure mode). However, the complex interaction between rockbolts and reinforced rock masses during strainbursts is hard to capture in this model setup due to the size limit, which prevents the model from being a potential design tool of rockbolting in burst-prone grounds. Therefore, to analyze the performance of rockbolts more realistically and accurately, the self-initiated strainburst occurring in a deep tunnel in an underground coal mine was modeled in this research rather than simulating it at a laboratory scale as previous studies. A widely used 2D DEM software UDEC was used to construct the numerical model. The model size is 30 m × 25 m. The shape of the tunnel cross-section is semicircular, with width and height

of 6 m and 4 m, respectively. Figure 4 shows the geometry of the numerical model, which is based on the lithology and designed size of a deep coal mine drift.
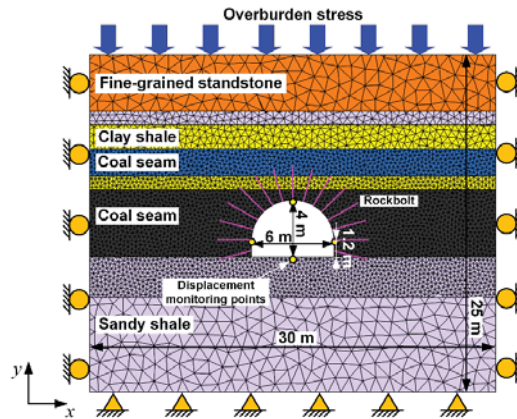
Figure 4. 2D numerical model of a deep tunnel in an underground coal mine.

The rock masses are divided into triangular blocks using the Trigon approach [38]. In the model, the average edge length of the blocks in two coal seams and nearby clay shale between them was set to 0.3 m. The block size with a range of 0.2–0.5 m was sufficiently acceptable to simulate the failure behavior of surrounding rock masses for a 2D model [38–40]. The average edge length of the blocks in the upper clay shale, sandy shale, and fine-grained sandstone was set to 0.5 m, 0.5 m, and 1 m, respectively. The average edge length of the blocks on the floor was set to 0.3 m and 1 m. A graded increasing edge length of blocks can avoid the resulting loss of simulation accuracy and enhance the calculation's reliability.

The upper boundary of the model was free and vertical stress of 24.3 MPa (assume the unit weight of overburden is 0.027 MN/m^3 and the buried depth is 900 m) was applied to the upper boundary to simulate the overburden weight. The roller constraints were applied on lateral boundaries, and the bottom boundary was fixed during the static stage (Figure 4). The ratio of horizontal to vertical stress (K) was assumed to be one since the hydrostatic stress state is a general in situ stress state in many deep excavations [45].

3.1.2. Modeling Large-Scale Strainbursts Based on the Stiffness Theory

The loading system stiffness (also called local mine stiffness at the engineering scale) and the post-failure stiffness of rock materials can distinguish stable or unstable failure (rockburst) effectively based on the stiffness theory [46]. If the loading system stiffness is smaller than the post-failure stiffness, the failure will be unstable and violent because the excess energy will transfer to the kinetic energy of ejected rocks. When the research object is a rock sample (e.g., [36,37]), it is simple to obtain the loading system stiffness K_L by the following equation:

$$K_L = \frac{AE}{L} \tag{1}$$

where A is the cross-section area of the loading platen; E is Young's modulus of the loading platen; L is the loading platen length.

However, unlike the unstable failure of rock samples, it is hard to identify the loading system when the focus is a strainburst that usually occurs in a tunnel or roadway. Thus, the determination of local mine stiffness becomes a more difficult task. Jaiswal and Shrivastva [47] proposed a method for calculating the local mine stiffness of a rock pillar by numerical modeling. The local mine stiffness is defined as a ratio of the load F_1 applied on the rock pillar over the distance difference ($d_1 - d_2$) with and without the modeling of the

rock pillar (Figure 5a). This study adopted this logic to calculate the local mine stiffness for a tunnel (see Figure 5b). In Stage 1, the internal pressure P_1 at the planned excavation boundary equals the in situ stress P_i. In Stage 2, P_1 is reduced to zero (P_2) after excavation. Similar to the calculation method of a rock pillar, the local mine stiffness for a tunnel can be determined as follows:

$$K_L = \frac{P_1}{(d_1 - d_2)} = \frac{P_i}{U} \qquad (2)$$

where d_1 and d_2 are the tunnel diameter before and after excavation; U is the convergence of tunnel walls after excavation. This method is the first attempt to calculate the local mine stiffness for a tunnel to the authors' knowledge. The excavation of the deep coal mine drift was simulated to obtain the local mine stiffness using the proposed method in this research. The obtained local mine stiffness is 174 MPa, where the tunnel convergence has been normalized by the tunnel diameter for convenient comparison with the post-peak characteristic stiffness of rock masses.
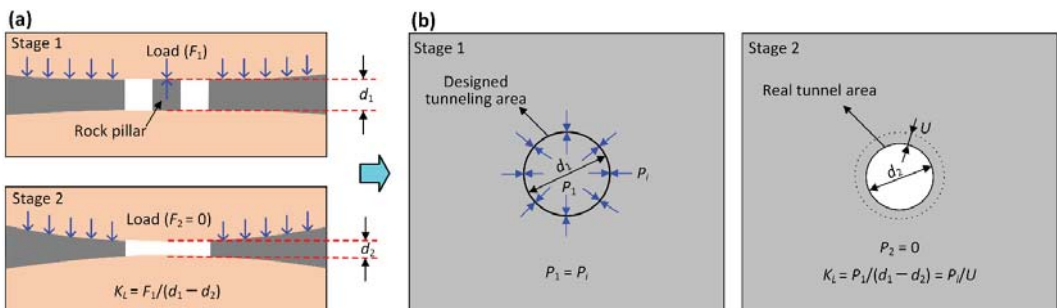
Figure 5. Determination of local mine stiffness by numerical modeling. (**a**) Local mine stiffness calculation for a rock pillar (after Jaiswal and Shrivastva [47]). (**b**) Proposed calculation method of local mine stiffness for a tunnel.

Since the main surrounding rock masses are coal seam and its strength is much lower than clay shale and sandy shale, only the post-peak characteristic stiffness of coal masses is determined using simulated uniaxial compression strength (UCS) tests. Considering that the rock mass property (e.g., strength and stiffness) is scale-dependent [48], the dimension of the rock mass model was determined based on the representative elementary volume (REV) concept [49]. The REV refers to the minimum scale of rock masses beyond which the material property becomes independent of the sample size (see Figure 6a). According to Bieniawski [50] (see Figure 6b), the UCS of coal masses declines gradually with increased sample side length. When the sample side length is less than 1.5 m, the UCS decreases remarkably with the growth of the specimen size. However, the UCS approaches a plateau when the sample side length exceeds 1.5 m, indicating that the scale dependency could be negligible. Thus, the REV size of the coal mass should be at least 1.5 m. In this study, the UCS model size is 4 m × 8 m, sufficient to eliminate the scale dependency. This model size is identical to Yang et al. [40].

Figure 7a shows the numerical model of UCS tests. In order to obtain the post-peak characteristic stiffness of the coal mass sample, the bulk and shear moduli of loading platens were set at an extremely high value (1000 GPa) to simulate an ideal rigid loading condition. As shown in Figure 7b, the obtained post-peak characteristic stiffness is 255 MPa, greater than the local mine stiffness (174 MPa). Hence, the self-initiated strainburst can happen. The material properties associated with coal masses are listed in Tables 2 and 3.
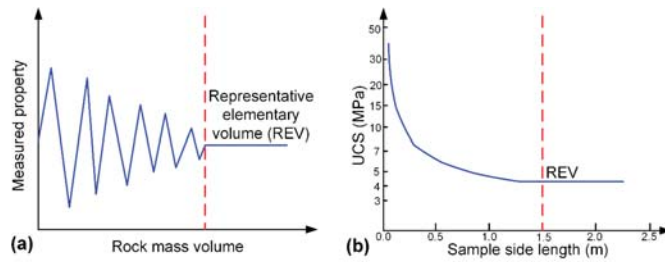
Figure 6. (**a**) Concept of the REV (after Bear, [49]). (**b**) The effect of sample size on the strength of coal (after Bieniawski, [50]).
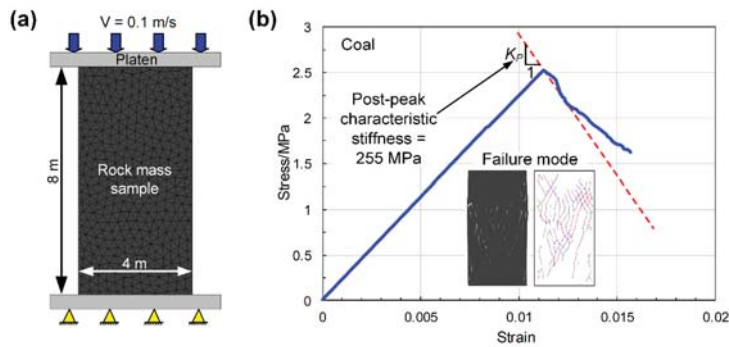
Figure 7. (**a**) UCS model. (**b**) Stress-strain curve of the coal mass sample under an ideal rigid loading condition.

3.1.3. Rock Mass Properties and Constitutive Model

The properties of rock masses (see Table 2) around the tunnel were obtained according to the laboratory tests of intact rock pieces (following ISRM recommended standards, [51]) and the generalized Hoek-Brown criterion [52] using the Geological Strength Index (*GSI*) system to evaluate rock mass qualities [53–55]. The UCS and deformation modulus of rock masses were estimated from the following equations [56,57]:

$$\sigma_{cm} = \sigma_{ci} \frac{(m_b + 4s - a(m_b - 8s))\left(\frac{m_b}{4+s}\right)^{as-1}}{2(1+a)(2+a)} \tag{3}$$

$$E_m = E_i \left(0.02 + \frac{1 - D/2}{1 + e^{((60+15D-GSI)/11)}} \right) \tag{4}$$

where D is a factor that depends upon the degree of disturbance to which the rock mass has been subjected by blast damage and stress relaxation. In this study, the value of D is assumed to be zero considering that the mechanical tunneling results in minimal disturbance to confined rock masses [56]. The calculated results of UCS and deformation modulus of rock masses are also summarized in Table 2.

The elastic constitutive model was chosen for blocks composed of finite-difference zones. The Coulomb slip model was used for contacts. The constitutive behavior of contacts is shown in Figure 8. A spring-rider simulates the behavior of contact, and the model deformation occurs when the contact stress is smaller than the contact strength, which is governed by the elastic modulus of blocks and contact stiffness; contact failure occurs when the stress exceeds its shear or tensile strength, and then blocks will slide or separate with each other [39].

Table 2. Physical and mechanical parameters of rock masses.

Lithology	Constant				Intact Rock				Rock Mass	
	m_i	m_b	s	a	ρ (kg/m³)	σ_{ci} (MPa)	E_i (GPa)	v	σ_{cm} (MPa)	E_m (GPa)
Coal	17	1.729	0.0008	0.5	1300	9.3	1.86	0.30	2.50	0.23
Clay shale	9	1.327	0.0022	0.5	2500	29.0	5.62	0.31	7.93	1.26
Fine-grained sandstone	17	2.851	0.0039	0.5	2580	90.0	9.52	0.26	24.53	2.92
Sandy shale	12	1.877	0.0031	0.5	2530	26.0	5.23	0.25	7.11	1.42

Note: m_i is a material constant for intact rocks. m_b, s, and a are constants for rock masses. ρ is the bulk density of intact rocks. σ_{ci} is the UCS of intact rocks. E_i is Young's modulus of intact rocks. v is the Poisson's ratio of intact rocks. σ_{cm} is the UCS of rock masses and E_m stands for the deformation modulus of rock masses.

Table 3. Calibrated micro parameters of rock masses in the model.

Lithology	Block Properties					Contact Properties				
	ρ (kg/m³)	K (GPa)	G (GPa)	k_n (GPa/m)	k_s (GPa/m)	c^j (MPa)	c_t^j (MPa)	φ^j (°)	σ_t^j (MPa)	σ_{tr}^j (MPa)
Coal	1300	0.16	0.09	18.7	7.5	0.99	0	33	0.25	0
Clay shale	2500	0.85	0.50	108.5	40.6	2.96	0	35	0.79	0
Fine-grained sandstone	2580	1.91	1.17	69.4	27.8	8.11	0	36	2.15	0
Sandy shale	2530	0.94	0.57	113.3	45.3	2.95	0	36	0.85	0
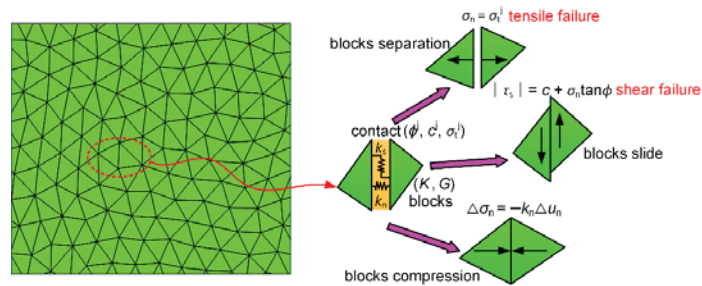
Figure 8. Constitutive behavior of contacts. (K and G are the bulk and shear moduli of blocks. c^j; Φ^j, and σ_t^j are the cohesion force, internal friction angle, and tensile strength of contacts. $\Delta\sigma_n$ and Δu_n are the effective normal stress increment and normal displacement increment. σ_n and τ_s are the normal and shear stresses of contacts).

In the Trigon approach, the deformation and failure of rock masses depend on the properties of blocks and contacts [38,39]. Thus, the micro parameters of blocks and contacts were calibrated against the rock mass properties (Table 2). Next, simulated UCS tests were conducted to calibrate the micro parameters [38]. To eliminate the effect of block size on simulation accuracy, the calibration model had a large scale (4 m × 8 m) [40] and identical block size with the tunnel model. A displacement loading mode was used in the simulation by applying a constant velocity of 0.1 m/s to the surface of the top platen, and the bottom platen was fixed. The loading rate of 0.1–0.15 m/s is slow enough to avoid the dynamic responses of models because UDEC automatically selects very small time steps (e.g., 10^{-7} s) in static analysis [37,58]. The initial micro parameters were first assumed based on the macro parameters of rock masses. Then, the modeling of UCS tests was conducted iteratively with the adjustment of micro parameters until the simulated results were consistent with the targeted material properties. The simulated failure modes and stress-strain curves of rock mass samples are shown in Figure 9. The main failure modes of rock mass samples are tensile (axial splitting) and tensile-shear failure, consistent with typical rock mass failure modes under no or low confining pressures [59]. The calibrated micro parameters of rock masses are listed in Table 3. The targeted and simulated deformation modulus and UCS errors are less than 3% (Table 4), suggesting that the targeted values agree well with calibrated rock mass parameters. Thus, the calibrated micro parameters in Table 3 could be used for further numerical analysis to evaluate the performance of yielding rockbolts during self-initiated strainbursts.

Table 4. Comparison between the targeted and simulated rock mass parameters.

Lithology	E_m (GPa)			UCS (MPa)		
	Target	Simulation	Error (%)	Target	Simulation	Error (%)
Coal	0.23	0.226	0.09	2.50	2.51	0.48
Clay shale	1.26	1.234	−1.82	7.93	7.91	−0.29
Fine-grained sandstone	2.92	2.852	−2.48	24.53	24.52	−0.05
Sandy shale	1.42	1.39	−2.11	7.11	7.02	−1.27
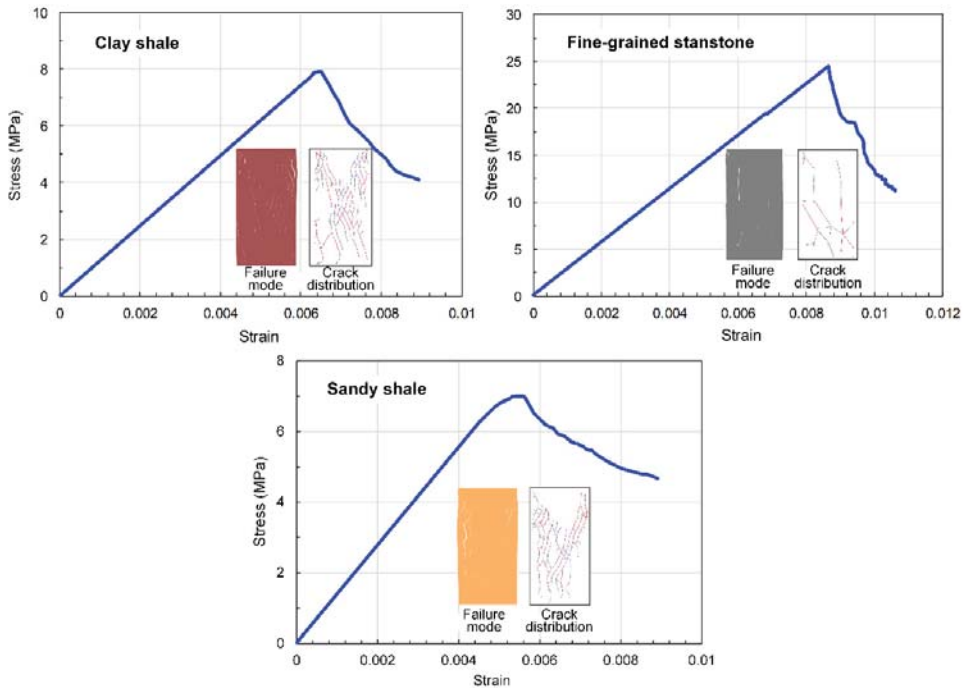
Figure 9. Simulated failure modes and stress-strain curves of rock mass samples.

3.2. Properties of Rockbolts

3.2.1. Introduction of the "Rockbolt" Element

In the past, the "cable" element in UDEC was more popular used than the "rockbolt" element to model a mechanically anchored or grouted cable or rockbolt, although both elements can simulate the shearing resistance along their length, which is provided by the shear bond between the grout and either the cable/rockbolt or the host rock [60]. This could be owing to more understandable input parameters and the more straightforward calibration process for using the "cable" element. Figure 10a shows the conceptual mechanical representation of the "rockbolt" element. It can be seen the "rockbolt" element is composed of several segments and nodal points located at segment ends. It has both shear and normal coupling springs, which are connectors that transfer forces and motion between the "rockbolt" element and the grid points associated with the block zone, while the "cable" element only has sliders (similar to shear coupling spring). Therefore, the "cable" element provides little resistance to bending, and thus it is more suitable for modeling cable bolts. In contrast, the "rockbolt" element can provide sufficient resistance for shearing and bending, appropriate for simulating rockbolts such as rebar bolts [61]. The other strength of the "rockbolt" element is that it can explicitly model the rockbolt breakage according to a user-defined tensile failure strain limit ε_{pl} [62]:

$$\varepsilon_{pl} = \sum \varepsilon_{pl}^{ax} + \sum \frac{d}{2} \frac{\theta_{pl}}{L} \qquad (5)$$

where ε_{pl}^{ax} is the axial plastic strain of rockbolt segment elements; d is the rockbolt diameter; L is the rockbolt segment length; θ is the average angular rotation over the rockbolt. The tensile failure strain limit provides a more accurate and realistic approach to reproduce rockbolt performances. Thus, the "rockbolt" element was used in this study to simulate the mechanical behavior of both yielding and conventional rockbolts.
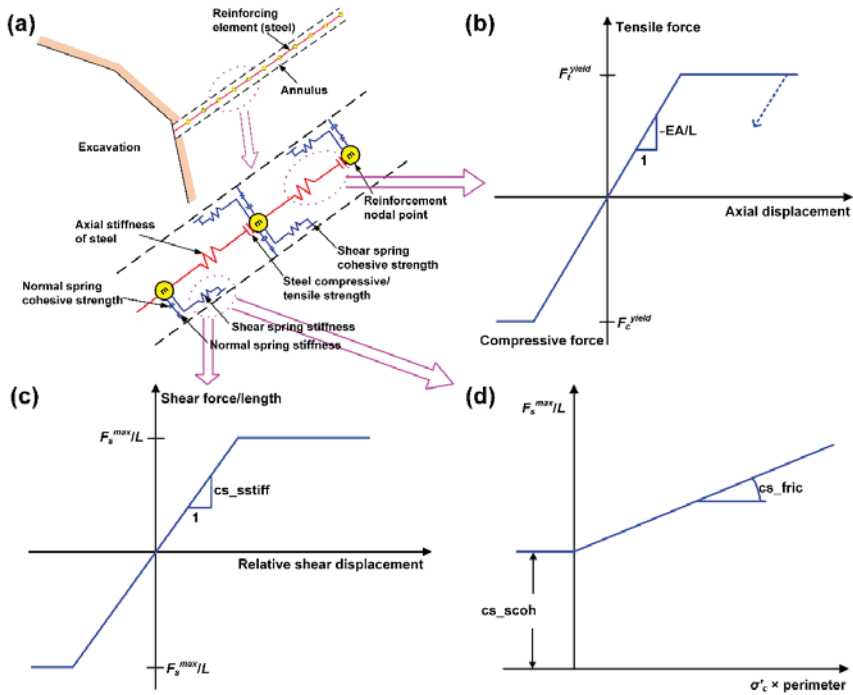
Figure 10. (**a**) Conceptual mechanical representation of the "rockbolt" element, which accounts for shear behavior of grout annulus and bending resistance of the reinforcement. (**b**) Mechanical behavior of the "rockbolt" element in the axial direction. (**c**) Shear force versus displacement of the shear coupling spring. (**d**) Shear criterion of the shear coupling spring ((**a**) is modified after Itasca [62]; (**b–d**) are from Itasca [62]).

The "rockbolt" element has a linearly elastic material behavior that it can yield in both tension and compression in the axial direction (Figure 10b). Therefore, the incremental axial force in a "rockbolt" element, ΔF_t, can be obtained by the calculation of the incremental axial displacement:

$$\Delta F_t = -\frac{EA}{L}\Delta u^t \tag{6}$$

where $\Delta u^t = \Delta u_i t_i = \Delta u_1 t_1 + \Delta u_2 t_2 = (u_1^{[b]} - u_1^{[a]})t_1 + (u_2^{[b]} - u_2^{[a]})t_2$; $u_1^{[b]}$, $u_1^{[a]}$, etc. are the displacements at the bolt nodes associated with each "rockbolt" element. Subscript 1 and 2 represent the x-direction and y-direction, respectively; the superscripts [a], [b] stand for bolt nodes. The direction cosines t_1, t_2 refer to the tangential (axial) direction of the "rockbolt" element.

The applied load is axial in an ideal pull-out test as simulated in this study. Thus, the parameters regarding resistance to bending (normal spring) are not discussed. The shear behavior of the "rockbolt" element were briefly introduced in this study. The shear behavior of the rockbolt/gridpoint interface is represented as a spring-slider system at the rockbolt nodal points. This behavior during relative displacement can be described numerically by the coupling spring shear stiffness (cs_{sstiff} in Figure 10c):

$$\frac{F_s}{L} = cs_{sstiff}\left(u_p - u_m\right) \tag{7}$$

where F_s represents the shear force that develops in the shear coupling spring (e.g., along with the interface between the rockbolt element and the gridpoint); cs_{sstiff} is the coupling

spring shear stiffness (coupling-stiffness-shear); u_p is the axial displacement of the rockbolt; u_m is the axial displacement of the medium (soil or rock); and L is the contributing element length.

The maximum shear force that can be developed along the rockbolt/gridpoint interface is a function of the cohesive strength of the interface and the stress-dependent frictional resistance along with the interface (Figure 10d). The following equation can be used to determine the maximum shear force per length of the rockbolt:

$$\frac{F_s^{max}}{L} = cs_{scoh} + \sigma_c' \times tan\left(cs_{sfric}\right) \times perimeter \tag{8}$$

where cs_{scoh} is the cohesive strength of the shear coupling spring (coupling-cohesion-shear); σ_c' is the average effective confining stress perpendicular to the "rockbolt" element; cs_{sfric} is the friction angle of the shear coupling spring (coupling-friction-shear), and *perimeter* is the exposed perimeter of the element.

3.2.2. Calibration of Rockbolt Properties

The pull-out test is a well-recognized test, and it can represent the static load-displacement characteristics of rockbolts before rockbursting [63,64]. Besides, the performance of rockbolts during strainbursts has been initially confirmed by in situ observations and others' experimental test and simulation results in this research. Hence, only the simulated pull-out tests were conducted to calibrate the input parameters of the "rockbolt" element with the comparison of the laboratory test results from Charette and Plouffe [10], Stillborg [65], and Li [17]. The model's size is 2 m × 1 m, and the bolt length is 2 m. This model size is almost identical to Bahrani and Hadjigeorgiou [60]. The model has a Young's modulus of 7.5 GPa and a Poisson's ratio of 0.25 to represent an elastic rock mass because it has been confirmed that the elastic properties of the rock mass do not influence the load-displacement response of the "rockbolt" element [61] which can significantly save computation time. The rockbolt was divided into 40 segments and 41 nodes to ensure that at least one node falls into each block zone [60]. The upper boundary of the model was free, and a vertical upward velocity of 0.08 m/s was applied to the end node of the bolt to simulate a pull action [66]. The roller constraints were applied on the side boundaries and the bottom boundary was fixed. A function was developed using the FISH language (built-in programming package) in UDEC to monitor the axial force and displacement of the last segment of the rockbolt in *y*-direction.

The modeling of pull-out tests was conducted iteratively to adjust input parameters (e.g., tensile yield strength, tension failure strain, shear coupling spring stiffness, and shear coupling spring cohesion, [62]) until the simulated results were consistent with the targeted properties of rockbolts. Other input parameters (e.g., the diameter, length, density, and elastic modulus of rockbolts) are the same as those used in laboratory tests. The simulated load-displacement curves and axial force of rockbolts and the block displacement are shown in Figure 11. The calibrated input parameters of rockbolts are listed in Table 5. The applied load is axial in an ideal pull-test as simulated in this study. Thus, the parameters regarding resistance to bending are not employed. The errors between the targeted and simulated ultimate load, rupture displacement, and static energy-absorption capacity of rockbolts are less than 5% (Table 6), indicating that the targeted values agree well with calibrated input parameters. Thus, the calibrated parameters in Table 5 could be used to further the numerical analysis of the performance of yielding and conventional rockbolts [9]. However, it should be noted that the sliding or extraction of Roofex was not simulated explicitly in the pull-out test, and its energy-absorption mechanism was simplified to the deformation or stretch of bolt shanks. This equivalent approach could be regarded as a relatively good selection at this stage since the complexity of simulating bolt sliding was ignored, and the time cost was thus significantly reduced.
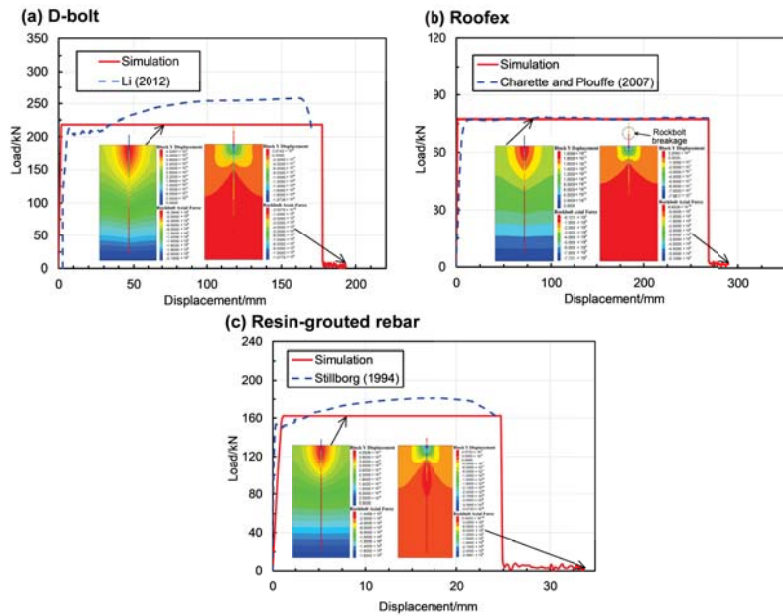
Figure 11. Simulated load-displacement curves and axial forces of rockbolts and deformation of rock masses. (Rockbolt axial force in N and block Y displacement in m.).

3.3. Simulation Procedures and Schemes

Modeling the effects of yielding rockbolts on controlling self-initiated strainbursts was performed with the following stages and schemes.

Stage I (static stage): The in situ stress field was applied to the model, and the geostatic equilibrium was achieved. Then, the tunnel was excavated by deleting the blocks. Adequate calculation steps were run to ensure gradual and slow release of surrounding rock stresses [38]. The installation of rockbolts was conducted immediately after the excavation of the tunnel.

Stage II (dynamic stage): The dynamic mode was activated. The local damping ratio was set 0.05. The viscous boundary [43] was used in the dynamic calculation to avoid propagating waves' reflection and allow the necessary energy radiation. The dynamic calculation time is set to 120 ms. The pattern layout of rockbolts in the tunnel is shown in Figure 4. The roof and two ribs of the tunnel were supported by 15 rockbolts in total, while the floor remained unsupported, as is a common practice. The roof and rib bolts have a length of 2.5 m and row spacing of 0.7 m. The spacing of rockbolts along the tunnel axis is one meter by setting the "spacing" parameter in UDEC. Besides, D-bolt, Roofex, and fully resin-grouted rebar were simulated in each scheme.

Table 5. Calibrated input parameters of rockbolts.

Rockbolt Type	Cross-Sectional Area (m²)	Moment of Inertia (m⁴)	Perimeter of Borehole (m)	Density (kg/m³)	Elastic Modulus (GPa)	Tensile Yield Strength (kN)	Tension Failure Strain	Shear Coupling Spring Stiffness (GN/m/m)	Shear Coupling Spring Cohesion (kN/m)	Shear Coupling Spring Friction Angle (°)
Resin-grouted rebar	3.14×10^{-4}	7.85×10^{-9}	0.08	7500	200	517	0.33	0.31	400	45
D-bolt	3.80×10^{-4}	1.15×10^{-8}	0.10	7500	200	575	1.36	0.29	438	45
Roofex	1.23×10^{-4}	1.20×10^{-9}	0.08	7500	200	630	1.66	0.21	353	45

Table 6. Comparison between the targeted and simulated rockbolt properties.

Rockbolt Type	Ultimate Load (kN)			Rupture Displacement (mm)			Static Energy-Absorption Capacity (kJ)		
	Laboratory Test	Simulation	Error/(%)	Laboratory Test	Simulation	Error/(%)	Laboratory Test	Simulation	Error/(%)
Resin-grouted rebar	162	162	0.0	24.1	24.9	3.3	4.15	3.96	−4.6
D-bolt	212	219	3.3	170	178	4.7	40.23	38.65	−3.9
Roofex	77.6	77.3	−0.4	274	269	−1.8	20.94	20.71	−1.1

4. Analysis of Simulation Results

4.1. Displacement and Velocity Analysis

The simulated displacement patterns of the tunnel supported by different types of rockbolts are shown in Figure 12a. The large deformation only occurs in a local tunnel area that D-bolts support. In contrast, noticeable roof subsidence and sidewall shrinkage are observed when the tunnel is supported with Roofex and resin-grouted rebar. To further investigate the effects of different types of rockbolts on controlling strainbursts, four monitoring points were arranged at the roof, floor, and two sidewalls of the tunnel to record the tunnel deformation (Figure 4). The comparison of the tunnel deformation in three support schemes is shown in Figure 12b. It can be seen that the tunnel supported by D-bolts suffers minor deformation (1411 mm in total). However, the total deformations of the tunnel supported with Roofex and resin-grouted rebar are 2159 mm and 2946 mm, respectively, which are 1.53 and 2.09 times that of the tunnel supported by D-bolts.

Figure 12. (**a**) Simulated displacement vectors of the surrounding rock masses along the tunnel supported by different types of rockbolts. (**b**). Comparison of the deformation of the tunnel supported by different types of rockbolts.

The most severe deformation is found when the resin-grouted rebar supports the tunnel. Although the resin-grouted rebar has relatively high strength (162 kN), its elongation rate is low and easy to break during dynamic shocks. As shown in Figure 13c, many resin-grouted rebar bolts are broken during the strainburst, and therefore they are unable to control rapid rock bulking or ejection effectively. Some in situ observations (see Figure 14) can confirm this phenomenon. Figure 14a shows that resin-grouted rebar bolts were broken in a rockburst while yielding rockbolts survive. Figure 14b,c also illustrate that many rebar bolts failed in rockbursts in deep tunnels. The match between simulation results and in situ observations verifies the reliability and rationality of the "rockbolt" element in modeling the performance of yielding rockbolts. Roofex also fails to restrain the large deformation because it possesses the lowest strength (77 kN) compared to D-bolt (219 kN) and resin-grouted rebar (162 kN). In summary, Roofex and resin-grouted rebar cannot effectively control the large deformation in self-initiated strainbursts.
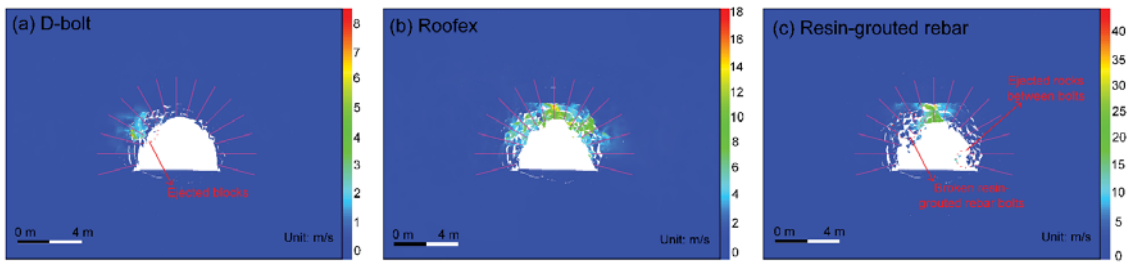
Figure 13. Simulated velocity distribution of the surrounding rock masses along the tunnel supported by different types of rockbolts. (**a**) D-bolt; (**b**) Roofex; (**c**) Resin-grouted rebar.
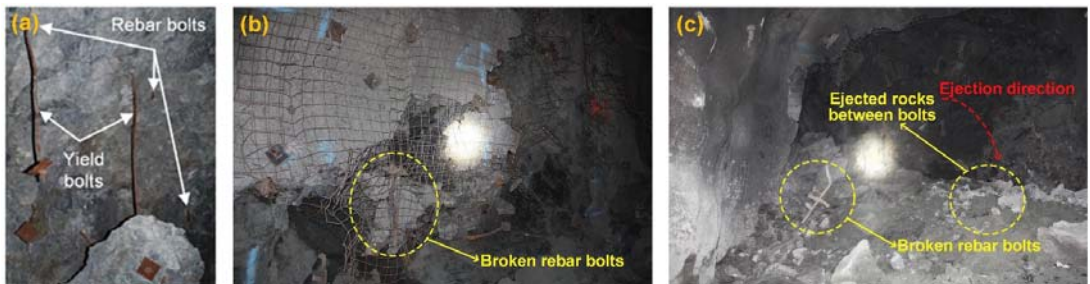
Figure 14. (**a**) Observed performance of fully resin-grouted rebar and yielding rockbolts in a rockburst [67]. (**b**,**c**) are in situ observations of broken rebar bolts after rockbursts in deep tunnels (photographs taken by authors).

The velocity distribution of tunnel surrounding rock masses in three support schemes is shown in Figure 13. It can be seen from Figure 13 that only a few rock blocks are ejected from a local zone when the D-bolt is adopted. For the tunnel supported by Roofex and resin-grouted rebar, much more rock blocks are ejected from the roof and sidewalls. To further study the effects of different rockbolts on mitigating rockburst damage, a function was developed using FISH language programming in UDEC to record the velocity and volume of all the detached rock blocks in the model. The detached rock blocks were detected when blocks or the clusters of blocks have no contact normal forces on their boundaries. The statistical analysis results are illustrated in Figure 15. As shown in Figure 15a, the average velocity of detached rock blocks in the tunnel supported by D-bolts is only 0.34 m/s, although a few blocks may have a relatively high velocity (e.g., 5–10 m/s). By comparison, the average velocities of detached rock blocks in the tunnel supported with Roofex and resin-grouted rebar are 3.22 and 3.97 m/s, respectively. Besides, the velocity distributions of rock blocks in these two scenarios are more extensive than those in the tunnel using D-bolts. Figure 15b shows that 99.8% of rock blocks in the tunnel supported by D-bolts possesses a velocity lower than 5 m/s, while the velocities of most rock blocks in the other two scenarios (95.1% for Roofex and 89.2% for resin-grouted rebar) are within the range of 0–10 m/s. In addition, many rock blocks focus on the volume range of 0.04–0.055 m^3. This is because the edge length of blocks near the tunnel was set to 0.3 m. These results suggest that the rock ejection is much more violent when the tunnel is supported by Roofex and resin-grouted rebar, which further confirms that these two types of rockbolts are unable to control strainbursts.
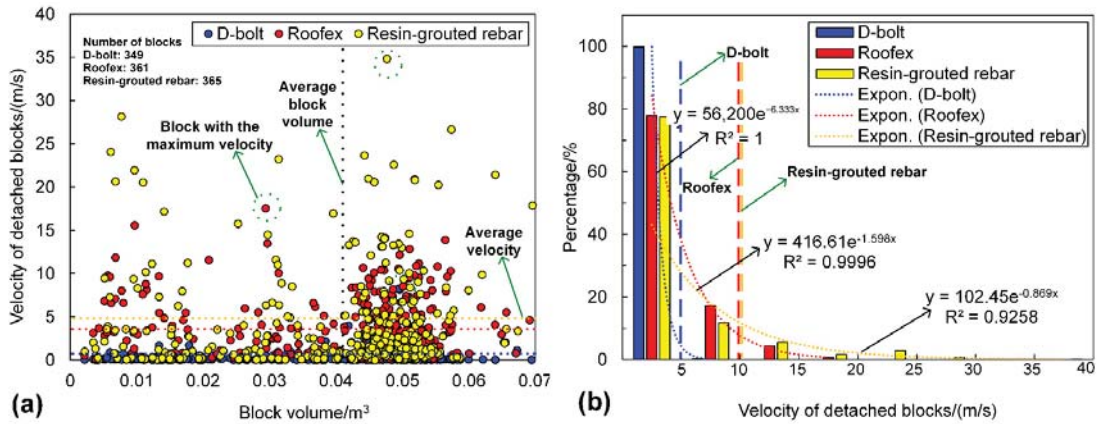
Figure 15. (**a**) is the velocity of all detached blocks versus block volume. (**b**) is the velocity distribution of all detached blocks. e is the Euler's number.

4.2. Rockburst Damage Analysis

In order to investigate the influences of different types of rockbolts on mitigating rockburst damage, the macroscopic failure pattern and damage degree of the tunnel induced by strainbursts were analyzed. In this study, the rockburst damage degree was evaluated by the volume of failed rocks [1]. A function was developed using FISH language programing in UDEC to sum the volume of detached rock blocks. It should be noted that the volume of detached rock blocks induced by static excavation was excluded in the calculation.

Figure 16 shows the macroscopic failure patterns of the tunnel supported by different types of rockbolts. As shown in Figure 16a, when D-bolts are adopted in the tunnel, the extent of the fractured zone is much smaller than that of the tunnel supported with Roofex and resin-grouted rebar. Only a few rock blocks are ejected between bolts, and the tunnel surrounding rock masses are overall stable. However, the surrounding rock masses are fractured for the tunnel using Roofex and resin-grouted rebar, and many ejected rock blocks are observed. As a result, the rockfall occurs, and the tunnel tends to be unstable.

The comparison of the volume of ejected rock blocks of the tunnel in three support schemes is shown in Figure 16b. The volume of ejected rock blocks is the least (1.07 m^3) when the tunnel uses D-bolt support. However, the volume of ejected rock blocks of the tunnel supported with Roofex and resin-grouted rebar is 1.54 m^3 and 1.79 m^3, respectively, which are 1.44 and 1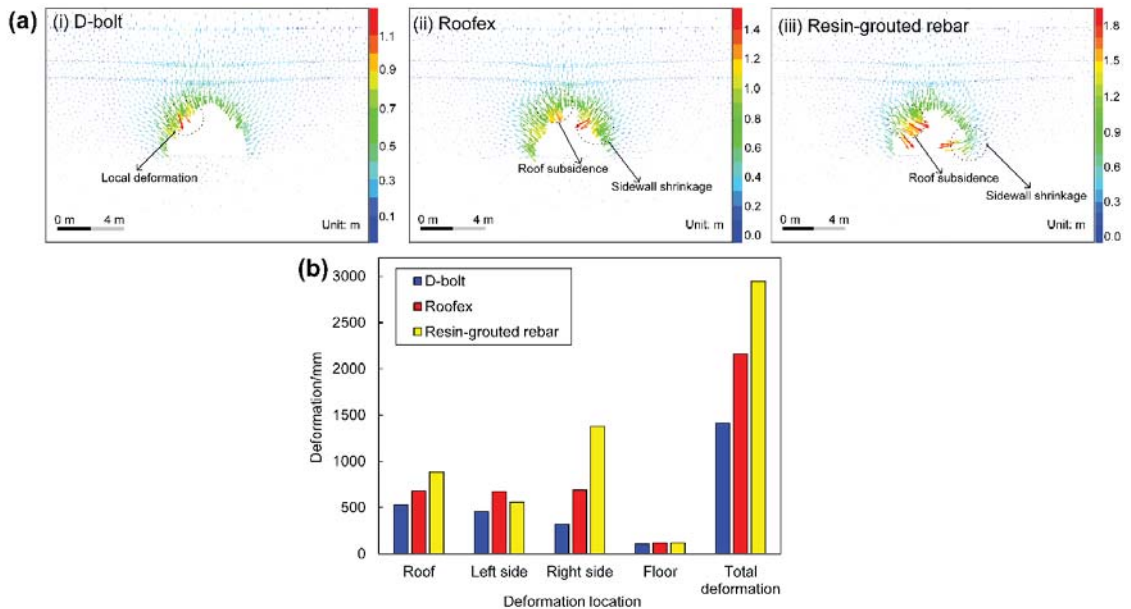.67 times that of the tunnel supported by D-bolts. The rockburst damage is the most serious when resin-grouted rebar supports the tunnel due to its low deformation capacity to restrain rapid rock bulking and ejection [1,7]. This finding further verifies that the conventional rockbolts (e.g., rebar bolts) are too stiff to control rockburst damage. Besides, the volume of ejected rock blocks of the tunnel supported with Roofex is moderate. This is because Roofex has the lowest strength, and its sliding mechanism can be easily activated. Thus, it is too "soft" or "smooth" to limit ejected rocks' movement compared to D-bolts.
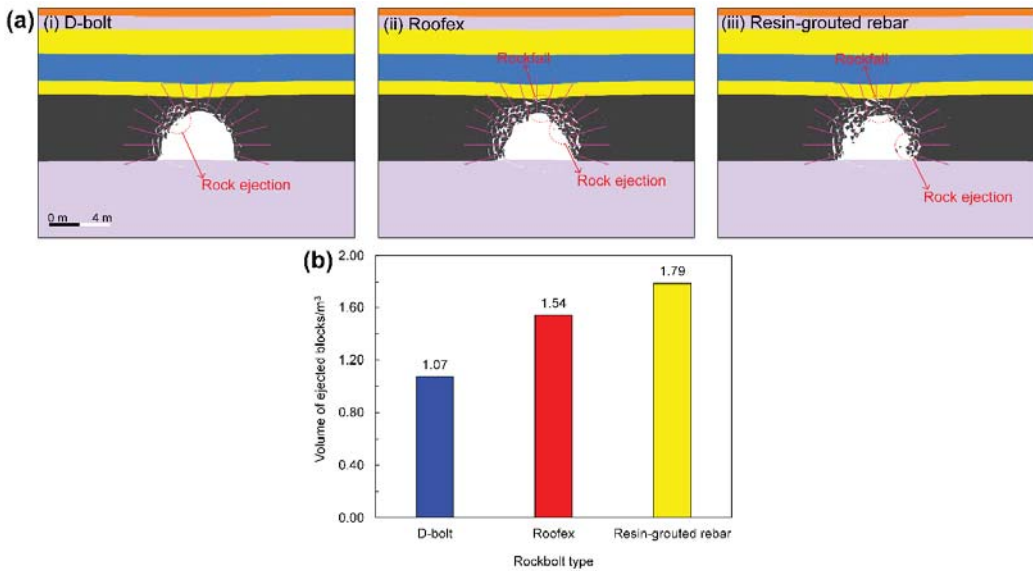
Figure 16. (**a**) Macroscopic failure patterns of the tunnel supported by different types of rockbolts. (**b**) is the volume of ejected rock blocks of the tunnel induced by rockbursts.

4.3. Energy Evolution Analysis

The severity of rockbursts is related to the magnitude of the kinetic energy of ejected rock materials [1,68]. The kinetic energy is one part of the total released energy that the whole supporting system (e.g., rockbolt, cable bolt, liner, and wire mesh) must absorb to reduce rockburst risks [69]. Therefore, the influences of rockbolt supporting on the distribution and change of kinetic energy were investigated in this study. The kinetic energy of ejected rock blocks was captured by the FISH language programing in UDEC using the following formula:

$$W_k = \sum \frac{1}{2}mv^2 \qquad (9)$$

where m and v are the mass and velocity of ejected rock blocks at the current time step.

The distribution of the kinetic energy of ejected rock blocks in three support schemes is shown in Figure 17. It can be seen that the kinetic energy pattern is very similar to that of velocity (see Figure 13). As shown in Figure 17a, only a few rock blocks have relatively high kinetic energy when the D-bolt is adopted. On the other hand, more rock blocks possess higher kinetic energy for the tunnel supported by Roofex and resin-grouted rebar. The variation of kinetic energy with time influenced by different rockbolt types is illustrated in Figure 17b. When the tunnel is supported with D-bolts, kinetic energy evolution can be divided into two stages: the kinetic energy first increases to the peak value from 0 to 26 ms and then gradually declines to almost zero. For Roofex, the kinetic energy experiences fast growth, especially after 80 ms, and reaches the peak value at 103 ms. Then, the kinetic energy drops with time but is still high. When the tunnel is supported by resin-grouted rebar, the kinetic energy first increases rapidly to the peak value from 0 to 54 ms and then suffers a sudden drop. Then, it surges again at 100 ms.
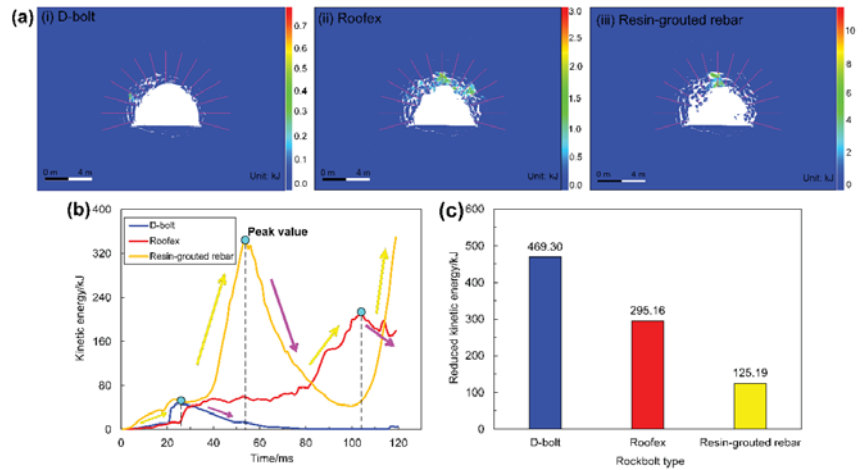
Figure 17. (**a**) Simulated kinetic energy distribution of ejected rock blocks in the tunnel supported by different types of rockbolts. (**b**) is the evolution of kinetic energy of ejected rock blocks. (**c**) is the comparison of reduced kinetic energy of ejected rock blocks.

Interestingly, kinetic energy grows again. This is because the ineffectiveness of resin-grouted rebar results in the "Domino-like" failure fashion during the strainburst. In summary, D-bolts absorb the kinetic energy of ejected rock blocks effectively, and the strainburst is controlled. However, Roofex and resin-grouted rebar fail to absorb the kinetic energy of ejected rock blocks effectively and cannot control the strainburst.

To further evaluate the dynamic energy-absorption capacity of three types of rockbolts, the tunnel without adopting any supports during the strainburst was simulated. Then, a new variable was defined as the reduced kinetic energy, which is the difference between the kinetic energy of ejected rock blocks in the tunnel without and using rockbolts. Figure 17c compares the reduced kinetic energy of ejected rock blocks in the tunnel supported by different rockbolts. The reduced kinetic energy is the highest (469.30 kJ) when the tunnel uses D-bolt support. In contrast, the reduced kinetic energy is the lowest (125.19 kJ) for the tunnel supported by resin-grouted rebar, while the performance of Roofex on reducing kinetic energy (295.16 kJ) is in between the D-bolt and resin-grouted rebar. These results are not surprising because they agree that D-bolt has both high strength and excellent deformation capacity, while Roofex has low strength and resin-grouted rebar has very limited deformation capacity.

4.4. Rockbolt Force Analysis

The simulated axial force distribution of rockbolts in three support schemes is shown in Figure 18. It can be seen that in all three cases, the tensile axial force tends to reach the peak value at a certain distance (around 1–1.5 m) from the bolt end (head) and then gradually decreases to a low value. The simulated axial force patterns of rockbolts agree with some published experimental test [70] and numerical simulation results [71,72]. The average peak values of axial forces for three rockbolt types are 214.87 kN, 76.99 kN, and 151.05 kN, respectively. Thus, both the D-bolt and resin-grouted rebar can bear the high load of rock masses, while the Roofex cannot provide sufficient resistance to control large rock deformation and rapid rock bulking during strainbursts.
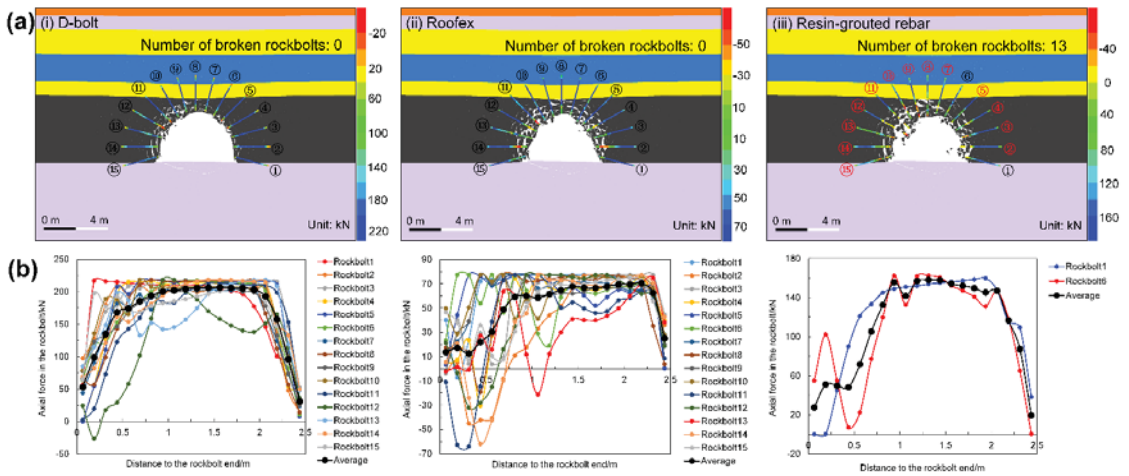
Figure 18. Simulated contours (**a**) and distribution of the axial force (**b**) in rockbolts for the tunnel supported by different rockbolts. The black and red numbers indicate intact and broken rockbolts, respectively. The positive value of axial forces represents a tensile load.

Additionally, it can be observed that 13 resin-grouted rebar bolts are broken, resulting in the unsuccessful control of the strainburst. Again, this is because the resin-grouted rebar has limited deformation capacity to accommodate rapid rock bulking and relieve rock ejection [1,7]. No broken rockbolts were found for the tunnel adopting D-bolt and Roofex supporting. In summary, the D-bolt and resin-grouted rebar can maintain a high axial force level during the strainburst to restrain rock ejection and rock bulking, but the resin-grouted rebar is prone to be broken due to a minimal elongate rate failing to mitigate rockburst damage effectively. Roofex's axial force is too low to control strainbursts, although it has an excellent deformation capacity over the other two rockbolt types.

5. Discussion

5.1. Influence of the Bolt Number

The effects of rockbolts on controlling self-initiated strainbursts not only depend on rockbolt types but also are affected by other factors, e.g., bolt number, bolt length, and row spacing. Therefore, it is interesting to explore the influences of these factors on the control and mitigation of strainburst damage, which can be used for optimizing the support design in burst-prone grounds. Since the D-bolt performs better on controlling strainbursts than Roofex and resin-grouted rebar based on previous analyses, it was decided to simulate the tunnel supported by D-bolts with different bolt numbers (9, 12, 15, and 18) as an example, while other influence factors (e.g., bolt length) can also be studied in the model.

The simulation results are shown in Figures 19 and 20. It can be seen from Figure 19a that many rock blocks with high velocities are ejected from the roof and sidewalls when 9 D-bolts support the tunnel. A moderate number of rock blocks are ejected from a local zone when 12 D-bolts are installed. However, only a few rock blocks are ejected for the tunnel supported with 15 D-bolts, and almost no ejected rock blocks are found when the bolt number is 18. The statistical analysis results of the velocity and volume of all the detached rock blocks in the model are illustrated in Figure 20. As shown in Figure 20a, the average velocity of rock blocks in the tunnel supported by 9 D-bolts is 4.54 m/s. By comparison, the average velocities of rock blocks in the tunnel supported with 12, 15, 18 D-bolts are 0.48, 0.34, and 0.04 m/s, respectively. These results suggest that the rock ejection is very violent when the tunnel is supported by 9 D-bolts, which fail to control the strainburst.
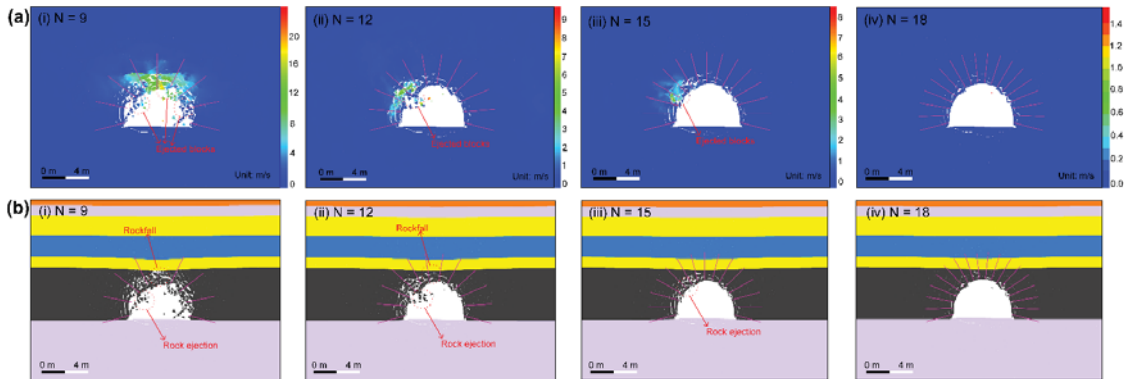
Figure 19. (**a**,**b**) are simulated velocity distribution and macroscopic failure patterns of the tunnel. N is the bolt number.
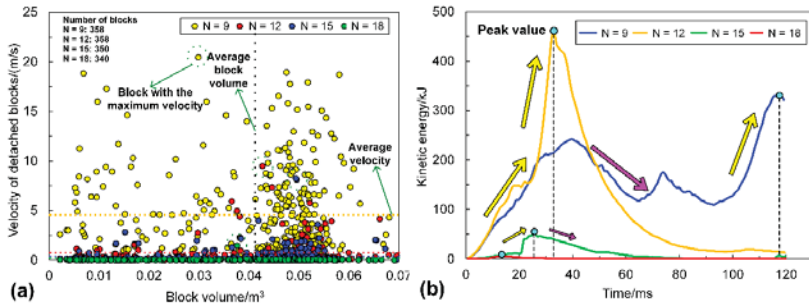
Figure 20. (**a**) is the velocity of all detached blocks versus block volume. (**b**) is the evolution of kinetic energy of ejected rock blocks in the tunnel. N is the bolt number.

Figure 19b shows the macroscopic failure patterns of the tunnel supported by different numbers of rockbolts. It can be seen that the extent of the fractured zone gradually decreases with the growth of bolt numbers. For the tunnel using 9 and 12 D-bolts, surrounding rock masses are very fractured, and rockfall and rock ejection are observed. The tunnel tends to be unstable. In contrast, only a few rock blocks are ejected when 15 D-bolts are installed. No obvious rockfall and rock ejection are observed, and the tunnel surrounding rock masses is very stable when the blot number is 18.

The variation of the kinetic energy of ejected rock blocks with time is illustrated in Figure 20b. When the tunnel is supported with 9 D-bolts, the kinetic energy first increases from 0 to 40 ms and then experiences several fluctuations. After that, the kinetic energy grows fast, especially after 100 ms, and reaches the peak value at 117 ms. In contrast, the kinetic energy evolution trends for the tunnel using 12, 15, and 18 bolts can all be divided into two stages: the kinetic energy first increases to the peak value and then gradually declines to lower values (almost zero when using 18 bolts). This is because more rockbolts are deformed to absorb the kinetic energy of ejected rock blocks, which the lower average velocity can confirm. However, the residual kinetic energy is still high (12.7 kJ) when adopting 12 D-bolts, indicating that this number is insufficient to control the strainburst. In summary, 9 and 12 D-bolts cannot control the strainburst, while 15 and 18 bolts can make the tunnel stable.

5.2. Influence of the Surface Retaining Element

The surface retaining element (e.g., fiber-reinforced shotcrete, wire mesh, and steel arch) is an indispensable component of the support system as it can prevent the unraveling of fractured rocks between rockbolts. Therefore, the effects of the combination of surface retaining elements and yielding rockbolts on controlling strainbursts should be investigated. In this research, the tunnel supported with D-bolts and a steel arch was simulated to demonstrate the benefits of surface retaining elements. The beam structural element modeled the steel arch in UDEC. The input parameters of the beam structural element are adopted from Małkowski et al. [53], as listed in Table 7.

Table 7. Input parameters of the beam structural element.

Input Parameter	Cross-Sectional Area (m^2)	Moment of Inertia (m^4)	Density (kg/m^3)	Poisson's Ratio	Elastic Modulus (GPa)	Tensile Yield Strength (kN)	Shear Coupling Spring Stiffness (GN/m/m)	Normal Coupling Spring Stiffness (GN/m/m)
Beam	4×10^{-3}	8.38×10^{-6}	7700	0.3	210	650	10^4	10^4

It should be noted that simulating both rockbolt and beam elements in the dynamic calculation mode in UDEC currently takes impracticable time (e.g., more than 1000 h) to approach the equilibrium state due to intrinsic difficulties in the program. Thus, the model's simulation results only running 20 ms were analyzed. Figure 21 shows the macroscopic failure patterns of the tunnel with and without a steel arch. It can be seen that the detachment and ejection of rock bocks between rockbolts are well restrained by the steel arch, although the surrounding rock masses are still fractured.
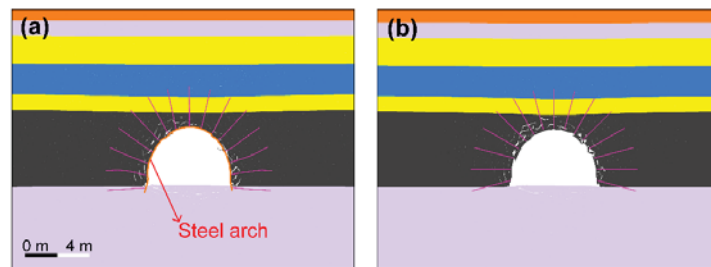
Figure 21. (**a**,**b**) are the macroscopic failure patterns of the tunnel with and without a steel arch. The dynamic calculation time is 20 ms.

5.3. Highlights and Limitations

The effects of yielding rockbolts on controlling self-initiated strainbursts were thoroughly numerically investigated using DEM. Instead of conventional drop tests, the performance of yielding rockbolts (e.g., the dynamic capacity of energy-absorption and control of rock damage) is evaluated during simulated strainbursts for the first time. The obtained results suggest that the D-bolt, as a type of high strength yielding rockbolt, can effectively control the large deformation, reduce kinetic energy, and mitigate rockburst damage, while Roofex (low strength yielding rockbolt) and resin-grouted rebar (stiff rockbolt) fail to control self-initiated strainbursts. This finding agrees well with many others' studies. For instance, Li et al. [21], Li [67], and Sharifzadeh et al. [22] suggested that the high strength yielding rockbolt should be used to control rockbursts, because this type of rockbolt can bear high loads and displace significantly, thereby absorbing a great amount of kinetic energy than other types of rockbolts.

This study highlights the usage of numerical modeling methods in assessing the performance of yielding rockbolts, which can be served as a promising tool to improve and optimize the design of rock supporting in burst-prone grounds following the presented modeling framework (including modeling sequence, parameter calibration method, model validation method, etc.). For example, the support scenarios with the combination of different bolt types (e.g., resin-grouted rebar and D-bolt), various bolt parameters (e.g., bolt number, bolt length, bolt strength, and row spacing), and surface retaining elements (e.g., fiber-reinforced shotcrete, wire mesh, and steel arch) can be modeled to select the optimal scheme that has best control effects and lowest cost.

The prerequisite for modeling self-initiated strainbursts is to determine whether the unstable failure will occur or not, which can be judged based on the local mine stiffness and the post-failure stiffness of rock masses. However, unlike the unstable failure of rock samples, it is hard to calculate the local mine stiffness when the focus is a strainburst that usually occurs in a tunnel or roadway. In this research, the authors first proposed a novel method to calculate the local mine stiffness of a tunnel: the ratio of the in situ stress at the designed excavation boundary to the convergence of tunnel walls. This method is straightforward, which can be easily fulfilled in 2D and 3D numerical modeling. The proposed method fills the gap about how to determine the local mine stiffness of a tunnel for modeling self-initiated strainbursts and provides a tool to predict the tendency of strainbursts using the stiffness theory during the design stage of mining and civil engineering projects.

The presented study and obtained results also point out some limitations for further research work:

1. The accuracy of simulation results can be improved if the dynamic mechanical properties of rock masses and joints and related constitutive relationships are known and used.

2. There is no energy dissipation when two contact faces are separated. Further studies (e.g., setting residual values of contacts or selecting more representative constitutive models) need to be conducted to consider the influences of fracture energy on simulation results.

3. The performance of yielding rockbolts during strainbursts has been initially confirmed by in situ observations and others' experimental test and simulation results. However, the simulation results will be more accurate and reliable if field monitoring data (e.g., dynamic strength and elongation rate) of yielding rockbolts during strainbursts are available to calibrate simulation parameters.

4. The sliding or extraction mechanism of Roofex should be simulated explicitly to better evaluate its performance during strainbursts. Setting reasonable parameters of the bolt-grout/rock interface will be a choice.

5. The performance of yielding rockbolts was mainly evaluated from the "macro" views of the dynamic energy-absorption capacity and the control of the deformation and damage of rock masses. Other "micro" behavior of rockbolts, e.g., the shear force and failure of bolt-grout/rock interfaces, can be studied in future research.

6. Conclusions

In this paper, a 2D DEM model of a deep tunnel in an underground coal mine is built to thoroughly evaluate the effects of yielding (D-bolt and Roofex) and the traditional rockbolt (fully resin-grouted rebar) on controlling self-initiated strainbursts. The occurrence of self-initiated strainbursts is judged based on the stiffness difference between the loading system and rock masses for the first time. The main conclusions are as follows:

(1) The total deformations of the tunnel supported with Roofex and resin-grouted rebar are 1.53 and 2.09 times that of D-bolts (1411 mm). The average velocities of detached rock blocks in the tunnel supported with Roofex and resin-grouted rebar are 3.22 and 3.97 m/s, respectively, which are much higher than that of D-bolts (0.34 m/s). 13 resin-grouted rebar bolts are broken during the strainburst, while D-bolts and Roofex

survive. This phenomenon agrees well with some in situ observations, verifying the reliability and rationality of the "rockbolt" element in modeling yielding rockbolts.

(2) The volume of ejected rock blocks can be obtained by the developed FISH function in the numerical model. The volume of ejected rock blocks in the tunnel supported by D-bolts is 1.07 m^3, which is the least compared with Roofex (1.54 m^3) and resin-grouted rebar (1.79 m^3).

(3) The dynamic energy-absorption capacity of rockbolts can be evaluated by a proposed variable, reduced kinetic energy. Compared with Roofex (295.16 kJ) and resin-grouted rebar (125.19 kJ), the D-bolt can reduce the most kinetic energy (469.30 kJ).

(4) The simulated axial force patterns of rockbolts agree with some published experimental test and numerical simulation results. The average peak values of axial forces for D-bolt, Roofex, and resin-grouted rebar are 214.87 kN, 76.99 kN, and 151.05 kN, respectively.

(5) The bolt number significantly influences the control effects of yielding rockbolts on strainbursts. For example, 9 and 12 D-bolts cannot control the strainburst, while 15 and 18 D-bolts can make the tunnel stable. In addition, the detachment and ejection of rocks between rockbolts can be well restrained using surface retain elements, e.g., steel arch.

In summary, D-bolt can effectively control the large deformation, reduce kinetic energy, and mitigate rockburst damage, while Roofex and resin-grouted rebar fail to control self-initiated strainbursts. This study highlights the usage of numerical modeling methods in assessing the performance of yielding rockbolts, which can be served as a promising tool to improve and optimize the design of rock supporting in burst-prone grounds.

References

1. Cai, M. Principles of rock support in burst-prone ground. *Tunn. Undergr. Space Technol.* **2013**, *36*, 46–56. [CrossRef]
2. Zhang, C.; Feng, X.T.; Zhou, H.; Qiu, S.; Wu, W. Case Histories of Four Extremely Intense Rockbursts in Deep Tunnels. *Rock Mech. Rock Eng.* **2012**, *45*, 275–288. [CrossRef]
3. Wang, J.; Apel, D.B.; Dyczko, A.; Walentek, A.; Prusek, S.; Xu, H.; Wei, C. Investigation of the Rockburst Mechanism of Driving Roadways in Close-Distance Coal Seam Mining Using Numerical Modeling Method. *Min. Metall. Explor.* **2021**, *38*, 1899–1921. [CrossRef]
4. Kaiser, P.K.; McCreath, D.; Tannant, D. *Canadian Rockburst Support Handbook*; Geomechanics Research Center: Sudbury, ON, Canada, 1996.
5. Kaiser, P.K.; Cai, M. Design of rock support system under rockburst condition. *J. Rock Mech. Geotech. Eng.* **2012**, *4*, 215–227. [CrossRef]
6. Mutke, G.; Dubiński, J.; Lurka, A. New Criteria to Assess Seismic and Rock Burst Hazard in Coal Mines/Nowe Kryteria Dla Oceny Zagrożenia Sejsmicznego I Tąpaniami W Kopalniach Węgla Kamiennego. *Arch. Min. Sci.* **2015**, *60*, 743–760. [CrossRef]
7. Diederichs, M.S. Early assessment of dynamic rupture hazard for rockburst risk management in deep tunnel projects. *J. S. Afr. Inst. Min. Metall.* **2018**, *118*, 193–204. [CrossRef]
8. Ortlepp, W. The design of support for the containment of rockburst damage in tunnels: An engineering approach. In *International Symposium on Rock Support*; Balkema: Rotterdam, The Netherlands, 1992.
9. Atlas Copco Construction Mining Technique. Roofex Rock Bolt. Available online: https://www.forconstructionpros.com/equipment/underground/vertical-drilling-equipment/product/10080325/atlas-copco-construction-mining-technique-usa-llc-roofex-rock-bolt (accessed on 22 May 2021).

10. Charette, F.; Plouffe, M. Roofex®–Results of laboratory testing of a new concept of yieldable tendon. In Proceedings of the Fourth International Seminar on Deep and High Stress Mining, Perth, Australia, 7–9 November 2007.
11. Varden, R.; Lachenicht, R.; Player, J.; Thompson, A.; Villaescusa, E. Development and implementation of the garford dynamic bolt at the kanowna belle mine. In Proceedings of the 10th Underground Operators Conference, Launceston, Australia, 14–16 April 2008.
12. Li, C.C.; Doucet, C. Performance of D-Bolts Under Dynamic Loading. *Rock Mech. Rock Eng.* **2011**, *45*, 193–204. [CrossRef]
13. Normet. Normet D-Bolt®—Dynamic Rock Bolt. Available online: https://www.normet.com/product/d-bolt/ (accessed on 22 May 2021).
14. Wu, R.; Oldsen, J.; Campoli, A. Application of yield-lok bolt for bursting and convergence grounds in mines. In Proceedings of the 30th International Conference on Ground Control in Mining, Morgantown, WV, USA, 26 July 2011.
15. He, M.; Xia, H.; Jia, X.; Gong, W.; Zhao, F.; Liang, K. Studies on classification, criteria and control of rockbursts. *J. Rock Mech. Geotech. Eng.* **2012**, *4*, 97–114. [CrossRef]
16. Kang, H.; Lin, J.; Wu, Y. High pretensioned stress and intensive cable bolting technology set in full section and application in entry affected by dynamic pressure. *J. China Coal Soc.* **2009**, *34*, 1153–1159.
17. Li, C.C. Performance of D-bolts Under Static Loading. *Rock Mech. Rock Eng.* **2011**, *45*, 183–192. [CrossRef]
18. Wu, Y.; Gao, F.; Chen, J.; He, J. Experimental Study on the Performance of Rock Bolts in Coal Burst-Prone Mines. *Rock Mech. Rock Eng.* **2019**, *52*, 3959–3970. [CrossRef]
19. Zhang, P.; Nordlund, E. Numerical investigation of dynamic response of a rockbolt under drop testing and simulated seismic loading conditions. In Proceedings of the Ninth International Symposium on Ground Support in Mining and Underground Construction, Perth, Australia, 23–25 October 2019.
20. Cai, M.; Champaigne, D.; Kaiser, P.K. Development of a fully debonded cone bolt for rockburst support. In Proceedings of the Fifth International Seminar on Deep and High Stress Mining, Santiago, MN, USA, 6–8 October 2010.
21. Li, C.C.; Stjern, G.; Myrvang, A. A review on the performance of conventional and energy-absorbing rockbolts. *J. Rock Mech. Geotech. Eng.* **2014**, *6*, 315–327. [CrossRef]
22. Sharifzadeh, M.; Lou, J.; Crompton, B. Dynamic performance of energy-absorbing rockbolts based on laboratory test results. Part I: Evolution, deformation mechanisms, dynamic performance and classification. *Tunn. Undergr. Space Technol.* **2020**, *105*, 103510. [CrossRef]
23. Bosman, K.; Cawood, M.; Berghorst, A. Relationship between energy per impulse and dynamic capacity of a rockbolt. In Proceedings of the Rock Dynamics–Experiments, Theories and Applications, Trondholm, Norway, 13 July 2018.
24. Wang, J.; Apel, D.B.; Pu, Y.; Hall, R.; Wei, C.; Sepehri, M. Numerical modeling for rockbursts: A state-of-the-art review. *J. Rock Mech. Geotech. Eng.* **2021**, *13*, 457–478. [CrossRef]
25. Ji, S.; Karlovšek, J. Calibration and uniqueness analysis of microparameters for DEM cohesive granular material. *Int. J. Min. Sci. Technol.* **2022**, *32*, 121–136. [CrossRef]
26. Ji, S.; Karlovšek, J. Optimized differential evolution algorithm for solving DEM material calibration problem. *Eng. Comput.* **2022**. [CrossRef]
27. Wang, J.; Apel, D.B.; Dyczko, A.; Walentek, A.; Prusek, S.; Xu, H.; Wei, C. Analysis of the damage mechanism of strainbursts by a global-local modelling approach. *J. Rock Mech. Geotech. Eng.* **2022**. [CrossRef]
28. Manouchehrian, A. Numerical Modeling of Unstable Rock Failure. Ph.D. Thesis, Laurentian University, Sudbury, ON, Canada, 2016.
29. Nie, W.; Zhao, Z.Y.; Ning, Y.J.; Guo, W. Numerical studies on rockbolts mechanism using 2D discontinuous deformation analysis. *Tunn. Undergr. Space Technol.* **2014**, *41*, 223–233. [CrossRef]
30. Marambio, E.; Vallejos, J.; Burgos, L.; Gonzalez, C.; Castro, L.; Saure, J.; Urzua, J. Numerical modelling of dynamic testing for rock reinforcement used in underground excavations. In Proceedings of the Fourth International Symposium on Block and Sublevel Caving, Australian Centre for Geomechanics, Vancouver, BC, Canada, 15–17 October 2018.
31. Yokota, Y.; Zhao, Z.; Nie, W.; Date, K.; Iwano, K.; Koizumi, Y.; Okada, Y. Development of a new deformation-controlled rockbolt: Numerical modelling and laboratory verification. In Proceedings of the Ninth International Symposium on Ground Support in Mining and Underground Construction, Australian Centre for Geomechanics, Sudbury, ON, Canada, 23–25 October 2019.
32. Zhao, T.; Xing, M.; Guo, W.; Wang, C.; Wang, B. Anchoring effect and energy-absorbing support mechanism of large deformation bolt. *J. Cent. South Univ.* **2021**, *28*, 572–581. [CrossRef]
33. Su, G.; Jiang, J.; Zhai, S.; Zhang, G. Influence of Tunnel Axis Stress on Strainburst: An Experimental Study. *Rock Mech. Rock Eng.* **2017**, *50*, 1551–1567. [CrossRef]
34. Su, G.; Zhai, S.; Jiang, J.; Zhang, G.; Yan, L. Influence of Radial Stress Gradient on Strainbursts: An Experimental Study. *Rock Mech. Rock Eng.* **2017**, *50*, 2659–2676. [CrossRef]
35. Hu, L.; Ma, K.; Liang, X.; Tang, C.; Wang, Z.; Yan, L. Experimental and numerical study on rockburst triggered by tangential weak cyclic dynamic disturbance under true triaxial conditions. *Tunn. Undergr. Space Technol.* **2018**, *81*, 602–618. [CrossRef]
36. Hu, L.; Liang, X.; Liang, Z.; Li, Y.; Zhang, Z.; Tang, C.A. Influence of radial stress on strainbursts under true triaxial conditions: Insights from a distinct element modelling. *Int. J. Rock Mech. Min. Sci.* **2021**, *138*, 104577. [CrossRef]
37. Hu, L.; Su, G.; Liang, X.; Li, Y.; Yan, L. A distinct element based two-stage-structural model for investigation of the development process and failure mechanism of strainburst. *Comput. Geotech.* **2020**, *118*, 103333. [CrossRef]
38. Gao, F.; Stead, D.; Kang, H. Numerical Simulation of Squeezing Failure in a Coal Mine Roadway due to Mining-Induced Stresses. *Rock Mech. Rock Eng.* **2015**, *48*, 1635–1645. [CrossRef]

39. Chen, M.; Yang, S.Q.; Zhang, Y.C.; Zang, C.W. Analysis of the failure mechanism and support technology for the Dongtan deep coal roadway. *Geomech. Eng.* **2016**, *11*, 401–420. [CrossRef]
40. Yang, S.Q.; Chen, M.; Jing, H.W.; Chen, K.F.; Meng, B. A case study on large deformation failure mechanism of deep soft rock roadway in Xin'An coal mine, China. *Eng. Geol.* **2017**, *217*, 89–101. [CrossRef]
41. Stavrou, A.; Vazaios, I.; Murphy, W.; Vlachopoulos, N. Refined approaches for estimating the strength of rock blocks. *Geotech. Geol. Eng.* **2019**, *37*, 5409–5439. [CrossRef]
42. Xu, Y.H.; Cai, M. Influence of Loading System Stiffness on Post-peak Stress–Strain Curve of Stable Rock Failures. *Rock Mech. Rock Eng.* **2017**, *50*, 2255–2275. [CrossRef]
43. Lysmer, J.; Kuhlemeyer, R.L. Finite dynamic model for infinite media. *J. Eng. Mech. Div.* **1969**, *95*, 859–877. [CrossRef]
44. Itasca. *Introductory Training Course UDEC7/3DEC7*; Itasca Consulting Group, Inc.: Minneapolis, MN, USA, 2021.
45. Dai, L.; Pan, Y.; Li, Z.; Wang, A.; Xiao, Y.; Liu, F.; Shi, T.; Zheng, W. Quantitative mechanism of roadway rockbursts in deep extra-thick coal seams: Theory and case histories. *Tunn. Undergr. Space Technol.* **2021**, *111*, 103861. [CrossRef]
46. Cook, N.G. The failure of rock. *Int. J. Rock Mech. Min. Sci. Geomech. Abstr.* **1965**, *2*, 389–403. [CrossRef]
47. Jaiswal, A.; Shrivastva, B.K. Stability analysis of the proposed hybrid method of partial extraction for underground coal mining. *Int. J. Rock Mech. Min. Sci.* **2012**, *52*, 103–111. [CrossRef]
48. Farahmand, K.; Vazaios, I.; Diederichs, M.S.; Vlachopoulos, N. Investigating the scale-dependency of the geometrical and mechanical properties of a moderately jointed rock using a synthetic rock mass (SRM) approach. *Comput. Geotech.* **2018**, *95*, 162–179. [CrossRef]
49. Bear, J. *Dynamics of Fluids in Porous Media*; Dover Publication: New York, NY, USA, 1972.
50. Bieniawski, Z. The effect of specimen size on compressive strength of coal. *Int. J. Rock Mech. Min. Sci. Geomech. Abstr.* **1968**, *5*, 325–335. [CrossRef]
51. Fairhurst, C.; Hudson, J.A. Draft ISRM suggested method for the complete stress-strain curve for intact rock in uniaxial compression. *Int. J. Rock Mech. Min. Sci.* **1999**, *36*, 279–289.
52. Marinos, P.; Hoek, E. GSI: A geologically friendly tool for rock mass strength estimation. In Proceedings of the ISRM International Symposium, Melbourne, Australia, 19 November 2000.
53. Małkowski, P.; Ostrowski, Ł.; Bachanek, P. Modelling the small throw fault effect on the stability of a mining roadway and its verification by in situ investigation. *Energies* **2017**, *10*, 2082.
54. Małkowski, P.; Ostrowski, Ł. Convergence monitoring as a basis for numerical analysis of changes of rock-mass quality and Hoek-Brown failure criterion parameters due to longwall excavation. *Arch. Min. Sci.* **2019**, *64*, 93–118.
55. Szott, W.; Słota-Valim, M.; Gołąbek, A.; Sowiżdżał, K.; Łętkowski, P. Numerical studies of improved methane drainage technologies by stimulating coal seams in multi-seam mining layouts. *Int. J. Rock Mech. Min. Sci.* **2018**, *108*, 157–168. [CrossRef]
56. Hoek, E.; Carranza-Torres, C.; Corkum, B. Hoek-Brown failure criterion-2002 edition. In Proceedings of the NARMS-Tac, Toronto, ON, Canada, 10 July 2002.
57. Hoek, E.; Diederichs, M. Empirical estimation of rock mass modulus. *Int. J. Rock Mech. Min. Sci.* **2006**, *43*, 203–215. [CrossRef]
58. Gao, F.; Kaiser, P.K.; Stead, D.; Eberhardt, E.; Elmo, D. Strainburst phenomena and numerical simulation of self-initiated brittle rock failure. *Int. J. Rock Mech. Min. Sci.* **2019**, *116*, 52–63. [CrossRef]
59. Diederichs, M.S. The 2003 Canadian Geotechnical Colloquium: Mechanistic interpretation and practical application of damage and spalling prediction criteria for deep tunnelling. *Can. Geotech. J.* **2007**, *44*, 1082–1116. [CrossRef]
60. Bahrani, N.; Hadjigeorgiou, J. Explicit reinforcement models for fully-grouted rebar rock bolts. *J. Rock Mech. Geotech. Eng.* **2017**, *9*, 267–280. [CrossRef]
61. Tomasone, P.; Bahrani, N.; Hadjigeorgiou, J. Practical considerations in the modelling of resin-grouted rockbolts. *J. S. Afr. Inst. Min. Metall.* **2020**, *120*, 385–392. [CrossRef] [PubMed]
62. Itasca. *UDEC, Version 7.0 Manual*; Itasca Consulting Group, Inc.: Minneapolis, MN, USA, 2020.
63. Skrzypkowski, K.; Korzeniowski, W.; Zagórski, K.; Zagórska, A. Modified Rock Bolt Support for Mining Method with Controlled Roof Bending. *Energies* **2020**, *13*, 1868. [CrossRef]
64. Skrzypkowski, K. An Experimental Investigation into the Stress-Strain Characteristic under Static and Quasi-Static Loading for Partially Embedded Rock Bolts. *Energies* **2021**, *14*, 1483. [CrossRef]
65. Stillborg, B. *Professional Users Handbook for RockBolting*; Trans Tech Publications: Clausthal, Germany, 1994.
66. Zhu, D.; Wu, Y.; Liu, Z.; Dong, X.; Yu, J. Failure mechanism and safety control strategy for laminated roof of wide-span roadway. *Eng. Fail. Anal.* **2020**, *111*, 104489. [CrossRef]
67. Li, C.C. Principles and methods of rock support for rockburst control. *J. Rock Mech. Geotech. Eng.* **2020**, *13*, 46–59. [CrossRef]
68. Gao, F.; Kaiser, P.K.; Stead, D.; Eberhardt, E.; Elmo, D. Numerical simulation of strainbursts using a novel initiation method. *Comput. Geotech.* **2019**, *106*, 117–127. [CrossRef]
69. Raffaldi, M.; Chambers, D.; Johnson, J. Numerical study of the relationship between seismic wave parameters and remotely triggered rockburst damage in hard rock tunnels. In Proceedings of the Eighth International Conference on Deep and High Stress Mining, Australian Centre for Geomechanics, Perth, Australia, 28–30 March 2017.
70. Hyett, A.; Moosavi, M.; Bawden, W. Load distribution along fully grouted bolts, with emphasis on cable bolt reinforcement. *Int. J. Numer. Anal. Methods Geomech.* **1996**, *20*, 517–544. [CrossRef]

71. Lisjak, A.; Young-Schultz, T.; Li, B.; He, L.; Tatone, B.S.A.; Mahabadi, O.K. A novel rockbolt formulation for a GPU-accelerated, finite-discrete element method code and its application to underground excavations. *Int. J. Rock Mech. Min. Sci.* **2020**, *134*, 104410. [CrossRef]
72. Ma, S.; Nemcik, J.; Aziz, N. Simulation of fully grouted rockbolts in underground roadways using FLAC2D. *Can. Geotech. J.* **2014**, *51*, 911–920. [CrossRef]

Article

Investigation and Stability Assessment of Three Sill Pillar Recovery Schemes in a Hard Rock Mine

Huawei Xu [1], Derek B. Apel [1,*], Jun Wang [1], Chong Wei [1] and Krzysztof Skrzypkowski [2,*]

[1] School of Mining and Petroleum Engineering, University of Alberta, Edmonton, AB T6G 2R3, Canada; hx1@ualberta.ca (H.X.); jun8@ualberta.ca (J.W.); cwei4@ualberta.ca (C.W.)

[2] Faculty of Civil Engineering and Resource Management, AGH University of Science and Technology, 30-059 Kraków, Poland

*   Correspondence: dapel@ualberta.ca (D.B.A.); skrzypko@agh.edu.pl (K.S.)

Abstract: In Canada, many mines have adopted the sublevel stoping method, such a blasthole stoping (BHS), to extract steeply deposited minerals. Sill pillars are usually kept in place in this mining method to support the weight of the overburden in underground mining. To prolong the mine's life, sill pillars will be recovered, and sill pillar recovery could cause failures, fatality, and equipment loss in the stopes. In this paper, three sill pillar recovery schemes—SBS, SS1, and SS2—were proposed and conducted to assess the feasibility of recovering two sill pillars in a hard rock mine by developing a full-sized three-dimensional (3D) analysis model employing the finite element method (FEM). The numerical model was calibrated by comparing the model computed ground settlement with the in situ monitored ground settlement data. The rockburst tendency of the stope accesses caused by the sill pillar recovery was assessed by employing the tangential stress (Ts) criterion and burst potential index (BPI) criterion. All three proposed sill pillar recovery schemes were feasible and safe to recover the sill pillars in this hard rock mine, and the scheme SBS was the optimum one among the three schemes.

1. Introduction

In underground mining, to improve production, several mining levels are generally active in the mining process at different mining depths, simultaneously. The mining process will cause redistributed stresses, which may transfer horizontally and vertically. The transferred stress may contribute to failure of the stopes and damage to the mining equipment. For the sake of mining zone safety, sill pillars are commonly reserved to prevent the transfer of the redistributed stress, especially in the steeply dipping orebodies. In most cases, sill pillars are recovered to prolong the mine life and maximize the usage of minerals. Pillar recovery is the practice of developing several pillars and then extracting the pillars, and it is considered the most hazardous form of underground mining [1,2]. It can trigger risks during pillar recoveries such as overlaying rock breakage, stope failure, and pillar failure [1–4].

To better assess the stability and improve the safety of miners and mining equipment during sill pillar recovery, scholars initiated and proposed empirical, analytical theories, and numerical modelling methods. To understand the mechanisms of pillar failures, Hudyma and Potvin [5,6] studied the conventional ground control instruments, in situ field visual observations, and numerical analysis modelling. Mark [1,7–13] and Iannacchione [14] assessed the major hazard risks and analyzed the MHRA techniques to evaluate sill pillar recovery in the room-and-pillar mining method. Zur [15] proposed the enhanced cemented rockfill to recover pillars and revealed that the pillars used the passive confinement effect of cemented rockfill (CRF) to increase the post-peak load-bearing ability. Zhukova [16]

employed the monitored underground seismic registrations and proposed mathematical models to improve the safety operations in pillar recovery. Langston [17] designed the stope layout, pillar extraction schedule, and ground support to recover sill pillars safely. Sainsbury [18–20] examined sill pillar stability and failure mechanisms and simulated pillar recovery by replacing the orebodies with laboratory-tested stabilized rockfill to solve the technical risks caused by the proposed extraction method. Ghasemi [21,22] assessed the risk of pillar recovery operations and classified that risk into four categories by using failure indicators. Beruar [23] and Valley [24] developed and optimized the mining sequence and suggested new directions for the different methods and potential shortcomings to avoid during pillar recovery. Townend [25] initiated five mitigation strategies to mitigate the high-stress concentration while mining sill pillars. Zhou [26] investigated the instability of large mined-out areas triggered by dynamic disturbance resulting from residual pillar recovery. Kyei [27] selected the suitable blasted rock particle size for making CRF to backfill the mined-out stopes for sill pillar recovery.

Cemented rockfill (CRF) is widely used to improve the stability and safety of the whole mining pipe and the sill pillar recovery, while, in many cases, compared with the host rocks, the strength of the CRF is relatively lower [18–20,28–33]. Sill pillar recovery with the influence of backfilled CRF in the blasthole stoping (BHS) mining method has not been widely discussed. In this paper, three schemes of sill pillar recovery were proposed and implemented to investigate and assess the feasibility of recovering the two sill pillars in a hard rock mine by applying the finite element method (FEM).

2. Background and Methodology

The hard rock mine in this study initially operated as an open pit mine. Once the open-pit mining was completed, the mining operation shifted to the underground. Due to the geological structure and deposition of the minerals, the blasthole stoping (BHS) mining method was used to excavate the steeply dipped mining pipe. According to the mining plan, there are three planned mining blocks in mining pipe MP#1, namely Block-A, Block-B, and Block-C, as shown in Figure 1. There are two initially kept sill pillars between the mining blocks—Sill-1 and Sill-2. The two sill pillars work as the protective pillars, which can effectively prevent the transfer of redistributed stress from one block to another [30]. After the completion of the excavation of three mining blocks, the feasibility of recovery of these two sills then plays a significant role in the resource development plan and prolonging the mine's life.
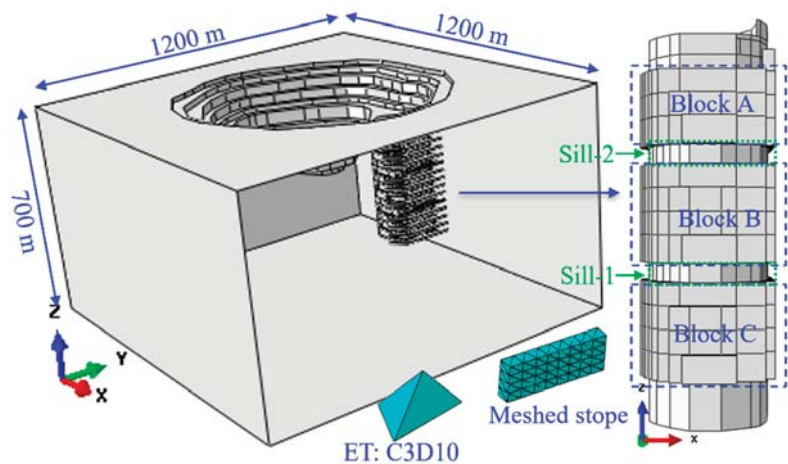
Figure 1. Two sill pillars in pipe MP#1.

Full-sized 3D models can estimate the deformations of underground openings and explore the mining-induced stress redistribution paths better than 2D analysis models [30,34–37]. Therefore, to better represent the complicated geometry of the stopes and haulages in the mining pipe at the hard rock mine, a full-sized elastoplastic three-dimensional (3D) model was developed by employing ABAQUS codes [38]. As illustrated in Figure 1, to better simulate the stress change paths in the stopes and haulages, the ten-node quadratic tetrahedron mesh element type (ET: C3D10) was used to mesh the stopes and analysis domain to conduct the simulation [38]. To make precise predictions, the model was created based on the real geometry of the stopes and haulages at the mine, and some modifications were made. To eliminate the influence of boundary effects of the model, an optimization study of the size of the analysis domain and a mesh convergence were conducted, and the analysis domain has a size of 1200 m × 1200 m × 700 m (length × width × depth), as shown in Figure 1 [39]. At the bottom of the model, the boundary conditions are applied to fix the bottom, and the top surface is set free. In addition, the horizontal restraints on both X and Y directions are applied to the four vertical boundaries of the model.

To achieve the parameters of the rock samples, several laboratory tests were conducted. Table 1 shows the rock mechanical properties applied in the model in this study [39]. Here, γ is the unit weight, C is the cohesive strength, ϕ is the angle of friction, E is the elastic Young's modulus, ν is the Poisson's ratio, and σ_c is the uniaxial compressive strength.

Table 1. Properties applied in the numerical model.

Rock Mass	γ (MN/m^3)	C (MPa)	ϕ (°)	E (GPa)	ν	σ_c (MPa)
MP#1	0.024	4.7	28.1	19.6	0.24	79
CRF	0.022	1.2	35	2	0.3	1.5
Granite	0.026	9.3	45	24	0.3	130

3. Calibration and Verification of the Finite Element (FE) Model

The finite element (FE) numerical analysis model is capable to conduct general study and helping the engineer to understand better the "real world" of the underground space [40–45]. Model calibration is a vital step in checking the reliability of the developed numerical model by comparing the monitored and recorded in situ data with the computed data from the developed numerical model.

In this paper, to calibrate the developed FE model, several monitor prisms were installed on the open pit benches to measure the ground surface subsidence induced by the mining activities in the mining pipe. Figure 2 presents the location of the installed monitor prisms on the benches. Monitoring zone 1 has two prisms: CRF-S01 and CRF-S02. Monitoring zone 2 has two prisms: CRF-N01 and CRF-N02. Both monitoring zone 1 and monitoring zone 2 are on the boundary of the top surface of the mining pipe MP#1. Monitoring zone 3 also has two prisms: 280-10 and 280-12.

Before implementing the simulation of the recovery process of the sill pillars, the developed numerical model was calibrated by comparing the ground surface settlement at monitoring zone 1 (prism CRF-S01, CRF-S02) and monitoring zone 2 (prism CRF-N01, CRF-N02) with the computed ground surface settlement from the numerical model. As a result, it takes 83 simulation steps, based on in situ production schedules, to excavate and backfill the three mining blocks in the developed analysis model.
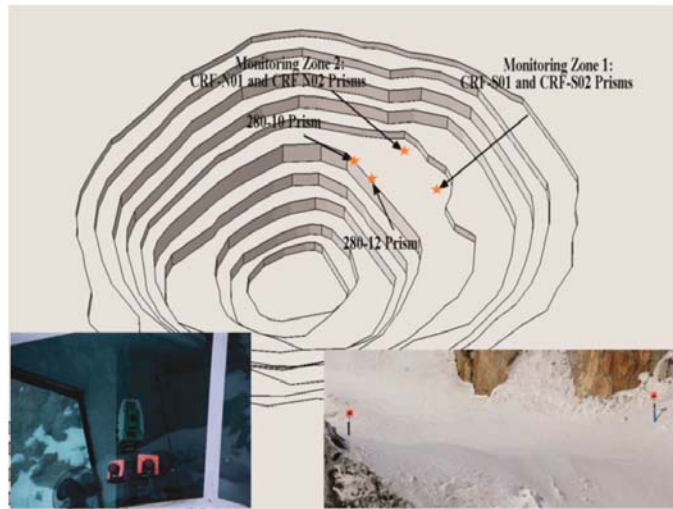
Figure 2. The open pit bench at the mine [30].

The profile of the computed displacement of the open pit slopes in the FE model is shown in Figure 3. The main areas with maximum ground settlement are over the mining pipe MP#1, where the mining activities are in active production. Though the three mining blocks were backfilled with cemented rockfill (CRF), the open pit boundary in the developed model, where the dike is located, still sees a tiny increase in displacement after the completion of the excavation and backfilling of the three mining blocks. The stability and safety of the protective dike play a significant role in mine site safety.
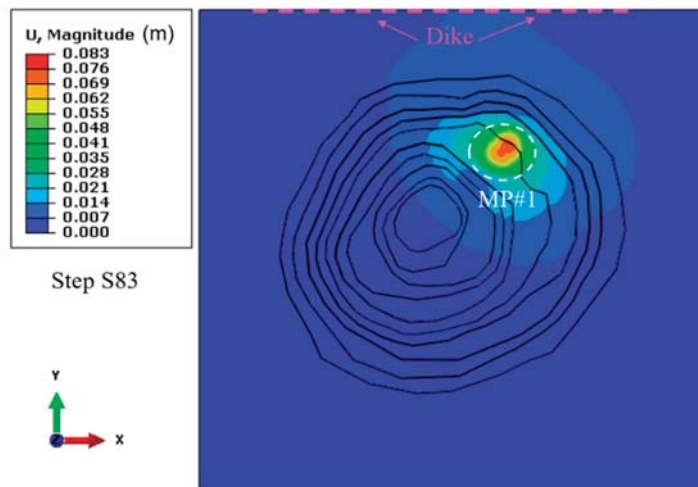
Figure 3. Computed displacement in the FE model before sill pillar recovery.

The comparison of the accumulated ground displacement between the in situ recorded data and the computed FE model results is shown in Table 2. The relative errors in different zones are 2.57% and 8.01% in zone 1 and 2, respectively. The average relative error is 5.29%, which is acceptable in mining engineering simulation analysis [30,46–48].

Table 2. In situ displacement and the FE model computed displacement.

Monitoring Prism Location	FE Model (mm)	In-Situ Data (mm)	Relative Error (%)
Monitoring zone 1 (Ave-S01 & S02)	45.50	46.7	2.57
Monitoring zone 2 (Ave-N01 & N02)	36.38	39.55	8.01
Average relative error			5.29

The analysis model calibration conducted via comparison of the ground displacement caused by the excavation and backfilling process of the three mining blocks, between the recorded in situ data and the computed simulation results of the FE model verifies that the developed FE analysis model is reliable and capable of conducting and implementing the simulation steps of the sill pillar recovery process.

4. Schemes of Sill Pillar Recovery

From the above FE model calibration, by comparison of the in situ recorded displacement and the computed results in the developed FE model, the developed FE model is capable and precise in conducting the numerical simulation to assess the feasibility of the recovery of the two sill pillars in the mining pipe MP#1.

4.1. Primary and Secondary Mining Sequence in Blasthole Stoping Mining Method

All three sill pillar recovery schemes follow the primary and secondary mining sequence to keep the sequence constant with the three mining blocks' mining schedules. The primary sequence stopes will be excavated firstly, and then the secondary sequence stopes will be excavated. Figure 4 shows an example configuration of the mining stopes of two mining levels. The colors orange, blue, purple, and green represent the mining sequence. Blue and green represent the primary mining sequence, and orange with purple for the second mining sequence. Here, P stands for the primary sequence, P1 means those stopes will be mined first in the primary sequence, and P2 stands for the second round of mined stopes in the primary sequence. Then, S stands for the secondary sequence, S1 means the first round of mined stopes in the secondary sequence, and S2 means the second round of mined stopes in the secondary sequence. When the stoping starts, stope P1-65 will first be mined out, followed by P1-95. After the first round in the primary sequence finishes, the second round of the primary sequence starts, and then the first round in the secondary sequence starts, followed by the second round in the secondary sequence. The stope of S2-193 will be the last mined-out stope in this level. Each stope will be backfilled as soon as it is mined.
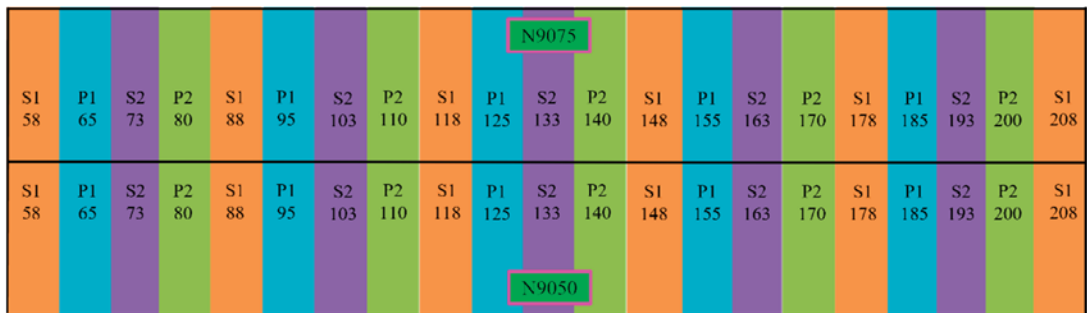
Figure 4. The stope mining sequence in the example two levels.

4.2. Three Proposed Sill Pillar Recovery Schemes

Three sill pillar recovery schemes are proposed to recover the two sill pillars. To keep the mining sequence consistent with the designed sequence schedule at the mine,

the mining sequence to recover the two sill pillars follows the sequence of mining and backfilled the three mining blocks in mining pipe MP#1. The first mined stopes in the three recovery schemes of the two sill pillars are labelled with the color magenta, as shown in Figure 5.

Figure 5. Profile of the sill pillar recovery scheme of SBS, SS1, and SS2.

The first proposed scheme of the recovery process starts at both sill pillars (SBS), from the stope P1-65 to the two sill pillars are excavated and backfilled, and the simulation steps start from step S84 to step S94. The second proposed scheme of the recovery process starts at Sill-1 (SS1), as shown in Figure 5, from the stope P1-65, and when all the stopes are excavated in Sill-1, then the mining process moves to Sill-2, until the two sill pillars are recovered and backfilled, and then simulation steps start from step S84 to step S98. Finally, the third proposed scheme of recovery process starts at Sill-2 (SS2), as shown in Figure 5, from the stope P1-65, and when all the stopes in Sill-2 are excavated, the mining process moves to Sill-1, until all the sill pillars are recovered and backfilled, and similarly with SS1, the simulation steps start from step S84 to step S98.

5. Displacement Caused by the Three Sill Pillar Recovery Schemes

5.1. Displacement at the Three Monitoring Zones

When conducting the recovery of the two sill pillars, the open pit benches are still in function to transport the orebodies from the sill pillars in mining pipe MP#1 to the ground surface. Then, the benches' stability is still a key issue to be considered.

From simulation step S84, the recovery process starts. Scheme SBS takes 11 simulation steps to recover and backfill the two sill pillars, and the simulation step ends at step S94. Both schemes SS1 and SS2 take 15 steps to recover and backfill the two sill pillars, and the simulation step ends at step S98. Though it takes different simulation steps to recover and backfill the two sill pillars, the mining-induced displacements at the monitored zones during the recovery process are almost the same. Figure 6 presents the computed displacement from the FE model at prisms 280-10 and 280-12. The final three displacements at prism 280-10 are −19.42 mm, −19.34 mm, and −19.43 mm, from recovery schemes SBS, SS1, and SS2, respectively. For the prism 280-12, the final three displacements are −22.24 mm, −22.20 mm, and −22.25 mm, respectively, from recovery schemes SBS, SS1, and SS2.
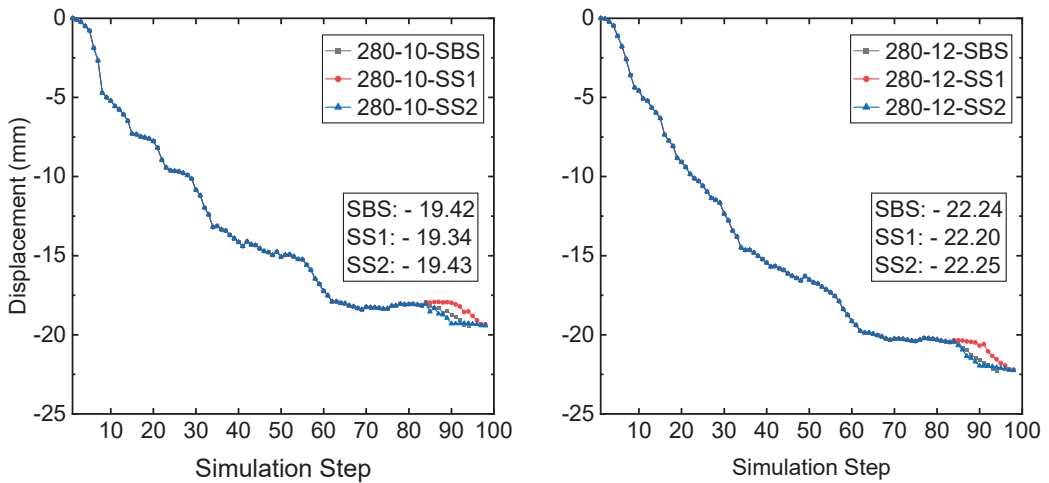
Figure 6. A comparison of displacement at monitored prism 280-10 and 280-12.

The displacements at monitoring zone 1 and zone 2 are shown in Figure 7. Like the displacement at monitoring zone 3, the final displacements of three different recovery schemes are very close at both monitoring zone 1 and zone 2. At the prism CRF-S, the three displacements are −48.49 mm, −48.39 mm, and −48.47 mm, respectively, from recovery schemes SBS, SS1, and SS2. The three displacements at the monitoring prism CRF-N are −38.45 mm, −38.38 mm, and −38.44 mm, from recovery schemes SBS, SS1, and SS2, respectively.
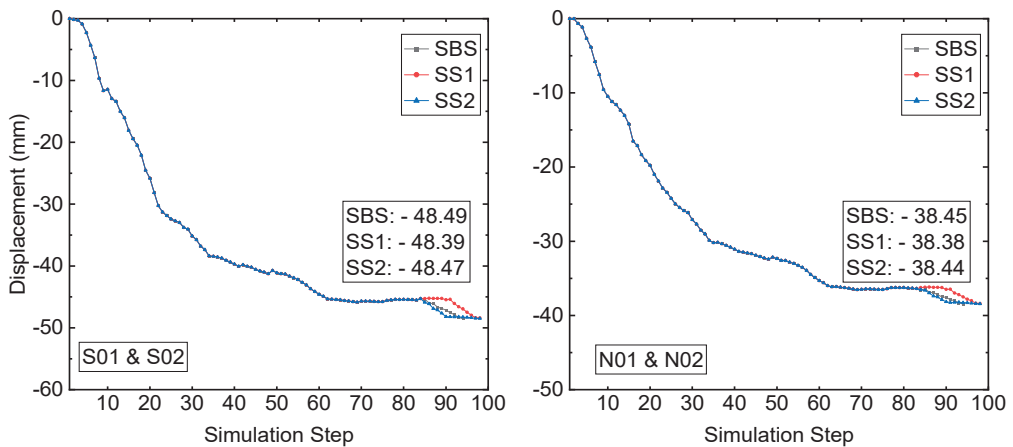
Figure 7. A comparison of the displacement at monitored sites S01-02 and N01-02.

During the mining and backfilling of the three mining blocks, the mining-induced displacement at the three monitoring zones reaches a value of 46.7 mm (CRF-S) and 39.55 mm (CRF-N), respectively. From the mining-induced displacement view, the three different schemes of sill pillar recovery have very close results at the two monitoring zones. Also, the displacement induced by the process of sill pillar recovery sees a slight increase at all three monitoring zones. Table 3 presents the displacement induced by the process of sill pillar recovery at the monitoring prisms.

Table 3. Sill pillar recovery induced displacement at monitoring zones.

Monitoring Zone	Displacement Caused by Recovery Scheme		
	SBS (mm)	SS1 (mm)	SS2 (mm)
280-10	1.77	1.73	1.78
280-12	0.97	0.86	0.98
CRF-S	2.99	2.89	2.97
CRF-N	2.07	2.00	2.06

All displacements induced by the three sill pillar recovery schemes are not more than 3 mm. Therefore, the backfilled CRF in the three mining blocks provides sufficient support for the process of sill pillar recovery. Furthermore, all three schemes of sill pillar recovery can be implemented.

5.2. Displacement of the Upper Levels

From the upper levels to the MP#1 mining pipe, there are four levels of open-pit benches, as shown in Figure 8. Several locations are chosen on bench levels in the numerical FE model to monitor the displacement on the benches caused by the mining activities and sill pillar recovery process in the mining pipe MP#1.
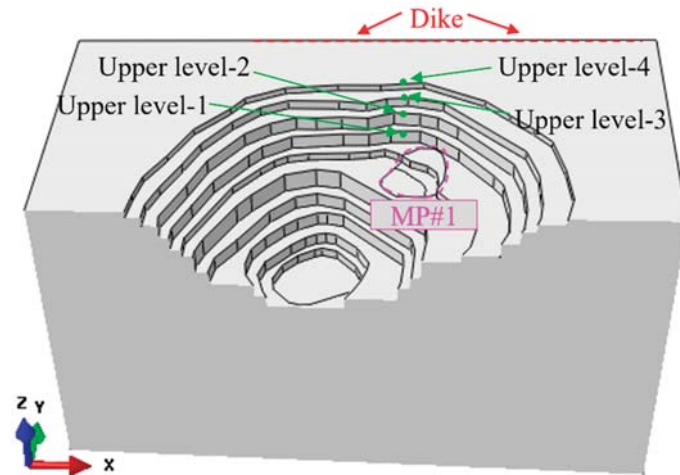
Figure 8. The chosen monitored location on the upper bench levels.

The four selected upper levels are marked with upper level-1 (UL-1), upper level-2 (UL-2), upper level-3 (UL-3), and upper level-4 (UL-4), as shown in Figure 8. Here, upper level-4 (UL-4) is the ground surface at the mine. The elevation between the top surface of mining pipe MP#1 and the ground surface is 94 m. Therefore, the depths of the four bench levels are 0 m, −14 m, −34 m, and −64 m, from upper level-4 (UL-4) to upper level-1 (UL-1), from the ground surface to the top surface of the bench level-1 (UL-1).

The average displacements at the analyzed locations on the four upper bench levels in the numerical model caused by the mining activities and the three sill pillar recovery schemes process are presented in Figure 9. From the beginning of the mining production in mining pipe MP#1 to the state of three mining blocks which were all mined and backfilled, the process of mining and backfilling in pipe MP#1 caused the displacement of −13.50 mm, −11.56 mm, −10.73 mm, and 9.76 mm, from upper bench level-1 (UL-1) to upper bench level-4 (UL-4). Compared to the displacement of the monitored prisms at the monitoring zones around the boundary of the top surface of mining pipe MP#1, the displacements at the upper bench levels caused by the mining activities of three mining blocks in mining

pipe MP#1 are much smaller. From upper bench level-1 (UL-1) to upper bench level-4 (UL-4), the mining-induced ground displacement at the bench level decreased constantly, which proves the influence on the displacement of the upper benches caused by the mining activities in mining pipe MP#1 decreasing with the increase of the distance between the upper benches and the top surface of the mining pipe MP#1.
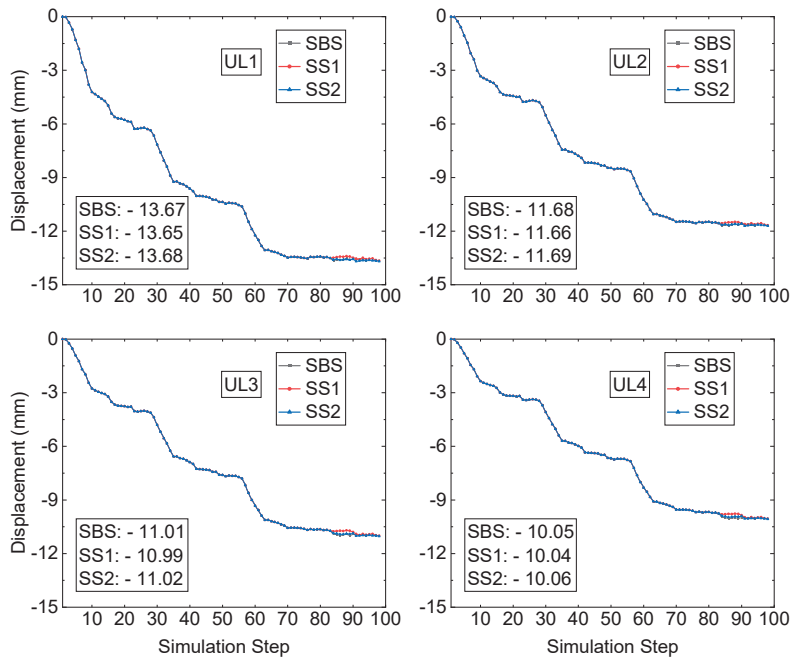
Figure 9. A displacement comparison at the monitored locations.

The sill pillar recovery process commences from simulation step S84 and ends at steps S94, S98, and S98 by scheme SBS, SS1, and SS2, respectively. Table 4 presents the average displacements at the upper bench levels of the analyzed locations induced by the sill pillar recovery and backfilling process.

Table 4. Sill pillar recovery induced displacement at upper levels.

Analyzed Location	Recovery Scheme		
	SBS (mm)	SS1 (mm)	SS2 (mm)
UL-1	0.168	0.147	0.180
UL-2	0.128	0.111	0.139
UL-3	0.284	0.294	0.294
UL-4	0.294	0.282	0.303

From Figure 9 and Table 4, the displacements of the analyzed locations at the upper bench levels caused by the process of sill pillar recovery conducted by the three sill pillar recovery schemes have a slight increase from upper level-1 (UL-1) to upper level-4 (UL-4). The maximum one is 0.303 mm at the upper level-4 (UL-4) from sill pillar recovery scheme SS2. The three sill pillar schemes are feasible because of the small displacements of the analyzed upper-level locations in the numerical model and monitoring prisms at the in-situ field.

6. Assessment of the Stope Accesses Stability among Three-Pillar Recovery Schemes

In underground mining, stope accesses are excavated to connect the stopes and haulages, and stope accesses are used as paths to transport the minerals and other materials between the ground surface and underground working sites. Compared to other underground mining structures, stope accesses serve the longest time for the production in the mine. Therefore, the stability of the stope accesses has a significant effect on the production schedule. Thus, assessing the stability of the stope accesses is critical in assessing the feasibility of the sill pillar recovery.

According to the studies done by Sepehri [30], Leveille [49,50], and Pu [51], kimberlite and granite in the hard rock mine have the potential for rockburst, which could cause severe damage to the roofs and sidewall surfaces in the stopes and crosscuts. In addition, some reported rockburst failure cases located near the stope accesses in this hard rock mine, as shown in Figure 10. Hence, the stability of the stope access is a key issue to be assessed.

Figure 10. Failure cases near the stope access.

6.1. Stress Condition in the Two Sill Pillars Pre-Sill-Pillar-Recovery

In this hard rock mine, the reserved sill pillar consists of several mining stopes, and each stope can contain thousands of tons of minerals. Compared with the backfilled CRF in the mined voids, the unmined stopes in the sill pillar will provide more support than the backfilled CRF [39]. After completing the excavation and backfilling of the three mining blocks, the stress field changed and was redistributed. Due to the vast volume of the backfilled CRF, there are some yield zones in the unmined sill pillars. Figure 11 presents the yield zone in the two sill pillars at steps S1 and S83. In Figure 11, in the mining pipe MP#1, the yellow areas are the two sill pillars, and the other zones are backfilled CRF.
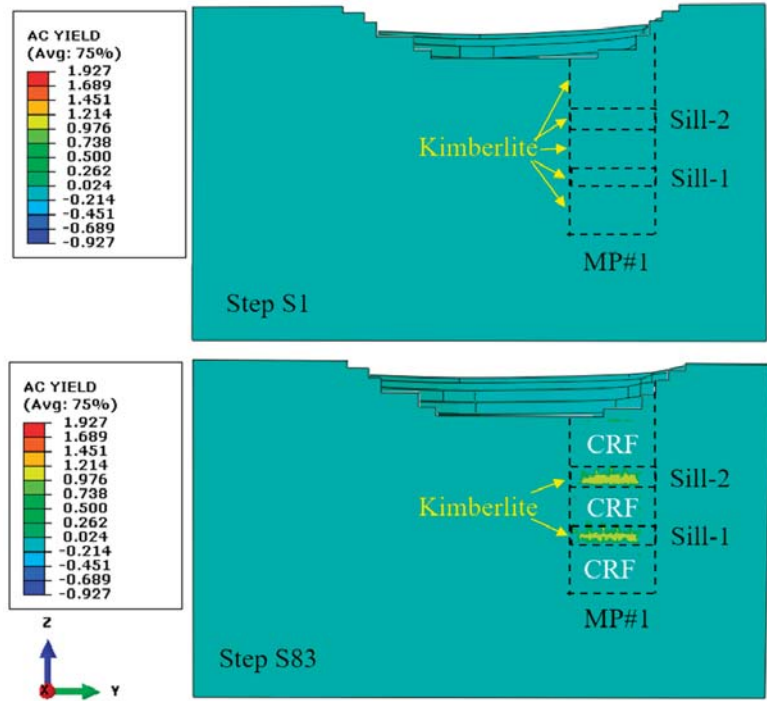
Figure 11. Yield zones in the MP#1 at step S1 and step S83.

6.2. Assessment of the Stope Access Stability among Three-Pillar Recovery Schemes

6.2.1. Tangential Stress Criterion (Ts)

For a rockburst to occur, the rock mass must have the ability to store a considerable amount of strain energy which can be released violently at failure, and there must be an environment for stress concentration and energy accumulation [33,52,53]. Here, the tangential stress criterion was used to compare the stability assessment among the three sill pillar recovery schemes, SBS, SS1, and SS2. According to Wang and Park [53], the rockburst tendency can be evaluated using *Ts* criterion, as presented in Table 5.

Table 5. Rockburst tendency prediction based on tangential stress criterion.

Tangential Stress Criterion (Ts)	Rockburst Tendency
Ts ≥ 0.7	Violent
0.5 ≤ Ts < 0.7	Strong
0.3 ≤ Ts < 0.5	Weak
Ts < 0.3	No rockburst

In a two-dimensional study, with the influence of the backfilled CRF, in the process of sill pillar recovery, the two edges of the mining pipe have a higher possibility of instability in the overcuts and undercuts compared to the crosscuts in the middle area of the mining level [32,33]. The stope access from three representative locations of left-edge, middle line, and right-edge are analyzed to conduct the assessment, as shown in Figure 12. Both the left-edge stope access and right-edge stope access are close to the boundaries between the mining pipe MP#1 and the host rock granite. The stope access has a section size of 5 m × 5 m (height × width).
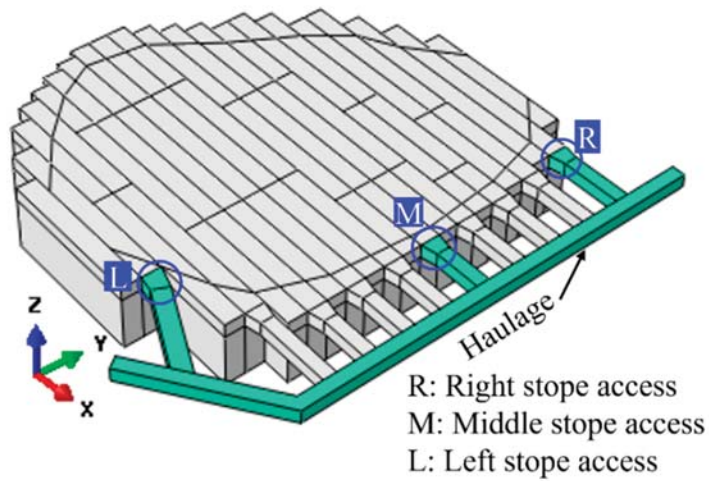
Figure 12. Analyzed stope access in sill pillar Sill-1.

According to Sepehri [30] and Xu [32,33,39], the boundaries of the mining pipe MP#1 have higher tangential stress than the center of the mining pipe, and with the increase of the mining depth, the possibility of the potential rockburst is higher. Hence, the stope accesses to the undercuts of stopes in Sill-1 from the three locations are chosen to conduct the assessment.

In underground rectangular openings, the four corners will easily generate the stress concentration effect, which may cause failures at these locations [33]. Four corners in the overcut and undercut are chosen to conduct the stability assessment comparison among the three sill pillar recovery schemes; UP1 is the left roof corner, UP2 is the right roof corner, DN1 is the left floor corner, and DN2 is the right floor corner, as shown in Figure 13.
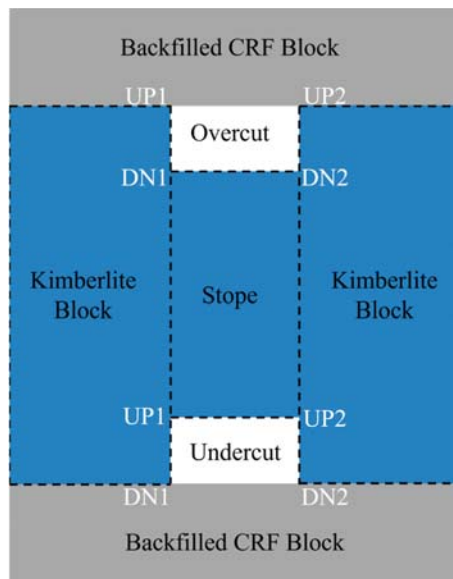
Figure 13. A profile of the chosen corners in the overcut and undercut accesses.

All three sill pillar recovery schemes start at simulation step S84; the following figures start from simulation step S83, which is the last step of excavation and backfilling of the three mining blocks, and simulation step S84 is the first step to recover the sill pillars by three recovery schemes. The Ts values are compared among three sill pillar recovery schemes at the four corners in the stope access section at three stope locations.

The Ts of the four corners at the undercut access in the right-edge stope in Sill-1 is shown in Figure 14. For the left roof corner UP1, the Ts value is less than 0.3, though at some step it reaches 0.3, and with the backfilling coming into effect at the flowing step, it goes down to a value under 0.1, then is safe for this corner based on the Ts value, and according to Table 5, there is no rockburst tendency. For the right roof corner UP2, from the beginning of the recovery, it is over 0.3, which means it is not stable as the left roof corner. Referring to Table 5, with a Ts value between 0.3 and 0.5, there is a rockburst tendency, though it is weak. For the left floor corner DN1, the Ts value is always under 0.1, which means there is no tendency of rockburst. For the right floor corner DN2, similar to the right roof corner, the value of Ts is between 0.3 and 0.5, presenting a weak tendency of rockburst. Comparing the Ts value at the four corners in the stope access to the undercut of the right edge in the Sill-1, the right side of the undercut access is more unstable than the left side. The right roof corner and floor corner present weak rockburst tendency, while the left side has no rockburst tendency.
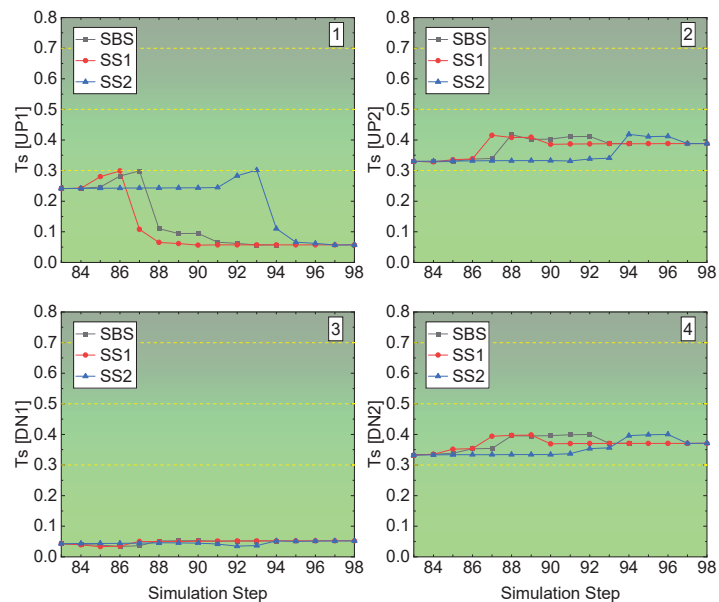
Figure 14. Ts value of the right-edge stope access to undercuts in Sill-1.

The rockburst tendency at the four corners in the middle stope undercut access in Sill-1 is shown in Figure 15. Unlike the right-edge stope access to the undercut, the four corners in the middle stope access to undercut show no rockburst tendency. Both the corners of the floor have a value of Ts less than 0.1, while the roof corners have a more considerable Ts value, though it is under 0.3. In Figure 13, the roof corners are in the unmined kimberlite rock mass, while the floor corners are in the backfilled CRF block. Although, according to the rock mechanics properties parameters in-put in the developed FE model in Table 1, the backfilled CRF has lower strength and elastic properties than the kimberlite block, when the backfilling finishes, the backfilled CRF could fail, but not in the type of rockburst.
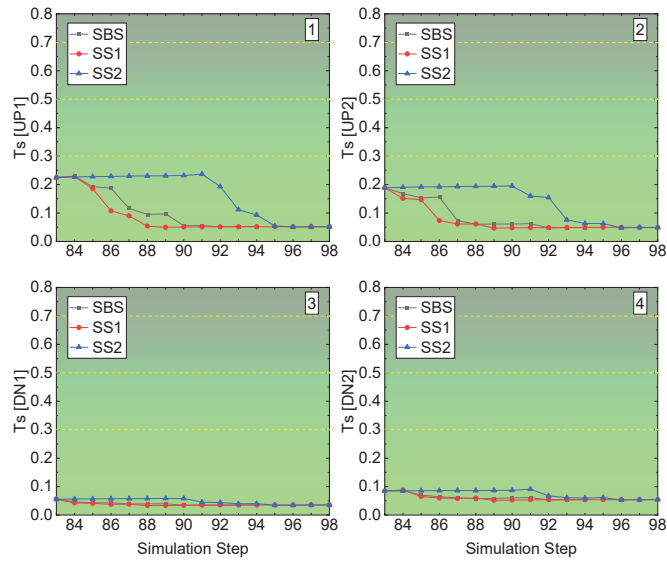
Figure 15. Ts value of the middle stope access to undercuts in Sill-1.

The rockburst tendency of the four corners in the left-edge stope access to the undercut is illustrated in Figure 16. Like the middle stope access to undercut, there is no rockburst tendency in the four corners. While compared with the floor corners, the roof corners have high values of Ts. The floor corners have a Ts value under 0.05 among the three sill pillar recovery schemes. For the roof corners, UP1 and UP2, though the three sill pillar recovery schemes cause a different value of Ts, the Ts is under 0.2, and after the completion of the recovery and backfilling of the two sill pillars, the Ts values of the three sill pillar recovery schemes reach the same final state of Ts.
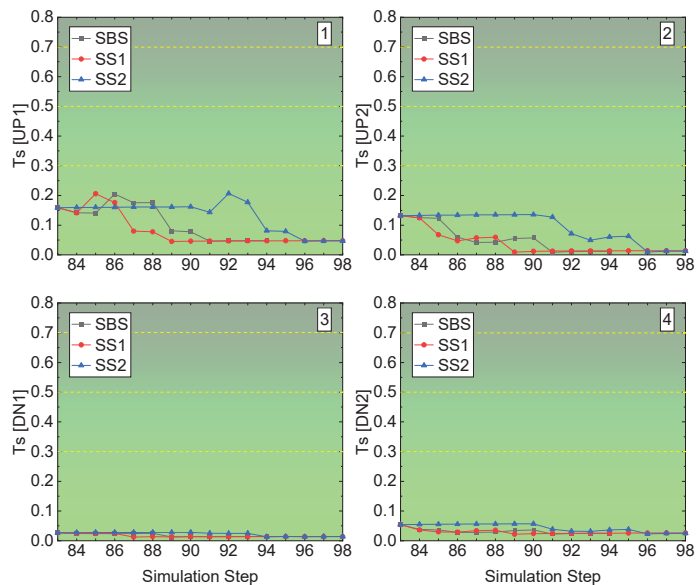
Figure 16. Ts value of the left-edge stope access to undercuts in Sill-1.

Referring to Figure 12, in which the locations of the three analyzed stope accesses were marked, based on the results presented in Figures 14–16, the right-edge stope access has a higher value of Ts, indicating the rockburst tendency at the right side of the right-edge stope access is higher than any other location in the other two stope accesses, the left-edge one and the middle one.

6.2.2. Energy-Based Burst Potential Index Criterion (BPI)

According to the studies of [30,49–51], the rockburst that occurred at this mine was classified as strainburst. Mitri [54] proposed the energy-based burst potential index (BPI) to better assess and predict the rockburst in the underground rock mass. Violent failure (rockburst) will occur when the energy stored in the rock mass exceeds the critical energy value (e_c) [54–58]. The e_c is the maximum capacity of the rock mass to store energy, and it can be obtained from the uniaxial compressive strength (UCS) test or the UCS hysteresis looping test curve with the following equation:

$$e_c = \sigma_c^2/2E \tag{1}$$

where σ_c is the UCS and E is Young's modulus in the UCS test. It should be noted that estimating e_c using Equation (1) is a conservative approach because the energy dissipated by fracturing and plastic deformations is neglected. Therefore, the BPI can be defined as

$$BPI = ESR/e_c \times 100\% \tag{2}$$

where ESR is the energy storage rate (kJ/m^3) in the rock mass, and e_c is the critical elastic strain energy density (SED) (kJ/m^3) of the rock. The larger the value of the BPI, the higher the probability of a rockburst occurring. According to Leveille [48], kimberlite's average critical energy (e_c) value in mining pipe MP#1 is 119.7 kJ/m^3.

Based on the computed ESR from the FE analysis model, the burst potential index (BPI) of the four corners of stope accesses to the undercuts and overcuts in the Sill-1 and Sill-2 during the process of recovery of two sill pillars conducted by the three recovery schemes can be calculated, and the following figures present the results.

At the right-edge stope access, all four corners have a low value of BPI, as shown in Figure 17. For the left roof corner UP1, during the whole process of recovery, among the three recovery schemes, the BPIs are less than 10%, though with a slight increase caused by the excavation. On the other hand, for the right roof corner UP2, the BPIs see a swift increase caused by the excavation of the stope access at the specific simulation steps among the three recovery schemes.

Before the excavation occurs, the BPIs stay at a stable value of 12.5%; due to the excavation, it increases to 20%, after the backfilling, and then comes down to the initial value of 12.5%, which proves the backfilled CRF can effectively lower the BPI by providing the immediate support. The left floor corner DN1 has the lowest BPI among these four corners in the stope access, and it is 5%, keeping stable. For the right floor corner, with an increase of 4.5% from 10.5% to 15%, all three recovery schemes end at 14%.

For the middle stope access to undercut in Sill-1, compared with the right-edge one, the BPIs are much smaller, as shown in Figure 18. For the two roof corners, UP1 and UP2, which have the highest BPI compared to the floor corners, the BPIs are not larger than 5%, and the excavation simulation step causes a decrease at both roof corners, as shown in the first and second pictures. On the two-floor corners, DN1 and DN2, as shown in the third and fourth pictures, the BPIs are even much smaller; both are less than 2%, though with the process of excavation, among the three recovery schemes, for recovery schemes SS2, before the excavation occurs, the BPI keeps stable as 2%.
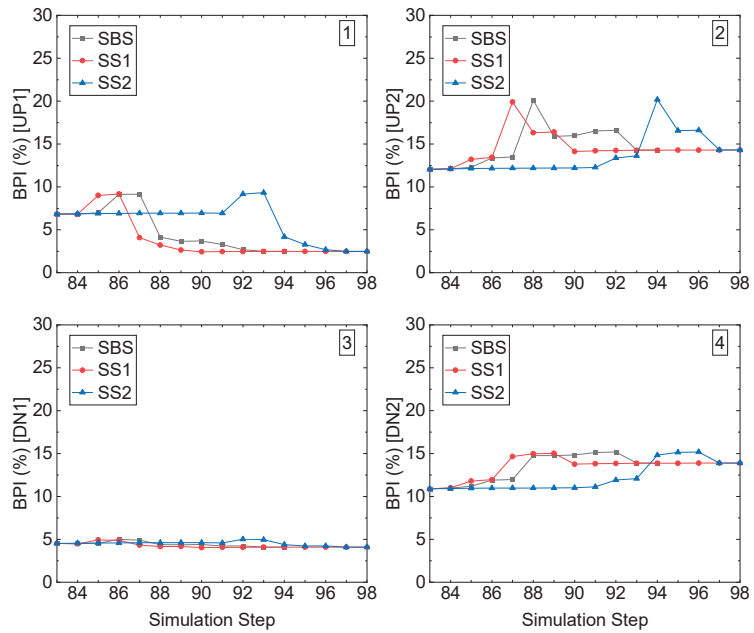
Figure 17. BPI value of the right-edge stope access to the undercut in Sill-1.
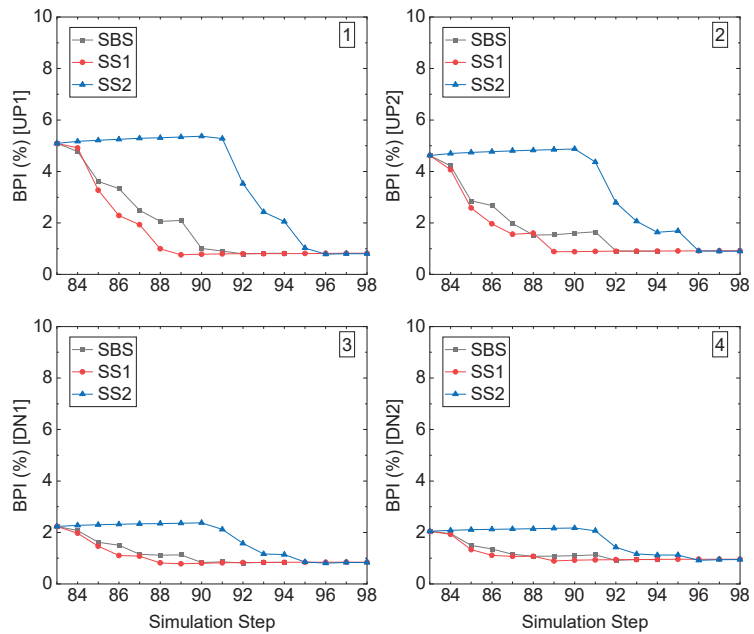
Figure 18. BPI value of the middle stope access to the undercut in Sill-1.

Figure 19 illustrates the BPI of the four corners in stope access to undercut in the left-edge stope in Sill-1. Like the right-edge stope access, the left roof corner UP1 increases, caused by the excavation, and the subsequent decrease, caused by the backfilled CRF,

among the three recovery schemes. All the BPIs of the three recovery schemes are less than 9%, though the excavation caused the increase. The right roof corner, UP2, sees a constant decrease during the excavation and backfilling sill pillar recovery, and it is under 6% the whole process. For the two-floor corners, DN1 and DN2, the BPIs are under 3%, and for DN2, the BPI is even under 1.5%.
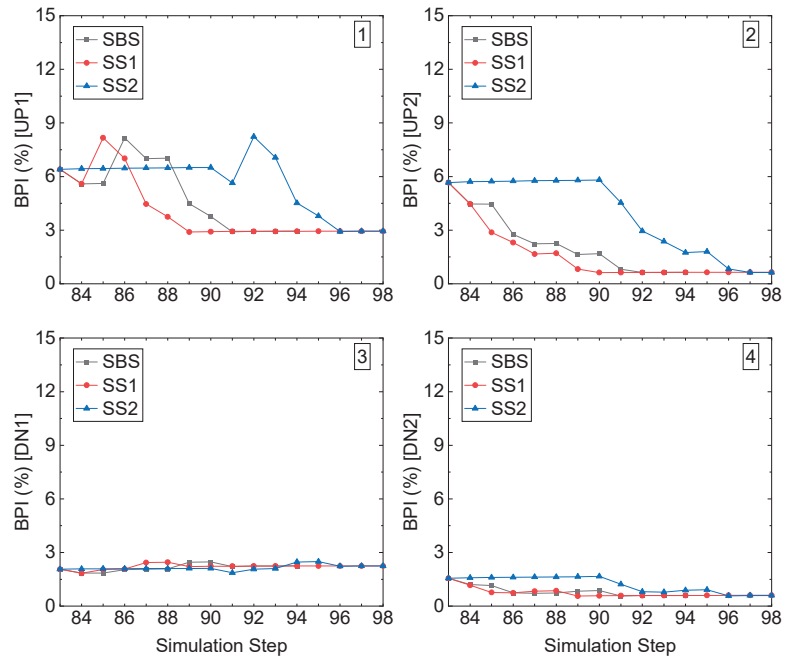
Figure 19. BPI value of the left-edge stope access to the undercut in Sill-1.

Similar to the tangential stress criterion (Ts) results, compared with the stope accesses to the undercuts in left edge-located stope and middle stope in Sill-1, the right-edge stope access has a higher value of BPI due to the contact boundary of kimberlite and granite.

7. Discussion

In the previous studies [32,33], the authors used the two-dimensional (2D) models to analyze the displacement of the crosscuts to assess the stability of the stopes, and the displacement was the only factor in conducting the assessment. To make a more precise and comprehensive analysis and prediction, a full-sized elastoplastic three-dimensional (3D) model was developed in this paper by simulating the whole mining schedule process of stope excavation and backfilling. Different from other studies [1–7,12,14,16,17], in the presented research, a full-size 3D analysis model of the mine was constructed to make the predication and analysis more precise and accurate by simulating the whole process of excavation and backfilling of the stopes, and rockburst tendency as the key factor was considered, and three different sill pillar recovery schemes were proposed.

The developed three-dimensional (3D) finite element (FE) analysis model was firstly calibrated and verified. Then, the sill pillar recovery simulation by three recovery schemes, SBS, SS1 and SS2, was conducted to investigate the feasibility of two sill pillars recovery. Finally, the displacement of the four monitoring prisms and four upper levels were chosen as indicators of the failure of the protective dike.

According to the displacement results of the four upper bench levels, the three sill pillar recovery schemes had an extremely low possibility of causing failures of the four

upper bench levels and the dike since the maximum displacements of the monitoring prism and the upper level was 2.99 mm (CRF-S) and 0.303 mm (UL-4), respectively.

The tangential stress criterion (Ts) and burst potential index criterion (BPI) were introduced and applied to assess the stability of the stope access to the two sill pillars during the process of the sill pillar recovery. The results of the sill pillar Sill-1 were presented since the mining depth of sill pillar Sill-1 was deeper. Though, at the access to the right-edge stope, weak rockburst tendency presented, advanced measures, such as stress-release, can be taken to reduce the damages caused by rockburst occurrence.

8. Conclusions

With an average relative error of 5.29% from the displacement comparison between the in situ recorded data and the FE model computed results, the developed numerical model was calibrated and proved to be capable of assessing the feasibility of the sill pillar recovery in the hard rock mine.

The maximum ground displacements caused by the recovery of the two sill pillars at the four monitoring prisms were 1.78 mm (280-10), 0.98 mm (280-12), 2.99 mm (CRF-S), and 2.07 mm (CRF-N), respectively. In addition, the displacements of the four upper bench levels caused by the sill pillar recovery were also presented, and the maximum displacement at each upper bench level was 0.18 mm (UL-1), 0.139 mm (UL-2), 0.294 mm (UL-3), and 0.303 mm (UL-4), respectively, which indicated that the protective dike would be stable during the sill pillar recovery.

During the process of sill pillar recovery, according to the tangential stress criterion (Ts) results, in Sill-1, the stope accesses to the right-edge stope had a weak rockburst tendency, while the accesses to the left-edge and middle stope did not tend rockburst. Similar to the Ts criterion scenarios, the results of BPI criterion showed that only the right-edge stope access in Sill-1 has a possible rockburst tendency at the right roof corner and the right floor corner.

Considering the displacement of the monitoring prisms and the upper bench levels above mining pipe MP#1, and the stability of the stope accesses in the sill pillar Sill-1, all three sill pillar recovery schemes are feasible and rational. Therefore, any scheme can recover the two sill pillars. However, the recovery scheme SBS, starting the sill pillar recovery process from both sill pillars, is the optimum one among the three schemes. This is because the recovery scheme SBS simultaneously conducts the mining activities in both two sill pillars, which takes less time than the other two recovery schemes. Hence, recovering the two sill pillars by scheme SBS is more productive than the other schemes. In addition, recovering the two sill pillars by scheme SBS will reduce the cost of ventilation and other maintenance by taking less time in the recovery process, thus increasing the profit of the mine.

Author Contributions: Data curation, H.X., J.W. and C.W.; Funding acquisition, D.B.A.; Methodology, H.X. and K.S.; Project administration, D.B.A.; Supervision, D.B.A.; Writing—original draft, H.X.; Writing—review & editing, D.B.A. and K.S. All authors have read and agreed to the published version of the manuscript.

Informed Consent Statement: Not applicable.

Conflicts of Interest: The authors declare no conflict of interest.

References

1. Mark, C.; Chase, F.; Pappas, D. Reducing the risk of ground falls during pillar recovery. *Trans.-Soc. Min. Metall. Explor. Inc.* **2003**, *314*, 153–160.
2. Mark, C.; Chase, F.E.; Pappas, D.M. Analysis of multiple seam stability. In Proceedings of the 26th International Conference on Ground Control in Mining, Morgantown, WV, USA, 31 July–2 August 2007; pp. 5–18.

3. Mark, C.; Gauna, M. Preventing roof fall fatalities during pillar recovery: A ground control success story. *Int. J. Min. Sci. Technol.* **2017**, *27*, 107–113. [CrossRef]
4. Henning, J.G.; Yu, T.R.; Zou, D.H. Rock mechanics aspects of sill pillar recovery at Kidd Creek Mine. In Proceedings of the 16th Canadian Rock Mechanics Symposium, Sudbury, ON, Canada, 11–15 June 1992.
5. Hudyma, M.R.; Potvin, Y.; Grant, D.R.; Milne, D.; Brummer, R.K.; Board, M. Geomechanics of sill pillar mining. In Proceedings of the 1st North American Rock Mechanics Symposium, American Rock Mechanics Association, Austin, TX, USA, 1–3 June 1994.
6. Potvin, Y.; Hudyma, M. Open stope mining in Canada. In Proceedings of the MassMin 2000, Brisbane, Australia, 29 October–2 November 2000.
7. Mark, C.; Tuchman, R.J. *Proceedings: New Technology for Ground Control in Retreat Mining*; U.S. Department of Health and Human Services: Pittsburgh, PA, USA, 1997.
8. Mark, C.; McCall, F.E.; Pappas, D.M. A statistical overview of retreat mining of coal pillars in the United States. In *Proceedings: New Technology for Ground Control in Retreat Mining*; No. 97–122; U.S. Department of Health and Human Services: Pittsburgh, PA, USA, 1997; pp. 2–16.
9. Mark, C.; Chase, F.E.; Campoli, A.A. Analysis of Retreat Mining Pillar Stability. In Proceedings of the 14th Conference on Ground Control in Mining, Morgantown, WV, USA, 1–3 August 1995; pp. 17–37.
10. Mark, C.; Zelanko, J.C. Sizing of final stumps for safer pillar extraction. In Proceedings of the 20th International Conference on Ground Control in Mining, Morgantown, WV, USA, 7–9 August 2001; pp. 59–66.
11. Esterhuizen, E.; Mark, C.; Murphy, M.M. Numerical model calibration for simulating coal pillars, gob and overburden response. In Proceedings of the 29th International Conference on Ground Control in Mining, Morgantown, WV, USA, 27–29 July 2010; pp. 46–57.
12. Zelanko, J.C.; Mark, C. Reducing roof fall accidents on retreat mining sections: Developing and following a mining plan, and using equipment properly could reduce miner exposure to ground falls. *Coal Age* **2005**, *110*, 26–31.
13. Mark, C. Deep cover pillar recovery in the US. In Proceedings of the 28th International Conference on Ground Control in Mining, Morgantown, WV, USA, 28–30 July 2009; pp. 1–9.
14. Iannacchione, A.T.; Mark, C. Major hazard risk assessment applied to pillar recovery operations. In Proceedings of the 28th International Conference on Ground Control in Mining, Morgantown, WV, USA, 28–30 July 2009; pp. 261–270.
15. Zur, K.J.; Apel, D.B. Use of cemented rock fill for enhanced pillar recovery in area 1 of the Doe Run Company. In Proceedings of the 5th International Conference on Case Histories in Geotechnical Engineering, New York, NY, USA, 13–17 April 2004; pp. 13–17.
16. Zhukova, S.; Korchak, P.; Streshnev, A.; Salnikov, I. Geodynamic rock condition, mine workings stabilization during pillar recovery at the level+ 320 m of the Yukspor deposit of the Khibiny Massif. In Proceedings of the VII International Scientific Conference "Problems of Complex Development of Georesources, Khabarovsk, Russia, 25–27 September 2018; Volume 56.
17. Langston, R.; Kirsten, H.A.; Niemi, E.; Marjerison, J. Extraction of a Remnant Sill Pillar Under Challenging Ground Conditions at the Stillwater Mine, Nye, MT. In Proceedings of the Golden Rocks 2006, the 41st US Symposium on Rock Mechanics (USRMS), Golden, CO, USA, 17–21 June 2006.
18. Sainsbury, D.P.; Cai, Y.; Hebblewhite, B.K. Numerical investigation of crown pillar recovery beneath stabilized rockfill. In *Numerical Modeling in Micromechanics via Particle Methods: International PFC Symposium, Gelsenkirchen, Germany, 6–8 November 2002*; Routledge: London, UK, 2003; pp. 225–231.
19. Sainsbury, D.P.; Sainsbury, B.L. Design and implementation of cemented rockfill at the Ballarat Gold Project. In Proceedings of the Eleventh International Symposium on Mining with Backfill, Perth, Australia, 20–22 May 2014; pp. 205–216.
20. Sainsbury, B.A.; Sainsbury, D.P.; Western, J.; Petrie, P.E.; Mutton, V. Pillar recovery adjacent to stabilised rockfill at the Ballarat Gold Project. In Proceedings of the Third Australasian Ground Control in Mining Conference, AUSIMM, Sydney, Australia, 5–6 November 2014; pp. 1–18.
21. Ghasemi, E.; Shahriar, K.; Sharifzadeh, M. A new method for risk assessment of pillar recovery operation. *Saf. Sci.* **2010**, *48*, 1304–1312. [CrossRef]
22. Ghasemi, E.; Ataei, M.; Shahriar, K.; Sereshki, F.; Jalali, S.E.; Ramazanzadeh, A. Assessment of roof fall risk during retreat mining in room and pillar coal mines. *Int. J. Rock Mech. Min. Sci.* **2012**, *54*, 80–89. [CrossRef]
23. Beruar, O.; Forsythe, A.S.; Yao, M. Sill Pillar Mining in the Main Orebody at Vale's Coleman Mine. In Proceedings of the 45th US Rock Mechanics/Geomechanics Symposium, San Francisco, CA, USA, 26–29 June 2011; American Rock Mechanics Association: Alexandria, VA, USA, 2011.
24. Valley, B.; Milkereit, B.; Pun, W.; Pilz, M.; Hutchinson, J.; Delaloye, D.; Forsythe, A. Rock mass change monitoring in a sill pillar at Vale's Coleman mine. In Proceedings of the 21st Canadian Rock Mechanics Symposium, Edmonton, AB, Canada, 5–9 May 2012; pp. 569–577.
25. Townend, S.; Sampson-Forsythe, A. Mitigation strategies for mining in high stress sill pillars at Coleman Mine–a case study. In Proceedings of the Seventh International Conference on Deep and High Stress Mining, Perth, Australia, 16–18 September 2014; pp. 65–78.
26. Zhou, Z.; Zhao, Y.; Cao, W.; Chen, L.; Zhou, J. Dynamic response of pillar workings induced by sudden pillar recovery. *Rock Mech. Rock Eng.* **2018**, *51*, 3075–3090. [CrossRef]

27. Amoah-Kyei, A.; Amoako, R.; Dumakor-Dupey, N.K. Fragmentation Analysis of Backfill Material for Paboase Modified Sublevel Caving (MSLC). In Proceedings of the 5th UMaT Biennial International Mining and Mineral Conference, Tarkwa, Ghana, 1–4 August 2018.
28. Belem, T.; Benzaazoua, M. Design and application of underground mine paste backfill technology. *Geotech. Geol. Eng.* **2008**, *26*, 147–174. [CrossRef]
29. Labrie, D.; Boyle, R.; Anderson, T.; Conlon, B.; Judge, K. Monitoring the behavior of a sill pillar at failure in a narrow vein mine. In Proceedings of the 1st Canada-US Rock Mechanics Symposium, Vancouver, BC, Canada, 27–31 May 2007; American Rock Mechanics Association: Alexandria, VA, USA, 2007.
30. Sepehri, M. Finite Element Analysis Model for Determination of In-Situ and Mining Induced Stresses as a Function of Two Different Mining Methods Used at Diavik Diamond Mine. Ph.D. Thesis, University of Alberta, Edmonton, AB, Canada, 2016.
31. Lingga, B.; Apel, D.B. Shear properties of cemented rockfills. *J. Rock Mech. Geotech. Eng.* **2018**, *10*, 635–644. [CrossRef]
32. Xu, H.; Apel, D.B. Optimum location of last-mined stope with the influence of backfilling. *J. Sustain. Min.* **2020**, *19*, 212–220. [CrossRef]
33. Xu, H.; Apel, D.B. Study of the influence of backfilling on stability and location of remaining stopes in sill pillar recovery. *Int. J. Geomate* **2021**, *21*, 43–49. [CrossRef]
34. Sepehri, M.; Apel, D.B.; Hall, R.A. Prediction of mining-induced surface subsidence and ground movements at a Canadian diamond mine using an elastoplastic finite element model. *Int. J. Rock Mech. Min. Sci.* **2017**, *100*, 73–82. [CrossRef]
35. Sainsbury, D.P.; Sainsbury, B.L.; Sweeney, E. Three-dimensional analysis of complex anisotropic slope instability at MMG's Century Mine. *Min. Technol.* **2016**, *125*, 212–225. [CrossRef]
36. Heidarzadeh, S.; Saeidi, A.; Rouleau, A. Evaluation of the effect of geometrical parameters on stope probability of failure in the open stoping method using numerical modeling. *Int. J. Min. Sci. Technol.* **2019**, *29*, 399–408. [CrossRef]
37. Rojek, J.; Nosewicz, S.; Thoeni, K. 3D formulation of the deformable discrete element method. *Int. J. Numer. Methods Eng.* **2021**, *122*, 3335–3367. [CrossRef]
38. Dassault Systemes. *ABAQUS/Standard User's Manual*; Dassault Systemes Simulia Corp.: Providence, RI, USA, 2015.
39. Xu, H. Stoping Sequence Optimization Based on Stope Stability Assessment Using Finite Element Modelling Method. Ph.D. Thesis, University of Alberta, Edmonton, AB, Canada, 2021.
40. Jing, L.; Hudson, J.A. Numerical methods in rock mechanics. *Int. J. Rock Mech. Min. Sci.* **2002**, *39*, 409–427. [CrossRef]
41. Jing, L. A review of techniques, advances and outstanding issues in numerical modelling for rock mechanics and rock engineering. *Int. J. Rock Mech. Min. Sci.* **2003**, *40*, 283–353. [CrossRef]
42. Manouchehrian, A.; Cai, M. Numerical modeling of rockburst near fault zones in deep tunnels. *Tunn. Undergr. Space Technol.* **2018**, *80*, 164–180. [CrossRef]
43. Wang, J.; Apel, D.B.; Pu, Y.; Hall, R.; Wei, C.; Sepehri, M. Numerical modeling for rockbursts: A state-of-the-art review. *J. Rock Mech. Geotech. Eng.* **2021**, *13*, 457–478. [CrossRef]
44. Wang, J.; Apel, D.B.; Dyczko, A.; Walentek, A.; Prusek, S.; Xu, H.; Wei, C. Investigation of the rockburst mechanism of driving roadways in close-distance coal seam mining using numerical modeling method. *Min. Metall. Explor.* **2021**, *38*, 1899–1921. [CrossRef]
45. Wang, J.; Apel, D.B.; Dyczko, A.; Walentek, A.; Prusek, S.; Xu, H.; Wei, C. Analysis of the damage mechanism of strainbursts by a global-local modeling approach. *J. Rock Mech. Geotech. Eng.* 2022; in press.
46. Kalenchuk, K.S.; Crockford, A.M.; Hume, C.D.; Milner, N.; Watson, J. Application of numerical modelling to predicted seismic probability and mitigate associated risks during the Craig pillar extraction at Morrison Mine, KGHM International. In Proceedings of the 48th US Rock Mechanics/Geomechanics Symposium, OnePetro, Minneapolis, MN, USA, 1–4 June 2014.
47. Kalenchuk, K. 2019 Canadian Geotechnical Colloquium: Mitigating a fatal flaw in modern geomechanics: Understanding uncertainty, applying model calibration, and defying the hubris in numerical modelling. *Can. Geotech. J.* **2022**, *59*, 315–329. [CrossRef]
48. Kang, Y.; Liu, H.; Aziz, M.M.A.; Kassim, K.A. A wavelet transform method for studying the energy distribution characteristics of microseismicities associated rock failure. *J. Traffic Transp. Eng. (Engl. Ed.)* **2019**, *6*, 631–646. [CrossRef]
49. Leveille, P. Rockbursting Properties of Kimberlite-Diavik Diamond Mine Case Study. Master's Thesis, University of Alberta, Edmonton, AB, Canada, 2015.
50. Leveille, P.; Sepehri, M.; Apel, D.B. Rockbursting potential of kimberlite: a case study of Diavik diamond mine. *Rock Mech. Rock Eng.* **2017**, *50*, 3223–3231. [CrossRef]
51. Pu, Y. Machine Learning Approaches for Long-Term Rock Burst Prediction. Ph.D. Thesis, University of Alberta, Edmonton, AB, Canada, 2019.
52. Park, H.D. Tensile Rock Strength and Related Behaviour Revealed by Hoop Tests. Ph.D. Thesis, Imperial College London, London, UK, 1994.
53. Wang, J.A.; Park, H.D. Comprehensive prediction of rockburst based on analysis of strain energy in rocks. *Tunn. Undergr. Space Technol.* **2001**, *16*, 49–57. [CrossRef]
54. Mitri, H.S.; Tang, B.; Simon, R. FE modelling of mining-induced energy release and storage rates. *J. S. Afr. Inst. Min. Metall.* **1999**, *99*, 103–110.
55. Jaeger, J.C.; Cook, N.G.; Zimmerman, R. *Fundamentals of Rock Mechanics*; John Wiley & Sons: Hoboken, NJ, USA, 2009.

56. Cai, M. Prediction and prevention of rockburst in metal mines—A case study of Sanshandao gold mine. *J. Rock Mech. Geotech. Eng.* **2016**, *8*, 204–211. [CrossRef]
57. Cai, M. Principles of rock support in burst-prone ground. *Tunn. Undergr. Space Technol.* **2013**, *36*, 46–56. [CrossRef]
58. Miao, S.J.; Cai, M.F.; Guo, Q.F.; Huang, Z.J. Rock burst prediction based on in-situ stress and energy accumulation theory. *Int. J. Rock Mech. Min. Sci.* **2016**, *100*, 86–94. [CrossRef]

Article

Back-Calculation Method for Estimation of Geomechanical Parameters in Numerical Modeling Based on In-Situ Measurements and Statistical Methods

Karolina Adach-Pawelus

Faculty of Geoengineering, Mining and Geology, Wroclaw University of Science and Technology, 50-370 Wroclaw, Poland; karolina.adach@pwr.edu.pl

Abstract: An important element of numerical modeling for specific mining issues is the selection of model parameters. The incorrect determination of geomechanical parameters can result in significant calculation errors carried throughout the entire problem. This paper presents a method for determining effective geomechanical parameters for technological and residual pillars through the use of numerical modeling, specifically, back-calculation. This is based on the results of numerical simulations, measurement data (e.g., excavation convergence measurements), and statistical methods (a non-linear regression model with "dummy" variables). The result is that appropriate parameters of pillars are set out iteratively so that the displacements of selected points in the numerical model correspond (with some approximation) to the results of mine measurements. The procedure of determining pillar parameters is presented using a case study of one mining field in an underground copper mine, where the deposit is mined using the room and pillar system. Numerical calculations were performed using a Phase2 v. 8.0 program (Rocscience, Toronto, Canada), while statistical calculations used a Statistica computer program. The results of excavation convergence measurements performed in the analyzed mine have been applied. This paper shows that for the presented method, the resulting matching of theoretical values of convergence determined numerically for specified pillar parameters to in-situ results of convergence measurements, is very good ($R^2 = 0.9896$). This work exemplifies a set of the parameters of pillars for an elastic model of rock mass, but this method can also be applied to other models.

Keywords: back-calculation in geomechanics; rock mechanics; numerical modeling; room and pillar mining system; non-linear regression

1. Introduction

In the past, rock mechanics was primarily described using empirical methods, based on experience and analytical methods giving a closed form of solution. As a result of the development of computer technology and computational methods, the most common methods used to solve geomechanics problems are numerical methods, which allow for the analysis of complex geometry (in close to real conditions) and different material behaviors. Both two- and three-dimensional tasks are solved. The most commonly used numerical calculation methods in geomechanics are the finite difference method, finite element method, and the boundary element method; though the discrete element method or hybrid methods (hybrid continuum/discrete methods) [1,2] are quite often used. Numerical modeling plays a very important role in the design of underground mines. It allows assessment of the current mining situation and predicts the behavior of rock mass along with the progress of work. Numerical methods in underground mining are used for, among others, stability analysis of mining excavations and the design of their support [3–10], to compare different types of support [11], for simulation of deposit excavation using various mining systems [12–20], for studies of the behavior and stability of pillars and remnants [21–29], for analysis of mining salt deposits with backfill and the determination of the backfilling

influence on the dynamics of deformation of the undermined rock mass [30], as well as for the assessment of seismic and rockburst hazard [20,22,27,28,31–35], etc.

A key element of any rock mass behavior modeling is the correct determination of its parameters and verification of obtained results. The introduction of incorrect parameters into the model will result in incorrect results. These parameters should be chosen so that the values set out as a result of numerical calculations correspond to actual values obtained on the basis of observations and mine measurements. The main source of input data for a numerical model are laboratory tests of rock samples and field tests. The impact of the sample size on the mechanical characteristics of rock samples is referred to as the "size effect" and is a significant issue [36,37]. The values of strength and deformation parameters set out by laboratory tests are often reduced to take into account the "size effect" between the sample (micro scale) and the rock mass (macro scale). The parameters of rock mass for numerical calculations can be set out using rock mass weakening factors chosen depending on the structure of the rock mass and the compressive strength of the rock samples or by using Hoek–Brown classification [38–40].

In practice, however, it happens that the obtained calculated values (e.g., of rock mass displacements) differ significantly from the values measured in mining conditions. The choice of suitable geomechanical parameters for numerical calculations is a particularly important issue in the case of technological and residual pillars in room and pillar mining systems and when considering their progressive destruction, when the mining front is moved. The yielding of pillars in numerical calculations is introduced by reducing their strength and deformation parameters. In order to make the best projection of the actual working conditions of pillars, the strength and deformation parameters are chosen most often using a method called "back-calculation". The required parameters are set out based on in-situ measurements in such a way, that a numerical model should fit best to the actual behavior of the object. Back-calculation based on measurements of displacements was initiated by Sakurai in 1981 [41] and is widely applied in geomechanics.

This paper presents a method for determining effective geomechanical parameters for technological and residual pillars used in numerical calculations for room and pillar mining systems using back-calculation, which is based on the results of numerical simulations, measurement data (e.g., excavation convergence measurements), and statistical methods. Numerical calculations have been performed as a plane strain problem using Phase2 v. 8.0 program (Rocscience, Toronto, Canada), which uses the finite element method, while the statistical analysis was done using Statistica. The above method is applied to one of the mining fields of the underground copper mines belonging to KGHM Polska Miedz SA. The analysis covered the D-IE mining field located in the Polkowice-Sieroszowice mine in south-western Poland. Copper ore deposit in the analyzed field was mined using the room and pillar system with a roof deflection. This work exemplifies how to set out the parameters of pillars for an elastic model of rock mass, but this method can also be used for other models.

2. The Method of Determination of Effective Geomechanical Parameters for Technological and Residual Pillars for Numerical Modeling Using Back-Calculation Based on the Results of Numerical Simulations, Measurement Data, and Statistical Methods

For the best projection of reality to determine the effective geomechanical parameters of technological and residual pillars applied to numerical calculations for room and pillar mining systems, back-calculation has been suggested based on the results of numerical simulations and measurement data, in which a non-linear regression model was applied with so-called dummy variables. This allows determining the values of the pillars parameters, for which the values of excavation convergence calculated in the numerical model will be most closely related to the results of convergence measured is-situ in this excavation. The model of non-linear regression with "dummy" variables is described by the formula:

$$Y = P_1 Z_1 + P_2 Z_2 + P_3 Z_3 + \ldots + P_k Z_k, \tag{1}$$

where:

Y—explained variable (results of in-situ measurements of convergence for a chosen excavation),

$Z_1, \ldots, Z_k$—so-called "dummy" variables (with a value of 1 or 0),

$P_1, \ldots, P_k$—quadratic functions acting as parameters of a regression model with "dummy" variables.

The established effective geomechanical parameters of technological and residual pillars are independent variables of quadratic functions $P_1, \ldots, P_k$. The number of variables in a quadratic function depends on the number of determined pillar parameters. Therefore, the actual determined parameters of a regression model with dummy variables are independent variables of the quadratic function being the parameters of pillars. In a case when all technological and residual pillars are characterized by one parameter such as E then functions $P_1, \ldots, P_k$ take the form of a quadratic function of one variable:

$$P = \beta_0 + \beta_1 E + \beta_{11} E^2 \tag{2}$$

If we use more parameters to characterize the work of technological and residual pillars, the Formula (1) takes the form:

— for two parameters (e.g., E, c):

$$P = \beta_0 + \beta_1 E + \beta_2 c + \beta_{11} E^2 + \beta_{12} E c + \beta_{22} c^2, \tag{3}$$

— for three parameters (e.g., E_1, E_2, c):

$$P = \beta_0 + \beta_1 E_1 + \beta_2 E_2 + \beta_3 c + \beta_{11} E_1{}^2 + \beta_{12} E_1 E_2 + \beta_{22} E_2{}^2 + \beta_{13} E_1 c + \beta_{33} c^2 + \beta_{23} E_2 c \tag{4}$$

The parameters of quadratic functions: $\beta_0, \beta_1, \beta_2, \beta_3, \beta_{11}, \beta_{12}, \beta_{13}, \beta_{11}, \beta_{22}$, and β_{33} are set out by the least square method on the basis of convergence values defined in numerical simulations for different combinations of established values of the parameters characterizing the pillars (the matrix of the numerical experiment). The matrix of the numerical experiment is selected iteratively in such a way that the calculations are based on interpolation, i.e., the calculated parameters of pillars should be within a space defined by the matrix of the numerical experiment.

In order to match the results of the numerical experiment to measurement data, the regression model parameters are set out using backward stepwise regression. This involves eliminating from the model the effective geomechanical parameters of pillars, which had no significant effect on the optimal adjustment of convergence values (identified on the basis of numerical modeling) to the measurement data. The statistical significance of respective parameters is evaluated on the basis of confidence intervals or p-values for the assumed level of significance α. The regression model with dummy variables, which incorporates all the selected parameters of pillars, is individually deprived of those where $p > \alpha$ (and therefore those for which there was no reason to reject the hypothesis, that the established parameter is equal to 0). In the next step, a new regression model is set out with a number of parameters reduced by 1. Finally, when all parameters of the pillars are considered statistically significant (significantly different from 0), the process of elimination is interrupted and matching of the results of the predicted excavation convergence to measurement data is estimated based on the coefficient of determination R^2. On this basis, a decision is made about the values of the geomechanical parameters for technological and residual pillars adopted for further numerical calculations.

The procedure of determining effective geomechanical parameters for technological and residual pillars based on the results of numerical simulations and data from mine measurements using statistical methods is presented in Figure 1. According to Figure 1, the first step (1) includes the choice of strength and deformation parameters of pillars, which have a decisive impact on the value of calculated vertical displacements for a given model of rock mass. Then, after construction of a numerical model of the selected mining field, (2) one should specify the number of quested effective geomechanical parameters charac-

terizing the work of technological and residual pillars (3) and select the values of these parameters, for which numerical simulations will be carried out (construction of the numerical experiment matrix) (4). In the case of a numerical experiment matrix consisting of three parameters describing the work of the pillars (e.g., E_1, E_2, and c) and three different values adopted for each parameter, the number of numerical simulations will be 27. Simulations performed for a numerical experiment matrix are a basis for determining a convergence graphs model in a chosen excavation in the following steps of mining excavation (5). On the established convergence curves, one should choose representative points for the regression analysis (6) and determine the quadratic functions of an appropriate number of variables depending on the number of sought geomechanical parameters of the pillars (7). Knowing the quadratic functions serving as model parameters, one can specify the non-linear regression model with "dummy" variables (8) and determine the values of effective geomechanical parameters for the technological and residual pillars (9). The next step is to examine whether the received parameters have physical meaning (e.g., $c \geq 0$, $E \geq 0$, $\varphi \geq 0$) (10). If not, calculations should be terminated (11), as this may mean that the numerical model has not been properly constructed: too small density of the grid, insufficient accuracy of calculations, etc. When the calculated parameters have physical meaning, it should be checked whether they belong to one type of parameter (12). If not, then one should check whether the set parameters are statistically significant (14) and if so, it should be checked whether the parameters belonging to one type are significantly different from each other (13). If among the established pillar parameters are those for which there are no grounds to reject the statistical hypothesis that they are equal, one should eliminate one of them, reduce the number of sought pillar parameters, (15) and repeat the procedure. If all set-out parameters are significantly different from each other and in the case of parameters not belonging to one type, one should check their statistical significance (14). In a case when among the established parameters are those not statistically significant, one of them must be eliminated (15), and following the steps of the procedure should be repeated. However, when all pillar parameters have been considered statistically significant, one should check whether they are in a space defined by the experiment matrix (16). If the set parameters do not belong to this space, one should return to the construction of the experiment matrix (4) and change the range of selected values. Otherwise, the set of effective geomechanical parameters for technological and residual pillars can be applied for further numerical modeling, evaluating the matching of numerical experiment data to measurement data on the basis of the coefficient of determination R^2 (17). The procedure of selecting pillar parameters based on numerical simulations and measurement data can be performed repeatedly for different models of rock mass, searching for optimal parameters that will produce the best match of numerical experiment data to measurement data.
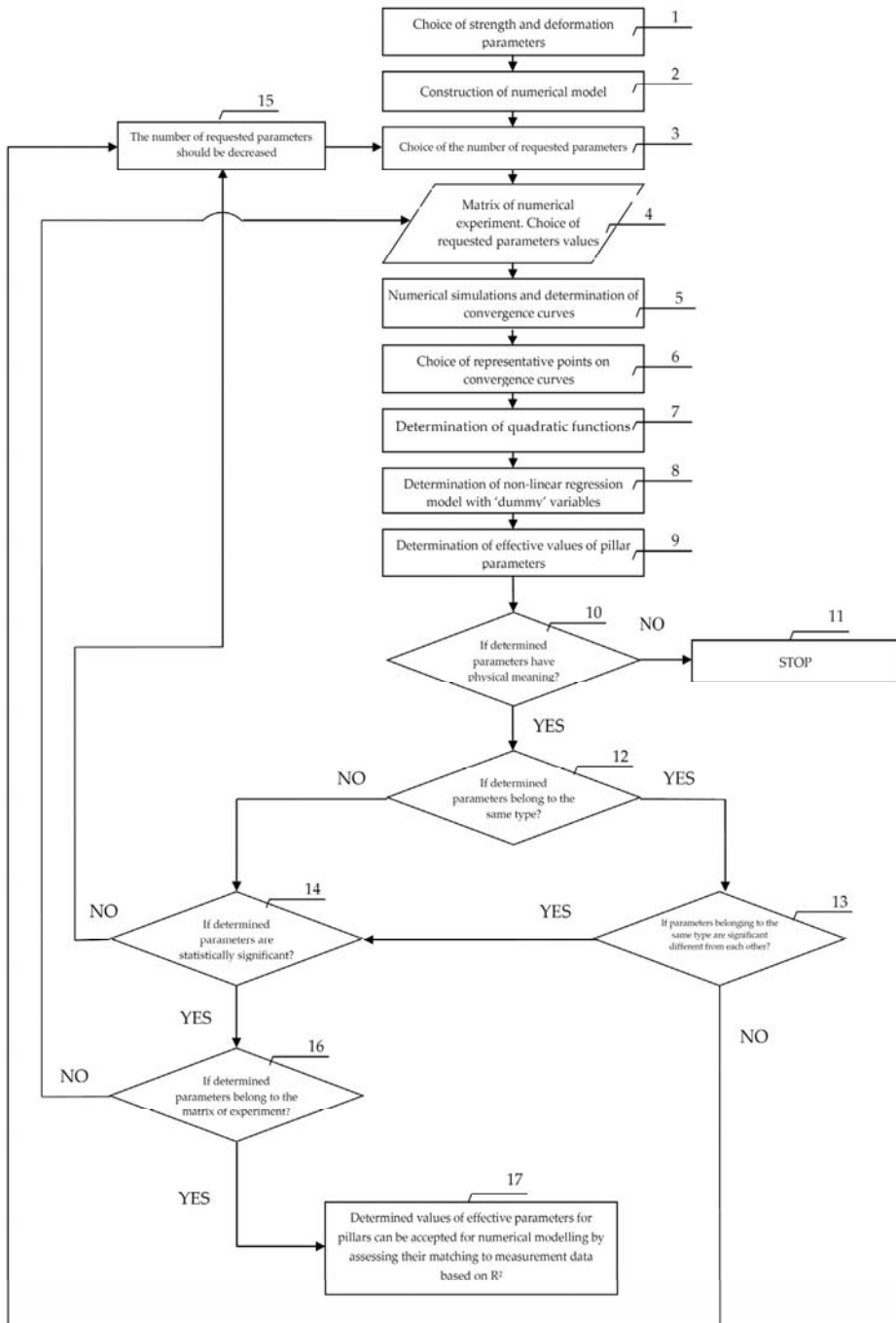
Figure 1. Method of determination of effective geomechanical pillar parameters on the basis of numerical simulations and measurement data using statistical methods.

3. Case Study in Polkowice-Sieroszowice Mine

3.1. Characteristics of Research Area

The method of determining effective geomechanical method parameters for technological and residual pillars for numerical modeling using back-calculation based on the results of numerical simulations, measurement data, and statistical methods are presented in the example of one mining field (D-IE) in Polkowice-Sieroszowice underground copper mine. The Polkowice-Sieroszowice mine belongs to KGHM Polska Miedz SA. It is located in the south-western part of Poland and mines the copper ore deposit which covers the central part of a geological unit known as Sudetic Monocline. Sudetic Monocline falls gently towards the northeast. It is constructed of Permian and Triassic sediments, which have a base made from Proterozoic crystalline rocks and Carboniferous sedimentary rocks. The deposit occurs in Permian formations, contacted by a dolomite limestone series, red sandstone, and Lower Permian limestone. Shaped in the form of a pseudobed of variable thickness (from 0.4 to approx. 20 m) and low gradient (approx. 4°), it lies at great depth (from 600 to 1400 m). The copper ore deposit is formed by an accumulation of sulfides, mainly chalcocite, bornite, and chalcopyrite. Sulfide mineralization occurs at the contact of red sandstone and Permian limestone layers. It includes carbonate rocks (dolomites and limestones), copper-bearing shales in the bottom part of the Permian limestone, and white sandstones. The deposits of the Polkowice-Sieroszowice mine subject to ore mineralization are mainly carbonate rocks and shales. Mining of the deposit is performed using a variety of room and pillar systems, depending on geological and mining conditions in a given mining field [29].

D-IE mining field was located in the mining area Sieroszowice I, in the Polkowice-Sieroszowice mine. It was a closing field explored since March 2005, where mining works were carried out in the vicinity of gobs. In February 2008, due to problems with maintaining roof stability, the remnant was left behind on the right side of the D-IE mining field (Figure 2).
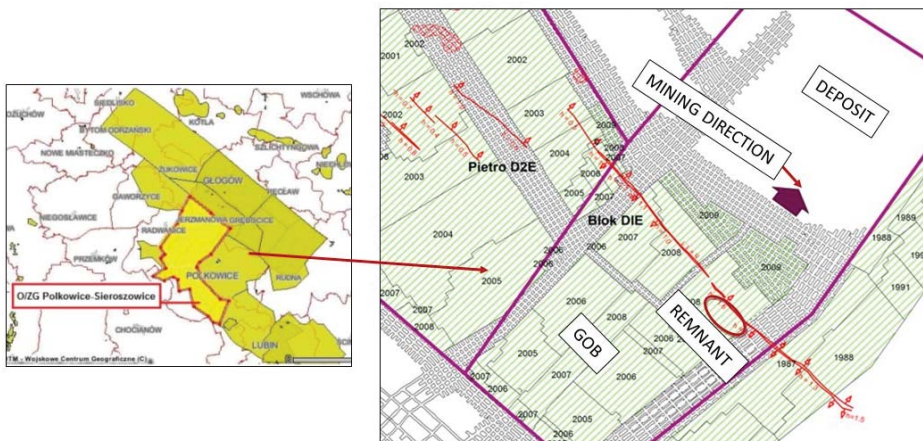
Figure 2. Mining field in the Polkowice-Sieroszowice mine where remnant has been left.

In the D-IE mining field, the deposit balance occurs in the lower part of a carbonate series of Permian limestones and the roof part of new red sandstone; it is comprised of grey quartz, fine-grained sandstone, loamy copper-bearing shale, and dolomite loamy shale, as well as streaked, dark grey, crypto-crystalline dolomite. The roof is made of rock layers, being part of a Permian limestone carbonate series, namely of calcareous dolomites with clear divisibility of bed (occurring in intervals of 0–2 m above the excavation roof), of concise calcareous dolomites with quite clear divisibility (occurring in intervals of 2–5 m above the excavation roof), and calcareous dolomites and dolomitic limestones with a bed structure (that occur in intervals of more than 5 m above the excavation roof). The carbonate

series is directly covered by anhydrites. The direct floor is built of grey sandstones of red Permian sediment rock. These are fine-grained quartz sandstones with a loamy bond, carbonate-loam bond, and locally anhydrite bond (in the eastern part of the area). The roof part of the sandstones, due to the larger amount of carbonate bond, is harder and more concise. The deposit is oriented towards NW-SE and its decline (2–3°) towards NE. The rock formation has marginal tectonic sensitivity. The height of the mined deposit is 2.0–2.8 m.

Until 2008 mining of the deposit in the discussed area was conducted using a room and pillar system with roof deflection and closing pillar (J-UGR-PS), while in 2008 the closing pillar was liquidated, and further works were performed using a room and pillar system with roof deflection (J-UG-PS). Exploration using the room and pillar system consists in cutting the deposit with rooms and strips with separation of technological pillars of a certain geometry, which protect the roof over the working area. The size of the pillars is chosen to provide its work in the post-critical state. In the D-IE mining field, the cutting work was carried out using technological pillars situated perpendicular to the mining front, with basic dimensions of 6 × 8 m (J-UGR-PS and J-UG-PS). In the discussed mining systems, the height of excavation in the cutting phase depends on the thickness of the deposit and the requirements of working machines and is not more than 4.5 m. The width of excavations does not exceed 7 m. The minimum size of the opening face of the mining front is equal to the sum of two strips and the length of two rows of pillars into undisturbed rock. In the D-IE mining field, the width of the opening was 4–5 strips. Along with the progress of the mining front, the technological pillars from the last row before gobs, depending on the degree of their disintegration, are adjusted or cleft into smaller ones. The resultant support pillars are adjusted to residual dimensions in elementary plots and then left in gobs. They work as supports to mitigate the deflection of roof layers. For D-IE field size of residual pillars left in the gobs amounted to approx. 5.2 m^2. In a room and pillar system with roof deflection and a closing pillar, the technological pillars are left in a separated part of the field, creating a gradually lengthening closing pillar. In one of the excavations of this pillar, a conveyor belt is assembled, which successively extends along with the progress of cutting. The width of a closing pillar depends on local geological and mining conditions and is generally 40–120 m [39]. The work of mining systems J-UGR-PS and J-UG-PS are shown in Figures 3 and 4.
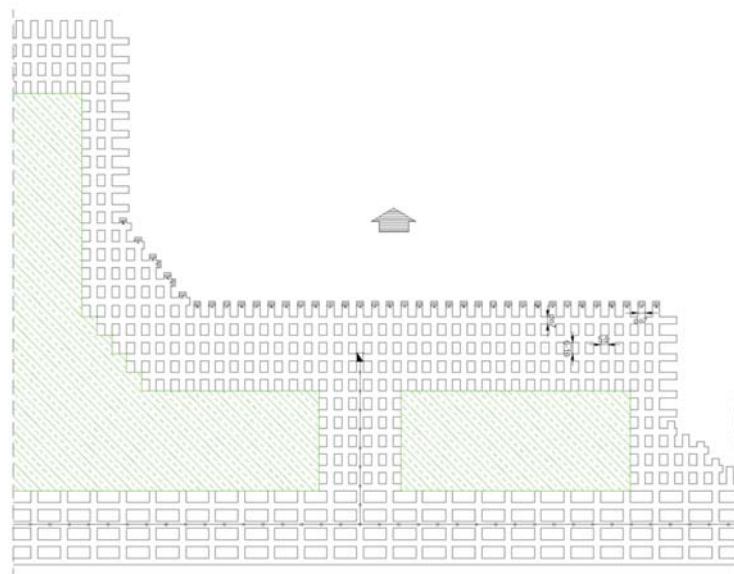
Figure 3. Room and pillar mining system with closing pillar J-UGR-PS [42].
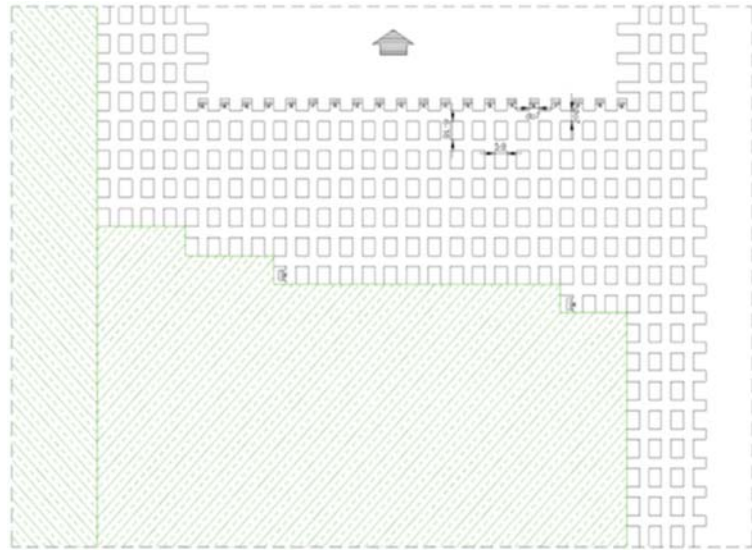
Figure 4. Room and pillar mining system with roof deflection J-UG-PS [42].

3.2. Characteristics of Numerical Modeling

Numerical calculations were performed in a plane strain state by a computer program Phase2 v. 8.0 (Rocscience, Toronto, ON, Canada) [43]. The computational model was a plate, which comprises the rock layers creating the rock mass (Figure 5). Construction of the mass resulted from geological recognition conducted in the analyzed field. The upper edge of the model was loaded with vertical pressure, replacing the influence of overlaying rocks. It was assumed that at the upper edge of the plate the stress should be equal to 17.657 MPa, corresponding to the value of the vertical stress set out for the D-IE mining field on the basis of data from the borehole S-294. The calculations considered the deadweight of rock layers. Horizontal stress values were determined on the basis of Poisson's ratio υ of a given rock layer. For the edges of the plate, the displacement edge conditions were assumed. At the lower edge of the model—lack of vertical displacements while at the side edges—no displacements in directions perpendicular to the surface of the edge. An applied grid of finite elements was composed of three nodal elements of triangular shape. In the central part of the plate, adjacent to the excavations, the grid was densified to improve the accuracy of numerical calculations.
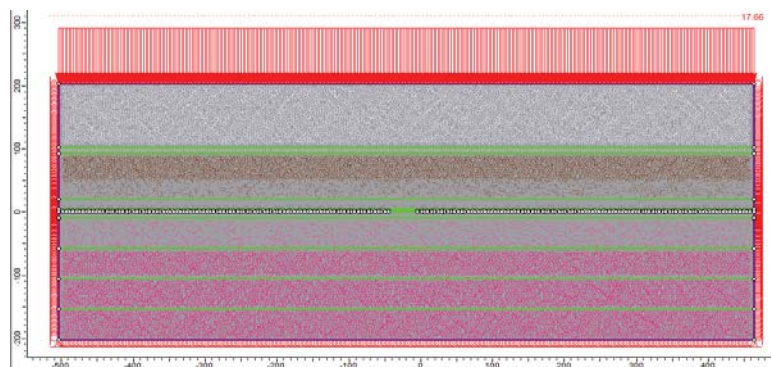
Figure 5. Calculation scheme for D-IE mining field.

The calculations were performed stepwise, simulating the mining carried out using a room and pillar system with parameters characteristic of an analyzed mining field (64 calculation steps). The first step covered the situation in the rock mass before the creation of mine excavations (Figure 6a). The second step consisted of the cutting of undisturbed rock into technological pillars (8 m in width) (Figure 6b). In the next steps, the size of the technological pillars was reduced to residual size (3 m width) and further technological pillars were cut out (Figure 6c). Cutting of the deposit was carried out with strips having dimensions 6 m width under the roof. Numerical simulations considered the width of the working area opening consisting of 5 strips.

(a)

(b)

(c)
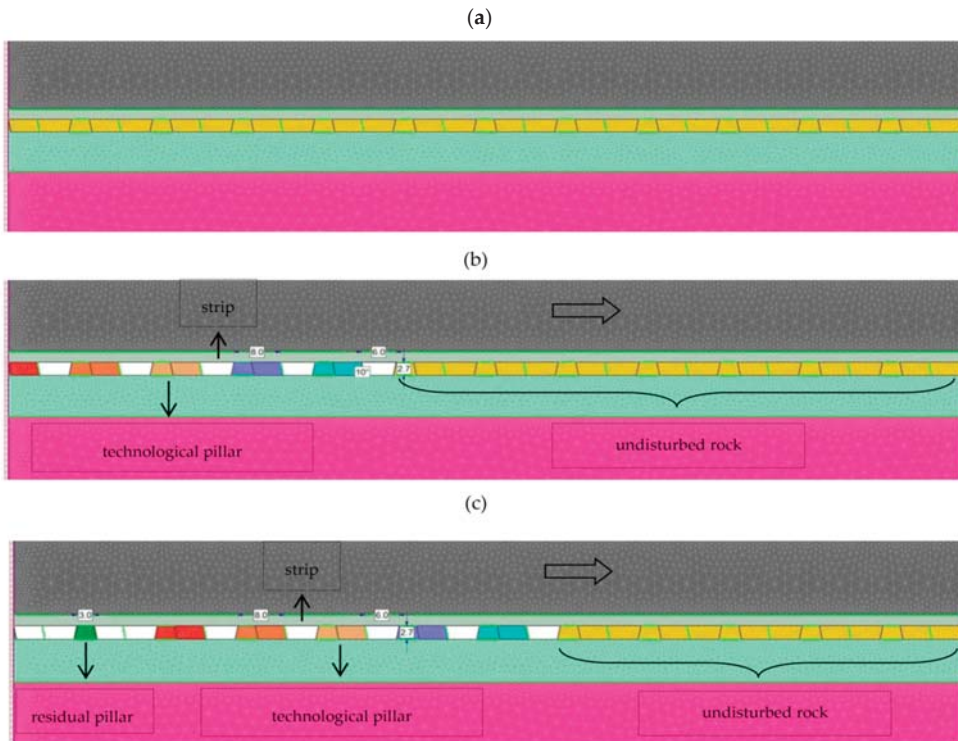
Figure 6. Simulation of room and pillar mining in the analyzed field: (**a**) step 1, (**b**) step 2, (**c**) step 4.

3.3. Determination of Parameters for Rocks and Rock Mass

The parameters of rock mass, which were assumed for numerical modeling, were determined based on Hoek–Brown classification. The results of laboratory tests of rock samples taken from geotechnical boreholes located in the analyzed mining field were applied. The averaged parameters of the rocks, which were designated in the laboratory for the D-IE field, are shown in Table 1, while the parameters of the rock mass are shown in Table 2.

Table 1. Averaged geomechanical parameters of rock.

Location	Name of Rock	h [m]	ρ [kg/dm^3]	R_c [MPa]	R_r [MPa]	E_s [MPa]	v [-]
	Main anhydrite	100.0	2.90	93.1	6.4	56,100	0.24
	Loamy anhydrite breccia	10.0	2.25	36.0	1.7	13,650	0.18
ROOF	Basic anhydrite	73.0	2.90	95.5	5.5	54,600	0.25
	Calcareous dolomite I	15.0	2.53	132.5	8.3	51,090	0.24
	Calcareous dolomite II	2.0	2.74	213.0	16.0	99,320	0.27
MINED DEPOSIT	Mined deposit	2.7	2.63	110.9	7.4	34,450	0.21
BOTTOM	Quartz sandstone I	8.2	2.12	22.1	1.4	8190	0.15
	Quartz sandstone II	194.5	1.95	16.7	0.7	6190	0.13

Table 2. Parameters of rock mass assumed for numerical modeling.

Location	Name of Rock	h [m]	E_s [MPa]	v [-]	σ_t [MPa]	c [MPa]	φ [°]
	Main anhydrite	100.0	41,110	0.24	0.746	6.967	38.66
	Loamy anhydrite breccia	10.0	7100	0.18	0.093	2.507	39.06
ROOF	Basic anhydrite	73.0	40,010	0.25	0.765	7.146	38.66
	Calcareous dolomite I	15.0	44,980	0.24	2.933	12.085	39.00
	Calcareous dolomite II	2.0	87,440	0.27	4.715	19.895	39.00
MINED DEPOSIT	Mined deposit	2.7	25,240	0.21	0.825	8.424	39.31
BOTTOM	Quartz sandstone I	8.2	4260	0.15	0.057	1.538	39.06
	Quartz sandstone II	194.5	3220	0.13	0.043	1.160	39.06

Marking in the above tables: h—thickness of rock layers, ρ—volume density, R_c—rock sample uniaxial compression strength, R_r—rock sample tensile strength, E_s—longitudinal elasticity modulus, v—Poisson coefficient σ_t—tensile strength of rock mass, c—coefficient of cohesion, ϕ—angle of internal friction.

3.4. Determination of Effective Geomechanical Parameters for Technological and Residual Pillars by Numerical Modeling Using Back-Calculation Based on the Results of Numerical Simulations, Measurement Data and Statistical Methods

The parameters of the technological and residual pillars described by an elastic model were determined using the procedure presented in the article. On the basis of in-situ tests carried out in the ZG Polkowice-Sieroszowice mine in 2002–2007, the course of the excavation convergence in time was determined for room and pillar mining systems with roof deflection and closing pillar. The pattern convergence curve, which was adopted as a reference for numerical calculations performed for the D-IE field, is shown in Figure 7. Each measurement of convergence made on a chosen test post was referred to as the mining step and the position of the working front line on a given day of measurement. This enabled the construction of a model that would fit the actual situation in the field and allow the determination of the effective geomechanical parameters of the technological and residual pillars.

The values of longitudinal elasticity modulus E were determined for an elastic model, (the parameter having a decisive impact on the numerically calculated values of displacements). Depending on the distance from the face of the mining front, the degree of pillar disintegration is varied. In the first step, the pillars were divided into three groups. Three technological pillars (located close to undisturbed rock) were characterized by longitudinal elasticity modulus E_1, the other two technological pillars with modulus E_2, and the residual pillars with modulus E_3 (Figure 8). It was assumed that $E_1 = E_2 + a$. The following values of E_1, E_2, and E_3 were adopted for the matrix of the numerical experiment:

E_1	E_2	E_3
2000 MPa	500 MPa	100 MPa
6000 MPa	1500 MPa	150 MPa
10,000 MPa	2500 MPa	200 MPa
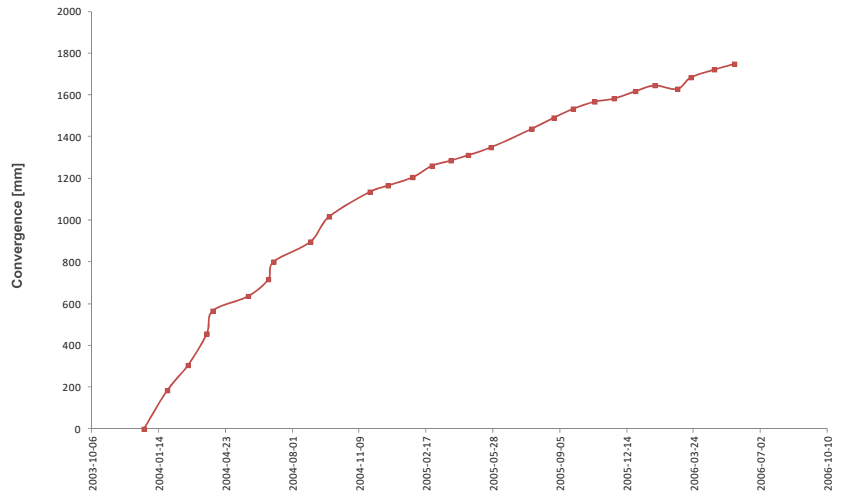
Figure 7. The results of excavation convergence measurements for J-UGR-PS mining system in Polkowice-Sieroszowice mine.
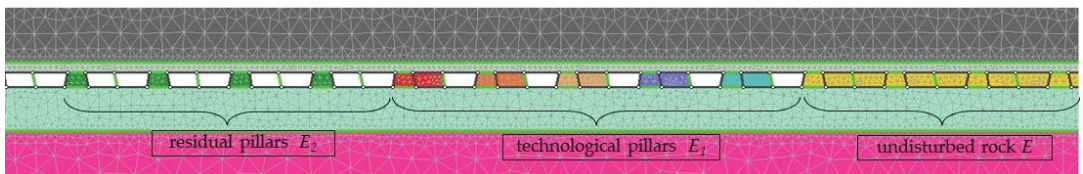
Figure 8. Fragment of the model of analyzed exploration field with marked division of pillars.

27 numerical simulations were performed for all combinations of assumed values of Young's modulus E. The convergence of the selected excavation in subsequent steps of the executed mining for a few chosen cases is presented in Figure 9.

Using the method of surface regression with Statistica v. 10 program, the quadratic function parameters of three variables were determined for selected points that are included in a non-linear regression model with dummy variables:

$$Y = Z_1(-145.75967 + 0.01(E_2 + a) - 0.00000046(E_2 + a)^2 + 0.05718E_2 - 0.00001043E_2{}^2 - 0.1659E_3 + 0.00054E_3{}^2$$
$$0.00000100(E_2 + a)E_2 + 0.00000087(E_2 + a)E_3 + 0.00000142E_2E_3) + \ldots + Z_9(-4620.2027 + 0.0405(E_2 + a) -$$
$$0.00000188(E_2 + a)^2 + 0.36882E_2 - 0.00006627E_2{}^2 + 22.9864E_3 - 0.04617E_3{}^2 - 0.00000146(E_2 + a)E_2 +$$
$$0.00002395(E_2 + a)E_3 - 0.00019174E_2E_3) \tag{5}$$

The values of a, E_2, and E_3 calculated using Statistica v. 10 are shown in Table 3.

$$E_1 = E_2 + a = 725.066 + 5541.145 = 6266.211 \text{ MPa}$$

Based on confidence intervals, statistical inference was performed to check whether E_1 and E_2 are significantly different from each other, namely if the added value of a is different from zero. The assumed level of significance $\alpha = 5\%$.

H_0: $a = 0$
H_1: $a \neq 0$

Table 3. Parameters of pillars determined for the elastic model using Statistica v. 10.

Parameter	Estimation	*p*	Lower Confidence Limit	Upper Confidence Limit
E_2	725.066	0.739776	−4582.5	6032.6
a	5541.145	0.893210	−95,323.3	106,405.6
E_3	135.808	0.000182	122.6	209.0
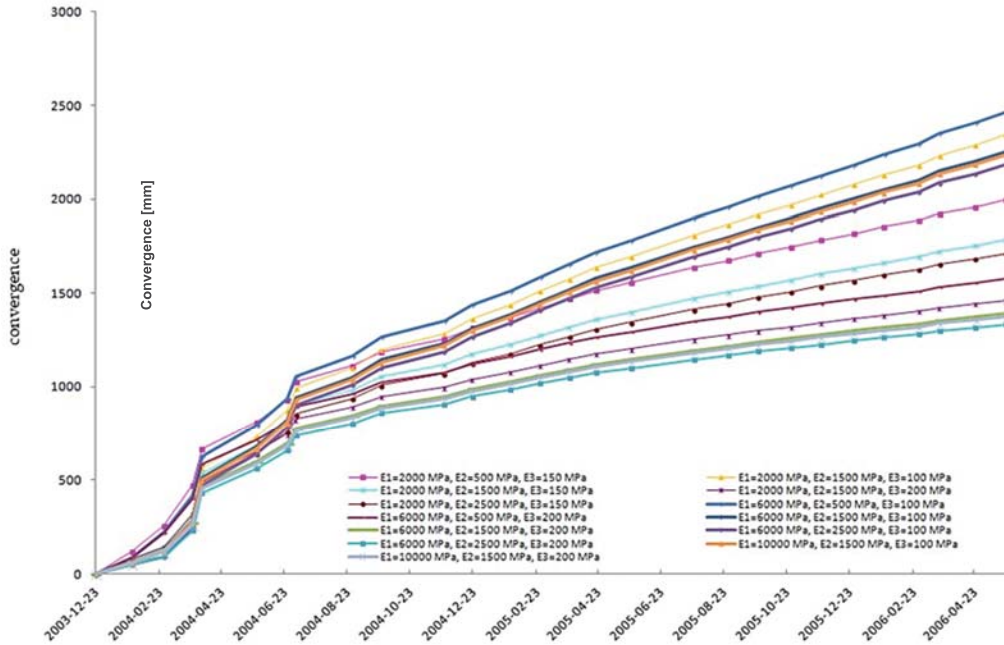
Figure 9. Chart of convergence determined numerically for chosen excavation in D-IE mining field for different combinations of parameter values assumed for pillars.

The $a = 0$ parameter is within 95% of the confidence interval, which indicates that there is no basis to reject the zero hypothesis H_0 (Figure 10). Therefore, it cannot be stated that at the level of significance $\alpha = 5\%$ $E_1 \neq E_2$. In addition, statistical inference based on test probability of *p*-value ($p = 0.893210 > \alpha = 0.05$) also indicates that there is no basis to reject H0: $a = 0$ hypothesis. In such a situation, it is assumed that $E_1 = E_2$ and the number of sought parameters of pillars was reduced to two. Technological pillars were characterized by longitudinal elasticity modulus E1, while residual pillars with longitudinal elasticity modulus E_2 (Figure 11). It was assumed, that $E_1 = E_2 + a$ and the following values of E_1 and E_2 were applied to the matrix of the numerical experiment:

E_1	E_2
200 MPa	80 MPa
400 MPa	120 MPa
600 MPa	160 MPa

There were nine numerical simulations. Convergence in the selected excavation is shown in Figure 12 in subsequent steps.
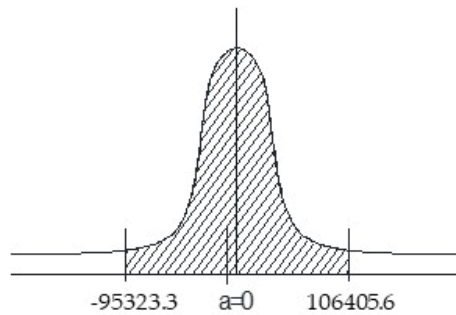
Figure 10. Intervals of confidence for *a*.
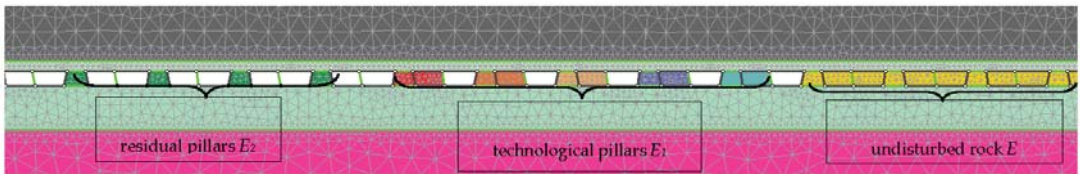
Figure 11. Fragment of the model of analyzed mining field with marked division of pillars.
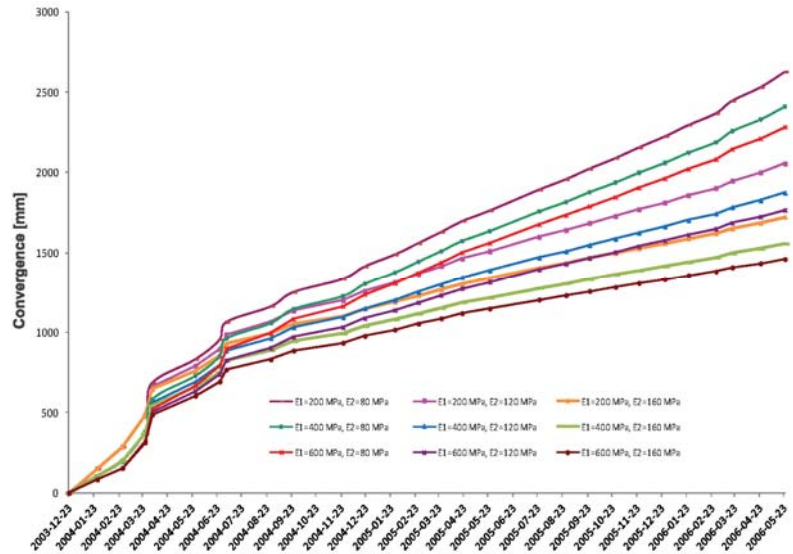
Figure 12. Results of convergence calculated numerically for the matrix of the experiment.

Using the method of surface regression with Statistica v. 10 program, the quadratic function parameters of two variables were determined for selected points that are included in the non-linear regression model with dummy variables:

$$
\begin{aligned}
Y = {} & Z_1(-220.077 + 0.424(E_2 + a) - 0.000322(E_2 + a)^2 - 0.0178E_2 + 0.00005993E_2{}^2 + 0.00000610(E_2 + a)E_2) \\
& + \ldots + Z_{16}(-4746.12 + 1.84(E_2 + a) - 0.000983(E_2 + a)^2 + 28.539E_2 - 0.06987090E_2{}^2 - 0.00252617(E_2 + a)E_2)
\end{aligned}
\tag{6}
$$

The values of a and E_2 were determined using Statistica v.10 presented in Table 4.

$$E_1 = E_2 + a = 136.931 + 174.424 = 311.355 \text{ MPa}$$

Table 4. Pillar parameters set for the elastic model using the Statistica v. 10 program.

Parameter	Estimation	p	Lower Confidence Limit	Upper Confidence Limit
E_2	136.931	0.0000000000119	122.134	151.729
a	174.424	0.0000162422638	238.441	391.832

Statistical inference carried out based on confidence intervals was performed to check whether E_1 and E_2 are significantly different from each other, namely if the added value of a is different from zero. The assumed level of confidence $\alpha = 5\%$.

H_0: $a = 0$

H_1: $a \neq 0$

The parameter $a = 0$ is located outside the 95% of confidence interval, which leads to rejection of zero hypothesis H_0 (Figure 13). It can therefore be stated that at significance level $\alpha = 5\%$ $E_1 \neq E_2$. Statistical inference based on test probability of p-value ($p = 0.010470 < \alpha = 0.05$) also suggests rejection of hypothesis H_0: $a = 0$.
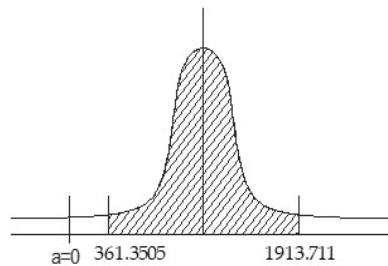
Figure 13. Confidence intervals for a.

The final values of E_1 and E_2 parameters determined using Statistica v.10 are shown in Table 5.

Table 5. Pillar parameters set for the elastic model using the Statistica v. 10 program.

Parameter	Estimation	p	Lower Confidence Limit	Upper Confidence Limit
E_1	311.355	0.0000364562557	198.823	423.887
E_2	136.931	0.0000000000119	122.134	151.729

On the basis of p-values it can be concluded that E_1 and E_2 parameters are statistically significant (E_1: $p = 0.0000364562557 < \alpha = 0.05$; E_2: $p = 0.0000000000119 < \alpha = 0.05$). The effective parameters of pillars $E_1 = 311.355$ MPa and $E_2 = 136.931$ MPa are also located in the space defined by the matrix of the numerical experiment. The resulting matching of theoretical values of convergence determined for specified pillar parameters, to in-situ results of convergence measurements is shown in Figure 14.

Reduced values of elasticity modulus for technological and residual pillars were adopted for further numerical modeling of the geomechanical situation in the D-IE mining field. The final validation of the numerical models was based on the results of convergence measurements of excavations carried out in this field.
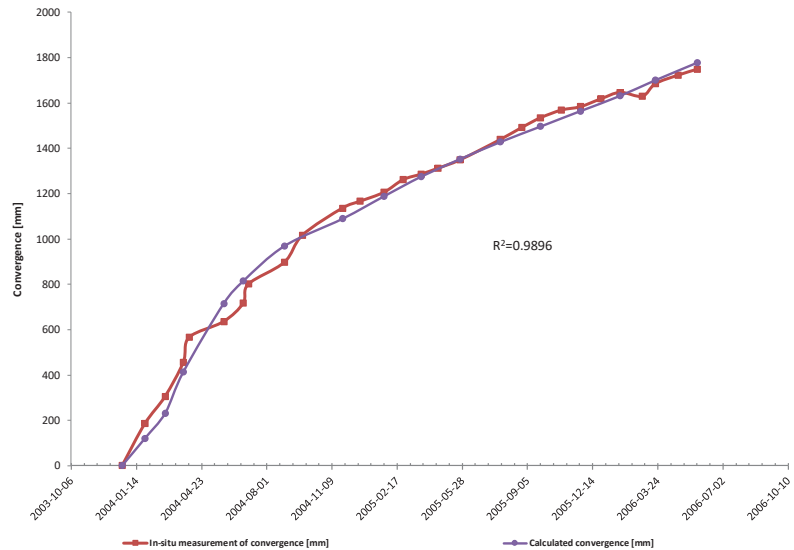
Figure 14. Matching of results of in-situ convergence measurements in Polkowice-Sieroszowice mine to convergence values obtained for effective parameters of pillars determined using statistical methods (elastic model).

4. Conclusions

In this paper, the innovative method for determining the geomechanical parameters of technological and residual pillars by numerical calculations using back-calculation based on the results of numerical simulations, in-situ measurement data, and a non-linear regression model with dummy variables, has been presented. The method has the potential to be useful in numerical modeling for specific mining issues due to the importance of model parameter selection. Incorrect determination of the geomechanical parameters results in significant calculation errors throughout the entire analyzed problem. These parameters should be chosen so that the values set out as a result of numerical calculations correspond to actual values obtained on the basis of observations and mine measurements.

In the case of room and pillar mining system modeling, a particularly difficult issue is the choice of parameters for technological and residual pillars (considering the progress of their destruction when a mining front is moved). Incorrect determination of the geomechanical parameters of pillars results in significant calculation errors throughout the whole analyzed mining field. The presented method enables the determination of pillar parameter values, for which the calculated numerical values of convergence of a chosen excavation in the model would be most closely related to the results of excavation convergence measurements carried out in mining conditions. This method facilitates estimation of the matching of predicted excavation convergence results to measurement data (based on the coefficient of determination, R^2. The case study presented in this paper proved that by using the described method, the matching between results of in-situ convergence measurements in mines to convergence values obtained for effective parameters of pillars determined using statistical methods is very good, with R^2 is equal to 0.9896.

The method has a lot of advantages and can be used to calibrate the numerical models of other engineering problems, e.g., for the determination of gob parameters for different mining systems. The method allows the determination of pillar parameters for different models of rock mass. In the case of an elastic-plastic model, it enables the description of the post-destructive part of stress-strain characteristics using the appropriate values of strength parameters such as the Coulomb–Mohr hypothesis. This is of vital importance for the accuracy of obtained results of numerical modeling and thus for the degree of real

situation representation (e.g., a real situation in a modeled mining area). An appropriately verified numerical model allows for accurate analysis of the current situation in an analyzed region, for forecasting rock mass behavior during the progress of work, and for identification of dangerous phenomena which might create a threat to people working in a particular area. Future research will include the application of the method described in this manuscript to the numerical analysis of different mining situations.

Institutional Review Board Statement: Not applicable.

Informed Consent Statement: Not applicable.

Data Availability Statement: The data presented in this study are available on request from the corresponding author.

Conflicts of Interest: The author declares no conflict of interest.

References

1. Jing, L.; Hudson, J.A. Numerical methods in rock mechanics. *Int. J. Rock Mech. Min. Sci.* **2002**, *39*, 409–427. [CrossRef]
2. Jing, L. A review of technics, advances and outstanding issues in numerical modelling for rock mechanics and rock engineering. *Int. J. Rock Mech. Min. Sci.* **2003**, *40*, 283–353. [CrossRef]
3. Beer, G.; Pousen, A. Efficient numerical modelling of faulted rock using the boundary element method. *Int. J. Rock Mech. Min. Sci.* **1995**, *32*, 117A. [CrossRef]
4. Kayupov, M.A.; Kuriyagawa, M. DDM modelling of narrow excavations and/or cracks in anisotropic rock mass. In Proceedings of the ISRM International Symposium-EUROCK 96, Torino, Italy, 2–5 September 1996; Balkema: Rotterdam, The Netherlands, 1996; pp. 351–358.
5. Cerrolaza, M.; Garcia, R. Boundary elements and damage mechanics to analyze excavations in rock mass. *Eng. Anal. Boundary Elements* **1997**, *20*, 1–16. [CrossRef]
6. Pan, E.; Amadei, B.; Kim, Y.I. 2D BEM analysis of anisotropic half- plane problems—Application to rock mechanics. *Int. J. Rock Mech. Min. Sci.* **1998**, *35*, 69–74. [CrossRef]
7. Shou, K.J. A three-dimensional hybrid boundary element method for non-linear analysis of a weak plane near an underground excavation. *Tunn. Undergr. Sp. Technol.* **2000**, *16*, 215–226. [CrossRef]
8. Mark, C.; Molinda, G.; Dolinar, D. Analysis of roof bolt stability. In Proceedings of the 20th International Conference on Ground Control in Mining, Morgantown, WV, USA, 7–9 August 2001; Peng, S.S., Mark, C., Khair, A.W., Eds.; West Virginia University: Morgantown, WV, USA, 2001; pp. 218–225.
9. Pawelus, D. Evaluation of corridor excavation stability in the area of R-XI shaft using elastic-plastic model of rock formation and Coulomb- Mohr criterion. *"Cuprum" Sci. Tech. Pap. Ore Min.* **2013**, *4*, 21–40.
10. Adach-Pawelus, K.; Pawelus, D. Influence of driving direction on the stability of a group of headings located in a field of high horizontal stresses in the Polish underground copper mines. *Energies* **2021**, *14*, 5955. [CrossRef]
11. Yassien, A.M.; Zhang, Y.; Han, J.; Peng, S.S. Comparison of Some Aspects of Bolting Mechanisms between Fully-Grouted Resin and Tensioned Bolts in Underground Mine Entries. In Proceedings of the 21st International Conference on Ground Control in Mining, Morgantown, WV, USA, 6–8 August 2002; Peng, S.S., Mark, C., Khair, A.W., Heasley, K.A., Eds.; West Virginia University: Morgantown, WV, USA, 2002; pp. 114–125.
12. Ghanmi, A.; Planeta, S.; Djelloud, J. Numerical modelling of mining sequences for steep orebodies. In *Mine Planning and Equipment Selection*; Balkema: Rotterdam, The Netherlands, 1998; pp. 53–57.
13. Board, M.; Brummer, R.; Seldon, S. Use of Numerical Modelling for Mine Design and Evaluation. In *Underground Mining Methods: Engineering Fundamentals and International Case Studies*; Society for Mining, Metallurgy and Exploration: Englewood, CO, USA, 2001; pp. 483–492.
14. Yasitli, N.E.; Unver, B. 3D numerical modelling of longwall mining with top-coal caving. *Int. J. Rock. Mech. Min. Sci.* **2005**, *42*, 219–235. [CrossRef]
15. Peng, S. *Coal Mine Ground Control*, 3rd ed.; Society for Mining Metallurgy: Englewood, CO, USA, 2008.
16. Villegas, T.; Nordlund, E. Numerical Analysis of the Hangingwall Failure at the Kiirunavaara Mine. In Proceedings of the InInternational Conference & Exhibition on Mass Mining, Luleå, Sweden, 9–11 June 2008; Schunnesson, H., Nordlund, E., Eds.; Luleå Tekniska Universitet: Luleå, Sweden, 2008.
17. Blachowski, J.; Ellefmo, S. Numerical Modelling of Rock Mass Deformation in Sublevel Caving Mining System. *Acta Geodyn. Geomater.* **2012**, *9*, 379–388.
18. Shabanimashcool, M.; Li, C.C. Numerical modelling of longwall mining and stability analysis of the gates in a coal seam. *Int. J. Rock. Mech. Min. Sci.* **2012**, *51*, 24–34. [CrossRef]

19. Suchowerska, A.M.; Merifield, R.S.; Carter, J.P. Vertical stress changes in multiseam mining under supercritical longwall panels. *Int. J. Rock. Mech. Min. Sci.* **2013**, *61*, 306–320. [CrossRef]
20. Lafont, G.; Gunzburger, Y.; Mitri, H.S.; Al Heib, M.; Didier, C.; Piguet, J.P. Influence of mining excavation on energy redistribution and rockburst potential. In Proceedings of the 23 World Mining Congress, Montreal, QC, Canada, 11 August 2013.
21. Ozbay, M.U.; Ryder, J.A. The effect of foundation damage on the performance of stabilizing pillars. *J. S. Afr. Inst. Min. Metall.* **1990**, *90*, 29–35.
22. Kaiser, P.K.; Tang, C.A. Numerical simulation of damage accumulation and seismic energy release during brittle rock failure part II: Rib pillar collapse. *Int. J. Rock. Mech. Min. Sci.* **1998**, *35*, 123–134. [CrossRef]
23. York, G. Numerical modelling of the yielding of a stabilizing pillar/foundation system and a new design consideration for stabilizing pillar foundations. *J. S. Afr. Inst. Min. Metall.* **1998**, *98*, 281–297.
24. Vieira, F.M.C.C.; Dede, T.; Maccelari, M.J.; Spottiswoode, S.M. Stabilizing and bracket pillar design to reduce seismicity. *J. S. Afr. Inst. Min. Metall.* **1998**, *98*, 11–17.
25. Yavuz, H. Yielding Pillar Concept and its Design. In Proceedings of the 17th International Mining Congress and Exhibition of Turkey–IMCET, Antalya, Turkey, 19–22 June 2001.
26. Watson, B.P.; Roberts, M.K.C.; Nkwana, M.M.; Kuijpers, J.; van Aswegen, L. The stress-strain behaviour of in-slope pillars in the Bushveld Platinum deposits in South Africa. *J. S. Afr. Inst. Min. Metall.* **2007**, *107*, 187–194.
27. Jia, P.; Zhu, W.-c. Dynamic−static coupling analysis on rockburst mechanism in jointed rock mass. *J. Cent. South Univ.* **2012**, *19*, 3285–3290. [CrossRef]
28. Adach, K. Impact of the Size of Remnants on Seismic and Rockburst Hazard in LGOM Mines. Ph.D. Dissertation, Wroclaw University of Science and Technology, Wroclaw, Poland, 2015. (In Polish).
29. Adach-Pawelus, K.; Pawelus, D. Application of hydraulic backfill for rockburst prevention in the mining field with remnant in the Polish underground copper mines. *Energies* **2021**, *14*, 3869. [CrossRef]
30. Rybak, J.; Khayrutdinov, M.; Kuziev, D.; Kongar-Syuryun, C.B.; Babyr, V.N. Prediction of the geomechanical state of the rock mass when mining salt deposits with stowing. *J. Min. Inst.* **2022**, *253*, 61–70. [CrossRef]
31. Tang, C. Numerical Simulation of Progressive Failure and Associated Seismicity. *Int. J. Rock. Mech. Min. Sci.* **1997**, *34*, 249–261. [CrossRef]
32. Wiles, T.D.; Lachenicht, R.; van Aswegen, G. Integration of deterministic modelling with seismic monitoring for the assessment of rockmass response to mining: Part I Theory. In Proceedings of the Fifth Internatioal Symposium on Rockburst and Seismicity in Mines, Johannesburg, South Africa, 17–19 September 2001; pp. 379–387.
33. Zhu, W.C.; Li, Z.H.; Zhu, L.; Tang, C.A. Numerical simulation on rockburst of underground opening triggered by dynamic disturbance. *Tunn. Undergr. Sp. Technol.* **2010**, *25*, 587–599. [CrossRef]
34. Adach-Pawelus, K.; Butra, J.; Pawelus, D. An attempt at evaluation of the remnant influence on the occurrence of seismic phenomena in a room-and-pillar mining system with roof deflection. *Studia Geotech. Mech.* **2017**, *39*, 3–16. [CrossRef]
35. Adach-Pawelus, K. Application of seismic monitoring and numerical modelling in the assessment of the possibility of seismic event occurrence in the vicinity of ore remnant. In *IOP Conference Series—Earth & Environmental Science, Proceedings of the World Multidisciplinary Earth Sciences Symposium, Prague, Czech Republic, 3–7 September 2018*; IOP Publishing Ltd.: Bristol, UK, 2019; Volume 221, pp. 1–10. [CrossRef]
36. Wang, S.; Masoumi, H.; Oh, J.; Zhang, S. *Scale-Size and Structural Effects of Rock Materials*; Woodhead Publishing: Sawston, UK, 2020.
37. Kashfia, M.; Shada, S.; Zivarba, D. Evaluation of sample scale effect on geomechanical tests. *Pet. Res.* **2022**. [CrossRef]
38. Hoek, E.; Brown, E.T. Practical estimates of rock mass strength. *Int. J. Rock. Mech. Min. Sci.* **1997**, *34*, 1165–1186. [CrossRef]
39. Hoek, E.; Marinos, P. GSI: A geologically friendly tool for rock mass strength estimation. Presented at the ISRM International Symposium, Melbourne, Australia, 19–24 November 2000.
40. Hoek, E.; Carranza-Torres, C.T.; Corkum, B. Hoek-Brown failure criterion—2002 edition. In Proceedings of the North American Rock Mechanics Society Meeting in Toronto, Toronto, ON, Canada, 7–10 July 2002.
41. Sakurai, S. Direct strain evaluation technique in construction of underground openings. In Proceedings of the 22nd US Symposium on Rock Mechanics, Cambridge, MA, USA, 29 June–2 July 1981; MIT Press: Cambridge, MA, USA, 1981; pp. 278–282.
42. *Catalogue of Copper Deposit Mining Systems in KGHM Polska Miedz SA Mines*; KGHM Polska Miedz SA Mines: Lubin, Poland, 2007. (In Polish)
43. *RocScience Phase2 Finite Element Analysis for Excavations and Slopes v. 8.0 Documentation*; RocScience Inc.: Toronto, ON, Canada, 2015.

Influence of a Type of Rock Mass on the Stability of Headings in Polish Underground Copper Mines Based on Boundary Element Method

Karolina Adach-Pawelus * and Natalia Szyry

Faculty of Geoengineering, Mining and Geology, Wroclaw University of Science and Technology, 50-370 Wroclaw, Poland
* Correspondence: karolina.adach@pwr.edu.pl

Abstract: This paper presents the results of a numerical analysis of the impact of rock mass geomechanical parameters on the stability of preparatory headings located within the Legnica-Glogow Copper District. The paper shows the results of numerical calculations prepared for headings driven in two rock mass types with different strength and deformation parameters, which allow illustrating their influence on the safety of mining performed in underground copper ore mines. Numerical modeling was performed using the Examine2D 7.0 software, in the plane strain state. Numerical simulations were performed for an isotropic and for a homogenous medium. The rock medium was described with an elastic model. The parameters of the rock mass for numerical modeling were calculated using the Hoek–Brown classification. The Coulomb–Mohr strength criterion was adopted as a measure for assessing the rock mass effort. Numerical simulations confirmed the dependance between the stability of the analyzed excavations and rock mass geomechanical parameters.

Keywords: rock mass stability; copper ore mining; numerical modeling

1. Introduction

Along with the development of deep underground mines appears an increasing difficulty in understanding the failure mechanism of a rock mass surrounding roadways and introducing deformational control. The geological surroundings of shallowly located headings are often simpler, e.g., lower values of the primary stress and less influenced by geological faults, while deep mining faces complicated problems such as in situ stress increase, a varied geological environment, and combinations of multi-type rock masses. Due to these factors, the instability mechanism of deep rock structures and the mechanical properties of underground rock masses are becoming more complex. It is difficult to precisely estimate the deformation of rock masses surrounding the headings located at a great depth, which makes the prevention of keeping their structural stability increasingly difficult. Unpredicted loss of rock stability may cause dynamic disasters such as roof collapse, rock bursts, gas and coal outbursts, or large-scale subsidence [1]. Owing to a large excavation dimension and heading height, any dynamic event can have a ruinous effect when it occurs [2]. In Poland, copper ore mining has exceeded 1200 m below the ground level and is strongly affected by difficult geology and mining conditions. Due to the extraction depth, copper ore mining is influenced by a growing number of problems connected with the rock mass stability and the occurrence of dynamic events. Therefore, there is a need to perform further research on the prediction and prevention of the potential stability loss in the future [3].

The deflection of the overlaying strata or block disintegration is related to the rock mass parameters. The most important factors playing a substantial role in forming subsidence and ground shifts are the strength and deformational characteristics of the rock mass [4]. For example, the strength and stiffness properties of the rock mass impact the angle of

draw, being one of the key parameters in subsidence analysis and prediction [5]. As the rock mass increases, the angle of draw decreases. In contrast, weak rocks extend the scope of subsidence at the surface. A strong rock layer tends to decrease the extent of subsidence, and a weak layer increases the area of deformation. Moreover, the weak strata could impact the scope of subsidences significantly more than the strong layer could [4].

The proper design of the rock headings demands an accurate understanding of the rock mass mechanical properties. There have been numerous attempts to find a way to correctly estimate the rock material parameters being used as the input for analytical and numerical simulations [6–9]. The results of these simulations are strongly influenced by the entered values. An undue trust in the simulation output without controlling the accuracy of the input parameters may cause devastating disasters in rock engineering ventures [4]. The parameters defining the rock mass material properties are mainly cohesion, tensile strength, internal friction angle, vertical stress, and the lateral pressure coefficient of the deeply located headings' surroundings [1]. Deformation of rock material is expressed, among others, through Poisson's ratio ν and the longitudinal modulus of elasticity E [3].

Understanding rock mass parameters enables the use of numerical analysis methods. Numerical simulations meaningfully expand the scope of research related to the evaluation of the rock mass stability [10,11]. Numerical modeling gives the possibility to define the stress concentration locations and potential regions endangered by the stability loss [12]. The numerical analysis approaches can be divided into the conventional and advanced data processing methods. Unlike the analytical approaches, numerical simulation can be applied to assess the stability of both the room and pillar or longwall mining methods. Numerical methods can be classified into one of three main groups. The first one, the continuous method, includes the Finite Element Method (FEM), the Boundary Element Method (BEM), and the Finite Difference Method (FDM). The second and third groups consist of more complicated and complex numerical methods, such as the Distinct Element Method (DEM) or the coupled Finite Element-Discrete Element Method (FEM-DEM), being recently introduced to the excavation stability analysis. Numerical methods allow the accurate assessment of mining subsidences and the magnitude of ground movements and preventing dynamic events. Numerical analysis considers the nonlinear behaviors of the pillars and rock floor materials. Moreover, numerical modeling enables the design of the complex deposit geometry and boundary conditions [4]. Numerical simulations and stability assessment performed may lead to further development of more efficient mining technologies and solutions designed to improve safety in underground mine plants [13].

This article aims to research the influence of the rock mass geological structure on the headings' stability and deep underground copper mining safety with the use of numerical analysis based on the boundary element method.

2. Geological Conditions of the Legnica-Glogow Copper District Mines

Copper deposits mined by KGHM Polska Miedz S.A. within the Legnica-Glogow Copper District are a fragment of the Fore-Sudetic monocline. The Fore-Sudetic monocline is a geological unit in southwest Poland, bordering the Zar pericline to the west, the Silesian-Krakow monocline to the east, the Fore-Sudetic block to the southwest, and the Szczecin-Lodz synclinorium to the northeast [14].

The Fore-Sudetic monocline consists of sedimentary rocks that cover a substrate made of Proterozoic crystalline rocks. The results of dating the copper-laden rock layers indicate that the balance reserves of this ore originated in the Permian. The top of the deposit is made of dolomite-limestone rocks of the Lower Zechstein, and the bottom is made of Rotliegend sandstones. The balance thickness of the deposit varies locally and ranges from several dozen centimeters to several meters. The rock layers that make up the monocline are inclined at an angle of 3–5°, and the depth at which they are located increases to the northeast [14].

As a result of geological and exploratory work around copper deposits in today's Legnica-Glogow Copper District, the presence of 1,403,467,000 balance tons of copper ore

resources was confirmed with an average thickness of 3.45 m and a copper content of 2.09%. The presence of 29,362,000 tons of copper has also been documented [15].

The area of the deposit is located between Legnica and Glogow. The deck has the shape of an elongated polygon 30–35 km long and 7–10 km wide, and its area is approximately 300 km^2. Copper mineralization includes Lower Zechstein limestones, dolomites and shales, and Weissliegend or Rotliegend sandstones. The copper content in the deposit rocks is heterogeneous. In practice, only those parts of the seam in which the copper-bearing series meets the balance criteria of at least 0.9% copper content are considered a deposit [16]. Copper shale has the highest content of copper. Sandstone mineralization is significant in the area of operation of the Rudna mine and irregular in the area of Polkowice. In some areas, the dolomites show little mineralization, and in others, they are the main carrier of copper (e.g., in the area of Polkowice) [17].

Violation of the original state of stress and deformation of the rock mass leading to the loss of stability are greater the more anisotropic the rock mass is. This type of rock mass occurs within the Legnica-Głogow Copper District mine. The anisotropy of the rock headings in this area results not only from the lithological variability of the rocks (the rock mass is made up of carbonate rocks, sandstones, and shales with different geomechanical properties), but also from the presence of tectonic geological disturbances. Roof rocks of established headings in the Lower Silesian Copper District have a layered structure, in which the spaces between the layers are filled with rock material with reduced strength parameters, composed of gypsum, calcite, or slate. The sandstones that make up the bottom part of the exploitation door contain binders of different compositions, which translates into the variability of the physical factors and strength properties of the bottom rocks [16].

Today, three copper ore mines of KGHM Polska Miedz S.A. operate in the area of the Legnica-Glogow Copper District. These include the mines "Lubin", "Polkowice-Sieroszowice", and "Rudna". The "Lubin" mine exploits the "Lubin-Malomnice" field. This deposit is dominated by sandstone rocks, which constitute about 67% of all rocks in this area. Eighteen percent of the resources are Zechstein limestone carbonate rocks and 15% Zechstein copper shales. The average thickness of the deposit is 2.33 m, and the depth of deposition varies from 368 to 1006 m. This part of the seam shows a high tectonic involvement of the deposit rocks. The deposit is shallow, not much deeper than the loose Cenozoic sediments. As a result of dislocation, the rock series building this fragment of the deck was divided into blocks of various shapes, which then moved relative to each other vertically and horizontally, creating ditches, frameworks, and stair systems. There are no clear discontinuous dislocation lines in the deposit area, only fault zones, the discharges of which range from a few centimeters to several dozen meters. The width of the faults ranges from 250 to 1500 m [18].

The "Polkowice-Sieroszowice" mine extracts the ore in the "Polkowice", "Sieroszowice", and "Radwanice-Wschód" deposits. Mining is carried out at a depth of 676 to 1084 m. In addition to copper, rock salt is present in the deposit rocks. The rock salt seam is the largest in the central and northern part of "Sieroszowice". The copper-bearing carbonate rocks of the Zechstein limestone dominate in the mine and account for 80%, 55%, and 93% of the deposit rocks of individual deposits, respectively. The resources of the Zechstein copper shale amount to 12%, 14%, and 7% of the total deposits, respectively. Weissliegend sandstone is found only in the "Polkowice" and "Sieroszowice" deposits, and its content is 8% and 31%, respectively. The series of copper-bearing shale located in the mining area contains large amounts of copper and silver, but the seam thickness does not usually exceed 1 m. The "Polkowice" and "Sieroszowice" deposits are located in the areas with developed tectonics. In zones deformed by faults or folds of the layers, the collapse of the series of rocks that make up the seam increases or decreases in relation to the usual inclination of the layers at an angle of 3–6°. The deviation from the general course of the layers varies locally, and the changes can be as high as 90°. There are numerous discontinuous dislocations in the "Polkowice" and "Sieroszowice" deposits. The range of shifts in the "Polkowice" area usually does not exceed 1 m, and the sum of shifts may

reach a value of several dozen meters. Apart from discontinuous dislocations, there are fold–fault structures around "Sieroszowice" [18].

The "Rudna" mine extracts from the "Rudna" and "Sieroszowice" deposits. The exploitation depth ranges from 920 to 1170 m. The average thickness of the seam within the "Rudna" deposit is 4.26 m. The deposit rocks are composed of Zechstein carbonate rocks and clay-dolomite shales, as well as Weissliegend sandstones. The presence of depression zones influenced the lithological development of the deposit rock layers. In depression zones, copper is found in sandstones, copper-bearing shales, as well as clay and dolomites. Carbonate ore constitutes 11%, shale ore 6%, and sandstone ore 83% of all ore resources of the Rudna deposit. The deposit layers fall at an average angle of 1–6°, but locally, the fall of the layers can even reach 45°. There are discontinuous dislocations in the deposit, which together form a system of numerous block structures [18].

3. Numerical Analysis of Headings' Stability in the Legnica-Glogow Copper District Mines

Numerical modeling in this article was performed with Examine2D 7.0, using the boundary element method. The boundary element method is a numerical modeling method that divides a given area into finite elements. In the connecting nodes of these elements, differential calculations are performed, the results of which allow modeling, e.g., the stress distribution around the analyzed element [19].

After a few decades of development, the Boundary Element Method (BEM) has found its place around numerical methods for differential equations. While more popular methods such as the Finite Element Method (FEM) or Finite Difference Method (FDM) can be classified as the domain method, the BEM differs in terms of the numerical discretization being conducted at a reduced spatial dimension. For three spatial dimensions, the discretization is only performed on the boundary surface of the analyzed element. For two spatial dimension problems, the discretization is performed only on the boundary contours. This solution leads to linear systems and computer memory requirement reduction, which makes the calculations more efficient. This effect is most visible when the domain is unbounded. Such domains need to be truncated and approximated in domain methods. The BEM automatically models the behavior of the element's surroundings without the need to construct a mesh to estimate it. Since mesh preparation seems to be the most labor intensive and cost consuming in numerical modeling, especially for the FEM, the BEM is more effective in terms of mesh deploying. When the problem includes moving boundaries, it is easier to adjust the mesh using the BEM, which makes the method preferably used. The advantages of the BEM are essential for choosing the right method to solve numerical problems [20]. The are several publications regarding the BEM, describing the characteristics of the method and the equations used during the calculations. Additional information on the method can be found in the studies performed by Beskos, Kythe, Balaš, and others [21–23].

3.1. Problem Geometry

In the Polish copper mines, the room and pillar mining system is used. Mining the ore using the room and pillar system consists of cutting the deposit with rooms and strips with the separation of technological pillars of a certain geometry, which protect the roof over the working area. The size of the pillars is chosen to provide the work in the post-critical state. In the discussed mining system, the shape of the excavation is an inverted trapezoid. The height of excavation in the cutting phase depends on the thickness of the deposit and the requirements of the working machines. The width of excavations does not exceed 7 m. The minimum size of the opening face of the mining front is equal to the sum of two strips and the length of two rows of pillars into undisturbed rock. Along with the progress of the mining front, the size of the technological pillars from the last row before gobs, depending on the degree of their disintegration, is reduced and remnant pillars are created. The remnant pillars are left in the gobs. They work as supports to mitigate the

deflection of roof layers [24]. The currently used mining system allows obtaining from 75% to even 90% of the deposit ore [17].

Mining the minerals in the KGHM mines includes the preparatory works, consisting of contouring the deposit with a network of underground roadways [18]. Preparatory excavations are protected with rock bolt support, which is the primary support for all excavations in the mines [17].

In this paper, preparatory excavations mined for the use of the room–pillar with roof deflection (J-UG-PS) mining system are analyzed. In the J-UG-PS system, the copper ore deposit is mined with rooms and strips up to 7 m wide, excavated to the full thickness of the deposit. During the work, technological pillars with the basic geometry of 6–9 m × 8–16 m are separated and located with the axis perpendicular to the mining front line [24]. Figure 1 shows a scheme of the J-UG-PS mining system.
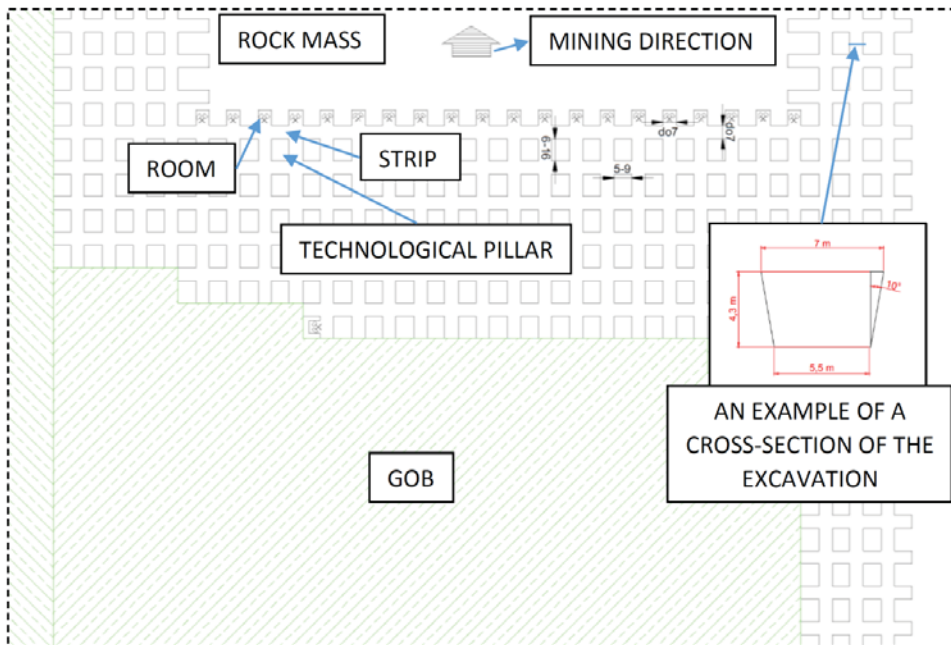
Figure 1. Room–pillar mining system with roof deflection (J-UG-PS) [24].

The geometry of the excavations analyzed in this study was determined based on two different cross-sections of the preparatory excavations driven around one of the mining fields located in the Legnica-Glogow Copper District, where ore was mined using the J-UG-PS system. The first cross-section runs through the ramps, the second through the entries. The geometrical data of the cross sections are presented in Table 1.

Table 1. Geometric cross-section data.

Parameter	Value (m)
Excavation height	4.30
Excavation roof length	7.00

In the Legnica-Glogow Copper District mines, the headings have the characteristic shape of an inverted trapezoid. Figure 2 presents ca ross-section through an analyzed single heading; Figure 3 shows cross-sections through ramps and entries.
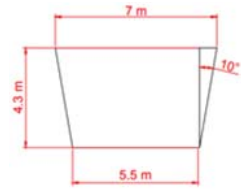
Figure 2. Heading profile.

(**a**)

(**b**)
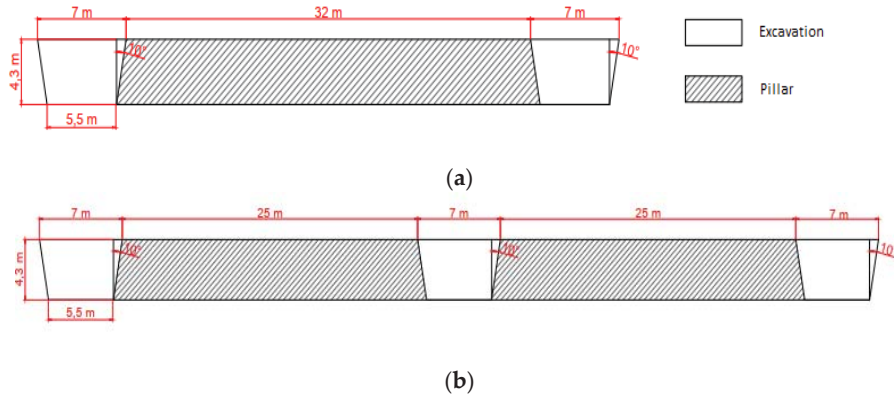
Figure 3. (**a**) Cross-section through the ramps; (**b**) cross-section through the entries.

3.2. Geological Conditions and Rock Mass Parameters

The analysis was performed for representative rock layers occurring in the Legnica-Glogow Copper District mines. Two different rock layer systems were analyzed, the parameters of which are presented in Tables 2 and 3. The headings are located at a depth of 1000 m, respectively in sandstone (Table 2) and in dolomite (Table 3).

Table 2. Rock mass parameters for the excavation drilled in sandstone.

Rock Layers	Rock Layer Thickness (m)	Rock Layer Density (g/cm³)	Rock Layer Poisson Ratio (-)
Overburden	500	$\rho = 2.70$	$v = 0.20$
Anhydrite	250	$\rho = 2.95$	$v = 0.25$
Dolomite	100	$\rho = 2.80$	$v = 0.25$
Sandstone I	100	$\rho = 2.40$	$v = 0.20$
Sandstone II	50	$\rho = 2.30$	$v = 0.15$

Table 3. Rock mass parameters for the excavation drilled in dolomite.

Rock Layers	Rock Layer Thickness (m)	Rock Layer Density (g/cm³)	Rock Layer Poisson Ratio (-)
Overburden	500	$\rho = 2.70$	$v = 0.20$
Anhydrite	250	$\rho = 2.95$	$v = 0.25$
Dolomite	100	$\rho = 2.80$	$v = 0.25$
Dolomite	100	$\rho = 2.80$	$v = 0.25$
Dolomite	50	$\rho = 2.80$	$v = 0.25$

Numerical modelling was performed using the Examine2D 7.0 software, in the plane strain state. Numerical simulations were performed for an isotropic and for a homogenous medium. The rock medium was described with an elastic model. The parameters of the

rock mass for numerical modeling were calculated using the Hoek–Brown classification. The Coulomb–Mohr strength criterion was adopted as a measure for assessing the rock mass effort [25]:

$$\sigma_1 = \sigma_3 \cdot \frac{1 + \sin\varphi}{1 - \sin\varphi} + \frac{2c \cdot \cos\varphi}{1 - \sin\varphi},$$ (1)

where:

σ_1, σ_3—maximum and minimum stress at failure;

φ—angle of internal friction;

c—cohesion.

The cohesion and the angle of internal friction were calculated based on the Hoek–Brown classification from the formulas [26–29]:

$$c = \frac{\sigma_{ci} \cdot \left[(1 + 2a) \cdot s + (1 - a) \cdot m_b \cdot \frac{\sigma_{3max}}{\sigma_{ci}} \right] \cdot \left(s + m_b \cdot \frac{\sigma_{3max}}{\sigma_{ci}} \right)^{a-1}}{(1 + a) \cdot (2 + a) \cdot \sqrt{1 + \frac{6 \cdot a \cdot m_b \cdot \left(s + m_b \cdot \frac{\sigma_{3max}}{\sigma_{ci}} \right)^{a-1}}{(1+a) \cdot (2+a)}}},$$ (2)

$$\varphi = \arcsin\left[\frac{6 \cdot a \cdot m_b \cdot \left(s + m_b \cdot \frac{\sigma_{3max}}{\sigma_{ci}} \right)^{a-1}}{2 \cdot (1 + a) \cdot (2 + a) + 6 \cdot a \cdot m_b \cdot \left(s + m_b \cdot \frac{\sigma_{3max}}{\sigma_{ci}} \right)^{a-1}} \right],$$ (3)

where:

$$\sigma_{3max} = \frac{\sigma_{ci}}{4}.$$ (4)

Performing these calculations allowed determining the parameters then adopted as assumptions for numerical modeling in Examine2D 7.0. The calculated parameters are shown in Table 4.

Table 4. The results of calculations based on the Coulomb–Mohr strength criterion.

Rock Type	h (m)	σ_{3max} (MPa)	σ_t (MPa)	c (MPa)	φ (°)
Sandstone	1000.0	3.75	−0.04	1.04	39.06
Dolomite	1000.0	37.50	−3.32	13.68	39.00

The numerical model was based on the values of primary stresses calculated according to the Therzagi formula, taking into account the weight of the overlying rock layers. The calculated vertical and horizontal stresses are included in Table 5.

Table 5. Primary stresses.

Rock Type	Thickness h (m)	Unit Weight of Rock γ (g/cm^3)	Vertical Stress σ_z (MPa)	Horizontal Stress σ_x (MPa)
Sandstone	50.0	2.30	26.71	4.71
Dolomite	50.0	2.80	27.22	9.07

The numerical model was a plate where boundary contours were discretized. The plate edges were assumed to be at a 150.0 m distance from the extreme points on each side of the analyzed headings (the roof, the floor, and the side walls). Based on the numerical calculations of the headings' stability for each model, the following parameters were determined:

- Distribution of principal stresses σ_1;
- Distribution of principal stresses σ_3;
- Horizontal stress distribution σ_{XX};
- Vertical stress distribution σ_{YY};

- Total displacements;
- Strength factor.

The analysis of the results indicated that the optimal measure of the stability of the headings is the range of the strength factor zone. The strength factor is calculated by dividing the rock strength (based on defined failure criteria) by the induced stress.

4. Discussion of Numerical Modeling Results

The distribution of the σ_{YY} stresses in the ramps and entries is shown in Figures 4–8. The conducted analysis showed that for both types of analyzed rock masses in which the excavations were established, the distribution of the σ_{YY} stresses in the vicinity of excavation was similar. Numerical simulations showed that the tensile stresses are concentrated in the roof and, to a lesser extent, in the bottom of the heading. Compressive stresses arise in the excavation's ribs, particularly in the corners. σ_{YY} stresses between the excavations obtain values like the ones within the primary stress field, which proves the correct design of the protective pillars. The proper selection of the pillar sizes is conducive in terms of maintaining the stability of the headings located in their vicinity. In the cross-section of the ramps and entries, it is shown that σ_{YY} stresses acting on the protective pillars located between the ramps have a shorter range than the stresses acting on the protective pillars between the entries. In the central zone of the protective pillars located between the sandstone entries, the stresses are lower than in the case of dolomite pillars.

(**a**)   (**b**)
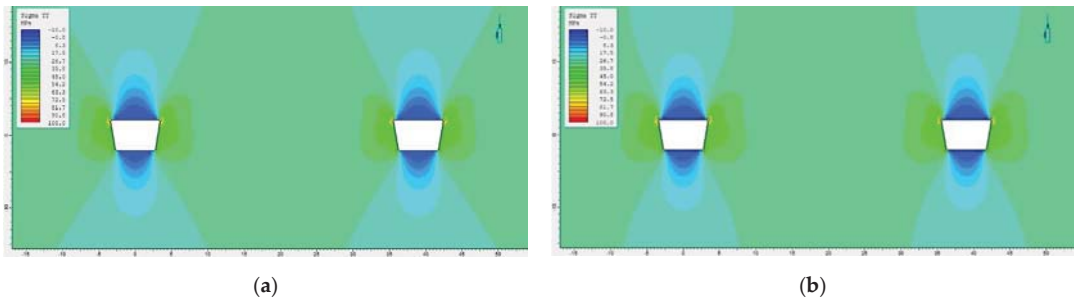
Figure 4. Distribution of σ_{YY} stresses in the cross-section through ramps drilled in: (**a**) sandstone; (**b**) dolomite.

(**a**)   (**b**)
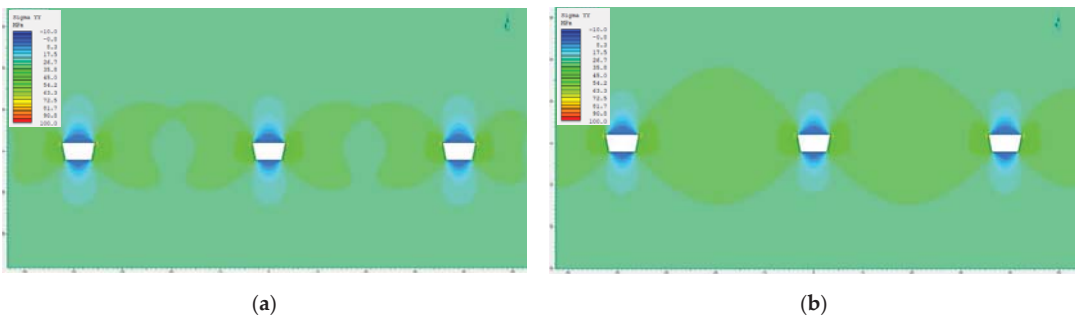
Figure 5. Distribution of σ_{YY} stresses in the cross-section through entries drilled in: (**a**) sandstone; (**b**) dolomite.
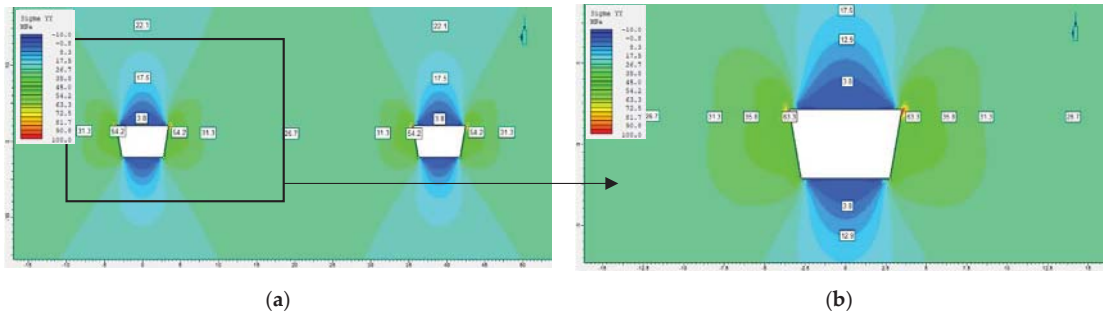
Figure 6. Distribution of σ_{YY} stresses in the cross-section through ramps drilled in sandstone: (**a**) view of both headings; (**b**) close-up of a single excavation.
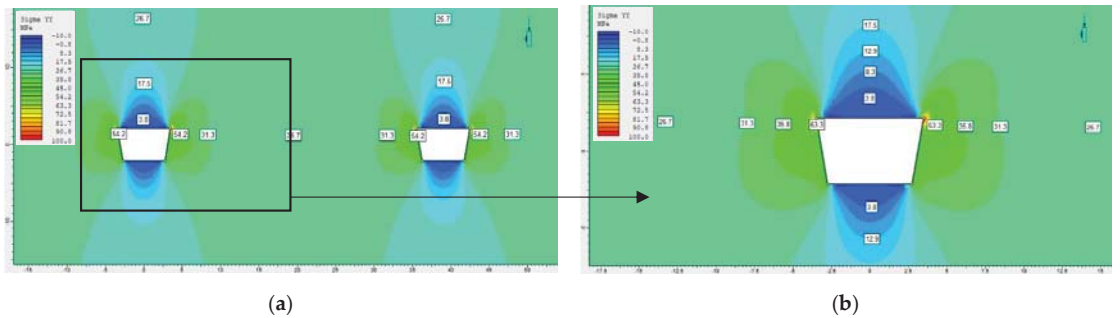
Figure 7. Distribution of σ_{YY} stresses in the cross-section through ramps drilled in dolomite: (**a**) view of both headings; (**b**) close-up of a single excavation.
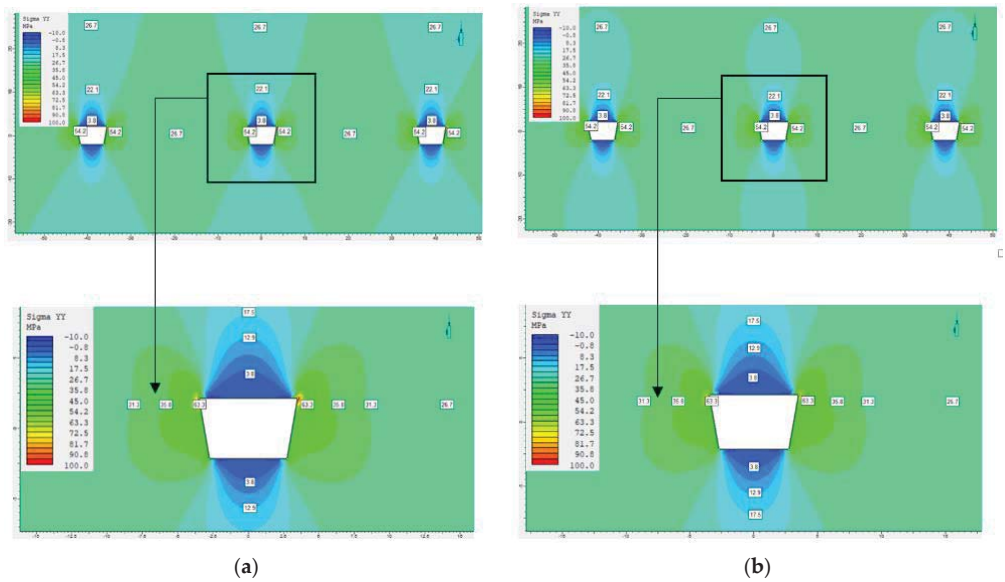
Figure 8. Close-up view of σ_{YY} stresses values in the cross-section through entries drilled in: (**a**) sandstone, (**b**) dolomite.

The location of roof stress measurement is presented in Figure 9. Graphs illustrating the dependence of distance to the excavation boundaries on the σ_{YY} values show that the tensile stresses acting on the heading roof in dolomite, having better strength and deformation parameters, reach slightly higher amounts than those occurring in sandstone (Figure 10).

(**a**)   (**b**)
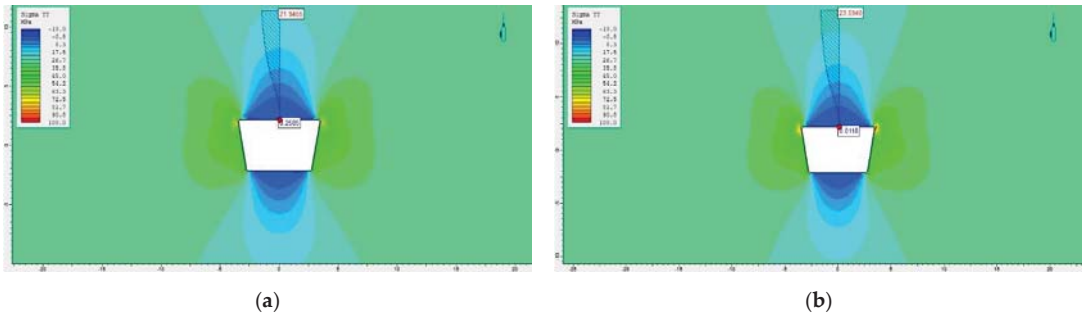
Figure 9. Stress measurement location used to create a graph presenting the distribution of stress acting on the excavation roof in cross-section through: (**a**) ramps; (**b**) entries.

(**a**)   (**b**)
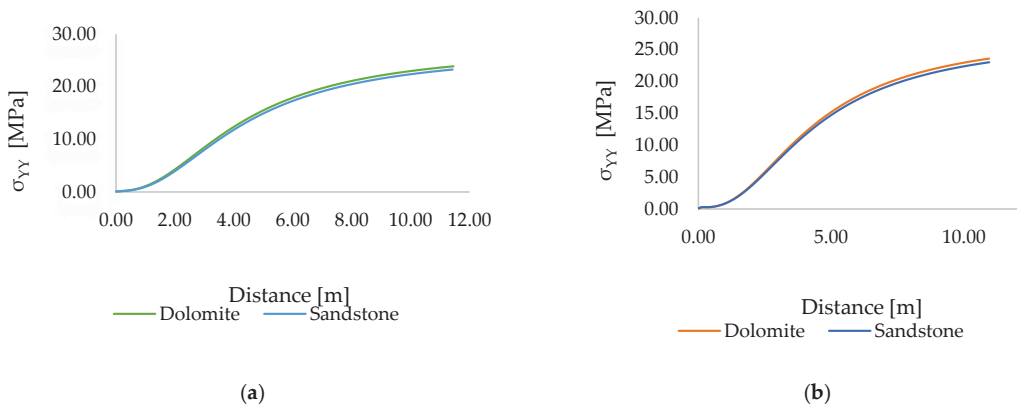
Figure 10. Distribution of σ_{YY} stresses acting on the excavation roof in the cross-section through the (**a**) ramps and (**b**) entries drilled in sandstone and dolomite.

The protective pillars' stress measurement location is shown in Figure 11. The stress values affecting the external part of the protective pillar in cross-section through the entries are bigger than the ones acting on the internal part of the pillar. The stresses affecting the protective pillars located between the ramps have similar values on both sides of the pillar. The stresses' distribution in the excavation ribs of the ramps and entries, drawn based on σ_{YY} distribution models in individual sections, prove that the compressive stresses reach similar values both in the internal and external ribs (Figures 12 and 13), comparable for sandstone and dolomite.

(**a**)   (**b**)
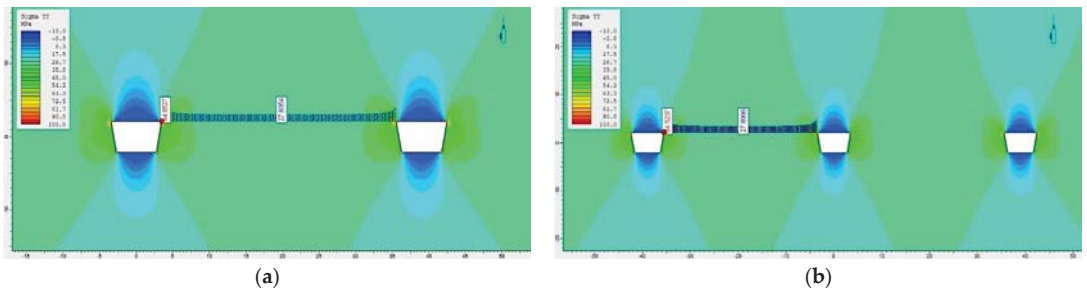
Figure 11. Stress measurement location used to create a graph presenting the distribution of stress acting on protective pillars in the cross-section through: (**a**) ramps; (**b**) entries.
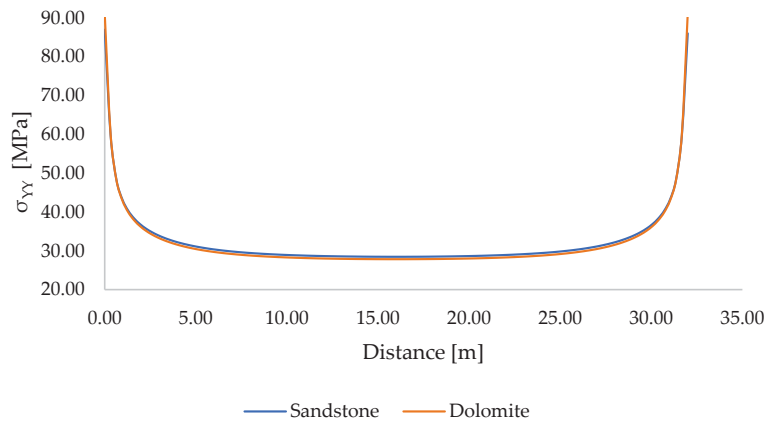
Figure 12. Distribution of σ_{YY} stresses acting on the protective pillars in the cross-section through the ramps.
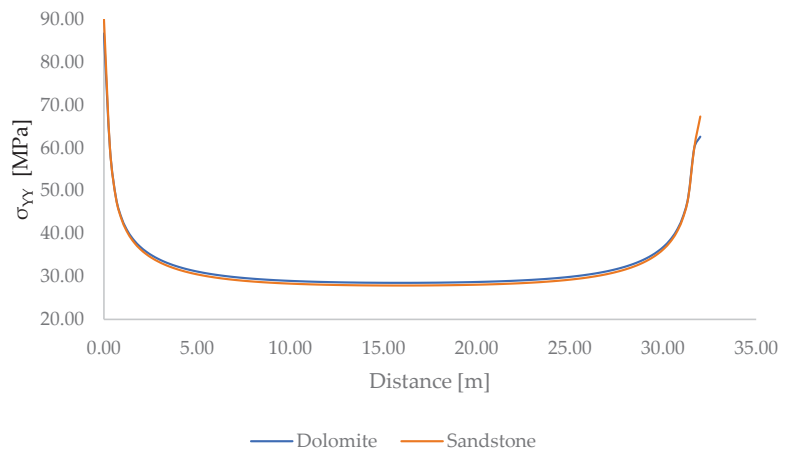
Figure 13. Distribution of σ_{YY} stresses acting on the protective pillars in the cross-section through the entries.

The stability of the analyzed headings was assessed based on the numerically defined distributions of the strength factor. The strength factor is calculated by dividing the rock

strength (based on the failure criteria) by the induced stress. The strength factor allows recognizing areas of potential rock mass instability, and its limit value is 1. Places where the index value falls below the limit are places of potential rock mass stability loss.

The strength factor value is related to the rock geomechanical parameter. The lower the strength and deformation parameters of the rock material in which the excavation is located, the greater the probability of losing the excavation stability is. A lower risk of instability occurs in the headings driven in dolomite and is greater in the headings created in sandstone (Figure 14).

(**a**)   (**b**)
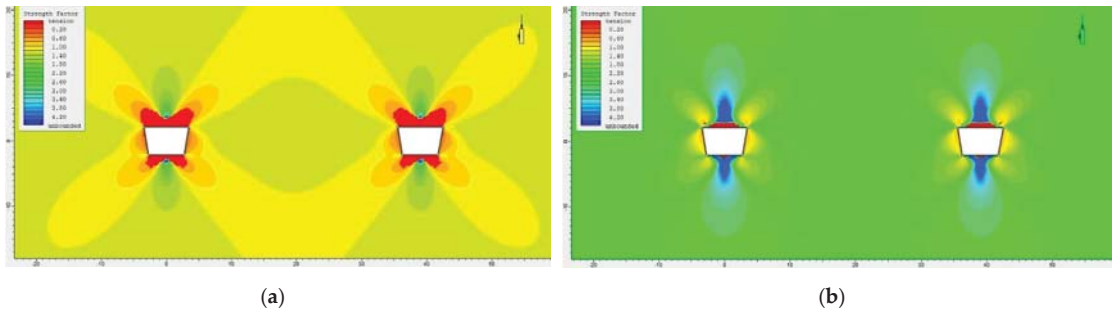
Figure 14. Distribution of strength factor values in the cross-section through ramps drilled in: (**a**) sandstone; (**b**) dolomite.

Figures 15 and 16 show close-up views of a single excavation with the extent of stability loss zone measured. The results of the strength factor distribution calculated using the numerical methods for headings located in sandstone show that the greatest risk of loss of stability occurs in the roof and floor of the excavation. The extent of the destruction zone is greater in the ribs than in the central part of the excavation, which may indicate the need to cover the area with longer bolts to protect the side fragments of the headings. As we move away from the boundaries, the strength factor reaches higher values, which is related to the rock mass returning to its primary stress field.

(**a**)   (**b**)
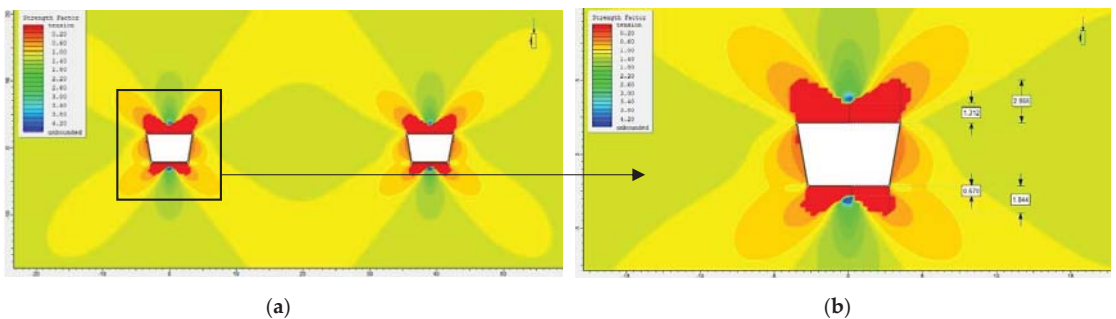
Figure 15. Distribution of strength factor values in the cross-section through ramps drilled in sandstone: (**a**) view of both headings; (**b**) close-up of a single excavation.
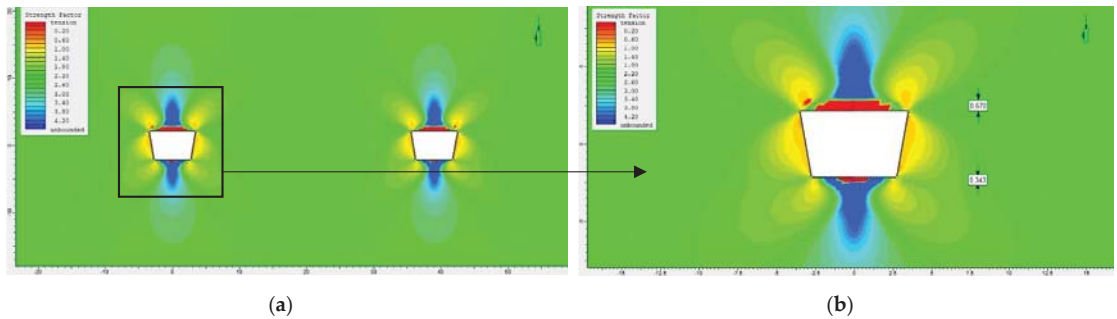
Figure 16. Distribution of strength factor values in the cross-section through ramps drilled in dolomite: (**a**) view of both headings; (**b**) close-up of a single excavation.

In the excavations driven in dolomite, being a material with high strength and deformation parameters, the risk associated with instability covers mainly the roof and floor of the excavation. The range of zones threatened by stability loss is greater within the roof and smaller within the floor, which is related to the intensification of the tensile stresses affecting the indicated heading fragments. In the immediate ribs' vicinity, the strength factor values are higher than in the roof and floor area, but remain lower than 1. The extent of the zones at risk of instability is noticeably smaller for dolomite than for sandstones. Directly after the zones at risk of stability loss within the roof and floor of the excavation, there are zones with a very high strength factor. Most of the area analyzed in the numerical simulations is covered by safe values of the strength factor, indicating the ability to maintain the rock mass stability. Distribution of strength factor values in the cross-section through entries drilled in sandstone and dolomite is presented in Figure 17.
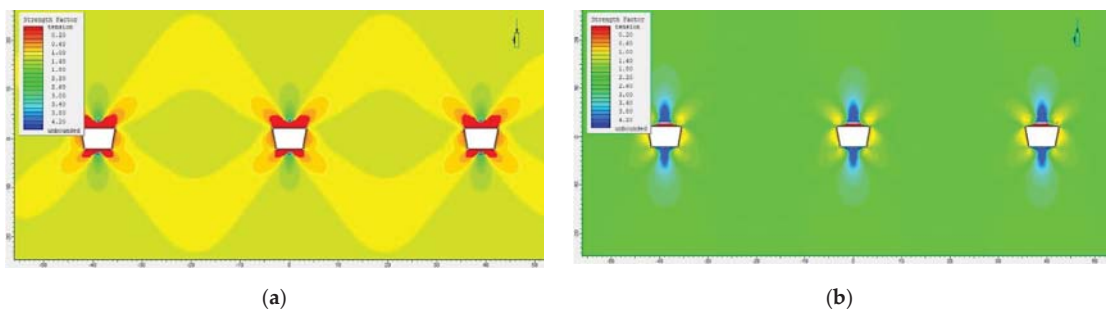
Figure 17. Distribution of strength factor values in the cross-section through entries drilled in: (**a**) sandstone; (**b**) dolomite.

5. Conclusions

The performed numerical modeling confirmed the dependence of the heading stability on the strength parameters of the rock mass. Having a lesser impact on the values of stresses affecting the driven heading, different geomechanical parameters of the rock mass determine its stability, as well as the size of emerging displacements. Rock material displacements create heading deformation, being a direct symptom of stability loss, and increase the probability of sudden roof collapses or (under appropriate conditions) even dynamic stress relief phenomena. Detailed analysis of the strength and deformation parameters of the rock mass type and the strength factor distribution will allow the optimal selection of the excavations' lining, creating less of a threat to miners' health and lives.

Numerical methods allow a broad analysis of mining excavations' stability. Accurate recognition of stresses affecting the excavation and modeling the effects of their impact

enable the development of appropriate prevention methods and excavation conditions' monitoring. Analysis of the models created for the needs of the article showed that having knowledge of the geomechanical parameters forming the rock mass is important in the context of ensuring safe and effective exploitation of copper ores in the conditions of the Legnica-Glogow Copper District. The results of the numerical modeling gave much crucial information about rock mass behavior in the vicinity of excavations. The innovativeness of the simulations performed is based on the possibility to predict the behavior of the rock mass in advance, without the need to perform labor-intensive and costly in situ experiments. This in turn allows the development of appropriate guidelines and new mining technologies designed to solve the problems of rock mass stability. Numerical modeling simulation results may enhance the deployment of the improved ongoing monitoring system of rock mass parameters, enabling the prediction of dynamic phenomena affecting the rocks. The future research will contain an analysis of the complex geological situation and different types of excavations located in Polish mines.

Author Contributions: Conceptualization, K.A.-P.; Data curation, K.A.-P. and N.S.; Formal analysis, K.A.-P.; Funding acquisition, K.A.-P.; Investigation, N.S.; Methodology, K.A.-P.; Project administration, K.A.-P. and N.S.; Resources, N.S.; Software, N.S.; Supervision, K.A.-P.; Validation, K.A.-P. and N.S.; Visualization, N.S.; Writing—original draft, N.S.; Writing—review & editing, K.A.-P. All authors have read and agreed to the published version of the manuscript.

Institutional Review Board Statement: Not applicable.

Informed Consent Statement: Not applicable.

Data Availability Statement: The data presented in this study are available upon request from the corresponding author.

Conflicts of Interest: The authors declare no conflict of interest.

References

1. Feng, X.; Ding, Z.; Hu, Q.; Zhao, X.; Ali, M.; Banquando, J.T. Orthogonal numerical analysis of deformation and failure characteristics of deep roadway in coal mines: A case study. *Minerals* **2022**, *12*, 185. [CrossRef]
2. Esterhuizen, G.; Dolinar, D.; Innacchione, A. Field observations and numerical studies of horizontal stress effects on roof stability in US limestone mines. *J. S. Afr. Inst. Min. Metall.* **2008**, *108*, 345–352.
3. Adach-Pawelus, K.; Pawelus, D. Influence of Driving Direction on the Stability of a Group of Headings Located in a Field of High Horizontal Stresses in the Polish Underground Copper Mines. *Energies* **2021**, *14*, 5955. [CrossRef]
4. Salmi, E. A numerical investigation of the mechanism of post-mining subsidence. In *Australian Research Council Centre of Excellence for Geotechnical Science and Engineering*; The University of Newcastle: Newcastle, Australia, 2016.
5. Li, J.; Ren, G. A study of Angle of Draw in Mining Subsidence Using Numerical Modeling Techniques. *Electron. J. Geotech. Eng.* **2008**, *13*, 1–14.
6. Aydan, Ö.; Ulusay, R.; Tokashiki, N. A new rock mass quality rating system: Rock mass quality rating (RMQR) and its application to the estimation of geomechanical characteristics of rock masses. *Rock Mech. Rock Eng.* **2013**, *47*, 1255–1276. [CrossRef]
7. Aydan, Ö.; Kawamoto, T. The assessment of mechanical properties of rock masses through RMR rock classification system. In Proceedings of the GeoEng 2000 Symposium International Society for Rock Mechanics, Melbourne, Australia, 19–24 November 2000.
8. Bieniawski, Z. Misconceptions in the applications of rock mass classifications and their corrections. In Proceedings of the ADIF Seminar on Advanced Geotechnical Characterization for Tunnel Design, Madrid, Spain, 29 June 2011; pp. 1–32.
9. Brown, E.T. Estimating the mechanical properties of rock masses. In *Proceedings of the 1st Southern Hemisphere International Bibliography 227 Rock Mechanics Symposium (SHIRMS)*; Potvin, Y., Carter, J., Dyskin, A., Jeffrey, R., Eds.; Australian Centre for Geomechanics: Perth, Australia, 2008; pp. 3–21.
10. Pawelus, D. Stability assessment of headings situated in a field of high horizontal stress in Polish copper mines by means of numerical methods. In Proceedings of the IOP Conference Series—Earth & Environmental Science, Proceedings of the World Multidisciplinary Earth Sciences Symposium, Prague, Czech Republic, 3–7 September 2018; IOP Publishing Ltd.: Bristol, UK, 2019; Volume 221, p. 221.
11. Zhang, L.; Scholtès, L.; Donzé, F. Discrete Element Modeling of Permeability Evolution During Progressive Failure of a Low-Permeable Rock Under Triaxial Compression. *Rock Mech. Rock Eng.* **2021**, *54*, 6351–6372. [CrossRef]

12. Stopka, G. Modelling of Rock Cutting with Asymmetrical Disc Tool Using Discrete-Element Method (DEM). *Rock Mech. Rock Eng.* **2021**, *54*, 6265–6279. [CrossRef]
13. Pawelus, D. Influence of Horizontal Stress on the Stability of Underground Excavations in Copper Mines. Ph.D. Thesis, Wroclaw University of Science and Technology, Wroclaw, Poland, 2010. (In Polish).
14. Kozłowski, T.; Kudełko, J. Verification of selection the rock bolt support in condition of tectonic disturbance in Lubin mine. *Cuprum. Sci. Tech. J. Ore. Min.* **2014**, *4*, 55–71. (In Polish)
15. Paździora, J. KGHM Polska Miedź S.A.—Monographic outline 1960–2020. *Cuprum. Sci. Tech. J. Ore. Min.* **2019**, *4*, 5–28. (In Polish)
16. Małkowski, P.; Juszyński, D. Assessment of a collapse risk in the mining plants of LGOM. *Min. Rev.* **2019**, *1*, 16–26. (In Polish)
17. *Technical Report on the Production of Copper and Silver by KGHM Polska Miedź S.A. in the Legnica-Głogów Copper District in South-West Poland*; KGHM Polska Miedź S.A.: Lubin, Poland, 2013. (In Polish)
18. *Mining Assets of KGHM Polska Miedź S.A. around the Legnica-Głogów Copper District*; KGHM Polska Miedź S.A.: Lubin, Poland, 2012. (In Polish)
19. Hoek, E. Practical Rock Engineering. *Environ. Eng. Geosci.* **2007**, *14*, 55–57.
20. Cheng, A.; Cheng, D. Heritage and early history of the boundary element method. *Eng. Anal. Bound. Elem. Methods* **2005**, *29*, 268–302. [CrossRef]
21. Beskos, D. Boundary Element Methods in Dynamic Analysis. *Appl. Mech. Rev.* **1987**, *40*, 1–23. [CrossRef]
22. Kythe, P. *An Introduction to Boundary Element Methods*; CRC Press: Boca Raton, FL, USA, 1995.
23. Balaš, J.; Sládek, J.; Sládek, V. *Stress Analysis by Boundary Element Methods*; Elsevier: Amsterdam, The Netherlands, 1989.
24. KGHM Polska Miedz, S.A.; KGHM Polska Miedz, S.A., Lubin, Poland. Catalogue of Copper Deposit Mining Systems in KGHM Polska Miedz SA Mines. Unpublished materials. 2007. (In Polish)
25. Adach-Pawelus, K.; Butra, J. Remnant influence on geomechanical situation in the mining field based on numerical modeling. *Ores Met. Recycl.* **2015**, *5*, 199–210. (In Polish)
26. Hoek, E.; Carranza-Torres, C.T.; Corkum, B. Hoek-Brown failure criterion—2002 edition. In Proceedings of the North American Rock Mechanics Society Meeting in Toronto in July, Toronto, ON, Canada, 7–10 July 2002.
27. Hoek, E. Strength of rock and rock masses. *ISRM News J.* **1994**, *2*, 4–16.
28. Hoek, E.; Brown, E.T. Practical estimates of rock mass strength. *Int. J. Rock Mech. Min. Sci.* **1997**, *34*, 1165–1186. [CrossRef]
29. Hoek, E.; Marinos, P. GSI: A geologically friendly tool for rock mass strength estimation. In *ISRM International Symposium*; OnePetro: Richardson, TX, USA, 2000.

Article

The Stress Evolution of Adjacent Working Faces Passing through an Abandoned Roadway and the Damage Depth of the Floor

Song Shi [1], Yichen Miao [2], Haikuan Wu [3], Zhipeng Xu [1] and Changwu Liu [1],*

[1] College of Water Resource & Hydropower, Sichuan University, Chengdu 610065, China
[2] Faculty of Civil Engineering and Mechanics, Kunming University of Science and Technology, Kunming 650500, China
[3] School of Emergency Science, Xihua University, Chengdu 610039, China
* Correspondence: liuchangwu@scu.edu.cn; Tel.: +86-(028)-85401154

Abstract: An advanced break or a vast region of pressurisation may occur when the working face passes through an abandoned roadway, resulting in a roof falling or water inrush. The stress evolution of the working face passing through an abandoned roadway in a coal mine was comprehensively discussed using theoretical analysis, numerical simulation, and field monitoring. In this study, the calculated critical width of the abandoned roadway where the main roof was bound to an advanced break was 5.4 m. Reducing the suspended length of the main roof is beneficial to the stability of the working face's passage across the abandoned roadway. The maximum abutment stress on the roof occurred at the working face through a semi-abandoned roadway, reaching 44.3 MPa. Subsequently, it decreased sharply until the working face completely passed and returned to the normal level. The damage depths of the floor strata from the field monitoring were 15 and 20 m, which showed that the use of hydraulic fracturing technology combined with floor grouting and hydraulic support for the abandoned roadway was proposed to stabilise the working face for safe mining.

Keywords: adjacent working face; abandoned roadway; stress evolution; numerical simulation; field monitoring

1. Introduction

The coalfields in northern China are an important coal mining base and mining in this region is often affected by Ordovician limestone aquifer, which hides the safety risk of major water-inrush accidents [1]. However, as most of China's traditional coal industry adopted a relatively crude operation method for mining, the resource utilisation rate remained low, and many old and abandoned roadways have been left as a result of disorderly mining, which has caused great difficulties in the recovery of working faces [2]. Consequently, mining is plagued by the working face passage through the front roadway. If the main roof of the coal seam breaks in advance when the working face passes through an abandoned roadway, the length of the primary fracture of the basic roof will be greater than that of the normal working face. The main roof may have an advanced or longer break than normal when the working face passes through the forward abandoned roadway [3,4]. This could result in a vast region of pressurisation, which could cause roof falling or coal wall spalling in less serious situations, or it could deepen the damage to the floor strata and result in a water-inrush accident.

Many studies have investigated the stability of roofs and working faces through abandoned roadways. Strength degradation is believed to be the root cause of fracturing of the main roof, which eventually leads to collapse [5–7]. Bai et al. suggested that roof collapse can be controlled by changing the width of coal pillars and the stopping time of excavation [8]. Coggan et al. suggested that the thickness of the weak layer of the roof

has a significant impact on the degree of damage, and this part needs to be reinforced [9]. Cheng and Jiang believed that the width of the coal pillar is the main factor affecting the stability of the roadway roof. Under in situ stress, structural integrity can be maintained through appropriate support [10,11]. Yu et al. analysed the differences in the stress and plastic zones of different support schemes and proposed a method of using long and short bolts for collaborative support, which can significantly improve the stability of the roadway [12]. Yuan et al. revealed the interaction mechanism of rock-bolt structures in large deformation roadways and increased the thickness of bolts to improve their compression and shear resistance [13]. Jing et al. examined numerous numerical simulation instances and concluded that numerical simulations are crucial for understanding the fundamentals of rock mechanics and the design of rock engineering systems [14]. Ma et al. improved the reinforcing performance of rock bolts by examining the interaction between the rock bolts and rock mass [15]. Xuesheng et al. [16] concluded that an increase in the working face length and mining thickness aggravates the degree of stress concentration, resulting in an increase in the height of the water-flowing fracture zone of the floor. Bai, Jiang, and Zhang et al. studied various support methods such as high-water materials, wooden piles, pumping pillar supporting, backfilling gangue, and anchor cables, and believed that the pre-filling and support method for the abandoned roadway could effectively reduce the stress concentration of the surrounding rock, and is an effective method to prevent the roof from an advanced break [17–20]. Pan et al. deduced the critical width of coal pillar instability using the key block theory [21]. Luo et al. believed that the existence of an abandoned roadway intensifies the joint action of water pressure, mining disturbances, and flooding, which is the main cause of water inrush accidents [22]. Yasitli et al. concluded that the uniform fracturing of the coal seam roof, which could form cracks on the roof, can maintain the uniform collapse of the roof and improve coal mining efficiency [23]. Wang et al. studied the influence of large-section abandoned roadways and the application of high-water-filling materials [24]. Ju et al. studied the influence of the coal pillar depth and interlayer thickness on the coal seam roof collapse and believed that the rotation and movement of the key blocks in the roof above the coal pillar might cause the overlying stress to concentrate on the coal pillar, resulting in coal pillar instability [25]. Esterhuizen et al. verified the feasibility of an entrance support system by monitoring the displacement and stress of a rock mass [26]. Pan et al. studied the stress state of short-distance coal mining and concluded that when mining under a goaf, the weighting step and abutment stress were lower than the normal level [27]. Sun et al. systematically studied the deformation mechanism and support technology of underground roadways and proved and improved the application of stress relief technique and pre-grouting technique underground [28–30].

In summary, most of these studies on the stability of the working face passing through the abandoned roadway are focused on a pre-filling and supportive manner of reducing the stress concentration at the abandoned roadway and restoring the original stress state of the coal seam. However, it is rare enough to support the roadway alone in engineering cases, owing to multiple influences, including groundwater, the small distance to other mining fields, and the layout of diagonally intersecting roadways. Additionally, most studies are based on underground mine pressure data, ignoring the influence of the depth of floor damage, which may cause floor water-inrush accidents. To comprehensively understand the stability of the working face through the abandoned roadway, both theoretical analysis and numerical simulations were utilised to model the stress evolution. The reliability of the calculated results was verified by field monitoring of the damage depth of the floor strata. Based on the results, comprehensive measures, including hydraulic fracturing technology to produce active roof release, auxiliary floor grouting reinforcement, and hydraulic support for the abandoned roadway, are proposed to improve the stability of the working face.

2. Project Overview

The Dongpang Mine is part of the Xingtai mining area of the coalfield in Xingtai City, Hebei Province, northern China. The main tectonic lines in this mine area are primarily east–west, north–east, and north–south. The Ordovician, Cambrian, Metasedimentary Great Wall System, and Taikoo Zanhuang Group are the underlying strata of the coal seam, with the Cambrian and Ordovician strata having a greater influence on coal mining. The No. 9119 working face at Dongpang Mine has an underground elevation of −220 to −274 m, leaving a 6 m net coal pillar in the middle of the No. 9118 working face that was previously recovered. An abandoned roadway is located between the track roadway and the belt roadway along the No. 9 coal seam. The sections of the roadway measure 4 m in width and 3 m in height. The layout of the working faces and the location of the abandoned roadway is shown in Figure 1.
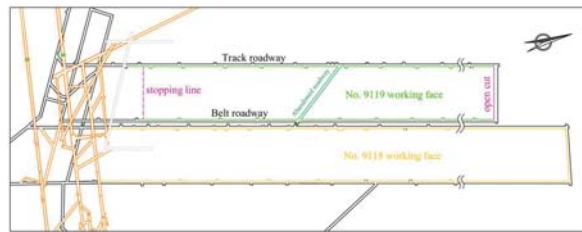
Figure 1. Layout of the working faces and location of the abandoned roadway.

The Daqing limestone aquifer in the roof strata, Benxi limestone aquifer, and Ordovician limestone aquifer in the floor strata constitute most of the water source for the No. 9119 working face. The water from the Daqing limestone aquifer is released along the No. 9118 mining field and roadways, posing no threat to this working face. From the base of the No. 9 coal seam, the heights of the Benxi limestone aquifer and the Ordovician limestone aquifer are approximately 13.39–33.38 m (average 22.86 m) and 30.78–54.57 m (average 43.92 m), respectively. The failure zone on the floor of the No. 9 coal seam serves as the primary conduit for water from the Benxi limestone aquifer. However, it can be employed as an early detection and release method because it has a low water head and a steady amount of water. The greatest danger to this mining operation comes from the irregular water-rich and somewhat high-head Ordovician limestone aquifer. A geological histogram of the No. 9119 working face is shown in Figure 2.

Histogram	Depth(m)	Tickness(m)	Rock structure	Rock formation
	256.78	10.88		Siltstone
	267.91	11.13	Main roof	Fine-sandstone
	272.92	5.01		Daqing limestone (aquifer)
	274.31	1.39	Immediate roof	No. 8 Coal
	280.23	5.92		Siltstone
	286.01	5.78	Coal seam	No. 9 Coal
	289.27	3.26	Immediate floor	Carbon mudstone
	295.15	5.88	Main floor	Mudstone
	308.87	13.72		Medium grained sandstone
	311.63	2.76		Benxi limestone (aquifer)
	317.95	6.32		Fine-sandstone
	329.68	11.73		Bauxite mudstone
				Ordovician limestone (aquifer)

Figure 2. Geological histogram.

3. Stress Evolution of the Working Face Passing through an Abandoned Roadway

With roadway excavation and working face mining, the in situ stress will be redistributed, so the coal walls on both sides of the abandoned roadway and in front of the working face will produce abutment stresses of different widths, W_1 and W_2. When W_1 and W_2 do not overlap, the working face is mined normally, preventing the coal pillar between the working face and the abandoned roadway from becoming unstable. With the continuous advancement of the working face, the coal pillar width gradually decreases, and the load above the pillar continues to increase, leading to a width where the coal pillar is bound to lose stability. This is known as the critical width of the coal pillar instability (W^*). There are three types of abutment stresses which can be distinguished by the width of the coal pillar (W).

(1) When $W \geq W_1 + W_2$, the working face is not impacted by the abandoned roadway; therefore, the abutment stress can be divided into the raised stress on each side and the original rock stress in the middle. The abutment stress state, which resembles an asymmetric saddle type, is shown in Figure 3. The peak value and width of abutment stress are greater on the goaf-side because the suspended length on the goaf-side is larger than that on the roadway-side. When $W > W_1 + W_2$, original rock stress exists in the coal pillar. When $W = W_1 + W_2$, the width of the original rock stress is exactly zero, and at that time, the abutment stresses on the goaf-side and roadway-side start to intersect. In this situation, the coal pillar has a good bearing capacity. The roof of the abandoned roadway can be approximated as a beam with a fixed support at both ends and an even load above, and the roof of the mining field can be approximated as a cantilever beam with an even load above. When the suspended length of the main roof (L_x) is greater than the periodic weighting step (l), that is, $L_x \geq l$, the cantilever beam cannot carry the top load, resulting in the fracture of the main roof at the fixed end. The periodic break line, in this instance, moves forward to the working face via a periodic weighting step.
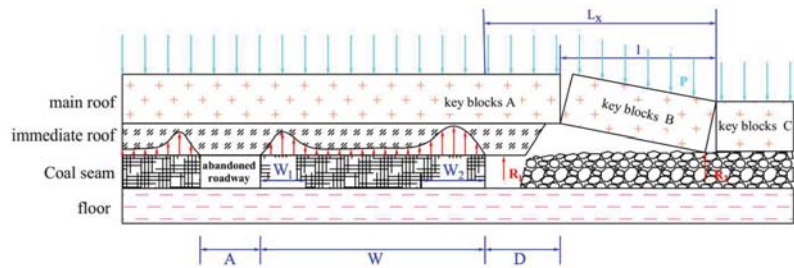
Figure 3. Saddle type.

(2) When $W^* < W < W_1 + W_2$, the evolution of the abutment stress changes from the saddle-type to the oblique-table type, as indicated in Figure 4, because of the overlap of the abutment stresses on the goaf- and roadway-side. The coal pillar is stable because W is greater than W^*, which means that the working face does not have an advanced break.

(3) When $W \leq W^*$, the distribution of abutment stress is presented as a solitary peak. The maximum abutment stress value is obtained when $W = W^*$. If the working face advances further, the middle coal pillar will remain in a state of plastic flow for a considerable amount of time, which will cause serious damage and deformation, and the strength and bearing capacity will be significantly reduced, resulting in instability and damage. At this moment, the suspended length of the main roof (L_x) increases from D to $A + W + D$, that is, $L_x = A + W + D$, which occurs in two ways. When $L_x = A + W + D < l$, the fixed end of the cantilever beam can support both its own weight and the upper loads without breaking. When $L_x = A + W + D \geq l$, the cantilever beam fractures at the fixed end, and the main roof undergoes an advanced break, creating a

vast region of pressurisation that might seriously threaten coal mining safety, as shown in Figure 5.
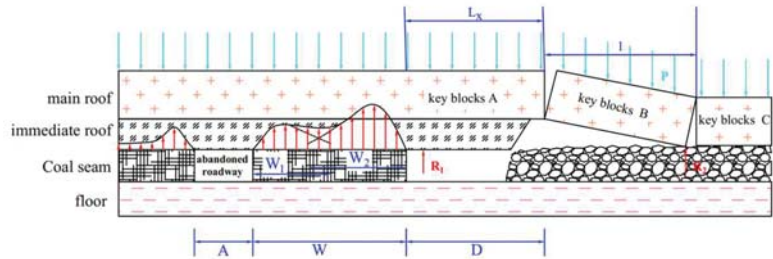
Figure 4. Oblique table type.
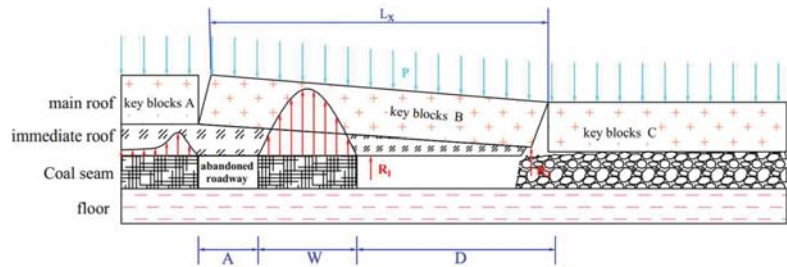
Figure 5. Solitary peak type.

Based on the Bieniawski formula [31]:

$$\sigma_p = 0.235\sigma_c(0.64 + 0.36\frac{W}{M}) \tag{1}$$

where σ_p is the ultimate compressive strength of the coal pillar (MPa), W is the width of the coal pillar between the working face and abandoned roadway (m), σ_c is the uniaxial compressive strength of the standard sample of the coal pillar (MPa), and M is the height of the coal pillar (m).

The coal pillar is not only required to carry the load of its own overlying strata but also the load of the overlying strata of one-half of the abandoned roadway and a significant portion of the load of the overlying strata of the cantilever beam on the goaf-side, so the static load set on the coal pillar is:

$$q = \gamma H(\frac{W + \frac{A}{2} + kD}{W}) \tag{2}$$

where q is the static load setting on the coal pillar, γ is the average volume weight of the overlying rocks (kN/m^3), H is the average thickness of the overlying strata (m), A is the width of the abandoned roadway (m), k is the stress concentration factor ($k = 1.5\sim5.0$), and D is the length of the cantilever beam (m).

When the ultimate compressive strength of the coal pillar is equal to its static load, that is $\sigma_p = q$, coupling (1) to (3) results in

$$0.235\sigma_c(0.64 + 0.36\frac{W}{M}) = \gamma H(1 + \frac{\frac{A}{2} + kD}{W}). \tag{3}$$

The critical width of coal pillar instability can be derived from Equation (4):

$$W^* = \frac{-b + \sqrt{b^2 - 4ac}}{2a} \tag{4}$$

where $a = \frac{0.085\sigma_c}{M}$, $b = 0.15\sigma_c - \gamma H$, and $c = -\gamma H(\frac{A}{2} + kD)$.

If the width of the coal pillar is less than the critical width, an advanced break occurs in the main roof. Because the suspended length on the goaf-side (D) is uncertain, the static load applied to the coal pillar is the smallest when D is 0, and at that time, the critical width of the abandoned roadway, where the main roof will inevitably experience an advanced break, can be deduced.

$$A^* = l - W^* - D = l - \frac{-b + \sqrt{b^2 - 4ac}}{2a}. \tag{5}$$

According to the field data, the periodic weighting step of the No. 9119 working face was 20 m, the height of the coal pillar was 6 m, the uniaxial compressive strength of the No. 9 coal seam was approximately 20 MPa, the overlying strata was 250 m from the ground level, and its average volume weight was 24,000 kg/m^3. Using Equation (5) and the above data, we can obtain A^* as 5.4 m. Therefore, an advanced break in the main roof will undoubtedly occur when the width of the abandoned roadway is greater than 5.4 m. Because the width of the abandoned roadway in this mining area is 4 m, which is less than the necessary width, an advanced break may not occur in the main roof.

According to $L_x = A + W + D$, the width of the coal pillar, suspended length of the main roof, and width of the abandoned roadway are all significant factors in determining whether the main roof will advance break. W^* is used as a rough alternative to W because the strength of the coal pillar rapidly declines when its width is below the critical width. W^* is positively correlated with D in Equation (4). Therefore, after the width of the abandoned roadway is established, there is a positive association between L_x and D. For the working face to pass through the abandoned roadway safely, it is crucial to reduce the suspended length of the main roof.

4. Numerical Simulation

Theoretical analysis is often based on idealised models and necessary assumptions. Considering the complexity of the project, a 3D numerical model created with Flac^{3D} software can more accurately depict the dynamic evolution of the No. 9119 working face passing through the abandoned roadway.

4.1. Three-Dimensional Numerical Model

A 3D model with an x-axis of 302 m, y-axis of 180 m, and z-axis of 80 m was created, as shown in Figure 6a. The working face was 90 m long. Each cross-section of the track, belt, and abandoned roadways measured 4 m in width and 3 m in height, with a 53° angle between them. Given the lateral abutment stress, two coal pillars of 50 m width were set aside on either side of the No. 9118 and No. 9119 working faces. The main roof fractured periodically owing to the large distance of the open cut from the roadway intersection, which allowed the model to be excavated from the boundary section. The bottom of the model was fixed, and the horizontal movement of its four sides was constrained. The upper surface of the model, whose boundary conditions are schematically depicted in Figure 6b, was subjected to an even load of $P = \gamma h = 6.0$ MPa.

The physical and mechanical parameters of the rock formation at the working face based on drilling data collected on-site are listed in Table 1.

(**a**) (**b**)
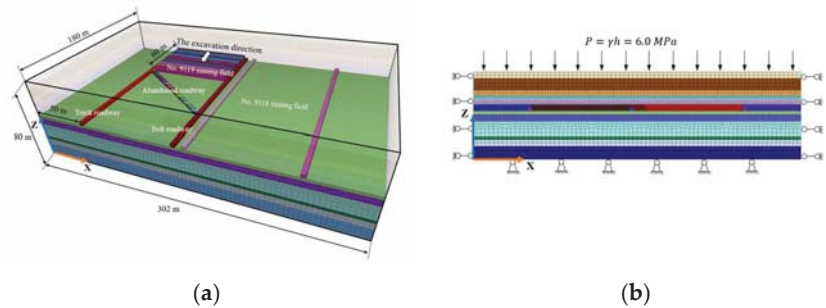
Figure 6. Three-dimensional model and boundary conditions: (**a**) three-dimensional model; (**b**) boundary conditions.

Table 1. Physical and mechanical parameters of rock formation.

Rock Formation	Thickness (m)	Bulk Modulus (GPa)	Shear Modulus (GPa)	Cohesion (MPa)	Internal Friction Angle (°)	Tensile Strength (MPa)	Density (kg/m^3)
Siltstone	6	13.7	9.4	6.0	35	1.5	2400
Fine-sandstone	11	17.9	11.8	4.9	36	2.5	2500
Daqing limestone	5	25.6	19.2	9.5	40	4.9	2700
No. 8 Coal	2	4.8	1.6	0.3	28	0.5	1400
Siltstone	6	12.8	8.1	3.8	32	1.0	2400
No. 9 Coal	6	4.8	1.6	0.3	28	0.5	1400
Carbon mudstone	3	11.1	5.4	2.6	29	0.8	2500
Mudstone	6	9.8	5.1	2.7	30	0.5	2500
Medium grained sandstone	14	8.9	6.1	3.6	29	1.8	2500
Benxi limestone	3	12.6	9.1	5.9	36	3.6	2800
Fine-sandstone	6	25.8	13.3	5.2	36	2.0	2400
Bauxite mudstone	12	15.7	6.0	1.7	28	0.5	2500

The fallen gravel in the mining field is a kind of loose medium, but Flac^{3D} belongs to the continuous medium simulation method. Therefore, we approximate the supporting effect of the gravel on the roof to elastic support [32]. The gravel will gradually be compacted by the overlying strata; therefore, the physical and mechanical parameters are positively correlated with time. Based on the physical and mechanical parameters of the rock formation and the actual mining pace, a demarcation line 40 m behind the working face is advised. The deformation parameters of gravel in the mining field, as determined using empirical formulas [32], are listed in Table 2.

$$\rho = 1600 + 800\left(1 - e^{-1.25t}\right), \tag{6}$$

$$E = 15 + 175\left(1 - e^{-1.25t}\right), \tag{7}$$

$$\mu = 0.05 + 0.2\left(1 - e^{-1.25t}\right), \tag{8}$$

where t is the time after the collapse of the immediate roof of the mining field (a).

In order to ensure that the roof elements would not invade the floor elements after the excavation, one contact surface with very large physical and mechanical properties was set on the floor of the coal seam. The stiffness-normal was 100 GPa/m, stiffness-shear was 100 GPa/m, tensile strength was 10 GPa, internal friction angle was 30°, cohesion was 10 GPa, and dilation was 6°.

Table 2. Physical and mechanical parameters of gravel in the mining field.

Distance from the Working Face (m)	Bulking Coefficient	Elastic Modulus (MPa)	Poisson Ratio	Bulk Modulus (MPa)	Shear Modulus (MPa)	Density (kg/m³)
<40	1.5	26.6	0.06	10.1	12.5	1650
>40	1.3	37.4	0.08	14.8	17.3	1700
NO. 9118 mining field	1.2	189.0	0.25	126.0	75.6	2400

4.2. Results

4.2.1. Initial Stress

The vertical stress cloud of the initial ground stress measured in Pa is shown in Figure 7. The following clouds and diagrams units are Pa unless otherwise indicated. Before the mining field was excavated, the initial ground stress reached an equilibrium. From there, the stress increased consistently with depth, peaking at 7.8 MPa at the bottom of the model.
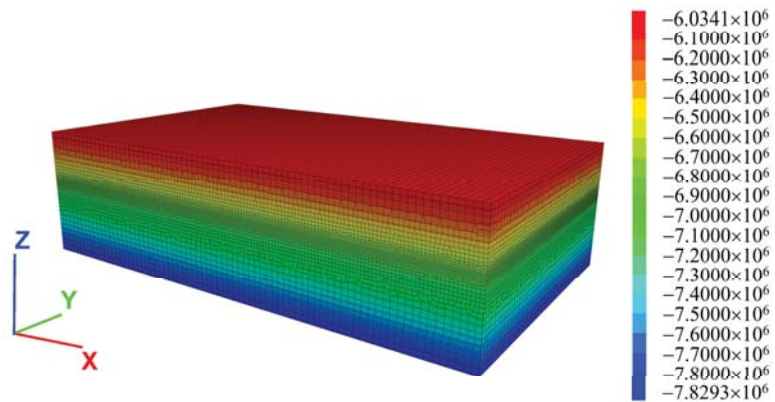
Figure 7. Initial ground stress.

The vertical stress cloud after the No. 9118 mining field was excavated is depicted in Figure 8. High compressive stress was produced by the two coal walls on either side of the No. 9118 mining field, which was partially concentrated in the No. 9119 working face, causing significant difficulties in the mining of the No. 9119 working face.

(**a**)   (**b**)
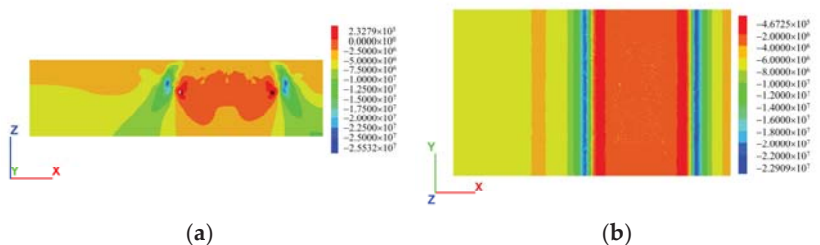
Figure 8. Vertical stress cloud after No. 9118 mining field was excavated: (**a**) front view of vertical stress; (**b**) top view of vertical stress.

4.2.2. Stress Evolution of the Roof

When the periodic weighting step is 10 m, 3D diagrams of the vertical stress at 1 m above the roof for excavations of 30, 60, 90, and 120 m are shown in Figure 9.
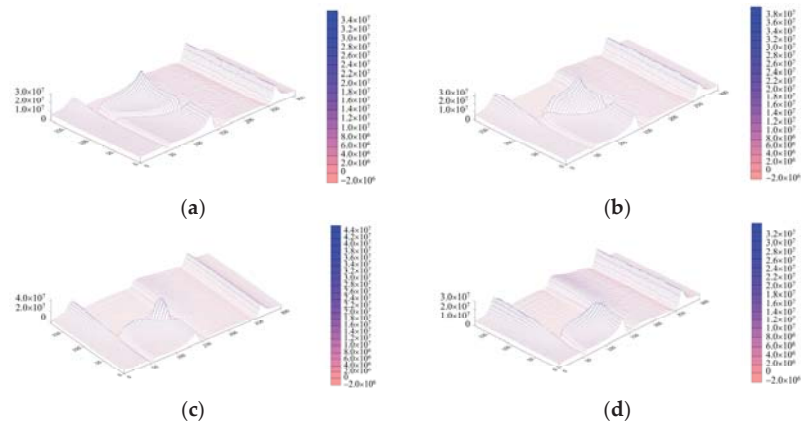
Figure 9. Three-dimensional diagrams of the vertical stress: (**a**) excavation of 30 m; (**b**) excavation of 60 m; (**c**) excavation of 90 m; (**d**) excavation of 120 m.

As the No. 9119 working face advanced by 30 m, the peak vertical stress on the roof, as can be seen in Figure 9a, occurred in front of the No. 9119 working face offset towards the No. 9118 mining field, reaching 34.0 MPa, with a stress concentration factor of 5.2. Only a 6 m wide coal pillar was reserved between the two working faces, which was insufficient to compensate for the lateral abutment stress and caused damage. As a result, there was a significant amount of stress concentration because the lateral abutment stress from the No. 9118 mining field was transferred to the inner side of the No. 9119 working face and superimposed on the front abutment stress.

The front abutment stress reached 36.9 MPa, and the stress concentration factor reached 5.7 when the working face advanced 60 m. At that point, the working face started to expose the abandoned roadway, as illustrated in Figure 9b. The No. 9118 mined-out area was compacted once more with the extraction of the No. 9119 working face. The working face passed half of the abandoned roadway at a distance of 90 m, where the abutment stress on the roof of the remaining triangular coal pillar reached its peak value of 44.3 MPa, as shown in Figure 9c. When the working face was entirely through the abandoned roadway, the peak abutment stress on the roof, as shown in Figure 9d, was 30.5 MPa.

The relationship between the peak vertical stress 1 m above the roof and the mining position of the working face is shown in Figure 10. The peak stress increased slowly when the working face was farther from the abandoned roadway. The area of the triangular coal pillar gradually decreased as the working face continued to advance beyond 60 m, and the peak stress on the roof began to increase sharply. The maximum stress occurred at 90 m, where the working face passed through a semi-abandoned roadway, where the maximum stress reached 44.3 MPa. This was because the abandoned roadway cut off the coal body behind it and the triangular coal pillar, resulting in the superposition of the front abutment stress, the lateral abutment stress of the No. 9118 mining field, and the abutment stress of the abandoned roadway, which caused a large degree of stress concentration. The triangular coal pillar area decreased as the working face advanced, and as a result, it could no longer support the roof. Most of the abutment stress began to transfer to the coal body behind the abandoned roadway, which led to a more uniform distribution of the abutment stress. As a result, the peak abutment stress began to decrease until the working face completely passed and returned to the normal level.
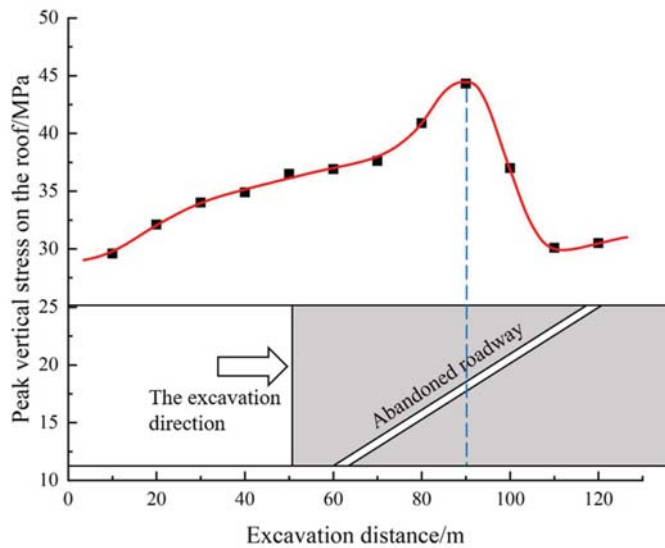
Figure 10. Relationship between the peak stress and the excavation distance.

Side views of the vertical stress cloud of the selected excavation are shown in Figure 11. Vertical stress appears in the sequence of the saddle type, oblique table type, and solitary peak type with the excavation of the working face.

(a)

(b)

(c)
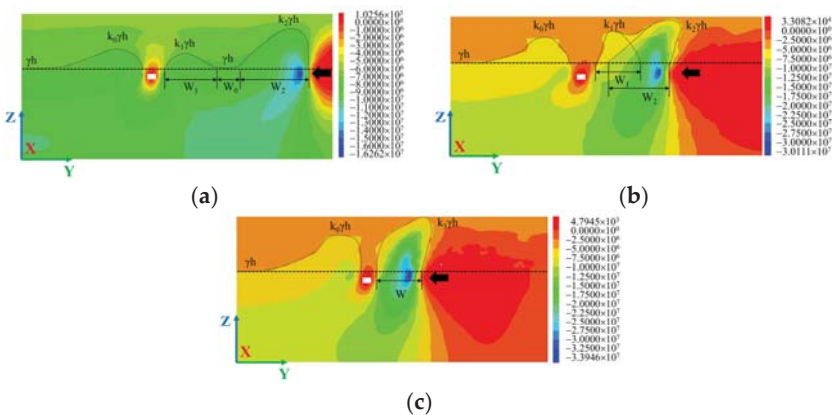
Figure 11. Side views of vertical stress cloud: (**a**) coal pillar width of 92 m; (**b**) coal pillar width of 52 m; (**c**) coal pillar width of 32 m.

(1) As shown in Figure 11a, when the width of the coal pillar was 92 m in the middle of the working face and the abandoned roadway, the vertical stress of the coal pillar exhibited an asymmetric saddle type, with the peak stress (16.3 MPa) on the goaf-side being larger. The coal pillar midsection still contained the original rock stress zone, indicating that the front abutment stress was not affected by the abandoned roadway.

(2) As shown in Figure 11b, when the width of the coal pillar was 52 m, the vertical stress of the coal pillar was an oblique table type, and the front abutment stress increased significantly, with peak stress of 30.1 MPa. The abutment stresses on both sides influenced one another.

(3)   As shown in Figure 11c, when the width of the coal pillar was 32 m, the vertical stress of the coal pillar was an asymmetrical peak type, with peak stress of 33.9 MPa. Currently, the abutment stress of the central coal pillar affects the abutment stress of the rear coal wall of the abandoned roadway, which results in a significant increase in the latter.

4.2.3. Effect of Weighting Steps on the Stability of the Roof and Floor

A common multiple of 60 m excavation length was selected for comparative analysis using Flac^{3D} to simulate the weighting steps of 10, 20, and 30 m, respectively. Figure 12 depict the vertical stress clouds of the coal pillar at 0.5 m above the floor before the roof collapses. When the weighting steps are 10, 20, and 30 m, the peak vertical stresses of the coal pillar are 43.8, 45.5, and 45.9 MPa, respectively, which indicates that reducing the weighting step can reduce the maximum front abutment stress on the coal pillar. Consequently, active roof cutting can be used to control the suspended length of the main roof behind the working face, thereby reducing the front abutment stress.

(a)

(b)

(c)
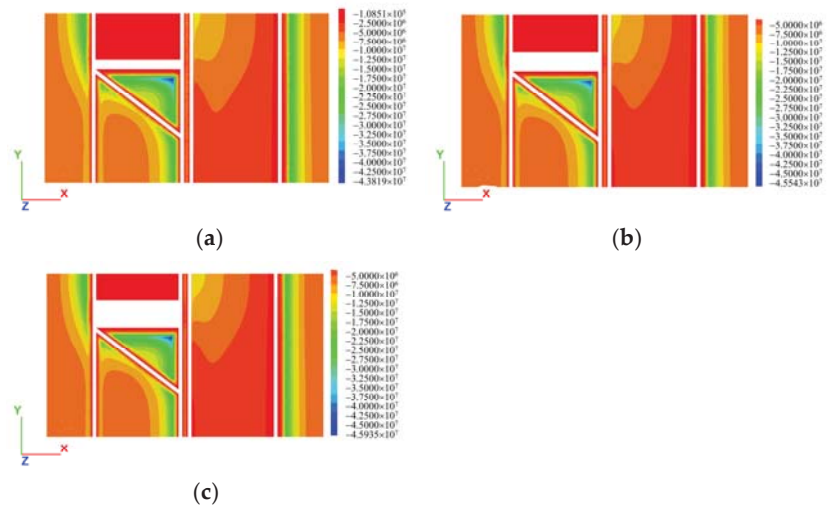
Figure 12. Top views of vertical stress cloud: (**a**) weighting step of 10 m; (**b**) weighting step of 20 m; (**c**) weighting step of 30 m.

From the above analysis, the largest front abutment stress occurred in front of the No. 9119 working face offset toward the No. 9118 mining field; therefore, the side views of the plastic zone near the No. 9118 mining field at 120 m of excavation were chosen, as shown in Figure 13. Shear failure primarily occurred in the plastic zone in the stope floor strata. Shear-n indicates that shear failure is occurring in the elements in the current cycle, while Shear-p indicates that shear failure has occurred in the elements in the previous cycle. Therefore, increasing the weighting step would cause the shear failure of the elements in front of the working face faster. The maximum depth of the plastic zone in the stope floor strata was 23 m when the weighing step was 10 m. The major portion of the plastic zone did not change significantly when the weighted step was increased to 20 and 30 m, but new plastic zones of various sizes appeared from 32 to 36 m below the floor, with the largest plastic zone occurring at 30 m. With the increase of the weighting step distance, the floor failure depth increased firstly and then tended to be stable [33]. Therefore, when the weighting step increased from 20 m to 30 m, the depth of the plastic zone did not change significantly. Combined with the physical and mechanical parameters of the floor strata, no plastic zone has arisen in the range of 23 m to 32 m below the floor because of the Benxi limestone and fine sandstone in this area, which are relatively hard in texture

and have large shear and tensile strengths. A certain zone of plasticity developed because of the lithological weakness of the bauxite mudstone that lies beneath the fine sandstone, which could still be inferred from the fact that as the weighting step increased, the extent of the plastic zone in the stope floor strata increased, indicating an increase in the depth of floor failure. However, the floor failure depth would not increase indefinitely and would eventually become stable.
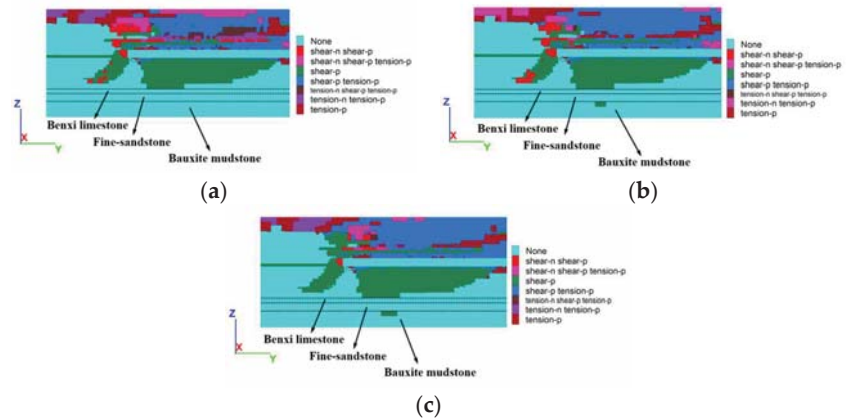
Figure 13. Side views of the plastic zone: (**a**) weighting step of 10 m; (**b**) weighting step of 20 m; (**c**) weighting step of 30 m.

5. Results

According to theoretical analysis and numerical simulation, the maximum front abutment stress of the coal pillar and roof can be reduced, and the depth of the plastic zone in the stope floor strata can be reduced by actively reducing the suspended length of the main roof. The Ordovician limestone aquifer had an impact on the No. 9119 working face, possibly causing water damage, so the floor strata could be grouted to strengthen the mechanical properties of the rock. Simultaneously, hydraulic supports were added to the interior of the abandoned roadway to ensure the safe passage of the No. 9119 working face.

5.1. Application of Hydraulic Fracturing Technology

The No. 9119 working face used hydraulic fracturing technology to actively cut the roof strata and control the weighting step to be 10 m. Holes were drilled in twin groups A and B. Group A was drilled from the top of the belt roadway to the interior of the roof strata of the mining field, with a length of 50 m, an elevation angle of 45°, and hole spacing of 10 m. It was used to cut the link between the main roof and the rock above and release the pressure. Group B was drilled vertically upward in the middle of the top of the belt roadway with a length of 34 m and a hole spacing of 10 m. The purpose of Group B was to cut the connection between the No. 9119 and No. 9118 mining fields and to reduce the impact of the No. 9118 mining field. Group A and group B holes were arranged in a staggered manner and extended close to the stopping line. Layout diagrams of the holes are shown in Figure 14.

(a)

(b)
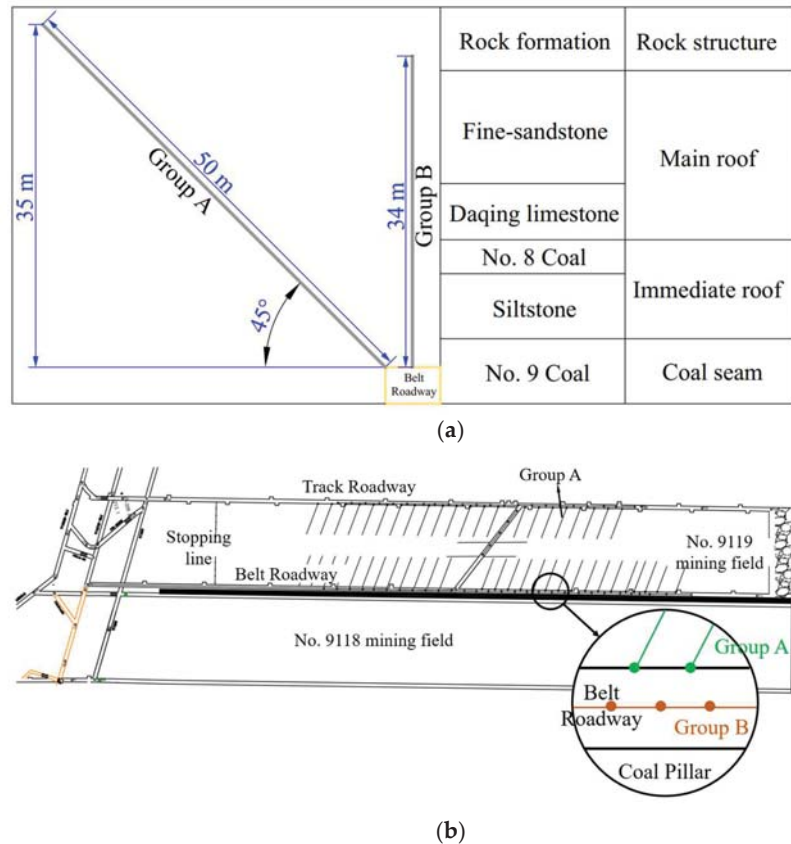
Figure 14. Layout of holes: (**a**) sectional view; (**b**) top view.

5.2. Floor Grouting Reinforcement

Underground structures are subject to weathering (for example, by water), which can reduce their mechanical strength and may eventually lead to unstable excavations [34,35], so the use of floor grouting reinforcement technology can significantly reduce the impact of groundwater on the strength of the floor strata. To achieve the best reinforcement effect and to consider the economics of the project, floor strata from 10 m below the floor to the top of the Ordovician limestone aquifer were used as the target rock strata for grouting. The key grouting reinforcement areas include the physical prospecting of unusual areas, typical hydrogeological areas, and areas where the overtopped hole has not been explored. A total of 360 advancing and grouting holes were constructed in the No. 9119 working face, with 23,895.5 m drill footage and 246.71 t grout.

5.3. Support for the Abandoned Roadway

The section size of the abandoned roadway at the No. 9119 working face is 4.2 m wide at the top, 4.5 m wide at the bottom, and 2.8 m high at the middle. DW-28 hydraulic supports with DJB (S) metal-hinged beams were used to strengthen the abandoned roadway. The hydraulic supports were spaced 0.8 m along the abandoned roadway, 0.3 m from the coal wall on both sides, and 1.3 m between each row of pillars, which provided 0.3 MPa for the abandoned roadway.

5.4. Verification Using the Field Monitoring

To monitor the displacement of the floor strata, vibrating wire multi-point displacement meters with two measuring stations were used at depths of 10, 15, 20, and 25 m below the floor. Station No. 1 was buried in the chamber of the track roadway away from and unaffected by the abandoned roadway, whereas station No. 2 was buried near the intersection of the track roadway and abandoned roadway, where it was affected by the abandoned roadway. The locations of the measuring stations and multi-point displacement meters are shown in Figure 15.
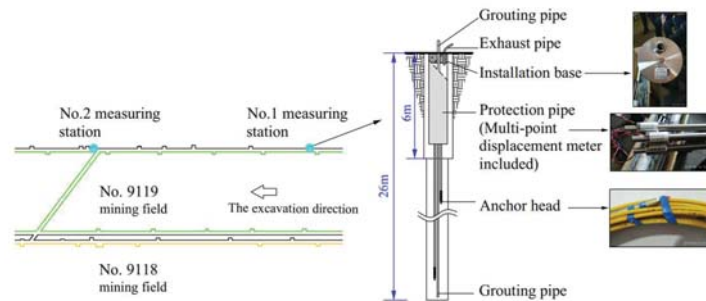
Figure 15. Locations of the measuring stations and multi-point displacement meters.

A peephole was used to inspect the borehole before the multi-point displacement gauge was buried. The conditions of borehole No. 1 from the peephole are shown in Figure 16a. A small number of fissures were produced at 5–8 m, which gradually decreased until they disappeared with increasing depth. The conditions of borehole No. 2 from the peephole are shown in Figure 16b. A small amount of water inflow is produced at 6–8 m, where mud occurs owing to the mudstone layer, and vertical fissures are produced at 12–15 m.

(**a**)   (**b**)
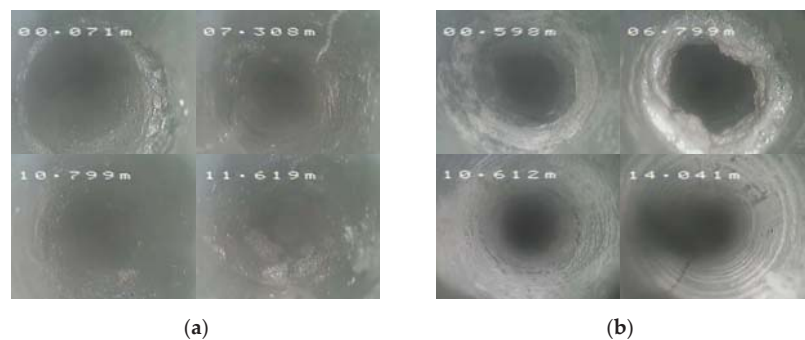
Figure 16. Borehole peephole views: (**a**) Conditions of borehole No. 1; (**b**) Conditions of borehole No. 2.

The relationship between the vertical displacement of each measuring point and the distance between the working face and station is shown in Figure 17. The vertical displacement of each measuring point decreased and then increased as the working face advanced, which was caused by the front abutment stress being transferred to the floor strata, resulting in compression deformation. As the working face moved forward, the peak front abutment stress passed through the measuring station, which decreased the stress concentration factor above the measuring point. The rock formation started to expand because of the floor strata pressure relief, which resulted in tensile deformation at the measuring point in the direction of the upper free space. The floor strata of the

No. 1 measuring station experienced discontinuous displacement changes between 10 and 15 m, whereas the floor strata of the No. 2 measuring station experienced discontinuous changes in displacement between 15 and 20 m. The damage depths of the floor strata, which are 15 and 20 m, respectively, are commonly regarded as the upper limit of the aforementioned interval to ensure the safety of pressure mining. This suggests that the abandoned roadway increased the stress concentration at the No. 2 measuring station, which in turn increased the damage depth and raised the possibility of water inrush of the floor strata. The peak front abutment stress under normal mining conditions was approximately 25 m in front of the working face, as shown in Figure 17a, where the turning point of the vertical displacement at the No. 1 measuring station was located. However, as shown in Figure 17b, the peak front abutment stress was approximately 30 m in front of the working face under No. 2 measuring station conditions. In the numerical simulation, the depths of the plastic zone at the two stations were extracted as 13 and 17 m, which is in error with the measured data by approximately 15% and 13%, respectively.

(**a**) (**b**)
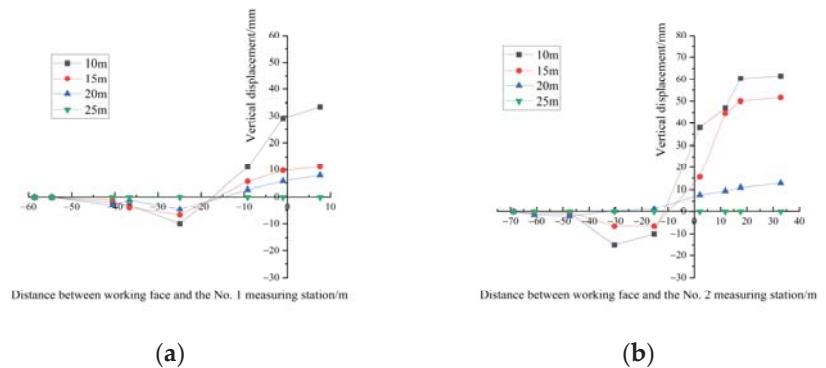
Figure 17. Relationship between the vertical displacement of each measuring point and the distance between the working face and the station: (**a**) No. 1 measuring station; (**b**) No. 2 measuring station.

The final monitoring results are in good agreement with the numerical simulation results, indicating that the application of hydraulic fracturing technology, floor grouting reinforcement, and support of the abandoned roadway can reduce the maximum front abutment stress of the mining field, thereby reducing the damage depth of the floor strata. In this case, the No. 9119 working face passed through the forward abandoned roadway without any advanced break or weighing over a great extent, and there were no water inrush accidents.

6. Conclusions

(1) The stress evolution of the working face passing through the abandoned roadway can be characterised by the types of saddle, oblique table, and solitary peak. The critical width of the abandoned roadway where the main roof is bound to advanced break was calculated to be 5.4 m. With the width of the abandoned roadway determined, the suspended length of the main roof was the key factor in determining whether the main roof will advance break.

(2) Using elastomeric expressions to approximate fallen gravel, a Flac^{3D} simulation method was proposed to simulate the stress evolution laws and the effect of different weighting steps. The error between the depths of the plastic zone obtained using this simulation method and the field monitoring data was within 15%.

(3) The peak stress on the roof increased slowly when the working face was farther away from the abandoned roadway and then increased sharply when the working face began to expose the abandoned roadway. The maximum stress occurred at the working face through a semi-abandoned roadway, where the maximum stress

reached 44.3 MPa. Subsequently, the area of the triangular coal pillar decreased, so the triangular coal pillar could no longer support the roof. The coal wall behind the abandoned roadway carried most of the front abutment stress, which caused the peak stress to slope downward.

(4) The use of hydraulic fracturing technology to produce active roof release, with the aid of floor grouting reinforcement and support for abandoned roadways, was proposed as a holistic management technique. The damage depths of the floor strata from the field monitoring were 15 and 20 m, respectively, which showed that the measurements enabled the No. 9119 working face at Dongpang Mine to safely pass through the forward abandoned roadway and provided a significant reference for similar projects.

Author Contributions: Writing—original draft, Software, Visualisation, Supervision, S.S.; Resources, Formal analysis, Y.M.; Data curation, Investigation, H.W.; Writing—review and editing, Resources, Z.X.; Methodology, Project administration, C.L. All authors have read and agreed to the published version of the manuscript.

Institutional Review Board Statement: Not applicable.

Informed Consent Statement: Not applicable.

Data Availability Statement: Not applicable.

Conflicts of Interest: The authors declare no conflict of interest.

References

1. Shi, L. Summary of Research on Mechanism of Water-inrush from Seam Floor. *J. Shandong Univ. Sci. Technol.* **2009**, *28*, 17–23. (In Chinese)
2. Fan, J.; Liu, W.; Jiang, D.; Chen, J.; Tiedeu, W.N.; Chen, J.; Deaman, J.J.K. Thermodynamic and applicability analysis of a hybrid CAES system using abandoned coal mine in China. *Energy* **2018**, *157*, 31–44. [CrossRef]
3. Liu, C.; Gong, P.; Wang, K.; Zhang, X.; Liu, Y. Roof stability for repeated mining workface passing through abandoned parallel gateway. *J. China Coal Soc.* **2015**, *40*, 314–322. (In Chinese)
4. Liu, C.; Yang, Z.; Gong, P.; Wang, K.; Zhang, J.; Li, Y.; Zhang, X. Mechanism and control technology of supports crushing induced by main roof's breaking ahead of workface when crossing abandoned roadway. *J. China Coal Soc.* **2017**, *42*, 1932–1940.
5. Bai, Q.; Tu, S.; Zhang, C.; Zhu, D. Discrete element modeling of progressive failure in a wide coal roadway from water-rich roofs. *Int. J. Coal Geol.* **2016**, *167*, 215–229. [CrossRef]
6. Chen, J.; Liu, P.; Liu, L.; Zeng, B.; Zhao, H.; Zhang, C.; Zhang, J. Anchorage performance of a modified cable anchor subjected to different joint opening conditions. *Constr. Build. Mater.* **2022**, *336*, 127558. [CrossRef]
7. Chen, J.; Zeng, B.; Liu, L.; Tao, K.; Zhao, H.; Zhang, C.; Zhang, J.; Li, D. Investigating the anchorage performance of full-grouted anchor bolts with a modified numerical simulation method. *Eng. Fail. Anal.* **2022**, *141*, 106640. [CrossRef]
8. Bai, J.; Shen, W.; Guo, G.; Wang, X.; Yu, Y. Roof Deformation, Failure Characteristics, and Preventive Techniques of Gob-Side Entry Driving Heading Adjacent to the Advancing Working Face. *Rock Mech. Rock Eng.* **2015**, *48*, 2447–2458. [CrossRef]
9. Coggan, J.; Gao, F.; Stead, D.; Elmo, D. Numerical modelling of the effects of weak immediate roof lithology on coal mine roadway stability. *Int. J. Coal Geol.* **2012**, *90–91*, 100–109. [CrossRef]
10. Cheng, Y.M.; Wang, J.A.; Xie, G.X.; Wei, W.B. Three-dimensional analysis of coal barrier pillars in tailgate area adjacent to the fully mechanized top caving mining face. *Int. J. Rock Mech. Min. Sci.* **2010**, *47*, 1372–1383. [CrossRef]
11. Jiang, L.; Zhang, P.; Chen, L.; Hao, Z.; Sainoki, A.; Mitri, H.S.; Wang, Q. Numerical Approach for Goaf-Side Entry Layout and Yield Pillar Design in Fractured Ground Conditions. *Rock Mech. Rock Eng.* **2017**, *50*, 3049–3071. [CrossRef]
12. Yu, H.; Niu, Z.; Kong, L.; Hao, C.; Cao, P. Mechanism and technology study of collaborative support with long and short bolts in large-deformation roadways. *Int. J. Min. Sci. Technol.* **2015**, *25*, 587–593. [CrossRef]
13. Yuan, X.; Yang, S.S. Interaction principle of rock-bolt structure and Rib control in large deformation roadways. *Arch. Min. Sci.* **2021**, *66*, 227–248.
14. Jing, L. A review of techniques, advances and outstanding issues in numerical modelling for rock mechanics and rock engineering. *Int. J. Rock Mech. Min. Sci.* **2003**, *40*, 283–353. [CrossRef]

15. Ma, S.; Nemcik, J.; Aziz, N. Simulation of fully grouted rockbolts in underground roadways using FLAC2D. *Can. Geotech. J.* **2014**, *51*, 911–920. [CrossRef]
16. Liu, X.; Tan, Y.; Ning, J.; Tian, C.; Wang, J. The height of water-conducting fractured zones in longwall mining of shallow coal seams. *Geotech. Geol. Eng.* **2015**, *33*, 693–700. [CrossRef]
17. Jiang, Z.; Wang, F.; Miao, K.; Cao, Q. Surrounding Rock Control Technology When the Longwall Face Crosses Abandoned Roadways: A Case Study. *Geofluids* **2021**, *2021*, 7867460. [CrossRef]
18. Liu, Z.; Ye, H.; Yang, L.; Wang, S.; Zhang, J.; Zhang, B.; Li, Z. Study on Control Technology for Working Faces Passing through Long-Span Abandoned Roadways. *Geofluids* **2020**, *2020*, 8822595. [CrossRef]
19. Zhang, X.; Gong, P.; Wang, K.; Li, J.; Jiang, Y. Characteristic and Mechanism of Roof Fracture Ahead of the Face in an LTCC Panel When Passing an Abandoned Roadway: A Case Study from the Shenghua Coal Mine, China. *Rock Mech. Rock Eng.* **2019**, *52*, 2775–2788. [CrossRef]
20. Bai, J.; Hou, C. Research on principle of roof stability of abandoned workings and supporting technology. *J. China Coal Soc.* **2005**, *30*, 8–11. (In Chinese)
21. Pan, W.; Deng, C.; Yang, Y.; Zhang, K.; Gao, S. Pressure Law of Roof and Supporting Technology of Roadway When Working Face Passing through Abandoned Roadway. *Shock Vib.* **2022**, *2022*, 7565629. [CrossRef]
22. Luo, B.; Sun, Y.; Xu, Z.; Chen, G.; Zhang, L.; Lu, W.; Zhao, X.; Yuan, H. Damage Characteristics and Mechanism of the 2017 Groundwater Inrush Accident That Occurred at Dongyu Coalmine in Taiyuan, Shanxi, China. *Water* **2021**, *13*, 368. [CrossRef]
23. Yasitli, N.E.; Unver, B. 3D numerical modeling of longwall mining with top-coal caving. *Int. J. Rock Mech. Min. Sci.* **2005**, *42*, 219–235. [CrossRef]
24. Wang, Y.; Xiong, Z.; Zhao, G. Three-dimensional stress evolution and comprehensive treatment technology for super-long working face over large section. *Coal Geol. Explor.* **2020**, *48*, 8. (In Chinese)
25. Ju, J.; Xu, J.; Zhu, W. Longwall chock sudden closure incident below coal pillar of adjacent upper mined coal seam under shallow cover in the Shendong coalfield. *Int. J. Rock Mech. Min. Sci.* **2015**, *77*, 192–201. [CrossRef]
26. Esterhuizen, G.S.; Gearhart, D.F.; Tulu, I.B. Analysis of monitored ground support and rock mass response in a longwall tailgate entry. *Int. J. Min. Sci. Technol.* **2018**, *28*, 43–51. [CrossRef] [PubMed]
27. Pan, W.D.; Zhang, S.P.; Liu, Y. Safe and Efficient Coal Mining Below the Goaf: A Case Study. *Energies* **2020**, *13*, 864. [CrossRef]
28. Sun, Y.; Li, G.; Zhang, J.; Sun, J.; Huang, J.; Taherdangkoo, R. New Insights of Grouting in Coal Mass: From Small-Scale Experiments to Microstructures. *Sustainability* **2021**, *13*, 9513. [CrossRef]
29. Sun, Y.; Li, G.; Zhang, J.; Huang, J. Rockburst intensity evaluation by a novel systematic and evolved approach: Machine learning booster and application. *Bull. Eng. Geol. Environ.* **2021**, *80*, 8385–8395. [CrossRef]
30. Sun, Y.; Bi, R.; Sun, J.; Sun, J.; Taherdangkoo, R.; Huang, J.; Li, G. Stability of roadway along hard roof goaf by stress relief technique in deep mines: A theoretical, numerical and field study. *Geomech. Geophys. Geo-Energy Geo-Resour.* **2022**, *8*, 45. [CrossRef]
31. Bieniawski, Z.T. The effect of specimen size on compressive strength of coal. In *International Journal of Rock Mechanics and Mining Sciences\& Geomechanics Abstracts*; Elsevier: Amsterdam, The Netherlands, 1968; Volume 5, pp. 325–335, IN5, 327–326, IN10, 335.
32. Xie, H.; Zhou, H.; Wang, J.; Li, L.; Kwasniewski, M.A. Application of flac to predict ground surface displacements due to coal extraction and its comparative analysis. *Chin. J. Rock Mech. Eng.* **1999**, *18*, 397. (In Chinese)
33. Li, C.; Zhang, Y. Relationship between deep depth and thin base rock roof pressurized and floor failure depth. *Coal Sci. Technol.* **2016**, *44*, 74–79. (In Chinese)
34. Kasim, M.; Shakoor, A. An investigation of the relationship between uniaxial compressive strength and degradation for selected rock types. *Eng. Geol.* **1996**, *44*, 213–227. [CrossRef]
35. Parise, M.; Lollino, P. A preliminary analysis of failure mechanisms in karst and man-made underground caves in Southern Italy. *Geomorphology* **2011**, *134*, 132–143. [CrossRef]

Real-Time Methane Prediction in Underground Longwall Coal Mining Using AI

Doga Cagdas Demirkan [1],*, H. Sebnem Duzgun [1],*, Aditya Juganda [1], Jurgen Brune [1] and Gregory Bogin [2]

[1] Mining and Earth Systems Engineering Program, Mining Engineering Department, Colorado School of Mines, Golden, CO 80401, USA
[2] Mechanical Engineering Department, Colorado School of Mines, Golden, CO 80401, USA
*   Correspondence: demirkan@mines.edu (D.C.D.); duzgun@mines.edu (H.S.D.)

Abstract: Detecting the formation of explosive methane–air mixtures in a longwall face is still a challenging task. Even though atmospheric monitoring systems and computational fluid dynamics modeling are utilized to inspect methane concentrations, they are not sufficient as a warning system in critical regions, such as near cutting drums, in real-time. The long short-term memory algorithm has been established to predict and manage explosive gas zones in longwall mining operations before explosions happen. This paper introduces a novel methodology with an artificial intelligence algorithm, namely, modified long short-term memory, to detect the formation of explosive methane–air mixtures in the longwall face and identify possible explosive gas accumulations prior to them becoming hazards. The algorithm was trained and tested based on CFD model outputs for six locations of the shearer for similar locations and operational conditions of the cutting machine. Results show that the algorithm can predict explosive gas zones in 3D with overall accuracies ranging from 87.9% to 92.4% for different settings; output predictions took two minutes after measurement data were fed into the algorithm. It was found that faster and more prominent coverage of accurate real-time explosive gas accumulation predictions are possible using the proposed algorithm compared to computational fluid dynamics and atmospheric monitoring systems.

Keywords: artificial intelligence (AI); computational fluid dynamics (CFD); underground coal mines; methane prediction; real-time; time series prediction; modified long short-term memory

1. Introduction

Despite alternative energy sources, worldwide coal production is still increasing each year [1]. Longwall mining is the most utilized coal mining method, due to its high productivity and safer operating conditions [2]. However, in usual mining operations and conditions, coal mining still faces serious challenges [3]. Despite advancements in technology and safety management, longwall face explosions from accumulated methane gas are known to be the most common causes of methane explosions [4]. Existing industry practices depend on point-type methane sensors in critical regions to prevent explosive gas accumulations [5]. However, point sensors are not reliable at spotting and warning about explosion hazards, especially in crucial areas, such as near the cutting drum, tailgate, and headgate areas of the longwall face [6]. One catastrophic example of a methane explosion accident was the 2010 Upper Big Branch Mine in West Virginia, U.S. [6]. Although atmospheric monitoring systems can report real-time methane concentrations, they fall behind due to their limited number of sensors and locations [7], which lack full coverage of the whole longwall face. Computational fluid dynamics (CFD) were employed to simulate ventilation conditions in longwall faces to reproduce airflow aerodynamics and the formation of hazardous gas mixtures which are not detectable using conventional monitoring and ventilation inspection practices [5]. Although CFD modeling can accurately predict explosive gas zones, high computational power and time requirements render its use for real-time ventilation monitoring purposes impossible [7].

Karacan (2008) proposed principle component analysis and an artificial neural network-based approach to predict methane emission rate throughout 63 longwall mines. The study shows that the volume of daily methane emission from each mine can be accurately predicted [8]. Dougherty and Karacan (2011) utilized the prediction model in [8] and developed software which can predict ventilation emissions with elastic properties [9]. Duda and Krzemień (2018) proposed a framework for forecasting methane emissions from seams to goafs; they predicted the average volume of methane per minute in each year of mine life [10]. Sidorenko et al. (2021) provided the necessary parameters to predict methane emissions from seams to goafs [11]. Although these studies discuss prediction, these predictions are neither real-time nor spatial outputs.

Previous studies demonstrate the successful implementation of Artificial Intelligence (AI) in various fields with real-time predictions. For example, Chen et al. (2019) proposed a real-time AI integration for cancer diagnosis by implementing image processing algorithms for body scans [12]. Nyanteh et al. (2013) implemented an AI for real-time fault detection [13]. To improve weather forecasting for high-impact weather, McGovern et al. (2017) integrated an AI with expert opinions [14]. Imran et al. (2014) classified real-time messages in social media using AI to help the public access important disaster response information [15]. Dong et al. (2021) used the AI model for real-time monitoring and predicting of slope failures [16]. Rodríguez-Rangel et al. (2022) incorporated big data analytics for autonomous vehicles' speed estimation [17]. Wahyono et al. (2022) proposed combining AI with data mining for real-time forest fire detection [18].

Real-time prediction of methane in a longwall face requires predicting explosive gas zone formation in time, and its location in 3D (x, y, and z coordinates). Predictions in time are mainly conducted using time series classification/analysis [19]. Spatiotemporal AI models and time series classification are relatively new to the field. Moreover, the vast majority of successful models only take into account one or two spatial dimensions, such as x and/or y coordinates, and the data of interest [20–28]. For example, whereas climate change studies that track carbon emissions use latitude, longitude, and carbon content [29], water quality studies use one-dimensional distance of the intersections and water content [19]. This study proposes a 3D spatiotemporal prediction model for the real-time prediction of methane in the coal face.

Current explosive gas accumulation monitoring practices in longwall coal mines rely on two methods, namely, point sensors and CFD modeling. Point sensors take real-time measurements along the face and provide methane concentration values at the installed locations. CFD modeling provides methane prediction for the whole longwall face. However, due to computational cost, predictions take days or weeks, depending on the resolution of the study area. In this study, a continuation of our previous work [7] benchmarking and analyzing the suitability of the dataset and off-the-shelf algorithms, we developed an AI algorithm and methodology for use as a real-time explosion hazard warning system. We used six CFD analyses with varying shearer locations to train, test, and validate our model. This approach lays the foundation for accurate methane predictions in real-time for underground mines by combining the most potent advantages of point sensors and CFD models, decreasing the computational cost of CFD modeling, and increasing the coverage of point sensors.

Previously conducted methane prediction studies mainly focused on total methane emissions from the seam or the whole mine. To the best of our knowledge, a 3D real-time methane prediction approach in longwall mining that integrates CFD data with an AI model has not been developed yet. Previous studies of methane prediction in longwall coal mines primarily focused on total methane emissions of the whole mine or the whole face with varying time intervals of years to minutes. Moreover, the predictions in these studies do not consider critical methane emission zones, such as near the drums or shearer locations. This paper fills these gaps. The approach presented herein can provide methane emission data not only in the 3D spatial domain but also in real-time throughout the mining

face, including, but not limited to, areas near cutting drums, the shearer, the tailgate, and the headgate.

The remainder of this paper is organized as follows. Section 2 describes materials and methods used in this study. Section 3 describes empirical results from the AI model. Section 4 discusses and compares results. Lastly, Section 5 summarizes the paper, makes concluding remarks, and outlines future work.

2. Materials and Methods

The developed research methodology exploits the advantages of CFD modeling and point sensors. Figure 1 illustrates how AI was integrated into real-time methane concentration prediction.
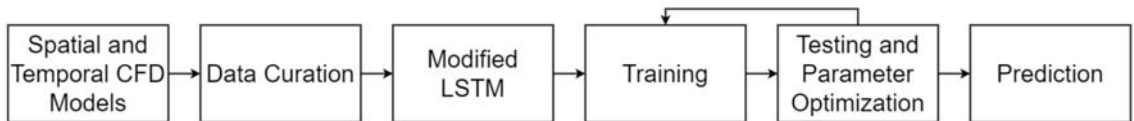
Figure 1. Research methodology.

The first step explains spatial and temporal CFD modeling and longwall face simulation. The second step presents extracted data and how they were processed and presented. The third step discusses an AI algorithm, referred to as the long short-term memory (LSTM) model, and how it was modified to meet this study's requirements; the algorithm was trained and tested, and parameters were optimized. In the last step, predictions for spatial and temporal results are discussed.

2.1. Spatial and Temporal CFD Modeling

Ansys Fluent software version 18.2 was utilized to model and simulate a longwall face. The modeled longwall face was 300 m long with a mining height of 3 m and a depth of 6 m. Two primary pieces of equipment were also modeled: (i) support equipment (shields) and (ii) cutting equipment (shearers). There were 150 shields; each shield was 2 m long, fixed in the model. One 10 m long shearer was placed along the longwall face in 6 locations. Location details are provided in Section 2.2. Lastly, the modeled area was covered with approximately 31 million hexagonal and octagonal meshes. Mesh sizes ranged from 3 cm to 30 cm, which increased prediction resolution.

The simulation exemplified a transient CFD model of methane (CH_4) gas emission from the coal face based on a bleeder ventilation system with a tailgate (TG) back return setup. Each transient model was simulated for 180 s and recorded at 1 s intervals.

2.2. Data Curation

Data were collected after modeling the longwall and simulating methane emissions. It should be noted that although each mine ventilation condition is unique, previously conducted studies [30–34] validate that simulated data are consistent with the actual situation that includes but is not limited to *"(i) continuous leakage of fresh air from the face to the gob, and the higher accumulation of methane as the supplied air travels from the headgate to tailgate side of the face; (ii) higher leakage around the headgate and tailgate corners of the face due to the high porosity and permeability around the edge of the gob; (iii) Methane accumulation seems to follow linear regression based on ventilation surveys done in several longwall operations."* [4].

Each simulation had approximately 31 million cells; data for each cell for each second of recording included pressure, airflow velocity (Vx, Vy, and Vz), CH_4 concentration, cell volume, and x, y, and z coordinates. Data collection was repeated for each of the shearer's six locations, which required 10 days for each location. Details of specific shearer locations and the cutting direction during data collection are provided in Figure 2.
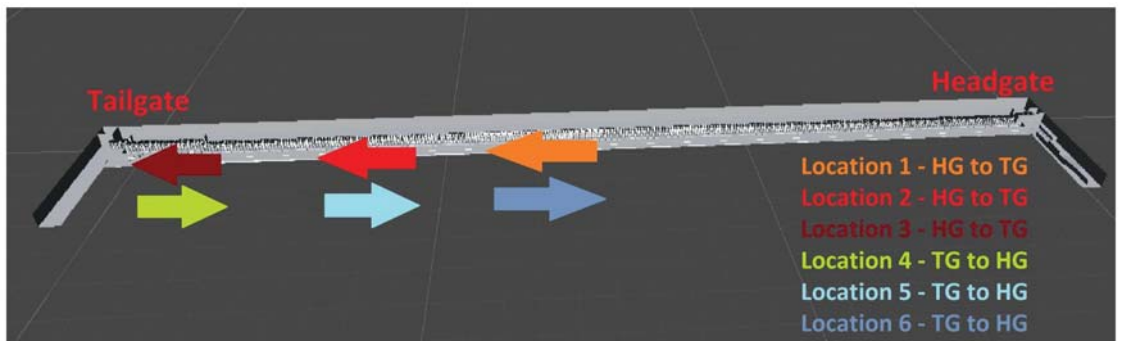
Figure 2. Six locations of the shearer and cutting directions during data collection.

Figure 3 represents a snapshot of the 120th second of location 3 as an example. Other locations and timestamps acted similarly; to avoid redundancy only one example is provided.
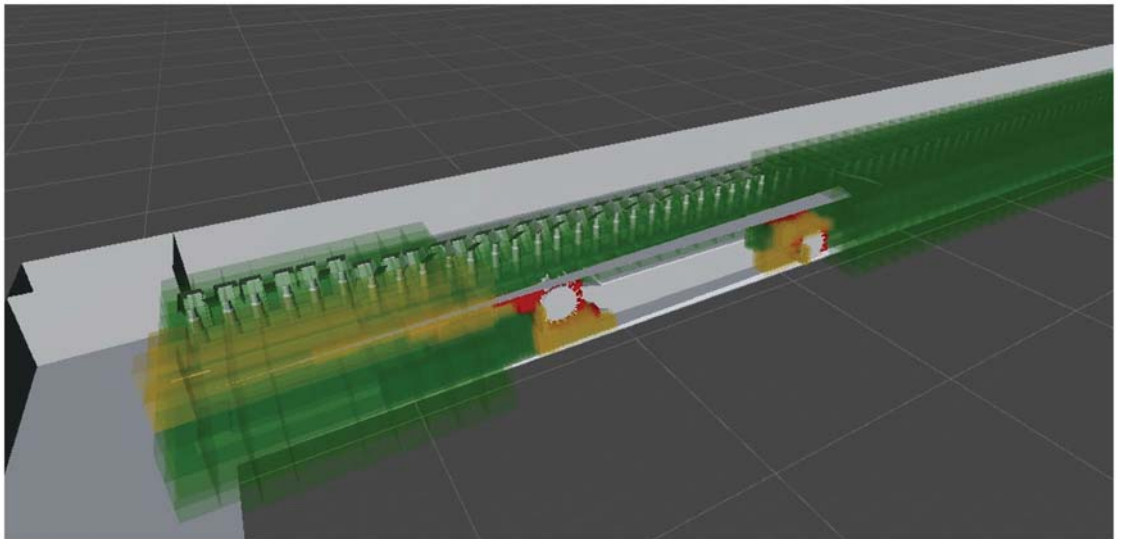
Figure 3. Snapshot of the 120th second of shearer location 3.

Raw data from the Fluent software were preprocessed, which included data conversion into CSV files, removing empty fields, adding cutting directions, and fixing the two significant figures for all fields. There were 2 terabytes (TBs) of end data for each location; 12 TBs of data were input into the AI.

2.3. The Modified LSTM

The literature discusses different methods for the spatiotemporal prediction of a parameter, namely, the Naïve 2 method, simple exponential smoothing, the Holt method, the ARIMA method, and the ETS method [35]. The primary disadvantage of using the Naïve 2, simple exponential smoothing, and HOLT methods is that these algorithms can only predict one step ahead of time within a confidence interval. In a dynamic environment such as longwall mining, continuous monitoring is the key to preventing explosive hazards; hence, one-step-ahead predictions were not sufficient for the aim of this study. Moreover, it was not feasible to implement these methods for real-time prediction considering the

required computational power and data size. For example, each location had approximately 32 million cells, which were connected to each other and affected methane concentration. In contrast, the ARIMA and ETS methods can predict long-term methane concentrations for a specific cell. However, the longwall's geometry was 3D, and these statistical methods are not effective at predicting in a 3D environment. Moreover, unlike AI models, statistical methods utilize interpolation that cannot learn data's extreme fluctuations.

AI and machine learning (ML) algorithms have been recently introduced to predict the time and location of a parameter of interest. Although applications are still limited, preliminary results of a range of studies (discussed briefly in Section 1) are promising. Moreover, in-depth analysis and benchmarking of the most promising algorithms for real-time methane prediction were examined in a previous study [7].

In light of the literature and previous tests, a recurrent neural network (RNN) was determined to be the best candidate for real-time methane prediction in longwall coal mines. An RNN contain cycles from previous time steps as network inputs to influence predictions at the current time step. These timestamps are stored in the RNN's internal states, allowing it to exploit a dynamically changing contextual window over the input sequence history [36–38].

Unfortunately, the range of contextual information that a standard RNN can access is, in practice, quite limited. The problem is that the influence of a given input on the hidden layer and, therefore, on the network output, either decays or blows up exponentially as it cycles around the network's recurrent connections. This shortcoming is referred to in the literature as the vanishing gradient problem. Long short-term memory (LSTM) is an RNN architecture specifically designed to address the vanishing gradient problem [39–41]. LSTMs were introduced in about 1997; their main advantages include that they are (i) algorithms that can store information for a specified time duration, (ii) resistant to noise, and (iii) trainable parameters [42,43]. In the light of our previous study [7], any future prediction using AI can be categorized into seven problem types (image, sensor, motion, spectrographs, electronic devices, electrocardiograms, and simulations). As methane prediction is similar to the sensor-type problem, one of the best performing algorithms, an LSTM network (a special type of RNN) was adapted for this study.

Figure 4 shows the simplified architecture of the LSTM model, modified from the blog post by Olah [37]. In the forget gate, the cell takes the previous time step and determines which information should be kept and which should be omitted. In the input gate, the cell takes information and keeps only what is relevant for prediction. In the update gate, the cell takes previous neural network information and updates prediction weights. Lastly, the output gate determines which parameters and data to output and feed to the next cell.

As LSTMs are viewed as feed-forward neural networks where each cell shares the same model parameters, they are considered deep architectures or deep neural networks [36]. In this study, the LSTM network was modified, trained, and tested with CFD outputs. A conventional LSTM network accepts 2D data. LSTM model modifications implemented in this study include (i) changing the input shape for the 3D space and (ii) adding 3D operations and vector calculations. The inputs to the modified LSTM model were; x, y, and z coordinates, the smallest distance to the shearer, airflow velocity, methane concentration, and the volume of each cell for 180 s, which were recorded at 1 s intervals.
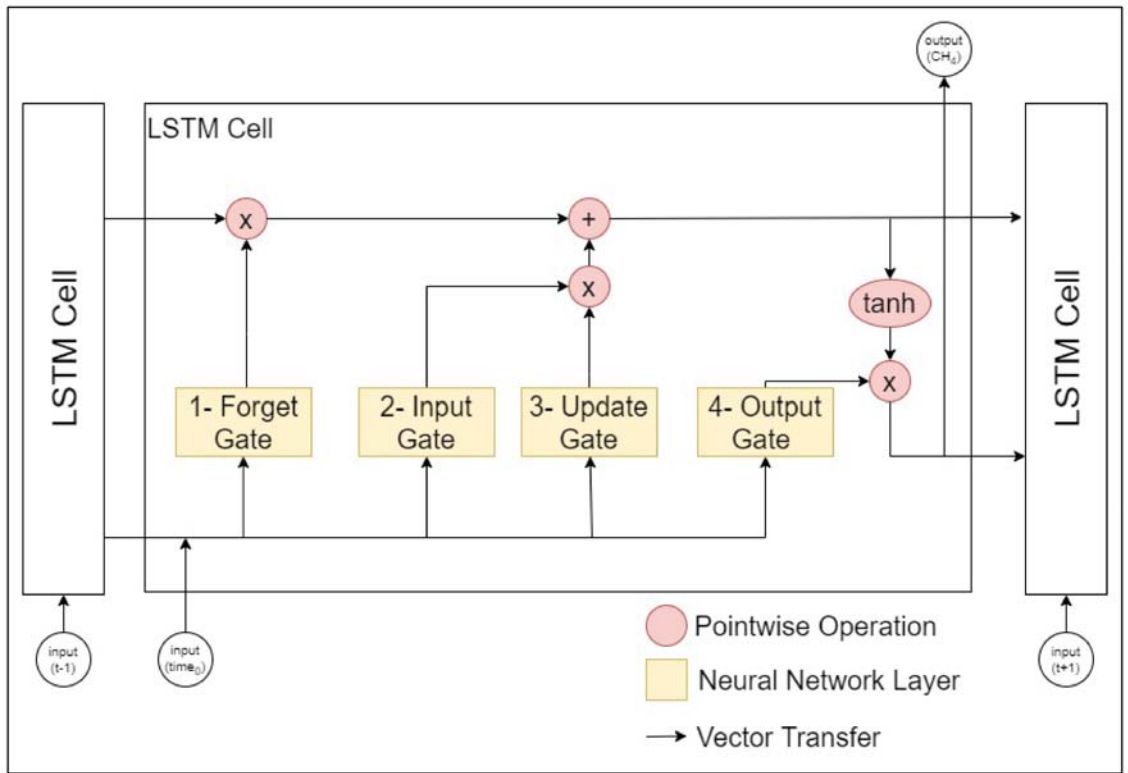
Figure 4. Simplified LSTM architecture (modified from [37]).

3. Results

Even the best-performing algorithms might fail to predict results without high-quality data. Therefore, training, validation, and testing of the algorithm are critical for reliable predictions; if these steps are not performed correctly results might be biased. Table 1 provides a data breakdown, and is followed by an explanation of each topic in respective subsections. Note that similar shearer locations were selected for training and predicting methane content. For example, Figure 2 illustrates that shearer locations 1 and 6 had a similar location in the middle of the longwall face, and locations 3 and 4 had a similar location on the tailgate side. In addition to slight changes in the exact positions of cutting equipment, cutting directions were also changed. Datasets for similar locations were divided 50–50 for training and testing. The first 50% was divided into 80% to 20% for training and validation; the detailed distribution is provided in Table 1.

Table 1. Training, validation, and testing datasets based on shearer locations.

Training DataSet	Validation DataSet	Cutting Direction	Testing DataSet	Cutting Direction
80% of Location 1	20% of Location 1	Headgate to Tailgate	Location 6	Tailgate to Headgate
80% of Location 2	20% of Location 2	Headgate to Tailgate	Location 5	Tailgate to Headgate
80% of Location 3	20% of Location 3	Headgate to Tailgate	Location 4	Tailgate to Headgate
80% of Location 4	20% of Location 4	Tailgate to Headgate	Location 3	Headgate to Tailgate
80% of Location 5	20% of Location 5	Tailgate to Headgate	Location 2	Headgate to Tailgate
80% of Location 6	20% of Location 6	Tailgate to Headgate	Location 1	Headgate to Tailgate

The common practice of splitting data into train, validation, and test sets depends on the dataset and might range from 50–50% to 80–20%. With a few data points ($n < 10,000$), 70–30% splitting is used. However, if the number of recordings is high ($n > 1,000,000$), the importance of split ratios decays. Overall, the most important element in splitting a dataset is having good data representation in the train and test sets. In this study, the number of recordings was close to 64,300,000; hence, training was conducted using a specific shearer direction and tested using the opposite direction but the same position [44–48].

The training and validation of each instance took approximately seven days; testing time was 15 min with high-performance computing using the following specifications:

- CPU: Intel Xeon COU E704830 v3@2.10GHz (4 CPUs/node, 48 cores/node)
- GPU: five Tesla K80
- Memory: 2133 MT/s, Dual Rank, x4 Data Width RDIMM (42.7 GB/Core)
- Storage: 20 TBs

Input data were approximately 5 TBs for each instance, with 2 TBs of output.

3.1. Training

Training data were used to teach patterns and features to the AI model. The same training data were repeatedly given to the model until a threshold level was reached. Feeding the same data repeatedly is called an epoch. The simple explanation of an epoch is one complete pass of the dataset through the designed network. The algorithm updated its parameters with each epoch while learning the input dataset. Training data were divided into 80% and 20% for each instance using the stratified K-folds cross-validation method. This yielded a balanced data division, which preserved the percentage of samples for each methane content. The divided 80% of data were used to train the model.

3.2. Validation

Validation data were separated from training data, which validated the AI's performance. Training and validation accuracy helps users evaluate their mode. Figure 5 illustrates a commonly used metric for assessing algorithm performance, validation, and training accuracy versus an epoch.
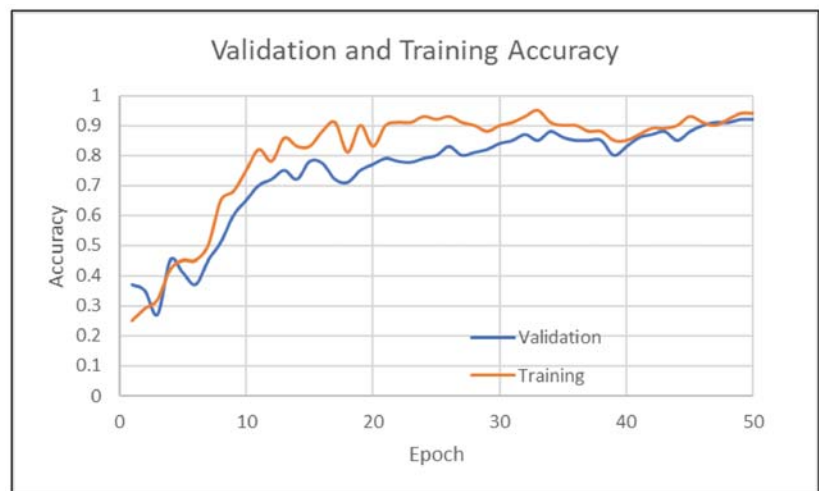
Figure 5. Validation and training accuracy.

In the training and validation accuracy graph, the curves' slopes approach horizontal after the 12th epoch, which indicates that data did not make a significant learning process over the algorithm. At approximately the 20th epoch, the learning curve becomes almost

horizontal. This indicates that no further training was necessary after the 20th epoch, as the accuracies did not change considerably and ranged from 89.1% to 93.8%. Lastly, the validation curve below the training curve indicates that the model was fed a good representation of data, was ready for testing, and able to provide reliable predictions.

3.3. Testing

After training and validation, test data were used to evaluate the AI model's performance predicting methane. The model's performance was analyzed using the actual and predicted methane content of the testing data for each training and testing coupled set, as provided in Table 2.

Table 2. Overall accuracies of tests.

Couple Name	Training DataSet	Testing DataSet	Overall Accuracy
L1L6	Location 1	Location 6	92.4%
L2L5	Location 2	Location 5	89.1%
L3L4	Location 3	Location 4	87.9%
L4L3	Location 4	Location 3	88.3%
L5L2	Location 5	Location 2	91.0%
L6L1	Location 6	Location 1	91.6%

These results show that the modified LSTM algorithm predicted methane concentration with an accuracy ranging from 87.9% to 92.4%.

4. Discussion

Analysis revealed that the modified LSTM algorithm can possibly combine effective aspects of CFD modeling and point sensor measurements. AI algorithms can achieve 3D coverage of CFD modeling and real-time point sensor data measurements. The overall accuracies of different locations ranged from 87.9% to 92.4%. Although accuracies were relatively high, some locations (such as locations 3 and 4) had less accurate results than others, possibly because the closer the shearer was to the headgate and tailgate (locations 1 and 6), the more methane emissions fluctuated. The algorithm was more agile when spotting fluctuations; therefore, relatively constant methane emissions might be the reason for lower test accuracies in locations 3 and 4. Although the accuracies showed promising results, with additional datasets they might increase. Even if a single location has approximately 32 million points, the entire measurement only contains 180 s of data. If these measurements could be increased, accuracies might also increase. Given the current data storage and computational power advancements in supercomputers, the required time for training was 45 days. Moreover, an increase in data size will increase the required computational power and time required for training; however, time requirements will change more exponentially than linearly. Training times will not affect prediction times; once the algorithm is trained, the required prediction time will not change drastically.

Whereas explosive gas zone monitoring relies on point sensors, the critical regions of the longwall face cannot be tracked in real time. Although CFD modeling can overcome the sensors' coverage, the required prediction time could be days to weeks, depending on the resolution of the simulation. This study's methodology eliminates these shortfalls. The system proposed herein yields highly accurate real-time predictions with detailed coverage of the longwall face. Therefore, modified LSTM-based methane prediction might help early warning systems for miners and engineers reduce safety risks and prevent accidents such as the Upper Big Branch. Lastly, the system can increase production by reducing unnecessary stops of the shearer.

However, the AI's prediction capabilities depend on the simulated CFD model results. Therefore, predictions can only be as accurate as similar longwall face models. Training

the AI model using different longwall face models can increase the AI model's capacity. If the AI model can be trained with more data, it might be used for all longwall mines in the world.

5. Conclusions

As was the case with the Upper Big Branch accident, longwall mine methane explosions can be fatal. Current explosive gas zone management practices are carried out either with point sensors or CFD modeling. Leveraging the power of AI might be crucial for monitoring explosive methane concentration. The primary objective of this study was to combine the advantages of current methane monitoring practices and eliminate their disadvantages. For this purpose, modified LSTM architecture was utilized for real-time methane prediction.

This study is unique as it provided real-time methane prediction in 3D space. Our study successfully leveraged a significant (12 TB) amount of CFD data for location and time prediction of possible explosive methane accumulation. Unnecessary stops, high fan speed, and other high operating costs can be reduced using the proposed method, which will help increase the safety and productivity of all longwall coal mines by monitoring the methane gas along the face.

Although the proposed methodology successfully predicted methane concentration throughout the longwall face, the results only contained numbers representing location, time, and methane content. Results consisted of lines of numbers that could not be interpreted or used by engineers and/or miners to determine if the explosive gas accumulation was hazardous.

Future research associated with this study will consist of two parts. First, the algorithm will be trained using other mines' methane emission models. This will increase the algorithm's prediction capabilities and enable its usage and implementation on all longwalls in the world. Second, the predictions of the AI model will be imported into Unity for visualization purposes. This will help facilitate the integration of real-time predictions with augmented and virtual reality environments, which are already implemented in other industries, such as construction, production, health, and many more. The final product might ease the judgement burden placed on engineers and workers in times of critical methane emission. We will convert results into more robust, understandable visualizations that resemble CFD output; providing a familiar output will help engineers and workers by decreasing their cognitive load.

We have started the second development phase; a side-by-side comparison of the CFD model and our visualizations for different time stamps are shown in Figure 6.
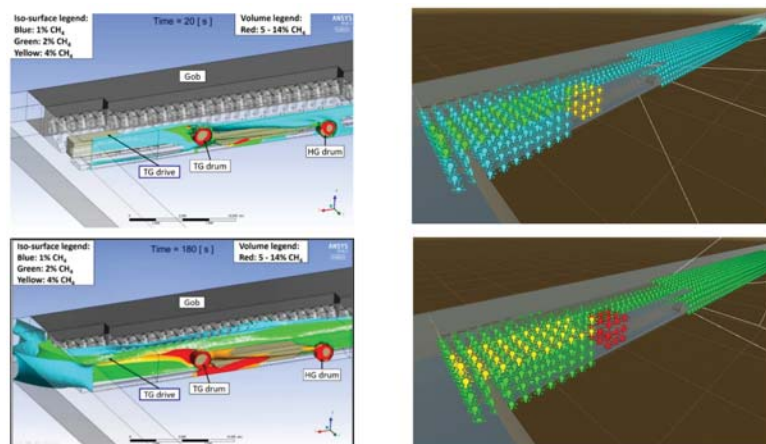
Figure 6. Side-by-side comparisons of CFD models and prediction visualizations modid.

These visualizations will help us conduct a user study with the aim of discovering a better way to visualize AI outcomes. The user study will also provide insights regarding the possible integration of these visualizations into a mixed-reality environment.

Author Contributions: Conceptualization, H.S.D., J.B. and G.B.; data curation, D.C.D. and A.J.; formal analysis, D.C.D.; funding acquisition, J.B.; investigation, D.C.D.; methodology, D.C.D. and H.S.D.; project administration, H.S.D., J.B. and G.B.; software, D.C.D. and A.J.; supervision, H.S.D., A.J., J.B. and G.B.; validation, D.C.D.; visualization, D.C.D.; writing–original draft, D.C.D.; writing–review and editing, H.S.D. and A.J. All authors have read and agreed to the published version of the manuscript.

Institutional Review Board Statement: The study did not require ethical approval.

Informed Consent Statement: The study did not involve humans.

Data Availability Statement: Data presented in this study are available on request from the corresponding author. On account of their large size (12 TB), data are not publicly available due to online data storage requirements and associated long-term maintenance costs. Data presented in this study were not previously used or published. Data contained in this study were not altered, modified, or changed using any means. Data were exported from a CFD model that simulates an actual working mine.

Conflicts of Interest: The authors declare no conflict of interest. The funders had no role in the design of the study; in the collection, analyses, or interpretation of data; in the writing of the manuscript; or in the decision to publish the results.

References

1. Dudley, B. BP Statistical Review of World Energy. *BP Stat. Rev. Lond. UK Accessed Aug.* **2018**, *6*, 116.
2. Peng, S.S. *Longwall Mining*; CRC Press: Boca Raton, FL, USA, 2019; ISBN 9780429260049.
3. Qiao, M.; Ren, T.; Roberts, J.; Yang, X.; Li, Z.; Wu, J. New Insight into Proactive Goaf Inertisation for Spontaneous Combustion Management and Control. *Process Saf. Environ. Prot.* **2022**, *161*, 739–757. [CrossRef]
4. Juganda, A. *Evaluation of Point-Based Methane Monitoring and Proximity Detection for Methane Explosive Zones in Longwall Faces of Underground Coal Mines*; Colorado School of Mines: Golden, CO, USA, 2020.
5. Juganda, A.; Strebinger, C.; Brune, J.F.; Bogin, G.E. Discrete Modeling of a Longwall Coal Mine Gob for CFD Simulation. *Int. J. Min. Sci. Technol.* **2020**, *30*, 463–469. [CrossRef]
6. Davis, S.G.; Engel, D.; van Wingerden, K. Complex Explosion Development in Mines: Case Study—2010 Upper Big Branch Mine Explosion. *Process Saf. Prog.* **2015**, *34*, 286–303. [CrossRef]
7. Demirkan, D.C.; Duzgun, S.; Juganda, A.; Brune, J.; Bogin, G. Evaluation of Time Series Artificial Intelligence Models for Real-Time/near-Real-Time Methane Prediction in Coal Mines. *CIM J.* **2022**, *1*, 1–10. [CrossRef]
8. Karacan, C.Ö. Modeling and Prediction of Ventilation Methane Emissions of U.S. Longwall Mines Using Supervised Artificial Neural Networks. *Int. J. Coal. Geol.* **2008**, *73*, 371–387. [CrossRef]
9. Dougherty, H.N.; Özgen Karacan, C. A New Methane Control and Prediction Software Suite for Longwall Mines. *Comput. Geosci.* **2011**, *37*, 1490–1500. [CrossRef]
10. Duda, A.; Krzemień, A. Forecast of Methane Emission from Closed Underground Coal Mines Exploited by Longwall Mining—A Case Study of Anna Coal Mine. *J. Sustain. Min.* **2018**, *17*, 184–194. [CrossRef]
11. Sidorenko, A.A.; Dmitriev, P.N.; Sirenko, Y.G. Predicting Methane Emissions from Multiple Gas-Bearing Coal Seams to Longwall Goafs at Russian Mines. *ARPN J. Eng. Appl. Sci.* **2021**, *16*, 851–857.
12. Chen, P.-H.C.; Gadepalli, K.; MacDonald, R.; Liu, Y.; Kadowaki, S.; Nagpal, K.; Kohlberger, T.; Dean, J.; Corrado, G.S.; Hipp, J.D.; et al. An Augmented Reality Microscope with Real-Time Artificial Intelligence Integration for Cancer Diagnosis. *Nat. Med.* **2019**, *25*, 1453–1457. [CrossRef]
13. Nyanteh, Y.; Edrington, C.; Srivastava, S.; Cartes, D. Application of Artificial Intelligence to Real-Time Fault Detection in Permanent-Magnet Synchronous Machines. *IEEE Trans. Ind. Appl.* **2013**, *49*, 1205–1214. [CrossRef]

14. McGovern, A.; Elmore, K.L.; Gagne, D.J.; Haupt, S.E.; Karstens, C.D.; Lagerquist, R.; Smith, T.; Williams, J.K. Using Artificial Intelligence to Improve Real-Time Decision-Making for High-Impact Weather. *Bull. Am. Meteorol. Soc.* **2017**, *98*, 2073–2090. [CrossRef]

15. Imran, M.; Castillo, C.; Lucas, J.; Meier, P.; Vieweg, S. AIDR: Artificial Intelligence for Disaster Response. In Proceedings of the 23rd International Conference on World Wide Web, Seoul, Korea, 7–11 April 2014; Volume 1, pp. 159–162. [CrossRef]

16. Dong, M.; Wu, H.; Hu, H.; Azzam, R.; Zhang, L.; Zheng, Z.; Gong, X. Deformation Prediction of Unstable Slopes Based on Real-Time Monitoring and Deepar Model. *Sensors* **2021**, *21*, 14. [CrossRef] [PubMed]

17. Rodríguez-Rangel, H.; Morales-Rosales, L.A.; Imperial-Rojo, R.; Roman-Garay, M.A.; Peralta-Peñuñuri, G.E.; Lobato-Báez, M. Analysis of Statistical and Artificial Intelligence Algorithms for Real-Time Speed Estimation Based on Vehicle Detection with YOLO. *Appl. Sci.* **2022**, *12*, 2907. [CrossRef]

18. Wahyono; Harjoko, A.; Dharmawan, A.; Adhinata, F.D.; Kosala, G.; Jo, K.H. Real-Time Forest Fire Detection Framework Based on Artificial Intelligence Using Color Probability Model and Motion Feature Analysis. *Fire* **2022**, *5*, 23. [CrossRef]

19. Bagnall, A.; Lines, J.; Bostrom, A.; Large, J.; Keogh, E. The Great Time Series Classification Bake off: A Review and Experimental Evaluation of Recent Algorithmic Advances. *Data Min. Knowl. Discov.* **2017**, *31*, 606–660. [CrossRef]

20. Lines, J.; Taylor, S.; Bagnall, A. Time Series Classification with HIVE-COTE: The Hierarchical Vote Collective of Transformation-Based Ensembles. *ACM Trans. Knowl. Discov. Data* **2018**, *12*, 1. [CrossRef]

21. Dempster, A.; Petitjean, F.; Webb, G.I. ROCKET: Exceptionally Fast and Accurate Time Series Classification Using Random Convolutional Kernels. *Data Min. Knowl. Discov.* **2020**, *34*, 1454–1495. [CrossRef]

22. Shifaz, A.; Pelletier, C.; Petitjean, F.; Webb, G.I. *TS-CHIEF: A Scalable and Accurate Forest Algorithm for Time Series Classification*; Springer: Berlin, Germany, 2020; Volume 34, ISBN 1061802000.

23. Ismail Fawaz, H.; Lucas, B.; Forestier, G.; Pelletier, C.; Schmidt, D.F.; Weber, J.; Webb, G.I.; Idoumghar, L.; Muller, P.A.; Petitjean, F. InceptionTime: Finding AlexNet for Time Series Classification. *Data Min. Knowl. Discov.* **2020**, *34*, 1936–1962. [CrossRef]

24. He, K.; Zhang, X.; Ren, S.; Sun, J. Deep Residual Learning for Image Recognition. *Proc. IEEE Comput. Soc. Conf. Comput. Vis. Pattern Recognit.* **2016**, *2016*, 770–778. [CrossRef]

25. Schäfer, P.; Leser, U. Fast and Accurate Time Series Classification with WEASEL. In Proceedings of the 2017 ACM on Conference on Information and Knowledge Management, Singapore, 6–10 November 2017; Association for Computing Machinery: New York, NY, USA, 2017; pp. 637–646.

26. Lucas, B.; Shifaz, A.; Pelletier, C.; O'Neill, L.; Zaidi, N.; Goethals, B.; Petitjean, F.; Webb, G.I. Proximity Forest: An Effective and Scalable Distance-Based Classifier for Time Series. *Data Min. Knowl. Discov.* **2019**, *33*, 607–635. [CrossRef]

27. Deng, H.; Runger, G.; Tuv, E.; Vladimir, M. A Time Series Forest for Classification and Feature Extraction. *Inf. Sci.* **2013**, *239*, 142–153. [CrossRef]

28. Li, K.; Principe, J.C. Transfer Learning in Adaptive Filters: The Nearest Instance Centroid-Estimation Kernel Least-Mean-Square Algorithm. *IEEE Trans. Signal Process.* **2017**, *65*, 6520–6535. [CrossRef]

29. Alléon, A.; Jauvion, G.; Quennehen, B.; Lissmyr, D. PlumeNet: Large-Scale Air Quality Forecasting Using a Convolutional LSTM Network. *arXiv* 2020, arXiv:2006.09204. Available online: https://arxiv.org/pdf/2006.09204.pdf (accessed on 3 May 2022).

30. Marts, J.A.; Gilmore, R.C.; Brune, J.F.; Bogin, G.E.; Grubb, J.W.; Saki, S. Dynamic Gob Response and Reservoir Properties for Active Longwall Coal Mines. *Min. Eng.* **2014**, *66*, 41–48.

31. Krickovic, S.; Findlay, C. Methane Emission Rate Studies in a Central Pennsylvania Mine. U S Bur Mines, Rep Invest 7591. 1971. Available online: https://www.cdc.gov/NIOSH/mining/UserFiles/works/pdfs/ri7591.pdf (accessed on 29 August 2022).

32. Peng, S.S.; Chiang, H.S. Air Velocity Distribution Measurements on Four Mechanized Longwall Coal Faces. *Int. J. Min. Geol. Eng.* **1986**, *4*, 235–246. [CrossRef]

33. Schatzel, S.J.; Krog, R.B.; Dougherty, H. Methane Emissions and Airflow Patterns on a Longwall Face: Potential Influences from Longwall Gob Permeability Distributions on a Bleederless Longwall Panel. *Trans. Soc. Min. Met. Explor. Inc* **2017**, *342*, 51–61. [CrossRef]

34. Gangrade, V.; Schatzel, S.J.; Harteis, S.P.; Addis, J.D. Investigating the Impact of Caving on Longwall Mine Ventilation Using Scaled Physical Modeling. *Min Met. Explor.* **2019**, *36*, 729–740. [CrossRef]

35. Hyndman, R.J.; Athanasopoulos, G. *Forecasting: Principles and Practice*; OTexts: Heathmont, VIC, Australia, 2018; ISBN 0987507117.

36. Sak, H.; Senior, A.; Beaufays, F. Long Short-Term Memory Based Recurrent Neural Network Architectures for Large Vocabulary Speech Recognition. *arXiv* 2014, arXiv:1402.1128. Available online: https://arxiv.org/pdf/1402.1128.pdf (accessed on 3 May 2022).

37. Olah, C. Understanding LSTM Networks. Available online: https://colah.github.io/posts/2015-08-Understanding-LSTMs/#fn1 (accessed on 6 September 2022).

38. Ismail Fawaz, H.; Forestier, G.; Weber, J.; Idoumghar, L.; Muller, P.A. Deep Learning for Time Series Classification: A Review. *Data Min. Knowl. Discov.* **2019**, *33*, 917–963. [CrossRef]

39. Graves, A.; Liwicki, M.; Fernández, S.; Bertolami, R.; Bunke, H.; Schmidhuber, J. A Novel Connectionist System for Unconstrained Handwriting Recognition. *IEEE Trans. Pattern Anal. Mach. Intell.* **2009**, *31*, 855–868. [CrossRef] [PubMed]

40. Greff, K.; Srivastava, R.K.; Koutnik, J.; Steunebrink, B.R.; Schmidhuber, J. LSTM: A Search Space Odyssey. *IEEE Trans. Neural Networks Learn. Syst.* **2017**, *28*, 2222–2232. [CrossRef] [PubMed]

41. Calin, O. *Recurrent Neural Networks B-Deep Learning Architectures: A Mathematical Approach*; Calin, O., Ed.; Springer International Publishing: Cham, Switzerland, 2020; pp. 543–559; ISBN 978-3-030-36721-3.
42. Hochreiter, S.; Schmidhuber, J. Long Short-Term Memory. *Neural. Comput.* **1997**, *9*, 1735–1780. [CrossRef]
43. Bengio, Y. Learning Long-Term Dependencies with Gradient Descent Is Difficult. *IEEE Trans. Neural Netw.* **1994**, *5*, 157–167. [CrossRef]
44. Gholamy, A.; Kreinovich, V.; Kosheleva, O. Why 70/30 or 80/20 Relation Between Training and Testing Sets: A Pedagogical Explanation. *Dep. Tech. Rep.* **2018**, *1*, 1–6.
45. Gholami, V.; Torkaman, J.; Dalir, P. Simulation of Precipitation Time Series Using Tree-Rings, Earlywood Vessel Features, and Artificial Neural Network. *Theor. Appl. Climatol.* **2019**, *137*, 1939–1948. [CrossRef]
46. Dubbs, A. Test Set Sizing Via Random Matrix Theory. *arXiv* **2021**, arXiv:2112.05977. Available online: https://arxiv.org/pdf/2112.05977.pdf (accessed on 29 August 2022).
47. Joseph, V.R. Optimal Ratio for Data Splitting. *Stat. Anal. Data Min.* **2022**, 531–538. [CrossRef]
48. Guyon, I. A Scaling Law for the Validation-Set Training-Set Size Ratio. *ATT Bell Lab.* **1997**, *1*, 1–11.

Review

A Review of Reliability and Fault Analysis Methods for Heavy Equipment and Their Components Used in Mining

Prerita Odeyar [1], Derek B. Apel [1,*], Robert Hall [2], Brett Zon [3] and Krzysztof Skrzypkowski [4,*]

[1] School of Mining and Petroleum Engineering, University of Alberta, Edmonton, AB T6G 2R3, Canada
[2] Department of Mining Engineering and Management (MEM), South Dakota School of Mines, Rapid City, SD 57701, USA
[3] North American Construction Group, 27287-100 Avenue, Acheson, AB T7X 6H8, Canada
[4] Faculty of Civil Engineering and Resource Management, AGH University of Science and Technology, 30-059 Kraków, Poland
* Correspondence: dapel@ualberta.ca (D.B.A.); skrzypko@agh.edu.pl (K.S.)

Abstract: To achieve a targeted production level in mining industries, all machine systems and their subsystems must perform efficiently and be reliable during their lifetime. Implications of equipment failure have become more critical with the increasing size and intricacy of the machinery. Appropriate maintenance planning reduces the overall maintenance cost, increases machine life, and results in optimized life cycle costs. Several techniques have been used in the past to predict reliability, and there's always been scope for improvement of the same. Researchers are finding new methods for better analysis of faults and reliability from traditional statistical methods to applying artificial intelligence. With the advancement of Industry 4.0, the mining industry is steadily moving towards the predictive maintenance approach to correct potential faults and increase equipment reliability. This paper attempts to provide a comprehensive review of different statistical techniques that have been applied for reliability and fault prediction from both theoretical aspects and industrial applications. Further, the advantages and limitations of the algorithm are discussed, and the efficiency of new ML methods are compared to the traditional methods used.

Keywords: reliability; fault diagnosis; predictive maintenance; machine learning; lifetime distributions

1. Introduction

Reliability refers to the probability of a system meeting its desired performance standards in yielding output for a specific time duration when used under specific conditions [1]. For instance, if a machine is designed to run continuously for 10,000 h with no faults in between, the machine is said to be 100% reliable for that period. However, if a failure occurs after 10,000 h of operation, the machine's reliability after 10,000 h is less than 100% [2]. Component reliability is a function of time and is always measured at a specific operating time. Reliable operation is interrupted or terminated by failures. A failure is an event that results in the inability to complete the required duties and meet the requirements. The theoretical definition of reliability is (Reliability = 1 − Probability of Failure), given by R(t). Availability and maintenance are related to reliability and are defined as essential components of it [3].

Understanding heavy equipment's complexities, efficiency, and failures can help achieve better production results and reduce unexpected and unneeded costs. Industries can maintain consistent levels of productivity by conducting regular reliability assessments [4]. Performance measurement is significant because it identifies existing performance gaps between existing and desired performance and shows how far the gaps have been closed [5,6]. A production system consists of many subsystems. In order to make the system efficient and viable to operate, each subsystem must be optimized concerning one another. The system's availability, reliability, and maintainability, as well as its ability

to perform as intended, significantly impacts the equipment's effectiveness. Since the mid-1980s, reliability analysis methodologies have steadily gained acceptance as standard tools for developing and operating automated and complex mining systems [7].

A proper maintenance plan is of paramount importance to increase or maintain the system's reliability at a standard level. The role of equipment maintenance has evolved in the last few decades, from merely being a part of the production to an essential strategic element in mining operations. Since the early 2000s, maintenance practices have been recognized as a profit contributor, giving more importance to maintenance practices, and elevating them to the same level as production [8]. With proper maintenance strategies many abrupt failures can be prevented, decreasing the downtime and increasing the system's reliability. This helps in achieving targeted levels of production in the industry.

Equipment maintenance is so vital that around 35% to 50% of the annual operating budget can be spent on equipment maintenance and repair alone in the mining industry, and around 30% in the construction industry [9,10]. The evolution of maintenance in the mining and construction industry has come a long way in the last decade, aided by real-time data availability. There are four common maintenance approaches that can be applied to mine assets: reactive, preventive, condition-based, and prescriptive [11,12].

Often known as unscheduled maintenance, corrective maintenance is only conducted when equipment fails. This is because it could result in a lot of equipment downtime and a lot of secondary failures, resulting in a loss of production [13].

Preventive maintenance (PM), is carried out at predetermined intervals and according to a prescribed criterion; "it is intended to reduce any cost of unplanned maintenance from unexpected equipment failure" (EN 13306 2001). All preventive management programs are time driven. The component to be maintained can either be replaced or reconditioned depending on its condition. PM can be further categorized into condition-based and predicted maintenance [14].

Condition-based monitoring (CBM) is a form of preventive maintenance that repairs a system before it fails by looking for signs of fatigue or other failure precursors. CBM creates an optimum maintenance period by extending the time between preventive maintenance and reducing the expense of unnecessary excessive maintenance and downtime. CBM is based on the study of maintenance of gathered data (such as vibration, crack propagation, oil, pressure, and viscosity) [15].

An overview of the maintenance classifications is shown in Figure 1. It is required that any maintenance strategy should minimize equipment failure rates, improve equipment reliability, prolong the equipment's life, and reduce maintenance costs. Many KPIs are used to monitor the long-term trends in reliability and maintenance performance. These KPIs help understand if all the small and large modifications in maintenance practices and system changes are having the desired effect over time. The mean time between failure (MTBF) and mean time to failure (MTTF) are two essential KPIs for determining the system's reliability and faults. A successful maintenance strategy and reliability policies lead to resolving issues that lead to equipment failures and show a steady increasing performance trend that stabilizes at industry benchmark levels [16].
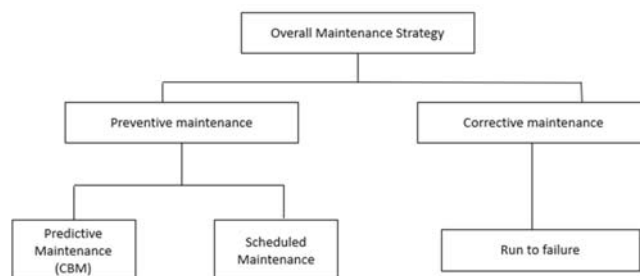
Figure 1. Different maintenance strategies [17].

Fault detection and reliability analysis of the system have evolved over the years. The history of the reliability field may be traced back to the early 1930s, when probability concepts were applied to problems associated with electric power generation. The beginning of the maintainability field may be traced back to 1901. By the 1960s, equipment maintenance activities started to be regarded as technical and involved optimizing maintenance solutions and activities [1]. Most literature on reliability and maintenance analysis in the mining and construction industry is present from 1975 onwards. During the 1975–1985 period, several literature works can be found on reliability analysis of mining equipment that was based on theoretical approaches [18–21]. Authors used manually drawn probability density functions and KS tests to identify the availability of continuous mine systems [22] and determined the reliability of bucket wheel excavators by doing probability calculations. In the next few years (1985–1995), graphical methods using total time on test and analytical methods using KS test and maximum likelihood estimations were used for reliability testing [4,23,24]. Authors used proportional hazard models to investigate the effects of two different designs and maintenance of power transmission cables [21]. Fault tree analysis, failure mode, effect and criticality analysis were used in the late 1980s for fault detection and reliability analysis [25–28]. By the 2000s best fit probability distribution using reliability software was extensively used in mining to predict reliability and schedule maintenance using information from reliability plots [29]. Weibull++6 software (from Reliasoft, Tuscon, AZ, USA) was used to determine best-fit distributions for characterizing the failure pattern of the two crushing plants and their subsystems. Authors used Statgraphic software to estimate parameters of probability distributions for the shovel and its subsystems [30]. Most work in reliability is found around estimating best fit distributions for independent and identically distributed data (I.I.D) and NHPP models for non-I.I. D data [31–33]. The genetic algorithm was first applied in the reliability analysis of equipment in mining in 2001 [34]. Authors used Pareto analysis and statistical modeling of failure and repair distribution for reliability analysis of a hydraulic shovel [35]. Machine learning applications for mine equipment reliability analysis were largely introduced from late 2000's. Several articles in the last ten years have used machine learning and deep learning for reliability and maintenance analysis. Genetic algorithms, discrete event simulations, SVM regression, KNN models, ANN, and reinforcement learning, have been widely used in the application of fault predictions and reliability analysis.

2. Methodology

Most of the relevant literature and research work reviewed in this study is regarding Machine learning applications in equipment fault detection and reliability analysis and their components, focusing on artificial intelligence and machine learning usage. This paper aims to provide a comprehensive review of advanced statistical and ML techniques widely applied for reliability and maintenance analysis by classifying the research according to the different statistical models and ML algorithms to offer guidelines and a foundation for further research. In addition, a critical analysis of previous articles was carried out to identify the advantages and shortcomings of the latest technological systems in the fault detection and maintenance field to identify areas for the future scope of the study.

To achieve the mentioned, the paper is organized into five sections. In the first section, there is a brief description of the current field of study. Section 2 presents the methodology in the literature that is employed to categorize the previous work. Section 3 presents the application of different traditional reliability methods. Section 4 discusses the application of ML methods used in failure and reliability predictions. Section 5 discusses the conclusions drawn based on the review and the potential future scope for the same.

Research databases, including Google scholar, Scopus, IEEE Xplore, ScienceDirect and SpringerLink were mainly used for this study. Strategic keywords like reliability/maintenance/failure analysis/fault detection and mine equipment (component) and machine learning/statistical/graphical method were used in the searches. Figure 2 shows the number of documents reviewed and used in each segment.
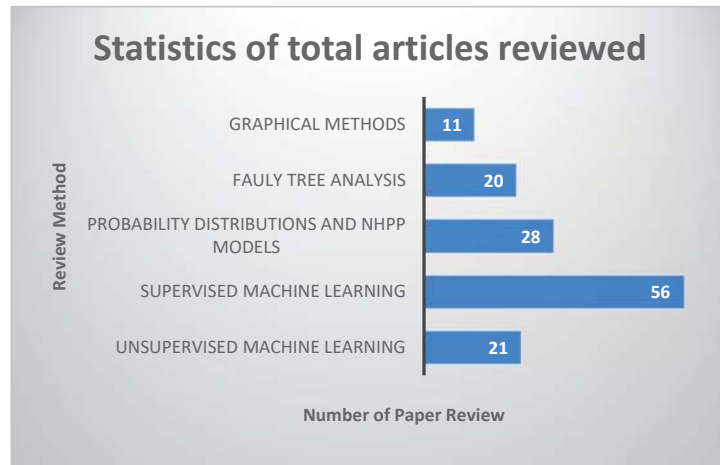
Figure 2. Statistics of number of documents reviewed.

3. Review on Application of Different Traditional Methods Used in Reliability and Fault Analysis

3.1. Graphical Methods

Graphical methods can identify fault time and monitor and schedule preventive maintenance. The graph plots the number of failures per unit versus the total time on test per unit. This method assumes the time between failures (TBFs) to be independently and identically distributed. Therefore, the actual chronological orderings of the TBFs can be ignored. Thus, using a TTT plot is not useful to evaluate failure data that has structures or is positive to the serial correlation test. However, a significant aspect of these plots is that they can be used to analyze incomplete data. The failure rate of the equipment can be inferred from the shape of the plot. If the plot is concave downwards, the equipment is deteriorating (increasing failure rate), but if it is concave upwards, the equipment improves over time [36]. If the plot crosses diagonal multiple times, the equipment has a constant failure rate [4]. Graphical methods can be used to arrive at maintenance intervals. TTT plots can be used to monitor health of equipment in terms of constant failure rate/increasing or decreasing failure rate. The technique of TTT-plotting, originally suggested by Barlow and Campo, is very simple to use for failure data analysis (Refs. [4,37,38]).

Graphical approaches can also be used to verify the presence of trends in failure and repair data by plotting the cumulative number of failures against the cumulative time [36]. Before modeling the reliability data, it should also be tested for mutual independence by testing it for the presence of serial correlation. The serial correlation can be tested by plotting the ith TBF X_i against $(I - 1)$ th TBF, X_{i-1}. If the plotted points exhibit no pattern, it can be interpreted that the TBFs are free from serial correlation. In case the plot reveals serial correlation, then the TBFs are plotted at greater lags, such as X_i against X_{i-2}, X_{i-3}, X_{i-4} .... etc., to search for serial correlation over greater lags [39]. Since the 1990s, reliability and maintenance engineering has incorporated graphical methods, and recent studies show that graphical methods are still in use for the initial exploratory investigation. The input data for the graphical approaches are TTF and TBF data. Graphical methods are typically used to estimate the reliability of large equipment like excavators, draglines, and LHDs. From the existing literature work, it can be deduced that graphical methods are mostly employed in planning maintenance intervals, identifying the machine's failure trends (increasing/decreasing failure rate), and testing the goodness of fit of other reliability estimating methods [40].

Authors used TTT plot to estimate the reliability of LHD machines and identified components that needed improvement in design [4]. In [23] scaled TTT was used to review

the goodness of fit of the power-law-process model using both graphical and analytical procedures. In [41] used TTT plots for i.i.d failure data to plan maintenance intervals for material handling equipment operating in the mining industry. In [42] authors collected failure data of hydraulic shovels for a period of 1.5 years, analyzed the machine's reliability using distribution plots and studied increasing/decreasing failure rates using a TTT plot. Authors used failure mode effect analysis (FMEA) and TTT plots to study the reliability of the cone crusher [40,43].

3.2. Fault Tree Analysis

Fault Tree analysis translates a physical system into a logical diagram, making it one of the industry's most popular approaches for reliability and safety calculations. It can also update a system's setup to make it less vulnerable and sensitive [44]. Fault trees can also assess the impact of design changes or proposed corrective actions [45]. The causes of an event are deduced using a top-down deductive analysis. The components of a fault tree analysis are "events" and "logic gates", which connect the events to determine the reason for the top unwanted event. The process of creating a fault tree is one of trial and error, and no failure causes should be overlooked [46]. The completed fault tree is assessed considering the analysis' goals. There are several stages to the evaluation: listing minimum cut sets, grading minimum cut sets, calculating probabilities, and so on. When there is quantitative data on the likelihood of events, FTA is very useful, although qualitative analysis is also possible [44]. Other risk analysis approaches aren't as effective at discovering faults as fault trees. Its visual presentation of the failure causes makes it simple to identify a single failure that leads to a complete system failure. A fault tree is often normalized to a given interval, and an event's probability depends on the relationship between the event risk function and this interval. The reliability is calculated using a sequence of gates, considering the probabilities of the outputs of a set of Boolean logic operations. It can also be used to assess the impact of design changes or proposed corrective actions [45]. Two major approaches used for determining minimal cut sets for fault trees are Monte Carlo simulation and deterministic methods. A basic fault tree structure is represented below (Figure 3). According to the literature, FTA is used in the fault analysis of HEMM. Several studies have been published in the last five years using SFT and DFT. From the previous work, it can be noted that FTA is used both with descriptive and numerical data combined with Boolean algebra to make decisions on optimized maintenance intervals, qualitative and quantitative fault analysis, and reliability estimations of the equipment [47]. FTA was helpful in identifying risk priority number (RPN), equipment value, and impact on value, identifying basic events that cause failures, and building mathematical models by logically correlating the events.
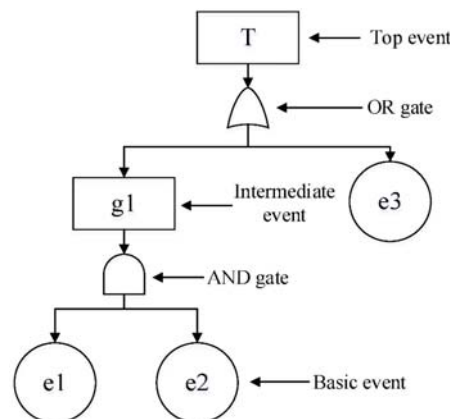
Figure 3. Basic fault tree representation [48].

In [49], authors used fault tree analysis to understand the effects of each component or subsystem of a dragline on its reliability, and to get an insight of an optimized maintenance schedule. Probability distribution that best defined TTF data of each subsystem of dragline was identified. The obtained distributions were then combined with a fault tree for defining the system to identify the influence of individual component reliability on a dragline. Dragging rope is predicted to have the highest contribution to a number of failures within a year, but the motors and generators will cause the longest downtime if they fail. Probability values were also useful in deciding which components need attention at certain time intervals. In [50], the authors used fault tree analysis for fault identification of CNC turning center. Boolean algebra was used to evaluate the fault tree (FT) diagram and to derive the machine's governing reliability model. Qualitative and quantitative analysis is carried out to identify critical sub-systems and components of CNC turning center. The results are the estimation of the reliability of the CNC machine after one year of the warranty period and identify the number of failures during this period. In [51], the authors used fault tree analysis to analyze failures associated with the mine cage conveyance while showing the various branches of events that can lead to failures and their order of criticality for the various associated components. Failures associated with one or more components compromised the effectiveness of the mine cage conveyance as a system, and efforts were geared toward managing the critical components identified in this study by reviewing the existing maintenance plans and developing more robust strategies. In [52], the authors developed a methodology to determine the critical machine of the company, based on impact on production, impact on value, availability standby and equipment value and this identified machine was further analyzed by using failure mode and effect analysis and fault tree analysis in detail to determine its risk priority number (RPN). The risk priority number (RPN) is the product of severity rating, probability of occurrence, and the probability of detection [53]. A case study used a fault tree for a heavy-duty machine's hydraulic system, and the result shows that there are 27 basic events that cause hydraulic failure in the hydraulic system, where oil pollution is the most critical basic event. As the outcome of quantitative analysis is entirely dependent on the precision of the numerical data used in the analysis, if uncertainties are left unresolved, then there is a chance of producing misleading results. Hence, different methodologies, mainly based on fuzzy numbers, were proposed to tackle the issue of uncertain failure data in FTA.

Standard fault trees (SFTs) can only assess the reliability of static systems. The dynamic nature of a system leads to several dynamic failure features such as functional dependent events and priorities of failure events. Although SFTs are commonly used for dependability analysis, they are incapable of capturing dynamic data. SFTs have been expanded in several ways to assist dynamic dependability analysis, such as dynamic fault trees (DFTs), state-event faults, and stochastic hybrid fault trees. The DFT is one of the most extensively used dynamic extensions of the SFT, and it captures sequence-dependent behavior, functionally dependent component behavior, and event priority [54,55]. In [56], the authors proposed a method to set the dynamic fault tree of a roadheader. The modular method was used to split the fault tree into dynamic and static states, and a binary decision tree was used to analyze the static state, and the logical relationship between faults was used to assess the dynamic module. In [57], the authors constructed a dynamic fault tree using a binary decision tree and Markov method in a modular approach for an electric haulage shearer. The study revealed that improper installation of the first shaft bearing, cage off of first shaft bearing, cutting motor damage and poor quality of lubricating oil were the major contributors to the faults of the shearer [44].

FTA's design concept can be used to demonstrate its limitations. It focuses on building a mathematical model of a complex physical condition by logically correlating events. The strategy is solely based on the analyst's judgement if all peripheral, environmental, and operating parameters are not given [58]. Another important difficulty with a quantitative FTA is the lack of reliable and meaningful failure data and the probabilities of events. The cost of development in a first-time application to a system is the most notable. For

investigating small systems, inductive analysis approaches such as failure-mode-and-effects analysis are significantly easier and less expensive to deploy [58].

Even though several fault tree extensions have been proposed, they all have a variety of shortcomings. Even when software tool help is available, many investigations involve a significant amount of manual work. Over the last two decades, researchers have focused on ways to automate the synthesis of dependability information from system models, with the goal of simplifying dependability analysis. As a result, the field of model-based dependability analysis has emerged (MBDA) [44]. As part of MBDA, many tools and approaches for automating the development of dependability analysis, such as fault trees, have been developed. Because the analyses in MBDA are carried out on formal models, they may be carried out iteratively, which helps to generate more results and new results if the system design changes. When compared to manual procedures, this process takes less time and costs less money, and because it is more structured, the chances of introducing errors in the analysis or producing incomplete results are reduced. Furthermore, by allowing sections of an existing system model or libraries of previously analyzed components to be reused, the MBDA methodologies give a higher degree of reusability [44,55].

3.3. Probability Distributions and NHPP Models

The reliability of the system and sub-system can be determined from the failure rate using probability distribution methods. Both parametric and non-parametric methods are used in reliability estimations. Trend and correlation tests can be used to check if the data points are independent and identically distributed. Parametric distributions can be used if no trend or correlation is observed in the data. Otherwise, non-parametric methods can be used to analyze data. In non-parametric methods, the failure data are analyzed without assuming any particular distribution. The non-parametric analysis methods include Kaplan–Meier, simple actuarial and standard actuarial methods. Reliability evaluation by parametric method considers fitting the failure rate to any statistical distribution, such as the exponential, normal, Weibull, or lognormal. This will result in a better understanding of failure, and the resulting model can be used for analytical evaluation of reliability parameters for the whole lifespan of the system.

Parametric probability distributions are used both in stochastic analyses of system reliability, where the systems are mostly assumed to be fully known, and corresponding properties of the system are analyzed, and for statistical inference, where process data are used to estimate the parameters of the distribution, often followed by a specific inference of interest [59]. Goodness of fit tests like the Chi-square test, Kolmogorov–Smirnov, Anderson–Darling and Shipiro–Wilk tests are used to analyze how best the distribution fits the given data. The model that most efficiently describes the data can be selected based on goodness-of-fit tests for reliability estimations. The Weibull distribution function, among all distributions, is usually the most used method to evaluate system reliability as the distribution could be used to show an assortment of life behaviors. In this distribution, cumulative probability, failure rate and probability density function (PDF) curves are changed by the influence of either shape parameter, β, scale parameter, η and location parameter, γ variation. The shape parameter mainly indicates the condition of the system. If $\beta < 1$, it indicates that the rate of failure of a system or component will be decreasing with respect to time. This condition can be treated as an early-life failure. Weibull distributions with β nearer to or equivalent to 1 have a constant rate of failure, also known as the useful life. Similarly, Weibull distributions with $\beta > 1$ have an increasing failure rate with respect to time, denoted as a wear-out failure. A typical 'bathtub curve' plot clearly depicts the three segments of failure zones. Figure 4 shows the bathtub curve representing the failure rate over time.
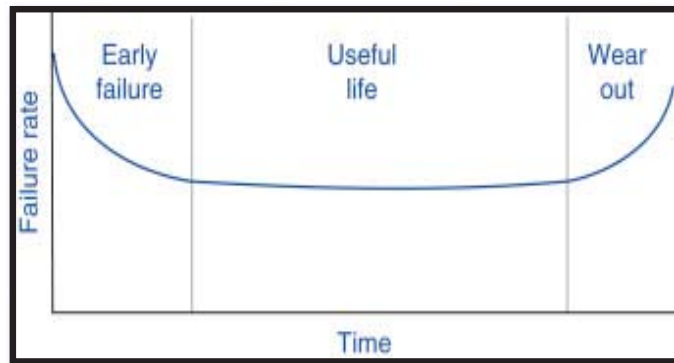
Figure 4. Bathtub curve representing equipment failure rate [60].

Most work in the literature is based on probability distributions in equipment reliability estimations and maintenance analysis. TBF, TTF and TTR data are mainly used in parametric and non-parametric estimations. Probability distribution and NHPP models are mainly used in reliability centered maintenance and to identify critical systems and sub-systems of the equipment. In [61], the authors presented reliability analysis based on probability density function and failure rate of a shovel-dumper system of an open pit coal mine using probability distribution functions. The KS test was used to evaluate the best fit distribution for TBF data of shovels and dumpers. In [62], the authors adopted a three-parameter Weibull distribution approach to analyze the data sets of load-haul-dumper (LHD) in underground mines using the 'Isograph Reliability Workbench 13.0' software package. The parameters were evaluated using best fit distributions, and Weibull likelihood plots and the percentage reliability of each individual subsystem of LHD were estimated. Using the results, the authors identified preventive maintenance time intervals and enhanced the overall reliability of the LHD. The equipment performance evaluation was based on availability and utilization. In [63], the authors presented a case study describing the reliability analysis of crushing plants in a bauxite mine where the crushing plants were divided into seven subsystems and reliability analysis was done for each subsystem using failures data. The parameters of some idealized probability distributions were estimated by using ReliaSoft's Weibull ++ 6 software, and the best fit distributions that characterized the failure pattern of the two crushing plants and their subsystems were identified. Further reliability of both the crushing plants and their subsystems were estimated at different time missions using the best fit distribution. Other aspects of system failure behavior were also analyzed briefly for machine improvement. Analysis of the total downtime, breakdown frequency, reliability, and maintainability characteristics of different subsystems shows that the reliability of crushing plant 1 and crushing plant 2 after 10 h reduce to about 64% and 35%, respectively. The study showed the importance of reliability and maintainability analysis for deciding maintenance intervals and for planning and organizing maintenance. In [64], the authors considered two approaches (a basic maintenance approach and a reliability-based approach) to analyze maintenance data. To find the best-fit distribution, different types of statistical distributions were tested by the Easyfit software. The developed model based on these data showed that the reliability of loader No. 1 and No. 2 decreased to a zero value after approximately 477 h and 309 h of operation, respectively, and suggested a review on the maintenance program to be performed to increase reliability. In [65], the authors presented a reliability analysis of load-haul-dumpers in an underground coal mine. The distribution parameters were estimated by both graphical and MLE processes and the goodness-of-fit test was carried out using the Cramer von mises statistical test. Further, using this analysis, the total cost of operation was reduced by estimating the reliability-based preventive maintenance time

intervals. In [66], the authors presented a case study describing reliability analysis and life cycle cost optimization of a band saw cutting machine. A few components followed the parametric distribution and certain components followed the non-parametric distribution. The failure distribution parameters for each component of the machine were estimated using ReliaSoft's Weibull++6 software. The result of the analysis indicates critical parts of the machine and with certain design changes indicated by the authors, there is around 16% improvement in the overall reliability of the system, and the life cycle costs are reduced by 22%. In [67], the authors used a renewal process (Poisson distribution) for modelling the LHD's mechanical failures. The graphical method tests if the data is independent and identically distributed (IID). The parameters of various distributions were found by using Math Wave Easy Fit 5.6 professional software. Chi-square test was applied to select the best-fit distribution model. Further, the study of the two-parameter log normal distribution theory and its parameters are presented using log-normal probability theory. The study reflects that reliability analysis is a powerful tool for determining maintenance intervals. Maintenance activity every week was suggested for the machine to achieve a reliability of 75%. In [68], the authors developed a basic methodology for the reliability modelling and development of a maintenance program for a fleet of four drilling rigs. Failure and performance data was collected from the Sarcheshmeh copper mine in Iran for two years. Then, the available data was classified and analyzed and the reliability of all subsystems and whole rigs were modelled and studied. Easyfit and MS Excel software were used for data analysis and finding the best-fit distributions and parameters, and the Kolmogorov–Smirnov (K-S) test was used to select the best distributions. NHPP and renewable processes were used for the reliability modelling of the subsystems of the drill rigs. The probabilistic possibility of all fleet states was calculated, and maintenance operations were suggested for 80% reliability.

In [69], the authors studied the reliability of a drum shearer machine using operation and maintenance data from an Iranian mine for a period of two years. The tests for trend and serial correlation showed that the times between successive failures for the cable system were not independent and identically distributed and the graphical tests revealed that the cable system of the shearer is a deteriorating system. A goodness-of-fit test showed that the power law process model is a good fit for this system's failure data. After parameter estimation for the power law model, reliability and failure rate plots were obtained. Based on analysis and results, a period of 125 h was defined as the reliability-based maintenance interval for the cable system of the shearer. The analysis shows that, using this strategy, the system's reliability would improve by at least 50%. In [70], the authors studied the reliability, availability, and maintainability (RAM) of a 36T dumper machine with failure and repair data using the KME method and outlined the constraints and reasons for machine unavailability. The results were verified using maximum likelihood estimation and piecewise exponential estimation methods. The reliability and maintainability of an LHD system are disappointing. They suggested maintenance planning and machine improvement from this analysis. The Kaplan–Meir estimator is used to find the design life and optimal maintenance period which are useful information in maintenance planning. In [71], the authors developed a computational tool and programming with VBA in Excel for reliability and failure analysis of underground rock bolters. The developed approach used the modelling of stochastic processes, such as the renewal process, the non-homogeneous Poisson process, and the Bayesian approach. The tool gives the best-associated model, the parameters estimation, the mean time between failure and the reliability estimate. This approach is validated with the reliability analysis of inter-failure times from underground rock bolters subsystems over a two-year period. Results show that Weibull and lognormal probability distribution fit to the most subsystem inter-failure times. The study revealed that the bolting head, the rock drill, the screen handler, the electric/electronic system, the hydraulic system, the drilling feeder and the structure have a high repair frequency. The hydraulic and electric/electronic subsystems represented the lowest reliability after 50 operation hours. In [23], the authors conducted a preliminary analysis of a fleet of LHD

machines, found that engine and hydraulic systems are the two most critical systems and selected hydraulic systems for further study. Maintenance data for two years for these machines were analyzed. The tests for trends and serial correlation showed that times between successive failures for the hydraulic systems were in most cases not independent and identically distributed. Goodness-of-fit tests (Cramer–von Mises test and graphical methods) showed that the power law process model is a good fit for the hydraulic systems' failure data. Methods for parameter estimation in the power law process model and estimation of optimal maintenance intervals for the LHDs are presented, emphasizing the use of graphical methods for data analysis.

4. Machine Learning Applications in Failure Predictions and Reliability Estimations

Machine Learning (ML) is a subclass of artificial intelligence (AI) that can be defined as a semi-automated system in which computers create an algorithm by learning from observed data. Machine learning algorithms create a model based on training data and use it to make predictions or judgments without having to be explicitly programmed to do so. In recent years, decision makers and the scientific community have paid close attention to the use of machine learning in risk and reliability assessment. Currently, quite a good amount of work is being carried out in mine equipment failure and reliability assessments and predictive maintenance analysis [72]. A machine learning approach can be used for predicting failures and also to identify important parameters that predict failures.

From the equipment failure perspective, machine learning can be useful to replace or repair a component before a fault happens and restore the original condition of the equipment to maintain reliability. The algorithms use previous failure data or the equipment's vibration/condition monitoring data to study failures and make predictions. This would lead to decreased downtime and achieve expected production levels at all times. Machine learning helps predict future failures to accurately schedule maintenance operations. ML techniques are designed to derive knowledge out of existing data. The following diagram (Figure 5) gives a basic understanding of ML application for fault analysis.
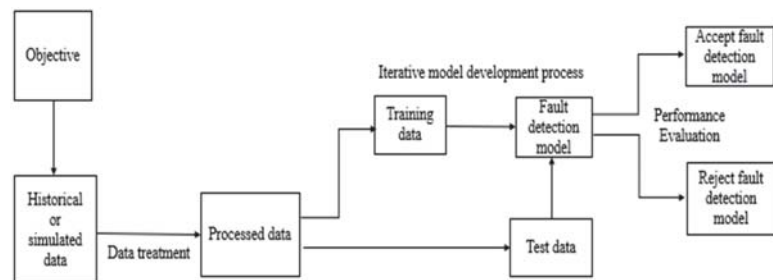
Figure 5. Workflow for developing data-driven ML model for fault detection.

Businesses can profit from big data since it aids in guiding systems with a prescriptive maintenance strategy. To improve the performance of machine learning algorithms, it is critical to acquire usable data from the dataset [73]. Depending on the availability of labelled data, ML-based data-driven methods can be further classified as supervised, semi-supervised or unsupervised approaches. Machine learning algorithms are classified into taxonomies based on the algorithm's expected outcome. The following are a list of common algorithm types:

- Supervised learning: The algorithm creates a function that maps inputs to outputs. Output variables are known. The classification problem is a common supervised learning challenge in which the learner must learn (or estimate the behaviors of) a function that maps a vector into one of many classes by studying multiple input-output samples of the function.

- Unsupervised learning: There is no target or outcome variable to predict/estimate in this method. It is used for clustering populations in different groups and when there is a lack of sufficiently labelled data [74].
- Semi-supervised learning: Combines both labelled and unlabeled examples to generate an appropriate function or classifier [75]
- Reinforcement learning: The machine is taught to make a certain decision using this algorithm. It works like this: the machine is placed in an environment where it would constantly train itself through trial and error. This system learns from its previous experiences and seeks to capture as much information as possible to make accurate decisions [74].

Predictive modelling can be described as the mathematical problem of approximating a mapping function (f) from input variables (X) to output variables (y). This is called the problem of function approximation. The algorithms are divided into two types: classification and regression based on the output variable. Classification predictive modelling is the task of approximating a mapping function (f), from input variables (X) to discrete output variables (y). The output variables are often called labels or categories. The mapping function predicts the class or category for a given observation. Regression predictive modelling is the task of approximating a mapping function (f) from input variables (X) to a continuous output variable (y). A continuous output variable is a real value, such as an integer or floating-point value. Classification models use different metrics like accuracy, precision, recall, F1-score, ROC, confusion metrics, specificity, sensitivity, and AUC to evaluate model performance. Regression models use mean square error (MSE), root mean square error (RMSE), mean absolute error (MAE), bias-variance and learning curves to estimate error and evaluate model performance [76]. Classification models are mostly used in the literature to predict and classify faults. A few ML algorithms used majorly in the literature of equipment reliability and fault analysis are discussed in this section.

4.1. Support Vector Machine (SVM)

Support vector machine (SVM) is a supervised machine learning algorithm that can be used for classification and regression problems. In the SVM algorithm, each data item is plotted as a point in n-dimensional space where n is the number of features considered, with each feature being the value of a particular coordinate [77]. Then, the aim is to perform classification by finding the hyper-plane that differentiates the two classes very well. SVMs maximize the margin around the separating plane, and the decision function is fully specified by a subset of training samples called the support vectors [78,79]. The optimal SVM hyperplane for binary classification is represented in Figure 6.

A separating hyper plane can be used to divide data that is linear. However, the data is frequently non-linear, and the datasets are closely linked. To account for this, the input data is non-linearly mapped to a high-dimensional space. After that, the new mapping is linearly separable. Kernel trick allows SVM's to form nonlinear boundaries. The kernel function's purpose is to allow operations to be conducted in the input space instead of the possibly high-dimensional feature space. As a result, the two classes can be separated in the feature space. Different kernel functions exist, such as polynomial, radial basis function (RBF), and sigmoid function, and the choice of a kernel function is determined by the application [80]. From the literature review, it can be noted that SVM is mainly used for forecasting failures, fault diagnosis and pattern recognition. The previous works used TTF, TBF, audio signals, vibration data, and fault states as input data for SVM algorithms. From the time horizon, it can be noted SVM was widely popular from 2010 to 2015 in mining.
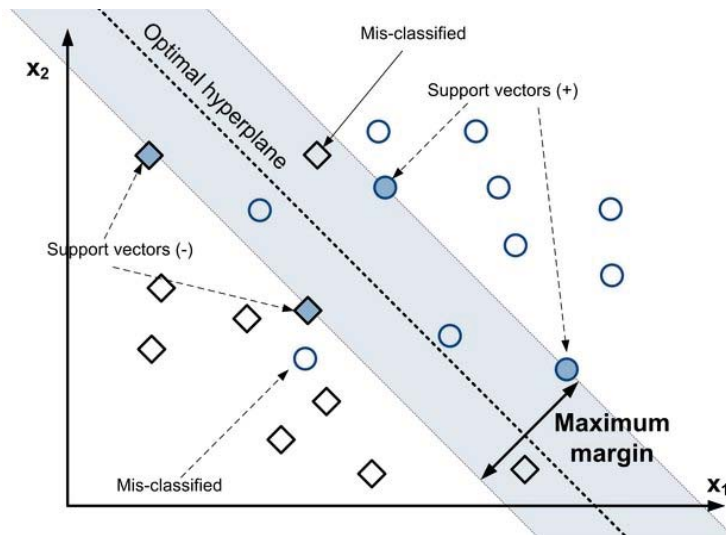
Figure 6. Optimal hyperplane for binary classification [81].

In [82], the authors used SVM to detect defects and fault patterns of unexpected heavy equipment failures. SVM classifier was used to divide data as normal and abnormal and only normal data was used for learning using restricted Boltzmann machine (RBM) and then based on patterns, faults in the system were identified. In [83], the authors used the SVM regression algorithm to forecast TBFs using historical observations of LHD failures. A Pareto analysis detected the LHD's engine as the most critical system. TBFs of 32 failures were obtained. Twenty-five records were used for SVR modelling and the remaining for testing. Mean absolute percentage error (MAPE) and normalized root mean square error (NRMSE) values were used to evaluate model performance. A polynomial kernel function of the third degree resulted in the best predictions (minimum errors). An absolute percentage error value of less than 2% was achieved, demonstrating excellent forecasting applicability of SVR. In [84], the authors have explored the application of the SVM classification approach for pattern recognition and failure forecasting on mining shovels. The failure behavior of a fleet of ten mining shovels during 1 year of operation was investigated and the shovels were classified into four clusters using k-means clustering algorithms, based on their reliability. Future failures were predicted using the support vector machine (SVM) classification technique. Historical failure (component type) and time to repair data were used to predict the next failure type for all shovels. Four different kernel functions, namely linear, polynomial, RBF and sigmoid function were examined in combination with different values of C parameter, using a grid search attempt. The best C–K pair that resulted in the maximum number of correct classes for the test dataset was selected for each shovel from each cluster using a grid search method, and the results were validated using particle swarm optimization. The SVM technique was shown to be successful with a prediction accuracy of over 75%. In [85], the authors proposed principal component analysis (PCA) with the SVM method for fault diagnosis of mine hoists. PCA was used to extract relevant time domain and frequency domain features and using these, a multi-class SVM algorithm model corresponding to nine different fault states output was built. Comparison of various methods showed the PCA-SVM method successfully diagnosed faults in the mine hoists system. The RBF kernel function system had the best classification properties and the accuracy of the model turned out to be around 98%. In [86], the authors developed a SVM based ensemble model for reliability forecasting of a mine dumper. The hyperparameters of the SVM were selected by applying a genetic algorithm. A case study

was conducted investigating a dumper operated at a coal mine in India. Time-to-failure historical data for the LHD were collected, and cumulative time to failure was calculated for reliability forecasting. The hyperparameters of the SVM models were selected using genetic algorithm-based learning. Study results demonstrate that the developed model performs well with high accuracy (determination coefficient R^2 = 0.97) in the prediction of LHD future failure times, and a comparison with other methods demonstrates the superiority of the proposed ensemble SVM model. In [87], the authors have proposed a classification method for an automated operating mode to increase the performance of vibration-based online condition monitoring systems for applications such as gearboxes, motors, and their constituent components. Several variations of the system have been tested and found to be successful. A swing machinery system of an electromagnetic excavator is used to see how this method functions on dynamic signals gathered from an operating machine. The empty and full swing cycles are the two classification classes with vibration and speed as input parameters. SVM and other classification models were used to analyze swing performance. Data were collected over a period of 45 h on an operation. In [88], the authors developed a method for monitoring and tracking both location and action for automated construction equipment. The authors have proposed an audio-based method for tracking and activity analysis of heavy construction equipment. The equipment generates distinct sound patterns while performing a certain task and these audio signals are filtered and converted into time–frequency representations. This data is classified into different activity representations using a multiclass SVM classification algorithm, and the results demonstrated the potential capacity to correctly recognize various equipment actions with 80% model accuracy.

4.2. The k-Nearest Neighbors KNN

The k-nearest neighbors (KNN) method is a supervised machine learning algorithm that can be used to address classification and regression problems [89]. KNN is a kind of instance-based learning (also known as lazy learning), in which the function is only estimated locally, and all computation is deferred until classification. When there is very little prior knowledge about the data distribution, the KNN is the most basic and simplest classification algorithm. The data points are categorized based on how their neighbors are classified. The algorithm's idea is that all data points with similar characteristics are in close proximity. Given a K value, the nearest K neighbors are chosen for any new point, and the class containing the most points out of the k points is allocated to the new point. The choice of K, as well as the distance measure used to pick the nearest K points, determine the performance of a KNN classifier. In the case of KNN, a small training sample size can significantly impact the selection of the optimal neighborhood size K, and the sensitivity of K selection can significantly decrease KNN classification performance. In general, KNN is susceptible to data sparsity, noisy mislabeled points, and outliers from other classes if the K value chosen is too small or too large [90–92]. From the literature review, it can be inferred that KNN data is recently gaining popularity in mining. It is mainly used in fault diagnosis and real time fault monitoring. Faults are monitored and identified both at system and sub-system levels.

In [93], the authors studied a historical failure dataset of a dragline to conduct predictive maintenance. The authors used the k-Nearest Neighbors algorithm to predict the failure mode but there was a chance of overfitting in the methodology. Hence, a combination of the genetic algorithm and k-Nearest Neighbor algorithm was applied for the failure dataset. This enhanced the model performance, and the results were better predicted. In another study, [94], the authors collected vibration signals of main journal-bearings of an IC engine from condition monitoring methods. The vibration signals were classified under normal, oil starvation, and extreme wear fault. Thirty features were extracted from the processing of signals, and KNN and ANN were applied to train the dataset and later for diagnostic use. Variable K ranging from 1 to 20 with the step size of 1 was used to get better classification results. The experimental results showed diagnostic methods were

reliable in separating fault conditions in the bearings. In [95], the authors proposed a new methodology of weighted k-Nearest Neighbor classifier where a square inverse weighting technique was used to improve the accuracy of the KNN model for fault diagnosis of rolling bearing elements. Three bearing conditions were classified: healthy, inner, and outer race fault. The algorithm indicated that this method enables fault detection in bearings with high accuracy. In [96], the authors presented a fault diagnosis technique based on acoustic emission (AE) analysis with the Hilbert–Huang transform (HHT) and data mining tool. In [97], the authors proposed a real-time online fault diagnosis method for rolling bearings based on the KNN algorithm. The rolling bearing vibration signal is preprocessed, and feature parameters are extracted. The data was preprocessed, with 100 raw points as one sample, for a total of 8496 samples. Different classification models like decision tree C4.5, CART algorithm and KNN were used to classify fault data. Real-time online extraction of the characteristic parameters of the vibration signal was used to realize real-time online faults through the fault diagnosis model. Results show that the fault diagnosis model based on the KNN algorithm is better than the fault diagnosis model.

4.3. Naïve Bayes Classifier

Naïve Bayes, a supervised machine learning algorithm, assumes an underlying probability distribution and captures uncertainty about the model logically by calculating probabilities of occurrences. It is used to solve diagnostic and predictive issues. It calculates explicit hypothesis probabilities and is robust to noise in the input data [98]. The naïve Bayes algorithm is a straightforward probability classifier that derives a set of probabilities by counting the frequency and combinations of values in a data set. When assessing the value of the class variable, the method applies Bayes' theorem and assumes that all variables are independent. In a range of controlled categorization challenges, the algorithm learns quickly [99].

There are different types of Naïve Bayes classifiers. When characteristic values are continuous, it is assumed that the values associated with each class are spread according to the Gaussian distribution, which is the Normal distribution. On multinomial distributed data, multinomial naïve Bayes is preferred. Bernoulli naïve Bayes is employed when data is distributed according to multivariate Bernoulli distributions. That is, multiple features exist, but each one is considered to have a binary value. As a result, binary values are required for features [100,101]. Naïve Bayes has recently earned a lot of attention because of its high learning and prediction accuracy, and more importantly, the algorithm works well for mining data and conditions. In the literature work, naïve Bayes was used in fault diagnosis and assessing faults' damage and fault classifications.

In [102], the authors predicted RUL of bearings using the naïve Bayes algorithm. Firstly, the statistical method is used to extract the features of the vibration signal, and the root mean square (RMS) is regarded as the main performance degradation index. Second, the correlation coefficient is used to select the statistical characteristics that have high correlation with the RMS. Then, in order to avoid the fluctuation of the statistical feature, the improved Weibull distributions (WD) algorithm is used to fit the fluctuation feature of bearings at different recession stages, which is used as the input of the naïve Bayes (NB) training stage. During the testing stage, the true fluctuation feature of the bearings is used as the input of NB. After the NB testing, five classes are obtained: health states and four states for bearing degradation. Finally, the exponential smoothing algorithm is used to smooth the five classes and to predict the RUL of bearings. The experimental results show that the proposed method is effective for RUL prediction of bearings. In [98], the authors used Naïve Bayes for bearing fault diagnosis on enhanced independent data. Data-based fault diagnostics of mechanical components has become a new hotspot. Their approach was based on processing the data vector (attribute feature and sample dimension) to reduce the limitations of Naïve Bayes by an independence hypothesis. The statistical characteristics of the bearings' original signal were extracted, decision trees were used to select important features of the signal, and low correlation features were selected. The

authors used SVM models in the next step to prune redundant vectors, and in the last step used Naïve Bayes on the processed data to diagnose faults. In [103], the authors studied non-repairable equipment with multiple and independent failure modes, where only incomplete information about the failure mode was obtained through condition monitoring. The study focused on obtaining a probability matrix representing the relationship between actual health and condition monitoring information of the equipment and Naïve Bayes was used as a classifier to classify each failure mode based on the degree of damage. An experimental planetary gearbox system is used to gather condition monitoring data for damage degree classification considering four failure modes. A forward feature selection is used in this paper to find the best set of features. The classification accuracy increases to 94.76%. In [104], the authors applied a Naïve Bayes classifier for diagnosing faults of rolling element bearings and indicated that the Naïve Bayes classifier presented higher levels of accuracy of 96% without any feature engineering requirement.

4.4. Decision Tree

Decision tree is a supervised machine learning method for constructing classification systems based on multiple parameters or generating prediction algorithms for a target variable. In this method, a population is divided into branch-like segments that form an inverted tree with a root node, internal nodes, and leaf nodes. The algorithm is non-parametric and can handle huge, complex datasets without imposing a complex parametric framework [105]. Decision trees are mainly effective in handling non-linear datasets. Like stepwise selection in regression analysis, decision tree methods can be used to pick the most relevant predictor variables from a large number of features in datasets and to assess the relative importance of these variables on the decision variable. Moreover, decision trees can also handle missing data very well. It is also easy to handle a variety of input data: nominal, numeric and textual [106].

However, other target functions of the decision tree can also include, minimizing the number of nodes or minimizing the average depth to find the most important predictors. Pruning is the practice of removing redundant nodes from a tree to obtain the best decision tree possible. A general decision tree structure is represented in Figure 7.
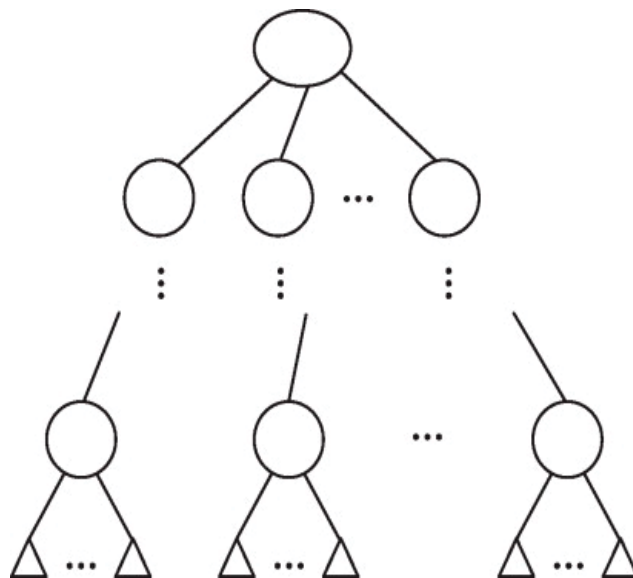
Figure 7. A general decision tree structure [107].

In [108], the authors in their work proposed an equipment reliability model for pumps, designed by applying a data extraction algorithm on equipment maintenance records residing in SAP applications. The author has initially applied unsupervised learning to perform cluster evaluation. Thereafter, the data from the finalized model was applied to a supervised learning algorithm where the classifier was trained to predict equipment breakdown. The classifier was tested on test data sets where it was observed that support vector machine (SVM) and decision tree (DT) algorithms were able to classify and predict equipment breakdown with high accuracy and a true positive rate (TPR) of more than 95 percent.

In [109], the authors proposed the fault diagnosis method of an industrial ventilator (Fan) based on analysis-decision trees. The operating of the fan was followed in five different conditions: a healthy condition and then affected by four different faults, those affecting inner and outer races of rolling bearings, the mass unbalance and mechanical looseness. Fifteen factors including mean, median, variance indicators (including the greatest three peaks by amplitude in each condition) that described the vibration signals were extracted for each spectrum. In each condition, 30 signals were recorded to have 150 indicator vectors, divided into two sets. Twelve trees were built on the base of numeric attributes, Decision-Stump, FT, J48, J48graft, LADTree, LMT, NBTree, RandomForest, RandomTree, REPTree, and SimpleCart. Genetic algorithms optimized the finding of the best choice representative tree. The RandomForest Tree is preconized for establishing a diagnostic tool for the studied industrial Fan. In [110], the authors emphasize the problem of finding out good features that discriminate the different fault conditions of the bearing. The selection of good features is an important phase in pattern recognition and requires detailed domain knowledge. Their paper illustrated the use of a Decision Tree that identifies the best features from a given set of samples for the purpose of classification. It uses Proximal Support Vector Machine (PSVM), which has the capability to efficiently classify the faults using statistical features. The criterion used to identify the best feature invokes the concepts of entropy reduction and information gain that are used in Decision Tree. The vibration signal from a piezoelectric transducer is captured for the following conditions: good bearing, bearing with inner race fault, bearing with outer race fault, and inner and outer race fault. The statistical features are extracted using decision tree and classified successfully using PSVM and SVM. In [111], the authors used Decision Tree combined with Bayesian network for fault diagnosis of motor faults. This paper describes the model structure and the basic ideas of Decision Tree and Bayesian network, combines the advantages of the two, and solves the uncertainty of diagnosis information effectively.

4.5. Logistic Regression

In binary classification, logistic regression analysis performs exceptionally well, particularly with categorical variables with [0, 1] classes. Based on the values of predictor variables, either categorical or numerical, logistic regression models can estimate the likelihood of a failure occurrence [112]. In logistic regression, the dependent variable has a Bernoulli distribution. Thus, for any given linear combination of independent variables, an unknown probability, P, of the response variable is estimated. To do so, a link function must be used to link the independent variables to Bernoulli's distribution, with the natural log of the odds ratio or the logit acting as the link function. This function converts a linear combination of explanatory variables to Bernoulli's probability distribution, which has a domain of 0 to 1.

Logistic regression is a supervised learning technique often used in failure predictions and preventive maintenance strategies. Cost data, failure data, sensor data and acoustic electric signals were the input data used in logistic regression in previous work. The algorithm was used to predict economic success, RPN, machine state in the next 24 h given the current state and equipment reliability.

In [113], the authors used logistic regression models based on cost to accurately predict economic success or failure using the fleet data for 378 single axle dump trucks. In [114],

the authors proposed a systematic approach for developing a standard equation for the risk priority number (RPN) measure, using the methodology of interval number-based logistic regression. The aim is to reduce risks of failure, using FMEA in terms of the risk priority number (RPN). The logistic regression model helped identify the probability of risk of failure of high-capacity submersible pumps. Another study aimed to propose a model for predicting mechanical equipment failure from various sensor data collected in the manufacturing process. This study constructed a Hadoop-based big data platform to distribute many datasets for research, and performed logistic regression modelling to predict the main variables causing the failure from various collected variables. As a result of the study, the main variables in the manufacturing process that cause equipment failure were derived from the collected sensor data, and the fitness and performance evaluations for the prediction model were made using the ROC curve [115]. In [116], the authors applied logistic regression to predict machine state 24 h in the future, given the current machine state. A confusion matrix was used to evaluate model performance. In [117], the authors used logistic regression models and acoustic emissions (AE) to evaluate the reliability of the cutting tool to determine best maintenance practice. As it is difficult to monitor cutting forces in practice, a combination of both AE and logistic models are effective in reliability analysis. Reliability models are constructed using AE signals and cutting force as parameters. The results show that AE feature extractions and logistic models work effectively in reliability estimations.

4.6. K-Means Algorithm

K-Means clustering is an unsupervised learning approach that is used in machine learning to handle clustering problems. It divides the unlabeled data into many clusters. The K-Means clustering method is easy and accurate, flexible to handle large data, has a good speed of convergence, and has adaptability to sparse data. K-Means clusters the data into different groups and provides a simple technique to determine the categories of groups in an unlabeled dataset without any training. It is a centroid-based approach, where each cluster has its own centroid. The goal of this algorithm is to minimize the sum of distances between the data point and their corresponding clusters. The K-means clustering algorithm finds the best value for K center points or centroids by an iterative process and assigns each data point to its closest K-center. Those points which are near to the K-center create a cluster. The distance of the point from the centroid in each step is calculated using Euclidean method. Hence data points from each cluster are similar in some way and are far from other clusters. The K value is user defined for the algorithm that is generated. The Elbow method is the most popular way that helps in selecting the optimal K value. The method is based on minimizing within cluster sum of square values (WCSS) that defines total variation in the data [118].

In [119], the authors have tried to implement a clustering method to group maintainable equipment based on their need for maintenance according to time to failure, and the location of these machines. The main aim was to reduce scheduling process and time and a standard maintenance procedure for the machines in each cell. In [120], the authors examined the condition-based equipment data using a data analytics approach to develop a predictive maintenance program. K-means for clustering the failure characteristic, support vector regression (SVR) model used for predicting equipment failure were the two models used in their study.

4.7. The Neural Network ANN

The neural network (NN) plays a vital part in the human brain, and ANN is an unsupervised learning technique created from biology. ANN stands for artificial neural networks, and biological neurons inspired it. It is a massively parallel computing system made up of many basic processors connected by a large number of interconnections. ANNs learn the basic rules from a series of given symbolic circumstances in instances rather than

following a set of laws specified by human experts. They are organized into three layers (i.e., input layer, several hidden layers, and an output layer).

Furthermore, the relationships between the network processing units are the source of the ANNs' analytical activity. ANNs are the most extensively used machine learning algorithms. Multilayer perceptrons (MLPs) with backpropagation learning are based on a supervised technique and have three layers: input, hidden, and output [121,122]. Compared to other classic machine learning techniques, ANN models have significant advantages in dealing with random, fuzzy, and nonlinear data. ANNs are best suited for systems with a complicated, large-scale structure and ambiguous data. They are commonly employed for a wide range of issues [123,124]. ANNs do, however, also have some drawbacks. As a hardware-dependent algorithm, ANN requires GPU for processing and to create them in the first place. ANN requires a large amount of training data to build the appropriate algorithm. When using the sigmoid activation function, ANN algorithms frequently encounter vanishing and expanding gradient difficulties and the challenge remains in finding the loss function. The algorithms of ANN are black boxes in nature, where results are based on the experience of training data and not a specified program, making it difficult for modification and explanation to business stakeholders. Despite the shortcomings of ANN, neural networks are gaining wide popularity in the mining industry and researchers are mostly moving towards the use of ANN in failure analysis and predictive maintenance. The sample neural network architecture is shown in Figure 8.
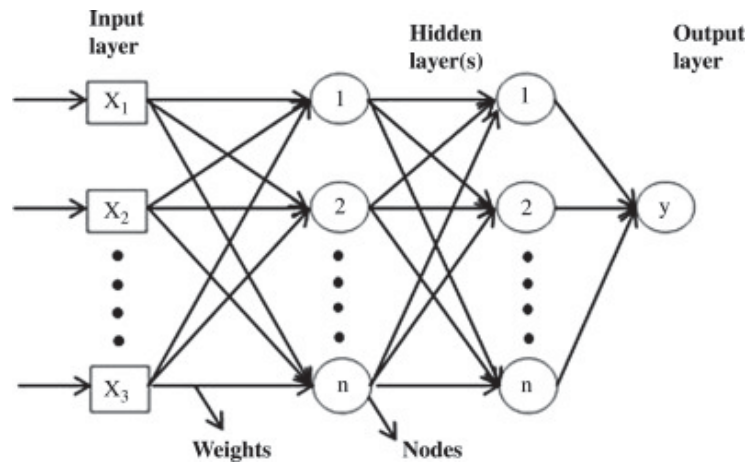
Figure 8. Sample neural network architecture [125].

ANN is widely used in reliability and fault analysis of mining machines. Several literature works can be found using ANN for analysis. ANN has been used in mining since the early 2000s. However, the ANN architecture was not as developed as it is today, and only feed-forward networks were used in the algorithm. Presently, ANN is used with higher accuracy and better results in predicting equipment failures and reliability. ANN is used for fault diagnostics of numerous types of rotating machinery that use signal processing techniques to extract features and further input these to the ANN model to classify faults [126–129]. In [130] the authors studied electric motor faults with ANN feedforward networks and self-organizing maps. Data was taken from stator current and mechanical vibration signals for major motor faults. The study showed the effectiveness of both algorithms and feedforward networks looked more promising for electric motor analysis. In [131], the authors used multilayer perceptrons (MLP) in ANN to classify dragline faults using two years failure data. There were 16 causes in total that lead to dragline failure. Two different models for analysis of these faults, using seven causes, seven symptoms and five fault parameters of drag systems have been developed. The prediction

accuracy of symptoms using the cause was 94.2% and that of fault using symptom was 97.1%. In [124], the authors demonstrated on how neural networks can be used in vibration monitoring analysis of rolling element bearing and derived how it can be effective in handling noisy data. In [132], presented a multi-state algorithm for dynamic condition monitoring of a gear. The algorithm information referred to the gear status and estimated the mesh stiffness per shaft revolution in case that any abnormality is detected. This network was fed with statistical parameters obtained from the wavelet coefficients derived for the most sensitive levels of decomposition to damage; the output resulted in the drop in the averaged torsional meshing stiffness when a failure appears, which is highly related to local failure. In [123], the authors proposed a rotor vibration fault diagnosis approach, that transforms multiple vibration signals into symmetrized dot pattern (SDP) images, and then identifies the SDP graphical feature characteristic of different vibration states using a convolutional neural network (CNN). A CNN can reliably and accurately identify vibration faults by extracting the feature information of SDP images adaptively through deep learning. The proposed approach was tested experimentally using a rotor vibration test bed, and the results obtained were compared to those obtained with an equivalent CNN-based image recognition approach using orbit plot images. The rotor fault diagnosis precision was improved from 92% to 96.5%.

5. Discussions and Conclusions

Various statistical techniques have been reviewed in this literature review and are categorized based on the method of application. Based on the literature review, it can be concluded that reliability and failure analysis play a significant role in tracking and improving efficiency of machine systems and subsystems and a significant amount of work is carried out with this regard. However, the effectiveness of statistical learning is based on the amount and quality of data that can be collected. The most common data used is historical failure data (TBF/TTF, TTR, failure component) and real-time vibration data. As the volume of data increases, the complexity increases. With the advancement in the integration of big data tools, the analysis should progress more efficiently. Often, incorrect and missing data lead to lower analysis quality and accuracy, and this problem can be mitigated by leveraging automation techniques to store failure data. At present, research is more focused towards the analysis of failure data and less attention is given to the process of automation of data collection and storage. This could be one of the significant areas of improvement. As per the literature review, reliability and failures can be analyzed using a wide range of algorithms. To sum up, every algorithm has its own advantages and limitations and should be chosen based on the stated problem and data availability. Choosing a sub-optimal or unsuitable algorithm can lead to reduced benefits or even loss of time and money. The business goals should be clearly specified, and the data driven framework should be properly established before the start of problem solving and actual statistical analysis.

Graphical methods, probability distributions, NHPP models, supervised and unsupervised classification models are discussed in the analysis. Based on the literature review, probability distributions and NHPP models are widely applied techniques in reliability and maintenance analysis of mine equipment and components. In the present day, artificial neural networks are gaining more importance and several works of literature are successfully leveraging ANN. Table 1 gives a summary of the methods reviewed in the literature, data type used in different literature for the algorithms reviewed, the application of each algorithm in the existing literature and the distinction of the methods from the other algorithms reviewed.

Table 1. Different methods, f reliability analysis and failure predictions, their applications and distinction.

Method	Data Types	Applications	Method Distinction
Graphical methods	• TBF	• Plan maintenance intervals • Know system conditions • Goodness-of-fit test	Works with both complete and incomplete data
FTA	• Qualitative • Quantitative	• Assessing risk priority number • Mathematical modelling • Root cause analysis	Can work with descriptive and numerical data
Probability distributions and NHPP models	• TBF • TTF • TTR	• RCM • Equipment design plan • Identifying critical components	Data can be easily and most accurately explained
SVM	• TTF • TBF • Fault types • Vibration data	• TBF forecast • Fault pattern recognition • Reliability forecast	Can work well with small datasets
KNN	• TTF • Fault types • Condition-monitoring	• Failure mode prediction • Fault diagnosis • Real-time fault detection	Can work when sub-classes and similarities in data are unknown
Naïve Bayes	• Vibration	• Fault diagnosis • Damage degree of faults	Works on probability of previous instances
Decision Tree	• Vibration • Fault types	• Features discriminating fault conditions • Diagnosis of equipment condition • Uncertainty of fault diagnosis	Information gain and pruning properties
Logistic Regression	• Cost per fault • TTF • Sensor • AE signals • TBF	• Assess RPN • Assess economic success • Assess machine state in next 24 h • Reliability prediction	Estimate the importance of each feature in binary decision models
K-Means	• TTF • Equipment Condition • TBF	• Classification of faults based on TTF • Predictive maintenance strategy	Can work with the output variable unknown (unsupervised algorithm)
ANN	• Signal processing • Stator current • Vibration image	• Fault diagnosis • Condition monitoring • Image recognition	Deep learning

Graphical methods are the oldest and most convenient techniques that can be used in reliability analysis to get an overview of the system condition (if it has a decreasing, increasing or constant failure rate) and only time between failure (TBF) data is required for the analysis. However, the process is time consuming, and a deep dive analysis of the problem is not possible using this technique. More importantly, the plots cannot be used if the data is not independently and identically distributed (i.i.d.). Graphical methods are used from the early 1990s to date in mining. As graphical methods are the easiest to use to determine the system condition, though trivial, the method is still existent and is used along with complex algorithms for initial data exploration.

Probability distributions and NHPP models work on both i.i.d and non-i.i.d data. Probability distributions can be applied if data is not correlated and shows no trend otherwise NHPP models can be used. TBFs or TTF or TTR are the input data for the analysis. A wide range of software is available in the market to make the analysis easier. The system's reliability, subsystems at any instance, the overall reliability, failure rate, and distribution parameters can be quickly obtained within seconds. Hence, this technique is widely used in reliability estimations. Maintenance intervals can be scheduled by studying

probability graphs to maintain certain reliability levels. However, the major limitation of this method lies in not capturing parameters that influence the failures. As mining is a very complex activity, the external and internal parameters that influence equipment failure keep changing constantly from one state to other, and this has a major effect in failure analysis. As Weibull distribution commonly explains a component behavior, the future scope for improvement of this method can be the development of machine learning algorithm that can enhance the Weibull -based curve through the integration of external knowledge.

Fault trees can effectively discover the underlying cause of every failure and troubleshoot the problem from its root. Its visual presentation of failure causes makes it simpler to identify a single failure that leads to complete system failure and find the probability of the same. However, FTA's design concept can be used to demonstrate its limitations. It focuses on building a mathematical model of a complex physical condition by logically correlating events. The strategy is solely based on the analyst's judgement if all peripheral, environmental, and operating parameters aren't given. A static fault tree cannot be applied if the system functions continuously change. Dynamic fault trees can be used in such conditions and even though several fault tree extensions have been proposed, they all have a variety of shortcomings. Even when software tool help is available, many investigations involve a significant amount of manual work.

Machine learning offers a wide range of algorithms that are excellent with failure analysis and predictions. Machine learning overcomes most of the limitations of the traditional statistical reliability techniques. Machine learning can work both with i.i.d and non-i.i.d data and the algorithm can easily capture underlying trends. ML can be faster than most other methods and can be less expensive if the input data is correctly fed. It considers external and internal feature parameters which influence failures. There are a variety of ML algorithms available and can be adopted based on the business problem requirement. Advantages and shortcomings of most common algorithms are discussed below.

SVM is one of the best classification and regression algorithms for failure analysis. It can generally categorize failure data very well into different groups with high classification accuracy. From the literature review, it can be seen that SVM is mainly used for fault pattern recognitions and predicting future failures. SVM can excellently deal with high dimension features, doesn't suffer from overfitting and outliers generally have less influence. However, SVM is not suitable for large data sets and data that has more noise. SVM was mostly used in combination with another pre-processing algorithm (genetic algorithms, principal component analysis) in the reviewed literature. Naïve Bayes and the ANN algorithm are replacing other classification models due to their high learning and prediction accuracy in mining.

K-NN is the easiest algorithm to implement and makes no assumptions about the underlying data. K-NN is used both for failure and real time monitoring data. K-NN presented high accuracy with failure data in the literature reviewed. However, the accuracy of data is susceptible to the quality of data. Overfitting is one of the major problems of K-NN and to eliminate this possibility K-NN was used with other algorithms like the genetic algorithm. KNN also does not work well with high dimensional data and needs feature scaling.

The Naïve Bayes algorithm is characterized by the explicit underlying probability model. Naïve Bayes was mainly applied in the bearing fault predictions that use vibration data. Naïve Bayes along with a forward feature selection method, provided excellent accuracy when data had incomplete information about failure mode. It can be used very well to analyze failure data where the predictors are independent of each other. The disadvantage of the method is the assumption of independent predictors, which might not actually be true and has a need of prior probability.

Decision trees need little data preparation and are used for constructing classification systems based on multiple parameters or generating prediction algorithms for a target variable. Decision trees in reliability and failure analysis are mainly used to identify important features influencing target variable. SVM, KNN and Naïve Bayes are used along

with decision trees to classify faults. The pruning method used in decision tree is one of the best techniques to accurately select parameters for classification models. Decision trees are very easy to understand and are able to handle multi-output problems. The major limitation of a decision tree is the time taken to process the algorithm and can be unstable due to small variations in data. Decision trees are piecewise constant approximations making it difficult to predict future faults. Decision trees were previously used in fault diagnosis of mining equipment. However, with the improvements of decision tree algorithms, new methods like random forest, or xgboost, have replaced the traditional decision tree algorithm.

Logistic regression performs well with failure classifications. They are mainly used in binary decision models and to estimate the importance of each feature. Logistic regression can be easily used for linearly separable data with a low dimensional dataset. Overfitting is the problem of high dimensional data. K-means models were mainly used to categorize data into groups, in order to plan a preventive maintenance strategy for each group. K-Means can also be to separate data into different fault classes and each of these classes can be an input parameter for a training dataset of SVM or KNN classification. K-Means is very easy to implement and computationally faster. But it is difficult to predict the value of K and it can have a strong impact on the final results. Rescaling data may result in completely different outputs.

ANN mimics the human brain structure to enable the model to approximate a complex non-linear function with multi-input and multi-output. As seen, ANN has a very high classification accuracy and a diverse use. It can very easily deal with complex non-linear functions. ANN is used in both failure and real time monitoring vibration data. As most other models, ANN is also prone to overfitting problems and there is an unexplained functioning of networks. There is no physical meaning to the training data of faults. ANN requires a large amount of training data and with the sigmoid activation function, ANN algorithms frequently encounter vanishing and expanding gradient problems. With the amount of quality data increasing in the mining industry, the scope for future applications of deep learning is massive. Equipment fault detection using image recognition, incorporating rule-based knowledge to implement logical procedures and formalizing knowledge on the algorithm of fault detection or equipment reliability can be few areas of exploration in future.

Overall, machine learning is a powerful tool in reliability and fault analysis. Although classifiers have presented excellent accuracy, they are required to be trained with complete data of all faults. Most of the literature reviewed uses single training set data and a single prediction method to carry out predictions which may not provide the best results. Multiple methods can be applied for a comprehensive understanding of data. Ensemble models can be created to predict outcome either by using different training datasets or by using different training models. Cross validations like K-fold cross validation techniques can also be employed to improve accuracy of the model and reduce the chance of randomness and overfitting. With the development of AI techniques and the rise of deep learning, intelligent diagnosis is going to be the future direction of fault diagnosis development. On the other hand, in the future diagnostic systems, not only data-driven AI methods, but also the consideration of failure mechanism and prior knowledge should be utilized and integrated closely to improve diagnostic performance. Statistical techniques like graphical methods and probability distributions can be used when there is no information on failure conditions and to get an overview of system conditions. Machine learning and deep learning algorithms can be employed where there is enough information for analysis. Combination of different techniques together might help in better analysis of reliability and faults. At present, fault diagnostic systems are mostly built as the combination of individual parts, such as data collection, feature extraction and dimensionality reduction, fault recognition, with little consideration of the whole diagnostic system. A complete end-to-end integrated and automated diagnostic system should be paid more attention.

References

1. Dhillon, B.S. *Mining Equipment Reliability, Maintainability, and Safety*; Springer: London, UK, 2008.
2. Carlo, F.D. *Reliability and Maintainability in Operations Management*; Massimiliano, S., Ed.; InTech: London, UK, 2013.
3. Mencik, J. Reliability of Systems. In *Concise Reliability for Engineers*; Mencik, J., Ed.; InTech: London, UK, 2016; p. 214.
4. Kumar, U.; Klefsjo, B. Reliability analysis of hydraulic systems of LHD machines using the power law process model. *Reliab. Eng. Syst. Saf.* **1992**, *35*, 217–224. [CrossRef]
5. Troy, D. The Importance of Efficient Mining Equipment. Available online: https://industrytoday.com/importance-efficient-mining-equipment/ (accessed on 12 February 2018).
6. Amy, H. What Is Equipment Reliability and How Do You Improve It? Available online: https://nonstopreliability.com/equipment-reliability/ (accessed on 15 October 2020).
7. Blischke, W.; Murthy, D. *Case Studies in Reliability and Maintenance*; Wiley: Hoboken, NJ, USA, 2003.
8. Kobbacy, K.; Murthy, D. *Complex Systems Maintenance Handbook*; Springer: London, UK, 2008; pp. 417–436.
9. Christiansen, B. Exploring Biggest Maintenance Challenges in the Mining Industry. Available online: https://www.mining.com/web/exploring-biggest-maintenance-challenges-mining-industry/#:~{}:text=Mining%20equipment%20maintenance%20is%20so,equipment%20maintenance%20and%20repair%20alone.&text=Deploying%20such%20technology%20in%20maintenance,can%20significant (accessed on 30 July 2018).
10. Norris, G. The True Cost of Unplanned Equipment Downtime. Available online: https://www.forconstructionpros.com/equipment-management/article/21104195/the-true-cost-of-unplanned-equipment-downtime (accessed on 3 December 2019).
11. Kumar, U. Reliability Analysis of Load-Haul-Dump Machines. Ph.D. Thesis, Lulea tekniska universitet, Lulea, Sweden, 1990.
12. Provencher, M. A Guide to Predictive Maintenance for the Smart Mine. Available online: https://www.mining.com/a-guide-to-predictive-maintenance-for-the-smart-mine/ (accessed on 16 April 2020).
13. Sellathamby, C.; Moore, B.; Slupsky, S. Increased Productivity by Condition-Based Maintenance Using Wireless Strain Measurement System. In Proceedings of the Canadian Institute of Mining (CIM) MEMO Conference, Sudbury, ON, Canada, 24–27 October 2010.
14. Coetzee, J.L. *Maintenance*; Trafford Publishing: Bloomington, IN, USA, 2004.
15. Correa, J.C.A.J.; Guzman, A.A. *Mechanical Vibrations and Condition Monitoring*; Academic Press: Cambridge, MA, USA, 2020.
16. Kendon, P. How Well Do You Understand the Key Metrics for Reliability and Maintenance? Available online: https://www.prometheusgroup.com/posts/how-well-do-you-understand-the-key-metrics-for-reliability-and-maintenance (accessed on 24 September 2019).
17. Alla, H.R.; Hall, R.; Apel, D. Performance evaluation of near real-time condition monitoring in haul trucks. *Int. J. Min. Sci. Technol.* **2020**, *30*, 909–915. [CrossRef]
18. Ambrose, D.H. *Research on Reliability of Mine Equipment: A Status Report*; Department of the Interior, Bureau of Mines: Washington, DC, USA, 1985.
19. Singh, B.P.; Tiari, S. Application of reliability and availability to underground mine transport. *J. Mines Met. Fuels (India)* **1984**, *32*, 23–30.
20. Zakharchenko, A.I.; Leusenko, Y.A. A comprehensive approach to solution of the problem of improving the quality of mine equipment. *Ugol'Ukr (Ukr. SSR)* **1980**, *7*, 16–17.
21. Viray, F.L. *Coal Mine Productivity Assessment as Influenced by Equipment Reliability and Availability*; ProQuest Dissertations Publishing: Ann Arbor, MI, USA, 1982; p. 338.
22. Dietl, W. Optimization of the structure of surface mine equipment systems. *Hebezeuge Foerdermittel* **1985**, *25*, 357–361.
23. Kumar, U.; Klefsjo, B.; Granholm, S. Reliability Investigation for a Fleet of Load Haul Dump Machines in a Swedish Mine. *Reliab. Eng. Syst. Saf.* **1989**, *26*, 341–361. [CrossRef]
24. Klefsjo, B.; Kumar, U. Goodness-of-fit tests for the power-law process based on the TTT-plot. *IEEE Trans. Reliab.* **1992**, *41*, 593–598. [CrossRef]
25. Soljacic, V.; Kosic, M. Reliability diagnostics of electronic equipment. *Measurement* **1990**, *8*, 141–144. [CrossRef]

26. Stanek, E.; Venkata, S. Mine power system reliability. *IEEE Trans. Ind. Appl.* **1988**, *24*, 827–838. [CrossRef]
27. Collins, E.W. Safety evaluation of coal mine power systems. In Proceedings of the Annual Reliability and Maintainability Symposium, Philadelphia, PA, USA, 27 January 1987; Sandia National Labs.: Albuquerque, NM, USA, 1987.
28. Samanta, B.; Sarkar, B.; Mukherjee, S.K. Reliability assessment of hydraulic shovel system using fault trees. *Min. Technol. Trans. Inst. Min. Metall. Sect. A* **2002**, *111*, 129–135. [CrossRef]
29. Barabady, J. Reliability and maintainability analysis of crushing plants in Jajarm bauxite mine of Iran. In *Annual Symposium on Reliability and Maintainability (RAMS)*; IEEE: Alexandria, VA, USA, 2005.
30. Samanta, B.; Sarkar, B.; Mukherjee, S.K. *Mineral Resources Engineering*; Imperial College Press: London, UK, 2001; pp. 219–231. [CrossRef]
31. Coetzee, J.L. The role of NHPP models in the practical analysis of maintenance failure data. *Reliab. Eng. Syst. Saf.* **1997**, *56*, 161–168. [CrossRef]
32. Roy, S.K.; Bhattacharyya, M.M.; Naikan, V.N. Maintainability and reliability analysis of a fleet of shovels. *Min. Technol. Trans. Inst. Min. Metall. Sect. A* **2001**, *110*, 163–171. [CrossRef]
33. Vagenas, N.; Runciman, N.; Clément, S.R. A methodology for maintenance analysis of mining equipment. *Int. J. Surf. Min. Reclam. Environ.* **1997**, *11*, 33–40. [CrossRef]
34. Vagenas, N.; Nuziale, T. Genetic Algorithm for reliability assessment of mining equipment. *J. Qual. Maint. Eng.* **2001**, *7*, 302–311. [CrossRef]
35. Hall, R.A.; Daneshmend, L.K. Reliability Modelling of Surface Mining Equipment: Data Gathering and Analysis Methodologies. *Int. J. Surf. Min.* **2003**, *17*, 139–155. [CrossRef]
36. Ascher, H.; Feingold, H. *Repairable Systems Reliability: Modeling, Inference, Misconceptions and Their Causes*; Marcel Dekker, Inc.: New York, NY, USA, 1984.
37. Barlow, R.E. Analysis of Retrospective Failure Data Using Computer Graphics. In Proceedings of the Annual Reliability and Maintainability Symposium, Los Angeles, CA, USA, 17–19 January 1978.
38. Crow, L.H. Reliability Analysis of Complex Repairable Systems. In *Reliability and Biometry*; Proschan, F., Serfling, R.J., Eds.; SIAM: Philadelphia, PA, USA, 1974.
39. Ahmadi, S.; Hajihassani, M.; Moosazadeh, S.; Moomivand, H. An Overview of the Reliability Analysis Methods of Tunneling Equipment. *CrossMark* **2020**, *14*, 218–219. [CrossRef]
40. Klefsjo, B. TTT-plotting—A tool for both theoretical and practical problems. *J. Stat. Plan. Inference* **1991**, *29*, 99–110. [CrossRef]
41. Rao, K.R.; Prasad, P.V. Graphical methods for reliability of repairable equipment and maintenance planning. In Proceedings of the Annual Symposium on Reliability and Maintainability (RAMS), Philadelphia, PA, USA, 22–25 January 2001; pp. 123–128.
42. Kumar, R.; Vardhan, A.; Kishorilal, D.B.; Kumar, A. Reliability analysis of a hydraulic shovel used in open pit coal mines. *J. Mines Met. Fuels* **2018**, *66*, 472–477.
43. Sinha, R.S.; Mukhopadhyay, A.K. Reliability centered maintenance of cone crusher: A case study. *Int. J. Syst. Assur. Eng. Manag.* **2015**, *6*, 32–35. [CrossRef]
44. Ruijters, E.; Stoelinga, M. Fault Tree Analysis: A survey of the state-of-the-art in modeling, analysis and tools. *Comput. Sci. Rev.* **2015**, *15–16*, 29–62. [CrossRef]
45. Yong, B.; Qiang, B. *Subsea Engineering Handbook*; Gulf Professional Publishing: Oxford, UK, 2018.
46. Singh, R. *Pipeline Integrity Handbook*; Gulf Professional Publishing: Oxford, UK, 2017.
47. Gharahasanlou, A.N.; Mokhtarei, A.; Khodayarei, A.; Ataei, M. Fault tree analysis of failure cause of crushing plant and mixing bed hall at Khoy cement factory in Iran. *Case Stud. Eng. Fail. Anal.* **2014**, *2*, 33–38. [CrossRef] [PubMed]
48. Kang, J.; Sun, L.; Soares, C.G. Fault Tree Analysis of floating offshore wind turbines. *Renew. Energy* **2019**, *133*, 1455–1467. [CrossRef]
49. Tuncay, D.; Nuray, D. Reliability analysis of a dragline using fault tree analysis. *Bilimsel Madencilik Derg.* **2017**, *56*, 55–64. [CrossRef]
50. Patil, R.B.; AMhamane, D.; Kothavale, P.B.; SKothavale, B. Fault Tree Analysis: A Case Study from Machine Tool Industry. In Proceedings of the An International Conference on Tribology, TRIBOINDIA-2018, Mumbai, India, 13–15 December 2018.
51. Iyomi, E.P.; Ogunmilua, O.O.; Guimaraes, I.M. Managing the Integrity of Mine Cage Conveyance. *Int. J. Eng. Res. Technol. (IJERT)* **2021**, *10*, 743–747. [CrossRef]
52. Relkar, A.S. Risk Analysis of Equipment Failure through Failure Mode and Effect Analysis and Fault Tree Analysis. *J. Fail. Anal. Prev.* **2021**, *21*, 793–805. [CrossRef]
53. Li, S.; Yang, Z.; Tian, H.; Chen, C.; Zhu, Y.; Deng, F.; Lu, S. Failure Analysis for Hydraulic System of Heavy-Duty Machine. *Appl. Sci.* **2021**, *11*, 1249. [CrossRef]
54. Jiang, G.-J.; Li, Z.-Y.; Qiao, G.; Chen, H.-X.; Li, H.-B.; Sun, H.-H. Reliability Analysis of Dynamic Fault Tree Based on BinaryDecision Diagrams for Explosive Vehicle. *Math. Probl. Eng.* **2021**, *2021*, 5559475. [CrossRef]
55. Kabir, S. An overview of fault tree analysis and its application in model based dependability analysis. *Expert Syst. Appl.* **2017**, *77*, 114–135. [CrossRef]
56. Yin, T.; Liu, Q.; Tang, X.; Zhao, Y.; Yang, J.; Wu, M. Fault Diagnosis of Roadheader Based on Dynamic Fault Tree. In Proceedings of the 3rd International Conference on Engineering Technology and Application, Singapore, 20–21 January 2017; p. 2016.

57. Wang, W.H.; Zhang, D.K.; Cheng, G.; Shen, L.H. The Dynamic Fault Tree Analysis of Not-Cutting Failure for MG550/1220 Electrical Haulage Shearer. *Appl. Mech. Mater.* **2011**, *130–134*, 646–649. [CrossRef]
58. Geitner, F.K.; Bloch, H.P. *Practical Machinery Management for Process Plants*; Gulf Professional Publishing: Oxford, UK, 2006; Volume 5.
59. Coolen, F. Parametric probability distributions in reliability. In *Quantitative Risk Analysis and Assessment*; Melnick, E.L., Everitt, B.S., Eds.; Wiley: West Sussex, UK, 2008.
60. Zuo, X.; Yu, X.R.; Yue, Y.L.; Yin, F.; Zhu, C.L. Reliability Study of Parameter Uncertainty Based on Time-Varying Failure Rates with an Application to Subsea Oil and Gas Production Emergency Shutdown Systems. *Processes* **2021**, *9*, 2214.
61. Kumar, N.S.; Choudhary, R.P.; Murthy, C. Reliability based analysis of probability density function and failure rate of the shovel-dumper system in a surface coal mine. *Modeling Earth Syst. Environ.* **2020**, *7*, 1727–1738. [CrossRef]
62. Balaraju, J.; Raj, M.G.; Murthy, C. Estimation of reliability-based maintenance time intervals of Load-Haul Dumper in an underground coal mine. *J. Min. Environ.* **2018**, *9*, 761–771.
63. Barabady, J.; Kumar, U. Reliability analysis of mining equipment: A case study of a crushing plant at Jajarm Bauxite Mine in Iran. *Reliab. Eng. Syst. Saf.* **2008**, *93*, 647–653. [CrossRef]
64. Taherı, M.; Bazzazı, A.A. Reliability Analysis of Loader Equipment: A Case Study of a Galcheshmeh. *J. Undergr. Resour.* **2016**, 37–46. Available online: https://dergipark.org.tr/en/pub/mtb/issue/32053/354893 (accessed on 3 March 2022).
65. Bala, R.J.; Govinda, R.; Murthy, C. Reliability analysis and failure rate evaluation of load haul dump machines using Weibull. *Math. Model. Eng. Probl.* **2018**, *5*, 116–122. [CrossRef]
66. Waghmode, L.Y.; Patil, R.B. Reliability analysis and life cycle cost optimization: A case study from Indian industry. *Int. J. Qual. Reliab. Manag.* **2016**, *33*, 414–429. [CrossRef]
67. Vashistha, S.; Agrawal, A.K.; Siddiqui, M.A.; Chattopadhyaya, S. Reliability and Maintainability Analysis of LHD Loader at Saoner Mines, Nagpur, India. *IOP Conf. Ser. Mater. Sci. Eng.* **2019**, *691*, 012013. [CrossRef]
68. Rahimdel, M.J.; Ataei, M.; Khalokakaei, R.; Hoseinie, S.H. Maintenance plan for a fleet of rotary drill rigs. *Arch. Min. Sci.* **2014**, *59*, 441–453.
69. Hoseinie, S.H.; Ataei, M.; Khalokakaie, R.; Ghodrati, B.; Kumar, U. Reliability analysis of the cable system of drum shearer using the power law process model. *Int. J. Min. Reclam. Environ.* **2012**, *26*, 309–323. [CrossRef]
70. Mouli, C.; Chamarthi, S.; Chandra, G.; Kumar, V. Reliability Modeling and Performance Analysis of Dumper Systems in Mining by KME Method. *Int. J. Curr. Eng. Technol.* **2014**, 255–258. [CrossRef]
71. Roche-Carrier, N.L.; Ngoma, G.D.; Kocaefe, Y.; Erchiqui, F. Reliability analysis of underground rock bolters using the renewal process, the non-homogeneous Poisson process and the Bayesian approach. *Int. J. Qual. Reliab. Manag.* **2019**, *37*, 223–242. [CrossRef]
72. Din, I.U.; Guizani, M.; Rodrigues, J.J.; Hassan, S.; Korotaev, V.V. Machine learning in the Internet of Things: Designed techniques for smart cities. *Future Gener. Comput. Syst.* **2019**, *100*, 826–843. [CrossRef]
73. Fahad, S.K.A.; Ala, M.M. Clustering, A modified K-Means Algorithm for Big Data. *IJCSET* **2016**, *6*, 129–132.
74. Abdi, A. Three Types of Machine Learning Algorithms. 2016. Available online: https://www.researchgate.net/publication/310674228_Three_types_of_Machine_Learning_Algorithms (accessed on 3 March 2022).
75. Ayodele, T. *New Advances in Machine Learning*; InTech: London, UK, 2010.
76. Jordan, J. Evaluating a Machine Learning Model. Available online: https://www.jeremyjordan.me/evaluating-a-machine-learning-model/ (accessed on 21 July 2017).
77. Ray, S. Understanding Support Vector Machine(SVM) Algorithm from Examples. Available online: https://www.analyticsvidhya.com/blog/2017/09/understaing-support-vector-machine-example-code/ (accessed on 13 September 2017).
78. Zisserman, A. The SVM Classifier. Available online: https://www.robots.ox.ac.uk/~{}az/lectures/ml/lect2.pdf (accessed on 5 March 2022).
79. Gordon, G. Support Vector Machines and Kernel Methods. Available online: https://www.cs.cmu.edu/~{}ggordon/SVMs/new-svms-and-kernels.pdf (accessed on 15 June 2004).
80. Jakkula, V. *Tutorial on Support Vector Machine (SVM)*; Report; Washington State University: Pullman, WA, USA, 2011.
81. Duc, H.N.; Kamwa, I.; Dessaint, L.-A.; Cao-Duc, H. A Novel Approach for Early Detection of Impending Voltage Collapse Events Based on the Support Vector Machine. *Int. Trans. Electr. Energy Syst.* **2017**, *27*, e2375.
82. Hwang, S.; Jeong, J. SVM-RBM based Predictive Maintenance Scheme for IoT-enabled Smart Factory. In Proceedings of the Thirteenth International Conference on Digital Information Management, ICDIM, Berlin, Germany, 24–26 September 2018.
83. Dindarloo, S.R. Support vector machine regression analysis of LHD failures. *Int. J. Min. Reclam. Environ.* **2014**, *30*, 64–69. [CrossRef]
84. Dindarloo, S.R.; Siami-Irdemoosa, E. Data mining in mining engineering: Results of classification and clustering of shovels failures data. *Int. J. Min. Reclam. Environ.* **2016**, *31*, 105–118. [CrossRef]
85. Chang, Y.-W.; Wang, Y.-C.; Liu, T.; Wang, Z.-J. Fault diagnosis of a mine hoist using PCA and SVM techniques. *J. China Univ. Min. Technol.* **2008**, *18*, 327–331. [CrossRef]
86. Chatterjee, S.; Dash, A.; Bandopadhyay, S. Ensemble Support Vector Machine Algorithm for Reliability Estimation of a Mining Machine. *Qual. Reliab. Eng. Int.* **2014**, *31*, 1503–1516. [CrossRef]

87. Timusk, M.A.; Lipsett, M.G.; McBain, J.; Mechefske, C.K. Automated Operating Mode Classification for Online Monitoring Systems. *J. Vib. Acoust.* **2009**, *131*, 041003. [CrossRef]
88. Cheng, C.-F.; Rashidi, A.; Davenport, M.A.; Anderson, D.V. Activity analysis of construction equipment using audio signals and support vector machines. *Autom. Constr.* **2017**, *81*, 240–253. [CrossRef]
89. Harrison, O. Machine Learning Basics with the K-Nearest Neighbors Algorithm. Available online: https://towardsdatascience.com/machine-learning-basics-with-the-k-nearest-neighbors-algorithm-6a6e71d01761 (accessed on 10 September 2018).
90. Imandoust, S.B.; Bolandraftar, M. Application of K-Nearest Neighbor (KNN) Approach for Predicting Economic Events: Theoretical Background. *Int. J. Eng. Res. Appl.* **2013**, *3*, 605–610.
91. Jabbar, M.A.; Deekshatulu, B.; Chandra, P. Classification of Heart Disease Using K- Nearest Neighbor and Genetic Algorithm. *Procedia Technol.* **2013**, *10*, 85–94. [CrossRef]
92. Zhang, Z. Introduction to machine learning: K-nearest neighbors. *Ann. Transl. Med.* **2016**, *4*, 218. [CrossRef] [PubMed]
93. Vahed, A.T.; Ghodrati, B.; Hosseinie, S.H. Enhanced K-Nearest Neighbors Method Application in Case of Draglines Reliability Analysis. In Proceedings of the 27th International Symposium on Mine Planning and Equipment Selection, Santiago, Chile, 20–22 November 2018.
94. Moosavian, A.; Ahmadi, H.; Khazaee, A.T. Comparison of two classifiers; K-nearest neighbor and artificial neural network, for fault diagnosis on a main engine journal-bearing. *Shock. Vib.* **2013**, *20*, 263–272. [CrossRef]
95. Sharma, A.; Jigyasu, R.; Mathew, L.; Chatterji, S. Bearing Fault Diagnosis Using Weighted K-Nearest Neighbor. In Proceedings of the 2nd International Conference on Trends in Electronics and Informatics (ICOEI 2018), Tirunelveli, India, 11–12 May 2018.
96. Pandya, D.; Upadhyay, S.; Harsha, S. Fault diagnosis of rolling element bearing with intrinsic mode function of acoustic emission data using APF-KNN. *Expert Syst. Appl.* **2013**, *40*, 4137–4145. [CrossRef]
97. Wang, H.; Yu, Z.; Guo, L. Real-time Online Fault Diagnosis of Rolling Bearings Based on KNN Algorithm. *J. Phys. Conf. Ser.* **2020**, *1486*, 032019. [CrossRef]
98. Zhang, N.; Wu, L.; Wang, Z.; Guan, Y. Bearing Remaining Useful Life Prediction Based on Naive Bayes and Weibull Distributions. *Entropy* **2018**, *20*, 944. [CrossRef]
99. Saritas, M.M.; Yasar, A. Performance Analysis of ANN and Naive Bayes Classification Algorithm for Data Classification. *Int. J. Ofintelligent Syst. Appl. Eng.* **2019**, *7*, 88–91. [CrossRef]
100. Gandhi, R. Naive Bayes Classifier. Available online: https://towardsdatascience.com/naive-bayes-classifier-81d512f50a7c (accessed on 5 May 2018).
101. Prabhakaran, S. How Naive Bayes Algorithm Works? (with Example and Full Code). Available online: https://www.machinelearningplus.com/predictive-modeling/how-naive-bayes-algorithm-works-with-example-and-full-code/ (accessed on 4 November 2018).
102. Zhang, N.; Wu, L.; Yang, J.; Guan, Y. Naive Bayes Bearing Fault Diagnosis Based on Enhanced Independence of Data. *Sensors* **2018**, *18*, 463. [CrossRef]
103. Moghaddass, R.; Zuo, M.J. Fault Diagnosis for Multi-State Equipment with Multiple Failure. In Proceedings of the 2012 Proceedings Annual Reliability and Maintainability Symposium, IEEE, Reno, NV, USA, 23–26 January 2012.
104. Yi, X.J.; Chen, Y.F.; Hou, P. Fault diagnosis of rolling element bearing using Naïve Bayes classifier. *Vibroengineering Procedia* **2017**, *14*, 64–69.
105. Lu, Y. Decision tree methods: Applications for classification and prediction. *Shanghai Arch. Psychiatry* **2015**, *27*, 130.
106. Rokach, L.; Maimon, O. *Data Mining With Decision Trees*, 2nd ed.; World Scientific Publishing Co. Pte. Ltd.: Singapore, 2015.
107. Du, C.-J.; Sun, D.-W. (Eds.) Object Classification Methods. In *Computer Vision Technology for Food Quality Evaluation*; Elsevier Inc.: Amsterdam, The Netherlands; Academic Press: Cambridge, MA, USA, 2008; pp. 57–80.
108. Kohli, M. Predicting Equipment Failure On SAP ERP Application Using Machine Learning Algorithms. *Int. J. Eng. Technol.* **2021**, *7*, 306. [CrossRef]
109. Karabadji, N.E.; Seridi, H.; Khelf, I.; Laouar, L. Decision Tree Selection in an Industrial Machine Fault Diagnostics. In Proceedings of the International Conference on Model and Data Engineering, Poitiers, France, 3–5 October 2012; Springer: Berlin/Heidelberg, Germany, 2012; pp. 129–140.
110. Sugumaran, V.; Muralidharan, V.; Ramachandran, K. Feature selection using Decision Tree and classification through Proximal Support Vector Machine for fault diagnostics of roller bearing. *Mech. Syst. Signal Process.* **2007**, *21*, 930–942. [CrossRef]
111. Gong, Y.-S.; Li, Y. Motor Fault Diagnosis Based on Decision Tree-Bayesian Network Model. In *Advances in Electronic Commerce, Web Application and Communication*; Jin, D., Lin, S., Eds.; Springer: Warsaw, Poland, 2012; pp. 165–170.
112. Kleinbaum, D.G.; Klein, M. *Logistic Regression*, 2nd ed.; Springer: New York, NY, USA, 2002.
113. Hildreth, J.; Dewitt, S. Logistic Regression for Early Warning of Economic Failure. In Proceedings of the 52nd ASC Annual International Conference Proceedings, Provo, UT, USA, 13–16 April 2016.
114. Bhattacharjee, P.; Dey, V.; Mandal, U.K. Risk assessment by failure mode and effects analysis (FMEA) using an interval number based logistic regression model. *Saf. Sci.* **2020**, *132*, 104967. [CrossRef]
115. Ku, J.-H. A Study on Prediction Model of Equipment Failure Through Analysis of Big Data Based on RHadoop. *Wirel. Pers. Commun.* **2018**, *98*, 3163–3176. [CrossRef]

116. Battifarano, M.; DeSmet, D.; Madabhushi, A.; Nabar, P. Predicting Future Machine Failure from Machine State Using Logistic Regression. Available online: https://www.researchgate.net/publication/324584543_Predicting_Future_Machine_Failure_from_Machine_State_Using_Logistic_Regression (accessed on 2 April 2022).
117. Li, H.; Wang, Y.; Zhao, P.; Zhang, X.; Zhou, P. Cutting tool operational reliability prediction based on acoustic emission and logistic regression model. *J. Intell. Manuf.* **2015**, *26*, 923–931. [CrossRef]
118. Na, S.; Xumin, L.; Yong, G. Research on k-means Clustering Algorithm: An Improved k-means Clustering Algorithm. In Proceedings of the 2010 Third International Symposium on Intelligent Information Technology and Security Informatics, Jinggangshan, China, 2–4 April 2010; pp. 63–67.
119. Abdelhadi, A. Heuristic Approach to schedule preventive maintenance operations using K-Means methodology. *Int. J. Mech. Eng. Technol.* **2017**, *8*, 300–307.
120. Riantama, R.N.; Prasanto, A.D.; Kurniati, N.; Anggrahini, D. Examining Equipment Condition Monitoring for Predictive Maintenance, A case of typical Process Industry. In Proceedings of the 5th NA International Conference on Industrial Engineering and Operations Management, Detroit, MI, USA, 10–14 August 2020.
121. Park, Y.S.; Lek, S. Ecological Model Types. In *Developments in Environmental Modelling*; Jørgensen, S.E., Ed.; Elsevier Ltd.: Amsterdam, The Netherlands, 2016; Volume 28, pp. 1–26.
122. Walczak, S.; Cerpa, N. Artificial Neural Networks. In *Encyclopedia of Physical Science and Technology*, 3rd ed.; Meyers, R.A., Ed.; Academic Press: Cambridge, MA, USA, 2001; pp. 609–629.
123. Zhu, X.; Hou, D.; Zhou, P.; Han, Z.; Yuan, Y.; Zhou, W.; Yin, Q. Rotor fault diagnosis using a convolutional neural network with symmetrized dot pattern images. *Measurement* **2019**, *138*, 526–535. [CrossRef]
124. Alguindigue, I.E.; Loskiewicz-Buczak, A.; Uhrig, R. Monitoring and diagnosis of rolling element bearings using artificial neural networks. *IEEE Trans. Ind. Electron.* **1993**, *40*, 209–217. [CrossRef]
125. Sairamya, N.J.; Susmitha, L.; George, S.T.; Subathra, M.S.P. Hybrid Approach for Classification of Electroencephalographic Signals Using Time–Frequency Images with Wavelets and Texture Features. In *Intelligent Data Analysis for Biomedical Applications*; Academic Press: Cambridge, MA, USA, 2019; pp. 253–273.
126. Jia, F.; Lei, Y.; Lin, J.; Zhou, X.; Lu, N. Deep neural networks: A promising tool for fault characteristic mining and intelligent diagnosis of rotating machinery with massive data. *Mech. Syst. Signal Process.* **2016**, *72–73*, 303–315. [CrossRef]
127. Jonathan, P.; Peck, J.B. On-line condition monitoring of rotating equipment using neural networks. *ISA Trans.* **1994**, *33*, 159–164.
128. Liu, R.; Yang, B.; Zio, E.; Chen, X. Artificial intelligence for fault diagnosis of rotating machinery: A review. *Mech. Syst. Signal Process.* **2018**, *108*, 33–47. [CrossRef]
129. Bin, G.; Bin, G.; Gao, J.; Li, X.J.; Dhillon, B. Early fault diagnosis of rotating machinery based on wavelet packets—Empirical mode decomposition feature extraction and neural network. *Mech. Syst. Signal Process.* **2012**, *27*, 696–711. [CrossRef]
130. Li, L.; Mechefske, C.K.; Li, W. Electric motor faults diagnosis using artificial neural networks. Insight Non-Destr. *Test. Cond. Monit.* **2004**, *46*, 616–621.
131. Sahu, A.R.; Palei, S.K. Fault prediction of drag system using artificial neural network for prevention of dragline failure. *Eng. Fail. Anal.* **2020**, *113*, 104542. [CrossRef]
132. Sanz, J.; Perera, R.; Huerta, C. Gear dynamics monitoring using discrete wavelet transformation and multi-layer perceptron neural networks. *Appl. Soft Comput.* **2012**, *12*, 2867–2878. [CrossRef]

Article

Automatic Determination of Rock-Breaking Target Poses for Impact Hammers

Daniel Cárdenas [1], Isao Parra-Tsunekawa [1], Francisco Leiva [1] and Javier Ruiz-del-Solar [1,2,*]

[1]   Advanced Mining Technology Center (AMTC), Universidad de Chile, Santiago 8370451, Chile
[2]   Department of Electrical Engineering, Universidad de Chile, Santiago 8370451, Chile
*   Correspondence: jruizd@ing.uchile.cl

Abstract: This paper describes a system for the automatic determination of rock-breaking target poses for impact hammers used in underground mines. The rock-breaking target pose is defined as the position and angle at which the impact hammer must strike a rock in order to break it. The automatic determination of this pose is essential for the autonomous operation of an impact hammer. The proposed system takes as input sensor data composed of point clouds and images, and automatically determines a rock-breaking target pose. The system consists of a *rock segmentation subsystem* that receives the sensor data and identifies and individualizes the rocks/boulders present above the grizzly, and a *rock-breaking target pose generation and evaluation subsystem* that receives the rock information produced by the rock segmentation subsystem, and generates a list of rock-breaking target pose candidates, it evaluates them, and it selects the best candidate as the rock-breaking target pose. The system is evaluated using real data. The reported experiments show the system's capability to generate appropriate target poses.

Keywords: impact hammers; industrial robotics; autonomous mining; underground mining

1. Introduction

Mining operations are progressively moving towards using autonomous and/or tele-operated equipment, because this improves their safety, productivity and reliability. This is especially important in underground mining, where workers are exposed to risks such as rock falls, mud rushes and continued exposure to dust [1]. All these hazards have been steadily increasing as underground mining operations go deeper, geo-mechanical conditions become more extreme and the time to enter and leave the mines becomes longer [2]. Consequently, great effort has been invested in improving the automation level of underground mining machines, especially those that operate in high-risk areas [1], such as load–haul–dump (LHD) machines, also known as scoop trams; and impact hammers, also known as rock breakers, rock-breaking manipulators, rock-breaking hammers or pedestal-mounted breaker booms [3].

Impact hammers are used to break rocks that are too large to pass through the steel grates, called grizzlies, placed on top of ore passes, which are vertical tunnels connecting different production levels. Thus, the material loaded and transported by the LHDs is dumped onto the grizzlies and fragmented, when needed, by impact hammers (see Figure 1).

In modern underground mines, impact hammers are usually tele-operated from a control room located in a safe place, often several kilometers away from the operation area. The tele-operation of the hammers is a complex task which requires skilled operators, not only because they must control these hammers effectively, but because they must do so by relying on visual information provided by cameras: there is latency produced by encoding, transmitting and decoding this information; there is often poor visibility of the environment (mainly because of the presence of dust and poor illumination); and

the visualization interfaces that are commonly available to the operators fail to properly characterize the 3D nature of the environment.

Figure 1. Interaction between an LHD dumping material onto the grizzly, and a hydraulic impact hammer. When the LHD is approaching the grizzly, the impact hammer moves to a safe position.

In order to improve this situation, assistive tele-operation systems for impact hammers (e.g., [3]) and autonomous control systems for impact hammers (e.g., [4]), are under development. A common problem to be solved in both kinds of applications is the automatic determination of the position where the hammer must impact the rock, and the angle of such an impact. In other words, it is essential to be able to automatically determine the so-called *rock-breaking target pose*, either for the autonomous operation of the hammer, or to provide this information to the operator. To the best of our knowledge, this problem has not been addressed properly in most of the literature [3,5–8]. In [4] a simple rock-breaking target pose methodology is proposed, but it does not take into account the orientation of the end-effector with respect to the rock surface or the shape of the rock, obtaining sub-optimal results in the proof-of-concept test when attempting to break the rocks.

Thus, the main goal of this paper is to describe a system for the automatic determination of rock-breaking target poses for impact hammers. The system takes as input sensor data composed of images and point clouds, and automatically determines a rock-breaking target pose. The system is composed of a *rock segmentation subsystem* that receives the sensor data and identifies and individualizes the rocks/boulders present above the grizzly, and a *rock-breaking target pose generation and evaluation subsystem* that receives the rock information produced by the rock segmentation subsystem, and generates a list of rock-breaking target pose candidates. It evaluates them and it selects the best candidate. The system is evaluated using real data.

To the best of our knowledge, autonomous impact hammers are not commercially openly available, so this work improves the state of the art in this topic by providing the following main contributions:

- The design of algorithms for generating rock-breaking target poses and assessing them, which are based on the way this task is performed by human operators in mining sites. This information was obtained from good practice manuals and from interviews with operators.
- A rock segmentation procedure that is the result of merging the segmentation obtained by processing the point-cloud data and the detection of rocks obtained by image processing techniques.
- The adaptation of image processing techniques used for image segmentation (e.g., flooding or watershed) to segment point-cloud data.
- Incorporating to the end-effector's target pose a criterion of a range of contact angles in which the hammer and the rock minimize the slippage due to impact.

This paper is organized as follows: In Section 2, the proposed system for determining the rock-breaking target pose is described. In Section 3, the results obtained when evaluating the system using both simulated and real data, are presented. In Section 4, we analyze the obtained results. In Section 5 the conclusions derived from this work are drawn. Finally, in Section 6 a patent derived from this work is mentioned.

2. Proposed System for Determining the Rock-Breaking Target Pose for Impact Hammers

2.1. General System Description

The proposed system implements a method that, based on sensor data composed of point clouds and images, automatically determines a rock-breaking target pose for an impact hammer, so that it can fragment oversized rocks within a pile of material. This system consists of two subsystems: a subsystem that performs rock segmentation, and a subsystem that generates and evaluates rock-breaking target poses. The rock segmentation subsystem receives sensor data (point clouds and images) and identifies and individualizes the rocks present above the grizzly. The rock-breaking target pose generation and evaluation subsystem receives sensor data and the rock's identification produced by the rock segmentation subsystem, and generates a list of rock-breaking target pose candidates, which are then evaluated to finally deliver the best candidate. Both subsystems may operate permanently and continuously, i.e., they are suited for constantly analyzing the environment, and determining the next rock-breaking target pose for the hammer.

Both subsystems are composed of several components, each of them performing different tasks. The overall system may be depicted by the diagram displayed in Figure 2. In this section each of these modules and their interactions are going to be described in detail.
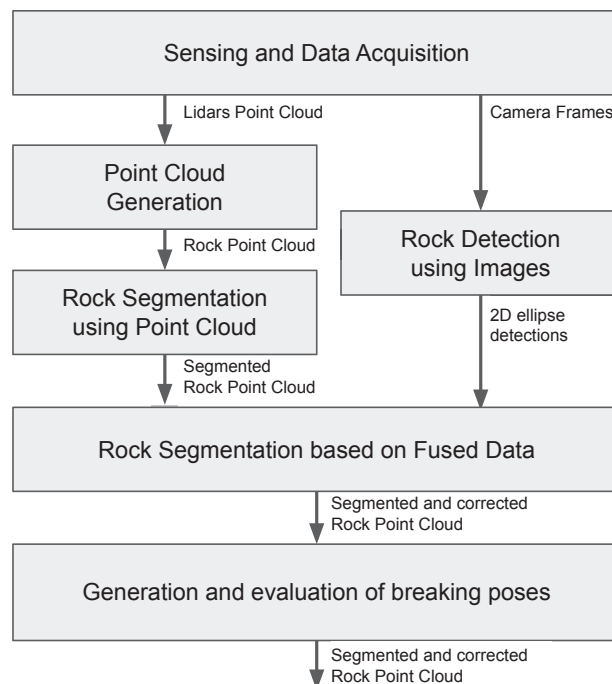
Figure 2. Block diagram of rock segmentation subsystem.

2.2. Rock Segmentation Subsystem

As mentioned above, the rock segmentation subsystem receives sensor data (point clouds and images), and through a series of logical and mathematical operations identifies and individualizes the rocks/boulders above the grizzly. This subsystem consists of the following modules: *Sensing and Data Acquisition*; *Point Cloud Generation*; *Rock Segmentation*

using Point Clouds; *Rock Detection using Images*; and *Rock Segmentation based on Fused Data* (see Figure 2).

2.2.1. Sensing and Data Acquisition

To determine the rock-breaking target poses, it is necessary to generate a representation in which each rock in a given rock pile is properly individualized. This individualization, referred to as instance segmentation, should provide a three-dimensional representation of the rocks, which would allow the hammer to strike them. To achieve this goal, 3D points and images are captured by sensors, allowing the generation of a 3D model of the workspace, as well as a characterization of the colors and textures present in the environment. Although the system may work with different range sensors and cameras, the current implementation uses two 3D LIDAR sensors (laser scanners), and two visible spectrum cameras.

The sensors must be properly positioned to capture a large percentage of the grizzly and the material above it. The data from these sensors are processed by an industrial computer, which performs the various operations required to implement the rock segmentation and rock-breaking target pose determination subsystems.

2.2.2. Point Cloud Generation

The raw captured point cloud contains points corresponding to the material on the ore pass, the impact hammer and the mine infrastructure. For this reason, the first stage of the segmentation process consists of eliminating the captured points associated to the mine infrastructure and the impact hammer, so a point cloud containing only data of the material above the ore pass's grizzly is obtained. To achieve this, a bounding box representing the working volume is defined, which allows eliminating all the points outside of it. Then, the points belonging to the impact hammer are eliminated using a model that represents its simplified geometry given its current configuration. This model is obtained using geometric primitives which, along with the measurements of the arm encoders, represent, approximately, the physical space that the impact hammer is currently using.

Then, the points that belong to the mine infrastructure (such as the floor, the grizzly, railings, and other adjacent structures) are eliminated using a previously constructed environment model. This model corresponds to a voxel representation of the empty grizzly and its surroundings (although, already limited by the workspace bounding box used to filter points). The environment model is generated prior to system operation and ensuring that the grill is free of material. This generation process starts by removing points that are outside the working volume, then the remaining points are integrated and merged into a single point cloud. Next, outlier points are removed using a predefined cluster filtering process [9]. Finally, this point cloud is stored for use in the operation. Using this model, it is possible to classify the points that correspond to the mine infrastructure as those points located within the voxels of the constructed model.

The points that belong to the constructed environment model are then separated from the rest of the point cloud. The remaining points are combined to represent in a unique and simplified way the information provided by the LIDARs. To achieve this, the measurements obtained from the LIDARs are temporally integrated using a time window of 1 s. This not only makes the obtained point cloud of the environment denser, but also allows filtering spurious measurements.

Finally, the resolution of the data is reduced to allow faster processing. To accomplish this, the data are subsampled using voxels, where the spatial locations of all the points contained within a given voxel, $p_1, p_2, ..., p_k$, are represented by a single centroid point, c_P. These centroids are defined by Equation (1), that is, their coordinates are the average coordinates of the points contained inside their corresponding voxel.

$$c_P = \frac{1}{k} \sum_{i=1}^{k} p_i \tag{1}$$

The result of applying all the steps described in this section is a point cloud containing a representation of the material above the grizzly.

2.2.3. Rock Segmentation Using Point Clouds

In order to segment each rock in the point cloud, a version of the *watershed* method adapted to point clouds defining a surface is applied (see details in [10]). This new version of the method allows applying the concept of "descent" and initial labeling on a point cloud, and performing a surface analysis without having to convert this point cloud to a polygon mesh, which is the way these types of methods are often applied (e.g., [11,12]). In general, using surface processing with polygonal meshes is convenient when an object is well defined, and it is required to generate a 3D visualization of it. Since in this case the information obtained from the surface is more relevant than the visualization itself, it is more convenient to use the point cloud directly, which is what the proposed method does. Furthermore, by not requiring a polygon mesh and directly processing a point cloud, this method avoids the construction of additional data structures, which could increase its processing cost.

In the proposed method, an initial labeling is performed by first identifying the convex surface points that are most similar to rocks. These points are called seeds. To obtain these seeds, it is first necessary to obtain the normal vector associated to each point. To obtain these normal vectors, a plane at the location of each point is estimated using the least squares algorithm.

Then, the so-called "height value" of each point is calculated, which determines what the initial labels will be, and how these labels will be propagated. The "height value" is determined by a height function. In traditional watershed segmentation algorithms, the Z-axis value or the surface curvature is usually used to segment point clouds. In our case, the height function is defined using the deviation between the normal component of the plane at the location of a given point, and a desired orientation. We are interested in finding the points whose planes have a normal component $(n_x, n_y, n_z)^\top$ that is aligned with the Z-axis direction. Given the aforementioned, the height function $H(p)$ is defined by Equation (2), that is, as the dot product between the normal of the plane (associated to a point), and the unit vector $\vec{r} = (0, 0, 1)^\top$.

$$H(p) = \vec{r} \cdot (n_x, n_y, n_z)^\top \tag{2}$$

With this function, a higher height value is assigned to points that belong to flattened geometric "peaks" in the point cloud. If the Z-axis were used directly, as in more commonly used height functions, the height values would be higher for metric peaks. This is not convenient when segmenting rocks, as they often come in different sizes, and consequentially, may possess widely different maximum heights when positioned above the grizzly.

With the above, a binary labeling of the points is performed by using the function defined by Equation (3), where H_t is a predefined threshold value.

$$L(p) = \begin{cases} 1 & \text{if } H(p) > H_t, \\ 0 & \text{otherwise.} \end{cases} \tag{3}$$

Afterwards, the morphological operations of dilation and erosion are applied on the binary labels assigned to the point cloud, "connecting" the labels of points that are close to each other, according to a predefined proximity radius. These morphological operations effectively remove small connected components of labeled points, whilst combining connected components that are close to one another. Finally, the resulting labels are clustered into new labels according to the proximity of their corresponding points, and these groups are individualized by re-labeling the points that conform them. These new labels are codified using natural numbers starting from 2 and up until N_l, depending on the number of groups.

When the flooding or watershed descent stage is carried out, a propagation of the labels from the seeds to points of lower height value is performed, which allows delimiting the points of contact between different rocks. Within this stage, a series of adaptations are made to apply a standard flooding 3D methodology [11] to our context in a meaningful manner.

First, a different height function is utilized for the descent stage. This new function will be referred to as $H_{\text{descent}}(p)$. This switch between height functions is based on the fact that the requirements for both stages (labeling, and descent) are different. In the initial labeling, the height function is designed to detect rocks using a single cut threshold, so it is convenient to generate seeds associated to geometric peaks, prioritizing their overall shape, and ignoring their metric height. On the other hand, for the descent stage, the objective is to propagate points (starting from the detected seeds) in a way such as to correctly limit the separations between different rocks. In this sense, using the same labeling criterion for this task would not be convenient, as it is not possible to reliably model a surface as a single plane at these intersections. If we consider the Z-axis values of the points in these intersections, however, their minimum value approximates reasonably well the boundary between different rocks. Therefore, $H_{\text{descent}}(p)$ is defined by Equation (4) as in standard watershed algorithms, that is, it assigns height values according to the points' Z-axis coordinate.

$$H_{\text{descent}}(p) = p_z \qquad (4)$$

Although this criterion does not generalize well in cases where a rock rests above another, in our application context this is not a problem: we are only concerned with segmenting rocks that are at the upper level of the material in the grizzly, since these are the rocks that take precedence at the time of the fragmentation.

In the flooding process, a hierarchical ranking of the height values is performed, assigning a certain height level, $N(p)$, to each point. Afterwards, a propagation of labels by the proximity of the points and their height level is carried out.

The height level of a point, $N(p)$, is assigned according to Equation (5), where $\Delta H_{\text{descent}}$ is a predefined resolution parameter. $\Delta H_{\text{descent}}$ is actually the same resolution parameter that is utilized in the voxelization process performed over the LIDAR data, as described in Section 2.2.2.

$$N(p) = \left\lceil \frac{H_{\text{descent}}(p)}{\Delta H_{\text{descent}}} \right\rceil \qquad (5)$$

After $N(p)$ is computed, the points are analyzed from highest to lowest hierarchy. If a point already has a label, the label is propagated to neighbor points in the next (inferior) level of hierarchy. On the contrary, if a point has no associated label, then it takes the label of the nearest labeled point. When doing this, the distance used in the neighbor search process is greater than the one used in the descending stage. This allows propagating the label to the nearest local maximum (or catchment basins of the surface) that are incorrectly generated by noisy Z values of the points. Label propagation by level allows labels to propagate uniformly through all points within the same hierarchy, thus producing the flooding effect of watershed for a point cloud.

Finally, the system labels the points that were not processed by associating them to the label of the nearest point to them. As a result, a segmented point cloud is obtained in which each point has a label that corresponds to a given rock instance. Figure 3 illustrates the result of applying the described process on a point cloud obtained from a scene where several rocks are present.
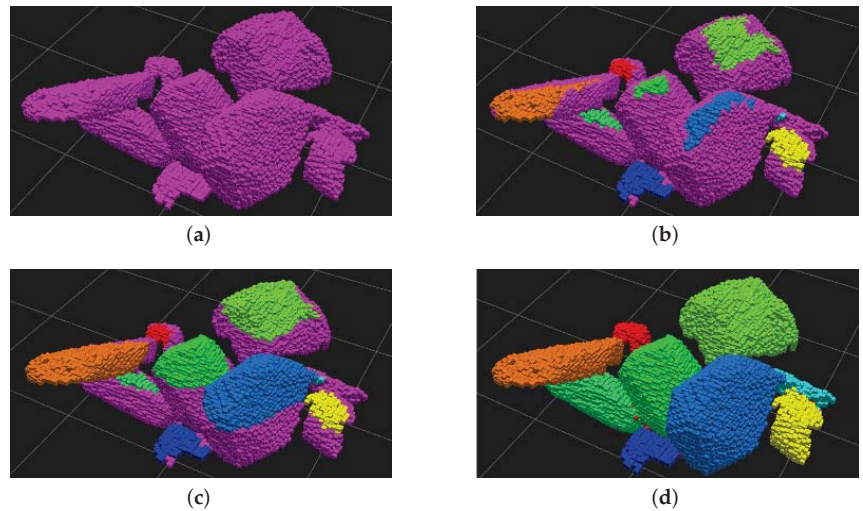
Figure 3. Example of rock segmentation using watershed on a point cloud. (**a**) Raw point cloud. (**b**) Result after initial labeling. (**c**) Intermediate result of the flooding process, where the initial labels are propagated from a higher level, up to an intermediate level. (**d**) Final result of flooding process, where all label are propagated until the lower level.

2.2.4. Rock Detection Using Images

Rocks are detected using a convolutional neural network called RockyCenterNet [13]. RockyCenterNet is based on CenterNet [14], which is a one-stage object detector in which center points are estimated, and then the other properties of a detection, such as bounding boxes' widths and heights, are regressed. Unlike CenterNet and most object detectors, RockyCenterNet uses ellipses to enclose a rock's bounds, enabling a better description of the shape of the rocks than a classical approach based on bounding boxes. According to the evaluation reported in [13], RockyCenterNet is a suitable choice for detecting rocks in mining applications when real-time operation and a good approximation of a rock's shape are needed.

2.2.5. Rock Segmentation Based on Fused Data

By using RockyCenterNet, rocks detected in the images are represented by ellipses, which in turn are represented by a coordinate and a set of parameters in the image space: a central position $(x_I, y_I)^\top$, and a major axis a_I, a minor axis b_I, and an orientation θ_I. Each ellipse is projected onto the point cloud containing the rocks already segmented, generating a new coordinate and set of parameters in the point cloud's space, according to the camera reference system: a centroid $(x_P, y_P, z_P)^\top$, a major axis a_P, a minor axis b_P, and an orientation θ_P. The centroids lie on the rock surface, and are calculated by intersecting a ray generated by the pinhole camera model of the cameras with the point cloud. The points $(x_r, y_r, z_r)^\top$ that conform this ray are defined by Equation (6), where $(f_x, f_y, c_x, c_y)^\top$ are parameters of the intrinsic matrix of the camera model [15]. The intersection is obtained using an octree voxel representation of the cloud spacing [16], and then recursively searching for the voxel closest to the ray.

$$\begin{pmatrix} x_r \\ y_r \\ z_r \end{pmatrix} = z_r \begin{pmatrix} (x_I - c_x)/f_x \\ (y_I - c_y)/f_y \\ 1 \end{pmatrix} \qquad (6)$$

Once the centroids $(x_P, y_P, z_P)^\mathsf{T}$ have been calculated, the other parameters of the ellipse in the point cloud space are computed according to Equations (7)–(9), with f_a and f_b defined by Equations (10) and (11), respectively.

$$a_P = a_I \cdot z_P / f_a \tag{7}$$
$$b_P = b_I \cdot z_P / f_b \tag{8}$$
$$\theta_P = \theta_I \tag{9}$$
$$f_a = \sqrt{f_x^2 \cos^2(\theta_I) + f_y^2 \sin^2(\theta_I)} \tag{10}$$
$$f_b = \sqrt{f_x^2 \sin^2(\theta_I) + f_y^2 \cos^2(\theta_I)} \tag{11}$$

Each properly segmented rock should contain a single centroid. Consequently, segmented rocks containing more than one centroid should be subdivided into smaller rocks. To subdivide a rock, the ellipse closest to each of the points on the rock is found, and assigned to that point.

This process goes as follows: For all segmented rocks, and each ellipse on its surface, the normal of the rock in the ellipse's centroid point is calculated, and then the depth of the centroid is corrected so that it is placed near the estimated center of the rock. Next, the Mahalanobis distance $d(p_j, c)$ between the point $p_j = (x_j, y_j, z_j)^\mathsf{T}$ of the cloud and the corrected centroid $c = (x_P, y_P, z_P)^\mathsf{T}$ of the ellipse is calculated according to Equation (12). The covariance matrix C is defined by Equation (13) where the ellipse parameters defined in Equations (7) and (8) are used as its first two diagonal components, and their product as its third diagonal component.

$$d(p_j, c) = \sqrt{(p_j - c)^\mathsf{T} C^{-1} (p_j - c)} \tag{12}$$

$$C = \begin{pmatrix} a_P^2 & 0 & 0 \\ 0 & b_P^2 & 0 \\ 0 & 0 & a_P b_P \end{pmatrix} \tag{13}$$

After the Mahalanobis distance for all ellipses and points is calculated, each point on the rock is associated with the ellipse that has the smallest distance to it. Finally, all the points associated to the same ellipse are clustered together. The result of the previous step is a set of clusters, each of them associated with a given ellipse.

Some of these point clusters may have a wrong ellipse assignment, as until this point no spacial information regarding their location is utilized. To detect these wrong assignments, it is verified that there are no different clusters associated with the same ellipse by performing the following additional checks:

- If an ellipse has only one associated cluster, that cluster is considered as correctly assigned.
- If an ellipse has multiple associated clusters, only the largest cluster is considered as correctly assigned, while the others are merged to the largest.
- The remaining clusters (which have associated ellipses but were not considered as correctly assigned) are disintegrated by reassigning their points to the nearest correctly assigned clusters.

The result of applying the point cloud correction using the ellipses is exemplified in Figure 4.

(**a**) (**b**)
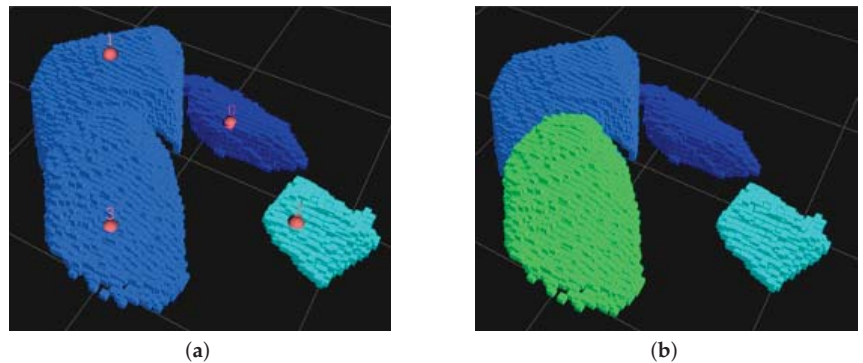
Figure 4. Example of correction in point cloud rock segmentation using image-based detections. (**a**) Segmented point cloud, and center projection of the ellipses detected in images. (**b**) Segmentation of the point cloud corrected from the information provided by the centers of the ellipses.

2.3. Subsystem for Generation and Evaluation of Rock Breaking Target Poses

This subsystem generates a set of feasible and hierarchized rock-breaking target poses. The resulting poses from this process should be such that a fracture would likely occur if the hammer's end effector aligns to them when impacting on rocks. Furthermore, the order in which these poses would be assigned as targets for the impact hammer should minimize the time that leaving the grizzly without material would take. To accomplish its objectives, this subsystem follows a set of flexible rules and criteria to select and prioritize the rock breaking target poses. These rules are based on good practice manuals and mine operators' feedback.

To generate a finite set of poses, the material's surface is divided into equidistant sub-regions on an *XY* plane parallel to the grizzly. The system then processes each of these sub-region to validate if it would be feasible to position the impact hammer's end effector on this region, considering both the material's surface geometry and the hammer's kinematic constraints. Afterwards, for each reachable region, a rock breaking target pose is generated. Finally, an evaluation and ranking of the generated poses is performed.

The following processing stages summarize the overall subsystem functioning:

- Generation of sub-regions.
- Validation of sub-regions.
- Generation and Hierarchization of rock breaking target poses.

The interaction between each stage is illustrated in Figure 5. In the following, each of these stages is described in detail.
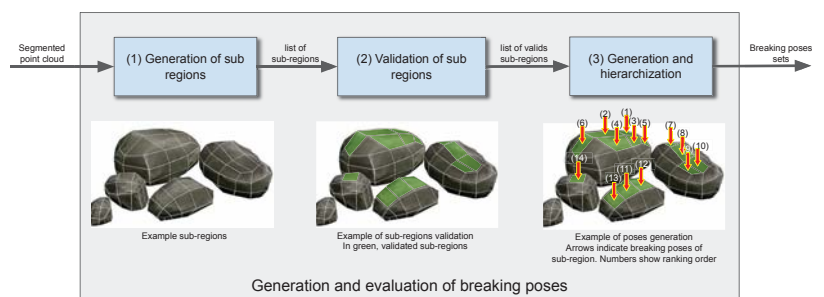
Figure 5. Block diagram of the target pose generation and evaluation subsystem.

2.3.1. Generation of Sub-Regions

As a first step, the segmented point cloud is processed to define a set of sub-regions. To generate these sub-regions, the points in the segmented point cloud are grouped according to their position in a plane parallel to the grizzly. This plane is divided in cells using a virtual grid. For each cell, the points that are at the upper level of the voxel representation of the segmented point cloud are grouped together. Figure 6 illustrates the virtual grid above the grizzly, whilst Figure 7 shows a representation of the projection of the segmented point cloud onto the *XY* plane's grid cells.
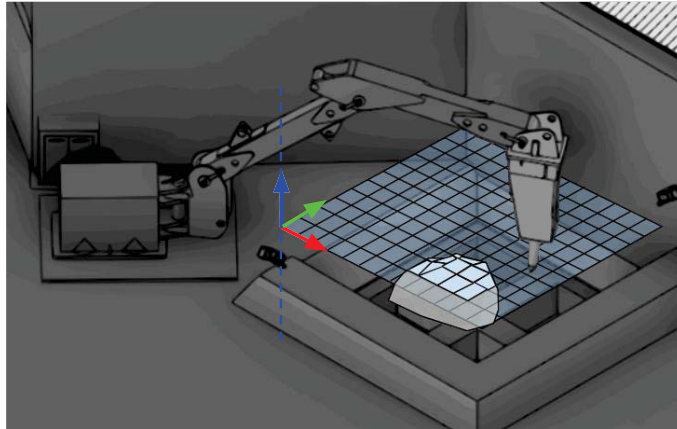
Figure 6. Grouping of points on the grizzly according to a parallel *XY* plane (the red, green and blue arrows represent the *X*, *Y* and *Z* axis, respectively). In light blue, a representation of the virtual grid utilized to perform the grouping of points. In white, the sub-regions found to be non-empty are displayed.
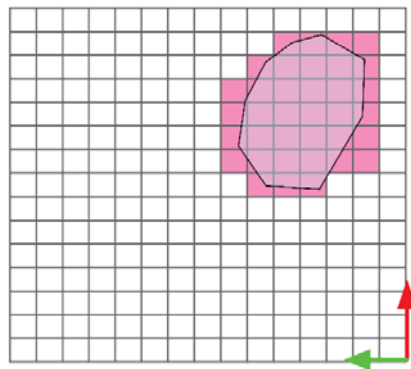
Figure 7. Representation of the rocks' projection on the *XY* plane (the red and green arrows represent the *X* and *Y* axis, respectively). The magenta grid cells are non-empty (below them there is at least a single point). The white grid cells are empty (below them there are no points).

To make a proper analysis of the breaking success related to each sub-region, it is necessary that these regions ensure that the tip of the chisel makes contact only with the points within the sub-region. In general, the chisel of an impact hammer that would be typically used in mining facilities is a steel cylinder with a diameter between 8 cm and 12 cm, ending in a rounded tip. Considering the most extreme case in which the wear on the tip is maximum, the tip of the hammer would cover the area of a circle with a radius

of 6 cm. For this reason, each sub-region is represented as a square of size 12 cm × 12 cm. This design decision ensures that, from a three-dimensional perspective, the contact area between the hammer's end effector and a rock is always less than the area covered by a given sub-region.

The generation of the sub-regions is obtained using the following method:

- To evaluate whether or not a rock would pass through the grizzly, a rough estimation of its enveloping volume is made. This allows identifying the rocks that, due to their large dimensions, would not be able to easily pass through the grizzly (i.e., the rocks that the system would target during the crushing process). To estimate the rock's enveloping volume, a 3D bounding box is constructed for each rock, using their respective point cloud. A graphic example of these bounding boxes is illustrated in Figure 8.

- The rocks that would likely pass through the grizzly (because of their low volume) are managed differently by the system, and are not considered during the rock breaking target poses' search. For instance, there might be rocks that possess a size and shape such that, although they could pass directly through the grizzly, are stuck. These cases are often dealt with by operators by redistributing the material on the grizzly.

    Another possible scenario that is managed differently is when rocks that, due to lack of visibility, are wrongly classified as "small". This case could happen, for instance, due to occlusions between rocks. These rocks are not considered for the breaking rock target pose generation, since, if they are small, they will likely fall through the grizzly after a material redistribution (performed by the hammer or due to more material being put on the grizzly) and if they are just occluded, it is likely that also because of redistributions of the material they will eventually become completely visible, and thus subject to being a target for the impact hammer.

- All the rocks that would not pass through the grizzly (because of their estimated volume) are considered for the breaking rock target pose search. In these cases, the rocks' corresponding points are grouped considering their position projected in the virtual *XY* grid cells (described previously). Thus, each of these groups of points is a sub-region associated with a particular rock. An example of these groupings is illustrated in Figure 9.

- Finally, the generated sub-regions that posses a low number of points, or whose points belong to different rocks, are discarded.
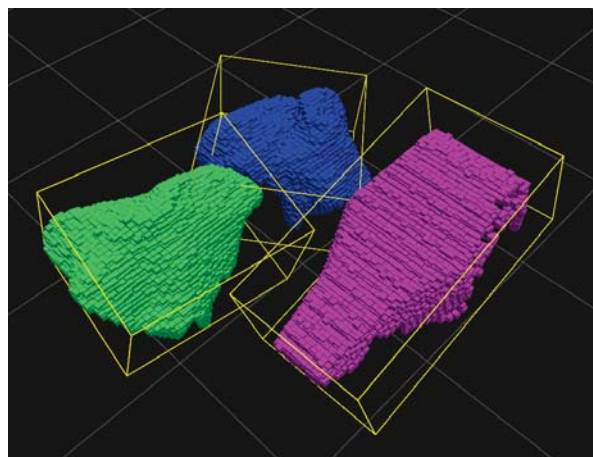
Figure 8. Segmented cloud input and bounding box representation of each rock model.
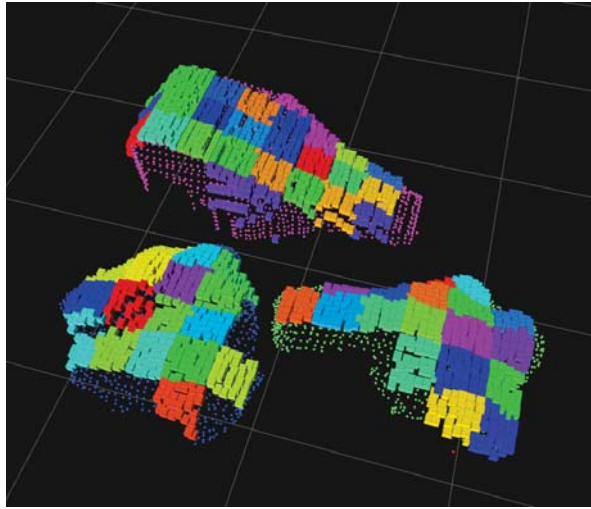
Figure 9. Example of the sub-regions generated by processing a segmented point cloud with three distinct rocks. The coloured groups of voxels on the surface of the point cloud represent each of the generated sub-regions.

2.3.2. Validation of Sub-Regions

Each generated sub-region is analyzed to determine whether or not it would be possible to find a rock breaking target pose within it, according to a set of rules. A sub-region would be discarded if at least one of these rule is not fulfilled. It is convenient to evaluate each rule considering its complexity to minimize the usage of system resources (that is, simpler rules should be evaluated before more complex rules).

For the proposed system design, three rules are considered:

- Rule 1: A vertical orientation of the impact hammer's end effector has to be maintained.
- Rule 2: The hammers' end effector should try to break the rocks by hitting them on low curvature regions.
- Rule 3: If a rock is very large, the attempts to break it should start by trying to hit it at its "edges".

The first rule seeks to ensure that the rock breaking is always done in a vertical orientation (that is, parallel to the Z axis). This is relevant because, when this rule is fulfilled, the impact force goes in the opposite direction of the force with which the rocks are supported on the grizzly. This allows the rock to be held firmly when pressure is applied to it. To evaluate this rule mathematically, the normal component of the surface within the sub-region, $\vec{n}$, is compared to the desired vertical component (that is, with the unit vector $\vec{r} = (0, 0, 1)^{\mathsf{T}}$) to obtain the angular error ϵ between the computed normal vector and $\vec{r}$. If this angular difference is greater than a predefined tolerance, the rule is considered to be not satisfied. The angular error ϵ, in radians, is defined according to Equation (14).

$$\epsilon = \arccos(\vec{n} \cdot \vec{r}) \tag{14}$$

In Figure 10 examples of applying "Rule 1" using different tolerances is illustrated.

The second rule seeks to ensure that the impact hammer does not slip when positioned on a rock. To accomplish this, the curvatures ρ of the surfaces conformed by the points within each sub-region are calculated. If a given curvature exceeds a predefined threshold, this rule is considered to be not satisfied.
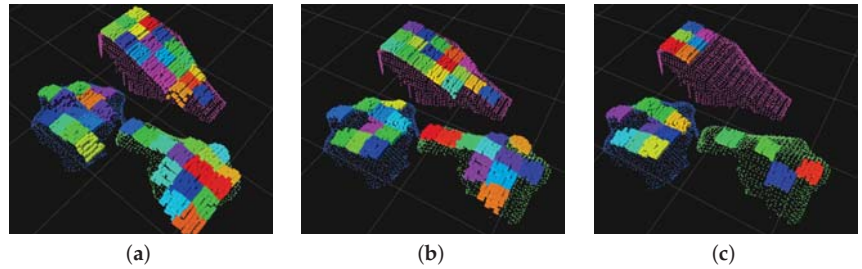
Figure 10. Results obtained by applying Rule 1 using different angular tolerances. (**a**) Tolerance 45°. (**b**) Tolerance 35° (used by the system). (**c**) Tolerance 20°.

The curvature of a given point may be computed along with the normals utilized to evaluate the first rule. To obtain these curvatures, the eigenvalues of the covariance matrix of the neighbor points (relative to the point for which $\vec{n}$ and/or ρ is being computed) are utilized, thus characterizing the curvature according to Equation (15).

$$\rho = \frac{\lambda_0}{\lambda_0 + \lambda_1 + \lambda_2}, \lambda_0 < \lambda_1 < \lambda_2 \tag{15}$$

In Figure 11 an example of applying "Rule 2" using different curvature thresholds is illustrated.
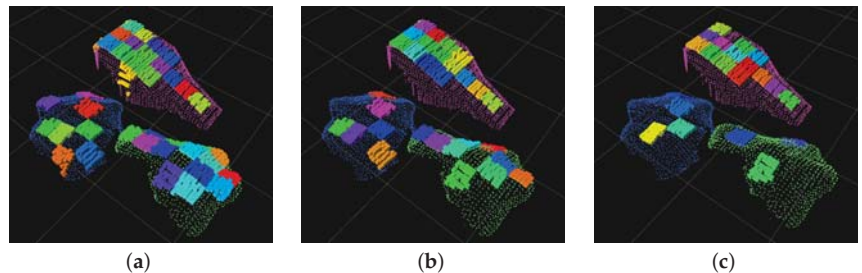
Figure 11. Results obtained after applying Rule 2 using different curvature thresholds. (**a**) Curvature tolerance = 0.02. (**b**) Curvature tolerance = 0.01 (used by the system). (**c**) Curvature tolerance = 0.007.

Finally, the third rule seeks to ensure two conditions that would allow a large rock to be fractured properly. Considering that the effort required to break a large rock by percuting on its geometric center would likely be greater than the effort required to break it by percuting near its edges, the operator manual we used as reference suggests that "large" rocks should be split from their edges to their center. To comply with this guideline, the system selects sub-regions that are not too far from the rocks' borders. On the other hand, trying to break rocks by percuting too near to their borders would probably be inefficient, as the largest resulting rocks would have a size similar to their related original rock, thus requiring several rock breaking attempts to significantly reduce their size.

Considering both scenarios, the system tries to select sub-regions that are in a certain distance range from the rocks' borders. To handle this, the position of each sub-region in relation to the edge of a rock is evaluated. If the distance of the sub-region to the borders is outside a range of 30 cm to 60 cm, then the region is discarded.

To calculate the distance of a sub-region to the rock's borders, the distance between the center of the sub-regions and the point associated to its nearest rock edge is measured. This measurement is performed by projecting both the sub-regions and the rock's edges to a *XY* plane.

To find the rocks' borders, the 2D concave hull algorithm is utilized in the aforementioned *XY*. This allows finding each rocks' "enveloping points". Figure 12 shows the effect of applying this method on a 2D point cloud.

<div align="center">(a) Segmented cloud (top-down view)   (b) Concave Hull of rocks</div>
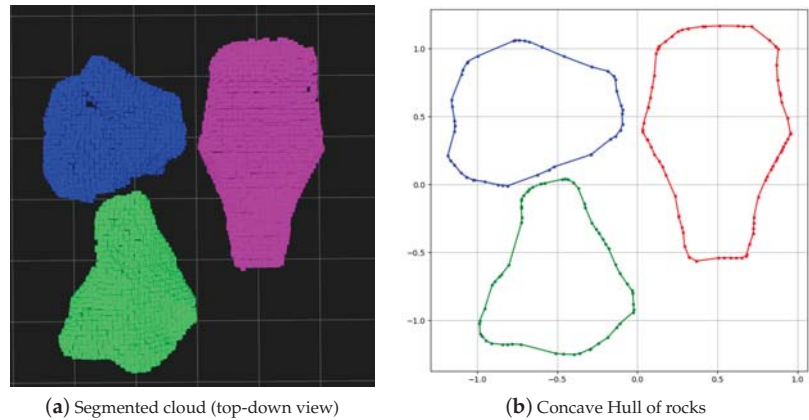
Figure 12. Example of the concave hull algorithm applied to a 2D projection of a segmented cloud. (**a**) Segmented cloud, where each rock instance is represented with a different color. (**b**) Concave envelope area generated by the algorithm.

There are cases when the rocks present narrow regions that should to be considered as possible rock breaking points because it would be easier to achieve a rock fracture if percuting on them. The "Rule 3", however, may consider that all the points contained in these narrow regions are too near to the rocks' borders. For this reason, the system also detects all the narrow regions of as given rock, and uses a lower threshold tolerance on them. This way, sub-regions that would belong to these narrow areas are not discarded.

To find the narrow regions, the system calculates the border-to-border distance on the second eigenvector coordinate system of the rock's cloud distribution. This way, a region is classified as "narrow" if its border-to-border distance is below a certain threshold. An example of this procedure is illustrated in Figure 13.
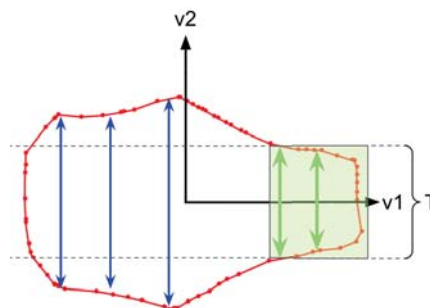
Figure 13. "Narrow" regions detection. The borders of the rock is represented in red. The v1 and v2 axes correspond to the coordinate system created with eigenvectors. T corresponds to the distance threshold used for the narrow detection process. The green arrows illustrate border-to-border distances that would be considered as valid for finding narrow regions, whereas the blue arrows are border-to-border distances that surpass the threshold defined by T. The green rectangle represents the narrow area detected in this case.

With all of the above, Figure 14 shows an example of applying Rule 3 and all its considerations.

(**a**) Tolerance = 0.15 m   (**b**) Tolerance = 0.30 m (used by the system).
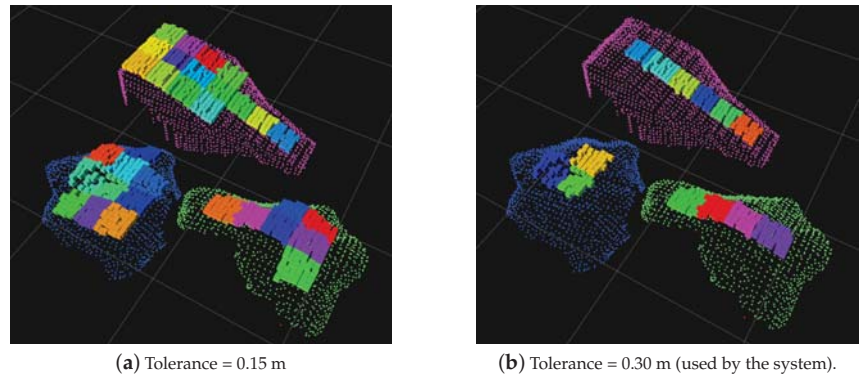
Figure 14. Results of Rule 3 with different thresholds.

2.3.3. Generation and Hierarchization of Rock Breaking Target Poses

A rock breaking pose from each sub-region is generated and then hierarchized. To generate a pose, the sub-region's center, projected in the XY plane, is assigned as the pose's position. The pose's orientation is always predefined as vertical, i.e., with an orientation parallel to $(0, 0, -1)^{\mathsf{T}}$.

To prioritize the obtained target poses, different criteria are combined. This criteria, however, may vary according to the operation state of the rock crushing process (e.g., the system might start by attempting to break the largest rock, but if this rock leaves residues after being fractured, then the following target might be an accessible rock residue instead of another rock). It is also possible to modify the system's behavior considering a user's priorities (e.g., it may be preferred by the user to clear a given quadrant of the grizzly if that quadrant is, for instance, utilized to discharge more material).

Currently, three hierarchization criteria are integrated into the system, and they are sequentially executed. These criteria are based on operation manuals and feedback provided by experienced operators, and are the following:

- Criterion 1: Picking the most accessible pose (that is, the pose that can be reached in the shortest possible time).
- Criterion 2: Attempting to break the largest rock.
- Criterion 3: Attempting to clear a specific grizzly's quadrant.

The purpose of Criterion 1 is to reduce the time that would take the impact hammer to reach the target pose starting from its current pose. To obtain an estimation of this time, it is necessary to know the current configuration of the impact hammer, and to have an inverse kinematics model of it. This allows generating trajectory plans for the hammer (from its pose to a target pose), and consequentially, getting an estimate of the time that it would take the hammer to follow such trajectories.

The result of applying this criterion is a list of ordered target poses according to the time it would take the impact hammer to reach them. The ordering goes from shortest to longest time. Different results obtained after applying Criterion 1 are illustrated in Figure 15.

(**a**)   (**b**)
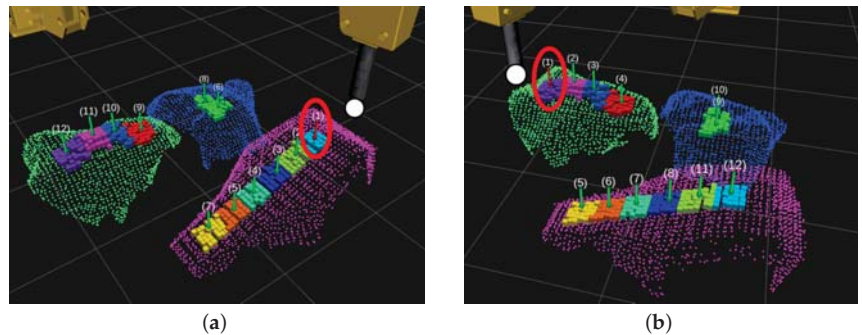
Figure 15. Results of applying Criterion 1 with different hammer states. Arrows represents the generated breaking pose. White point is the end effector pose (in the chisel tip). Circled arrow is the first preferred pose. Numbers are the ranking of each breaking pose. (**a**) Accessibility criterion with arm state with effector near to pink rock. (**b**) Accessibility criterion with effector near to green rock.

Criterion 2 is related to starting the breaking rocks' process addressing the most critical case, since the rock with the largest dimension is the one that produces the greatest spatial obstruction on the grizzly. This criterion is in charge of finding the rock with the largest volume, and keeping track of the target poses associated with that rock, ignoring the rest. Naturally, it is convenient to use this criterion in combination with Criterion 1 for ranking the breaking poses associated with the preferred, largest, rock. An example of this combination is illustrated in Figure 16.
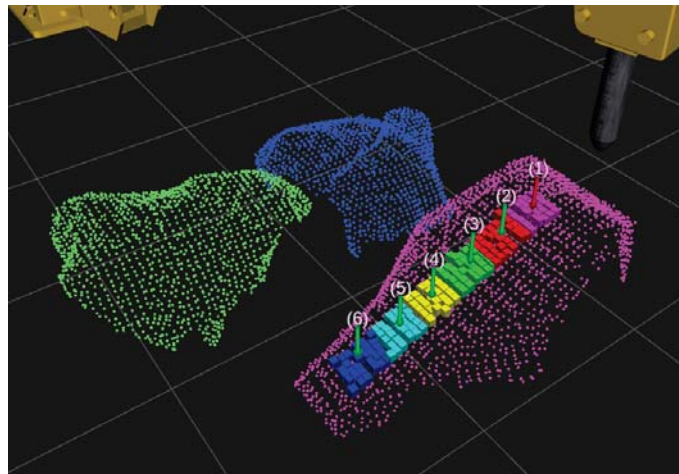
Figure 16. Result of applying Criterion 1 and Criterion 2. In this case, the pink rock corresponds to the largest rock and numbered arrows represents the generated breaking poses.

Besides prioritizing a specific quadrant to target rocks, Criterion 3 may establish a termination condition for the operation, as in some cases it is not desired to completely clear the grizzly, but rather to only clear a region to allow the unloading of more material. This is because the process of clearing the grizzly prevents LHDs from unloading material in the ore pass, which in turn, may slow the whole operation, therefore diminishing the production throughput of the mine.

In the rock breaking operation, the grizzly is usually divided into four quadrants within the *XY* plane. Operating on a given quadrant allows limiting the use of the hammer to that specific quadrant, which is also convenient when trying to reduce the use of the impact hammer whilst ensuring that the grizzly is never completely full. To implement this criterion, all the poses that correspond to a rock outside of the selected quadrant are discarded. An example of using this criterion is illustrated in Figure 17.
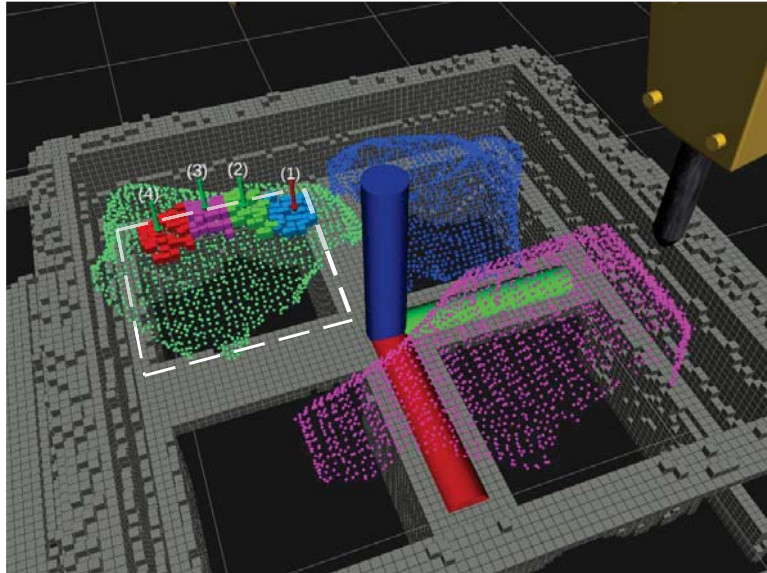
Figure 17. Result of applying Criterion 1 and Criterion 3. The blue, green, and red cylinders, correspond to the grill axes (*Z*, *Y* and *X*, respectively). The red and green axes representation, in this case, also determine the quadrant's separation. The white dashed line delimits the preferred quadrant. The green rock corresponds to the rock that is positioned within the preferred quadrant. The gray voxels correspond to the grizzly model. Numbered arrows represents the generated breaking poses.

3. Experiments

3.1. Experimental Configuration

The proposed system was implemented and continuously tested in simulations during development, using Gazebo [17] and ROS [18]. Furthermore, using ROS allowed us to seamlessly integrate the resulting software to real-world environments for validation.

To evaluate the system, experiments in the real world were conducted. We constructed a scaled experimental setup conformed by a hydraulic mini-excavator (a Bobcat E10 which we modified), a scaled steel grizzly, and four sensors: two Livox MID-40 LiDARs, and two Arecont AV 5225P MIR cameras. This setup is displayed in Figure 18.

Although several scenarios simulating real mining sites' conditions were built for Gazebo, to adjust the system's parameters for this setting, and to model the mini-excavator itself, we replicated the real world's experimental configuration in the simulator, as shown in Figure 19.
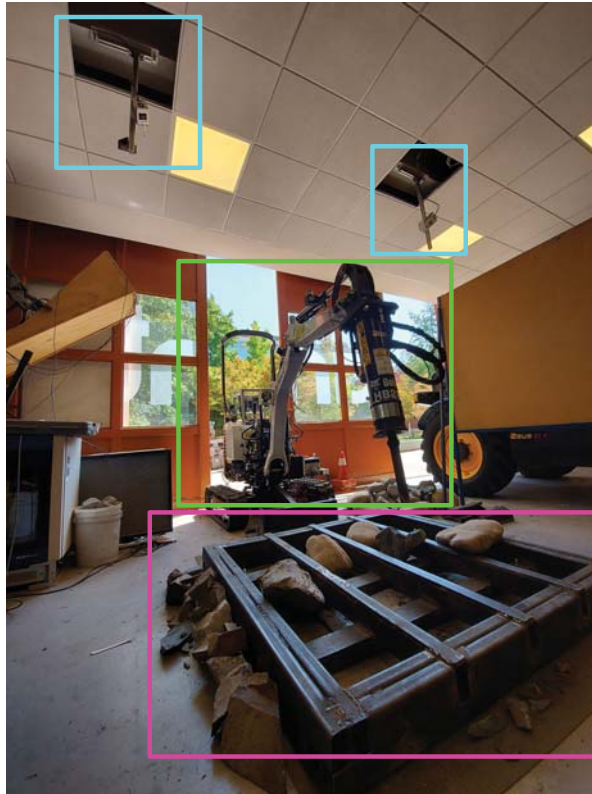
Figure 18. Experimental setup used for real-world testing. The Bobcat E10 hydraulic mini-excavator is marked with a green frame, the grizzly is marked with a magenta frame, and the sensors (LIDARs and cameras) are marked with cyan frames.
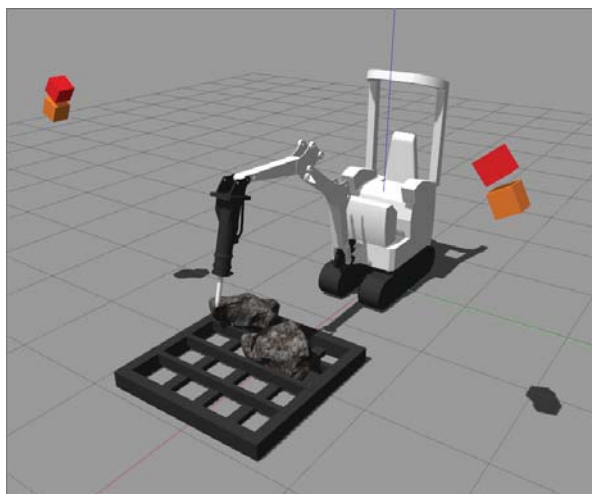
Figure 19. Simulation of the Bobcat E10 mini-excavator and a simplification of its working environment. The red and orange boxes correspond to the simulated cameras and LIDARs.

To evaluate the performance of the developed system (and its different modules), rocks that would not pass through the grizzly are positioned in several configurations, and both the segmentation of rocks and the generation of target rock-breaking poses are assessed. Although the system may use cameras to detect rocks using visual information, and in this manner, improve the performed instance segmentation, we do not use this part of the system for the real world experiments. In the constructed scenario, the visual cameras are only used to evaluate the system's performance and rate the generated rock-breaking target poses.

The hydraulic mini-excavator and the scaled steel grizzly have, approximately, a 1:2 scale with respect to a typical impact hammer used in mining sites. Furthermore, the grizzly has 16 cells for which small sized material could pass. Let us assign a pair of indices to each of these cells, counting rows and columns from 1 to 4, as illustrated in Figure 20.

Bobcat E10
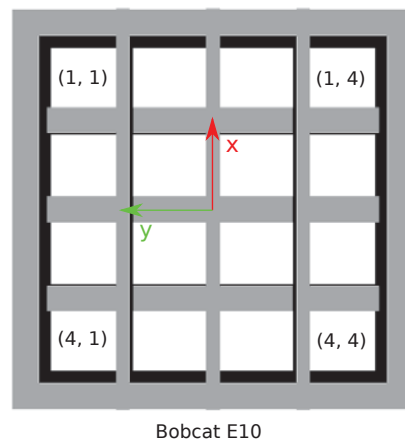
Figure 20. Reference for the scaled steel grizzly cells.

Given the aforementioned, the experiments described in Table 1 were conducted.
To quantitatively measure the system's performance, the following metrics are considered:

- For the rocks' segmentation: Precision and recall, measured as if we were detecting rocks. The metrics typically used for segmentation tasks using images (such as the intersection over union) are not utilized, as manually labeling ground truths for the point clouds processed by the system would be highly prone to error.
- For the rocks' instance segmentation: The number of correctly and incorrectly individualized rocks is measured.
- For the generation of rock-breaking target poses: An average score over the generated poses (limiting the generated poses to a maximum of 10), and an average score over only the highest priority pose are considered. The scores are 1 (bad), 2 (could be improved), and 3 (good), and the evaluation is performed by humans who are knowledgeable about good practices for rock-breaking mining operations. We will refer to the average score over all the generated rock-breaking poses as "Overall Rock-breaking Pose score" (ORP score) and to the average score for the highest priority pose as "Best Rock-breaking Pose score" (BRP score).

Table 1. Experimental configurations used to conduct the evaluation of the developed system, in the real world.

Experimental Configuration		Description
1 rock	(i, j)	A single rock is sequentially positioned above the grizzly in a single cell (i, j), for (i, j) ∈ {(1, 1), (1, 4), (4, 1), (4, 4), (2, 2), (2, 3), (3, 2), (3, 3)}.
4 rocks	corners	Four rocks that do not overlap are positioned in the corners of the grizzly, that is, in (1, 1), (1, 4), (4, 1), and (4, 4).
	center	Four rocks that do not overlap are positioned around the center of the grizzly, that is, in (2, 2), (2, 3), (3, 2) and (3, 3).
	center + overlap	Four rocks are again positioned around the center of the grizzly, but this time they overlap.
5 rocks	upper/bottom row leftmost/rightmost column	The rocks are sequentially positioned in the upper row, lower row, leftmost column, and rightmost column of the grizzly. They overlap.
5 to 6 rocks + clutter	upper/bottom row leftmost/rightmost column	The same four settings as in the "5 rocks" case are considered (that is, overlapping rocks are sequentially positioned in the upper row, lower row, leftmost column, and right most column of the grizzly), however, this time small rocks cluttering the environment are present.
8 rocks	center + corners	Eight rocks are positioned in both the corners and the center of the grizzly, without overlap.
	center + overlap	Eight rocks are positioned around the center of the grizzly, overlapping each other.
8 to 9 rocks + clutter	center + corners	The same two configurations for eight rocks are considered, that is, rocks positioned in the corners and center of the grizzly, without overlapping, and then near the center of the grizzly, overlapping each other, however, this time small rocks are added to the environment.
	center + overlap	

3.2. Evaluation Results

According to the configurations described in Table 1, we positioned rocks in the grizzly of the scaled real environment. For each configuration, the proposed system was run and we captured its output, that is, the point cloud containing the rocks' segmentation (and instance segmentation), and the set of generated target breaking-rock poses. The obtained data were labeled and scored to generate the results presented in Table 2. A summary of the scores provided by experts, regarding the generated target poses' quality, is presented in Table 3. Finally, some examples of the performed experiments are shown in Figure 21.

(**a**) 1 rock (3,3) (**b**) 5 rocks, bottom row
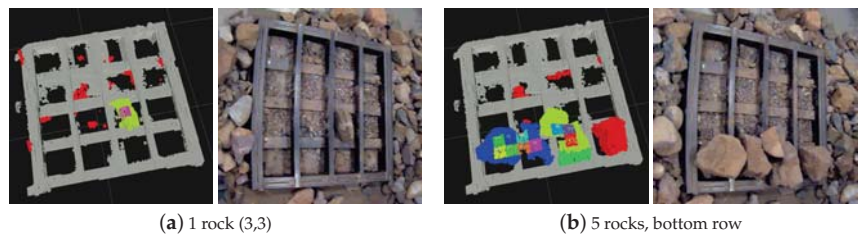
Figure 21. Examples of two of the performed experiments. (**a**) A single rock near the center of the grizzly, and (**b**), rocks occupying the cells of the bottom row of the grizzly.

Table 2. Performance metrics for the experiments conducted in the real world. ORP score: Overall Rock-breaking Pose score. BRP score: Best Rock-breaking Pose score.

Experimental Configuration		Segmentation		Instance Segmentation		Rock-Breaking Pose Evaluation	
		Precision	*Recall*	*Correct*	*Incorrect*	*ORP Score*	*BRP Score*
1 rock	(1,1)	1.0	1.0	1	0	3.00	3.00
	(1,4)	1.0	1.0	1	0	1.67	1.67
	(4,1)	1.0	1.0	1	0	3.00	3.00
	(4,4)	1.0	1.0	1	0	3.00	2.67
	(2,2)	1.0	1.0	1	0	3.00	3.00
	(2,3)	1.0	1.0	1	0	3.00	2.67
	(3,2)	1.0	1.0	1	0	3.00	3.00
	(3,3)	1.0	1.0	1	0	3.00	3.00
4 rocks	corners	1.0	1.0	4	0	2.67	3.00
	center	1.0	1.0	4	0	2.67	3.00
	center + overlap 1	1.0	1.0	0	4	2.33	2.33
	center + overlap 2	1.0	1.0	1	3	2.67	2.67
5 rocks	upper row	1.0	1.0	0	5	3.00	3.00
	bottom row	1.0	1.0	1	4	1.67	1.00
	leftmost column	1.0	1.0	3	2	2.33	2.33
	rightmost column	1.0	1.0	3	2	2.00	2.33
5 to 6 rocks + clutter	upper row	1.0	1.0	1	4	2.33	2.00
	bottom row	1.0	1.0	1	4	2.33	3.00
	leftmost column	1.0	1.0	1	5	2.67	3.00
	rightmost column	1.0	1.0	0	6	2.33	2.67
8 rocks	center + corners 1	1.0	1.0	8	0	2.67	3.00
	center + corners 2	1.0	1.0	8	0	2.67	2.33
	center + corners 3	1.0	1.0	8	0	2.67	3.00
	center + overlap 1	1.0	1.0	3	5	2.33	3.00
	center + overlap 2	1.0	1.0	2	6	2.33	3.00
	center + overlap 3	1.0	1.0	2	6	3.00	3.00
8 to 9 rocks + clutter	center + corners 1	1.0	1.0	5	4	3.00	3.00
	center + corners 2	1.0	1.0	4	5	2.33	3.00
	center + corners 3	1.0	1.0	2	7	3.00	3.00
	center + overlap 1	1.0	1.0	1	7	3.00	3.00
	center + overlap 2	1.0	1.0	1	7	2.33	3.00
	center + overlap 3	1.0	1.0	2	7	2.67	3.00

Table 3. Summary of the performance metrics for the target poses' quality. ORP score: Overall Rock-breaking Pose score. BRP score: Best Rock-breaking Pose score.

Experimental Configuration		Rock-Breaking Pose Evaluation	
		ORP Score	*BRP Score*
1 rock	8 trials	2.83	2.75
4 rocks	4 trials	2.59	2.75
5 rocks	4 trials	2.25	2.17
5 to 6 rocks + clutter	4 trials	2.42	2.67
8 rocks	6 trials	2.61	2.89
8 to 9 rocks + clutter	6 trials	2.72	3.0

4. Discussion

The obtained results, presented in Table 2, provide information that allows characterizing the system's overall performance, as well as its strengths and weaknesses. As the proposed system performs several operations (each of them with a given output), we will divide the analysis based on its segmentation, instance segmentation, and rock-breaking pose generation performance.

4.1. Segmentation

The data presented in Table 2 show that the system's segmentation performance is approximately perfect. This result is expected, as the segmentation process is fundamentally a background subtraction method, where the points corresponding to the rocks are separated from those that belong to an environment model that is constructed when no material above the grizzly is present.

Following this approach results in an almost perfect segmentation, where the main challenge corresponds to the creation of the environment model, the parameterization of the workspace to filter unwanted LIDAR measurements, the correct construction of the simplified geometric model of the impact hammer, and the calibration of the sensors.

Taking into account that the environment model and the workspace are relatively easy to construct, the main weakness of the segmentation subsystem is that it depends on the grizzly not moving relative to the LIDARs, and the impact hammer's encoders providing correct measurements, that is, it mainly relies on proper sensor calibration.

4.2. Instance Segmentation

The data show that the instance segmentation performance for all the experiments when no overlapping between rocks occurs is correct (that is, experimental configurations "1 rock", "4 rocks corners and center", and "8 rocks center + corners"). This result showcases that the instance segmentation subsystem easily differentiates rocks when they are represented by disconnected clusters of points.

When there are overlapping rocks (be these the rocks that should be targeted by the impact hammer, or small sized boulders that have not passed through the grizzly), the instance segmentation subsystem fails to achieve a good performance. This behavior may be explained due to the difficulty of differentiating rock instances by only relying on the information provided by the rocks' segmented point cloud.

However, it is important to remark that the main objective of the developed system is not to accurately represent each rock, but to characterize them with enough accuracy to select the best possible rock-breaking pose (which is, conceptually, one of the tasks the operators of impact hammers currently perform).

In addition, even though a correct instance segmentation is difficult to achieve when overlapping occurs, since the rock's segmentation is approximately perfect (refer to Section 4.1), no information regarding where the rocks are located is lost for the target rock-breaking poses generation step.

4.3. Rock-Breaking Pose Generation

The obtained results show that, in most cases, the rock-breaking target poses generated by the system are appropriate, both when rating all of them (ORP score) and when only rating the highest priority pose (BRP score). It is important to remember that the goal of the proposed system is to determine a rock-breaking target pose for the hammer. This is achieved in most cases.

Furthermore, by inspecting the results presented in Table 2, it is noted that the BRP score is, in general, higher than the ORP score. As the criteria to prioritize a target rock-breaking pose over other poses are related to factors such as the impact hammer's end effector pose, or a quadrant, the variation on the rocks' overall shape (product of a bad instance segmentation), or the presence of multiple rocks (resulting in a scenario where it would be difficult to determine which rock should be fragmented first), it is not going to necessarily negatively alter the quality of the generated highest priority pose, as its priority largely depends on factors based on geometric measures and overall rock segmentation, and not on a proper rock individualization.

We recognize, however, that there might be situations where the quality of the target rock-breaking poses would be affected by a bad instance segmentation. This could happen, for instance, when small boulders artificially make a potential target rock appear larger

than what it really is. This might result in target poses being generated near the edge of the rock that needs to be fragmented, or worse yet, on top of the small boulders.

The BRP being in general rated higher than the ORP is also a positive metric for the developed system, since it is the highest rated pose the only pose that the impact hammer would attempt to break. After this attempt, the system would be run again to obtain an updated characterization of the environment and select the best possible target rock-breaking pose, attempt to break the associated rock, and repeat the cycle.

5. Conclusions

In this paper we presented a system for generating and selecting rock-breaking target poses for impact hammers. The system and its components were described, and a real-world performance evaluation was conducted to assess its capabilities. It was found that the proposed system can generate rock-breaking target poses for the rock-breaking task performed by impact hammers in mining operations in a reliable way, complying with standard rules of operation and different criteria to prioritize poses.

6. Patents

This research has a PCT patent application on WIPO under the title "*METHOD AND SYSTEM FOR DETERMINING AND SELECTING ROCK BREAKING TARGET POSES FOR A ROCK BREAKER*" (application number: PCT/IB2021/059373) [10].

Author Contributions: Conceptualization, J.R.-d.-S. and I.P.-T.; methodology, J.R.-d.-S., I.P.-T. and D.C.; software, D.C.; validation, F.L. and D.C.; formal analysis, D.C., I.P.-T., F.L. and J.R.-d.-S.; investigation, D.C., I.P.-T., F.L. and J.R.-d.-S.; resources, J.R.-d.-S.; data curation, D.C. and F.L.; writing—original draft preparation, D.C., J.R.-d.-S., I.P.-T and F.L.; writing—review and editing, D.C., J.R.-d.-S., I.P.-T. and F.L.; visualization, I.P.-T., F.L. and D.C.; supervision, J.R.-d.-S.; project administration, J.R.-d.-S.; funding acquisition, J.R.-d.-S. All authors have read and agreed to the published version of the manuscript.

Institutional Review Board Statement: Not applicable.

Informed Consent Statement: Not applicable.

Data Availability Statement: The data presented in this study are contained in the article itself.

Conflicts of Interest: The authors declare no conflict of interest.

References

1. Salvador, C.; Mascaró, M.; Ruiz-del Solar, J. Automation of unit and auxiliary operations in block/panel caving: Challenges and opportunities. In Proceedings of the MassMin2020—The 8th International Conference on Mass Mining, Santiago, Chile, 9–11 December 2020; pp. 9–11.
2. Espinoza, J.P.; Mascaró, M.; Morales, N.; Ruiz Del Solar, J. Improving productivity in block/panel caving through dynamic confinement of semi-autonomous load-haul-dump machines. *Int. J. Min. Reclam. Environ.* **2022**, 1–22. [CrossRef]
3. Correa, M.; Cárdenas, D.; Carvajal, D.; Ruiz-del Solar, J. Haptic Teleoperation of Impact Hammers in Underground Mining. *Appl. Sci.* **2022**, *12*, 1428. [CrossRef]
4. Lampinen, S.; Niu, L.; Hulttinen, L.; Niemi, J.; Mattila, J. Autonomous robotic rock breaking using a real-time 3D visual perception system. *J. Field Robot.* **2021**, *38*, 980–1006. [CrossRef]
5. Takahashi, H.; Sano, K. Automatic detection and breaking system for boulders by use of ccd camera and laser pointer. *Fragblast* **1998**, *2*, 397–414. [CrossRef]
6. Hubert, G.; Dirdjosuwondo, S.; Plaisance, R.; Thomas, L. Tele-operation at Freeport to reduce wet muck Hazards. *MassMin 2000* **2000**, 173–179.
7. Tang, X.; Zhao, D.; Yamada, H.; Ni, T. Haptic interaction in tele-operation control system of construction robot based on virtual reality. In Proceedings of the 2009 International Conference on Mechatronics and Automation, Changchun, China, 9–12 August 2009; pp. 78–83.

8. Xu, X.; Song, A.; Ni, D.; Li, H.; Xiong, P.; Zhu, C. Visual-haptic aid teleoperation based on 3-D environment modeling and updating. *IEEE Trans. Ind. Electron.* **2016**, *63*, 6419–6428. [CrossRef]
9. Rusu, R.B.; Marton, Z.C.; Blodow, N.; Dolha, M.; Beetz, M. Towards 3D point cloud based object maps for household environments. *Robot. Auton. Syst.* **2008**, *56*, 927–941. [CrossRef]
10. Cárdenas, D.; Mascaró, M.; Parra-Tsunekawa, I.; Ruiz-del Solar, J. Method and System for Determining and Selecting Rock Breaking Target Poses for a Rock Breaker. PCT Patent PCT/IB2021/059373, 12 October 2021.
11. Mangan, A.P.; Whitaker, R.T. Partitioning 3D surface meshes using watershed segmentation. *IEEE Trans. Vis. Comput. Graph.* **1999**, *5*, 308–321. [CrossRef]
12. Koschan, A. Perception-based 3D triangle mesh segmentation using fast marching watersheds. In Proceedings of the 2003 IEEE Computer Society Conference on Computer Vision and Pattern Recognition, Madison, WI, USA, 18–20 June 2003, Volume 2, pp. 27–32.
13. Loncomilla, P.; Samtani, P.; del Solar, J.R. Detecting rocks in challenging mining environments using convolutional neural networks and ellipses as an alternative to bounding boxes. *Expert Syst. Appl.* **2022**, *194*, 116537. [CrossRef]
14. Zhou, X.; Wang, D.; Krähenbühl, P. Objects as Points. *arXiv* **2019**, arXiv:1904.07850.
15. Hartley, R.; Zisserman, A. *Multiple View Geometry in Computer Vision*; Cambridge University Press: Cambridge, UK, 2003.
16. Revelles, J.; Urena, C.; Lastra, M. An Efficient Parametric Algorithm for Octree Traversal. *J. WSCG* **2000**, *8*, 1–3.
17. Koenig, N.; Howard, A. Design and use paradigms for gazebo, an open-source multi-robot simulator. In Proceedings of the 2004 IEEE/RSJ International Conference on Intelligent Robots and Systems (IROS) (IEEE Cat. No. 04CH37566), Sendai, Japan, 28 September–2 October 2004; Volume 3, pp. 2149–2154.
18. Quigley, M.; Conley, K.; Gerkey, B.; Faust, J.; Foote, T.; Leibs, J.; Wheeler, R.; Ng, A.Y. ROS: An open-source Robot Operating System. In Proceedings of the ICRA Workshop on Open Source Software, Kobe, Japan, 12–17 May 2009; Volume 3, p. 5.

Article

Determining the Stability of a Mobile Manipulator for the Transport and Assembly of Arches in the Yielding Arch Support

Krzysztof Krauze [1], Kamil Mucha [1,*], Tomasz Wydro [1], Ryszard Klempka [2], Andrzej Kutnik [3], Waldemar Hałas [3] and Piotr Ruda [3]

[1] Faculty of Mechanical Engineering and Robotics, AGH University of Science and Technology, al. Mickiewicz 30, 30-059 Kraków, Poland; krauze@agh.edu.pl (K.K.); wydro@agh.edu.pl (T.W.)
[2] Faculty of Electrical Engineering, Automatics, Computer Science and Biomedical Engineering, AGH University of Science and Technology, al. Mickiewicz 30, 30-059 Kraków, Poland; klempka@agh.edu.pl
[3] FAMA Sp. z o.o., ul. Przemysłowa 1, 83-140 Gniew, Poland; andrzej.kutnik@fama-gniew.com (A.K.); waldemar.halas@fama-gniew.pl (W.H.); piotr.ruda@fama-gniew.com (P.R.)
* Correspondence: kmucha@agh.edu.pl

Abstract: The yielding arch support is transported and installed in the face with the use of auxiliary machines. These activities in underground mining cause many problems, which have as yet not been solved. Currently, transport and assembly are carried out manually, using the roadheader and suspended rail, or various types of mounting platforms. The analysis of the structure of the existing solutions resulted in the development of an original structure that met the requirements of Polish mines. Developed jointly by FAMA Sp. z o.o. and the AGH University of Science and Technology in Krakow, Poland, the mining modular transport and assembly unit (MZT-M) will enable the transport and assembly of support arches in the mining face. Additionally, it can also be used to reload works, which is related to the work ergonomics in underground coal mining, which is the main energy resource in Poland. The most important problem to be solved in the case of this manipulator, due to the limited space in the excavation, is how to ensure its stability during various phases of its operation. Therefore, analyses were carried out to find a solution, which resulted in determining specific conditions and design requirements related to the operation of this manipulator.

Keywords: coal mining; transport and assembly manipulator; stability; safety; work ergonomics

1. Introduction

In hard coal mines, one of the key processes is tunnelling. During tunnelling and later during the exploitation of such an excavation, it is deformed due to the pressure of the rock mass [1,2]. The floor may be deformed [3,4], but the more serious danger is caused by the roof deformation [5–7]. Hence, various types of support for tunnels are used [8–11], but the most commonly used in hard coal mines are yielding arch support frames [12–14].

The use of yielding arch support frames in galleries of underground mines involves installing their elements in the face using a roadheader [15,16]. For this purpose, apart from the aforementioned roadheader, a suspended monorail [17] and moving equipment are used. It is easy to notice that this process, i.e., the transport of support arches and other elements of the support, the lining, as well as the assembly itself, is performed manually. Delivering the support elements to the face is particularly cumbersome and requires a lot of physical effort. Hence, an idea arose to use a device enabling the transfer of elements of the support frame from the place of their storage to the face, in front of the roadheader, and to deliver them to the place of assembly [18–20].

The current solutions do not enable one to perform the above-mentioned functions due to the dimensions of the excavation. This is clearly visible in the attached photo (Figure 1), where the manipulator is attached to the platform. Examples of such solutions are GTA [21]

and Deilmann–Haniel Mining Systems GmbH [22] platforms. However, in this situation, it is not possible for the platform to ride over the roadheader (Figure 2).

Figure 1. Roadway Support Machine AMG 5000 produced by GTA [21].

Figure 2. View of the mining face of a gallery drilled with a roadheader.

A conceptual diagram of the manipulator, consisting of a boom mounted on one runway beam with a stabilizing foot and a hydraulic power unit, and consisting separately of a haulage drive (haulage unit) moving along the suspended monorail track, is shown in Figure 3a [19,20].
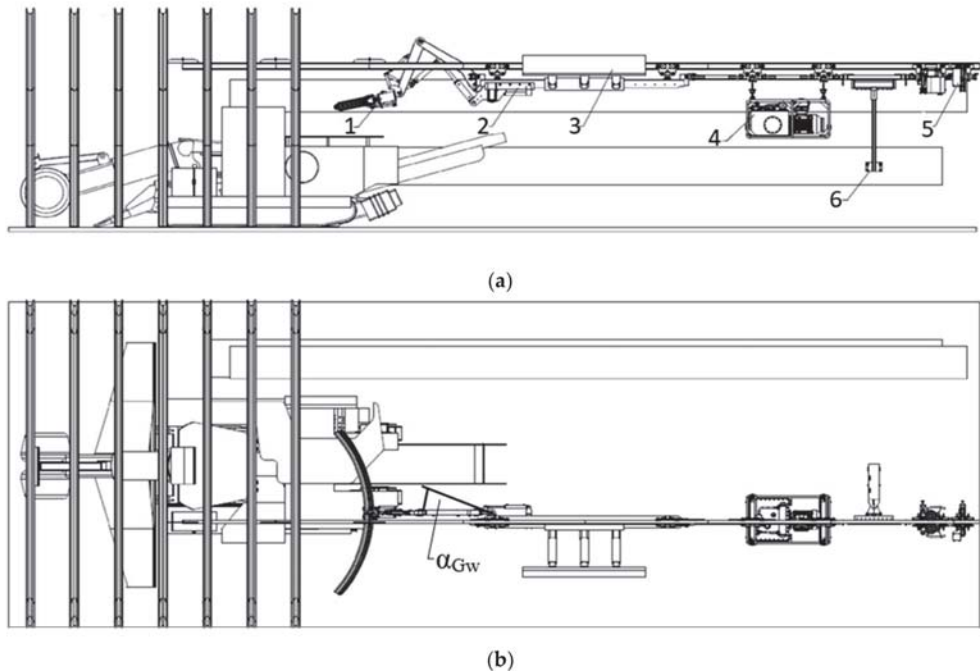
Figure 3. Diagram of the MZT-M in a gallery system with the arch in the transport position: (**a**) side view, (**b**) top view: 1—boom, 2—beam, 3—support slide, 4—hydraulic power unit, 5—CHM-15 tractor, 6—control panel [19,20].

A characteristic feature of this solution is the asymmetrical mounting of the suspended monorail in the gallery and the need to stabilize (balance) the modular transport and assembly unit (MZT-M) during the transport of support elements, whereas the manipulator can only be operated when the stabilizing foot is unfolded.

Bearing in mind the above, the following assumptions were formulated:

- the manipulator with a boom and its drive mounted on one monorail with a useful weight of up to 440 kg or without it in the transport position (boom raised, folded, twisted) can be moved without the possibility of maneuvering at the same time only when the stabilizing foot is folded;
- the maneuvering of the boom itself, with or without a load, is possible only after stoppage, with the use of a stabilizing foot stretched against the yielding support arches.

Therefore, the manipulator balancing process was performed for a transport position with a permissible boom rotation with an angle $\alpha_{Gw} \leq 30°$ (Figures 3b and 4). The model of the boom with its individual elements marked is shown in Figure 5.
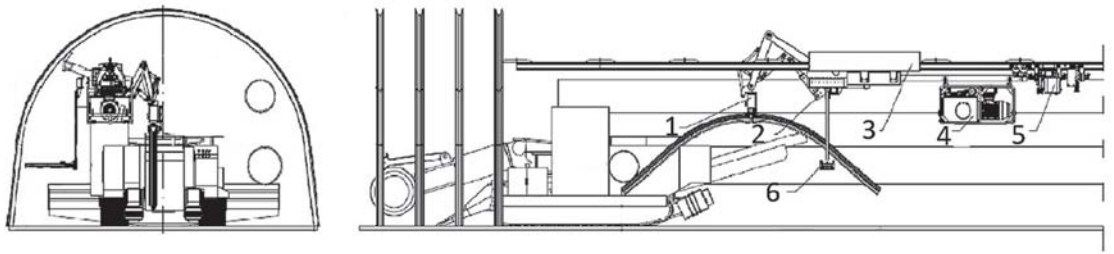
Figure 4. Diagram of the MZT-M in the transport position: 1—boom, 2—beam, 3—support slide, 4—hydraulic power unit, 5—CHM-15 tractor, 6—control panel.
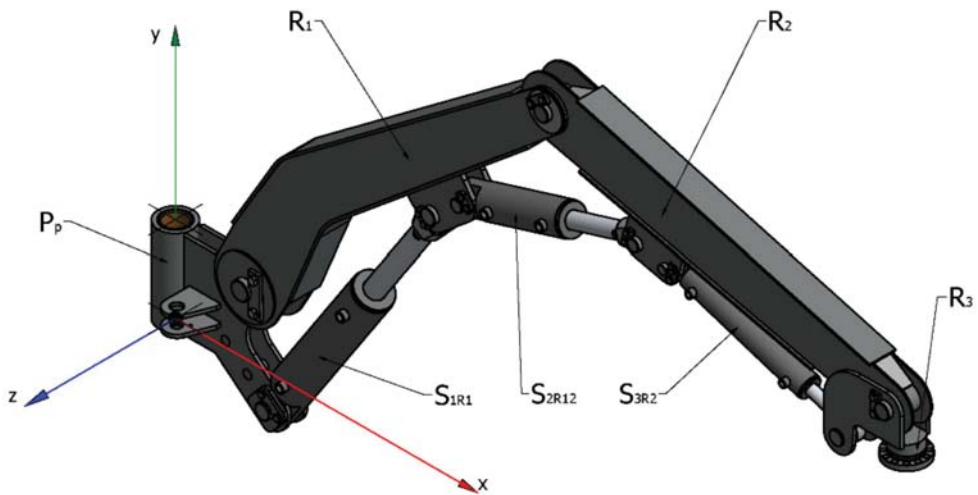
Figure 5. Boom model: P_p—vertical joint, R_1—first arm, R_2—second arm, R_3—third arm with a handle, S_{1R1}—first arm cylinder, S_{2R12}—second arm cylinder, S_{3R2}—third arm cylinder.

The article's main objective is to present the process of analytically determining the stability of the manipulator during various phases of its operation and to determine the counterweight mass for the boom in the transport position. A solution was searched for, resulting in specific conditions and design requirements related to the operation of this manipulator being obtained and specified.

2. Analytical Model of the Manipulator and Methodology for Determining Its Stability

As mentioned before, the aim of this article was to determine the counterweight for the boom in the transport position. Therefore, the boom model shown in Figure 5 was adapted, with the boom elements being marked in Figures 6 and 7.
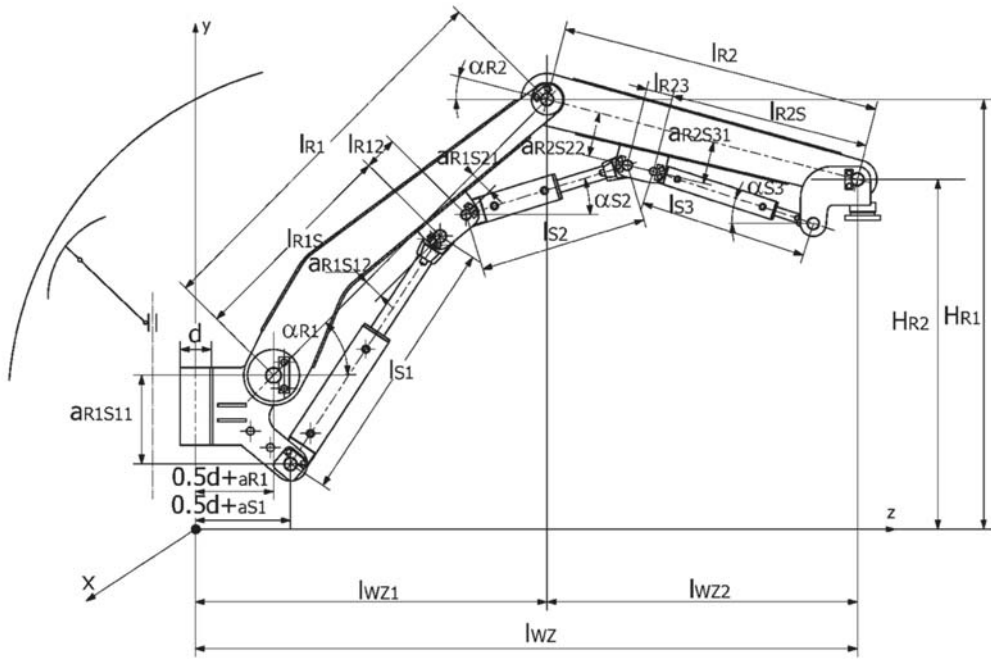
Figure 6. Diagram of the boom with marked dimensions.
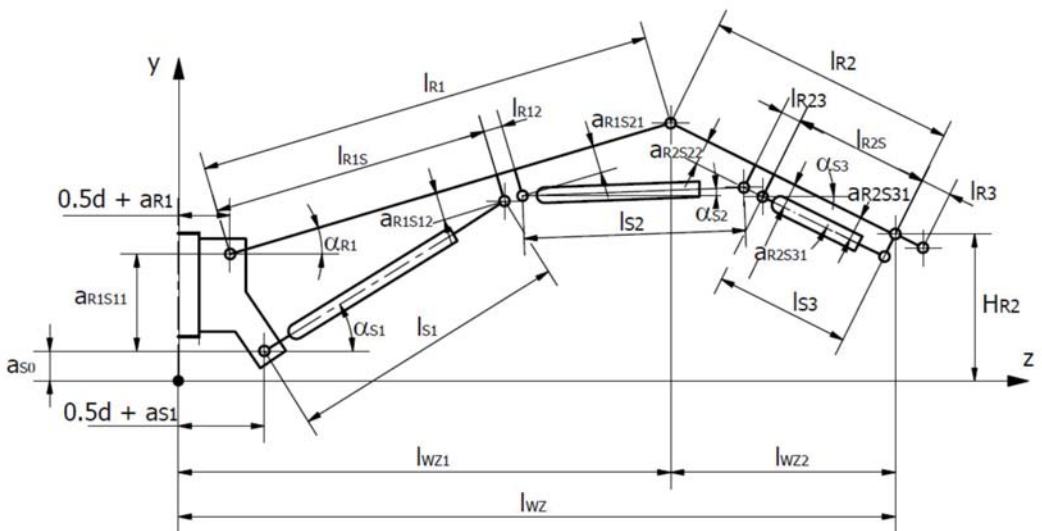
Figure 7. Analytical model of the boom for determining stability.

Based on the analytical model (Figure 7), the structure and kinematics of the R1 arm were considered (Figures 5 and 8). Bearing in mind the diagram (Figure 8), the dependencies that allowed one to describe the quantities that were important for the assessment of the arm's stability as a function of the construction parameters were determined.

$$\alpha_{R1} = \alpha_{R11} + \alpha_{R12} \tag{1}$$

$$\alpha_{R11} = arctg\left(\frac{a_{R1S12}}{l_{R1S}}\right) \tag{2}$$

$$\alpha_{R12} = \arccos\left[\frac{\left[(a_{S1} - a_{R1})^2 + a_{R1S11}^2 + \left(l_{R1S} \cdot \cos\alpha_{R11}^{-1}\right)^2\right] - l_{S1}^2}{2 \cdot l_{R1S} \cdot \cos\alpha_{R11}^{-1} \cdot \sqrt{(a_{S1} - a_{R1})^2 + a_{R1S11}^2}}\right] - arctg\left(\frac{a_{R1S11}}{a_{S1} - a_{R1}}\right) \tag{3}$$

$$\alpha_{S1} = 90° + arctg\left(\frac{a_{S1} - a_{R1}}{a_{R1S11}}\right) - \arccos\left[\frac{a_{R1S11}^2 + (a_{S1} - a_{R1})^2 - l_{R1S}^2 \cdot \cos\alpha_{R11}^{-1} + l_{S1}^2}{2 \cdot l_{S1} \cdot \sqrt{(a_{S1} - a_{R1})^2 + a_{R1S11}^2}}\right] \tag{4}$$

$$H_{R1} = a_{SO} + a_{R1S11} + l_{R1} \cdot \sin\alpha_{R1} \tag{5}$$

$$l_{WZ1} = 0.5 \cdot d + a_{R1} + l_{R1} \cdot \cos\alpha_{R1} \tag{6}$$

Figure 8. Computational diagram of the R1 arm.

The same was done for the R2 arm, whose computational diagram is presented in Figure 9.

$$\alpha_{R21} = arctg\left[\frac{a_{R2S22}}{l_{R2} - (l_{R2S} + l_{R23})}\right] \tag{7}$$

$$\alpha_{R10} = arctg\left[\frac{a_{R1S21}}{l_{R1} - (l_{R1S} + l_{R12})}\right] \tag{8}$$

$$A = \frac{l_{R2} - (l_{R2S} + l_{R23})}{\cos \alpha_{R21}} \tag{9}$$

$$B = \frac{l_{R1} - (l_{R1S} + l_{R12})}{\cos \alpha_{R10}} \tag{10}$$

$$\alpha_{R1R2} = \arccos \left(\frac{A^2 + B^2 - l_{S2}^2}{2 \cdot A \cdot B} \right) \tag{11}$$

$$\alpha_{R2} = 180^{\circ} - (\alpha_{R21} + \alpha_{R10} + \alpha_{R1} + \alpha_{R1R2}) \tag{12}$$

$$\alpha_{S2} = \alpha_{R10} + \alpha_{R1} - \alpha_{R1S1} \tag{13}$$

$$\alpha_{R1S1} = \arccos \left(\frac{B^2 + l_{S2}^2 - A^2}{2 \cdot l_{S2} \cdot B} \right) \tag{14}$$

$$H_{R2} = H_{R1} - l_{R2} \cdot \sin \alpha_{R2} \tag{15}$$

$$l_{WZ2} = l_{R2} \cdot \cos \alpha_{R2} \tag{16}$$

$$l_{S1} = l_{S1min} + \Delta S_{S1} \tag{17}$$

$$l_{S2} = l_{S2min} + \Delta S_{S2} \tag{18}$$

$$l_{S3} = l_{S3min} + \Delta S_{S3} \tag{19}$$

$$l_{WZ} = l_{WZ1} + l_{WZ2} \tag{20}$$
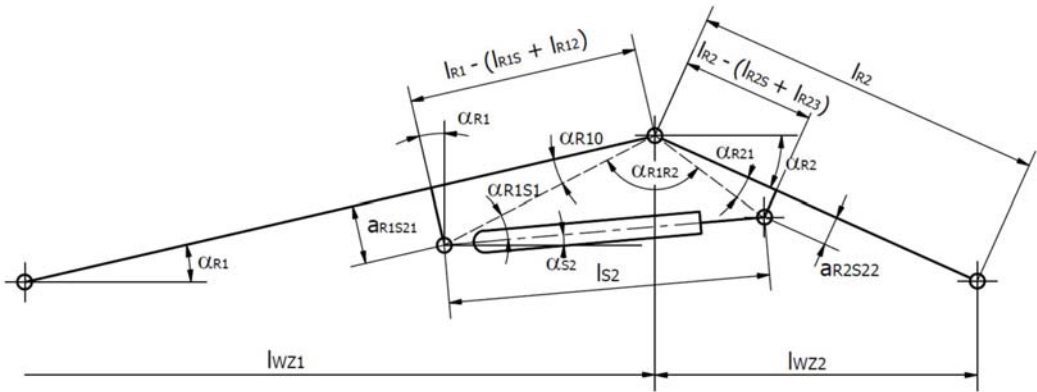
Figure 9. Computational diagram of the R2 arm.

The computational diagram of the R2 arm and more specifically its end, consisting of a gripping part that is moved by the S3 actuator, is presented in Figure 10.

$$\alpha_{R22} = arctg \left(\frac{a_{R2S31}}{l_{R2S}} \right) \tag{21}$$

$$\alpha_{R2S31} = \arccos \left[\frac{l_{S3}^2 + \left(l_{R2S} \cdot \cos \alpha_{R22}^{-1} \right)^2 - a_{R2S32}^2}{2 \cdot l_{S3} \cdot l_{R2S} \cdot \cos \alpha_{R22}^{-1}} \right] \tag{22}$$

$$\alpha_{S3} = \alpha_{R2} - \alpha_{R22} + \alpha_{R2S31} \tag{23}$$

$$\alpha_{R2S32} = \arccos \left[\frac{\left(l_{R2S} \cdot \cos \alpha_{R22}^{-1} \right)^2 + a_{R2S32}^2 - l_{S3}^2}{2 \cdot l_{R2S} \cdot \cos \alpha_{R22}^{-1} \cdot \alpha_{R2S32}} \right] \tag{24}$$

$$\alpha_{R2SC} = \arccos\left(\frac{a_{R2S32}^2 + l_{R3}^2 - l_{aR3}}{2 \cdot a_{R2S32} \cdot l_{R3}}\right) \tag{25}$$

$$\alpha_{lR3} = \alpha_{R2SC} - [90 - \alpha_{R2S32} + (\alpha_{R2} - \alpha_{R22})] \tag{26}$$

$$l_{R3X} = l_{R3} \cdot \sin \alpha_{lR3} \tag{27}$$

$$l_{R3Y} = l_{R3} \cdot \cos \alpha_{lR3} \tag{28}$$

Figure 10. Computational diagram of the R2 arm with an actuator.

Based on the above dependencies, it is possible to determine the location of the center of mass (x_s, y_s) for the boom system. The boom diagram is shown in Figure 11, whereas Figures 12 and 13 show the diagrams that provided a basis for determining the missing parameters related to the installation of the S1, S2 and S3 actuators (l_{R12}, l_{R23}).

$$G_W = G_{S_1} + G_{R_1} + G_{S_2} + G_{R_2} + G_{S_3} + G_M + G_U \tag{29}$$

where:

Figure 11. Diagram of the boom for determining the resultant of the center of mass x_s and y_s.
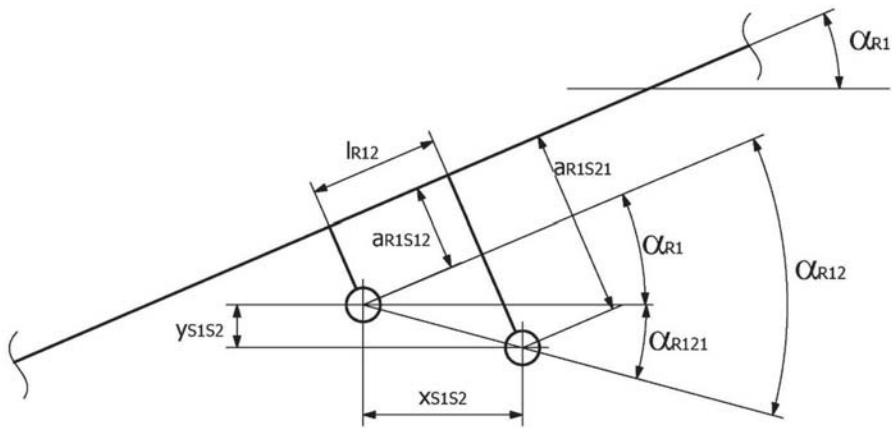
Figure 12. Diagram of the S1 and S2 actuators' mounting.
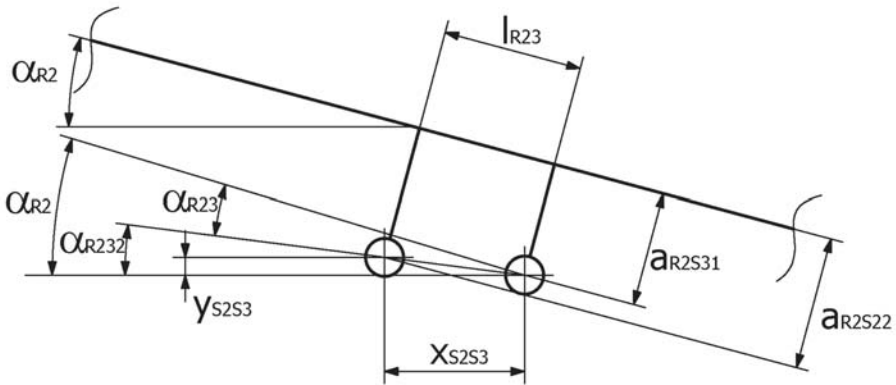
Figure 13. Diagram of the mounting of the S2 and S3 actuators.

G_W—resultant mass (weight), kg
G_{S1}—mass (weight) of the first actuator, kg
G_{R1}—mass (weight) of the first arm, kg
G_{S2}—mass (weight) of the second actuator, kg
G_{R2}—mass (weight) of the second arm, kg
G_{S3}—mass (weight) of the third actuator, kg
G_M—mass (weight) of the gripping part, kg
G_U—useful mass (weight) (support arch), kg.

$$l_{GS1} = 0.5 \cdot d + a_{S1} + x_{GS1} \cdot \cos \alpha_{S1} + l_p \tag{30}$$

$$l_{GR1} = 0.5 \cdot d + a_{R1} + x_{GR1} \cdot \cos \alpha_{R1} + l_p \tag{31}$$

$$l_{GS2} = 0.5 \cdot d + a_{S1} + x_{GS2} \cdot \cos \alpha_{S2} + l_p + x_{S1S2} + l_{S1} \cdot \cos \alpha_{S1} \tag{32}$$

$$l_{GR2} = x_{GR2} \cdot \cos \alpha_{R2} + l_p + l_{WZ1} \tag{33}$$

$$\alpha_{R12P} = arctg \left(\frac{a_{R1S21} - a_{R1S12}}{l_{R12}} \right) \tag{34}$$

$$\alpha_{R121} = \alpha_{R12P} - \alpha_{R1} \tag{35}$$

$$\Delta l_{R12} = l_{R12} \cdot \cos \alpha_{R12}^{-1} \tag{36}$$

$$x_{S1S2} = \Delta l_{R12} \cdot \cos \alpha_{R121} \tag{37}$$

$$y_{S1S2} = \Delta l_{R12} \cdot \sin \alpha_{R121} \tag{38}$$

$$\alpha_{R23} = arctg \left(\frac{a_{R2S22} - a_{R2S31}}{l_{R23}} \right) \tag{39}$$

$$\alpha_{R232} = \alpha_{R2} - \alpha_{R23} \tag{40}$$

$$\Delta l_{R23} = l_{R23} \cdot \cos \alpha_{R23}^{-1} \tag{41}$$

$$x_{S2S3} = \Delta l_{R23} \cdot \cos \alpha_{R232} \tag{42}$$

$$y_{S2S3} = \Delta l_{R23} \cdot \sin \alpha_{R232} \tag{43}$$

$$l_{GS3} = 0.5 \cdot d + a_{S1} + l_p + l_{S1} \cdot \cos \alpha_{S1} + x_{S1S2} + l_{S2} \cdot \cos \alpha_{S2} + x_{S2S3} + x_{GS3} \cdot \cos \alpha_{S3} \tag{44}$$

$$x_s = \frac{G_{S1} \cdot l_{GS1} + G_{R1} \cdot l_{GR1} + G_{S2} \cdot l_{GS2} + G_{R2} \cdot l_{GR2} + G_{S3} \cdot l_{GS3} + (G_M + G_U) \cdot (l_{WZ} + l_{R3X})}{G_{S1} + G_{R1} + G_{S2} + G_{R2} + G_{S3} + G_M + G_U} \tag{45}$$

$$h_{GS1} = a_{S0} + x_{GS1} \cdot \sin \alpha_{S1} \tag{46}$$

$$h_{GR1} = a_{S0} + a_{R1S11} + x_{GR1} \cdot \sin\alpha_{R1} \tag{47}$$

$$h_{GS2} = a_{S0} + l_{S1} \cdot \sin\alpha_{S1} + y_{S1S2} + x_{GS2} \cdot \sin\alpha_{S2} \tag{48}$$

$$h_{GR2} = H_{R1} - x_{GR2} \cdot \sin\alpha_{R2} \tag{49}$$

$$h_{GS3} = a_{S0} + l_{S1} \cdot \sin\alpha_{S1} + y_{S1S2} + l_{S2} \cdot \sin\alpha_{S2} + y_{S2S3} - x_{GS3} \cdot \sin\alpha_{S3} \tag{50}$$

$$h_{GMU} = H_{R2} - l_{R3Y} \tag{51}$$

$$y_s = \frac{G_{S1} \cdot h_{GS1} + G_{R1} \cdot h_{GR1} + G_{S2} \cdot h_{GS2} + G_{R2} \cdot h_{GR2} + G_{S3} \cdot h_{GS3} + (G_M + G_U) \cdot h_{GMU}}{G_{S1} + G_{R1} + G_{S2} + G_{R2} + G_{S3} + G_M + G_U} \tag{52}$$

The location of the center of the entire boom (x_s, y_s) and its resultant mass G_w allows one to determine the counterbalance weight G_{st} (stabilizing foot) for the variant of the manipulator's ride with the support arches. In such a case, it is required for the stabilizing foot not to be in contact with the already installed arch or arches of the support (Figure 14).

$$G_W \cdot x_{St} = G_{St} \cdot l_{GStt} \tag{53}$$

$$l_{GStt} = l_{GSt} \cdot \cos\alpha_{GSt} + l_t \tag{54}$$

where:

G_{St}—mass (weight) of the stabilizing foot, kg

l_{Gst}—length of the arm of the stabilizing foot, m

For the transport position, the value of α_{GW} cannot be greater than $30°$, and then:

$$x_{St} = x_S \cdot \sin\alpha_{GW} \tag{55}$$
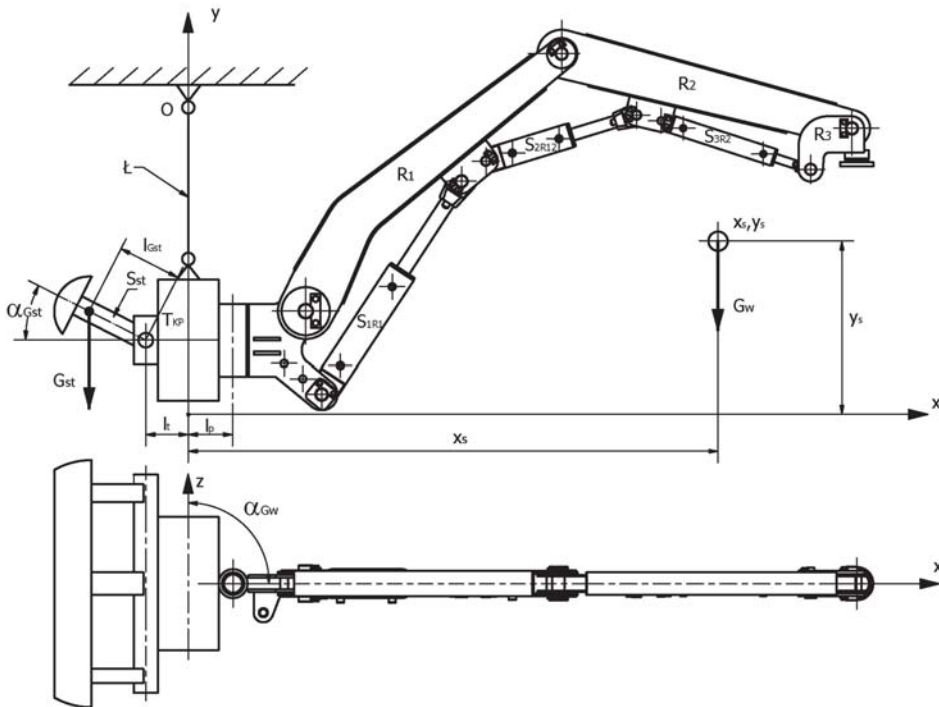
Figure 14. Diagram of the manipulator in the transport position.

Therefore, taking into account the dependencies of Equations (53)–(55), we obtain the following Equation (56), where:

$$G_{St} = \frac{G_W \cdot x_{St}}{l_{GStt}} = G_W \cdot \frac{x_S \cdot \sin \alpha_{GW}}{l_{GSt} \cdot \cos \alpha_{GSt} + l_t} \tag{56}$$

It is equally important to determine the load on the trolleys of the transport beam (points A and B), a simplified diagram of which is shown in Figure 15. Then, the beam is loaded with an additional mass (weight) with the G_z hydraulic power unit and G_n drive.

$$l_1 + l_2 + l_3 + l_4 = 1$$
$$\sum P_{iz} = 0 \rightarrow R_{AZ} = 0$$
$$\sum P_{iy} = 0 \rightarrow -G_z - G_n - G_{st} + R_{BY} - G_w + R_{AY} = 0$$

$$R_{AY} = G_z + G_n + G_{st} + G_w - R_{By} \tag{57}$$

$$\sum M_{iA} = 0 \rightarrow -(G_z + G_n) \cdot l_1 - G_{st} \cdot (l_1 + l_2) + R_{BY} \cdot (l_1 + l_2 + l_3) - G_w \cdot (l_1 + l_2 + l_3 + l_4)$$

$$R_{By} = [(G_z + G_n) \cdot l_1 + G_{st} \cdot (l_1 + l_2) + G_w \cdot (l_1 + l_2 + l_3 + l_4)] \cdot (l_1 + l_2 + l_3)^{-1} \tag{58}$$
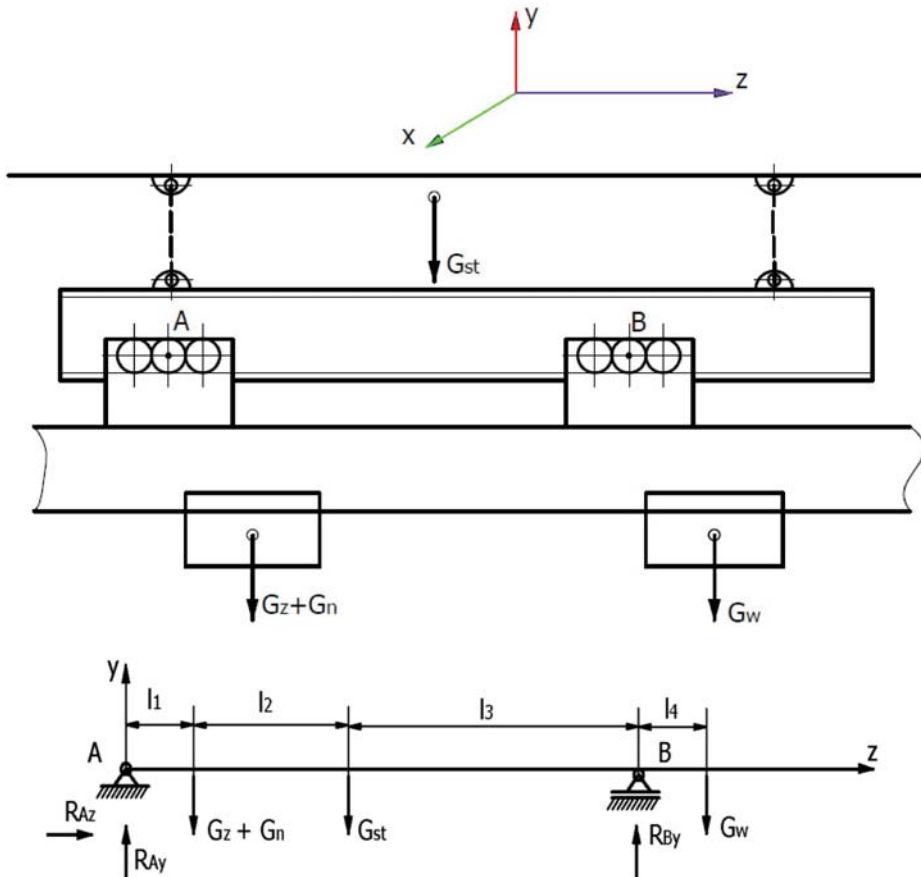
Figure 15. Simplified diagram of the transport beam loading.

3. Calculation Results and Their Analysis

The previously described manipulator model, especially the one dedicated to the transport and assembly of the arch support, was used to develop a preliminary design and, next, a basic design and technical documentation used to create a real object (Figure 16). At the same time, as previously mentioned, data (design parameters) was obtained on the basis of the technical documentation so as to determine the manipulator's stability, especially in the transport position (no contact of the stabilizing foot with the excavation sidewall or with the support elements). It is then important to determine the counterbalance weight, so that the manipulator can move along the excavation axis without the stabilizing foot coming into contact with the sidewall, in the case of movement without or with a load (useful weight of up to 400 kg). Of course, before the MZM-T was used in a tunnel, the results of the counterweight calculations were verified on a test stand, using specialized software (Figure 17).

Figure 16. The MZM-T on the test stand.

The construction and mass parameters of the manipulator obtained on the basis of the technical documentation made it possible to carry out a simulation that enabled the determination of its movement trajectory and stability [19]. It was assumed that the manipulator would be suspended 4 m from the floor (a_{so}), on the left side of the excavation (Figure 16). For such a system, the movement trajectory of the manipulator tip was determined for the minimum and maximum extensions of the actuators (Figures 18 and 19). It turned out that the manipulator movement capabilities determined analytically were consistent with the research carried out on the test stand, which allowed the support arches (usable weight of up to 440 kg) to be effectively moved to the face, i.e., in front of the roadheader. This eliminated the previous process, where the elements of support arches were provided manually. At the same time, the stability of the boom-counterweight system was determined analytically for the arch transport phase, so that the stabilizing foot did not come into contact with the support. This case was considered in the system of the support, stabilizing the foot (l_{GST}, α_{GST}) and boom, with a maximum rotation of up to 15° and a load

of up to 5 kN. As before, there was no contact between the stabilizing foot and the support, i.e., the model was consistent with the real object (test stand).
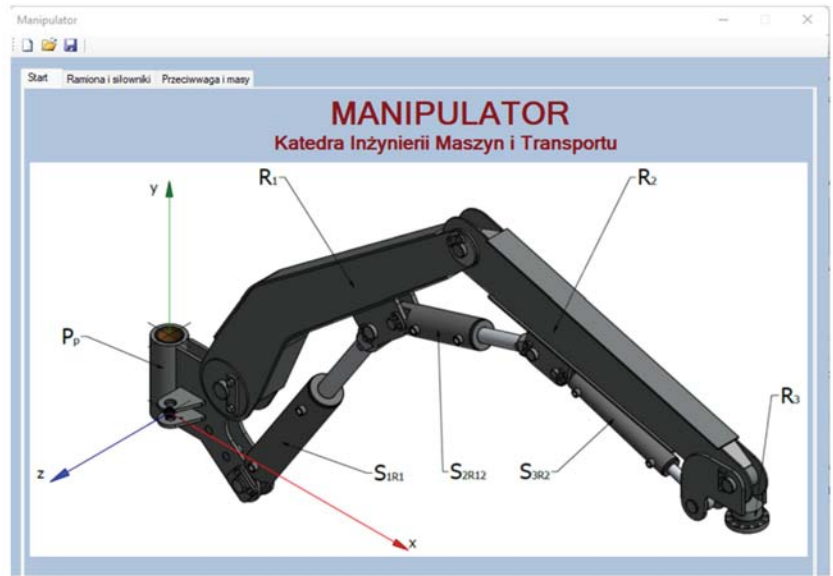
Figure 17. Application page of the program for determining the manipulator's stability.
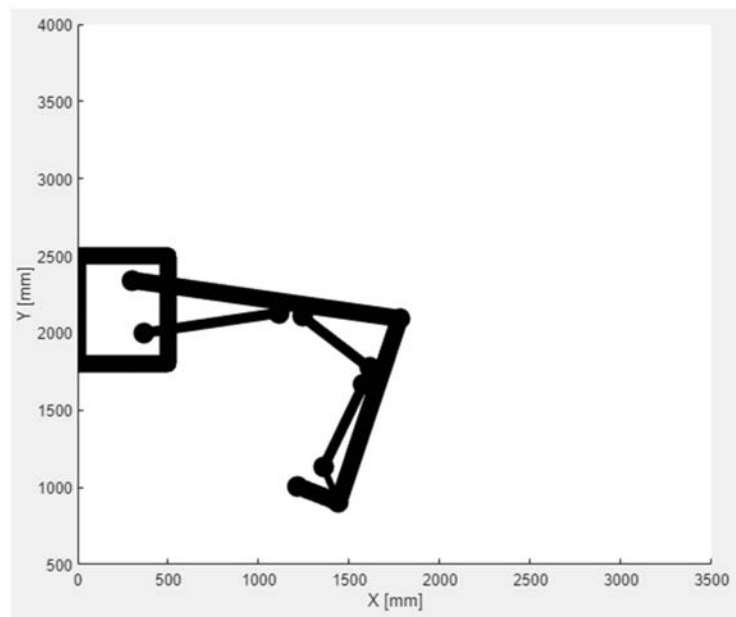
Figure 18. Movement trajectory of the manipulator tip's movement for the minimal extension of the actuators.
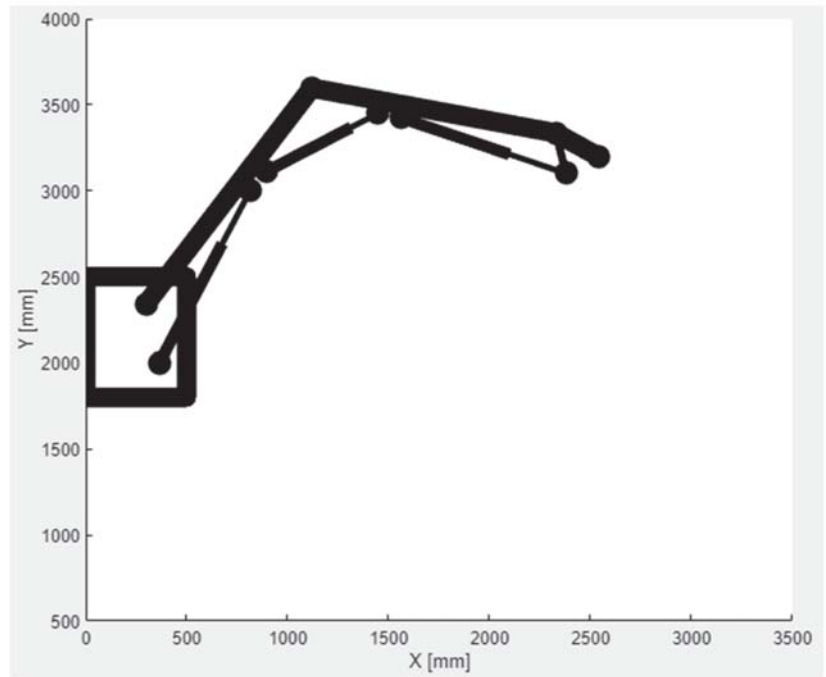
Figure 19. Movement trajectory of the manipulator tip's movement for the maximum extension of the actuators.

4. Conclusions

The aim of developing this manipulator model for supporting assembly works in mining excavations was to describe its basic functions (kinematics, stability) in an analytical way. The model and the calculation results were finally verified in an excavation of a hard coal mine, where the movement capabilities of the manipulator were tested (Figure 20). Given that the design, documentation and working assumptions have been fulfilled, the manipulator can be recommended for practical use in underground workings, and the model and software can be used for design purposes.

Figure 20. View of the MZT-M installed in an underground excavation.

References

1. Cao, J.; Zhang, N.; Wang, S.; Qian, D.; Xie, Z. Physical model test study on support of super pre-stressed anchor in the mining engineering. *Eng. Fail. Anal.* **2020**, *118*, 104833. [CrossRef]
2. Zhu, W.; Xu, J.; Li, Y. Mechanism of the dynamic pressure caused by the instability of upper chamber coal pillars in Shendong coalfield, China. *Geosci. J.* **2017**, *21*, 729–741. [CrossRef]
3. Xu, Y.; Pan, K.; Zhang, H. Investigation of key techniques on floor roadway support under the impacts of superimposed mining: Theoretical analysis and field study. *Environ. Earth Sci.* **2019**, *78*, 436. [CrossRef]
4. Małkowski, P.; Ostrowski, Ł.; Bednarek, Ł. The Effect of Selected Factors on Floor Upheaval in Roadways—In Situ Testing. *Energies* **2020**, *13*, 5686. [CrossRef]
5. Yuan, H.H.; Shan, R.L.; Su, X.G. Deformation characteristics and stability control of a gateroad in fully mechanized mining with large mining height. *Arab. J. Geosci.* **2018**, *11*, 767. [CrossRef]

6.   Mu, W.; Li, L.; Chen, D.; Wang, S.; Xiao, F. Long-term deformation and control structure of rheological tunnels based on numerical simulation and on-site monitoring. *Eng. Fail. Anal.* **2020**, *118*, 104928. [CrossRef]
7.   Tsesarsky, M.; Hatzor, Y. Tunnel roof deflection in blocky rock masses as a function of joint spacing and friction—A parametric study using discontinuous deformation analysis (DDA). *Tunn. Undergr. Space Technol.* **2006**, *21*, 29–45. [CrossRef]
8.   Bednarek, Ł.; Majcherczyk, T. An analysis of rock mass characteristics which influence the choice of support. *Geomech. Eng.* **2020**, *21*, 371–377. [CrossRef]
9.   Cai, M.; Champaigne, D.; Coulombe, J.; Challagulla, K. Development of two new rockbolts for safe and rapid tunneling in burst-prone ground. *Tunn. Undergr. Space Technol.* **2019**, *91*, 103010. [CrossRef]
10. Wang, Q.; Luan, Y.; Jiang, B.; Li, S.; He, M.; Sun, H.; Qin, Q.; Lu, W. Study on key technology of tunnel fabricated arch and its mechanical mechanism in the mechanized construction. *Tunn. Undergr. Space Technol.* **2019**, *83*, 187–194. [CrossRef]
11. Xue, G.; Cheng, J.; Guan, J.; Chai, J.; Zhang, G.; Hao, X.; Wu, M. The method for determining working resistance of advance support bracket in deep fully mechanized roadway based on Flac3D. *Adv. Mech. Eng.* **2018**, *10*, 6. [CrossRef]
12. Wu, K.; Shao, Z.; Qin, S.; Wei, W.; Chu, Z. A critical review on the performance of yielding supports in squeezing tunnels. *Tunn. Undergr. Space Technol.* **2021**, *115*, 103815. [CrossRef]
13. Rotkegel, M.; Szot, Ł.; Fabich, S. The analysis of selected methods of the yielding of a circular arch support made of V profiles. *Arch. Min. Sci.* **2020**, *65*, 531–550.
14. Horyl, P.; Snuparek, R.; Marsalek, P.; Pacześniowski, K. Simulation of Laboratory Tests of Steel Arch Support. *Arch. Min. Sci.* **2017**, *62*, 163–176. [CrossRef]
15. Nowak, P.; Kilan, Ł. Sandvik experiences with remote controlled machinery. *Min. Inform. Autom. Electr. Eng.* **2019**, *2*, 45–58. [CrossRef]
16. Korski, J. The efficiency of a bolter miner-requirements and constraints. *Min. Inform. Autom. Electr. Eng.* **2020**, *1*, 37–44. [CrossRef]
17. Pytlik, A. Tests of steel arch and rock bolt support resistance to static and dynamic loading induced by suspended monorail transportation. *Studia Geotech. Mech.* **2019**, *41*, 81–92. [CrossRef]
18. Krauze, K.; Bołoz, Ł.; Mucha, K.; Wydro, T. The mechanized supporting system in tunnelling operations. *Tunn. Undergr. Space Technol.* **2021**, *113*, 103929. [CrossRef]
19. Krauze, K.; Mucha, K.; Wydro, T. Ocena Stateczności Górniczego Manipulatora Transportowo-Montażowego w Różnych Fazach Jego Pracy, a Szczególnie w Czasie Transportu Obudowy do Przodka Wyrobiska Korytarzoweg. The Report from re-Search Conducted in the Department of Machinery Engineering and Transport AGH UST 2020, Kraków, Poland. 2020. *unpublished*. (In Polish)
20. Krauze, K.; Mucha, K.; Wydro, T.; Kutnik, A.; Hałas, W.; Ruda, P.; Osowski, D. Operational Tests of a Modular Installation and Transport Assembly of Steel Arch Support in Underground Excavations. In *Multidisciplinary Aspects of Production Engineering—MAPE*; Sitko, J., Ed.; De Gruyter: Warsaw, Poland, 2021; Volume 4, p. 1. [CrossRef]
21. GTA Roadway Support Machines. Available online: https://www.gta.eu/en/ (accessed on 3 December 2021).
22. Maas, M. Equipment for underground mining: Projects and new developments at Deilmann-Haniel Mining Systems GmbH. *Min. Rep.* **2014**, *150*, 223–227. [CrossRef]

Research on Calculation Method for Discharge Capacity of Draining Well in Tailing Ponds Based on "Simplification-Fitting" Method

Sha Wang [1,2], Guodong Mei [1,2,*], Lijie Guo [1,2,*], Xuyang Xie [1,2] and Krzysztof Skrzypkowski [3]

[1] BGRIMM Technology Group, No. 22, Beixing Road, Daxing District, Beijing 102628, China; wangsha@bgrimm.com (S.W.); xiexuyang@bgrimm.com (X.X.)

[2] National Centre for International Research on Green Metal Mining, No. 22, Beixing Road, Daxing District, Beijing 102628, China

[3] Faculty of Civil Engineering and Resource Management, AGH University of Science and Technology, 30-059 Krakow, Poland; skrzypko@agh.edu.pl

* Correspondence: meiguodong@bgrimm.com (G.M.); guolijie@bgrimm.com (L.G.)

Abstract: The existing empirical formulas concerning draining systems are complex in their expression: there are difficulties in locating the intersection point among different flow patterns and parameters vary depending on the water level, resulting in a large amount of data to be processed and low calculation efficiency. To solve these problems, a "simplification-fitting" method was proposed herein to calculate the discharge capacity of a window-type draining well, and optimal and reasonable locations were selected as discrete points of water level to deduce the increasing progressive relationship of free flow discharge capacity among discrete points according to the window size and longitudinal layout of window-type draining wells. Additionally, the algorithm simplified the discharge formulas of half-pressure flow and pressure flow and defined the convergence criteria for water level-discharge capacity to further simplify the expression of pressure flow. The comparison and contrast between the simplified calculation method and empirical formula method show that the method herein is of high precision. It is able to resolve the shortcomings of the traditional theoretical formula method in solving the discharge capacity curve of a window-type draining well and simplify the algorithm integration.

Keywords: simplification fitting; discharge capacity; window type; draining well; empirical formula

1. Introduction

A tailing pond stands as a critical facility affiliated with mines. Its safe operation is vital to the daily production of mining companies and the safety of the downstream area. The flood-discharging system of the tailing pond serves as an essential approach to discharge catchment water on the slope surface and to supply mining company with production water [1,2].

An insufficient discharge capacity in this system will increase the risk of flood overflow atop the tailing pond and simultaneously cause the water level in the tailing pond to be higher than its safety control value, thus driving the saturation line to exceed the safety threshold, increasing the seepage, deformation and damage risks and even directly inducing the dam break [3,4].

It is a critical measure to guarantee the safe operation of tailing ponds by specifying the permissible water level in tailing pond reservoir through flood routing calculation before the flood season [5]. Li [6] highlighted that the drainage system has the characteristics of multiple inlets and complex flow patterns, and that the calculation of the discharge capacity of a flood-discharging system is a crucial step in flood routing [6]. Its calculation accuracy directly influences the precision of the calculation results of the flood routing

program. Therefore, scholars conducted many analyses and discussions to research the variation pattern and the specific quantity of discharge capacity of the flood-discharging system in a tailing pond. Li [7] and Tan [8] summarized the problems existing in the hydraulic calculation of discharge system in a tailing pond, and suggested that free flow is recommended to estimate the discharge system, especially the combined patterns discharge system. As the primary method of studying the hydraulic characteristics of the flood-discharging system, the hydraulic model test was taken as the basic method for researching the changing process of discharge capacity in complex flood-discharging systems. Liu [9] carried out a hydraulic experimental model to research the flow characteristics of the curved section of the spillway tunnel, and found that the flow pattern and its change tendency was the basic influence factor for the designing of the tunnel. Wang [10] studied the influence of shaft depth on the discharge capacity through a typical tailing dam heightening project, and established the fitting function relation between discharge and shaft depth. Han [11] and Du [12] carried out an experimental model based on the principle of similarity to simulate the process of the water level rising in a tailing pond and to obtain the complex ternary water flow movement laws, they found that the angle of the turning can be adjusted to reduce the backwater height. Djillali [13] proposed a new design for the shaft spillway, replacing the circular section with a polygonal configuration of 12 sections, thus making the hydraulic structure more reliable. Fraga [14] proposed a model under unsteady part-full and pressure flow conditions. Zakwan [15] established the relationship between the coefficient and flow of side weir. Ebtehaj [16] recommended a multi-objective method for the prediction of the side weir discharge coefficients. Sen [17] used a stabilized finite-element method to discrete the conservation equations of incompressible fluid flow in two dimensions. Dennis [18] suggested the small to moderate values of the Reynolds number for higher accuracy. These research results were subject to theoretical generalization and analysis, and applied to practical projects.

In complicated and unconventional flood-discharging systems, numerical simulation methods can be adopted as a simple, cheap, and reliable means of analyzing the hydraulic variation characteristics. Mo [19], Zhao [20] and Bao [21] carried out the numerical simulation analysis of different discharge systems; in these simulations, the flow pattern, velocity distribution, water surface profile and other hydraulic characteristics were analyzed, and the simulation results showed that the use of numerical simulation is of high accuracy. The numerical simulation software adopted includes Flow-3D, 3D VOF model, Fluent, etc. Three-dimensional hydraulic simulation is usually adopted to modify the parameters of theoretical formulas, especially when the design of a discharge system is unconventional and thus theoretical formulas cannot accurately calculate the discharge capacity. For example, Wang [22] adopted Flow-3D to simulate the downstream of the sluices; Ling [23] built a 3D water quality model coupled VOF method and the k-ε turbulence model; Yi [24] chose Flow-3D to simulate the water characteristic of window type, frame type and chute type water-discharge system, respectively. Yu [25] simulated the flow in a siphon-shaped overflow tower under both steady and unsteady flow conditions using CFD. However, calculation results may deviate from actual projects because some basic assumptions were adopted in numerical simulation or the selected parameters are unreliable. In this situation, a method combining numerical simulation with the model test can be adopted [26] to invert calculating parameters for a numerical simulation with model test results. Then, simulation results more consistent with reality can be obtained. Meanwhile, repeated numerical simulations can be exploited to predict the discharge results under multiple operating conditions. The analysis combining the empirical calculation formula of discharge capacity with monitoring results also serves as a key research method. Based on the real-time monitoring results of water level and discharge capacity, the parameters of the empirical calculation formula can be modified, and a more accurate prediction formula can be obtained [27]. In addition to the aforementioned methods, the empirical formula and the numerical simulation results of computational fluid dynamics have been compared to achieve mutual verification and calibration. For example, Wu [28] compared the calcula-

tion results of the empirical formula and computational fluid dynamics flow simulation (CFD), and found that the discharge capacity of half-pressure flow calculated by CFD method is higher but more reasonable than that of the empirical formula method. Ning [29] found that LUSGS preconditioning is slightly better than the ILU preconditioning. Liu [30] and Dang [31] stated that chute plate type, chute slope, water head and flow patterns on flow capacity should be adequately considered in the design stage. These achievements lay a theoretical basis for the optimal design of the flood-discharging system of tailing ponds [32–35].

In recent years, as the information construction rapidly progresses and develops, it has become a development trend to establish the flood routing algorithm system for tailing ponds based on the dynamic monitoring data of rainfall and water level so as to realize a real-time analysis and calculation on flood routing for tailing ponds. This trend has put forward new requirements on the accuracy and efficiency of hydraulic calculation concerning flood-discharging systems [36–38]. On this basis, the "window-type draining well plus tunnel/draining pipe" draining system was chosen herein to research the algorithm for discharge capacity.

Theoretical Calculation Formulas

According to the References for Tailing Pond Design [39], the working conditions of a "window-type draining well plus tunnel/draining pipe" flood-discharging system vary in function of the size of the discharge water head, which can be divided into free flow, half-pressure flow and pressure flow. Their specific calculation methods are listed in Table 1:

Table 1. Theoretical calculation formulas of "window-type draining well plus tunnel/draining pipe" flood-discharging system.

Working Conditions	Calculation Formulas	
Free Flow (a) When the water level is between two layers of windows. (b) When the water level is in the window position.	$Q_a = Q_2 = 2.7 n_c \omega_c \sum \sqrt{H_i}$ $Q_b = Q_1 + Q_2$ For square orifice, $Q_1 = 1.8 n_c \varepsilon b_c H_0^{1.5}$ For round orifice, $Q_1 \approx n_c A D_c^{2.5}$	(1)
Half-Pressure Flow	$Q = \varphi F_s \sqrt{2gH}$ $\varphi = \dfrac{1}{\sqrt{1 + \lambda_j \frac{l}{d} f_1^2 + \zeta_1 f_2^2 + \zeta_2 + 2\zeta_3 f_1^2}}$	(2)
Pressure Flow	$Q = \mu F_s \sqrt{2gH_z}$ $\mu = \dfrac{1}{\sqrt{1 + \sum \lambda_g \frac{l}{D} f_3^2 + \sum \zeta f_3^2 + \zeta_1 f_4^2 + \zeta_2 f_9^2 + 2\zeta_3 f_5^2}}$	(3)

Notes: Descriptions of symbols in the table.

H_i—Discharging water head calculated at the working window fully submerged on the *i*th floor, m;
H_0—Discharging water head at the working window not submerged on the *i*th floor, m;
H—Water head calculated, the difference between the water level in the pond and the elevation of the inlet section center of the draining pipe, m;
H_z—Water head calculated, the difference between the water level in the pond and the elevation of downstream outlet section center of the draining pipe, or the height difference between the water level in the pond and the level of tail water when there is water downstream, m:
ω_c—The area of one draining window, m²;
ω_s—Flow shrinkage area at the wellhead, m², $\omega_s = \varepsilon_b \omega_j$;
ω—The total window area within the water depth range, m²;
ω_j—Cross-section area of draining well shaft, m²;
ω_1—Total window area of draining well, m²;
ω_2—External surface area of draining well shaft, m²;
F_s—Water flow shrinkage area at draining pipe inlet, m², $F_s = \varepsilon_b F_e$;

F_e—Sectional area of draining pipe inlet, m^2;

F_x—Sectional area of downstream outlet of draining pipe, m^2;

F_g—Sectional area of calculating pipe segment of draining pipe, m^2;

ζ—Local head loss coefficient of draining pipeline, including angle, bifurcation, section change, etc., which can be obtained by referring to relevant tables;

ζ_0—Coefficient, related to the shape of gate pier head;

ζ_1—Local head loss coefficient of draining window, $\zeta_1 = \left(1.707\frac{\omega_1}{\omega_2}\right)^2$;

ζ_2—Local head loss coefficient of draining pipe inlet, rectangular entrance $\zeta_2 = 0.5$, fillet angular or oblique angular entrance $\zeta_2 = 0.2\sim0.25$, flare opening entrance $\zeta_2 = 0.1\sim0.2$;

ζ_3—Local head loss coefficient of water diversion in a draining well;

ε—Lateral contraction coefficient, $\varepsilon = 1 - \frac{0.25\zeta_0 H_h}{b_c}$;

ε_b—Sectional sudden contraction coefficient;

d—Inner diameter of draining well, m, but if the well shape is not circular, $d = 4R_j$;

D—Inner diameter of calculating pipe segment, m, but if the pipe is not circular, $D = 4R_g$;

L—The calculated length of the pipe segment of draining pipe (when there is no change in the cross section, the length is the full length of pipeline), m;

A—Coefficient, obtained with reference to relevant tables and based on $\frac{H_0}{D_c}$;

R_g—Hydraulic radius of calculating pipe segment of draining pipe, m;

R_j—Hydraulic radius of shaft section of drainage well, m;

D_c—Draining well diameter, m;

b_c—Width of one draining window, m;

n_c—Number of draining windows on the same cross-section;

λ_j—Frictional head loss coefficient of draining well, $\lambda = \frac{8g}{C^2}$;

λ_g—Frictional head loss coefficient of draining window, $\lambda = \frac{8g}{C^2}$;

C—Chezy coefficient, with reference to relevant documents and according to n and R;

n—Pipe wall roughness coefficient;

$$f_1 = \frac{F_s}{\omega_j}; \; f_2 = \frac{F_s}{\omega}; \; f_3 = \frac{F_x}{F_g}; \; f_4 = \frac{F_x}{\omega}; \; f_5 = \frac{F_x}{\omega_j}; \; f_9 = \frac{F_x}{F_e}$$

There will be the following problems when these formulas are adopted to calculate the discharge capacity:

(1) In the free discharge stage, as the water level increases, there will be three combined flow regimes—the weir flow, the orifice flow, and the weir flow + orifice flow. These correspond to the water levels within the elevation range of the first window, between two layers of windows, and within the elevation ranges of windows other than the first window. Therefore, the relationship between the water level and window position should be judged whenever necessary in the calculation. The discharge capacity under three flow regimes can be obtained by choosing and combining reasonable formulas, thus resulting in a complicated calculation process.

(2) There are many parameters, iterations among parameters and applications in this method, and the water level is also closely involved. Furthermore, fluctuations in water level result in constant changes in calculation parameters.

(3) The empirical formula method has to locate the intersection point among the free flow curve, the half-pressure flow curve, and the pressure flow curve, and choose the discharge capacity calculation formula according to the relative position relationship between the actual water level and the intersection point. This requirement will bring about logical difficulties in algorithm integration.

In order to overcome the shortcomings of the existing theoretical calculation method, a simplified calculation method needs to be proposed to enhance the significance of discharge capacity calculation efficiency of the "window-type draining well plus tunnel/draining

pipe" flood-discharging system, thus realizing algorithm simplification and program-based treatment, and delivering a higher calculation accuracy.

The literature review showed a very small number of studies similar to the simplification-fitting method. Discharge capacity calculation is critical to flood routing calculation, which is an important measurement to guarantee the safety of the tailing pond. However, the theoretical formulas recommended in books are enormously complex in expression, and are thus those algorithm cannot be implemented to flood the routing calculation program. Therefore, this article presents for the first time research on a simplification method of calculation equations for a discharge system in tailing pond. The proposed method determines discrete water level points according to the shape, size, and spacing of windows. The simplified formulas for free flow, half-pressure flow, and pressure flow were obtained through a specific discrete method. The discrete values calculated by the simplified formula were adopted to fit those data, and to obtain the discharge capacity value on a random water level. A series of comparative analyses was carried out during the free flow stage, half-pressure flow stage, and pressure flow stage, respectively, the purpose of which was to verify the accuracy of the simplified algorithm proposed in this study. The obtained analysis results indicate that the proposed simplification method made it possible for discharge algorithm computer integration with the flood routing program in a low-cost, high-efficient and steady way.

2. Physical Model

In the window-type draining system in a tailing pond shown in Figure 1 [39], there are six draining windows on each floor of the well; the window size is 0.5×0.5 m; the clear vertical distance between windows is 0.2 m; the inner diameter of draining well is 5.0 m; the draining well wall is as thick as 0.2 m; the elevation of cover plate is 400.0 m; the pedestal elevation is 398.7 m; the draining tunnel has the shape of a horseshoe, whose bottom is as wide as 1.52 m; and the height of the straight wall is 0.76 m. The curve of the relationship between the discharge capacity of this draining system and the water level in the tailing reservoir was calculated.
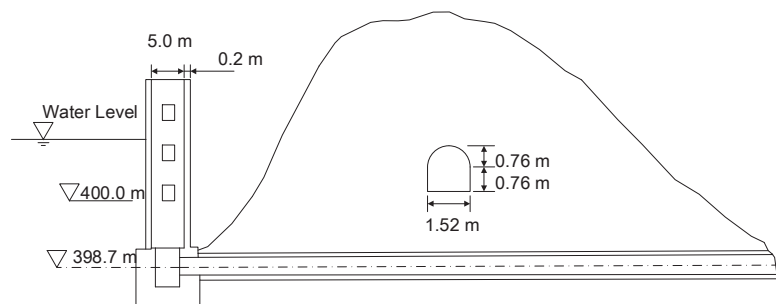
Figure 1. A window-type draining system in a tailing pond.

3. Method

A unique discrete point selection method was proposed based on a systematical summary of the empirical calculation formula of a window-type draining well to simplify the formula in the free discharge stage. Simultaneously, calculation parameters in half-pressure flow and pressure flow stages were simplified according to the characteristics of draining wells in tailing ponds to simplify calculation expressions. The flow chart of the simplified algorithm for the discharge capacity of window-type draining wells is shown in Figure 2.
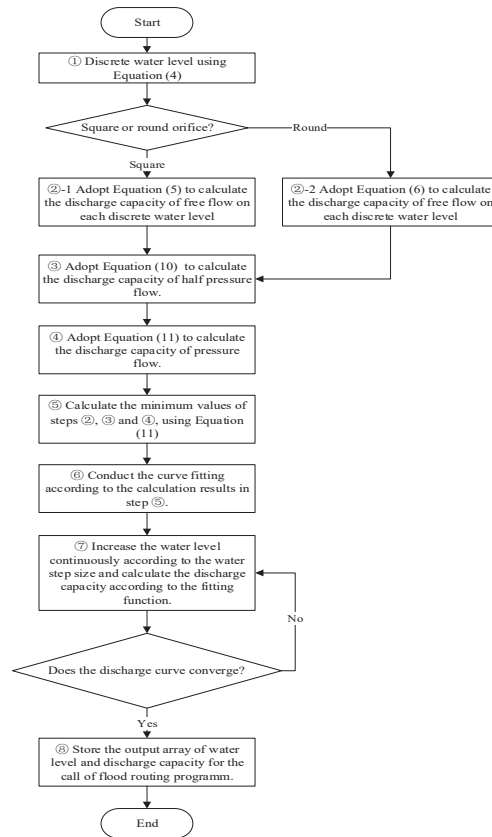
Figure 2. Flow chart of the simplified algorithm for discharge capacity of window-type draining wells.

The specific "simplification-fitting" calculation processes are shown as follows:

1. Step 1. The coordinates of discrete points for the simplified algorithm were obtained according to the dimension parameters of the window-type draining well input, including the window number on the same longitudinal section n_z, the window height h_c (or inner diameter D_c), the inlet elevation z_j, etc.

Positions of discrete points were located at the center point of each window. The first point takes the bottom level of the first window (namely, inlet elevation z_j). The coordinates of each discrete point value are shown in Figure 3. The same discrete law was adopted for calculating the water level beyond the well height. According to the aforementioned method, the formula of discrete point coordinates regarding water level should be expressed as follows:

$$z_i = \begin{cases} z_j, i = 0 \\ z_j + 0.5 h_c (\text{or } D_c), i = 1 \\ z_j + 0.5 h_c + (n_z - 1) \cdot (h_c (\text{or } D_c) + h_k), i \geq 2 \end{cases} \quad (4)$$

where z_i represents the coordinate value corresponding to the ith discrete water level point, m; z_j represents the inlet elevation, m; h_c represents the window height, m; D_c represents the window diameter, m; n_z represents the window number on the vertical section; h_k represents the window spacing, m.
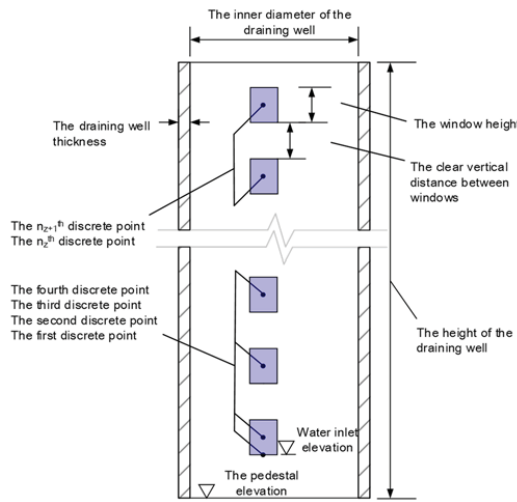
Figure 3. Water level discrete method.

2. Step 2. The free flow curve was calculated by the simplified algorithm according to the dimension parameters of a window-type draining well, such as the window number on the same cross-section n_c, the window width b_c (or window diameter D_c), and the draining well thickness δ. The simplified algorithm was shown as follows:

When the window takes the shape of a square orifice, the simplified algorithm is shown as follows:

$$Q_{1i} = \begin{cases} 0, i = 0 \\ 1.8 n_c \varepsilon b_c (0.5 \times h_c)^{1.5}, i = 1 \\ Q_{1(i-1)} + 2.7 n_c \omega_c \sqrt{(i-1)(h_c + h_k)}, i \geq 2 \end{cases} \quad (5)$$

where Q_{1i} represents the discharge capacity of free flow corresponding to the i-1st discrete water level point, m^3/s; n_c represents the window number on the same cross-section; b_c represents the window width, m; ε represents the lateral contraction coefficient; ω_c represents the area of one draining window, m^2.

When the window takes the shape of a round orifice, the simplified algorithm is as follows:

$$Q_{1i} = \begin{cases} 0, i = 0 \\ n_c A D_c^{2.5}, i = 1 \\ Q_{1(i-1)} + 2.7 n_c \omega_c \sqrt{(i-1)(D_c + h_k)}, i \geq 2 \end{cases} \quad (6)$$

According to the discrete water level method, flow regimes at all discrete points will be simplified into two components, namely weir flow and orifice flow. The discharge capacity of weir flow is constant, while the discharge capacity of the orifice flow regularly presents a progressive increase with the water head. According to the aforementioned formula, the difference in discharge capacity between point $i - 1$ and point i should be:

$$\Delta Q_{1i} = 2.7 n_c \omega_c \sqrt{(i-1)(h_c (or D_c) + h_k)}, i \geq 2 \quad (7)$$

The above formula will express the flow difference between the adjacent points. As the position of discrete water level points increases, the flow difference between the adjacent points will increase according to the aforementioned law. Therefore, only the discharge capacity at the second point ($i = 1$) needs to be calculated, namely the discharge capacity

under the state of weir flow, and the discharge capacity at the rest of the points can be superimposed automatically according to Equation (7).

Simultaneously, as for the lateral contraction coefficient $\varepsilon = 1 - 0.2\zeta_0 H_h/b_c$, the coefficient ζ_0 was taken as 0.8 in the flood routing system of tailing ponds according to relevant specifications since sidewalls on both sides of the window are rectangular and have no structure with irregular shape. Therefore, $\varepsilon = 1 - 0.16H_h/b_c$.

Meanwhile, as for coefficient A in Equation (6), since the water level chosen for the simplified algorithm is the center point of the window, $H_0/D_c = 1/2$; according to the relevant table, A = 0.45.

The point set was converted into a smooth curve and fitted into a function relation between the water level and discharge capacity in the free flow stage.

3. Step 3. According to the design characteristics of the flood-discharging system of tailing ponds, the parameters in empirical Formula (2) were simplified to determine the simplified calculation formula for half-pressure flow and the discharging curve under half-pressure flow according to the simplified algorithm. The simplification process of parameters is shown as follows:

① Simplification Process for Submerged Window Area

The water level step size for half-pressure flow was the same for free flow. The submerged window area ω_i at different positions can be calculated as follows.

The calculation method for the submerged window area of the square window is as follows:

$$\omega_i = \begin{cases} 0, i = 0 \\ [0.5 + (i-1)]n_c b_c h_c, i \geq 1 \end{cases} \tag{8}$$

The calculation method for the submerged window area of the circular window is as follows:

$$\omega_i = \begin{cases} 0, i = 0 \\ \left[\frac{\pi}{8} + (n_z - 1) \cdot \frac{\pi}{4}\right] n_c D_c^2, i \geq 1 \end{cases} \tag{9}$$

According to Equations (8) and (9), the submerged window area can be directly obtained at the specified water level step size.

② Simplification process for parameters f_2 and f_4. Parameters f_2 and f_4 can be determined when ω_i is determined.

③ Simplification process for parameter f_3. The downstream outlet section of the draining pipe in a tailing pond is generally consistent with the designed shape of calculating a pipe segment of draining pipe, so the parameter is $f_3 = 1$ in the simplified algorithm.

④ Simplification process for parameter ζ_2 and ζ_3. Since the draining pipe inlet is generally perpendicular to the draining well in a tailing pond, in the simplified algorithm for discharge capacity, the local head loss coefficient ζ_2 of the draining pipe inlet is =0.5 and the local loss coefficient ζ_3 of water diversion is =1.1.

⑤ Simplification process for parameter λ_j. Since the height of the draining well in tailing ponds is limited, and the well surface is smooth due to long-term exposure to water, the frictional head loss coefficient λ_j of the draining well in the simplified algorithm is 0.

⑥ Simplification process for parameter ε_b. There is no contraction section at the inlet section of draining pipe in tailing ponds, so the sectional contraction coefficient ε_b is 1.0.

Based on the simplified results of six parameters above, the discharge capacity calculation formula under half-pressure flow can be simplified as follows:

$$Q_{2i} = \frac{1}{\sqrt{1.5 + 3.2\left(\frac{F_e}{\omega_j}\right)^2 + \zeta_1\left(\frac{F_e}{\omega_i}\right)^2}} F_e \sqrt{2g(z_i - z_{jc})} \tag{10}$$

where Q_{2i} represents the discharge capacity of the half-pressure flow corresponding to the ith discrete water level point; F_e represents the sectional area of draining pipe inlet; ω_j represents the sectional area of draining well j shaft; ω_i represents the submerged window area corresponding to the ith discrete water level point; z_{jc} represents the center elevation of the entrance section of water conveyance structure; g represents gravitational acceleration.

The number and the type of parameters for the simplified calculation formula of discharge capacity under half-pressure flow were significantly reduced, facilitating the algorithm compilation.

The discharge capacity results under half-pressure flow at discrete points on different water levels were obtained according to Equation (10), and the results were then converted into the curve representing the functional relationship between the water level and discharge capacity.

4. Step 4. According to the design characteristics of the flood-discharging system of tailing ponds, the parameters in empirical Formula (3) were simplified to work out the simplified calculation formula for pressure flow and the discharging curve under pressure flow according to the simplified algorithm.

Simplification process for parameter ζ. The local head loss coefficient ζ on the draining pipeline is 0 as the draining pipe is generally short, and there are few corners, bifurcations and section changes in tail ponds. The rest of the parameters adopted the simplified results such as those in Step 3.

$$Q_{3i} = \frac{1}{\sqrt{1.5 + \sum \lambda_g \frac{L}{D} + \zeta_1 \left(\frac{F_e}{\omega_i}\right)^2 + 2.2 \left(\frac{F_e}{\omega_j}\right)^2}} F_x \sqrt{2g(z_i - z_{cc})} \tag{11}$$

where Q_{3i} represents the pressure flow discharge capacity corresponding to the ith discrete water level point, m^3/s; λ_g represents the frictional head loss coefficient of the draining pipe; L represents the length of the calculating pipe segment of the draining pipe, m; D represents the inner diameter of calculating the pipe segment of draining pipe, m; F_x represents the sectional area of the downstream outlet of the draining pipe, m^2; z_{cc} represents the center elevation of the draining pipe outlet section, m; ζ_1 represents the local head loss coefficient of the draining window.

The number and the type of parameters for the simplified calculation formula of the pressure flow discharge capacity were significantly reduced, which facilitated the algorithm compilation.

The calculation results of the pressure flow were re-fitted to the functional relationship between water level and discharge capacity.

5. Step 5. The curve of the final discharge capacity within the well height was calculated and fitted to a function. The method to determine the final discharge curve is as follows:

At each discrete water level point, the minimum value of discharge capacity results of the free discharge, half-pressure flow and pressure flow calculated in steps 2, 3 and 4, respectively, were taken as the final discharge capacity and the calculated results were stored.

$$Q_i = \min\{Q_{1i}, Q_{2i}, Q_{3i}\}, i = 0, 1, 2 \cdots \cdots n_z \tag{12}$$

6. Step 6. Judgment of discharge curve convergence beyond well height.

According to the fitted curve through Step 5, the water head increased at the set step size to determine the discharge capacity. $|Q_{k+1} - Q_k| < \varepsilon$, ε serves as a convergence criterion. The discharge capacity will no longer change upon the rising of the water level. The discharge capacity beyond the convergence water level point will be a constant value.

4. Results and Discussion

The simplified algorithms were adopted to calculate the process of the water head-discharge capacity of the physical model displayed in Figure 1, and the results were fitted, as shown in Figure 4.
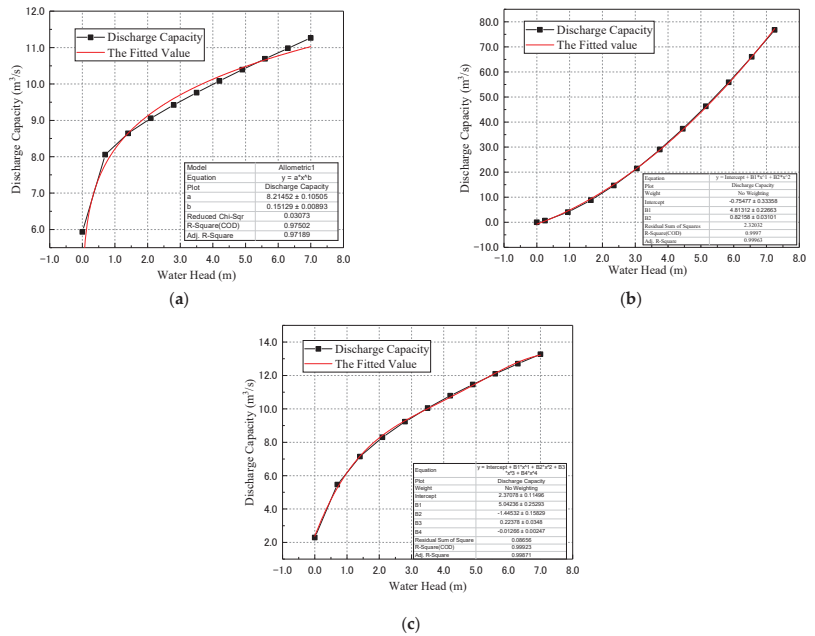
Figure 4. Fitted value of results calculated through simplified algorithm for discharge capacity: (**a**) free flow; (**b**) half-pressure flow; and (**c**) pressure flow.

Based on those fitted results, the water level elevation was gradually increased in a water level step size of 0.1 m. Then, the resulting curve on the water level-discharge capacity process and the calculation error compared with the accurate algorithm method in the free discharge stage were shown in Figures 5 and 6.

Figure 5. Figure on discharge capacity results from both simplified and accurate algorithms in the free discharge stage.

Figure 6. Figure on the errors of simplified and accurate algorithms in the free flow stage.

The calculation error of Figure 6 represents the difference between the results of an accurate algorithm method and the results of the simplified method, which was calculated according to Equation (13):

$$E_r = \frac{|Q' - Q|}{Q} \cdot 100\% \tag{13}$$

where Q represents the discharge capacity calculated by the accurate algorithm listed in Equations (1)–(3) for free flow, half-pressure flow and pressure flow, respectively, m³/s; Q' represents the discharge capacity calculated by the simplified method listed in Equation (5) (or Equation (6)), Equations (10) and (11) for free flow, half-pressure flow and pressure flow, respectively, m³/s.

The statistical data on calculation errors between the simplified and accurate algorithms are displayed in Table 2. According to the calculation results, the average error in the simplified algorithm is +4.19% as compared with the accurate algorithm. Errors in the early discharge stage are significant, with a maximum error of +15.8%. However, the discharge capacity is generally small in the early stage. The resulting difference inflow has little influence on the holistic process of flood routing. In the later period, as the water level rises, the calculation accuracy gradually improves and has relatively high overall accuracy.

Table 2. Statistical table on errors in both simplified and accurate algorithms in the free discharge stage.

Water Level (m)	Discharge Capacity from the Accurate Algorithm (m³/s)	Discharge Capacity from Simplification-Fitting Algorithm (m³/s)	Error (%)	Average Error (%)
400.5	1.60	1.86	15.80	
401.5	7.70	8.31	8.01	
402.5	16.04	16.41	2.31	
403.5	26.34	26.16	0.69	4.19
404.5	37.94	37.54	1.06	
405.5	51.30	50.57	1.42	
406.5	65.30	65.24	0.08	

Based on the fitted results, the water level is gradually increased in a water level step size of 0.1 m. The discharge capacity on each water level was calculated based on fitted results and compared with those calculated by the accurate algorithm. The resulting curve on the water level-discharge capacity process is shown in Figure 7, and the calculation errors compared with the accurate algorithm method calculated by Equation (12) in the half-pressure flow stage are shown in Figure 8.
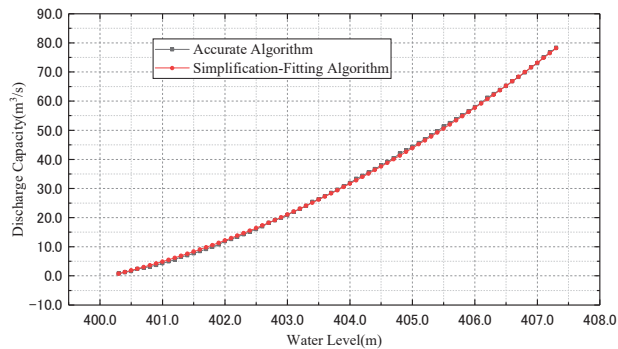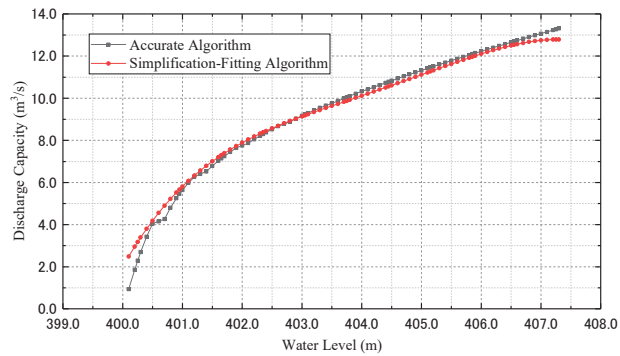
Figure 7. Figure on discharge capacity results from both simplified and accurate algorithms in the half-pressure flow stage.
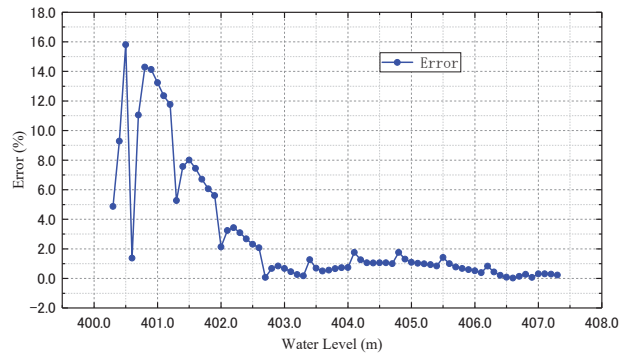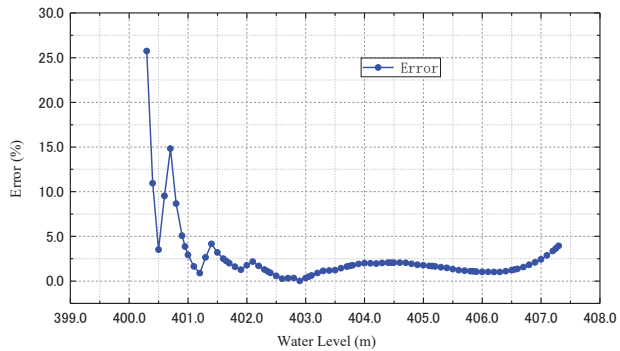

Figure 8. Figure on errors of simplified and accurate algorithms in the half-pressure flow stage.

The statistical data on the calculation errors between the "simplification-fitting" algorithm and the accurate algorithm are displayed in Table 3. According to the calculation results above, the average error in the "simplification-fitting" algorithm is +1.87%, as compared with the accurate algorithm. The error is large in the early stage of half-pressure flow. However, in light of the entire discharge process, the early stage belongs to the free discharge so the results from the simplified algorithm of half-pressure flow in the early stage will not be adopted; therefore, errors arising from this stage can be ignored.

Table 3. Statistical table on errors between the simplified and accurate algorithms in the half-pressure flow stage.

Water Level (m)	Discharge Capacity from the Accurate Algorithm (m³/s)	Discharge Capacity from Simplification-Fitting Algorithm (m³/s)	Error (%)	Average Error (%)
400.5	4.04	4.19	3.52	
401.5	6.79	7.00	3.20	
402.5	8.52	8.57	0.57	
403.5	9.75	9.63	1.22	1.87
404.5	10.83	10.61	2.07	
405.5	11.78	11.63	1.34	
406.5	12.66	12.50	1.21	

Based on those fitted results, the water level elevation is gradually increased in a water level step size of 0.1 m. The discharge capacity on each water level was calculated based on fitted results and compared with those calculated by the accurate algorithm. Then, the resulting curve on the water level-discharge capacity process is shown in Figure 9, and the calculation errors compared with the accurate algorithm method calculated by Equation (12) in the pressure flow stage are shown in Figure 10.
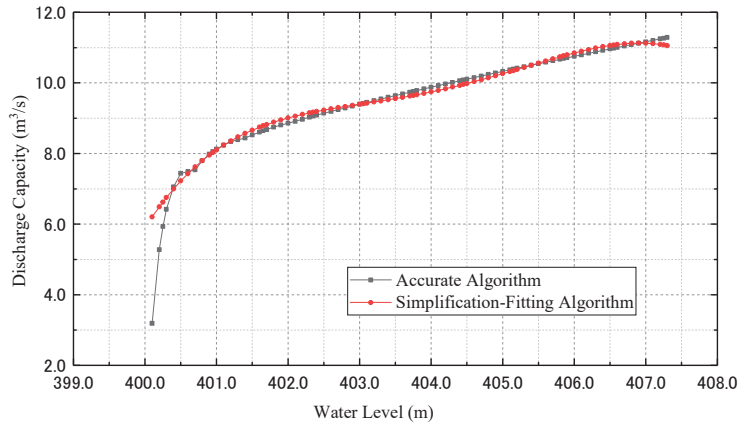
Figure 9. Figure on discharge capacity results from both simplified and accurate algorithms in the pressure flow stage.
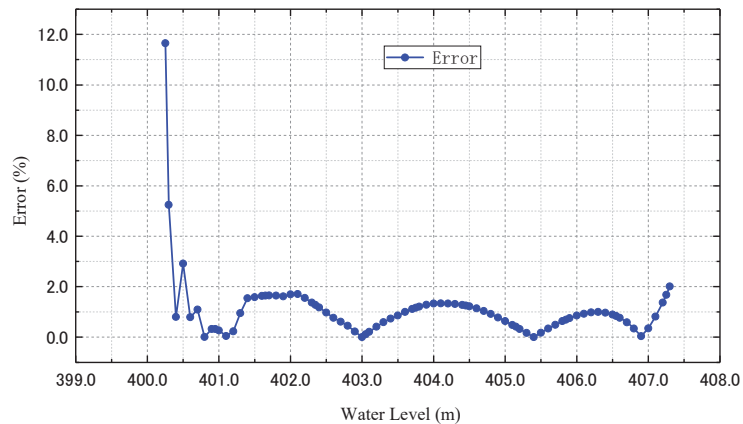
Figure 10. Figure on errors of simplified and accurate algorithms in the pressure flow stage.

The statistical data on calculation errors between the "simplification-fitting" algorithm and the accurate algorithm are displayed in Table 4. According to the calculation results, the average error in the simplified algorithm is +1.23%, as compared with the accurate algorithm. The error is large in the early stage. However, in light of the entire discharge process, the early stage belongs to the free discharge; therefore, the results from the simplified algorithm of pressure flow in the early stage will not be adopted; thus, errors arising from this stage can be ignored.

Table 4. Statistical table on errors between the simplified and accurate algorithms in the pressure flow stage.

Water Level (m)	Discharge Capacity from the Accurate Algorithm (m^3/s)	Discharge Capacity from Simplification-Fitting Algorithm (m^3/s)	Error (%)	Average Error (%)
400.5	7.44	7.22	2.91	
401.5	8.53	8.66	1.59	
402.5	9.14	9.23	0.97	
403.5	9.64	9.56	0.86	1.23
404.5	10.10	9.98	1.21	
405.5	10.54	10.56	0.17	
406.5	10.96	11.06	0.89	

In terms of the determination of the curve on the final discharge capacity within the well height, $Q_i = \min\{Q_{1i}, Q_{2i}, Q_{3i}\}, i = 0, 1, 2 \cdots\cdots n_z$, the results on the final discharge capacity within well height in this example are displayed in Table 5.

Table 5. Table on results of final discharge capacity within well height.

Water Level (m)	Discharge Capacity (m^3/s)
400.5	1.86
401.5	7.00
402.5	8.57
403.5	9.56
404.5	9.98
405.5	10.56
406.5	11.06

According to the determined convergence criterion $|Q_{k+1} - Q_k| < \varepsilon$, ε is the convergence criterion. The convergence criterion should match the distance between the discrete water level points. In this example, $\varepsilon = 0.50$. Therefore, the discharge capacity converged when the water level reached 406.5 m. Thus, in terms of water level above 406.5 m, a constant discharge capacity of 11.06 m^3/s should be the maximum discharge capacity value of this flood-discharging system.

5. Conclusions

This paper derived a "simplification-fitting" calculation method for window-type draining wells of a tailing pond. Several conclusions can be drawn:

- The "simplification-fitting" algorithm, together with the mathematical fitting method introduced, facilitated the expression of calculation formula for discharge capacity;
- The mathematical relationship existing in the discharge capacity between windows was deduced, thus the discharge capacity at the rest of the discrete points can be directly deduced once the discharge capacity at the first discrete point is known, and the calculation step of orifice flow can be omitted;
- Due to the unique discrete method concerning the water level, the parameters related to the water level in empirical calculation formulas under half-pressure flow and pressure flow were simplified;
- The final discharge capacity curve adopted the minimum value among the free flow, half-pressure flow and pressure flow on each water level step and thus avoided the difficulty in calculating the intersection point among the three discharge capacity curves;
- The average error in the "simplification-fitting" algorithm compared with the accurate algorithm for free flow, half-pressure and pressure flow stage is +4.91%, +1.87%, +1.23%, respectively.

The presented study refers to the simplification of a calculation method in a flood discharge system for a tailing pond. According to the empirical formulas, discharge capacity and water level are bonded by a complicated non-linear relationship, During the process of developing a flood routing system, if the discharge capacity under three flow regimes is calculated in strict accordance with the theoretical calculation formula, not only is it challenging to locate the intersection points of three discharge curves, but also formulas will grow complicated and parameters must be constantly changed, which will result in difficulties in terms of computer programming. The simplified method proposed in this study can meet the accuracy and efficiency requirements of automatic discharge capacity calculation by the flood-discharging system.

Institutional Review Board Statement: Not applicable.

Informed Consent Statement: Not applicable.

Data Availability Statement: Data will be available upon reasonable request.

Conflicts of Interest: The authors declare no conflict of interest.

References

1. Clarkson, L.; Williams, D. An Overview of Conventional tailing Dam Geotechnical Failure Mechanisms. *Min. Metall. Explor.* **2021**, *38*, 1305–1328. [CrossRef]
2. Koppe, J.C. Lessons Learned from the Two Major tailing Dam Accidents in Brazil. *Mine Water Environ.* **2021**, *40*, 166–173. [CrossRef]
3. Shahriari, M.; Aydin, M.E. Lessons learned from analysis of Los Frailes tailing dam failure. In Proceedings of the International Conference on Applied Human Factors and Ergonomics, San Diego, CA, USA, 16–20 July 2017; Springer: Cham, Switzerland, 2017; pp. 309–317.
4. Marti, J.; Riera, F.; Martínez, F. Interpretation of the Failure of the Aznalcóllar (Spain) tailing Dam. *Mine Water Environ.* **2020**, *40*, 189–208. [CrossRef]
5. Zhou, Z.G.; Li, P.; Guo, R. Reliability Analysis on Flood Control Capacity of Drainage System of a Certain tailing Pond in Huanren. *Min. Eng.* **2016**, *14*, 52–54.
6. Li, B.H.; Diao, M.J.; Yang, H.B. Hydraulic calculation of drainage system of tailing ponds. *J. Southwest Univ. Natl. Nat. Sci. Ed.* **2007**, *33*, 613–617.
7. Li, Y.H.; Dai, C.J. Discussion on discharge capacity calculations of drainage system of tailing ponds. *Heilongjiang Metall.* **2009**, *29*, 26–29.
8. Tan, J.J. Discharge capacity analysis of a tailing pond after drainage system combined. *Mod. Min.* **2016**, *7*, 220–221.
9. Liu, X.L.; Zhang, P.H.; Wang, X. Hydraulic Characteristic Research of Longtan Reservoir Spillway Diversion Tunnel. *J. Water Resour. Archit. Eng.* **2015**, *13*, 4.
10. Wang, Y.Y.; She, C.X.; Chen, Y.Q.; Chen, J.Y.; Jia, P.; Yin, Z.Q.; Li, Y.; Jin, J.C. Influence of Shaft Depth on Discharge Capacity of tailing Pond Flood System. *J. Water Resour. Archit. Eng.* **2017**, *15*, 133–137, 205.
11. Han, C. Hydraulic Model Test and Hydraulic Calculation of Tailing Pond Drainage System. Master's Thesis, Shijiazhuang Tiedao University, Shijiazhuang, China, 2017.
12. Du, Z.F.; Wu, W.W.; Wu, Y.G. Hydraulic Model Test of Flood Discharge System of a Large tailing Reservoir. *Nonferrous Met. Min. Sect.* **2019**, *71*, 64–71.
13. Djillali, K.; Abderrezak, B.; Petrovic, G.A.; Sourenevan, B.E. Discharge capacity of shaft spillway with a polygonal section: A case study of Djedra dam (East Algeria). *Water Sci. Technol. Water Supply* **2021**, *21*, 1202–1215. [CrossRef]
14. Fraga, I.; Cea, L.; Puertas, J. Validation of a 1D-2D dual drainage model under unsteady part-full and surcharged sewer conditions. *Urban Water J.* **2017**, *14*, 74–84. [CrossRef]
15. Zakwan, M.; Khan, I. Estimation of Discharge coefficient for side weirs. *Water Energy Int.* **2020**, *62*, 71–74.

16. Ebtehaj, I.; Bonakdari, H.; Gharabaghi, B. Development of more accurate discharge coefficient prediction equations for rectangular side weirs using adaptive neuro-fuzzy inference system and generalized group method of data handling. *Measurement* **2018**, *116*, 473–482. [CrossRef]
17. Sen, S. Surface pressure and viscous forces on inclined elliptic cylinders in steady flow. *Sādhanā* **2020**, *45*, 172. [CrossRef]
18. Dennis, S.C.R.; Young, P.J.S. Steady flow past an elliptic cylinder inclined to the stream. *J. Eng. Math* **2003**, *47*, 101–120. [CrossRef]
19. Mo, S.J. Numerical Simulation of Hydraulic Characteristics of Tailing Pond. Master's Thesis, Shijiazhuang Tiedao University, Shijiazhuang, China, 2016.
20. Zhao, J.Y. The Hydraulic Characteristic Research for Volute. Master's Thesis, Northwest A & F University, Xianyang, China, 2017.
21. Bao, Z.J.; Wang, Y.H. Three-Dimensional Numerical Simulation of Spillway Based on Flow—3D. *Zhejiang Hydrotech.* **2012**, *2*, 5–9.
22. Wang, Y.H.; Bao, Z.J.; Wang, B. Three-dimensional Numerical Simulation of Flow in Stilling Basin based on Flow-3D. *Eng. J. Wuhan Univ.* **2012**, *45*, 454–457, 476.
23. Ling, L.; Chen, R.C.; Li, Y.H. Three-dimensional VOF Model and its Application to the Water Flow Calculation in the Spilway. *J. Hydroelectr. Eng.* **2007**, *26*, 83–87.
24. Yi, C. Numerical Simulation of Hydraulic Characteristics of Tailing Pond. Master's Thesis, Nanchang University, Nanchang, China, 2016.
25. Yu, K.; Cheng, Y.; Zhang, X. Hydraulic characteristics of a siphon-shaped overflow tower in a long water conveyance system: CFD simulation and analysis. *J. Hydrodyn.* **2016**, *28*, 564–575. [CrossRef]
26. He, M.M. Discussion on Hydraulic Model Test and Numerical Simulation of tailing Pond Drainage System. *Constr. Decor.* **2021**, *7*, 48.
27. Wang, S.X. Discharge Capacity of Shaft Spillway with Framed Inlettower for High tailing Dam. *Met. Mine* **1994**, *5*, 36–39,47.
28. Wu, G.G.; Liu, X.F.; Lu, J.J.; Shen, L.Y. Comparison of Two Hydraulic Calculation Methods for Drainage System of tailing Pond. *Nonferrous Met. Eng. Res.* **2011**, *32*, 6–8.
29. Ning, F.; Li, X.U. Application of GMRES Algorithm in the Predictions of Two-Dimensional Inviscous Steady Flows. *Chin. J. Comput. Phys.* **2001**, *33*, 442–451.
30. Liu, C. Discussion on Flow Capacity of Chute Flood Drainage System in tailing Pond. *Ment. Mine* **2012**, *1*, 15–18.
31. Dang, N. Tailing Drainage Wells Experimental Study on Shape Optimization of Flood Discharge System. Master's Thesis, Xi'an University of Technology, Xi'an, China, 2010.
32. Shi, W. Discussion on Flood Discharge System Design of tailing Pond. *Nonferrous Mines* **2002**, *31*, 43–46.
33. Yu, D.X. Design and Optimization Method of Flood Discharge System in tailing Reservoir. *China Met. Bull.* **2018**, 268–269.
34. Shang, X.J.; Su, X.L. Design and Optimization Method of Flood Discharge System in tailing Reservoir. *Hydroelectr. Sci. Tecnol.* **2019**, *2*, 90–91.
35. Yang, M.J. Study on Optimization Technology of flood discharge system of a tailing pond. *World Nonferrous Met.* **2020**, *9*, 273–274.
36. Zhang, C.H. Software Development and Engineering Application of the Tailing Dam Complex Flood Drainage. Master's Thesis, Shijiazhuang Tiedao University, Shijiazhuang, China, 2015.
37. Ma, W.J. Software Development and Application of HydraulicCalculation of the Tailing Dam Drainage System. Master's Thesis, Shijiazhuang Tiedao University, Shijiazhuang, China, 2014.
38. Chen, H.; Li, R.L.; Jia, Y.; Wang, J.R. Discussion on calculation method of discharge capacity of drainage system. *Mod. Min.* **2015**, *31*, 180–183.
39. Reference Materials for Tailing Facility Design Writing Group. *Reference Materials for Tailing Facility Design*; Metallurgical lndustry Press: Beijing, China, 1980; pp. 621–628.

Piotr Mertuszka [1,*], Bartlomiej Kramarczyk [2], Mateusz Pytlik [3], Marcin Szumny [1], Katarzyna Jaszcz [4] and Tomasz Jarosz [4,*]

[1] KGHM Cuprum Ltd. Research & Development Centre, 2-8 Sikorskiego Street, 53-659 Wrocław, Poland
[2] NITROERG S.A., 1 Alfred Nobel Square, 43-150 Bieruń, Poland
[3] Conformity Assessment Body, Central Mining Institute, 1 Gwarków Square, 40-166 Katowice, Poland
[4] Department of Physical Chemistry and Technology of Polymers, Silesian University of Technology, 44-100 Gliwice, Poland
[*] Correspondence: piotr.mertuszka@kghmcuprum.com (P.M.); tomasz.jarosz@opayq.com (T.J.)

Abstract: Explosives are commonly used in the mining industry to extract minerals from hard rock deposits. Therefore, an efficient explosive should ensure that the appropriate blast outcome is achieved, taking into account the desired rock-breaking parameters and the costs of drilling and blasting works. Depending on the type of deposit and follow-up processes, a proper blast result may be characterized by fragmentation, muckpile shape, overbreaks, etc. Industry has struggled to respond to the demand for bulk emulsion explosives with improved energetic parameters, having so far been unable to do so safely, effectively, and cost-efficiently. Methods of improving blasting parameters mainly rely on introducing a variety of additives to the emulsion explosive formulation during production, which creates additional hazards at that stage. Alternative, safe methods of achieving an improved energetic performance of emulsion explosives are, therefore, highly desirable. This paper is focused on one such proposed method as a continuation of previous research works and the performance of a novel bulk emulsion formulation under real mining conditions during the firing of mine faces is described. The tests included density measurements over time, measurements of impact and friction sensitivity, measurements of the detonation velocity in blastholes, determination of brisance via Hess test, and analysis of rock fragmentation. Results were compared with those obtained with a commercially available bulk emulsion explosive, highlighting that the performance improvement achieved by the proposed emulsion modification method is not limited to artificial test conditions, but translates well into actual application conditions.

Keywords: underground mining; blasting; explosives; detonation velocity

1. Introduction

The growing demand for metals and minerals translates into the need for economically sound, effective, time- and material-efficient methods of mining. However, there are still some technical constraints associated with underground mining. Over the last few decades, the development of mining explosives has led to a continuous improvement in their energetic parameters while maintaining the highest effectiveness and safety of blasting operations. Emulsion explosives, frequently referred to as "the latest generation explosives", are a prime example of this trend, even though they were invented more than 50 years ago [1]. According to the data provided by the Federation of Explosives Manufacturers, the share of bulk emulsion explosives in the total usage of emulsions in Europe is more than 85%, with this share expected to increase even further in the coming years. This is mainly because no alternative methods of solid rock extraction have so far proven to be effective enough [2,3].

The mining industry is facing various challenges, such as the need for increased production, reducing the time of the entire technological cycle, lowering deposit exploitation costs and ensuring personnel safety, including the issue of the stability of underground openings [4,5]. One such challenge, related to drilling and blasting operations, is the general effectiveness of blasting, mainly in terms of explosive performance. The effect of blasting is directly influenced by the working capacity of explosives—which, in a much wider sense, may be defined as the quality of explosives. It should, however, be noted that, apart from a number of manufacturing parameters which influence the working capacity [6,7], the results of blasting are affected by many different technological parameters. They are only observed in real mining conditions and cannot be evaluated under laboratory conditions [8,9]. The most important factors from the adopted technology point of view are the diameter of the blastholes, method of initiation or time between charging of explosives, and firing.

According to recent studies [10], the detonation velocity increases with an increase in blasthole diameter. Velocity of detonation (VOD) is used as a basic parameter in the determination of the detonation pressure, which in turn represents the energy of the explosive [11,12]. The problem of the blasthole diameter is especially significant when high rock pressures are observed. This may lead to a reduction in blasthole diameters, while causing a reduction in the charge diameter, but may also cause some problems with charging (when using bulk emulsions). The initiation method in turn is important for the effectiveness of the production. When initiating with the detonator only, the distance between the detonator position and the stable detonation velocity value is much greater than when using proper boosters. However, according to previous research studies, this does not affect the final detonation velocity value of bulk emulsions [13] but may affect the VOD of ANFO explosives [14]. From a safety point of view, the time between charging the blastholes and firing seems to be the most important factor. This problem should be considered from two perspectives. The first is associated with the density changes in time, which means that detonation velocity decreases with reductions in density. Such an explosive becomes less energetic over time [15,16]. The second problem is connected with the sleep time of bulk emulsions [17]. The sleep time is the time after which the bulk emulsion loses its detonation capacity. As shown during field investigations, the sleep time may even reach 6 months after the charging [18], meaning that each undetonated explosive should be treated with extreme caution.

Other important factors that may only be observed in underground mines are the temperature of rock mass and ambient temperature. With the increase in depth, the primary rock mass temperature increases. Under such conditions, lower thermodynamic parameters of bulk emulsions may be expected and their efficiency, expressed as velocity of detonation, may be much lower [19,20]. A very important issue in the field of blasting effectiveness is also detailed identification of the interaction between the explosive and the rock mass, i.e., propagation of blast-induced fractures around the blasthole [21,22]. This should be treated as the first step in the selection of relevant explosives for given geologic and mining conditions. Therefore, it may be concluded that the determination of relationships between the above parameters and their efficiency is critical in formulating reliable and credible computational models describing the detonation process [23].

A recent study was conducted to develop and evaluate, under laboratory conditions, a novel sensitizing agent formulation for bulk emulsion explosives with improved energetic parameters [24]. The purpose of the study was to improve the effectiveness of blasting by replacing the commonly used sensitizer by novel formulations. The results proved that energetic parameters of new formulas were actually better in every aspect in relation to the standard explosive, used commercially. The greatest advantage is that the sensitization process is much faster and much more stable. Moreover, it was confirmed that new formulations are capable of detonation after 5 min and the final density remains stable after 30 min.

Since the mixing of components using mixing–charging units in mines is not as precise as manual mixing in laboratory conditions [25], the authors have made an attempt to verify selected detonation parameters under real mining conditions. For this purpose, one of the developed formulas was verified during regular faces firing and compared with the standard bulk emulsion. Finally, the effectiveness evaluation of such an emulsion was conducted. The tests included: density measurements over time, measurements of the detonation velocity in blastholes, determination of brisance via Hess test, and analysis of blasted rock fragmentation. In this paper, results of in situ trials using the underground mixing–charging units are presented, which should be treated as the continuation of work under development of a novel formulation of bulk emulsion explosive with improved energetic parameters.

2. Materials and Methods

Evaluation of the blasting effect has been conducted under real mining conditions in a deep mine in Poland and consisted of two rounds of trials, in each of which explosives in four faces were fired. Each trial included the firing of two faces charged with BK-2 and two with the commercially available E8L explosive for reference. The time interval between the two rounds of trials was two weeks.

2.1. Trial Site

A trial panel was located in a deep underground copper mine in Poland, in which the room-and-pillar mining method with roof deflection and pillar softening is practiced. The average depth of excavations is approximately 800 m below the surface. The orebody thickness does not exceed 1.8 m and is almost flat. It is formed from sandstone (2.8 m) and a thin shale stratum located near the roof (Figure 1).
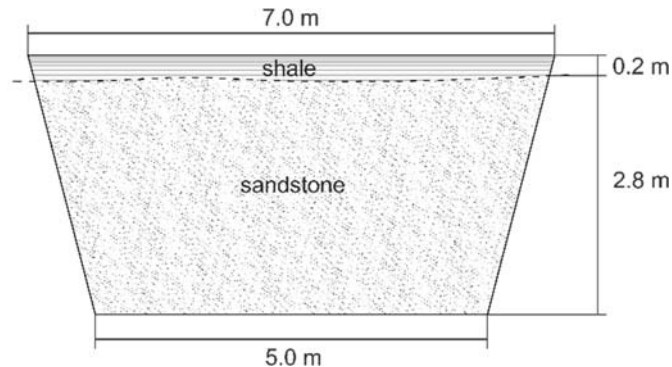
Figure 1. Scheme of the mining face cross-section, depicting the geologic structure and dimensions of the typical face over the considered panel.

Drifts are excavated using the drilling and blasting method. The shape of excavations is in the form of an inverted trapezoid, with the average base of 5 m and an average width of 7 m in the roof stratum. The height is approximately 3 m. Faces are fired using bulk emulsion explosives charged by standardized mixing–charging units installed on blasting utility vehicles. Explosives are initiated by non-electric detonators and explosive boosters. No stemming is used in blastholes.

The same drilling and blasting pattern with the V-cut was used on each trial and each face (same distribution of blastholes, same mass of explosives, same delays, etc.), as presented in Figure 2. The blastholes had a length of 3 m, except those charged with 2.5 kg of explosives (central ones), which were slightly shorter, and a diameter of 48 mm; thus, 3 m was also the expected advance per blast. The total number of blastholes was 41 per face,

total mass of explosives per face was 138.5 kg, and the total firing time was 5000 ms. The calculated powder factor was 2.40 kg/m^3.
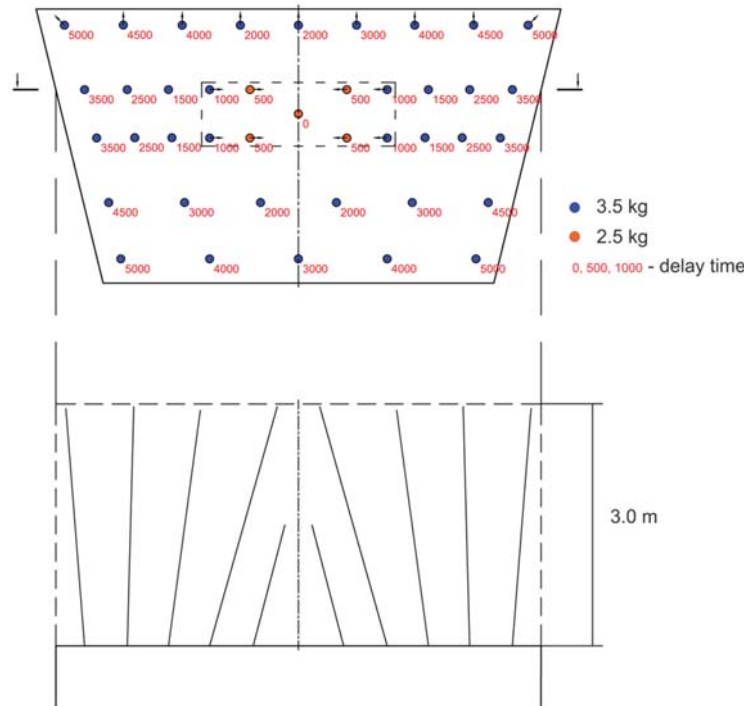
Figure 2. Drilling and blasting pattern used during underground trials: cross-section of the face (**upper**), topside view of the drilled blastholes (**lower**).

2.2. Formulations of Explosives and Mixing–Charging Unit

All tests, except the impact and friction sensitivity tests, were performed on the same batch of emulsion matrix (supplied by Nitroerg, Bieruń, Poland) for the underground bulk emulsion formula. The matrix contains ammonium nitrate, calcium nitrate, water, oil, emulsifier, and auxiliary components. The E8L emulsion was sensitized with a standard sensitizing agent—an aqueous solution of sodium nitrite. For the modified BK-2 formulation, a more comprehensive sensitizing agent formulation was utilized, as per the authors' earlier work [24], characterized by a lower water concentration (Table 1).

Table 1. Tested sensitizing agent formulations.

Component	Concentration (wt.%)	
	E8L	BK-2
Ammonium nitrate	–	47
Water	95.45	41
Sodium perchlorate	–	8
Sodium nitrate	4.5	3.3
ph modifier and dye	0.05	0.7

The mixing–charging unit was installed on a blasting utility vehicle. It mainly consists of the matrix and sensitizer tanks and pumps for the transfer of these components (Figure 3). The production unit is controlled by a computer for accurate dosing of ingredients. The mixing takes place in the middle of the loading hose, using a static mixer

(Figure 4). Former constructions were based on a single mixer, while new ones already have a double static mixer.
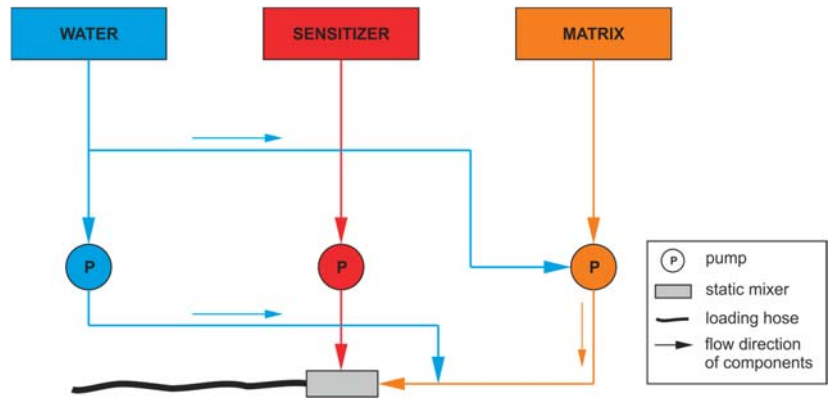
Figure 3. Simplified scheme of the mixing–charging units for bulk emulsions. Arrows indicate flow direction of the components.
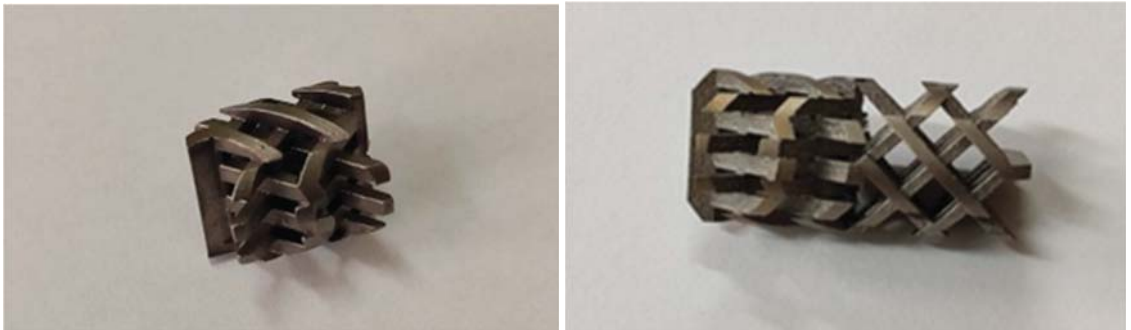
Figure 4. Photographs of the single (**left**) and double (**right**) static mixers.

The flow of components in the loading hose is laminar, thus, the mixing takes place using a cross-stream static mixer. However, due to large differences in the viscosity of components, the fast flow, and relatively short mixing time limited by the length of the static mixer, complete mixing is not possible, compared with manual mixing under laboratory conditions. Thus, in order to investigate the significance of this aspect for the first and second rounds of trials, a single mixer and a double mixer were employed, respectively.

2.3. Auxiliary Materials and Software

The probes used for the determination of detonation velocity were manufactured by MREL (Kingston, ON, Canada). They were VOD ProbeCables green with a unit resistance of 10.80 Ω/m. Dedicated software, DAS—Data Acquisition Suite, was used for data analysis from the VOD recorder.

Fragmentation analysis was carried out using WipFrag software, version 3.2.11.1, developed by WipWare (North Bay, ON, Canada). Photos of the muckpile after firing were taken using an Olympus Tough TG-6 camera (resolution 12 megapixels, lens aperture f/2.0) dedicated for extreme environments.

Statistical analyses were conducted using Statistica 13 software developed by StatSoft (Kraków, Poland).

2.4. Preparation of Explosive Samples and Charging of Blastholes

The explosive components were blended mechanically via standardized mixing–charging units used for charging blastholes in the mine hosting the study. In the case of the BK-2 formulation, the dosing settings of the sensitizer have been reduced by 3.5% due to much greater reaction activity.

Blastholes were loaded following a standard procedure, using the charging hose with 3.5 kg of bulk emulsion, except the cut holes, into which 2.5 kg were loaded. Due to the bottom initiation, the VOD in blastholes could be measured. The average length of the explosive column was 130–140 cm.

During the blastholes charging, the samples for the density measurements and brisance determination were loaded from the mixing–charging unit to the piping bag and then were carefully elaborated into the relevant plastic cups. For this purpose, a precise mobile digital balance was used.

The samples for the impact and friction sensitivity tests in turn were produced by the manual mixing of components, due to the relatively small mass of the sample required for such tests—the sample volume was insufficient for the use of a mechanical stirrer. After mixing, 10 mg samples were accurately weighed. The tests were conducted after the density had stabilized.

2.5. Measurements of the Density over Time

Plastic cups with a set volume of 500 cm^3 were used for the determination of density changes over time. They were weighed and filled with the mixture of the matrix and sensitizer directly from the mixing–charging unit. Due to the chemical reaction (sensitization), the mixture increased in volume, thus, the excess was removed from the top edge of the cup to maintain the set volume of the samples, followed by weighing of the cup. Each sample was weighed using an electronic balance, first at 5 min intervals for 60 min and then once each after 180 min and 1440 min. The density was determined based on the ratio of the net sample mass to the cup volume.

2.6. Determination of the Detonation Velocity

Detonation velocity values were obtained using the electrical method, via the continuous resistance wire technique. In this method, a precise measuring probe of known linear resistance is placed axially in the explosive column. When the detonation front progresses, the probe is destroyed, and the resistance of the entire circuit drops in proportion to the length reduction of the probe. Thus, a decrease in probe voltage vs. time is recorded by a dedicated measuring device.

In this research, a DataTrap II Data/VOD recorder manufactured by MREL (Kingston, ON, Canada) was used. This device allows independent measurements of detonation velocity to be taken using eight channels, allowing the simultaneous measurement of VOD in eight blastholes. The maximum recording rate in this system is 10 MHz per channel. The uncertainty of the measurements declared by the manufacturer is ±2%.

During underground trials, six-meter sections of the VOD ProbeCables were attached by electrical tape to the booster with a detonator and placed at the end of the loading hose. Blastholes were then charged according to the standard procedure, i.e., the loading hose was inserted to the bottom of the blasthole and the desired mass of the explosive was loaded. After that, the VOD probes from each tested face were connected to the communication (coaxial) cable and plugged to the recorder, which was located between the fired faces (Figure 5). The VOD probes were put into two cut holes in each of the four tested faces, which were fired with the first delay (same).
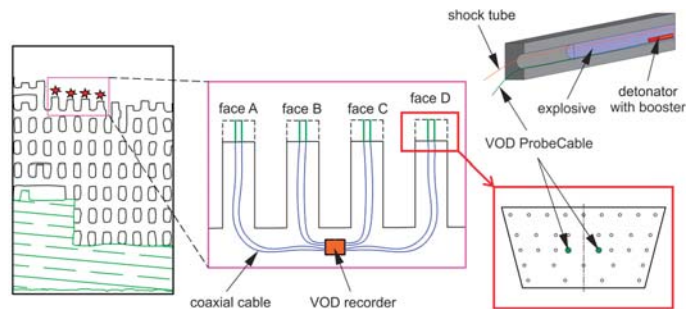
Figure 5. Scheme of the VOD measurements in blastholes with construction of the explosive charge.

The data analysis was performed with Data Acquisition Suite software, which converts the recorded data into a graph as a function of distance versus time. The software automatically calculates and displays the VOD of an explosive at any selected location in the graph.

2.7. Determination of Rock Fragmentation

Determination of the rock fragmentation was based on the image analysis method, which is one of the most common methods utilized to measure rock fragment size distribution in mines. It was carried out using a 2D photogrammetry method based on analysis of digital images of the muckpile using WipFrag software. The software applies an algorithm to detect edges, which are used to render a polygon around the particles, in order to determine the size–distribution [26,27]. To avoid issues caused by the spatial distribution of rock fragments in the muckpiles, each one was imaged multiple times during the hauling process (Table 2).

Table 2. Summary of images used for fragmentation analysis.

Trial Round	Face No.	Explosive Type	Number of Images
#1 (single mixer)	1	E8L	11
	2		12
	3	BK-2	10
	4		12
#2 (double mixer)	1	E8L	15
	2		14
	3	BK-2	16
	4		14

The photogrammetry method includes the following steps: (1) acquisition of multiple images representing each muckpile—pictures should be taken during hauling to depict different cross-sections of the muckpile, (2) image processing and analysis using a dedicated application—fragmentation analysis, and (3) determination of the size–distribution curve.

Since underground conditions are very difficult (no natural light, dust, humidity), one of the challenges is to ensure good quality of the photographs and reliable input data for analysis. Hence, pictures were taken by a camera with a low aperture and an additional light source in the form of a high-power LED flashlight. It should, however, be noted that this fragmentation assessment method has certain limitations caused by the image resolution and delineation algorithm. Therefore, photos were delineated automatically and corrected manually by adding or removing particle boundaries. At this stage, some fine areas were also indicated if needed. The images were scaled using an object with known dimensions; in this case, a bright foam ball, as presented in Figure 6.
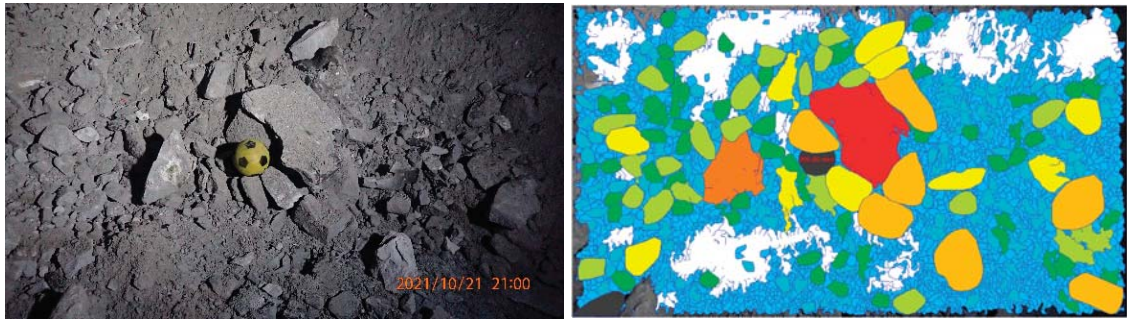
Figure 6. Sample photo of muckpile cross-section with a scaling ball (**left**) and part of the delineation process (**right**).

Any systems using photogrammetry methods can be characterized by a limiting size called fines cut-off (FCO), which means that below this value, the delineation is not reliable. Consequently, for fines regions (below FCO), an error between the real size of particles and those determined by analysis reaches the maximum value. Calculations of size–distribution below FCO can be performed using calibrated distribution models, such as Rosin-Rammler or Swebrec [28]. It should be noted that the calibration of distribution models requires the provision of sieving analysis data, which is very problematic or even impossible in normal underground operations. Thus, the model parameters were calculated statistically with the input of raw data obtained from image analysis. Statistical analysis was conducted using Statistica software. Calculation of model parameters was performed using the non-linear estimation method (user regression, least squares method). As the estimation function, the Swebrec equation was applied, which seems to be much better suited for blasting fragmentation and determination of fines regions [29,30].

The Swebrec model can be expressed by the following equation:

$$f(x) = \frac{1}{1 + [ln(x_{max}/x)/ln(x_{max}/x_{50})]^b} \tag{1}$$

where: $f(x)$—cumulative percent passing [%], x_{max}—size of the largest particle [mm], x—particle size [mm], x_{50}—particle size at 50% passing [mm], b—curve undulation.

The size of the largest particle was estimated in WipFrag software. Other parameters, such as x_{50} and b, were calculated in Statistica. In addition, it must be noted that, even in calibrated models, the error level below FCO can be significant (maximum value reaches 25–30% of FCO). Nevertheless, even non-calibrated models can provide valuable information on the fines distribution.

The rock fragmentation analysis consisted of firing explosives in 8 faces divided into 2 trials differing in mixer type, i.e., 4 faces per trial (2 charged with E8L and 2 with BK-2). Hence, all images in each trial concerned with a given type of explosive were analyzed together as one database. This was the basis for the determination of histograms and fragmentation curves.

2.8. Determination of Brisance via the Hess Method

Cylindrical lead rods of 99.97% purity were used for the determination of brisance, from which the cylinders with a diameter of 40 ± 0.2 mm and height of 60 ± 0.15 mm were made. The face surfaces were machined to 10 grade. They were placed vertically on the floor of excavation. Then, on the top of this cylinder, a cylindrical 1.7035 steel disc with a diameter of 41 ± 0.2 mm and height of 10 ± 0.2 mm was placed. Surfaces of steel discs were machined to 2.5 grade and hardened to 150–200 HB. A 50 g explosive sample loaded into a 3D printed plastic (PET-G) testing cup with an inner diameter of 40 mm and

height of 65 mm was placed on this plate and initiated, according to the scheme in Figure 7. As a result of firing, the lead cylinder was axially compressed. The change in the cylinder height was used as a measure of brisance. Samples were initiated using a standard 0.65 g PETN detonator. Since no reference material was tested underground due to the relatively high temperature, the results were compared with each other.
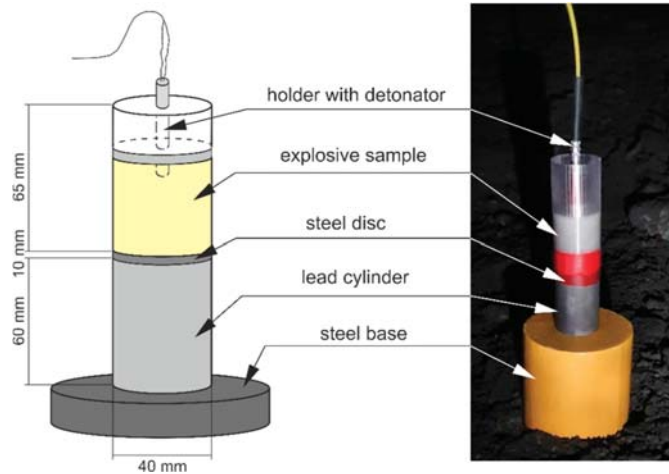
Figure 7. Scheme (**left**) and view of the sample (**right**) for determining brisance via the Hess method.

2.9. Determination of Impact and Friction Sensitivity

Determination of the sensitivity of explosives to mechanical stimuli covered the impact and friction sensitivity tests. As accepted, due to dynamic stimuli, stress and strain may appear in the explosive, which results in local heating. Those areas of local heating are the most likely causes of the explosive's initiation [31]. Both tests were conducted under laboratory conditions prior to large-scale underground trials.

The principle of the impact sensitivity test is that the sample of the tested explosive is subjected to the action of a drop weight. As a result, the mass of the drop weight and the drop height at which the initiation may occur is determined. For the impact sensitivity determination, the Kast fall hammer was used (Figure 8). In this test, a 40 mm^3 sample of the explosive was placed using a spatula into the open piston device, which is comprised of two steel rollers and a hollow cylinder. Then, the second roller was carefully placed onto the piston to not damage the structure of chemical sensitization and pushed up to the sample. The drop weight was then positioned at the desired height using a locking device. In this test, drop weights with a mass of 5 kg and 10 kg were used. The height varied from 20 cm to 50 cm, which represents the impact energy from 10 J to 50 J (5 J interval from 10 J to 40 J and also 50 J). Six trials were conducted for each energy and each type of explosive, which gives 2 × 48 samples. The results of the test are reported as initiation (sound, light effect, smoke) or non-initiation, in accordance with the EN 13631-4:2002 standard [32].

For the friction sensitivity determination in turn, the Peters friction apparatus was used (Figure 9), in which friction is created electromechanically between the porcelain cylinder and the plate with the explosive sample. In this test, similar to the impact sensitivity test, a 10 mm^3 sample of explosive was placed on a flat porcelain plate attached to the sliding carriage of the device. The porcelain cylinder clamped on the carriage was then lowered using the weight mounted on the loading arm. The movement of the plate with the sample was provided by a motor (stroke length 10 mm). In this test, six trials were conducted for each loading, representing the normal force starting from 360 N (load of 10.8 kg lowered at a distance of 360 mm). If detonation was observed at least once in six trials, the next

six samples were tested using smaller loading at intervals specified in the EN 13631-3:2004 standard [33]. As before, the tests were conducted for each type of explosive.
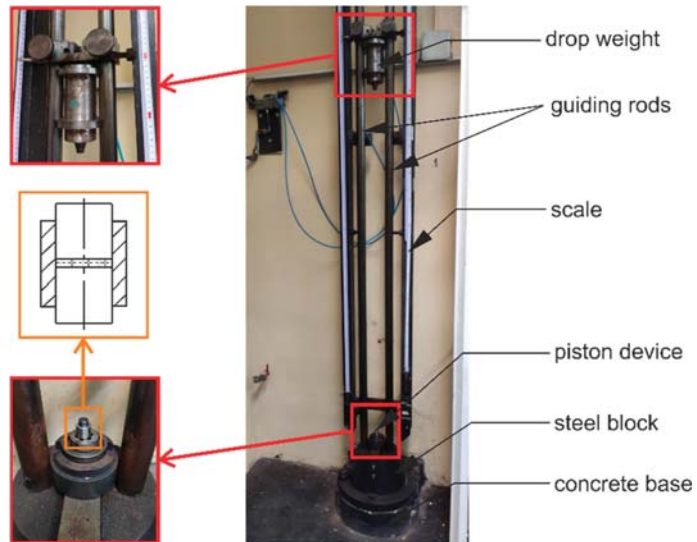
Figure 8. Scheme of the Kast fall hammer test.
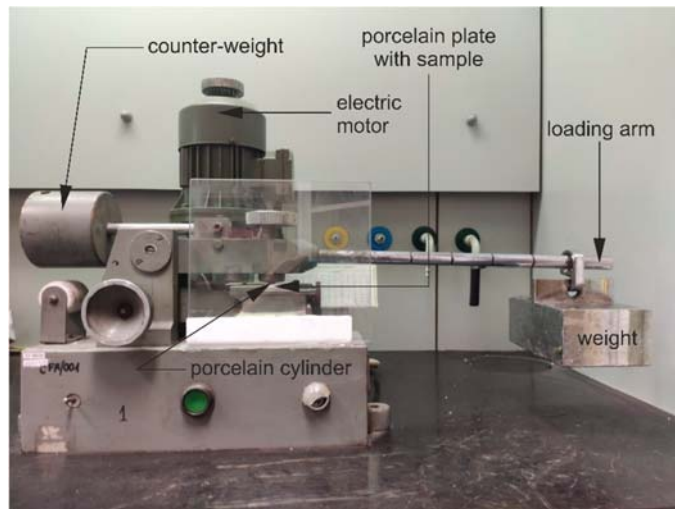
Figure 9. Peters friction apparatus.

3. Results

3.1. Impact and Friction Sensitivity

The tests of impact and friction sensitivity were carried out under laboratory conditions to verify the sensitivity level of explosives to mechanical stimuli, before underground trials could be conducted. A criterion was set that the proposed explosive formulation cannot be more sensitive to impact and friction than the commercial E8L explosive.

Among 48 samples tested in the energy from 10 J to 50 J, no sample showed initiation (no sound, no light effect, no smoke) by impact. The same applies to the E8L

and BK-2 formulations, which means that the impact sensitivity value of both explosives exceeded 50 J.

No detonation was observed during the friction sensitivity tests of the two explosive formulations either. None of the 12 tested samples were initiated under the loading of 10.8 kg lowered at a distance of 360 mm, indicating that the friction sensitivity value of both the E8L and BK-2 explosives exceeded 360 N.

3.2. Density

The explosive samples were sensitized chemically and, due to the reaction of ammonium nitrate and sodium nitrite, a gradual decrease in sample density over time was observed. This directly affects the detonation parameters and is the key issue for mine operators to maintain high effectiveness of mining. Thus, such emulsions are desired, achieving the final density and stabilizing within a relatively short and practically justified time. This time depends on the type of mine and adopted technology. The density measurements were conducted for each trial and each type of explosive was tested based on three samples. The results are presented in Figure 10 as the average values from three samples and deviation between the maximal and minimal.
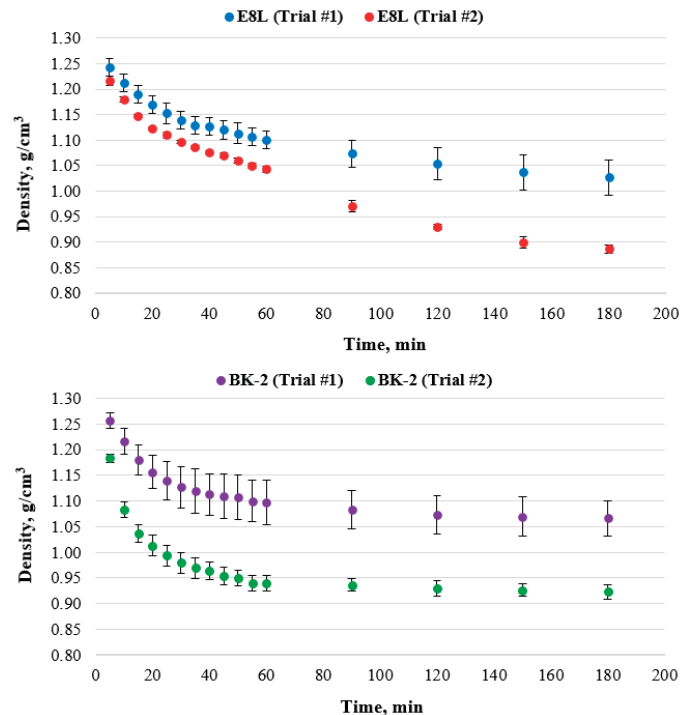
Figure 10. Graphs of changes in the density of explosives in time: E8L (**top**) and BK-2 (**bottom**).

The analysis results indicate that the blending of components using a double static mixer (#2) is much more precise than blending with a single mixer (#1). This is shown by different density values of specific samples in trial #1. In turn, the differences between densities measured in trial #2 are much closer to each other. Smaller dispersion is also observed. This indicates that thorough blending is critical for maintaining higher detonation parameters, since the sensitizer is more evenly distributed throughout the entire mass of the matrix—greater reaction surface, and thus, greater gas volume and lower density. Thus, a double static mixer is highly recommended for further blasting operations.

The novel BK-2 formulation initially showed a much more rapid density decrease than the E8L formulation. However, the density of the BK-2 formulation stabilized after approximately 30 min, unlike E8L, whose density continued decreasing noticeably, even after 180 min. In fact, all the densities measured in trial #2 reached a similar final density value; nevertheless, the decrease observed between 30 min and 180 min for BK-2 was approximately 0.06 g/cm^3, and as much as 0.21 g/cm^3 for E8L.

3.3. Brisance

Detonation performance is fundamental in the evaluation of high explosive power and describes the energetic capacity of explosives, and therefore, their power, strength, or energy. The results are presented without units using other parameters, such as degree of compression of the metal cylinder in the case of the brisance test. The results of Hess lead block compression tests for the E8L and BK-2 formulations are presented in Figure 11.
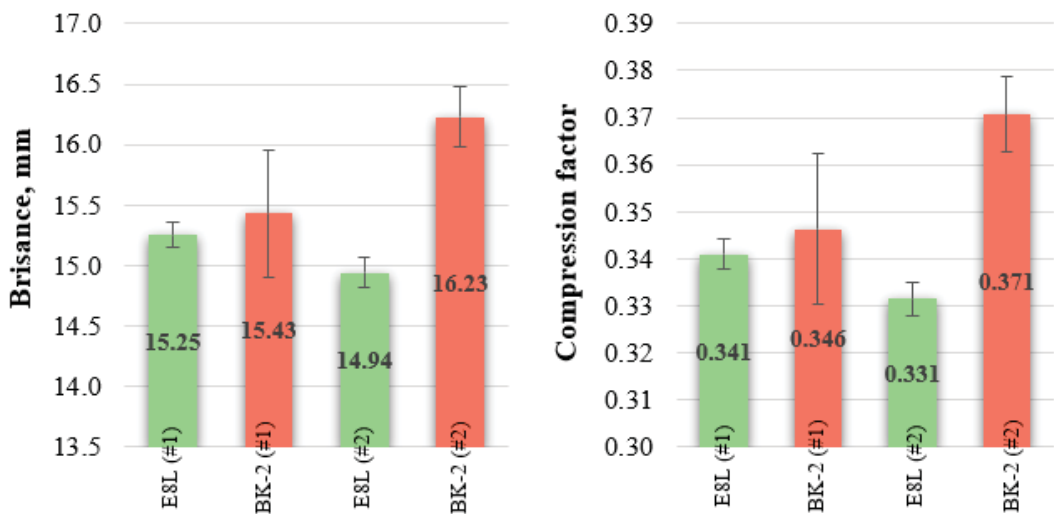
Figure 11. Comparison of brisance (**left**) and compression factors (**right**) determined for the tested explosives using the Hess method.

The in situ trials have proven that the brisance of the BK-2 formulation is higher than that of the standard E8L explosive. This may be mainly observed for the BK-2 samples in trial #2, in which a double mixer was used. The average compression factors for a single mixer in trial #1 for both explosives are similar and remained within the uncertainty of measurement. However, high dispersion between samples for BK-2 in trial #1 may be observed, indicating some mixing problems and that the explosive was not homogeneous. In the case of the double mixer, a 12% increase in the compression factor was observed for BK-2 in relation to E8L.

3.4. Detonation Velocity

In principle, the results of detonation velocity measurements of confined explosives (in blastholes) are higher than those detonated in the open air. This is mainly because the force and pressure produced by detonation is intensified on a much smaller area. However, as stated before, the VOD is affected by many parameters, especially when measuring in situ. The VOD measurements were conducted during each trial and each type of explosive was tested (four tests per explosive per trial). The time between charging the blastholes and faces firing was approximately 150 min. The results are presented in Table 3.

Table 3. Summary of the results of detonation velocity measurements.

Trial no.	Test No.	Velocity of Detonation [m/s]	
		E8L	BK-2
	1	3710	3760
#1 (single mixer)	2	3850	3735
	3	3880	3890
	4	3720	3895
	1	4030	4000
#2 (double mixer)	2	4060	3990
	3	4000	4060
	4	3990	4070

As proven during laboratory tests, the lower water content in the new formulation causes an increase in the velocity of detonation. However, such a conclusion has not been confirmed by underground tests. The average VOD of E8L measured in trial #1, in which a single static mixer was used, reached 3790 m/s, while the average VOD of BK-2 was 3820 m/s. The difference in the average values was 30 m/s only. However, having in mind that the uncertainty of the measurements in the system used is ±2%, it may be assumed that the achieved VOD is similar for both explosive formulations.

Similar conclusions may be drawn from trial #2, in which a double mixer was applied. The average value of VOD in the case of E8L was 4020 m/s and 4030 m/s for BK-2. This means that the detonation velocity of BK-2 was not improved during the large-scale field tests in comparison with the results obtained during laboratory testing.

When analyzing the average VOD from both trials, an almost 6% increase was observed in trial #2, in which the double static mixer was used. The average detonation velocity (based on eight blastholes) increased from 3805 m/s in trial #1 to 4025 m/s in trial #2. This proved that precise blending is crucial to maintain higher detonation parameters of AN-based bulk emulsions.

3.5. Rock Fragmentation

Taking of the muckpile pictures started after approximately 90 min following the completion of blasting. This was required for ventilation and removing of post-blast fumes. A loader with a bucket capacity of 4 m^3 was used to haul the excavated rocks. The total volume of the ore from a single face was approximately 55 m^3. The pictures were taken immediately after each bucket was collected. While hauling, 104 pictures in total were taken, including 45 in trial #1 and 59 in trial #2.

The analysis of the data collected during trial #1 included 23 pictures for E8L and 22 for BK-2 (sum from two faces). In the case of trial #2, the analysis of the size–distribution curves was based on 29 and 30 images, respectively, for the E8L and BK-2 explosives. The calculated fragmentation curves for both trials are shown in Table 4.

Based on Table 4, one may conclude that there is a slight difference in fragmentation between faces blasted with E8L and BK-2. The size–distribution of the outcome from E8L in trial #1 shows that more "fines" were produced in comparison with BK-2, which is a little coarser. Nevertheless, the differences do not exceed 10%. The difference in fines fraction (<3.16 mm) is approximately 5% and the content of particles bigger than 465 mm reaches 4.9% for BK-2 and 9.7% for E8L. In trial #2 in turn, there is hardly any difference in fragmentation between faces blasted using E8L and BK-2. In the range of 3.16 mm up to 1000 mm, the difference does not exceed 2% (the content of fines was approximately 35.00% for E8L and 34.05% for BK-2). Similar results were observed for coarse fractions (>465 mm), in which the content was 3.14% for E8L and 2.34% for BK-2.

For reliable determination of the fines content in both cases, the Swebrec model was applied and model data parameters were estimated using WipFrag software. Determination of parameters was based on data above FCO, which was set for 10.0 mm. Below this value, the fragmentation curve is almost flat up to 3.16 mm, which is a limit value for the applied system (lower particles cannot be recognized by the algorithm). This indicates that resolution of the system in this area was poor and the error increased rapidly. All estimated parameters for both trials are presented in Table 5. The confidence level was 95%.

As mentioned before, the Swebrec function is much more reliable for the description of the fines region in terms of blasting. Since very good fitting of the model to the data (above FCO) was observed, cumulative fragmentation curves for both trials and both types of tested explosives using the Swebrec function were compared, as shown in Figure 12.

Table 4. Cumulative fragment size–distribution curves (blue) and histograms (red) for considered cases.
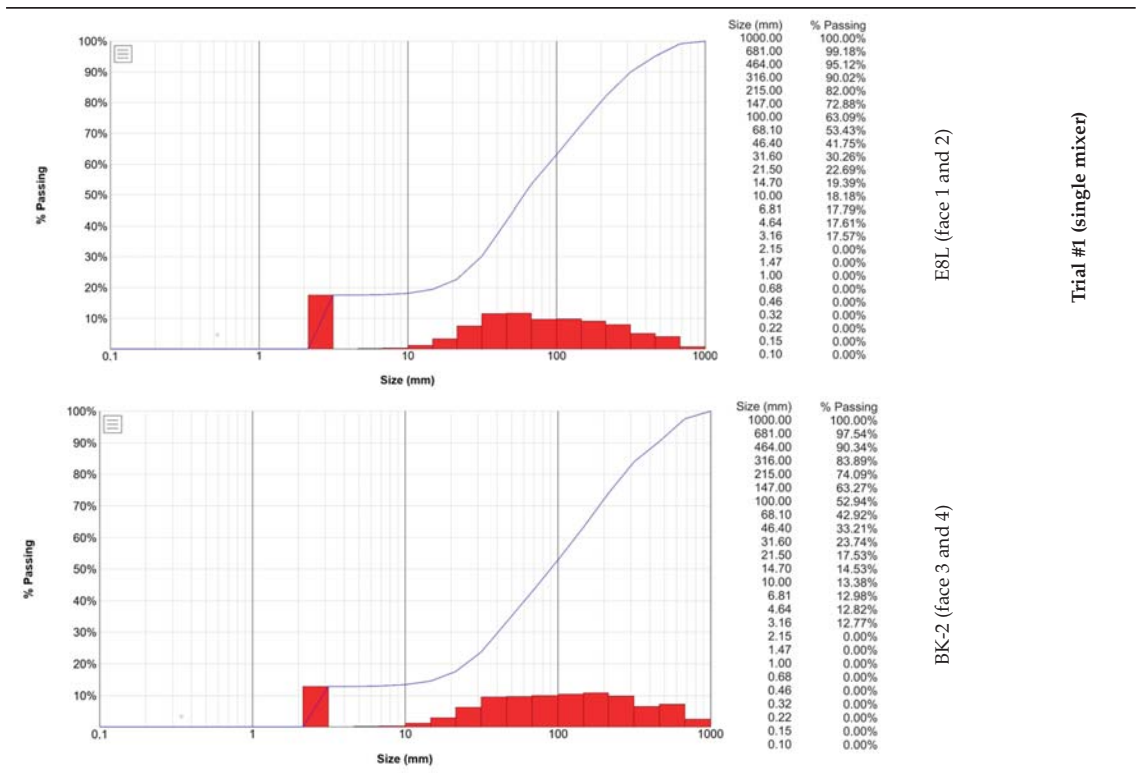
Table 4. *Cont.*
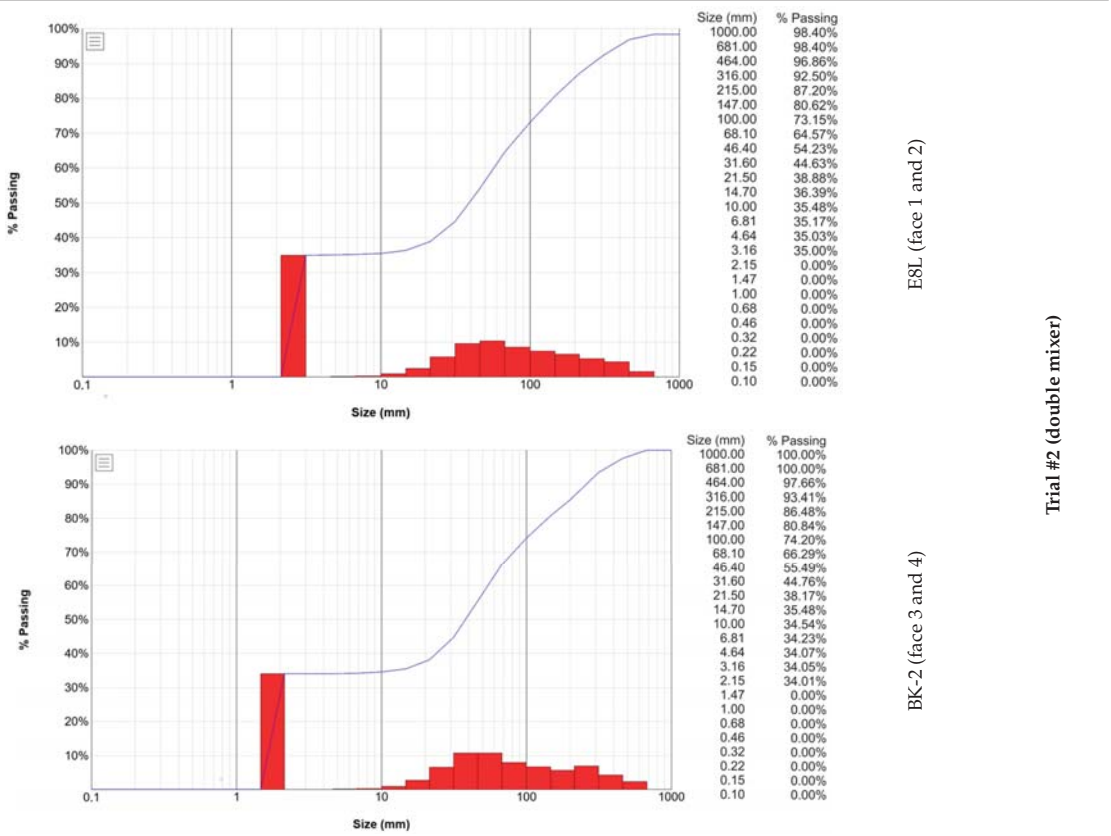
Table 5. Estimated model parameters of the distribution model for both trials.

Explosive Type	Parameter	Value	Standard Error	Confidence Limit	
				Lower	Upper
Trial #1 (single mixer)					
E8L	x_{max}	684 mm	n/a	n/a	n/a
	x_{50}	69.50 mm	3.03 mm	62.75 mm	76.25 mm
	b	2.50	0.13	2.21	2.82
BK-2	x_{max}	866 mm	n/a	n/a	n/a
	x_{50}	100.14 mm	4.30 mm	90.57 mm	109.72 mm
	b	2.48	0.13	2.20	2.77
Trial #2 (double mixer)					
E8L	x_{max}	1080 mm	n/a	n/a	n/a
	x_{50}	35.09 mm	1.56 mm	31.66 mm	38.52 mm
	b	2.61	0.11	2.37	2.86
BK-2	x_{max}	608 mm	n/a	n/a	n/a
	x_{50}	35.86 mm	1.85 mm	31.73 mm	39.99 mm
	b	2.08	0.11	1.83	2.32
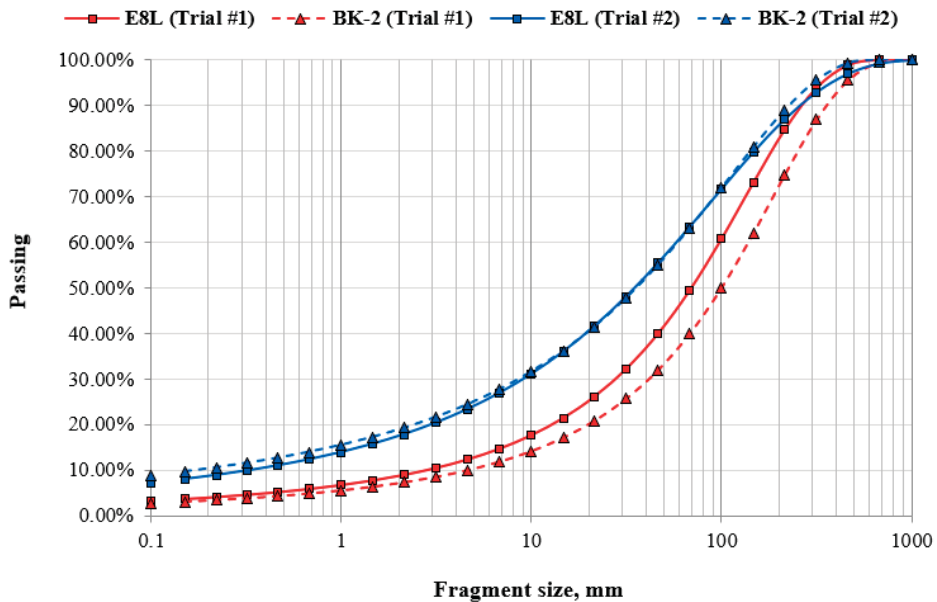
Figure 12. Comparison of Swebrec models for both trials.

From Figure 10, one may conclude that the maximum differences between the given fractions in trial #1 slightly exceed 11%. The maximum difference is 11.1% and can be observed in the range of particle size between 50 mm and 200 mm. In the fines region in turn, the differences are negligible. Finally, it can be concluded that, from a practical point of view, the changes in the fragmentation distribution obtained in trial #1 using two types of explosive are insignificant and do not have a major impact on the blast outcome in relation to fragmentation. Similar conclusions may be drawn from the results of trial #2, in which a double static mixer was used. The plotted curves showed that there was hardly any difference between both cases. It can, therefore, be concluded that the type of explosive and the mixing method did not affect the fragmentation of blasted rocks. However, it should be emphasized that there is a visible difference between the fragmentation achieved in trial #1 and trial #2, indicating a significant influence of the mixing method. Much better fragmentation was achieved for both explosives in trial #2, in which a double mixer was used.

4. Discussion

The results of the research showed that parameters of the novel bulk emulsion explosive with improved energetic parameters obtained during underground trials are not, in principle, consistent with results obtained in the first phase of investigations under laboratory conditions. Differences in the energetic performance of the two explosive formulations are relatively minor. Most of the tested parameters are similar for each type of explosive and each type of component mixing (single or double static mixer). The novel BK-2 formulation exhibits a similar sensitivity level to mechanical stimuli (impact and friction) as the standard E8L explosive.

The sensitization of BK-2 is much faster and much more stable than that of E8L. In underground conditions, where temperature usually ranges from 25 °C to 35 °C, it is capable of detonation after 5 min. Moreover, the final density is obtained after approximately 30 min. In comparison, the standard E8L explosive in such conditions is capable of detonation after at least 30 min. It usually achieves the final density after more than 12 h. In addition, the time between the loading of blastholes and firing varies depending on the location of the blasting site, which is limited by the ventilation constraints.

It should, however, be noted that sensitization cannot be too rapid, because an excessively fast reaction will cause certain difficulties from a practical point of view, such as an increase in pressures and other problems related to the mixing–charging unit. However, the were no significant problems with the loading unit for the BK-2 formulation and all the pressures and flows were normal. On the other hand, it is much better and safer, while charging, to operate with emulsion that is not capable of detonation. Thus, this time should not be too short. It should definitely be reduced in relation to the standard E8L, but within reason. More important, however, is the stability of the BK-2 formulation, which became stable after about 30 min.

In terms of the brisance determination via the Hess method, the BK-2 and E8L formulations achieved comparable values when using a single mixer. In the case of a double mixer (trial #2), an approximately 12% increase in the compression factor was observed for the BK-2 formulation in relation to E8L. In comparison, the difference in brisance obtained under laboratory conditions for BK-2 was almost 32% higher than the brisance of E8L. This shows how precise mixing influences the working capacity of novel formulations of explosives. It should also be noted that the brisance results cannot be referenced to results of high explosive samples due to safety constraints. Moreover, the impact of high temperatures of lead cylinders on results has not been defined so far. Thus, the results were compared with each other.

The measurements of detonation velocity did not prove the results obtained during laboratory tests., i.e., that lower water content in the new formulation will cause an increase in the detonation velocity. In conditions where the emulsion components were blended manually, the VOD of BK-2 was, on average, almost 19% higher than that obtained for E8L. The in situ tests have confirmed that the differences in the average values remained within the uncertainty of the measuring system in both trials, which means that the detonation velocity of novel formulations was not improved during the large-scale field tests.

In the case of blast fragmentation analysis, it may be stated that the differences in the fragment size–distribution in both trials are insignificant. The shape of plotted curves from each trial and for each type of explosive are similar. Thus, it may be concluded that for given mining and geologic conditions, the type of explosive and the method of component mixing did not affect the fragmentation of blasted rocks.

There is, however, one issue to which special attention should be paid. This is the method of component mixing using a static mixer. In this research, single (trial #1) and double (trial #2) static mixers were implemented and verified. The mixture of the matrix and sensitizer is much more homogeneous when using a double mixer than when using a single one. In fact, the mixture is not homogeneous, but far better blended using a double mixer, which was confirmed by different density values of specific samples in trial #1. Meanwhile, the differences between densities measured in trial #2 are much closer to each other. This proves that precise blending is critical for maintaining higher detonation parameters and a double static mixer is recommended for both the E8L and BK-2 formulations. In the case of BK-2, a much greater effect of precise mixing on the spread of density values may be observed. Thus, one can expect that the refinement of the mixing system for a novel formulation will result in a significant improvement in energetic parameters, which has been proven during laboratory tests where the mixing was very precise and almost perfect. In contrast to E8L, the BK-2 formulation is based on a hybrid sensitization, i.e., that apart from the gassing reaction, the reaction of precipitating fine ammonium perchlorate crystals in the matrix occurs in parallel, which can only be achieved with very precise mixing of components.

The same conclusion can be drawn from the brisance tests, in which the highest compression factor was obtained for BK-2 when a double mixer was used. From a detonation velocity point of view, an approximately 5–6% increase in average values was observed in tests with a double static mixer. The average VOD measured for E8L increased from 3790 m/s to 4020 m/s and from 3820 m/s to 4030 m/s for BK-2. This proves that slightly higher detonation velocities may be achieved when a double static mixer is used. Finally,

this finding also applies to the results of fragmentation, which was improved by more than 20% in some fragment size ranges, when the double mixer was used.

5. Conclusions

A comparison of the results of experiments conducted in actual use conditions and those conducted in laboratory conditions, discussed in our previous work [24], shows that the emulsion explosive densities obtained under laboratory conditions cannot be obtained using commonly used mixing–charging units, due to the method of component mixing. Despite the inadequate mixing of BK-2, its performance is comparable to that of E8L.

Consequently, developing a mixing–charging system that would allow a sufficient degree of mixing to be achieved and, therefore, allow peak performance of BK-2, is an important aspect of future work on modifying emulsion explosive formulations. Taking into account the prospective results of laboratory tests and the observations from the presented work, achieving the above goal necessitates further tests, so as to refine and redevelop the mixing method for the BK-2 formulation.

On the other hand, despite the use of a single mixer and inaccurate mixing, no misfires were observed for BK-2, and the produced explosive has similar physical parameters to those of the standard E8L emulsion explosive formulation. This indicates that the BK-2 formulation exhibits a high degree of tolerance to technical issues or errors taking place during the charging of the blastholes, potentially alleviating occurrences which would otherwise compromise the viability of a less error-tolerant emulsion explosive formulation. It should also be highlighted that the faces were loaded using a mixing–charging unit that was designed specifically for the standard E8L emulsion explosive formulation. Nevertheless, the results achieved for the novel BK-2 formulation are very promising. From a mining point of view, the greatest advantage of this formulation is its rapid stabilization of the density over time.

In summary, a significant improvement in the sensitization rate, a shorter time required to reach the final emulsion explosive density, and an increased stability of the sensitized bulk emulsion have all been achieved. This is especially important when firing several faces loaded at different times. Although the rate, at which the final parameters of the bulk emulsion explosive are achieved can in principle be further shortened, further work needs to take into account that the sensitization process cannot be too rapid, because an excessively fast reaction will cause certain practical and technical difficulties, such as increased pressure in the blastholes, as well as possibly introducing inhomogeneity defects in the sensitized emulsion explosives.

Author Contributions: Conceptualization, P.M. and B.K.; methodology, P.M., B.K. and M.P.; validation, P.M., T.J. and K.J.; formal analysis, P.M., B.K., M.P. and M.S.; investigation, P.M., B.K., M.P. and M.S.; data curation, P.M., B.K., M.P. and T.J.; writing—original draft preparation, P.M., B.K., M.P., M.S. and T.J.; writing—review and editing, P.M., T.J. and K.J.; visualization, P.M., B.K., M.P., M.S. and T.J.; supervision, P.M. and T.J.; project administration, P.M. and B.K.; funding acquisition, T.J. and K.J. All authors have read and agreed to the published version of the manuscript.

Data Availability Statement: Not applicable.

Conflicts of Interest: The authors declare no conflict of interest.

References

1. Bluhm, H.F. Ammonium Nitrate Emulsion Blasting Agent and Method of Preparing Same. U.S. Patent 3447978, 3 June 1969.
2. Sifferlinger, N.A.; Hartlieb, P.; Moser, P. The importance of research on alternative and hybrid rock extraction methods. *BHM Berg- und Hüttenmännische Monatshefte* **2017**, *162*, 58–66. [CrossRef]
3. Pickering, R.G.B.; Young, C. Controlled foam injection: A new and innovative non-explosive rockbreaking technology. *J. S. Afr. Inst. Min. Metall.* **2017**, *117*, 237–243. [CrossRef]
4. Ranjith, P.G.; Zhao, J.; Ju, M.; De Silva, R.V.S.; Rathnaweera, T.D.; Bandara, A.K.M.S. Opportunities and challenges in deep mining: A brief review. *J. Eng.* **2017**, *3*, 546–551. [CrossRef]
5. Fairhurst, C. Some challenges of deep mining. *J. Eng.* **2017**, *3*, 527–537.

6. Sil'vestrov, V.; Plastinin, A.; Karakhanov, S.; Zykov, V. Critical diameter and critical thickness of an emulsion explosive. *Combust. Explos. Shock Waves* **2008**, *44*, 354–359. [CrossRef]
7. Mendes, R.; Ribeiro, J.; Plaksin, I.; Campos, J.; Tavares, B. Differences between the detonation behavior of emulsion explosives sensitized with glass or with polymeric micro-balloons. *J. Phys. Conf. Ser.* **2014**, *500*, 427052030. [CrossRef]
8. Balakrishnan, V.; Pradhan, M.; Dhekne, P. Field investigation in the detonation behavior of emulsion explosive column induced with air gaps. *Min. Sci.* **2019**, *26*, 55–68. [CrossRef]
9. Lyashenko, V.; Vorob'ev, A.; Nebohin, V.; Vorob'ev, K. Improving the efficiency of blasting operations in mines with the help of emulsion explosives. *Min. Miner. Depos.* **2018**, *12*, 95–102. [CrossRef]
10. Mertuszka, P.; Szumny, M.; Fułaska, K.; Maślej, J.; Saiang, D. The effect of the blasthole diameter on the detonation velocity of bulk emulsion explosive in the conditions of selected mining panel of the Rudna mine. *Arch. Min. Sci.* **2019**, *64*, 725–737.
11. Kabwe, E. Velocity of detonation measurement and fragmentation analysis to evaluate blasting efficacy. *J. Rock Mech. Geotech. Eng.* **2018**, *10*, 523–533. [CrossRef]
12. Cooper, P.W. Acceleration, formation and flight of fragments. In *Explosives Engineering*, 1st ed.; Cooper, P.W., Ed.; Wiley-VCH: New York, NY, USA, 1996; pp. 385–394.
13. Mertuszka, P.; Fułaska, K.; Cenian, B.; Kramarczyk, B. Impact of initiation method of bulk emulsion explosive on the velocity of detonation based on Emulinit 8L. *Przegląd Górniczy* **2017**, *5*, 8–16. (In Polish)
14. Gupta, R.N.; Adhikari, G.R.; Venkatesh, H.S.; Theresraj, A.I.; Verma, H.K. Evaluation of explosives performance through in-the hole detonation velocity measurement. In *Research Work of National Institute of Rock Mechanics*; National Institute of Rock Mechanics: Kolar Gold Fields, India, 2001.
15. Agrawal, H.; Mishra, A.K. A study on influence of density and viscosity of emulsion explosive on its detonation velocity. *Model. Meas. Control* **2017**, *78*, 316–336. [CrossRef]
16. Mertuszka, P.; Fułaska, K.; Pytlik, M.; Wincenciak, J.; Wawryszewicz, A. The influence of time on the density and detonation velocity of bulk emulsion explosives–a case study from Polish copper mines. *Cent. Eur. J. Energ. Mater.* **2019**, *16*, 245–258. [CrossRef]
17. Pradhan, M. Sleep time: Its consequences on performance of bulk emulsion explosive. *J. Sci. Ind. Res.* **2010**, *69*, 125–128.
18. Mertuszka, P.; Kramarczyk, B. The impact of time on the detonation capacity of bulk emulsion explosives based on Emulinit 8L. *Propellants Explos. Pyrotech.* **2018**, *43*, 799–804. [CrossRef]
19. Pradhan, M. Effect of charge temperature on the detonation velocity of bulk emulsion explosives. *J. Inst. Eng.* **2009**, *90*, 3–7.
20. Mertuszka, P.; Fułaska, K.; Pytlik, M.; Szastok, M. The influence of temperature on the detonation velocity of selected emulsion explosives. *J. Energ. Mater.* **2020**, *38*, 336–347. [CrossRef]
21. Baranowski, P.; Mazurkiewicz, Ł.; Małachowski, J.; Pytlik, M. Experimental testing and numerical simulations of blast-induced fracture of dolomite rock. *Meccanica* **2020**, *55*, 2337–2352. [CrossRef]
22. Baranowski, P.; Kucewicz, M.; Pytlik, M.; Małachowski, J. Shock-induced fracture of dolomite rock in small-scale blast tests. *J. Rock Mech. Geotech. Eng.* **2022**, *in press*. [CrossRef]
23. Türker, L. Velocity of detonation-a mathematical model. *Acta Chim. Slov.* **2010**, *57*, 288–296. [PubMed]
24. Kramarczyk, B.; Pytlik, M.; Mertuszka, P.; Jaszcz, K.; Jarosz, T. Novel sensitizing agent formulation for bulk emulsion explosives with improved energetic parameters. *Materials* **2022**, *15*, 900. [CrossRef] [PubMed]
25. Kramarczyk, B.; Mertuszka, P. Study of the influence of sensitizer content on the density of a bulk emulsion explosive used in underground operations. *Cent. Eur. J. Energ. Mater.* **2021**, *18*, 429–447.
26. Wimmer, M.; Ouchterlony, F. 2D image analysis using WipFrag software compared with actual sieving data of Kiruna magnetite loaded from a draw point. In *Swebrec Report*; Luleå University of Technology, Swedish Blasting Research Centre: Luleå, Sweden, 2009.
27. Nanda, S.; Pal, B. Analysis of blast fragmentation using WipFrag. *Int. J. Innov. Sci. Res. Technol.* **2020**, *5*, 1561–1566. [CrossRef]
28. Sanchidrián, J.A.; Segarra, P.; Ouchterlony, F.; López, L.M. On the accuracy of fragment size measurement by image analysis in combination with some distribution functions. *Rock Mech. Rock Eng.* **2009**, *42*, 95–116. [CrossRef]
29. Ouchterlony, F. The Swebrec© function: Linking fragmentation by blasting and crushing. *Min. Technol. Trans. Inst. Min. Metall.* **2005**, *114*, 29–44. [CrossRef]
30. Coello-Velázquez, A.L.; Quijano Arteaga, V.; Menéndez-Aguado, J.M.; Pole, F.M.; Llorente, L. Use of the Swebrec function to model particle size distribution in an industrial-scale Ni-Co ore grinding circuit. *Metals* **2019**, *9*, 882. [CrossRef]
31. Sućeska, M. Test Methods for Explosives. Springer Science + Business Media: New York, NY, USA, 1995.
32. *EN 13631-4:2002*; Explosives for Civil Uses. High Explosives–Part 4: Determination of Impact Sensitiveness to Impact of Explosives. European Committee for Standardization (CEN): Brussels, Belgium, 2002.
33. *EN 13631-3:2004*; Explosives for Civil Uses. High Explosives–Part 3: Determination of Impact Sensitiveness to Friction of Explosives. European Committee for Standardization (CEN): Brussels, Belgium, 2004.

Article

Relationships between the Petrographic and Abrasive Properties of Sandstones in the Aspect of Their Cutting

Iwona Jonczy [1] and Kamil Mucha [2,*]

[1] Faculty of Mining, Safety Engineering and Industrial Automation, Silesian University of Technology, Akademicka 2 Street, 44-100 Gliwice, Poland; iwona.jonczy@polsl.pl

[2] Faculty of Mechanical Engineering and Robotics, AGH University of Science and Technology, Mickiewicza 30 Street, 30-059 Kraków, Poland

* Correspondence: kmucha@agh.edu.pl

Abstract: The research described in this article was carried out on samples of sandstone obtained from the underground excavations of four hard coal mines that operate in the region of Poland with the highest energy resources, i.e., Upper Silesia. The majority of underground tunnel excavations are mainly drilled using roadheaders, the organs of which are equipped with conical picks. The selection of pick type is usually based on rock compressive strength. However, sandstones often cause more problems during cutting compared to other waste rocks because of their variety. This article's primary purpose is to emphasize the importance of researching various properties of waste rock in addition to uniaxial compression strength, which is crucial in the selection of both the appropriate cutting method and appropriate cutting tools. Accordingly, relations between mineralogical, petrographic, physical and mechanical properties were examined in this study, with special attention paid to the abrasive properties that comprise rock abrasivity. Sandstones from the regions of Upper Silesia are characterized by a heterogeneity of mineralogical and petrographic features that strongly affect the physical and mechanical properties of these rocks, especially their abrasive properties. The determined correlations can aid understanding of the behavior of rocks during their mechanical cutting and facilitate the selection of appropriate cutting tools.

Keywords: underground mining; rock properties; cutting; conical picks; abrasive wear

1. Introduction

Although global coal production is declining, it is still a vast industrial sector in many countries. In 2016, 7.4 billion tons of coal were extracted worldwide, 6.7 billion tons of which was steam coal and 700 million tons of which was coking coal. China is currently the largest coal producer globally; second is the USA, and India is third. Among the European Union countries, which are producers of hard coal, Poland is at the forefront and extracted 63.4 million tons of coal in 2018. In the same year, Polish hard coal mines employed over 80,000 employees [1].

However, to exploit the coal resources mentioned above, accessing excavations should be made. About 200–300 km of workings of this type are performed annually in Poland [1]. Many aspects are considered when preparing work related to drilling excavations, including the properties of the rocks in which the excavation will be drilled. Unfortunately, mines mainly pay attention to the value of the uniaxial compressive strength of rocks. The mining method, cutting machine and cutting tools are often selected on this basis, and this can cause severe consequences that lead to negative impacts on the volume of extraction via the increased drilling time [2,3].

Although uniaxial compressive strength is a significant parameter, mechanical parameters alone do not provide all the information needed to assess the actual behavior of a material during cutting [4]. Such an assessment can be rationally conducted by understanding mineralogical, petrographic, physical, and mechanical rock properties, as well

as their correlations [5]. This article's primary purpose is to emphasize the importance of conducting research regarding the determination of the properties of waste rock to explain the different states of the behavior of these rocks during cutting. Particular attention was paid during research to the relationship between mineralogical, petrographic, and abrasive properties because, apart from the strength properties, rock abrasivity has the most significant impact on the wear of cutting tools (Figure 1) and rock workability.

Figure 1. Examples of conical picks' wear.

There are two frequently confused terms associated with abrasive rock properties: abrasiveness and abrasivity. Abrasiveness is defined as the ability of rocks to reduce their volume and mass under the action of abrasive forces [6]. It can also be defined as the effect of a tool on a rock, i.e., how easily the rock wears away. It is determined using Boehme Shield, Amsler Shield, Los Angeles drum, or Micro-Deval drum [7,8]. However, these methods are more often used to determine the abrasion resistance of aggregates [8].

Rock abrasivity is more interesting in the case of the cutting tool selection. Abrasivity is defined as the effect of a rock on a tool, i.e., the amount of the tool's abrasive wear [9]. It can be determined using the Cerchar method [10,11] or the proprietary method developed at the AGH University of Science and Technology [3,12].

In this research, tests were carried out for Carboniferous sandstones (characterized by mineralogical and petrographic features) and selected physical and mechanical properties. Sandstones have higher uniaxial compressive strength than other waste rocks and are very abrasive [13,14]. Additionally, mineral composition, especially the quantitative share of quartz in the crumb material, and the type of binder-building mineral have significant impacts on the determination of these properties in sandstones.

2. Research Material

The tests were carried out for seven different sandstones taken from the underground mining excavations of four hard coal mines located in the following cities: Katowice, Jaworzno, Bieruń, and Libiąż, all located within the Upper Silesian Coal Basin (Southern Poland) (Figure 2).

The Upper Silesian Coal Basin is a triangular basin filled with Upper Carboniferous formations. Its area is about 6100 km^2, 1600 km^2 of which lies on the Czech side, forming the Ostrava–Karviná Basin. The Upper Silesian Coal Basin is an orogenic basin formed in the foothills of the Moravian–Silesian fold zone of variscite, with paralic and limnic formations. The coal-bearing zone occurs at various depths: down to 2400 m deep in the eastern part and down to 4600 min the western part. With drilling, it can reach even deeper to 6000 m. A significant position of the rocks accompanying coal seams next to claystone and silt is occupied by sandstone [15,16].
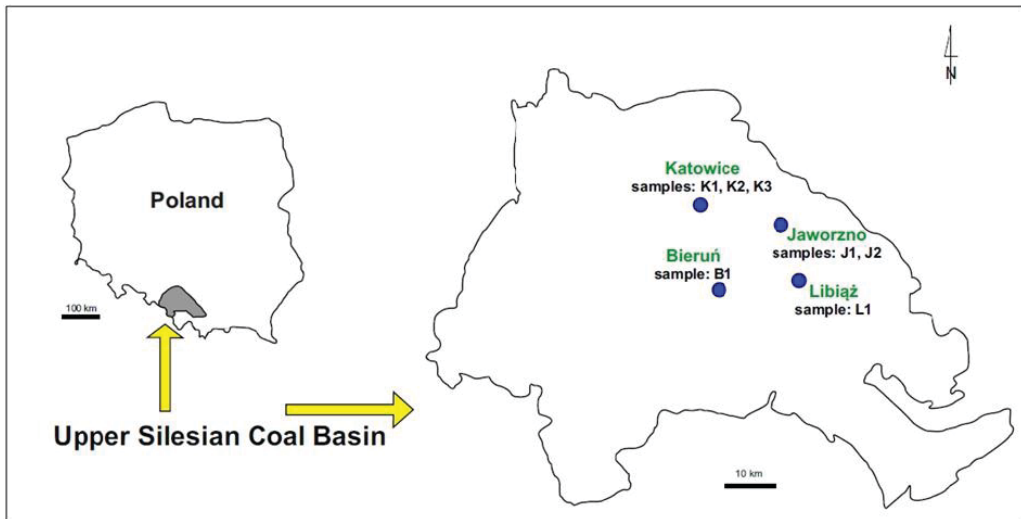
Figure 2. Schematic map of the location of the Upper Silesian Coal Basin with marked sampling sites.

3. Research Methodology

After collecting sandstones from mining excavations, appropriate laboratory samples were prepared and tests were carried out following the established plan and research methodology. Thanks to the research, mineralogical and petrographic analyses were performed and physical and mechanical properties were assessed.

3.1. Petrographic and Mineralogical Analyses

Microscopic observations were carried out with transmitted light in thin sections (Figure 3a) using the OPTA-TECH LAB-40 HAL polarizing diagnostic microscope from the OPTA-TECH company equipped with an image analyzer (Figure 3b).

The quantitative analysis of the components was performed using the point method using a polarizing microscope equipped with an eyepiece with a cross of spider threads and an integration table. A planimetric analysis of the entire surface of the preparations was performed, with about 500 counts from each sample in 0.2 mm increments.

3.2. Analysis of Physical Properties

In terms of physical properties, the effective porosity, bulk density, and water absorption of the tested sandstones were determined. Effective porosity, also known as active or discovered porosity, is the content of pores that connect with the outer surface of the rock (i.e., open pores), allowing the liquid to move through the medium. Effective porosity is determined by saturating samples of known volume with a liquid of known bulk density. Five cylindrical samples with a diameter and height equal to 50 ± 0.5 mm were prepared for each type of sandstone (Figure 4). Effective porosity was determined using a hydrostatic balance using the following formulas based on Archimedes' law [5]:

$$V_w = \frac{W_w - W_d}{\gamma_w} \left[\text{cm}^3\right] \tag{1}$$

$$V_s = \frac{W_w - W_h}{\gamma_w} \left[\text{cm}^3\right] \tag{2}$$

where W_d is the mass of the dry sample measured in the air, W_w is the mass of the saturated sample measured in the air, W_h is the mass of the saturated sample measured on the hydrostatic balance, γ_w is the density of the liquid at ambient temperature, V_s is the volume

of the sample, and V_w is the volume of water in the pores [5]. Therefore, the effective porosity P_w can be calculated as [17]:

$$P_w = \frac{V_w}{V_s} \cdot 100 \ [\%] \tag{3}$$
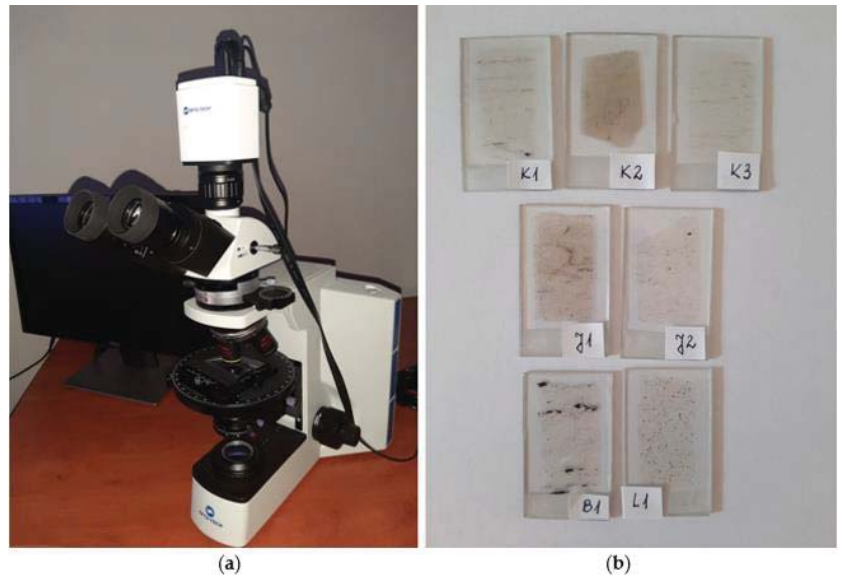
Figure 3. Petrographic and mineralogical analyses: (**a**) OPTA-TECH LAB-40 HAL polarizing diagnostic microscope; (**b**) thin sections.

Figure 4. Examples of rock samples for physical and mechanical property tests.

After calculating the mass of the above-mentioned rock samples and their dimensions, it was also possible to determine the bulk density γ_s as the ratio of the mass of the dry sample to its volume:

$$\gamma_s = \frac{W_d}{V_s} \left[\frac{\text{g}}{\text{cm}^3} \right] \tag{4}$$

The N_s water absorption of the tested sandstones, i.e., their ability to absorb water, was determined as the third physical property. To that end, five cylindrical samples with a diameter and height equal to 50 ± 0.5 mm were also prepared for each type of sandstone. After determining their dry weight (W_d), each sample was dipped in distilled water and

weighed regularly until saturation was stabilized. The water absorption coefficient in weight percentage was determined as the ratio of the mass of water absorbed to the mass of the sample in the dry state, and it was calculated as [5]:

$$N_s = \frac{W_w - W_d}{W_d} \cdot 100 \ [\%] \tag{5}$$

3.3. Analysis of Mechanical Properties

The considered mechanical properties of the tested sandstones were their uniaxial compression strength and tensile strength, which were determined using the Brazilian method, and abrasivity, which was determined using the proprietary rock abrasivity assessment method that has been described in several publications [3,12,18].

To determine the value of uniaxial compressive strength (UCS) for each tested sandstone, five cylindrical samples with a diameter and height equal to 50 ± 0.5 mm were prepared in accordance with the EN 1926:2007 standard. Laboratory tests were carried out using a testing machine in accordance with the PN-G-04303:1997 standard. The load was perpendicularly applied to the bedding planes at a constant stress rate of 1 ± 0.5 MPa/s. The uniaxial compressive strength (R_c) of each sample was expressed as the ratio of the failure load (F) and its cross-sectional area (A) before the test:

$$R_c = \frac{F}{A} [\text{MPa}] \tag{6}$$

The Brazilian method (BTS—Brazilian Tensile Strength Test) was used to determine tensile strength by compressing the cylinder on the side surface with two linear balancing loads. Loading the cylindrical sample perpendicular to the sample axis causes cracking along the surface passing through the cylinder axis and is mainly caused by tensile forces [19]. In this case, five cylindrical samples with a diameter of 50 ± 0.5 mm but a sample thickness of 25 ± 0.5 mm were also prepared for each tested sandstone, as the thickness to diameter ratio had to have been 0.5–0.6. The load was applied with a constant stress rate of 0.1 ± 0.05 MPa/s. The uniaxial tensile strength was determined as:

$$R_t = \frac{2F}{\pi dh} [\text{MPa}] \tag{7}$$

where R_t is uniaxial tensile strength, F is the maximum force at which the sample is destroyed, d is the diameter of the sample, and h is the thickness of the sample [20].

The third mechanical property that was determined for the tested sandstones was abrasivity. It was determined with a method comprising the assessment of the mass abrasive wear of a standard steel sampler that was in contact with a rock sample with a constant clamping force of 300 N and was moving in a uniform motion along a circle at a speed of 50 rpm for 8 min (Figure 5). The parameter characterizing rock abrasivity is the abrasivity index (W_z), which is defined as the ratio of the weight loss of the steel pin to the weight loss of the sample and is calculated as:

$$W_z = \frac{M_{pa}}{M_{pi}} \tag{8}$$

where W_z is the abrasivity index, M_{pi} is the mass loss of the rock sample, and M_{pa} is the mass loss of the steel pin [3,12,18].
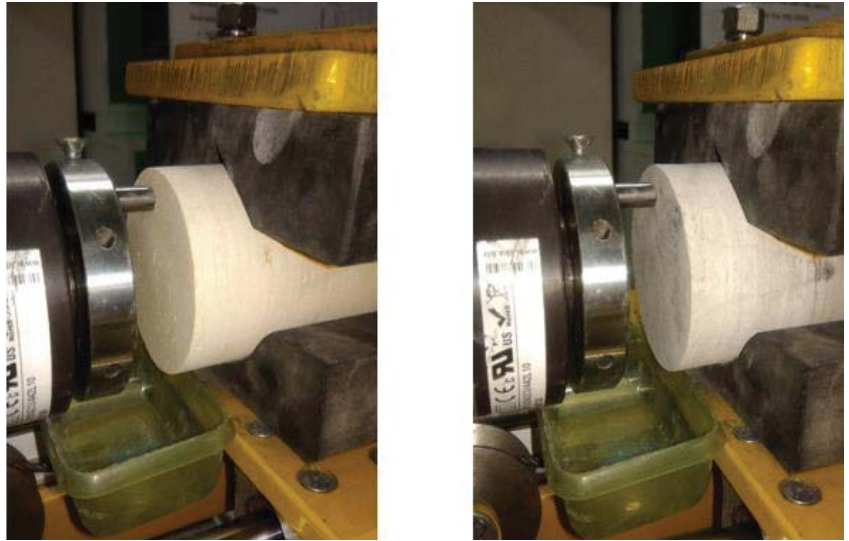
Figure 5. View of selected sandstone samples during the abrasivity test.

4. Results

The tests were carried out following the previously established and above-described methodology. Petrographic properties were determined for seven types of sandstone and the values of selected parameters, enabling the determination of physical and mechanical properties.

4.1. Mineralogical and Petrographic Characteristics of Sandstones

The analysis of the mineralogical and petrographic features of sandstones was carried out based on macroscopic observations, microscopic observations in transmitted light, and planimetric analysis. Macroscopic observations showed that the analyzed sandstones had similar features (Figure 6).

Figure 6. Examples of tested Carboniferous sandstones.

The sandstones were light to dark grey. Their structure was psammitic and fine-grained, and the degree of sorting of crumb material was high. The texture of the sandstones was usually dense and disorderly. A directional texture could be seen in some sandstones and was caused by fine laminates of a carbonaceous matter. Next to them, carbonaceous matter was observed in crumbs of irregular shapes and a scattered form throughout the rock volume as a pigment.

Macroscopically, in the mineral composition of sandstones, transparent or grey grains of quartz could be seen and were characterized by a glassy luster, pink feldspar grains with a matte luster, and single grains of mica: biotite with black color and transparent muscovite with a visible pearly luster. When in contact with moisture, the mortar could be smelled, which indicated the presence of clay minerals in the binder.

A detailed analysis of the mineral composition of sandstones was conducted during microscopic observations in thin sections. The mineral composition of the crumb material included quartz, muscovite, biotite, plagioclase and heavy minerals. The binder was represented by microcrystalline quartz, clay minerals, and carbonate minerals. An admixture of a carbonaceous matter was found in each tested sandstone.

Quartz grains were characterized by varying sizes from 0.1 to 1 mm and varying degrees of coating. Next to individuals with rounded edges, sharp-edged grains could be seen. Previous research indicates that sharp-edged quartz grains arise due to crushing larger individuals exhibiting network defects whose weak structure promotes the disintegration into smaller fragments [21,22]. With one polar, the surface of quartz grains was often scratched and covered with a network of irregular cracks, and the presence of slight inclusions could also be noted. The occurrence of inclusions in quartz is a fairly common phenomenon; quartz originating from plutonic rocks most often contains liquid and gas inclusions, while quartz of volcanic rocks is rich in glass inclusions. With crossed polars, optical anomalies caused by dynamic deformations of the quartz network structure could be observed. The effect of this was a wavy quenching of light. As a result of this phenomenon, the surface of individual grains was fragmentarily, not evenly, quenched, which was visible as locally quenched spots within the grain (Figure 7). This is usually the effect of quartz deformation due to dynamic deformations caused by, e.g., tectonic movements.
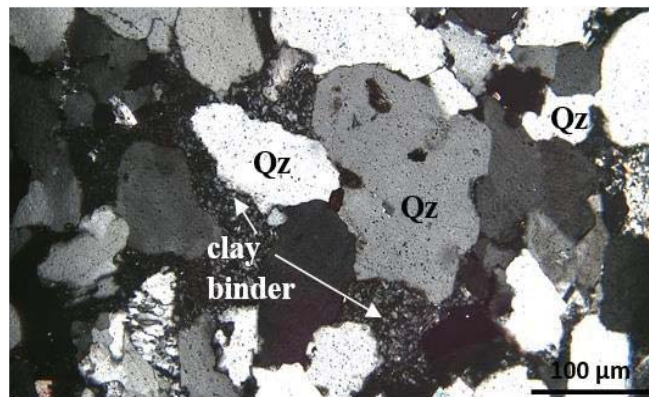
Figure 7. Wavy quenching of light on quartz grains (Qz), surrounded by clay binder: crossed polars—100× magnification.

The micas were primarily represented by well-preserved muscovite grains that create idiomorphic and elongated forms, often bent on contact with other minerals. At one polar, muscovite was colorless with clearly visible unidirectional cleavage (Figure 8).

In addition to muscovite, biotite was found in smaller amounts in the tested sandstone. The biotite grains were strongly weathered, often with jagged edges, and rarely well preserved, and idiomorphic crystals could be observed. At one polar, biotite had a reddish to dark brown color and strong pleochroism. One-way cleavage was visible on the surface of the grains (Figure 9). The cleavage cracks were usually filled with biotite-weathering products, often emitting iron oxides. For some specimens, it was observed that iron oxides could also focus on the periphery of the grains, forming black borders around them. This phenomenon is called "opacite fringes".
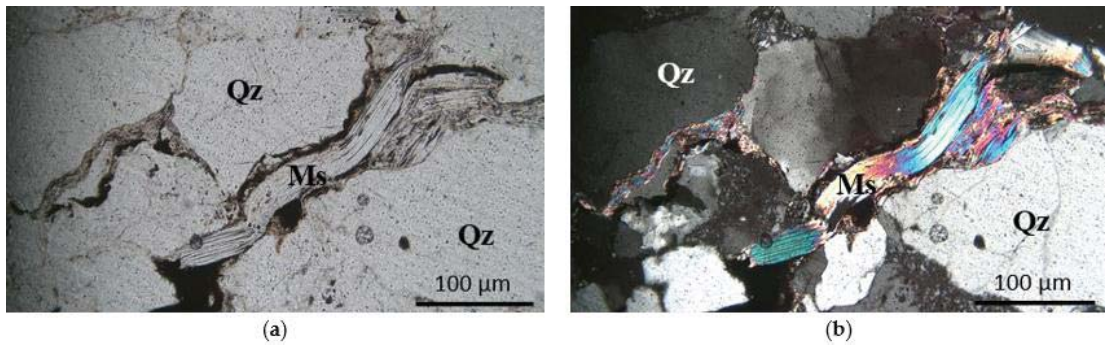
Figure 8. Muscovite (M_s) and quartz grains (Q_z): (**a**) one polar and (**b**) crossed polars—100× magnification.
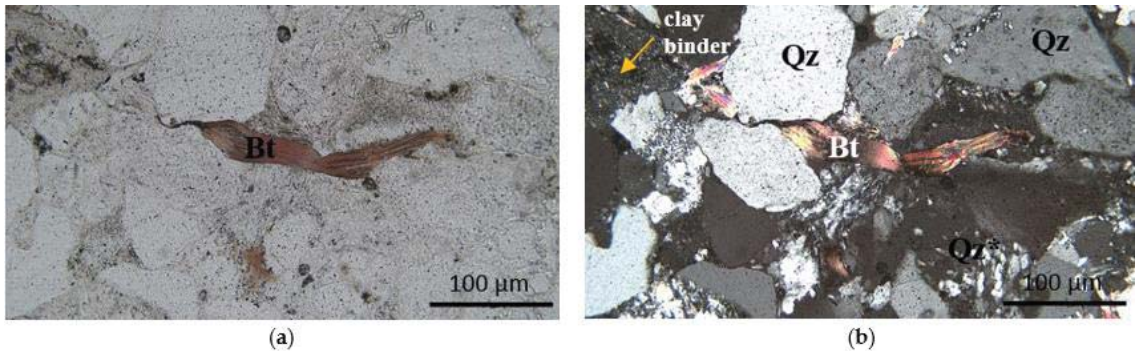
Figure 9. Biotite (B_t) and quartz (Q_z) surrounded by clay binder and microcrystalline quartz (Q_z*): (**a**) one polar; (**b**) crossed polars—100× magnification.

Feldspars formed table-like grains that were strongly weathered. Often, the edges of the grains were ragged and their surface was scratched. There were also signs of sericitization, i.e., the formation of sericite (a small-grain variety of light mica) due to the transformation of feldspar grains. Fine sericite plates usually formed in feldspars according to their cleavage planes. For feldspars, the phenomenon of peritite formation (on the micropertite scale) was also characteristic and is associated with the heterogeneous chemical composition of individual feldspar grains (Figure 10). The feldspars formed a series of mixed crystals with sodium and potassium and calcium cations. Because sodium and potassium are not diadochic elements, they cannot freely substitute in the structure of minerals. However, due to the significant network tolerance of feldspar structures, sodium–potassium feldspar crystallizing at high temperatures can produce a continuous series of homogeneous mixed crystals. As a result of lowering the temperature, these crystals become unstable and are mixed into more potassium feldspar with sodium and sodium feldspar with potassium [23]. During microscopic observations, fine lamellas were observed to be arranged parallel to each other within single feldspars. The way they generally develop depends on the conditions of temperature decrease during feldspar crystallization; the slower this process is, the thicker the structures of veins generally are.
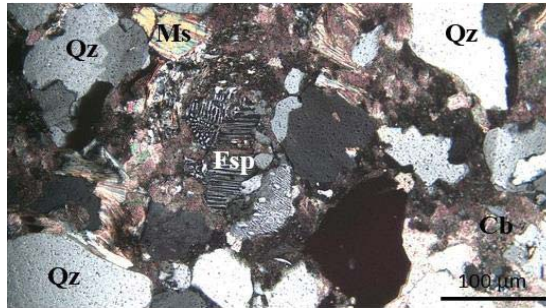
Figure 10. Micropertites on feldspar grains (F_{sp}), surrounded by quartz (Q_z), muscovite (M_s), and carbonate binder (C_b): crossed polars—100× magnification.

In the group of feldspars, plagioclases could be distinguished. They formed fine grains with grey interference colors and polysynthetic twinning (Figure 11).
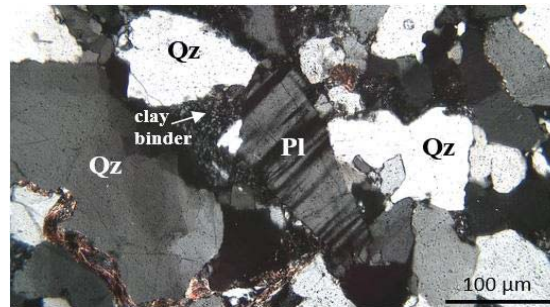
Figure 11. Grains of plagioclase (Pl) and quartz (Q_z) surrounded by clay binder: crossed polars—100× magnification.

Heavy minerals were mainly represented by zirconium grains (Figure 12). Zirconium was found in the form of well-coated, oval, colorless grains with characteristic black pleochroic borders. Pleochroic borders or fields testified to the occurrence in the network structure of zirconium of substitutions of radioactive elements, mainly thorium and less often uranium. For crossed polars, the fourth order's interference colors were characteristic of zirconium.
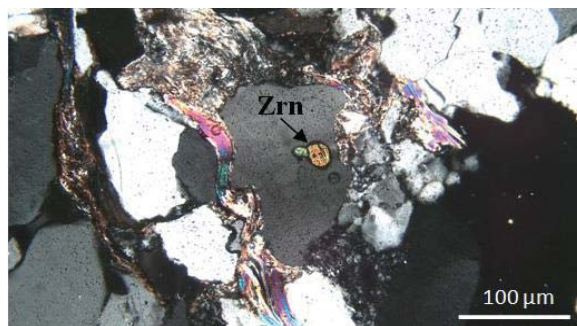
Figure 12. Zirconium (Zrn): crossed polars—100× magnification.

In the K2 sample, tourmaline grains were observed, forming characteristic elongated forms with rounded tops and not showing cleavage (Figure 13).
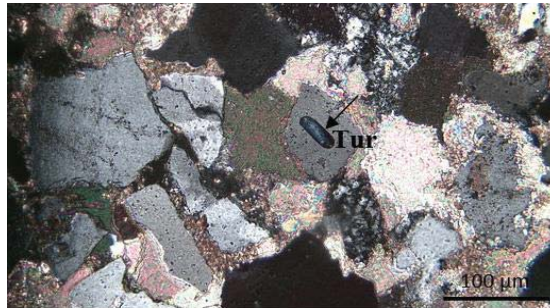
Figure 13. Tourmaline (Tur): crossed polars, 100× magnification.

The sandstone binder represented a pore or primary type; its share ranged from 26% to 52.3%. It is a cement-type mixed binder in which the mineral composition was dominated by microcrystalline quartz, carbonate minerals, and clay minerals. No matrix type binder was found; in single samples only, these were small amounts associated with the presence of fine quartz grains.

The microcrystalline quartz created aggregates. Individual crystals were colorless, non-pleochroic with zero or slightly positive relief, and without cleavage (Figure 9).

Clay minerals formed microcrystalline aggregates with dark grey interference colors, often mixed with other binder components, e.g., carbonates (Figure 14).
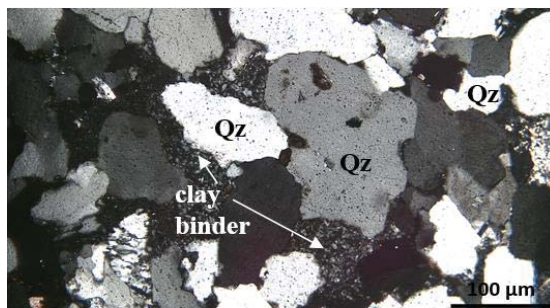
Figure 14. Quartz grains (Q_z) surrounded by clay binder: crossed polars—100× magnification.

Carbonates, like clay minerals, could occur in the form of microcrystalline aggregates or single, larger grains characterized by rhombohedral cleavage and variable relief (Figure 7).

Carbonaceous matter in the sandstones occurred in various forms. The elongated forms comprising laminates were macroscopically visible. Moreover, the presence of a dispersed carbonaceous matter in the form of a pigment, giving the sandstones a dark grey color, could be found. During microscopic observations, a carbonaceous substance was observed in the form of small crumbs (Figure 15).

Figure 15. Crumbs of carbonaceous matter: one polar—100× magnification.

Planimetric analysis (Tables 1 and 2) showed varied contents of framework grain content in the tested sandstones. For the B1, L1, and J1sandstones, the framework grains' contentswere75, 74, and 73%, respectively. The second group consisted of K1 and K3 sandstones, where the framework grains' contents were 70.9 and 69.7% respectively, and the third group consisted J2 and K2 sandstones, where the framework grains' contents were the lowest at 58.5 and 47.7%, respectively.

Table 1. Planimetric analysis of sandstones.

	Mineral	Content of Minerals [%]						
		No of Sample						
		K1	K2	K3	J1	J2	B1	L1
Framework grains	Quartz	61.5	45.7	61.3	60.0	46.4	56.3	56.6
	Feldspars	2.0	1.0	4.5	3.5	3.4	2.1	5.2
	Muscovite	6.7	-	2.6	4.4	3.0	4.2	4.1
	Biotite	-	-	1.3	5.1	5.7	9.4	8.1
	Lithic fragments	-	-	-	-	-	3.0	-
	Heavy minerals	0.7	1.0	-	-	-	-	-
Cement	Microcrystalline quartz	5.2	2.9	7.7	15.3	6.9	9.3	8.1
	Clay minerals	14.2	3.8	11.6	6.5	6.6	6.3	15.6
	Carbonates	6.7	45.6	9.7	2.2	28.0	4.2	2.3
	Iron compounds	-	-	1.3	3.0	-	-	-
	Carbonaceous matter	3.00	-	-	-	-	5.2	-
	Σ	100.0	100.0	100.0	100.0	100.0	100.0	100.0

Table 2. Participation of framework grains and cement in sandstones.

Component	Content [%]						
	No of Sample						
	K1	K2	K3	J1	J2	B1	L1
Framework grains	70.9	47.7	69.7	73	58.5	75	74
Cement	29.1	52.3	30.3	27	41.5	25	26
Σ	100.0	100.0	100.0	100.0	100.0	100.0	100.0

The dominant component in the crumb material was quartz (the K1 sandstone had the highest percentage of 61.5%, while the K2 sandstone had the lowest percentage of 45.7%);

next were minerals from the group of feldspars (1.0–5.2%) and mica: muscovite (3.0–6.7%) and biotite (5.1–9.4%). Heavy minerals during observations in thin sections were found in only two sandstone samples, and their quantitative share was about 1%. The presence of rock crumbs (3%) was determined in a single sample.

According to the content of framework grains, the B1sandstone (25%) had the lowest percentage of binder, while the K2 sandstone had the highest (52.3%). Microcrystalline quartz, clay minerals, and carbonates were found in all sandstone samples in the binder. Their content varied within relatively wide limits: 2.9–15.3% for microcrystalline quartz, 3.8–15.6% for clay minerals, and 2.2–45.6% for carbonates. One sample was found to have a ferruginous binder (3%). In all sandstones, the binder was of a mixed type. However, the dominant component could be indicated. The binders of the K1, K3, and L1 sandstones were clay minerals—14.2, 11.6, and 15.6%, respectively. The second group comprised the J1 and B1sandstones, where the binder was full of microcrystalline quartz (J1: 15.3%; B1: 9.3%), while carbonates dominated the K2 and J2 binder sandstones. For the K2 sandstone binder, the content of carbonates was found as high as 45.6%.

Carbonaceous matter was observed in various forms among the sandstone components. Its content ranged from 3.0 to 5.2%.

The results of planimetric analysis enabled the classification of sandstones (Figures 16 and 17). For this purpose, two triangular classifications were used: according to Folk and according to Dott–Pettijohn geological classification [24,25].
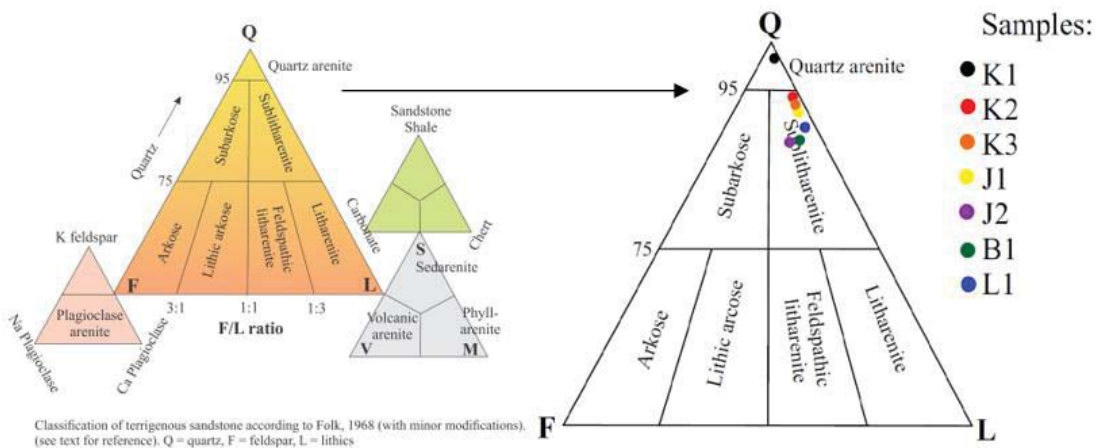
Figure 16. Classification of tested sandstones according toFolk triangle [24,25].

According to the Folk classification, the tested sandstones were classified as sublitharenite, while according to the Dott–Pettijohn classification, they were classified as subarcoses. Only the K1 sample, according to both classifications, was included in the quartz arenite group.

4.2. Characteristics of Physical and Mechanical Properties of Sandstones

The results obtained from the determination of the bulk density, effective porosity, and water absorption coefficient of seven types of sandstone are presented in Table 3. The table summarizes the average values of five replicates for the determination of a given parameter.
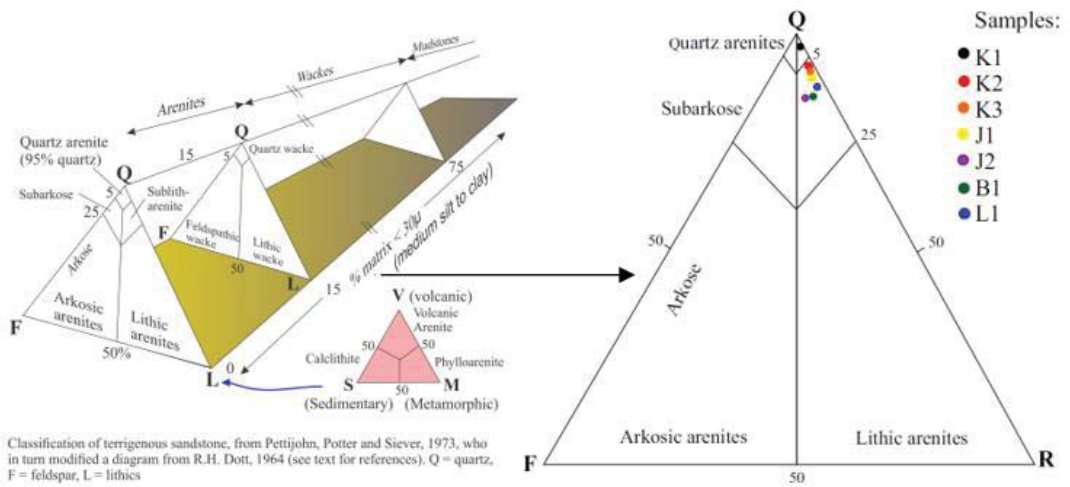
Figure 17. Classification of tested sandstones according to the Dott–Pettijohn triangle [24,25].

Table 3. Bulk density, effective porosity, and water absorption coefficient of the tested sandstones.

Property	No of Sample						
	K1	**K2**	**K3**	**J1**	**J2**	**B1**	**L1**
γ_s [g/cm^3]	2.34 ± 0.01	2.69 ± 0.04	2.31 ± 0.01	2.25 ± 0.00	2.62 ± 0.03	2.28 ± 0.01	2.28 ± 0.01
P_w [%]	5.5 ± 0.6	1.5 ± 0.1	4.8 ± 0.5	6.8 ± 0.7	2.3 ± 0.2	10.1 ± 1.0	8.2 ± 0.9
N_s [%]	2.12 ± 0.48	0.58 ± 0.05	1.85 ± 0.20	2.62 ± 0.61	0.88 ± 0.07	3.88 ± 0.90	3.16 ± 0.72

It can be seen that the highest effective porosity was found in the B1 and L1 sandstones at over 8%. This porosity was almost twice as high as for other sandstones. On the other hand, the most negligible effective porosity was in the K2 sandstone at only 1.5%. As can be seen, the porosity of individual sandstones directly affected their water absorption (Figure 18). The highest values of the water absorption coefficient were found in sandstones with the highest porosity, i.e., B1 and L1. Their water absorption coefficient was over 3%. The lowest values of the water absorption coefficient belonged to the K2 and J2 sandstones, and their coefficients were below 1%. While analyzing the bulk density of the tested sandstones, it could be seen that it was inversely proportional to both the effective porosity (Figure 19) and the water absorption coefficient. The highest bulk density was characteristic of the K2 and J2 sandstones at over 2.6 g/cm^3, while the lowest density was found in theJ1, B1, and L1 sandstones and at below 2.3 g/cm^3.

Table 4 presents the results obtained from the determination of uniaxial compressive and tensile strength, as well as the values of abrasivity indexes. As mentioned above, the tests were performed in five replicates for each sandstone, and the average values are summarized in the table. Due to uniaxial compressive strength values, the vast majority of the tested sandstones belonged to the rocks with a low uniaxial compressive strength [19], with values in the range of 20–30 MPa. Only the J2 sandstone had an average compressive strength of over 60 MPa. Comparing uniaxial compressive strength (UCS) with tensile strength (BTS), a linear relationship could be seen between these properties (Figure 20). The J2 sandstone with the highest uniaxial compressive strength also had the highest uniaxial tensile strength of over 6 MPa. The uniaxial tensile strength of other sandstones was in the range of 2.8–3.6 MPa. Analyzing the values of the abrasivity indexes (W_z) showed that the most abrasive sandstone wasK1, whose index was almost 4, which identifies it as a rock with a high abrasivity. The J1 sandstone was classified as medium abrasive. The

most abrasive sandstones are K3, L1, J2 and B1. Only the K2 sandstone had a very low abrasivity index. Sandstones were classified based on the classification included in Mucha's publication [3]. In addition, it could be seen that there was no clear relationship between uniaxial rock compressive strength and abrasive properties (Figure 21).
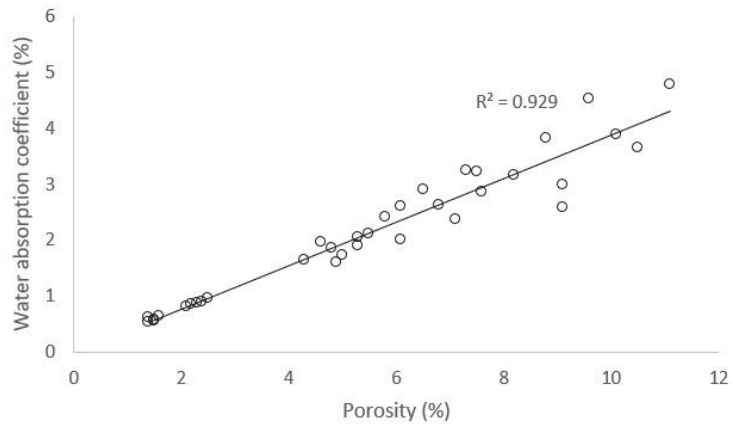
Figure 18. Relationship between effective porosity and water absorption coefficient.
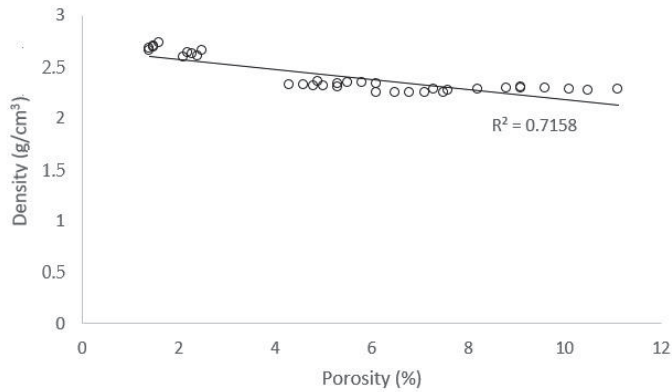
Figure 19. Relationship between porosity and bulk density.

Table 4. Uniaxial compression strength, tensile strength, and abrasivity index of the tested sandstones.

Property	No of Sample						
	K1	K2	K3	J1	J2	B1	L1
UCS [MPa]	29.4 ± 2.7	24.7 ± 2.5	19.4 ± 1.6	22.4 ± 2.2	64.6 ± 5.8	30.1 ± 2.8	20.8 ± 2.0
BTS [MPa]	3.32 ± 0.04	3.18 ± 0.03	2.81 ± 0.02	3.11 ± 0.03	6.10 ± 0.7	3.58 ± 0.04	2.92 ± 0.02
W_z [-]	3.9 ± 0.3	0.2 ± 0.0	1.7 ± 0.2	2.4 ± 0.2	1.5 ± 0.1	1.2 ± 0.1	1.6 ± 0.1
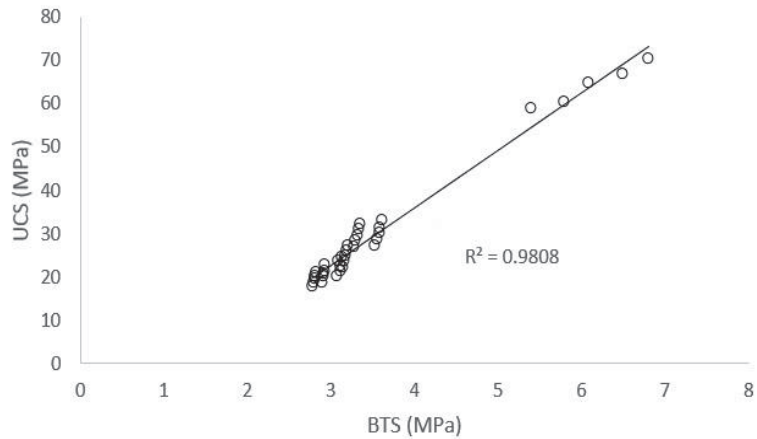
Figure 20. Relationship between USC and BTS.
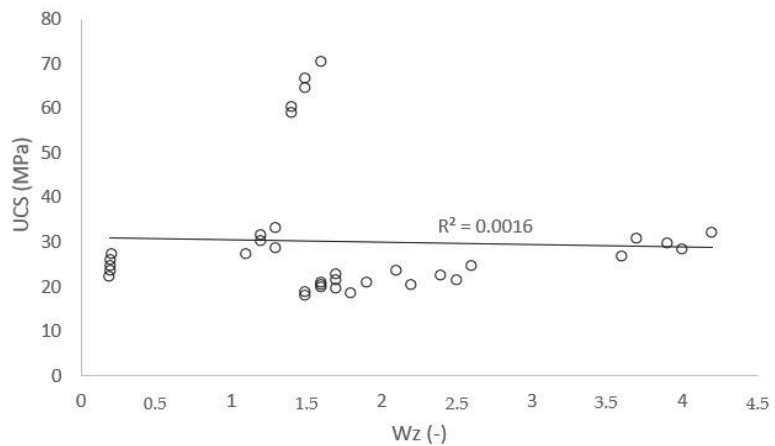
Figure 21. Graph illustrating the lack of relationship between USC and abrasivity index W_z.

4.3. Influence of Petrographic Properties on Abrasive Properties of Tested Sandstones

The influence of the quartz percentage (Figure 22) and the binder (Figure 23) on the abrasivity of the tested rocks was also analyzed. In this case, it was only possible to compare the average values of the W_z index with the results of the petrographic analysis on the charts because analyses were performed once for each sandstone. However, in the case of the tested sandstones, it could be seen that the more quartz and minor binder (sample K1), the more abrasive the sandstone was. A similar dependence was also noticed by West [26].

However, in the case of the tested sandstones, the results did not clearly show this. For the K1, K3 and J1 sandstones, the quartz percentage was about 60% and the cement percentage was about 30%, but the sandstones significantly differed in their abrasive properties (the value of the W_z index). Hence, it can be assumed that another crucial factor influences the abrasivity index's value. This factor could be the size of the quartz grains, as indicated by the research results of Kotwica [2], Käsling and Thuro [13], and Yarali et al. [27].
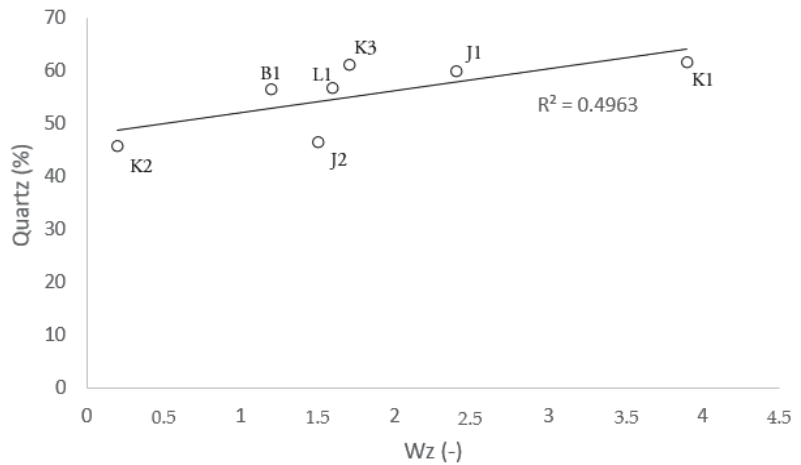
Figure 22. Relationship between quartz content and abrasivity index W_z of tested sandstones.
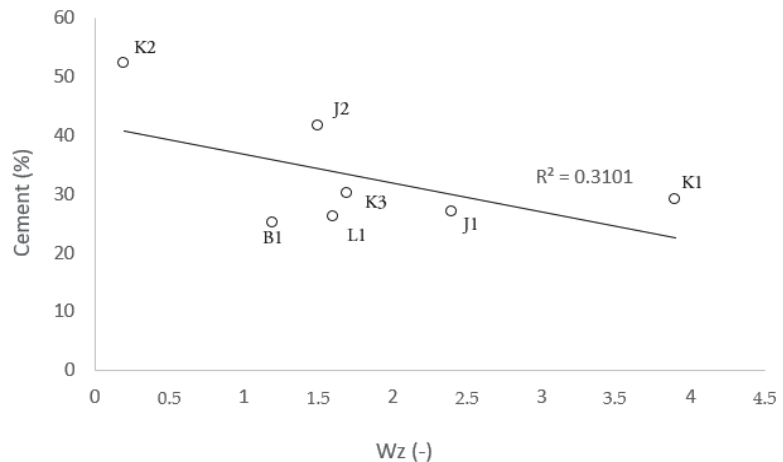
Figure 23. Relationship between cement content and abrasivity index W_z of tested sandstones.

5. Discussion

Carboniferous sandstones' physical and mechanical properties partially depend on the mineral composition, including the qualitative differentiation of components and their mutual quantitative relations, rock structures (with particular emphasis on the size of the mineral of the framework grains), and the degree of weathering of the rocks.

In the case of the tested Carboniferous sandstones, these relationships were particularly visible when analyzing the results of determinations of mechanical properties, i.e., strength and abrasivity tests. The mineral composition of the rocks played a crucial role in both cases. However, the uniaxial compressive strength test results did not show too much differentiation. The range of uniaxial compressive strength results was 19.4–30.1 MPa, which designates the tested sandstones as rocks of low strength (Polish standard specifies the range of 15–60 MPa for rocks of poor strength for uniaxial compressive strength). Only in the J2 sample did the value of this parameter slightly exceed the limit of 60 MPa, which designates it as a rock with a medium uniaxial compressive strength. Similarly, a small range of results was obtained regarding tensile strength (Table 4). However, as already

mentioned, the higher the sandstone's compressive strength, the higher its tensile strength, which was confirmed by Nazir [28], Karaman [19] and Ribeiro [29].

An extensive range of results was obtained while determining the rock abrasivity. Due to the abrasivity index values, the tested sandstones could be divided into four groups: insignificant abrasivity (sample K2), low abrasivity (samples K3, J2, B1, and L1), medium abrasivity (sample J1), and high abrasivity (sample K1). Abrasivity is a property that, in the case of polymineral rocks, is the resultant of the hardness of individual minerals, especially those that form the grain skeleton of the rock. The mineral of crucial importance for sandstones is quartz—a weatherproof mineral with a hardness of 7 on the Mohs scale. Its content in the tested sandstones was on average 55.4%, which is typical of Carboniferous sandstones from the Upper Silesian Coal Basin—Łukaszewski's reports [30] showed that sandstones from the Katowice region contain about 60% quartz.

In the case of the tested rocks, the largest group comprised sandstones with low abrasivity—samples B1, J2, L1, and K3. The abrasivity index ranged from 1.2 to 1.7, with a quartz content from 46.4 to 61.3% and a relatively high proportion of silica binder, the primary component of which was finely crystalline microcrystalline quartz (6.9–9.3%). The J1sandstone was a rock with a medium abrasivity. The abrasivity index for this rock was 2.4—which was slightly higher than the abrasivity index for the K3, J2, B1, and L1 sandstones—due to the high content of quartz (60.0%) and an equally high proportion of silica binder (15.3%). Extreme abrasivity index values were obtained for two samples: 3.9 for the K1 sample and 0.2 for the K2 sample, which means that the first one was ahigh abrasivity sandstone and the second one was an insignificant abrasivity sandstone.

The highest abrasivity of the K1 sandstone was directly related to it having the highest quartz content (61.5%) of the tested sandstones. The K1 sandstone was characterized by a high content of crumb material (70.9%) and a low binder content (29.1%). In addition, the good abrasive properties of the K1 sandstone also influenced various grain structures, especially the abundant quartz grains that were larger than 1 mm, estimated based on observations in thin sections. However, issues related to the sandstone grain size and thus the determination of exact quartz grain sizes requires additional analyses, which the authors will carry out in the next stage of tests.

On the other hand, it was noted that the K2 sandstone had the lowest content of crumb material (47.7%), with a binder share of 52.3%. These values also directly led that K2 sandstone has the highest density value and lowest porosity (1.5%) and water absorption (0.58%) values of the tested samples.

The tested sandstones were also diverse in terms of their physical properties. Their density remained at the level of about 2.3 g/cm^3. Only the K2 and J2 sandstones were characterized by higher densities of 2.69 and 2.62 g/cm^3, respectively. They were much more diverse in porosity, ranging from 1.5% to 10.1%. In the case of the tested sandstones, the variable porosity was also associated with different water absorption values, which ranged from 0.58% to 3.88%. It can be seen that the quantity of binder had the most significant impact on porosity and water absorption, which was confirmed by the results of theB1 sandstone, which was characterized by the highest porosity value, water absorption value, and (thus) the smallest amount of binder with the highest content of crumb material. A similar relationship was noticed by Karman and Kesimal [31] when examining 22 types of rocks from the Black Sea region.

The results presented in this paper are directly connected to the rock workability of the tested sandstones. The K1, K3, and J1 sandstones were characterized by a high quartz content of 60%, a small amount of binder (28%), and a high abrasivity index W_z of 1.7–3.9. As a result, the K1, K3, and J1 sandstones were classified as middlingly hard to cut rocks. On the other hand, the J2sandstone—despite a lower quartz content (46.4%) and therefore higher amount of binder (41.5%) and abrasivity index value W_z = 1.5 but high compressive strength (64.6 MPa)—could also be classified as a middlingly hard to cut rock. The B1 and L1 sandstones, which had a quartz content of 56%, a binder amount of about 25%, a compressive strength value of 20–30 Mpa, and an abrasivity index value

of W_z 1.2–1.6, could be classified as easy to cut rocks. Finally, the K2 sandstone, which was characterized by the lowest quartz content (45.7%), the highest binder content (52.3%), and the lowest abrasivity index W_z (only 0.2), could be classified as a very easy to cut rock. The rock workability classification was based on the efficiency and quantity of wear tools in excavations from which samples were taken. Detailed results were published by Mucha [3,12].

The above analysis was aimed to indicate how to improve cutting efficiency in mines from which the tested samples were taken, the properties of mined rocks have an especially significant influence on selecting appropriate cutting tools. The higher the compressive strength and abrasivity index value, the faster the tool is worn [3,27,32]. Thus, a tool of better quality with special protection should be selected, e.g., in the form of a particular hard-faced layer or sintered carbide rings [2,33]. If a cutting tool has better durability, the adequate working time of the mining machine becomes longer [4,34] and the energy demand decreases [35].

6. Conclusions

Based on the conducted petrographic tests and the determinations of selected physical and mechanical properties, it was found that:

- According to the Folk classification, the sandstones were classified as sublitharenite, and according to the Dott–Pettijohn classification, sandstones were classified as subarcoses. The exception was sample K1, in which both classifications represented quartz arenite.
- Along with the decrease in the size of minerals and the increase in the amount of binder, the strength properties of sandstones increased.
- The determination of physical properties showed that the sandstones were diverse in porosity. The variable porosity was also associated with different water absorption values.
- Various engineering properties were found to characterize the sandstones. The determination of uniaxial compressive strength showed that most sandstones from the regions of Upper Silesia were characterized as rocks of low strength. Only the J2 sandstone was classified as a rock with medium strength.
- The abrasive properties of the sandstones were affected by their different grain structures. The sandstones were found to contain a relatively significant content of quartz of varying grains size from 0.1 to 1 mm, and they were also characterized by a high content of crumb material and a low binder content.
- The insignificant abrasivity of one of the sandstone samples was directly related to its fine-grained rock structure. It was also found that this type of sandstone was characterized by a lower share of crumb material concerning the binder content, which directly impacted its low porosity and water absorption.
- The rock workability was found to depend on the quartz percentage (more quartz grains lead to more difficulty in cutting), strength properties, and rock abrasivity (the higher the compressive strength and the value of the abrasivity index Wz, the more difficult it is to cut a rock).
- The rock properties were found to significantly influence the selection of the cutting tool because these properties are the main causes of tool wear during mining. For harder rocks, better quality tools should be selected, with special focus on the proper protection of their working parts (e.g., wear-resistant coatings and hard facing).

Author Contributions: Conceptualization, I.J. and K.M.; methodology, I.J. and K.M.; software, I.J.; formal analysis, I.J. and K.M.; investigation, I.J. and K.M.; resources, K.M.; data curation, I.J. and K.M.; writing—original draft preparation, I.J. and K.M.; writing—review and editing, I.J. and K.M.; visualization, I.J. and K.M.; supervision, I.J.; project administration, K.M.; funding acquisition, I.J. and K.M. All authors have read and agreed to the published version of the manuscript.

Institutional Review Board Statement: Not applicable.

Informed Consent Statement: Not applicable.

Data Availability Statement: Data presented in the article are original and not inappropriately selected, manipulated, enhanced, or fabricated.

Conflicts of Interest: The authors declare no conflict of interest.

References

1. Bartkowska, I. Program for the Hard Coal Mining Sector in Poland Ministry of Energy, Warsaw 2019, Poland. Available online: https://www.gov.pl/web/aktywa-panstwowe/program-dla-sektora-gornictwa-wegla-kamiennego-w-polsce (accessed on 15 February 2022).
2. Kotwica, K. Atypical and innovative tool, holder and mining head designed for roadheaders used to tunnel and gallery drilling in hard rock. *Tunn. Undergr. Space Technol.* **2018**, *82*, 493–503. [CrossRef]
3. Mucha, K. The new method for assessing rock abrasivity in terms of wear of conical picks. *New Trends Prod. Eng.* **2019**, *2*, 186–194. [CrossRef]
4. Tiryaki, B.; Dikmen, A. Effects of Rock Properties on Specific Cutting Energy in Linear Cutting of Sandstones by Picks. *Rock Mech. Rock Eng.* **2005**, *39*, 89–120. [CrossRef]
5. Cantisani, E.; Garzonio, C.; Ricci, M.; Vettori, S. Relationships between the petrographical, physical and mechanical properties of some Italian sandstones. *Int. J. Rock Mech. Min. Sci.* **2013**, *60*, 321–332. [CrossRef]
6. Hobler, M. *Badania Fizykomechanicznych Własności Skał*; Państwowe Wydawnictwo Naukowe: Warszaw, Poland, 1977.
7. Cobanoglu, I.; Celik, S.B.; Alkaya, D. Correlation between "Wide wheel abrasion (capon)" and "Bohme abrasion" test results for some carbonate rocks. *Sci. Res. Essays* **2010**, *5*, 3398–3404.
8. Hydzik-Wiśniewska, J.; Bednarek, Ł. Statistical analysis of mechanical properties on the example of aggregates of Carpathian sandstones. *Stud. Geotech. Mech.* **2020**, *42*, 366–375. [CrossRef]
9. Plinninger, R.J.; Restner, U. Abrasivity testing, Quo Vadis?—A commented overview of abrasivity testing methods. *Geomech. Tunn.* **2008**, *1*, 61–70. [CrossRef]
10. Plinninger, R.; Käsling, H.; Thuro, K.; Spaun, G. Testing conditions and geomechanical properties influencing the CERCHAR abrasiveness index (CAI) value. *Int. J. Rock Mech. Min. Sci.* **2003**, *40*, 259–263. [CrossRef]
11. Torrijo, F.J.; Garzón-Roca, J.; Company, J.; Cobos, G. Estimation of Cerchar abrasivity index of andesitic rocks in Ecuador from chemical compounds and petrographical properties using regression analyses. *Bull. Eng. Geol. Environ.* **2018**, *78*, 2331–2344. [CrossRef]
12. Mucha, K. Ścierność skał w Aspekcie Prognozowania Zużycia Noży Kombajnowych (Rock Abrasivity in Terms of Forecasting the Abrasive Wear of Cutting Picks). Ph. D. Thesis, AGH University of Science and Technology, Kraków, Poland, 2019.
13. Käsling, H.; Thuro, K. Determining Abrasivity of Rock in the Laboratory. Engineering Geology. Technische Universität München, Germany 2010, 1973–1980. Available online: https://www.researchgate.net/profile/Kurosch-Thuro/publication/26520682 7_Determining_rock_abrasivity_in_the_laboratory/links/559f8bf408ae424c1e6a6dd9/Determining-rock-abrasivity-in-the-laboratory.pdf (accessed on 12 February 2022).
14. Karaca, Z.; Yılmaz, N.G.; Goktan, R.M. Considerations on the European Standard EN 14157 Test Methods: Abrasion Resistance of Natural Stones Used for Flooring in Buildings. *Rock Mech. Rock Eng.* **2011**, *45*, 103–111. [CrossRef]
15. Bukowska, M. The rockbursts in the Upper Silesian Coal Basin in Poland. *J. Min. Sci.* **2012**, *48*, 445–456. [CrossRef]
16. Cabała, J.; Ćmiel, S.R.; Idziak, A.F. Environmental impact of mining activity in the Upper Silesian Coal Basin. *Geol. Belg.* **2004**, *7*, 225–230.
17. He, M.; Zhang, Z.; Zhu, J.; Li, N. Correlation Between the Constant mi of Hoek–Brown Criterion and Porosity of Intact Rock. *Rock Mech. Rock Eng.* **2021**, *55*, 923–936. [CrossRef]
18. Mucha, K.; Krauze, K. Planning experiment for laboratory tests on rock abrasivity. *Min. Inform. Autom. Electr. Eng.* **2018**, *3*, 535. [CrossRef]
19. Karaman, K.; Cihangir, F.; Ercikdi, B.; Kesimal, A.; Demirel, S. Utilization of the Brazilian test for estimating the uniaxial compressive strength and shear strength parameters. *J. South. Afr. Inst. Min. Met.* **2015**, *115*, 185–192. [CrossRef]
20. Gong, F.; Zhang, L.; Wang, S. Loading Rate Effect of Rock Material with the Direct Tensile and Three Brazilian Disc Tests. *Adv. Civ. Eng.* **2019**, *2019*, 1–8. [CrossRef]
21. Jonczy, I.; Borówka, B. Wykształcenie litologiczne warstw orzeskich na południowym skrzydle siodła głównego GZW. *Przegląd Górniczy* **2015**, *71*, 52–55.
22. Jonczy, I.; Borówka, B. Characteristics of Near-Surface Part of the Orzesze Beds in the Region of the Main Saddle in View of Weathering Processes. *Gospod. Surowcami Miner.* **2016**, *32*, 111–124. [CrossRef]

23. Lee, M.; Parsons, I. Diffusion-controlled and replacement microtextures in alkali feldspars from two pegmatites: Perth, Ontario and Keystone, South Dakota. *Miner. Mag.* **2015**, *79*, 1711–1735. [CrossRef]
24. Garzanti, E. Petrographic classification of sand and sandstone. *Earth Sci. Rev.* **2018**, *192*, 545–563. [CrossRef]
25. Geological Digressions. Available online: https://www.geological-digressions.com/classification-of-sandstones (accessed on 12 February 2022).
26. West, G. A relation between abrasiveness and quartz content for some Coal Measures sediments. *Geotech. Geol. Eng.* **1986**, *4*, 73–78. [CrossRef]
27. Yaralı, O.; Yaşar, E.; Bacak, G.; Ranjith, P. A study of rock abrasivity and tool wear in Coal Measures Rocks. *Int. J. Coal Geol.* **2008**, *74*, 53–66. [CrossRef]
28. Nazir, R.; Momeni, E.; Armaghani, A.J.; Amin, M. Correlation between unconfined compressive strength and indirect tensile strength of limestone rock samples. *EJGE* **2013**, *18*, 1737–1746.
29. Ribeiro, P.C.P.D.S.; Oliveira, M.M.; Nelson, P.P. Correlation Between Uniaxial Compressive Strength and Brazilian Tensile Strength Using Different Rock Types. In Proceedings of the ISRM VII Brazilian Symposium on Rock Mechanics-SBMR 2016, Belo Horizonte, Minas Gerais, Brazil, 19 October 2016. [CrossRef]
30. Ukaszewski, P. Development of fracture processes in Silesian Carboniferous sandstones. *Geol. Q.* **2003**, *47*, 29–38.
31. Karman, K.; Kesimal, A. Evaluation of the influence of porosity on the engineering properties of rocks form the Eastern Black Sea Region: NE Turkey. *Arab. J. Geosci.* **2015**, *8*, 557–564. [CrossRef]
32. Abu Bakar, M.; Majeed, Y.; Rostami, J. Influence of moisture content on the LCPC test results and its implications on tool wear in mechanized tunneling. *Tunn. Undergr. Space Technol.* **2018**, *81*, 165–175. [CrossRef]
33. Bołoz, Ł. Directions for increasing conical picks' durability. *New Trends Prod. Eng.* **2019**, *2*, 277–286. [CrossRef]
34. Krauze, K.; Bołoz, Ł.; Wydro, T.; Mucha, K. Durability testing of tangential-rotary picks made of different materials. *Min. Inform. Autom. Electr. Eng.* **2017**, *1*, 529. [CrossRef]
35. Krzysztof, K.; Piotr, M. Methods of Mechanical Mining of Compact-Rock—A Comparison of Efficiency and Energy Consumption. *Energies* **2019**, *12*, 3562. [CrossRef]

MDPI

Article

Vapour Sorption on Coal: Influence of Polarity and Rank

Katarzyna Czerw, Andrzej Krzyżanowski, Paweł Baran and Katarzyna Zarębska *

Faculty of Energy and Fuels, AGH University of Science and Technology, Al. Mickiewicza 30, 30-059 Cracow, Poland; kczerw@agh.edu.pl (K.C.); krzyzano@agh.edu.pl (A.K.); baranp@agh.edu.pl (P.B.)
* Correspondence: zarebska@agh.edu.pl; Tel.: +48-12-617-21-41

Abstract: The surface properties of coal, interactions with gaseous and vapour media, and knowledge of the pore structure are important in terms of preparation, use, and utilisation of coal. This publication combines new unpublished data with analyses included in earlier publications by the research team to expand and systematise information on the sorption of water vapour, methanol vapour, and the saturated and unsaturated hydrocarbons hexane, 1-hexene, heptane, 1-heptene, octane on coals of different ranks. The study showed that the affinity of coal for water and methanol is related to the content of oxygen in the coal rather than the rank of the coal. Water sorption is a multilayer phenomenon, while methanol sorption is a monolayer phenomenon. The water monolayer is greater than that of methanol for low-rank coal, but for the higher-rank coals it is the opposite. The sorption capacity of the applied hydrocarbons depends on the presence or absence of a double bond and the size of the molecule. It increases in the order: n-octane < n-heptane/n-hexane < 1-heptene < 1-hexene. The effect of a double bond is dominant over the influence of the length and shape of the molecule.

Keywords: coal; adsorption; water vapour; methanol vapour; saturated hydrocarbons; unsaturated hydrocarbons

1. Introduction

Coal surface properties, pore structure, and closely correlated sorption properties, are important issues to address in coal preparation, application, and use processes, in particular coal bed methane (CBM) recovery and CO_2 geosequestration. Coal is a porous material characterised by the presence of voids (pores) in the bulk of the material, which vary in size and shape and are interconnected in a complex irregular network. In this space, diffusion processes and sorption processes of liquid and gaseous media take place. The study of interfacial phenomena in systems based on heterogeneous sorbents is often directed toward the understanding of the mechanism of retention of molecules of a given medium in the porous structure of the sorbent. The reasons lie in the theoretical and practical aspects from the point of view of the natural environment of the sorbent, the original conditions of its occurrence, and the conditions under which the sorbent is used. The coal substance has the ability to sorb low molecular weight substances such as water vapour [1–7], methanol vapour [8–11], and hydrocarbons [12–17]. The process can occur on its surface by physical bonding (physical adsorption) or by formation of covalent chemical bonds (chemical adsorption, chemisorption) or by volumetric absorption that affects its structure (absorption). In the case of physical adsorption, different mechanisms may be involved. There can be intermolecular interactions of van der Waals forces, nonspecific dispersion forces, or forces of a specific nature, including dipole interactions or hydrogen bonds.

Adsorption magnitude and course depend on the nature of the adsorbate, the nature of the adsorbent, and the conditions under which adsorption takes place. Factors that are related to the structure of the adsorbent are (1) the amount and type of surface area potentially accessible to the sorbate and (2) the texture and structure of the pores. The nature and accessibility of the surface area is of particular importance in sorbent-sorbate systems based on specific interactions related to the presence of specific sorption sites.

This factor is also particularly significant in the case of multilayer sorption and in the mechanism of volumetric filling of micropores. The interpretation of isotherms of sorption of small molecule size substances allows one to obtain information about the size and properties of the internal surface of sorbents. Texture and structure parameters such as specific surface area and pore volume with a range of diameters and their distribution, as well as information on which atomic groups are present on the surface of the pores, are of key importance for the practical application of commercial sorbents, and to understand, interpret, and predict the behaviour of natural sorbents in situ. The mechanism of sorption in the case of polar substances vapours involves the binding of sorbate molecules to the polar sorption sites of the sorbent. In the case of bituminous coals, these are oxygen reactive groups, mostly hydroxyl OH, including hydroxyl and phenol groups, carbonyl groups C=O, less often carboxyl groups COOH [18]. The approximate proportion of oxygen contained in reactive groups compared to total oxygen varies between 30–50% on the entire coalification scale up to a C^{daf} content of approximately 89% [19]. Therefore, coal can be considered a system with a double feature: hydrophilic and hydrophobic [20].

In planning the study presented in this paper, the authors were motivated by the recognition of a literature gap regarding studies on the sorption of small-molecule sorbates on coal, including polar compounds, but especially apolar hydrocarbon molecules. This paper aims to gather suitable analytical data and provide an analysis of the relationship between sorption capacity and the physicochemical structure of coal.

1.1. Sorption of Water and Methane

By analysing the relevant literature, it can be concluded that coals as adsorbents show good sorption properties with respect to polar compounds, methanol, and water. Differences in the interaction of these compounds with the porous structure of coal have already been observed in measurements of the real density of coals [21]. In relation to helium density, the results obtained with water are higher for low-rank and medium-rank coals (71–89% C) and lower for high-rank coals. This is due to the progressive loss of oxygen content in the coal and the associated gradual change in the character of the coal surface from hydrophilic to hydrophobic. As noted by Liu et al. [22], water vapour has been used to characterize the pore structure of porous material due to its lower kinetic diameter (0.28 nm) when compared to N_2 (0.38 nm) and CO_2 (0.33 nm). However, surface functional groups may provide extra sorption sites for water molecules that act as secondary sites for further adsorption, forming clusters. The density values obtained with methanol are generally higher than the helium density, irrespective of the coal rank. This regularity is explained by the compression of methanol in small pores as a result of significant specific interactions with the coal surface. Czuchajowski and colleagues [19] studied the sorption of methanol and water vapours on vitrinites of 18 bituminous coals in the range of C^{daf} 69.31–94.30%. The authors postulated chelate bond formation as the sorption mechanism, and proposed that for coals up to 81% C^{daf}, some of the reactive groups are inaccessible to polar sorbates because of the presence of internal hydrogen bonds between them. Korta et al. [23] analysed the effect of the petrographic composition of coal lithotypes of different rank on the sorption properties towards methanol and water vapour at 20 °C. The sorption capacity of vitrains was found to be slightly higher than that of their durain counterparts, but this effect decreases with an increase in the degree of coalification. Allardice and Evans [18] carried out desorption and resorption of water vapour from lignite (66.6% C) at several temperatures (30–60 °C). Type II sigmoidal curves were obtained (according to the IUPAC classification). The authors correlated this fact with three effects: capillary condensation, responsible for the upper part of the isotherm; multilayer sorption, which determines the linear middle part of the curve; and monolayer sorption, which is reflected in a shape of sorption isotherm at low sorbate pressures. The studies conducted by Bhattacharyya [1] aimed to measure the rate of heat release from eight coals (80.7–94.2% C^{dmmf}) during the sorption of water vapour under isothermal (30 °C) conditions with different relative humidity. It was observed that the rate of heat release increases with a deficiency in the equilibrium moisture content of

the coal and depends on its hygroscopicity and not directly on its degree of coalification. Lasoń and Żyła [20] carried out measurements of multiple sorption of water and methanol vapours on five Polish bituminous coals of varying ranks (C^{daf} 73.52–94.30%) to observe the phenomenon of swelling of the coal accompanying adsorption. The obtained water vapour isotherms were assigned to type II for the lower-rank coals, and type III for the higher-rank coals. The work of Spitzer's team [10] presents the results of a study of the sorption of methanol vapour on 20 coals differing in their rank (64–91% C^{daf}) at 20, 40 and 70 °C. The obtained data were described using the Dubinin-Kagener-Radushkewich (DKR) equation and the BET equation in the range of relative pressure from 0.05 to 0.35. Comparable values of the parameters corresponding to the monolayer capacity were obtained in terms of both models. Ceglarska-Stefańska et al. [2] have studied the course of the sorption of water vapour under low pressure isothermal-isobaric conditions, at 25 °C, on two bituminous coals and concentrates of liptinite and vitrinite macerals. It was confirmed that because of the low degree of ordering of the liptinite structure, the low aromaticity, and the significant content of aliphatic compounds these macerals have a higher water vapour sorption capacity than base coals and vitrinite. Takanohashi et al. [11] reported the results of studies of the effect of coal extraction on the sorption of methanol vapour in coal at 30 °C. Coals with low extraction efficiency sorbed similar amounts of methanol as their post-extraction residues, but the sorption on the residue from the high extraction-efficiency coal increased significantly compared to that of the base coal, suggesting that the extraction resulted in a more microporous system. Krzyżanowski and Żyła [9] presented the results of studies on sorption of water vapour, methanol, and benzene on three coals of different rank. The authors found that the sorption of water vapour on bituminous coals depends not only on the polar character of the coal surface but also on its capillary structure. On the other hand, the sorption of vapours of organic compounds occurs in both polar and in apolar sites as a result of dispersion forces. Charrière and Behra [3] carried out isothermal studies of water vapour adsorption and desorption on bituminous coal and lignite 298 K. Water sorption isotherms corresponding to type II were obtained and were described with a modified BET model to estimate water adsorption on primary and secondary adsorption sites. The authors assumed that the sorption of water vapour in coals with increasing relative pressure can be divided into four stages: (I) adsorption on primary sites, i.e., on oxygen-containing functional groups; (II) adsorption on secondary sites, via hydrogen bonding between water molecules; (III) formation of water clusters; and (IV) filling of micropores by water clusters and capillary condensation in narrow pores. The amount of water adsorbed at the primary sites was estimated to be 50% and 35% of the total sorption for bituminous coal and lignite, respectively. Švábová and co-workers [7] conducted a study of water vapour adsorption on three coals at temperatures: 25, 35, and 45 °C to observe the role of primary and secondary adsorption sites on the adsorption process. It was observed that at low relative pressures, adsorption at primary adsorption sites dominates, while adsorption at secondary sites becomes more important with increasing pressure. The percentage of adsorption at secondary sites depends on the concentration of the oxygen-containing functional groups. Baran et al. [8] presented the results of methanol sorption on three coals of different rank and elemental and petrographic composition. A positive relationship was found between the amount of adsorbed methanol and the oxygen content of the coal. The authors assumed that methyl alcohol molecules can be adsorbed at both the polar and a polar adsorption sites because of the dual nature of the molecule: the –OH group is polar and the methyl group –CH_3 is apolar. Orzechowska-Zięba et al. [24] investigated the sorption of water vapour on five coals of varying rank. The sorption and desorption isotherms obtained at 303 K were classified as type II characteristic for sorbents containing micro- and mesopores. As part of their study, Chen and co-workers [4] measured the water vapor adsorption/desorption isotherms and the corresponding kinetics at preset relative humidity (P/P_0) steps on five coals of different rank (R_0 0.65–3.18%). Samples of low-rank coal and high-rank anthracite exhibit higher sorption capacity, pronounced hysteresis features, and a sharp step-down of the desorption isotherms at a P/P_0 of approximately 0.5. On the contrary, the desorption

curves of the other three samples follow a path approximately parallel to the adsorption curves. In their review, Liu and co-workers [5] focused on the relationship between the occurrence of H_2O and the metamorphism of the coal, the presence of functional groups containing oxygen, the influence of mineral matter and other internal factors. The authors postulate that the H_2O adsorption process can be well described by the modified Brunauer–Emmet–Teller (BET) model with the assumption of double adsorption sites.

1.2. Sorption of Hydrocarbons

Coal is an adsorbent with a dual-surface nature, which is also of particular importance for the sorption of apolar sorbates. This area of research is based primarily on practical aspects, since apolar compounds are the main constituents of a mine gas. In addition to methane, nitrogen, and carbon dioxide, the lower hydrocarbons (C1–C5) and medium hydrocarbons (C6–C9) present in the gas mixture are also of great importance as their content in some sections of coal-bearing formations may exceed even 10% [25] and are sorbed on coals to varying degrees [26,27]. However, the literature on this subject is not extensive. Dudzińska [26] investigated the sorption capacities of bituminous coals toward gases present in the mine atmosphere. It was found that the volume of gas sorption on bituminous coal decreases in the following order: $CO_2 \sim C_2H_2 > C_2H_4 > C_3H_6 > C_2H_6 > C_3H_8 > CO > H_2$. Relatively high sorption of unsaturated hydrocarbons was attributed to the interaction of double- and triple-bond electrons with the energy centres of the coal surface. It has been found that lower-rank coals with higher porosity are characterised by the highest sorption capacity. According to Dudzińska [26], it can be assumed that when in contact with the surface of the coal, a pair of binding electrons in the molecules of unsaturated hydrocarbons is shifted and a dipole structure is formed and they can electrostatically interact with polar adsorption sites with donor or acceptor properties. Dudzińska et al. [13] conduct research in the field of assessing the self-heating rate of coal by studying sorption/desorption of gases released into the mine atmosphere as a result of coal oxidation including unsaturated hydrocarbons: ethylene, propylene, acetylene. The volume of sorbed gases is closely related to the rank of coal and its porous structure and the volume of adsorbed acetylene is approximately 2–3 times larger than the volume of adsorbed ethylene or propylene [15]. Acetylene molecules are smaller than those of ethylene and propylene and due to the triple bond between the carbon atoms, have a higher electron availability of weak π bonds than ethylene and propylene. Wojtacha–Rychter and Smoliński [16,17] studied the effects of transporting a multicomponent gas mixture through a sorption column filled with granular coal and inert material and the sorption of multicomponent gas mixtures of ethane, ethylene, propane, and propylene during flow through coal masses of different degrees of coalification. The gases migrated through the coal bed at different rates. The presence of a double bond was found to be responsible for the strongest selectivity of propylene on coal. However, the selectivity of ethylene on coal was the lowest, which was contrary to expectations. The authors emphasised that the complex mechanisms of adsorption on coal for multicomponent gas mixtures have not been fully elucidated, leaving this issue open for further research. Zhao and co-workers [28] conducted adsorption and desorption measurements of carbon dioxide, methane, ethane, propane, n-butane, and iso-butane on two different shales and kerogen at temperatures of 35, 50, and 65 °C, in a wide pressure range. At 2 bar, the highest adsorption was observed for n-butane, followed by isobutane, propane, carbon dioxide, ethane, and methane. Longer molecules were found to provide a stronger interaction with the sorbent surface and higher adsorption. Krzyżanowski and Zarębska [29] carried out measurements of n-heptane and 1-heptene vapour sorption in bituminous coals and concluded that the sorption of vapours of apolar substances is mainly surface-bound and significantly depends on the porosity of coals and that the presence of a double bond influences the sorbent-sorbate type interactions and the sorption capacity. These results were confirmed by Baran and co-workers [12] who performed sorption studies of hexane, 1-hexene, heptane, 1-heptene, octane, and benzene vapours on low-rank bituminous coal.

The study of the course of sorption of vapours and gases with different physico-chemical properties is a source of information on the porous structure of coals and the mechanism of adsorption of sorbates. The paper is a continuation of research carried out in the Adsorption and Environmental Engineering Group, Faculty of Energy and Fuels, AGH University of Science and Technology. The publication combines information presented in previous works of the team [8,9,12,29] with new, unpublished data to summarize, expand and systemise information on the sorption of water vapour, methanol vapour, and saturated and unsaturated hydrocarbons: hexane, 1-hexene, heptane, 1-heptene, and octane, on bituminous coal.

2. Materials and Methods

The research was carried out on three selected Polish coals, provided by three operating coal mines of the Upper Silesian Coal Basin, that differ in the degree of coalification. The samples weighing several kilograms were acquired in accordance with the Polish standard PN-G-04502:2014-1, crushed in a jaw crusher, ground, sieved on Fritsch sieves to the fractions 0.500–0.700 mm, 0.125–0.250 mm, and 0.063–0.075 mm, and stored in nitrogen atmosphere.

Coal analysis was carried out at the Department of Solid Fuel Quality Assessment of the Central Mining Institute in Katowice (Poland) and at the Faculty of Energy and Fuels of the AGH University of Science and Technology in Kraków (Poland), using the requirements and procedures specified in Polish standards (Table 1). Micropore surface area and volume determined on the basis of carbon dioxide sorption at 298 K using Dubinin–Raduszkiewicz model (D-R) were presented in Table 1. The tests were performed using the Micromeritics ASAP 2010 apparatus.

Table 1. Specification of coal samples C1, C2, C3: proximate and ultimate analysis, petrographic analysis, vitrinite reflectance, densities, and porosity.

Coal	C1	C2	C3
Proximate analysis			
W^a [%]	1.75	1.85	11.11
A^a [%]	3.01	14.18	14.45
V^{daf} [%]	27.12	29.88	35.63
Ultimate analysis			
C^{daf} [%]	84.24	70.82	57.83
H^{daf} [%]	4.58	3.35	3.37
N^{daf} [%]	1.52	1.28	0.87
S^{daf} [%]	0.39	3.50	1.10
O^{daf} [%]	4.58	6.29	11.30
Petrographic analysis and vitrinite reflectance			
vitrinite [%]	73	60	67
liptinite [%]	7	9	5
inertinite [%]	20	31	28
mineral matter [%]	1	14	11
R_0 [%]	0.92	0.78	0.51
Structural properties			
d_{real} [g/cm^3]	1.26	1.27	1.37
d_{bulk} [g/cm^3]	1.22	1.23	1.16
porosity [%]	3.20	3.40	15.90
V_{micro} [cm^3/kg]	0.070	0.063	0.229
S_{micro} [m^2/g]	115.8	103.2	419.6

W: moisture content, A: ash content, V: volatile matter content, C, H, N, O, S: content of element C, H, N, O, S, respectively, a: analytical basis, daf: dry–ash–free basis, R_0: vitrinite reflectance, d_{real}: real density (helium density), d_{bulk}: apparent/bulk density (mercury density), V_{micro}: D-R micropore volume, S_{micro}: D-R micropore surface area.

FTIR spectra of the samples C1, C2, and C3 are presented in Figure 1. The FTIR results provided information on the structure of our 3 coals in terms of carbon and hydrogen

groups and oxygen groups, enabling the assessment of differences in the structure and character of sample surfaces. Spectra are characterized by:

- a broad hydroxyl stretching region, with peak at 3425 cm^{-1} for C1 and C2 and shifted peak at 3390 for C3,
- a clearly visible aliphatic stretching region, with two peaks for asymmetric bonds at 2920 cm^{-1} and symmetric bonds at 2855 cm^{-1}; the latter is most pronounced for C1 and least pronounced for C2,
- a prominently displayed aromatic carbon region with a peak at 1600 cm^{-1}, most pronounced for C1,
- an aliphatic bending region with peak at 1435 cm^{-1} for C1 and C2 and peak at 1430 cm^{-1} for C3,
- peaks at 1032 cm^{-1} assigned to the stretching vibration of minerals, such as Si-O-Si or Si-O-C, most pronounced for C3 and almost indistinct for C1,
- noticeable three aromatic out-of-plane peaks within 900–650 cm^{-1} region,
- peaks at 535 and 460 cm^{-1} region assigned to the Si-O bending vibration of feldspar and quartz minerals, most pronounced for C3 and indistinct for C1.

Figure 1. FTIR spectra of coals C1, C2 and C3.

Scanning electron microscopy–energy dispersive X-ray spectroscopy (SEM/EDS) analysis was carried out with the aid of JEOL JSM-7500F, coupled with an AZtecLiveLite Xplore 30 (Oxford Instruments) system. The secondary electron detector provided SEI images, and the back-scattered electron detector provided BSE (COMPO) micrographs. SEM images were recorded for the samples coated with 30 nm Cr. SEM (Scanning Electron Microscopy) makes use of secondary electron signal imaging to observe the surface morphology of the sample, to infer material components and to reveal the microstructure on the micro- and

nanometre scale. The SEM photographs in Figure 2 present the topography of the coal's surface and its phase diversity for fraction below 0.075 mm.
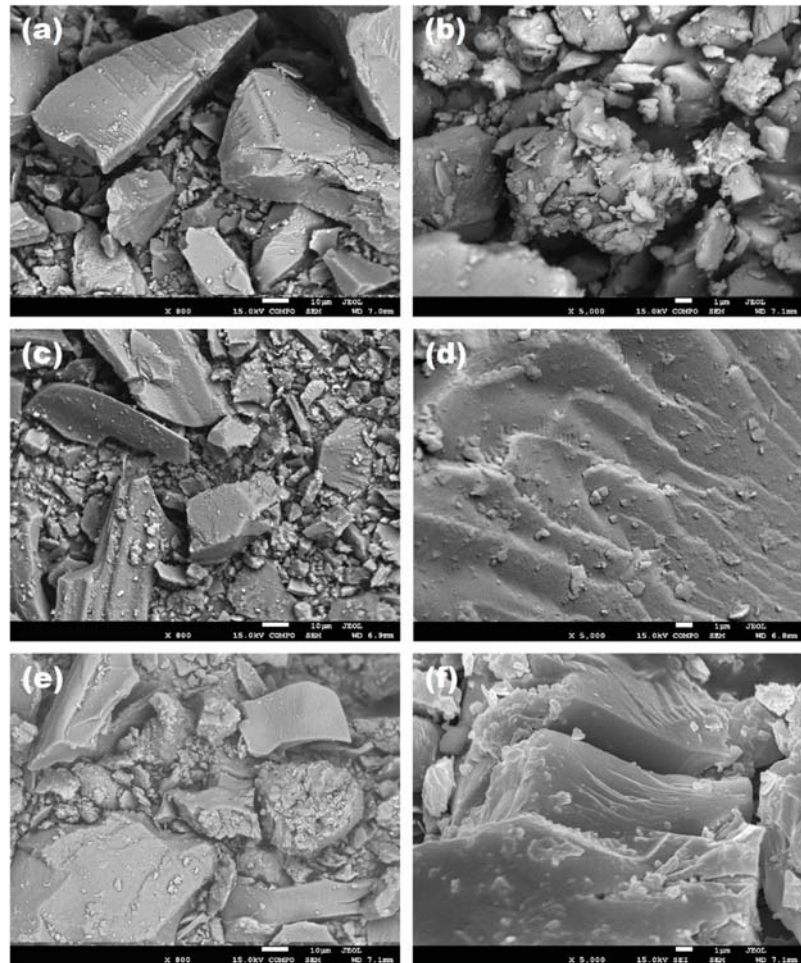
Figure 2. The surface morphological characteristics of the SEM pore-fracture system in (**a**,**b**) coal C1, (**c**,**d**) coal C2, (**e**,**f**) coal C3. Magnification = 800 (**left**), magnification = 5000 (**right**).

The choice of sorbates was dictated by both cognitive and practical aspects. Water vapour and liquid water occur naturally in coal seams. The amount of water vapour and its form of bonding with the coal is determined by hydrogeological conditions and the depth of deposit. The sorption of water vapour on coal depends on the polar character of the coal surface and its capillary structure, which enables the formation of multilayer clusters. The sorption of methanol has a more universal character because of the specific structure of the molecule, containing a polar and an apolar section. Medium hydrocarbons (C6–C9), saturated and unsaturated, can be present in the mine atmosphere; thus, the results of the studies can be used to determine the predisposition of selected coals for their storage. The selected sorbates differ in structure (saturated and unsaturated hydrocarbons), size and shape of the molecules (molar mass; angular, spatial, linear structure of the molecule) and

physical properties (equilibrium vapour pressure), they are also present as components of gas mixtures, including coal seam gas (Table 2).

Table 2. Characteristic of sorbates.

Sorbate	T_C [°C]	p_C [MPa]	M [g/mol]	d_{kin} [nm]	p_0 [Pa]	μ [D]
water	373.99	22.06	18.02	0.265	4240	1.85
methanol	240.00	78.50	32.04	0.380	21,065	1.70
n-hexane	234.64	3.04	86.18	0.430	24,598	0.00
1-hexene	230.83	3.21	84.16	0.430	30,507	0.44
n-heptane	266.87	2.74	100.20	0.430	7786	0.00
1-heptene	264.08	2.92	98.19	0.430	9533	0.44
n-octane	295.75	2.49	114.23	0.430	2240	0.00

T_C: critical temperature, p_C: critical pressure, M: molecular weight, d_{kin}: kinetic diameter, p_0: vapour pressure at 303 K, μ: dipole moment.

The sorption isotherms were determined using a volumetric technique with so-called liquid microburettes, at a temperature of 303 K. This technique allows the determination of isotherms of adsorption and desorption of vapours of polar substances, such as water or alcohols, and nonpolar compounds, for example, benzene, carbon tetrachloride, hydrocarbons, ether, and amines, in the entire range of relative pressures, i.e., from absolute vacuum to equilibrium vapour pressure. The measuring instrument is made almost entirely of glass and is placed inside an air thermostat to maintain a constant temperature with an accuracy of 0.1 °C. The apparatus consists of several independent basic units. A schematic of a single measuring unit is shown in Figure 3.

Figure 3. Schematic of sorption apparatus (C: measuring capillary, CN: narrower part of capillary tube, B: glass bubble, WT: cotton tampon damp in water, A: sample ampoule, MM: mercury manometer and valve, MV: mercury valve, MD: helium dosing unit with mercury valve, FV: float valve, V_1–V_8: valves and glass taps).

Measuring capillary C is filled with liquid by immersing the open narrower part of measuring capillary CN in adsorbate, creating 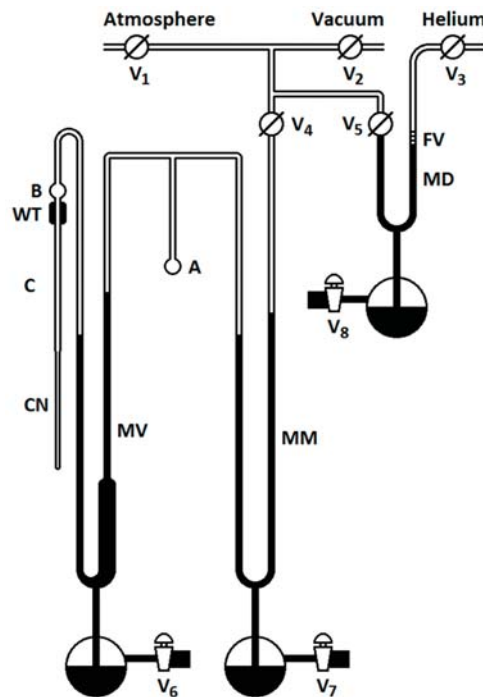negative pressure by MV valve, and sucking the liquid into bubble B (half of the volume). After closing the MV valve, the end of the CN capillary is sealed. Then, with the MV and MM valves open and valve V$_4$ open, the liquid is degassed to remove its vapours and dissolved gases and to obtain a uniform column of liquid in capillaries C and CN. When this stage is complete, the MM and V4 valves are closed. Below the meniscus of the liquid, on the measuring capillary C, a cotton swab pre-soaked in water WT is placed in order to locally lower the temperature in order to counteract the predistillation and condensation of the adsorbate outside the measuring capillary C. The next step is to plot the curve of the dependence of the lowering of the meniscus level of the liquid in the measuring capillary C on the vapour pressure of the sorbate in the adsorption space, to determine the correction for the dead space of the system. The glass sample ampoule A containing the adsorbent is connected to the system with a gas burner. The sorption space and sample are then degassed to remove the free gas and previously sorbed compounds from the pore system and the surface of the coal. In the case of coal, the heating of samples is not practiced to remove the vapours and gases contained in the pores of the sorbent. Instead, the so-called helium bath is used. After the initial degassing of the sample, a portion of helium (pressure of several kPa) is introduced into the system for 1–2 h, after which the degassing is continued (10-3 Pa). Helium atoms, which are not adsorbed themselves, provide the necessary kinetic energy to the molecules of sorbed gases and vapours, forcing them off the sorbent surface [30].

Sorption experiments were carried out for 0.125–0.25 mm grain samples of coal weighing approximately 1 g. Prior to the main test, the samples were outgassed (10^{-7} Pa) and flushed under helium atmosphere at least 3 times in total, and next kept under vacuum at the room temperature to a stable residual pressure. The actual measurement begins by reading the baseline liquid level in capillary C using a cathetometer with an accuracy of 0.02 mm. Opening the MV valve results in the distillation of a certain amount of liquid into the adsorption space. The amount of adsorbed vapour is calculated from the difference in the level of the meniscus of the liquid in the measuring capillary C, taking into account the dead volume of the apparatus and the volume of the sample. The equilibrium pressure of sorption is checked on the MM manometer using a cathetometer, with the MV valve closed. The MM gauge acts as a pressure gauge and a valve between the sorption part of the system and the section for degassing and aeration of the system. During the measurements, the optimum equilibrium waiting time of 24 h was selected, after which no change in equilibrium pressure was detected.

The multilayer adsorption model of the Brunauer, Emmett, and Teller equation (BET) [31] was used to describe the experimental data. It assumes that if a sorbate molecule encounters an occupied adsorption site on the surface of an adsorbent, it does not leave it immediately, but it forms an adsorption complex. With increasing vapour pressure, the number of available unoccupied adsorption sites decreases, as well as the number of sites occupied by one molecule, because complexes are formed which are dual-molecular and with more molecules. The interpretation of the obtained curves is based on the linear form of the BET equation:

$$\frac{\frac{p}{p_0}}{a \cdot \left(1 - \frac{p}{p_o}\right)} = \frac{1}{a_m \cdot C} + \frac{C - 1}{a_m \cdot C} \cdot \frac{p}{p_0}, \tag{1}$$

where: p—equilibrium vapour pressure of the sorbate [Pa], p_0—saturated vapour pressure of the sorbate at the measurement temperature [Pa], a—sorption capacity of the adsorbed vapour at equilibrium pressure p [mmol/g], a_m—adsorption capacity of the monolayer [mmol/g], C—equation constant, depending on the heat of adsorption and measurement temperature.

3. Results

3.1. Sorption Isotherms

The course of sorption isotherms is presented as a dependence of the sorption capacity of the sorbate (mmol/g) and the relative pressure of the sorbate (p/p_0). The sorption isotherms of water and methanol for the studied systems are presented in Figure 4. The isotherms of hydrocarbon sorption on samples C1, C2, and C3 are illustrated in Figure 5.

3.2. BET Parameters

The BET adsorption model was used to describe the experimental adsorption data. Classically, the BET method is used to describe the low temperature (77 K) sorption of nitrogen and to determine the specific surface area of the adsorbents from the a_m values. Korta et al. [23] postulated that the monolayer capacity (a_m) determined for the coal-water sorption system corresponds to the number of polar active groups that make up the water sorption sites and not to the compact sorbate monolayer capacity. In our present study, the characteristic parameters of the BET equation, the monolayer capacity (a_m), were calculated. However, we followed the view presented by Allardice and Evans [18] that the determined parameters represent the capacity of a single first adsorbent layer. For the purposes of this theoretical analysis, the data were not differentiated in terms of similarity to type II isotherms and calculations were carried out for each isotherm obtained. It was assumed that the agreement of the experimental data with the linear equation of BET is in the range of relative pressures from 0.05 to 0.4.

The monolayer capacity values (a_{BET}) were presented graphically in relation to the maximum sorption capacity values (a_{max}) in Figure 6. The values of the maximum sorption capacities (a_{max}) of the sorbents with respect to each sorbate were correlated with the molar mass of the sorbates and the kinetic diameter of the sorbate molecules (Figure 7) in order to evaluate the presence or absence of dependence of these parameters on the determined quantities.
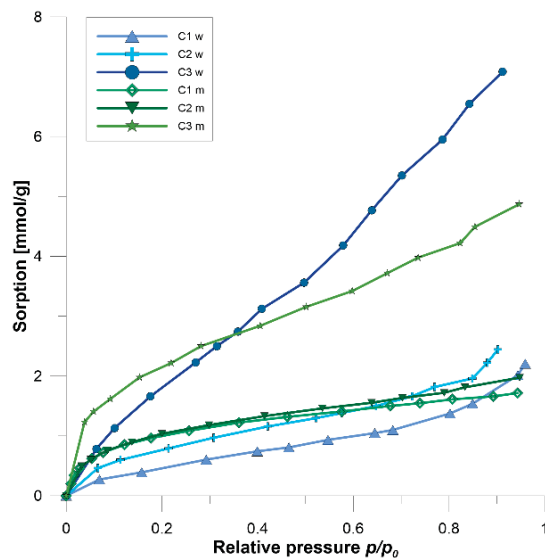
Figure 4. Sorption isotherms of water vapour (Ci w) and methanol vapour (Ci m) on coals C1, C2, C3.
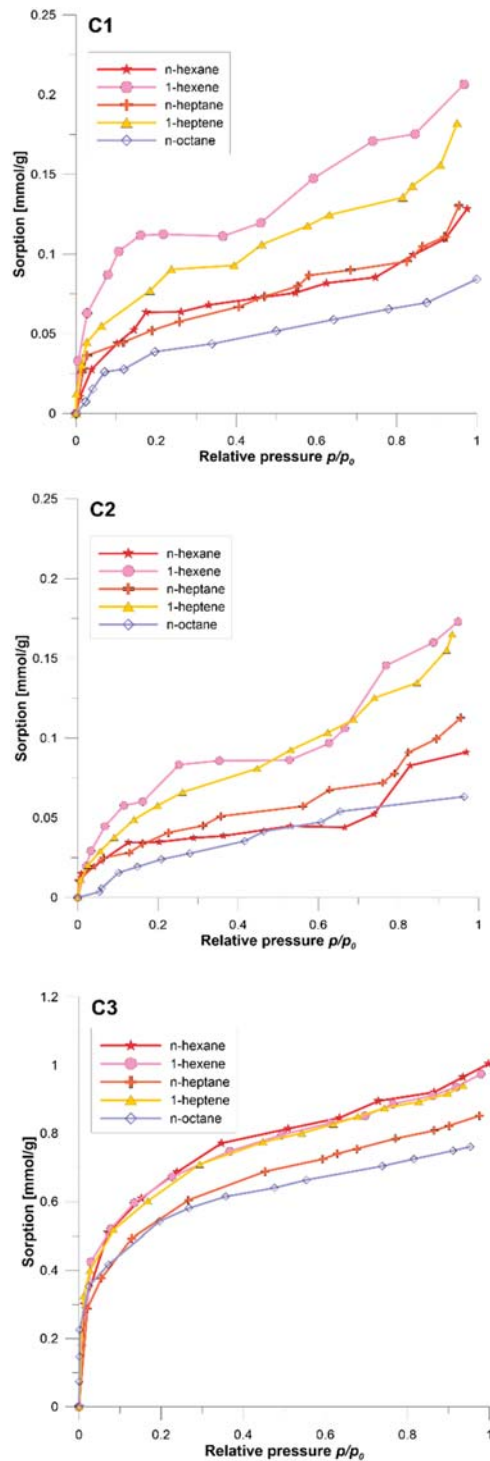
Figure 5. Sorption isotherms of n-hexane, 1-hexene, n-heptane, 1-heptene, and n-octane on coals: C1, C2 and C3.
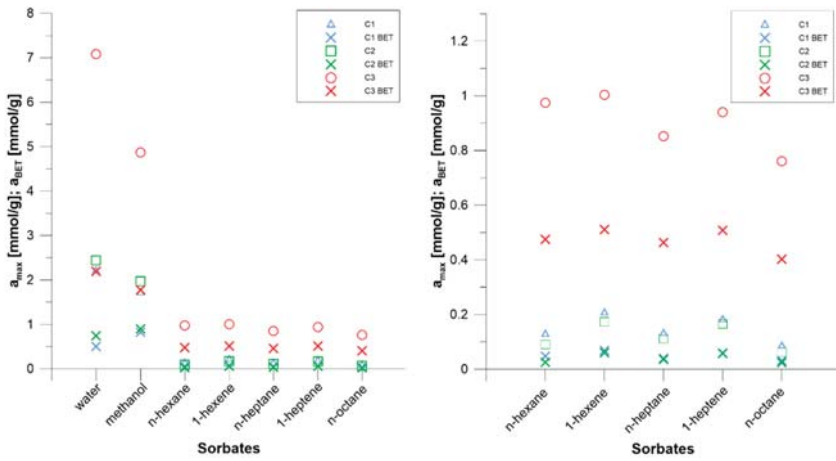
Figure 6. Maximum values of sorption (Ci max) and BET monolayer adsorbed quantities (Ci BET) of water vapour, methanol vapour, n-hexane, 1-hexene, n-heptane, 1-heptene, and n-octane on coals C1, C2, C3.
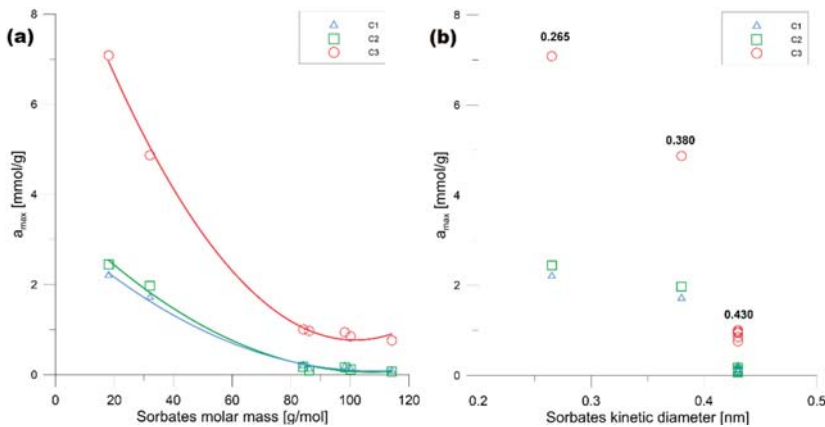
Figure 7. Maximum values of sorption a_{max} of water vapour, methanol vapour, n-hexane, 1-hexene, n-heptane, 1-heptene, and n-octane on coals C1, C2, C3: (**a**) in relation to molar mass of sorbates and (**b**) in relation to kinetic diameter of sorbates.

4. Discussion

The shape of the water sorption isotherms is sigmoidal and corresponds to type II according to the IUPAC classification (Figure 4), characteristic for sorbents containing micro- and mesopores. It indicates the initial monolayer adsorption followed by multilayer filling. The formation of a sorption monolayer corresponds to the initial part of the isotherm. The slope of the isotherm is steeper along this section, the greater the accumulation of polar sorption sites, which are identified with oxygen groups. The phase of filling subsequent adsorption layers corresponds to the transition of isotherms into a linear line. Previously adsorbed water molecules become sorption sites for the next sorbate molecules. This is a cluster-type phenomenon. At higher relative pressures, the isotherms tend to shift in the vertical direction. The cause may be the appearance of sorption in the network of the coal matrix, followed by swelling of the coal or condensation of sorbate vapours on the surface

of the pores [9]. For higher-rank coals, the filling of the monolayer takes place at a lower relative pressure than for lower-rank coals and the part of the isotherm that is close to the linear line is sloped at a smaller angle to the relative pressure axis. The Type II isotherm corresponds to processes with higher adsorption energy of the first layer compared to the subsequent layers, in contrast to type III, which corresponds to a process with opposite characteristics [20].

The shape of methanol sorption isotherms corresponds to type I according to the IUPAC classification, characteristic for microporous adsorbents (Figure 4). In the initial part of the isotherm, corresponding to the monolayer filling process, adsorption is limited by the number of adsorption sites. In the case of methanol, this number is potentially higher than in the case of water. Methanol molecules can be adsorbed not only by polar sites but also by non-specific apolar sites. Methanol sorption is less dependent on the nature of the coal surface than water sorption. The possibility of the formation of another layer after the formation of the first layer is limited by both the capillary structure of the sample and the interactions strength between the sorbate molecules.

The open pore structure of coal promotes the clustering and association of strongly interacting water molecules with dipole-dipole and hydrogen-bonding interactions. In the case of methanol, these interactions also occur, but are much weaker, and even with favourable coal texture the sorption increases slightly with increasing relative pressure. In general, the texture of higher-rank coals does not favour the formation of multiple layers of adsorbed methanol. This is reflected in the course of the relevant curves (Figure 4). The isotherm of water sorption on the C2 coal lies above that determined for the C1 coal, while the isotherms of methanol sorption on these coals are in their initial part above the mentioned curves and have a very close course. The sorption of methanol vapour is higher than that of water vapour on a significant part of the relative pressure scale. This trend persists longer for the lower-rank coals. The curves crossfor C3 coal at a value of $p/p0$ of approximately 0.35, for C2 coal at a value of $p/p0$ of approximately 0.72, and for C1 coal at a value of $p/p0$ of approximately 0.87. When saturation vapour pressure was reached, maximum sorption capacities were obtained, which are higher for coal-water systems than for coal-methanol systems (Figures 4 and 6). The sorption capacity of the investigated coals toward water and methanol depends to some extent on their degree of coalification. As the photographs in Figure 1 show, the organic matter morphology of the samples is similar. The presence of mineral matter in the C2 and C3 coals is responsible for the differences in the images. Hence, it is inferred that the differences in sorption amounts in the systems in question are strongly related to the chemical nature of the coal surface and not directly to its nanostructure. However, this regularity has different magnitude. The differences in sorption capacity between low-rank C3 coal and C2 and C1 coals are greater than between C2 and C1. The parameter that corresponds much better to the sorption properties of coal relative to those of low-molecular-weight polar sorbents is the content of element O in the coal. In the case of water, the dominant factors determining the sorption capacity of coal are (1) the capillary structure of the coal sorbent, enabling diffusion of the medium in the pores and creating conditions for multilayer sorption and condensation of sorbate vapours on the pore walls, and (2) the accessibility of polar adsorption sites, associated with functional groups, mainly oxygen groups. In the case of methanol, the capillary structure of the coal sorbent and the accessibility of the adsorption sites also play a key role. However, two aspects should be kept in mind. First, methanol molecules consist of a polar hydroxyl group and an apolar methyl group, therefore, they can be bonded to the coal surface by specific interactions with polar sites and nonspecific (dispersive) interactions with the apolar surface of the coal matrix. A methanol molecule can screen for more than one sorption site. Second, methanol molecules are larger than water molecules. Their kinetic diameters are 0.38 nm and 0.265 nm, respectively (Figure 7b).

The water sorption results obtained in our study were compared with the sorption capacity values obtained by Švábováet al. [7] and by Chen at al. [4] (Table 3). Coal marked Vitrinite sorbed about 43 mg of water/g of coal [7]. This is just slightly higher than

the 39.7 mg/g obtained for C1 coal. This leads to the conclusion that for coals with a similar degree of coalification expressed by vitrinite reflectance of about 0.9%, the maceral composition does not affect the magnitude of water sorption. The coal marked as Huminite sorbed about 170 mg of water/g of coal [7]. This is considerably higher than the 127.6 mg/g obtained for C3 coal. This is in accordance with the conclusions presented above regarding the relationship of the magnitude of water sorption with the capillary structure of the coal sorbent and the availability of polar adsorption sites, the amount of which decreases with increasing coal rank. The coal marked YZG2 sorbed approximately 82 mg of water/g of coal and the coal marked LH7 sorbed approximately 21 mg of water/g of coal [4]. These values are consistent with the findings from this publication Analogously, the methanol sorption results presented in this paper were compared with the sorption absorption values obtained by Takanohashi et al. [11] (Table 3). Coal marked as Upper Freeport sorbed approximately 1.2 mmol of methanol/g of coal [11]. This is a little lower than the 1.715 mmol/g obtained for C1 coal. In contrast, the Beulah–Zap marked coal sorbed approximately 6.5 mmol of methanol/g of coal [11]. This is significantly higher than the 1.97 mmol/g obtained for C2 coal. This is in accordance with the deductions presented above concerning the relationship of the magnitude of methanol sorption with the availability of polar adsorption sites. The ratio of sorption capacity of these low-rank coals is 3.3, while the ratio of the amount of elemental O content in these coals is 3.45. This indicates that there may be a near-linear relationship between oxygen content and sorption capacity toward methanol for coals with a similar degree of coalification.

Table 3. Comparison of selected relevant self-reported and literature data.

Coal	R_0 [%]	C^{daf} [%]	O^{daf} [%]	TV [%]	a_w [mg/g]	a_m [mmol/g]	$a_{w,prim}$ [%]
C1	0.92	84.24	4.6	73	39.7	1.715	-
C2	0.78	70.82	6.29	60	44.0	1.97	31
C3	0.51	-	-	67	127.6	-	-
Vitrinite [7]	0.88	-	-	93	43	-	-
Huminite [7]	0.37	-	-	n.a.	170	-	-
YZG2 [4]	0.65	-	n.a.	-	82	-	-
LH7 [4]	1.16	-	n.a.	-	21	-	-
Upper Freeport [11]	n.a.	86.2	4.6	-	-	1.2	-
Beulah-Zap [11]	n.a.	71.6	21.7	-	-	6.5	-
Albert [3]	0.75	-	10.7	-	-	-	50

R_0: vitrinite reflectance, C, O: content of element C, respectively, daf: dry–ash–free basis, T: vitrinite content, a_w: water sorption capacity, a_m: methanol sorption capacity, $a_{w,prim}$: water sorption share on primary sorption sites calculated as: $a_{BET} \cdot 100\%/a_{max}$, n.a.: data not available, -: data not available or irrelevant for purpose of comparison.

The shape of the isotherms of sorption of unsaturated hydrocarbons is close to sigmoidal (Figure 5). When they were assigned type II according to the IUPAC classification, they were supported by the elevation of the curve toward the vertical in the final part of the isotherm. In the case of saturated hydrocarbon sorption, this feature of the curve decreases with increasing length of the aliphatic chain and decreasing degree of coalification, which is well illustrated by isotherms for the sorption of n-octane and n-heptane (Figure 5). The shape of these isotherms is closer to type I according to the IUPAC classification (Figure 5). The sorption of vapours of nonpolar substances mainly involves a surface process and depends primarily on the porosity of the bituminous coal, in particular on the presence and distribution of micro- and mesopores. Coal appears as a molecular sieve in this system. Therefore, the sorption absorptivity of the C3 coal is definitely several times higher than that of the C2 and C1 coals. Therefore, the ratios of the sorption capacities of individual sorbates on the same coal are the smallest for the C3 coal (Figure 5).

The molecular dimensions of unsaturated hydrocarbons and their saturated counterparts are similar (Table 2 and Figure 7). The presence of a double bond in the hydrocarbon molecule affects the sorption mechanism, changes the course of the isotherm with respect

to the saturated counterpart, and leads to higher sorption values. This results from the interaction of the double bond (πelectrons) with the polar groups present on the surface of the coals [29]. This effect is more evident in the case of the C1 and C2 coals. The association of unsaturated hydrocarbon molecules on the surface of micropores is likely to occur because adsorbate-adsorbate interactions play a more significant role than adsorbate-adsorbent processes. It should also be noted that in the sorption of unsaturated hydrocarbons, the presence of π-electrons in the aromatic structures of coal is also important. Higher-rank coals have a higher degree of aromatic condensation resulting, on the one hand, in the presence of adsorption sites in the form of a delocalised sextet of π-electrons and, on the other hand, in a lower porosity, which reduces the possibility of interaction of the coal substance with the sorbate molecules. These interactions lead to higher sorption capacities of alkenes relative to alkanes of a chain/molecule length similar to that of these alkanes. Hence, the sorption capacity of the C1 coal toward these sorbates is higher than that of the lower-rank C2 coal (Figures 5 and 6). The sorption capacity of the hydrocarbon sorbates used increases in order: n-octane < n-heptane/n-hexane < 1-heptene < 1-hexene. This pattern is influenced by two factors: the presence or absence of a double bond and the size/length of the molecule. In relation to the maximum sorption values of 1-hexene and 1-heptene obtained for coal C3, 6 and 5 times lower sorption capacities were obtained for coal C2 and C1, respectively (Figure 6). The alkane sorption ratios obtained for coal C3 and coals C2 and C1 are 8 to 12 and 6 to 9, respectively (Figure 6). However, n-hexane and n-heptane sorb on coals C2 and C1 with close capacities and n-octane with lower capacity. For coal C3, the curves for these three homologues differ most clearly (Figure 5). Coal with a lower degree of coalification more clearly differentiates the course of sorption isotherms of alkanes. The higher sorption capacity of alkenes in comparison to that of their saturated counterparts indicates that the effect of double bonding is dominant over the influence of molecule length and shape. The pattern is more evident for higher-rank coals (Figure 5). Moreover, the curves obtained for 1-heptene are above those corresponding to the sorption of n-hexane, which further confirms which feature of the molecule has a greater influence on the sorption capacity.

When considering the relationship between the obtained values of the monolayer capacity a_{BET} and the maximum sorption capacity a_{max}, the criteria of the type of sorbate should first be taken into account, and then the influence of the type of sorbent should be analysed. This is supported, among other reasons, by the fact that for the higher-rank coals C1 and C2, the a_{BET} values differ only by water sorption, while for the rest of the sorbates, their a_{BET} values are almost the same (Figure 6).

For the sorption of water vapours, a_{BET} represents about 31% of the a_{max} values for C2 and C3 coals and about 23% for the highest rank C1. For methanol, higher values of a_{BET} relative to a_{max} were recorded. A clear dependence on the degree of coalification can also be seen, as the a_{BET} contributions to a_{max} are 36%, 45%, and 48% for the C3, C2, and C1 coals, respectively. Comparison of the a_{BET} for these sorbates reveals that the a_{BET} of methanol for the C1 and C2 coals is higher than that of water and for the C3 coal the ratio is reversed. In other words, the sorption of water on the higher rank C1 and C2 coals is higher than that of methanol but the water monolayer capacity is lower than that of methanol. This is most likely due to the overlapping of two phenomena. First, both sorbates undergo multilayer adsorption, but in the case of water molecules the process is more efficient because of strong dipole-dipole interactions and hydrogen bonds. The second aspect is the affinity of methanol for both polar and nonpolar sorption sites. The effect of decreasing the amount of the former with increasing degree of coalification is reflected in a larger difference between the a_{BET} of water and the a_{BET} of methanol for the C1 coal than for the C2 coal (Figure 6). On the other hand, on low-rank C3 coal, the sorption of water and methanol takes place mainly at numerous polar sorption sites. Because of the shape and larger size of the methanol molecules, they are less efficient at using the available sites effectively, hence the lower a_{BET} value for this sorbate.

The self-reported monolayer capacities obtained a_{BET} and the maximum sorption capacity a_{max} of water were compared with the values obtained by the authors Charrire and Behra [3] (Table 3). For the coal marked Albert in their work, the amount of water adsorbed on the primary sorption sites was 50% [3]. For our C2 coal, the ratio of a_{BET} and a_{max} is 31%. The ratio of the fraction of sorption at the primary sorption sites to the fraction of total multilayer sorption of the compared coals is 1.6, while the ratio of the amount of element O content in these coals is 1.7. These values indicate the possibility of a linear relationship between the oxygen content and the monolayer capacity in water sorption for coals with similar degrees of coalification. This is in agreement with the arguments and conclusions presented earlier in the paper. In the case of hydrocarbon sorption, a_{BET} provides between 28% and 38% of the a_{max} values for C1 and C2 coals. Slightly higher proportions are shown for systems with C2 coal. For the lowest rank C3 coal, the ratios are between 49% and 54%. No clear dependence on hydrocarbon type was observed in this regard. The a_{BET} values for the C1 and C2 coals overlap as in the case of methanol sorption (Figure 6).

5. Conclusions

On the basis of the analysis of the literature on the subject and on the studies carried out and the obtained results, it was concluded that the nature of the adsorbate determines the course and magnitude of adsorption due to the kinetics of the process and in terms of specific interaction with the sorbent surface.

- The shape of water sorption isotherms corresponds to type II according to the IUPAC classification, while the shape of methanol sorption isotherms corresponds to type I according to the IUPAC classification. The sorption in the coal-water system follows a course characteristic for sorbents containing micro- and mesopores with the formation of a monolayer and then a multilayer structure. Sorption in the coal-methanol system follows a course characteristic for microporous adsorbents, including formation of the monomolecular adsorbent layer.
- The difference in the maximum sorption value between low-rank coal C3 coal and higher rank coals C2 and C1 is greater than between C2 coal and C1 coal. The parameter that corresponds better to the sorption properties of coal toward water and methanol is the content of element O in the coal.
- The sorption of methanol vapour is higher than that of water vapour in the initial part of the relative pressure scale. This tendency remains longer for lower-rank coals. The maximum sorption capacity is higher for coal-water systems than for coal-methanol systems. The open-pore structure of coal is responsible for this diversity. It enables the formation of association of water molecules with dipole-dipole and hydrogen bonding interactions. In the case of methanol, these interactions are weaker.
- The factors that determine the sorption capacity of coal toward water are (1) the capillary structure of the sorbent, in terms of diffusion in pores and conditions for the occurrence of multilayer sorption and condensation of sorbate vapours, and (2) the availability of polar adsorption sites, associated with oxygen functional groups. In the case of methanol, the second aspect also includes the availability of an apolar coal surface, since methanol molecules can bond to specific polar sites and nonspecific apolar sites. In addition, one methanol molecule can screen for more than one sorption site.
- The shape of the sorption isotherms of unsaturated hydrocarbons is close to type II according to the IUPAC classification. In the case of saturated hydrocarbons, the shapes of the sorption isotherms change from type II to type I as the length of the aliphatic chain in the molecule increases and the degree of coal coalification decreases. The sorption of vapours of nonpolar substances on coal has a surface character. The pores present in coal act as a molecular sieve in this system.
- The sorption capacity of the applied hydrocarbon sorbates depends on (1) the presence or absence of a double bond and (2) the size of the molecule. The sorption capacity of these sorbates increases in the order: n-octane < n-heptane/n-hexane < 1-heptene < 1-hexene.

- The effect of differentiating the sorption amounts of the studied sorbates increases with the degree of coal coalification. Coal with a higher degree of coalification shows greater differentiation of the course of isotherms of alkane sorption, due to higher microporosity, and greater sorption of alkane and their unsaturated counterparts, due to the presence of π-electrons in aromatic structures of coal. It is significant that the double bond effect is dominant over the influence of the length and shape of the hydrocarbon molecule.

- Based on the analysis of the data description with the BET sorption isotherm equation, it was found that the water monolayer capacity is higher than that of methanol in low-rank C3 coal. The sorption of water and methanol takes place mainly at numerous polar sorption sites. Smaller water molecules are more efficient at using the available adsorption sites.

- Analysis of data using the BET sorption isotherm showed that the water monolayer sorption capacity is lower than that of methanol on the higher-rank coals C1 and C2, although the maximum sorption capacity of water is higher than that of methanol. The affinity of methanol for both polar and nonpolar sorption sites results in a higher monolayer capacity. Multilayer sorption based on strong dipole-dipole interactions and hydrogen bonds between water molecules results in a higher sorption capacity.

Author Contributions: Conceptualization, P.B. and K.Z.; methodology, P.B. and K.Z.; investigation, A.K.; resources, A.K.; data curation, K.C.; writing—original draft preparation, K.C.; writing—review and editing, K.C. and P.B.; visualization, K.C. and P.B.; supervision, K.Z.; funding acquisition, K.Z. All authors have read and agreed to the published version of the manuscript.

Data Availability Statement: Not applicable.

References

1. Bhattacharyya, K. The Role of Sorption of Water Vapour in the Spontaneous Heating of Coal. *Fuel* **1971**, *50*, 367–380. [CrossRef]
2. Ceglarska-Stefańska, G.; Brzóska, K.; Winnicki, J. Sorption of Water Vapour on Exinite Concentrates. *Adsorption* **1998**, *4*, 313–319. [CrossRef]
3. Charrière, D.; Behra, P. Water Sorption on Coals. *J. Colloid Interface Sci.* **2010**, *344*, 460–467. [CrossRef]
4. Chen, M.; Yang, Y.; Gao, C.; Cheng, Y.; Wang, J.; Wang, N. Investigation of the Fractal Characteristics of Adsorption-Pores and Their Impact on the Methane Adsorption Capacity of Various Rank Coals via N_2 and H_2O Adsorption Methods. *Energy Sci. Eng.* **2020**, *8*, 3228–3243. [CrossRef]
5. Liu, S.; Zhang, D.; Lun, Z.; Zhao, C.; Wang, H. Occurrence of Water within Different Rank Coals: A Review. *Energy Sources Part A Recovery Util. Environ. Eff.* **2020**, 1–19. [CrossRef]
6. Mo, Q.; Liao, J.; Zhang, Y.; Chang, L.; Han, Y.; Bao, W. Kinetic Analysis on Water Adsorption of Thermally Upgraded Lignite. *Fuel Process. Technol.* **2021**, *211*, 106603. [CrossRef]
7. Švábová, M.; Weishauptová, Z.; Přibyl, O. Water Vapour Adsorption on Coal. *Fuel* **2011**, *90*, 1892–1899. [CrossRef]
8. Baran, P.; Jodłowski, G.S.; Krzyżanowski, A.; Zarębska, K. Experimental Testing of Methanol Sorption on Selected Coal Samples from Upper Silesian Basin. *Geol. Geophys. Environ.* **2014**, *40*, 261–269. [CrossRef]
9. Krzyżanowski, A.; Żyła, M. Characteristics of Water, Methanol and Benzene Vapours Sorption Properties of Selected Metamorphic Types of Hard Coal. *Gospod. Surowcami Miner.* **2007**, *23*, 139–147.
10. Spitzer, Z.; Bíba, V.; Boháč, F.; Málková, E. Micropore Structure Analysis of Coal from Adsorption Isotherms of Methanol. *Fuel* **1977**, *56*, 313–318. [CrossRef]
11. Takanohashi, T.; Terao, Y.; Iino, M. Sorption Behaviors of Methanol Vapor by Coal Extracts and Residues. *Fuel* **2000**, *79*, 349–353. [CrossRef]
12. Baran, P.; Cygankiewicz, J.; Krzyżanowski, A.; Zarębska, K. Sorption of Saturated and Unsaturated Hydrocarbons on Selected Coal Sample from the Pniówek Mine. *Geol. Geophys. Environ.* **2013**, *39*, 341–349. [CrossRef]
13. Dudzińska, A.; Cygankiewicz, J.; Włodarek, M. Natural Content of Gases: Carbon Monoxide, Carbon Dioxide, Hydrogen and Unsaturated Hydrocarbons of Ethylene, Propylene and Acetylene in Selected Bituminous Coal Seams. *Int. J. Coal Geol.* **2017**, *178*, 110–121. [CrossRef]

14. Dudzińska, A.; Howaniec, N.; Smoliński, A. Effect of Coal Grain Size on Sorption Capacity with Respect to Propylene and Acetylene. *Energies* **2017**, *10*, 1919. [CrossRef]
15. Dudzińska, A. Analysis of Sorption and Desorption of Unsaturated Hydrocarbons: Ethylene, Propylene and Acetylene on Hard Coals. *Fuel* **2019**, *246*, 232–243. [CrossRef]
16. Wojtacha-Rychter, K.; Smoliński, A. Multi-Component Gas Mixture Transport through Porous Structure of Coal. *Fuel* **2018**, *233*, 37–44. [CrossRef]
17. Wojtacha-Rychter, K.; Smoliński, A. Selective Adsorption of Ethane, Ethylene, Propane, and Propylene in Flammable Gas Mixtures on Different Coal Samples and Implications for Fire Hazard Assessments. *Int. J. Coal Geol.* **2019**, *202*, 38–45. [CrossRef]
18. Allardice, D.; Evans, D. The-Brown Coal/Water System: Part 2. Water Sorption Isotherms on Bed-Moist Yallourn Brown Coal. *Fuel* **1971**, *50*, 236–253. [CrossRef]
19. Czuchajowski, L.; Lasoń, M.; Żyła, M. Tlenowe Grupy Reaktywne Węgla Kamiennego w Świetle Badań Sorpcji Par Polarnych. *Chem. Stosow.* **1960**, *1*, 3–13.
20. Lasoń, M.; Żyła, M. Wielokrotna Sorpcja i Desorpcja Par Wody i Alkoholu Metylowego Na Węglach Kamiennych. *Zesz. Nauk. Akad. Górniczo-Hutniczej. Górnictwo* **1973**, *366*, 21–32.
21. Krevelen, D.W.; Schuyer, J. *Coal Science: Aspects of Coal Constitution*; Elsevier: Amsterdam, The Netherlands, 1957.
22. Liu, Z.; Zhang, Z.; Choi, S.K.; Lu, Y. Surface Properties and Pore Structure of Anthracite, Bituminous Coal and Lignite. *Energies* **2018**, *11*, 1502. [CrossRef]
23. Korta, A.; Laskowski, T.; Lasoń, M.; Żyła, M. Sorpcja Par Metanolu i Wody Na Petrograficznych Odmianach Węgli Kamiennych. *Koks-Smoła-Gaz* **1962**, *7*, 1–6.
24. Orzechowska-Zięba, A.; Baran, P.; Zarębska, K.; Cygankiewicz, J. Sorpcja Pary Wodnej Na Próbkach Wytypowanych Węgli Kamiennych w Aspekcie Określenia Potencjału Magazynowego Złoża. *Zesz. Nauk. Inst. Gospod. Surowcami Miner. I Energią PAN* **2017**, *97*, 71–82.
25. Kotarba, M.J. Composition and Origin of Coalbed Gases in the Upper Silesian and Lublin Basins, Poland. *Org. Geochem.* **2001**, *32*, 163–180. [CrossRef]
26. Dudzińska, A. Analiza Sorpcji Gazów Współistniejących w Atmosferze Kopalnianej. *Przegląd Górniczy* **2016**, *72*, 10–16.
27. Dudzińska, A.; Cygankiewicz, J.; Włodarek, M. Gaseous Emissions from Freshly Extracted Coal in the Inert and Air Atmosphere in Terms of Natural Desorption and Early Coal Oxidation. *Fuel* **2021**, *285*, 119066. [CrossRef]
28. Zhao, H.; Lai, Z.; Firoozabadi, A. Sorption Hysteresis of Light Hydrocarbons and Carbon Dioxide in Shale and Kerogen. *Sci. Rep.* **2017**, *7*, 16209. [CrossRef]
29. Krzyżanowski, A.; Zarębska, K. Sorpcja Par Cieczy Apolarnych Na Węglu Kamiennym o Różnym Składzie Petrograficznym. *Gospod. Surowcami Miner.* **2007**, *23*, 175–181.
30. Saha, S.; Sharma, B.K.; Kumar, S.; Sahu, G.; Badhe, Y.; Tambe, S.; Kulkarni, B. Density Measurements of Coal Samples by Different Probe Gases and Their Interrelation. *Fuel* **2007**, *86*, 1594–1600. [CrossRef]
31. Brunauer, S.; Emmett, P.H.; Teller, E. Adsorption of Gases in Multimolecular Layers. *J. Am. Chem. Soc.* **1938**, *60*, 309–319. [CrossRef]

Article

Modified Activated Carbon as an Effective Hydrogen Adsorbent

Paweł Baran *, Bronisław Buczek and Katarzyna Zarębska

Faculty of Energy and Fuels, AGH University of Science and Technology, Al. Mickiewicza 30,
30-059 Cracow, Poland
* Correspondence: baranp@agh.edu.pl; Tel.: +48-12-617-20-79

Abstract: Hydrogen adsorption measurements were taken by the weighting method using the Sartorius low-pressure microbalance. Experiments were conducted at two temperatures: 77.5 and 300 K; the adsorbent used was active carbon obtained from wood and modified with potassium hydroxide. The porous structure of the carbon prior to and after modification was evaluated based on the nitrogen adsorption and desorption data. Thus, the densimetric characteristic of active carbon was modified; porous structures were developed in the range of micro-, meso- and macropores and the volume of hydrogen adsorbed at 77.5 K showed an almost four-fold increase. Modified active carbons are found to be suitable for applications in hydrogen storage systems.

Keywords: hydrogen; adsorption; storage; active carbon

1. Introduction

Hydrogen has become one of the most important energy sources in the 21st century. In a long term, it may actually replace oil and petroleum. It is an ideal fuel because of its easy availability and for environmental reasons. The product of hydrogen burning is water vapour, which does not add to air pollution. Currently, hydrogen is mainly used in industrial applications, but it can also be used as a source of energy for the lighting and heating of buildings, for electricity generation and as an engine fuel. Fuel cells that utilise the reaction between hydrogen and oxygen are used to produce electricity; their first application was aerospace technology [1,2].

No matter the actual application, of particular importance is the hydrogen storage method. The simplest strategy involves the storage of compressed H_2. The main drawback, however, is the low density of H_2 in this phase. Storage of liquid H_2 does not have this disadvantage, although the hydrogen tank temperature needs to be maintained below the critical point for hydrogen (33.145 K). In the context of supplying power to the fuel cells, a most interesting option involves metal hydride storage using the reversed sorption, although a heavyweight hydrogen tank is required, and that still remains a major disadvantage. The density of stored hydrogen can be increased through the physical process of gas adsorption in porous adsorbents. The method relying on the adsorption processes seems promising, because hydrogen can be recovered from the adsorbent's surface at the room temperature without necessitating the use of the heating system to trigger gas desorption. There are studies exploring potential applications of such adsorbents as carbon nanotubes [3], graphene [4], carbon nanofibers [5], and active carbon [6–9]. Despite extensive research efforts made so far to obtain high-porosity carbon adsorbents with enhanced storage capacity, their practical applications for hydrogen storage are still limited.

In the gravimetric method the quantity of adsorbed gas is obtained directly from the increase in the adsorbent's weight, and measurements are taken using high-precision and high-sensitivity microbalances [10,11]. Jagiełło et al. investigated [12] gas adsorption under 0–6 MPa and at 119–319 K using a weight-type apparatus in which measurable weight was 4 μg. Cazorla-Amoros et al. [13] used the DMT Sartorius 4406 high-pressure sorption microbalance to investigate carbon dioxide adsorption on active carbon and obtained

adsorption isotherms at a pressure of up to 4 bars. The repeatability of measurement results was reported to be 1%. The same type of weight apparatus [14] was used in studies on adsorption of N_2, Ar and CH_4 with microporous adsorbents at a temperature of 258–418 K and under pressure of 0.1–20 MPa. The article [15] summarises the contents of previous research studies on hydrogen storage in porous materials, provides a thorough review of current work of its authors and outlines the directions for further research efforts.

This paper summarises the results of research work aimed at developing the porous structure of active carbons. With regards to storage projects, the adsorbent ought to contain micropores in the size range of approximately 1 nm. For that reason carbon was activated with KOH, which is a most effective method used to prompt the development of porous structure in carbon sorbents [16,17].

2. Materials and Methods

Testing was done on active carbon made from pinewood (Picazine) modified with potassium hydroxide (PicazineK) [18]. Picazine carbon was dried and then mixed with ground KOH in the ratio 1:3 (m/m). The treatment was carried out in a muffle furnace at a temperature of 1023 K in the atmosphere of neutral gas (N2). The mixture was rapidly heated up to 973 K, and then the temperature was raised to 1023 K at a rate of 10 K/min. Once this temperature was reached, the mixture was maintained at this temperature for 30 min and then cooled to ambient temperature. During the entire treatment process, the neutral gas (N_2) was flowing inside the furnace at a rate of 30 L/min. When the reaction mixture reached the ambient temperature, the potassium hydroxide present in the mixture was neutralized with 5% HCl solution. Thus, modified carbon produced a solution which remained green-colored during the initial period of rinsing. After each subsequent rinsing of the potassium base, the suspension was decanted and diluted with distilled water and its pH value was measured. This treatment was repeated several times, until the pH readout of the filtrate became 6.5. When the specified pH level was achieved, the active carbon was separated from the solution by filtration under reduced pressure of 10–15 mmHg, and the filter cake was rinsed with distilled water and dried at 393 K. The modified product was obtained with a yield of 60.5% (m/m). The KOH modified active carbon sample was denoted as Picazine K.

Active carbon is originally produced by chemical activation using orthophosphoric acid by Societe PICA, France [19]. Adsorption tests were also performed on 5.0 pure hydrogen supplied by Linde Gaz.

Bulk density of carbon was determined using the type PT-E Powder Characteristics Tester apparatus, its apparent density measurements were taken with the EDA GeoPyc 1360 system, and real density (helium density) was obtained using the Accu-Pyc 1330 pycnometer. Density measurement and calculation data are summarized in Table 1.

Table 1. Properties of the activated carbons used.

Properties	Picazine	Picazine K
Bulk density (n), g/cm^3	0.204	0.120
Apparent density (p), g/cm^3	0.450	0.325
Real density ((r), g/cm^3	1.777	2.669
Total porosity (εc), cm^3/cm^3	0.885	0.631
Volume of pores (V), cm^3/cm^3	1.660	2.702

The characteristics of the porous structure were determined basing on the low-temperature adsorption and desorption isotherms for nitrogen (77 K). High-precision sorption measurements were taken with the ASAP 2020 apparatus over a wide range of relative pressures, from approx. 10^{-7} down to 0.99. Prior to the measurements, carbon samples were vacuum heated at 423 K for 16 h. The obtained measurement data were used to determine key parameters of the porous structure of active carbon (Pic) and of carbon

modified with potassium hydroxide (PicK). The following porous structure parameters were calculated for the samples:

- Specific surface area according to Brunauer—Emmet—Teller (BET) methodology.
- Total pore volume for relative pressure $p/p_0 = 0.99$;
- Microporous structure parameters (pores with diameter up to 2 nm) according to Dubinin—Radushkevich, Dubinin—Astakhov and t-plot methods;
- Mesoporous structure parameters (pores with diameters of 2–50 nm)—volume and area distributions of mesopores according to Barrett-Joyner-Halenda (BJH) methodology;

The analysis was performed according to the recommendations of standards:

- ISO 9277:2010(E), Determination of the specific surface area of solids by gas adsorption—BET method;
- ISO 15901-2:2006(E), Pore size distribution and porosity of solid materials by mercury porosimetry and gas adsorption—Part 2: Analysis of mesopores and macropores by gas adsorption;
- ISO 15901-3:2007(E), Pore size distribution and porosity of solid materials by mercury porosimetry and gas adsorption—Part 3: Analysis of micropores by gas adsorption;
- NIST 2006, Porosity and Specific Surface Area Measurements for Solid Materials.

Measurement and calculation data are summarized in Table 2.

Table 2. Structural parameters of active carbons.

Parameter	Picazine	Picazine K
Specific surface area calculated using the BET method, S_{BET}, m^2/g	1462	2939
Total volume of pores for p/p$_0$ = 0.99, $V_{total}^{0.99}$, cm^3/g	1.024	1.488
Parameters of texture of micropores by Dubinin and Radushkevich (DR)		
Surface of micropores, S_{mikro}^{DR}, m^2/g	1392	2817
Volume of micropores, V_{mikro}^{DR}, cm^3/g	0.494	1.001
Adsorption energy in micropores, E_{mikro}^{DR}, kJ/mol	16.22	17.77
Parameters of texture of micropores by Dubinin and Astakhov (DA)		
Surface of micropores, S_{mikro}^{DA}, m^2/g	1127	2229
Volume of micropores, V_{mikro}^{DA}, cm^3/g	0.500	0.938
Adsorption energy in micropores, E_{mikro}^{DA}, kJ/mol	16.11	18.49
Mean diameter of pores, d_r, nm	1.78	1.68
Dominant diameter of pores, d_d, nm	1.60	1.54

Figures 1 and 2 presented the results of the DFT analysis.

A diagram of the apparatus used in hydrogen adsorption and desorption experiments is shown in Figure 3.

Adsorption and desorption isotherms were obtained using the low-pressure microbalance Sartorius [20,21]. A sample with a mass of approximately 0.1 g was used for the tests. The accuracy of the microbalance in the tested measurement range was 10 μg. The microbalance was placed in the air thermostat where the constant temperature of 300 K was maintained. The sample to be tested was placed on one pan and the counterweight was filled with a non-sorptive material. To remove adsorbed gases and vapors from the sample's surface, the system (with open valves V1 and V3) was degassed for 8 h using a vacuum pump to reach the static vacuum of 10^{-2} Pa, and to maintain a constant weight. Afterwards, the glass arms of the microbalance were immersed in vessels filled with liquid nitrogen. Subsequent points of the isotherm were determined using the pressure progression method by dosing gas to the system through valves V1 and V2. The adsorption equilibrium was obtained after about 15 min. Pressure control in the system was effected using a pressure

transducer P operating in the range of 0–1 bars. The desorption isotherm was obtained by gradually reducing the pressure in the system using the vacuum pump, via valves V1 and V3. The waiting time to determine the desorption equilibrium was approx. 30 min. Measurements of adsorption and desorption isotherms were carried out at 77.5 K and 300 K for both carbon samples. The results are summarized in Figures 4–7.
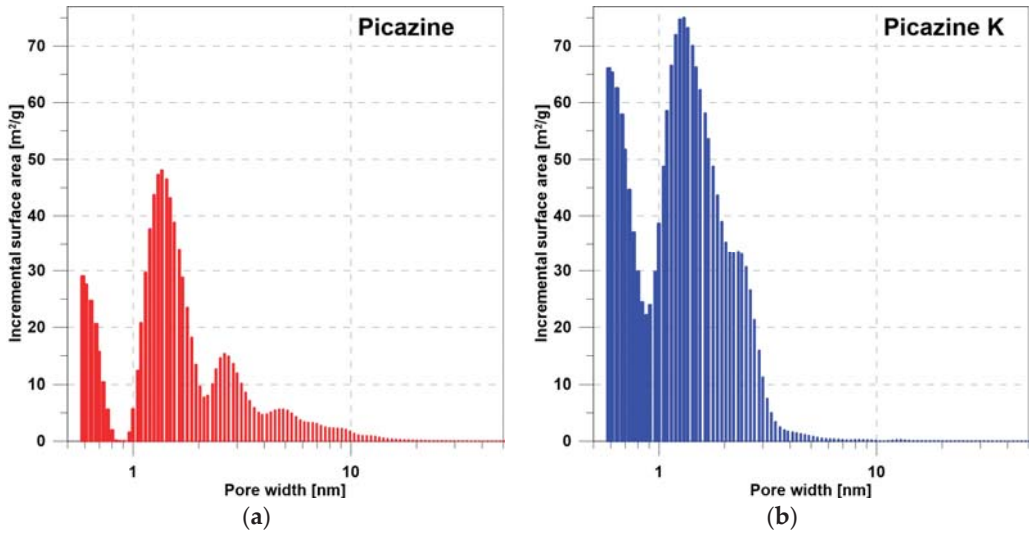
Figure 1. The dependence of the pore surface on the pore diameter determined by the DFT method for the (**a**) Picazine and (**b**) Picazine K samples.
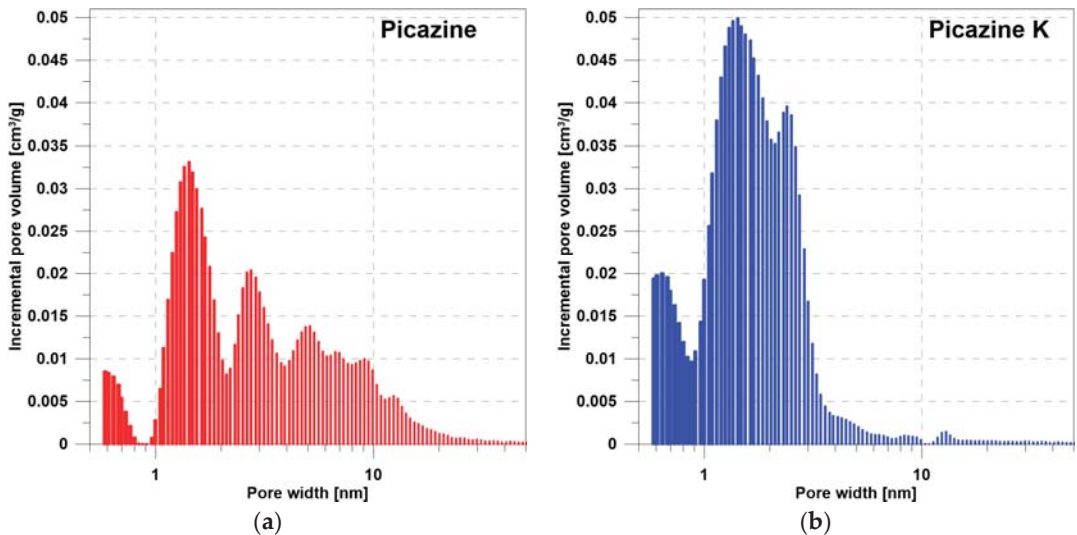
Figure 2. The dependence of the pore volume on the pore diameter determined by the DFT method for the (**a**) Picazine and (**b**) Picazine K samples.
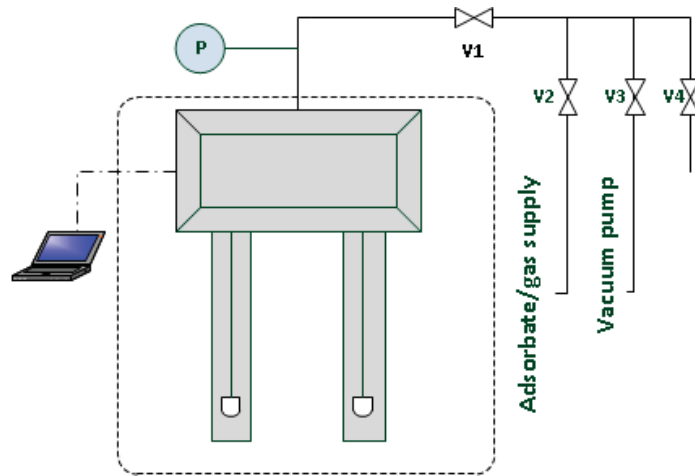
Figure 3. Apparatus used for measurements of hydrogen adsorption-desorption (V1-V4-valves, P-pressure transducer).
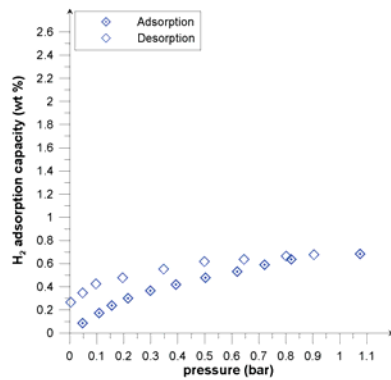
Figure 4. Adsorption/desorption isotherms of hydrogen onto Picazine at 77 K.
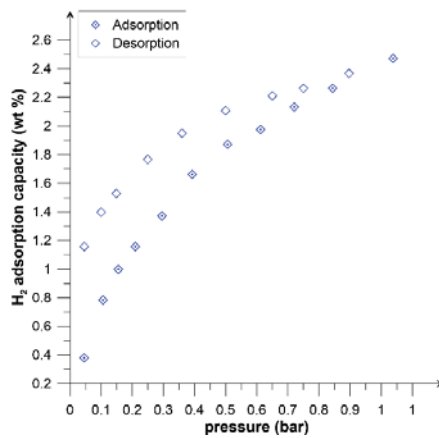
Figure 5. Adsorption/desorption isotherms of hydrogen on Picazine K at 77 K.
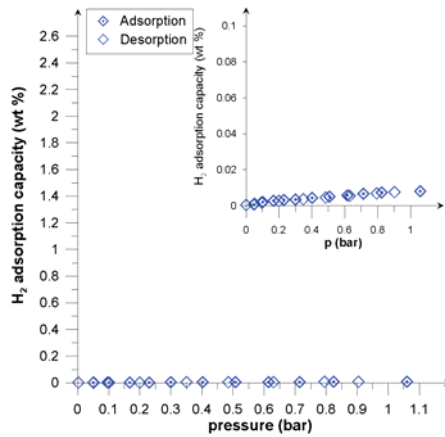
Figure 6. Adsorption/desorption isotherms of hydrogen on Picazine at 300 K.
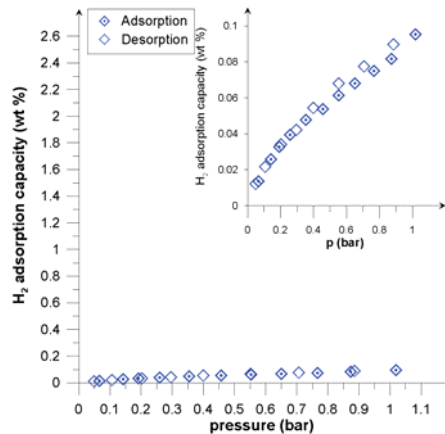
Figure 7. Adsorption/desorption isotherms of hydrogen on Picazine K at 300 K.

3. Results and Discussion

Based on the DFT analysis (Figures 1 and 2), it can be seen that the Picazine sample (before modification) was characterized by a dominant share of micropores, with a certain range of mesopores. Chemical activation of KOH changes the pore structure in the adsorbent. The presence of pores in the meso range disappears, while the share of micropores and submicropores increases significantly. This correlates with the pore volume values shown in Tables 2 and 3. In Table 2, the given volume values were calculated based on real and apparent densities. Table 3 shows the results of the analysis of adsorption isotherms which were fitted by the DR and DA equations. Both equations are applicable to describe adsorption isotherms on microporous materials. The calculated pore volume values presented in the manuscript are different, but this is due to the way they are calculated and the limitations of the models. Analyzing the results of the DFT analysis, we see that the range of pores includes both the range of micropores (in dominant quantity) and the range of narrower mesopores. Therefore, the values of constants calculated from the DR and DA equations may be subject to some uncertainty. Regardless, we see that there have been changes in these values after activation of the carbon material. In all cases, an increase is observed, a phenomenon which is also observed on hydrogen adsorption isotherms.

The analysis of measured hydrogen adsorption/desorption isotherms obtained at the temperature of liquid nitrogen reveals that the hydrogen adsorption capacity of the PicazineK carbon was nearly three times higher than that of the unmodified sample.

In both cases a hysteresis loop was registered. The potential occurrence of the capillary condensation phenomenon could be excluded due to the low critical temperature of hydrogen. The reported loop can be attributable to certain kinetic restrictions during the process of desorption.

The presence of a hysteresis loop has been previously registered in tests on other adsorbents. In the case of zeolites [22,23], it is reasonable to assume the occurrence of sealed micropores from which hydrogen cannot be removed. As regards nanotubes, the occurrence of a well-pronounced hysteresis loop in the H_2 adsorption/desorption isotherms measured at 77.5 K is consistent with a high energy barrier for desorption of H_2 molecules due to the presence of nanotubes with submicroporous inside-tube characteristics [24]. In the case of porous metal organic frameworks, it has been established that desorption restrictions are stronger at lower temperatures [25], and that they are also a function of the micropore radius [26]. Consequently, when pores are very narrow, they require higher temperature for desorption.

In the case of the investigated active carbons, the registered effects were similar to MOFs in relation to the nature of the microporous material. Calculations of the dominant pore diameters revealed a significant proportion of sub-micropores (Table 2). Recalling the McEnaney equation [27] for micropore size calculations, it was established that for the adsorption energy $E_0 = 16.22$, the micropore size becomes 0.40 nm, whilst for $E_0 = 17.77$, the size equals 0.36 nm in the slit pore model. An adsorbent having a high proportion of pores in this size will be a most promising material to be used in hydrogen storage systems [28,29]. Accordingly, the presence of hydrogen in the carbon structure was found to be molecular in nature. Similar values of sorption capacity at 77.5 K (excess hydrogen uptake) were obtained by Geng et al. [30]. Adsorption/desorption isotherms obtained at the ambient temperature are shown in Figures 6 and 7. In the case of the unmodified Picazine carbon, the adsorption capacity was found to be low (comparable to the measurement error). The modified PicazineK carbon had an adsorption capacity of 0.1 wt% (which corresponds to 12 cm^3 STP/g) (Figure 7). At room temperature, low-pressure sorption and desorption processes were found to be reversible, and in the context of practical applications this adsorbent does not seem appropriate for hydrogen storage. However, when comparing the results obtained for similar carbon adsorbents, including KOH activated ones, it is reasonable to suppose that in the elevated pressure range the properties of investigated samples might be more favorable in the context of potential applications. In their work, Minoda et al. [31] studied hydrogen sorption on active carbons, with rice hulls or PAN (Poly-acrylonitrile) as precursors. The specific surface and pore density of the samples thus obtained were similar to those of the carbon samples investigated in this study. One has to bear in mind, however, that experiments were conducted at elevated pressures. For the sample having the surface area 1600 m^2/g under the pressure 10 MPa the hydrogen uptake was 0.5%. Similarly, the hydrogen storage capacity of the sample S_{BET} 3000 m^2/g was found to be 0.7%.

According to the results of Panel et al. [32] and their literature analysis, the density of the adsorption monolayer is less than that of liquid hydrogen. This is directly due to the surface area of the hydrogen molecule that settles on the adsorbent, and it is also closely related to the distances between hydrogen molecules in the adsorption layer. This corresponds to Chahine's Rule which states that, in general, for every 500 m^2/g of surface area there is 1 wt% of hydrogen adsorption. Note, however, that the rule indicates the potential value of stored hydrogen relative to the specific surface area. The results obtained, show that KOH activation allowed the storage of about 2.5% of H^2 already at a pressure of 1 bar. This already relatively high adsorption value is related to the high proportion of micropores. Theoretical calculations [33,34] as well as experimental results [35] show that significant adsorption occurs in pores below 1.3 nm. These reports confirm a significant

increase in hydrogen adsorption on the PicazineK sample, resulting from an increase in the division of micropores formed by activation with KOH (Figure 1b).

Table 3. Hydrogen storage in various conditions using activated carbons.

Type of Adsorbent	S_{BET} (m²/g)	H₂ Uptake (wt. %)	Storage Conditions	Additional Information	Ref.
AC from coffee beans	2070 2070	0.6 0.4	120 bar, 298 K 40 bar, 77 K	KOH activated	[36]
AC from anthracite	1149 2029 2849 3220 1308 2451 3073	3.2 4.9 6.0 5.7 2.9 5.8 5.7	40 bar, 77 K	KOH/NaOH activated	[37]
AC from pine	1055 1409	1.61 1.93	1 bar, 77 K	CO₂ activated	[38]
AC from low rank coal	640	0.29	40 bar, 77 K	KOH activated	[39]
AC from oil palm shell	3503	6.7 2.86	40 bar, 77 K 1 bar; 77 K	KOH activated	[40]
Carbon monolith from lignite	973	1.28	60 bar, 293 K	CO₂ activated	[41]
AC from stone of cherry laurel	1624	2.9	1 bar, 77 K	KOH activated	[42]

Investigations carried out using active carbon (Table 3) have shown that adsorption in activated carbon can be more efficient than compressed gas, but only at low temperatures. Chemical modification of adsorbents using KOH is known, although its impact varies [43]. In work by Lendzion-Bieluń et al., [44] the influence of chemical activation on WG-12 activated carbon was analyzed. This AC is obtained as a result of steam activation of hard coal with low ash content. As a result of the activation process with KOH, the surface area has remained virtually unchanged. It was different in the case of activated carbon obtained from the KOH activation of finger citron residue [45]. The use of KOH caused a very large development of the surface to acquire an adsorbent value similar to that obtained in this work (PicazineK). It seems, therefore, that a carbon precursor plays an important role in the chemical activation process using KOH. In the case of a compact structure that occurs in the case of low-ash hard coal, only the chemical surface area will change, and the nature of the texture will remain unchanged.

4. Conclusions

Adsorption experiments have demonstrated a substantial increase in adsorptive capacity of active carbon produced from pinewood on an industrial scale and then subjected to chemical activation with potassium hydroxide. It appears that the hydrogen adsorption capacity of the thus obtained active carbon is significantly higher than that of the unmodified sample at a temperature of 77.5 K. Key parameters of the porous structure of active carbon measured before and after the modification correlate well with the hydrogen adsorption rate determined by the gravimetric method.

In the context of those findings, the main consideration is whether the active carbon is a suitable material for practical applications, such as storage of gaseous fuels and distribution of gases which do not readily condense.

References

1. Broom, D.P. *Hydrogen Storage Materials: The Characterisation of Their Storage Properties*; Springer: London, UK, 2011; ISBN 9780857292216.
2. Sherif, S.A.; Goswami, D.Y.; Stefanakos, E.K.; Steinfeld, A. *Handbook of Hydrogen Energy*; CRC Press: Boca Raton, FL, USA, 2014; ISBN 9781420054477.
3. Singh, A.K.; Lu, J.; Aga, R.S.; Yakobson, B.I. Hydrogen Storage Capacity of Carbon-Foams: Grand Canonical Monte Carlo Simulations. *J. Phys. Chem. C* **2011**, *115*, 2476–2482. [CrossRef]
4. Darkrim Lamari, F.; Levesque, D. Hydrogen Adsorption on Functionalized Graphene. *Carbon N. Y.* **2011**, *49*, 5196–5200. [CrossRef]
5. Ryu, Z.; Rong, H.; Zheng, J.; Wang, M.; Zhang, B. Microstructure and Chemical Analysis of PAN-Based Activated Carbon Fibers Prepared by Different Activation Methods. *Carbon N. Y.* **2002**, *40*, 1144–1147. [CrossRef]
6. Texier-Mandoki, N.; Dentzer, J.; Piquero, T.; Saadallah, S.; David, P.; Vix-Guterl, C. Hydrogen Storage in Activated Carbon Materials: Role of the Nanoporous Texture. *Carbon N. Y.* **2004**, *42*, 2744–2747. [CrossRef]
7. Bhat, V.V.; Contescu, C.I.; Gallego, N.C.; Baker, F.S. Atypical Hydrogen Uptake on Chemically-Activated, Ultramicroporous Carbon. *Carbon N. Y.* **2010**, *48*, 1331–1340. [CrossRef]
8. Xiao, J.; Mei, A.; Tao, W.; Ma, S.; Bénard, P.; Chahine, R. Hydrogen Purification Performance Optimization of Vacuum Pressure Swing Adsorption on Different Activated Carbons. *Energies* **2021**, *14*, 2450. [CrossRef]
9. Ramirez-Vidal, P.; Canevesi, R.L.S.; Sdanghi, G.; Schaefer, S.; Maranzana, G.; Celzard, A.; Fierro, V. A Step Forward in Understanding the Hydrogen Adsorption and Compression on Activated Carbons. *ACS Appl. Mater. Interfaces* **2021**, *13*, 12562–12574. [CrossRef]
10. Ziemiański, P.P.; Derkowski, A.; Szczerba, M.; Guggenheim, S. Smectite Crystallite Swelling Under High Pressure of Methane. *J. Phys. Chem. C* **2021**, *125*, 7598–7610. [CrossRef]
11. Karbownik, M.; Dudzińska, A.; Strzymczok, J. Multi-Parameter Analysis of Gas Losses Occurring during the Determination of Methane-Bearing Capacity in Hard Coal Beds. *Energies* **2022**, *15*, 3239. [CrossRef]
12. Jagiełło, J.; Bandosz, T.J.; Schwarz, J.A. Application of Inverse Gas Chromatography at Infinite Dilution to Study the Effects of Oxidation of Activated Carbons. *Carbon N. Y.* **1992**, *30*, 63–69. [CrossRef]
13. Cazorla-Amorós, D.; Alcañiz-Monge, J.; Linares-Solano, A. Characterization of Activated Carbon Fibers by CO_2 Adsorption. *Langmuir* **1996**, *12*, 2820–2824. [CrossRef]
14. Salem, M.; Braeuer, P.; Szombathely, M. Thermodynamics of High-Pressure Adsorption of Argon, Nitrogen, and Methane on Microporous Adsorbents. *Langmuir* **1998**, *7463*, 3376–3389. [CrossRef]
15. Park, N.; Choi, K.; Hwang, J.; Kim, D.W.; Kim, D.O.; Ihm, J. Progress on First-Principles-Based Materials Design for Hydrogen Storage. *Proc. Natl. Acad. Sci. USA* **2012**, *109*, 19893–19899. [CrossRef] [PubMed]
16. Yoon, S.-H.; Lim, S.; Song, Y.; Ota, Y.; Qiao, W.; Tanaka, A.; Mochida, I. KOH Activation of Carbon Nanofibers. *Carbon N. Y.* **2004**, *42*, 1723–1729. [CrossRef]
17. Lillo-Ródenas, M.A.; Cazorla-Amorós, D.; Linares-Solano, A. Understanding Chemical Reactions between Carbons and NaOH and KOH: An Insight into the Chemical Activation Mechanism. *Carbon N. Y.* **2003**, *41*, 267–275. [CrossRef]
18. Buczek, B. Adsorption of Methane and Carbon Dioxide on a Potassium Hydroxide-Modified Activated Carbon. *Przem. Chem.* **2013**, *92*, 535–537.
19. Perrin, A.; Celzard, A.; Marêché, J.F.; Furdin, G. Improved Methane Storage Capacities by Sorption on Wet Active Carbons. *Carbon* **2004**, *42*, 1243–1249. [CrossRef]
20. Baran, P.; Cygankiewicz, J.; Zarębska, K. Carbon Dioxide Sorption on Polish Ortholignite Coal in Low and Elevated Pressure. *J. CO_2 Util.* **2013**, *3–4*, 44–48. [CrossRef]
21. Baran, P.; Krzak, M.; Zarebska, K.; Szczurowski, J.; Zmuda, W.A. Adsorption of Sulfur(IV) Oxide on Activated Carbon from Pyrolysis of Waste Tires. *Przem. Chem.* **2016**, *95*, 1164–1166. [CrossRef]
22. Fujiwara, M.; Fujio, Y.; Sakurai, H.; Senoh, H.; Kiyobayashi, T. Storage of Molecular Hydrogen into ZSM-5 Zeolite in the Ambient Atmosphere by the Sealing of the Micropore Outlet. *Chem. Eng. Process. Process Intensif.* **2014**, *79*, 1–6. [CrossRef]
23. Masika, E.; Mokaya, R. Preparation of Ultrahigh Surface Area Porous Carbons Templated Using Zeolite 13X for Enhanced Hydrogen Storage. *Prog. Nat. Sci. Mater. Int.* **2013**, *23*, 308–316. [CrossRef]
24. Czosnek, C.; Baran, P.; Grzywacz, P.; Baran, P.; Janik, J.F.; Rózycka, A.; Sitarz, M.; Jeleń, P. Generation of Carbon Nanostructures with Diverse Morphologies by the Catalytic Aerosol-Assisted Vapor-Phase Synthesis Method. *Comptes Rendus Chim.* **2015**, *18*, 1198–1204. [CrossRef]

25. Rowsell, J.L.C.; Yaghi, O.M. Effects of Functionalization, Catenation, and Variation of the Metal Oxide and Organic Linking Units on the Low-Pressure Hydrogen Adsorption Properties of Metal−Organic Frameworks. *J. Am. Chem. Soc.* **2006**, *128*, 1304–1315. [CrossRef] [PubMed]

26. Panella, B.; Hirscher, M.; Ludescher, B. Low-Temperature Thermal-Desorption Mass Spectroscopy Applied to Investigate the Hydrogen Adsorption on Porous Materials. *Microporous Mesoporous Mater.* **2007**, *103*, 230–234. [CrossRef]

27. McEnaney, B. Estimation of the Dimensions of Micropores in Active Carbons Using the Dubinin-Radushkevich Equation. *Carbon N. Y.* **1987**, *25*, 69–75. [CrossRef]

28. Wang, J.; Kaskel, S. KOH Activation of Carbon-Based Materials for Energy Storage. *J. Mater. Chem.* **2012**, *22*, 23710–23725. [CrossRef]

29. Wang, H.; Gao, Q.; Hu, J. High Hydrogen Storage Capacity of Porous Carbons Prepared by Using Activated Carbon. *J. Am. Chem. Soc.* **2009**, *131*, 7016–7022. [CrossRef]

30. Geng, Z.; Zhang, C.; Wang, D.; Zhou, X.; Cai, M. Pore Size Effects of Nanoporous Carbons with Ultra-High Surface Area on High-Pressure Hydrogen Storage. *J. Energy Chem.* **2015**, *24*, 1–8. [CrossRef]

31. Minoda, A.; Oshima, S.; Iki, H.; Akiba, E. Synthesis of KOH-Activated Porous Carbon Materials and Study of Hydrogen Adsorption. *J. Alloys Compd.* **2013**, *580*, S301–S304. [CrossRef]

32. Panella, B.; Hirscher, M.; Roth, S. Hydrogen Adsorption in Different Carbon Nanostructures. *Carbon N. Y.* **2005**, *43*, 2209–2214. [CrossRef]

33. Rzepka, M.; Lamp, P.; de la Casa-Lillo, M.A. Physisorption of Hydrogen on Microporous Carbon and Carbon Nanotubes. *J. Phys. Chem. B* **1998**, *102*, 10894–10898. [CrossRef]

34. Wang, Q.; Johnson, J.K. Molecular Simulation of Hydrogen Adsorption in Single-Walled Carbon Nanotubes and Idealized Carbon Slit Pores. *J. Chem. Phys.* **1998**, *110*, 577–586. [CrossRef]

35. Gogotsi, Y.; Portet, C.; Osswald, S.; Simmons, J.M.; Yildirim, T.; Laudisio, G.; Fischer, J.E. Importance of Pore Size in High-Pressure Hydrogen Storage by Porous Carbons. *Int. J. Hydrog. Energy* **2009**, *34*, 6314–6319. [CrossRef]

36. Akasaka, H.; Takahata, T.; Toda, I.; Ono, H.; Ohshio, S.; Himeno, S.; Kokubu, T.; Saitoh, H. Hydrogen Storage Ability of Porous Carbon Material Fabricated from Coffee Bean Wastes. *Int. J. Hydrog. Energy* **2011**, *36*, 580–585. [CrossRef]

37. Fierro, V.; Szczurek, A.; Zlotea, C.; Marêché, J.F.; Izquierdo, M.T.; Albiniak, A.; Latroche, M.; Furdin, G.; Celzard, A. Experimental Evidence of an Upper Limit for Hydrogen Storage at 77 K on Activated Carbons. *Carbon N. Y.* **2010**, *48*, 1902–1911. [CrossRef]

38. Rowlandson, J.L.; Coombs OBrien, J.; Edler, K.J.; Tian, M.; Ting, V.P. Application of Experimental Design to Hydrogen Storage: Optimisation of Lignin-Derived Carbons. *C J. Carbon Res.* **2019**, *5*, 82. [CrossRef]

39. Harjanto, S.; Noviana, L.N.; Diniati, M.; Yunior, S.W.; Nasruddin. Hydrogen Adsorption Capacity Reduction of Activated Carbon Produced from Indonesia Low Rank Coal by Pelletizing. *Sains Malays.* **2015**, *5*, 747–752. [CrossRef]

40. Zhao, W.; Luo, L.; Chen, T.; Li, Z.; Zhang, Z.; Fan, M. Activated Carbons from Oil Palm Shell for Hydrogen Storage. *IOP Conf. Ser. Mater. Sci. Eng.* **2018**, *368*, 12031. [CrossRef]

41. Alfadlil, B.R.; Knowles, G.P.; Parsa, M.R.; Subagyono, R.R.D.J.N.; Daniel; Chaffee, A.L. Carbon Monolith from Victorian Brown Coal for Hydrogen Storage. *J. Phys. Conf. Ser.* **2019**, *1277*, 12024. [CrossRef]

42. Toprak, A. Production and Characterization of Microporous Activated Carbon from Cherry Laurel (*Prunus laurocrasus* L.) Stone: Application of H_2 and CH_4 Adsorption. *Biomass Convers. Biorefinery* **2020**, *10*, 977–986. [CrossRef]

43. Williams, N.E.; Oba, O.A.; Aydinlik, N.P. Modification, Production, and Methods of KOH-Activated Carbon. *ChemBioEng Rev.* **2022**, *9*, 164–189. [CrossRef]

44. Lendzion-Bieluń, Z.; Czekajło, Ł.; Sibera, D.; Moszyński, D.; Sreńscek-Nazzal, J.; Morawski, A.W.; Wrobel, R.J.; Michalkiewicz, B.; Arabczyk, W.; Narkiewicz, U. Surface Characteristics of KOH-Treated Commercial Carbons Applied for CO_2 Adsorption. *Adsorpt. Sci. Technol.* **2017**, *36*, 478–492. [CrossRef]

45. Dai, W.; Liu, Y.; Su, W.; Hu, G.; Deng, G.; Hu, X. Preparation and CO_2 Sorption of a High Surface Area Activated Carbon Obtained from the KOH Activation of Finger Citron Residue. *Adsorpt. Sci. Technol.* **2012**, *30*, 183–191. [CrossRef]

Article

Good Practices to Counteract Epidemic Emergency in Mining Companies in Poland

Patrycja Bąk

Faculty of Civil Engineering and Resource Management, AGH University of Science and Technology, A. Mickiewicza Av. 30, 30-059 Krakow, Poland; pbak@agh.edu.pl

Abstract: The date assumed as the beginning of the pandemic in Poland is 4 March 2020, the date of the first confirmed case of the virus. This article presents the actions undertaken by the management of underground hard coal mining plants concerning the risk of epidemic related to SARS-CoV-2. This work shows a set of implemented recommendations, guidelines and decisions, which were established after the appearance of the first wave of cases in Poland. What is more, it discusses measures aiming at reducing the risk of spreading the coronavirus among the mineworkers. The suggestions for different variants of the decision-making process concerning the pandemic and which have an enormous impact on the operating expenses of the company are also made. The paper presents the results of the study on actions taken in individual mining companies and good work practices recommended to be applied.

Keywords: COVID-19; pandemic; mining company; epidemic emergency; prevention; good practices

1. Introduction

In March 2020, an epidemic emergency appeared in Poland due to the spread of the coronavirus SARS-CoV-2, causing acute respiratory disease COVID-19, which in some cases, may even lead to the death of the infected person. It was acknowledged that the virus is very easily transmitted from one person to another. The virus is mainly transmitted by the droplets created, when a person infected coughs, sneezes or speaks. These droplets are too heavy to float in the air, so they fall quickly on surfaces. Then, a person may become infected after touching the contaminated surface, followed by touching their eyes, nose or mouth. The risk of a severe course of the coronavirus disease appeared to be serious and led to making high-level decisions concerning the announcement of the state of epidemic emergency in the Republic of Poland, commencing 14 March 2020, and the state of epidemic commencing 20 March 2020 [1–3]. On that basis, a number of radical actions were implemented in the field of isolation and distancing of people. The isolation involved mainly the large scale, temporary suspension of their activities, especially closures of many businesses, offices, schools and retail outlets. Whenever possible, the so-called remote working system was implemented. This created a dilemma—what decisions should be made and what will be the consequences for mines? These decisions were left to be made by the mining companies and mine managements. These had to be made having insufficient information concerning a threat of this kind, which actually "only just" emerged. Therefore, what decisions need to be made (as soon as possible) with regard to the functioning of mines, without having any reliable knowledge about the sources of the spread of the threat itself and methods of preventing it? Further, knowledge of the risks involved is essential at each mining company management level. Although it would be more favourable to implement decisions that would involve "no risk", the basis of the security concept involves "acceptable risk". If it is adopted in relation to a mining company, it is necessary to anticipate and predict the possibility of occurrence for a risk. This term should be understood as a risk included between the desired upper and lower levels of safety, taking into account a set of

necessary criteria. In the analysed case, the criteria should concern epidemic emergency in relation to the employees. It should be clearly emphasised that a lack of knowledge on the virus concerns not only the mining industry. The COVID-19 pandemic spread worldwide and has had economic, environmental and social impacts [4–8]. All countries where the virus causing the previously unknown disease appeared have undertaken basic actions, primarily aimed at limiting the possibility of its spread by forcing social distancing. This has often involved the introduction of a lockdown of all social activities ("stay at home"—closure of educational, commercial and cultural facilities) and economic activities (forced production stops of many industrial plants). However, due to the specific nature of mining production, such recommendations could not completely be implemented in mining companies—neither the vast majority of mine workers can "stay at home", nor, due to the deformation of underground excavations, can the mine's operation be stopped for a long time. In such a situation, their managers had to make quick decisions concerning both reducing the spread of infections and preventing adverse effects on the operation of individual mines and plants. This study consists of an overview of the various solutions used in various mining companies to counteract the emerging epidemic emergency.

2. Research Material

The SARS-CoV-2 virus (severe acute respiratory syndrome coronavirus 2) is a coronavirus of animal origin, causing acute respiratory infectious disease in humans that can even lead to death, called COVID-19 (Coronavirus Disease 19) [9]. According to the World Health Organization, SARS-CoV-2 is mainly spread via respiratory droplets [10]. Infection can occur through direct or close contact with the virus carrier or indirectly through contact with an object or surface contaminated with the pathogen. When speaking, coughing or sneezing, the carrier of the virus (a person with COVID-19 disease or asymptomatic infection) produces respiratory secretions or saliva that carry the pathogen. Such molecules contain the virus and, through another person's mouth, nose or eyes, leads to a viral infection [11–13]. According to the literature, coronaviruses can survive from 2 h to 9 days on the surfaces of various materials, such as plastic, metal or glass. A synthesis of the results of the studies included in the papers [14,15], containing detailed data on the survival of different types of coronaviruses depending on the type of surface, in relation to human coronaviruses being an equivalent to SARS-CoV-2 virus in the study, is presented in the publication [16] (Table 1). Based, among other things, on the analyses carried out by Carraturo and co-workers, the following coronavirus life span is assumed for each type of surface: aluminum 2–8 h, metal 5 days, wood 4 days, paper and glass 5 days, and plastic 2–5 days. Another team of researchers assessed the amount of virus retaining its infectious properties for different surface types. The experiment to determine the duration of virus persistence in the air spray was carried out for three hours from the moment of spraying. During the whole time it was conducted, the following environmental conditions were maintained: temperature 21–23 °C and air humidity $\geq$ 40%.

Table 1. Survival of the two main SARS-CoV-2 virus surrogates (HCoV 229E and SARS-CoV) on different types of inanimate surfaces.

Surface Type	Strain	Temperature	Life Span
Aluminium	hCoV 229E and OC43	21 °C	2–8 h
Metal	SARS-CoV P9	room	5 d
Wood	SARS-CoV P9	room	4 d

Table 1. *Cont.*

Surface Type	Strain	Temperature	Life Span
Paper	SARS-CoV GVU6109 and P9	room	3 h–5 d
Glass	SARS-CoV P9	room	2–5 d
Plastic	SARS-CoV FFM1, HKU39849 and P9	20–25 °C	2–5 d
PVC	hCoV 229E	21 °C	5 d
Silicone	hCoV 229E	21 °C	5 d
Latex	hCoV 229E and OC43	21 °C	≤8 h
Disposable apron	SARS-CoV GVU6109	room	1 h–2 d
Ceramics	hCoV 229E	21 °C	5 d
Teflon	hCoV 229E	21 °C	5 d

Source: [16].

The amount of the virus in the sample was expressed as TCID50. On the basis of the conducted tests, it was found that the SARS-CoV-2 coronavirus had the shortest life span on the copper (4 h) and cardboard (24 h) surfaces, while the longest was on plastic and stainless-steel surfaces (up to 72 h). As mentioned, the concentration of viruses in the aerosol was measured within three hours. A decrease in the concentration of infectious virus particles in the air was found—the virus half-life span of the analysed strains reached a similar value and was approximately 1.1–1.2 h. It was noted, however, that at the end of the experiment, the value of TCID50 remained above the set detection threshold. The half-life span of SARS-CoV-2 on particular types of surfaces was: 6.8 h for plastic, 5.6 h for stainless steel, 3.8 h for cardboard and about 1 h for copper [17]. The results of the study on the influence of temperature on coronavirus activity were presented, among others, in the paper [18]. Its authors evaluated, in laboratory tests, the stability of SARS-CoV-2 on steel plates incubated at: room temperature and 4 °C and 30 °C, at constant ambient humidity of 30–40%. The research proved that while there was a significant decrease in the viral load within 1 h after spraying at room temperature, its value remained stable within the next 4–8 h of incubation. A minimum decrease in values was recorded for 30 °C and for samples incubated at 4 °C, a large discrepancy in results was observed in individual series of measurements. After eight hours of incubation, a stable, slow decrease of the viral load was observed in all analysed temperatures during the following days of the experiment. However, the authors pointed out that it was possible to recover (reactivate) the amount of infectious SARS-CoV-2 even after 180 h incubation on a metal surface. The humidity of the environment in relation to coronavirus molecules was considered in the study in two ways—in terms of the influence of environmental humidity on its life span and the influence on the size of respiratory droplets being the direct carrier of the pathogen. The paper [19,20] presents the results of the research, which show that:

- Very high humidity (99.5%) induces a hygroscopic increase in liquid droplets, while humidity of 40% causes water to evaporate, reducing droplet size,
- Ambient humidity has a significant impact on the size of medium-sized respiratory droplets (50–100 μm)—high humidity is conducive to slowing down the evaporation of the droplets, so that the droplets will settle on the substrate more quickly and evaporate more quickly in dry air, which will cause them to stay longer in the air spray.

The mining production process consists primarily of a selection of the applicable technology for mining the deposit while maintaining occupational safety. Concerning the management of a mining company and its individual mines, particularly vital are decisions involving [21]:

■ Ensuring high standards of occupational safety,

- Implementation of modern technical and technological solutions for deposit mining,
- Ensuring the required quality of commercial coal produced,
- Protection of the mining area where the effects of the carried-out mining and the natural environment may be visible.

Additionally, from an economic point of view, the mining production process should be efficient, or at least not generate financial losses. Such requirements for mining production are shown in Figure 1.

Figure 1. Features of standard for carrying out mining production process. Source: own study based on [21].

In underground mining, the basis for decisions, especially those related to industrial safety and natural hazards, are the laws, regulations, guidelines and various rules and procedures developed. In many cases, those are established based on past experience and are often supported by scientific research. These regulations are, or at least should be, well known to individual decision-makers. This allows for proper management of a mine and a mining company—proper, i.e., in a way that ensures the highest possible level of safety and avoids unjustified risks concerning mining production.

Hazards present in underground mining have been either technological or natural. The method of conducting works in the conditions of their occurrence and the scope of necessary anti-hazard measures have been developed over many years, based on operational experience and scientific research conducted on a large scale. On the other hand, in the case of an epidemic emergency caused by the virus, we are dealing with a wide range of ignorance concerning the decision-making process in relation to the operation of a mining plant.

As opposed to other hazards, in the case of an epidemic emergency caused by the SARS-CoV-2 virus, there are no specific procedures that could be strictly followed in the operation of a mining company. For example, the Website of the Republic of Poland provides only five general guidelines [22]:

1. Regularly wash your hands with soap and water.
2. Cover your mouth and nose with your bent elbow or tissue when you cough.
3. Avoid touching your eyes, nose and mouth.
4. Stay at least 2 m from other people.

5. Stay home.

This means that the primary means of protection against becoming infected is to keep a distance from other people or even to avoid any contact at all. Implementation of such rules is absolutely not feasible in mines where the limited space of shaft hoist cages, underground means of transport and excavations and where a large number of people work, make it impossible to maintain two-meter space between people.

Various measures have been taken by various mining companies to counteract the epidemic emergency related to SARS-CoV-2 coronavirus. Today we can say that they brought good results—after the initial perturbations resulting from a large number of infections among employees, the situation has been managed and stabilised. With the continuous enforcement of the newly developed and implemented procedures, mining companies now operate without the major turmoil that might have been brought by the spreading pandemic. As they have fulfilled their role, they can be described as "good practices used to counteract the epidemic emergency". The research problem undertaken is an attempt to develop a set of such practices, which could be recommended for use in conditions of epidemic emergency.

3. Research Methodology

In order to conduct research on the activities undertaken in mining companies and their effects, it was decided to use a qualitative research method, a case study. As the name itself indicates, the primary purpose of this method is to illustrate and analyse the "selected case" in detail. The reasons for its use are most often atypical character of the case and a desire to learn about the analysed phenomenon in detail. As American scientist Wilbur Schramm, the pioneer of social communication research, stated: "*The essence of a case study (. . .) is to explain the decisions: why it was made, how it was made and what was the effect*" [23]. It indicates that in the case study, the main focus is on the decisions made. This is the preferred method in situations where [24]:

- ■ The main questions are "how?" or "why?",
- ■ The researcher has little influence on behavioural factors,
- ■ The study concerns a contemporary phenomenon.

With regard to the issues related to actions to combat the epidemic emergency caused by the previously unknown coronavirus, all the above conditions are undoubtedly met.

In order to obtain information on how to counteract the epidemic emergency, nine mining companies (seven from the hard coal mining industry and two from the metal ore mining industry) were sent a question about all undertakings—organisational, operational, informational—related to the preventive actions (ad. 1).

As mentioned, in mining companies, actions concerning combating the threats occurring so far are undertaken based on the applicable legal regulations. On the other hand, the study assumed (re. 2) that due to the lack of regulations imposing a specific course of action, independent solutions were introduced in each company.

The assumed unit of enquiry (re. 3), i.e., a specific case, was each separate company and solutions implemented in it.

Surveyed companies sent back various answers consisting of descriptions, drawings, diagrams and tables concerning the scope of undertaken actions. Some solutions were used in all of the companies, others in individual cases. For the sake of comparability, all of the solutions were summed up together, regardless of frequency of their implementation. The only condition for inclusion in the list was usefulness in combating the threat (re. 4).

The list of solutions used in various mining companies was analysed in terms of the frequency of their implementation and the results (effects) obtained. Next, on this basis, a set of so-called good practices, recommended to use in the area concerned, was developed (re. 5).

At the first stage of the case study, an assumption (theory) was made, which should be proved by the result of the study (a negative result was also considered). The assumption was as follows:

So far, no methods of combating the epidemic threat in underground mines caused by an unknown virus have been formulated clearly. However, if various actions were taken in different mining plans and were successful in all such plants, it is possible to prepare a list of standardised recommendations to be used in practice in the future.

Figure 2 shows the procedure and assumptions adopted in the conducted study.
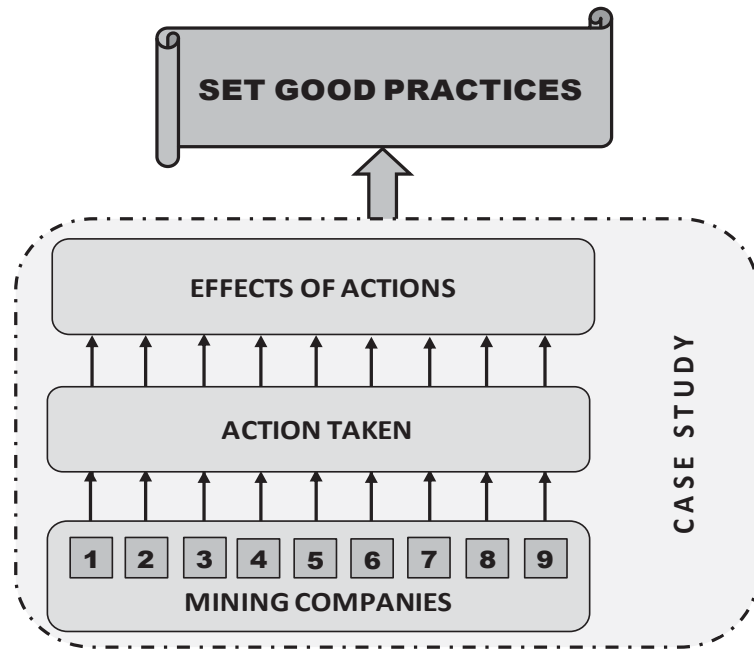
Figure 2. Object and expected result of the case study. Source: author's own elaboration based on the research carried out in mining companies.

4. Result

The first step consisted of asking managers of the nine mining companies to draw up a brief description of all action taken to combat the epidemic threat that had been spreading since March and to assess the effects of their implementation. From descriptions received, 33 various, specific projects were isolated and tabulated. Assuming that in some cases, the descriptions focused only on the vital counteractions concerning a given company, the compiled summary table was sent to all companies, asking them to analyse the list and mark all the actions that were taken in individual companies. In addition, acknowledging that some of them may not have been included in the submitted descriptions, companies were asked to add others, not included in the table in order to include all the implemented projects. As a result, the total number of actions amounted to 40; they are presented in Table 2. Before analysing the list, one should note that the descriptions showed that in all companies, the first actions were taken even before the official announcement of epidemic threat (14 March). Most frequently, those actions included the obligation to use any available protective masks, introducing an option to (or obligation to) measure the temperature of all people entering the premises and making urgent purchases of disinfectants and protective masks and gloves (in order to speed up their acquisition, purchase procedures were significantly simplified in all companies). This clearly shows that there is an awareness of the need to counteract a widespread and unknown threat as soon as possible. Seventeen of all forty actions were introduced in all mining companies. The majority of the actions concerned the possibility of maintaining social distance by:

- Limiting all company-wide meetings to a minimum, including business-related meetings with customers/applicants, while maintaining special care when dealing with co-workers,
- Implementing changes to the schedule and working hours of underground workers in order to divide them into smaller groups, which led to smaller concentrations of people in places where they had gathered in larger groups, with such places being mainly pitbottoms, pitheads, means of vertical and horizontal transport, baths,
- Introducing remote work for workstations that can be operated remotely.

Table 2. List of actions taken in mining companies to combat the epidemic threat.

No.	Actions Taken	LW Bogdanka SA	PGG SA	Węglokoks Kraj Sp. z o.o.	TAURON Wydobycie SA	JSW SA	SRK SA	ZG Bolesław SA	KGHM Polska Miedź SA	PG Silesia
1.	Before 14 March—making a decision to wear dust masks available in the mine obligatorily.	♦	♦	♦	♦	♦	♦	♦	♦	♦
2.	Before 14 March—introducing the possibility of measuring the body temperature of people entering the workplace.	♦	♦		♦	♦	♦		♦	
3.	Establishing a crisis management team—ongoing monitoring of the situation, developing appropriate recommendations and guidelines if necessary.	♦	♦	♦	♦	♦	♦	♦	♦	♦
4.	Specifying the so-called critical areas in which workers may contract the virus the fastest due to large concentrations of people.	♦	♦	♦	♦	♦	♦	♦	♦	♦
5.	Introducing mandatory quarantine for people who may have had contact with the virus.	♦	♦	♦	♦	♦	♦	♦	♦	♦
6.	Obliging workers to provide information when they, their household members, or people with whom they have close contact return from abroad where there were COVID-19 cases.	♦	♦	♦		♦	♦	♦	♦	♦
7.	Suspending all business trips and trips/events organised by the Social Department.	♦		♦	♦	♦	♦	♦	♦	♦
8.	Suspending the distribution of tickets for sporting and cultural events by the Social Department.	♦	♦	♦	♦	♦		♦	♦	♦
9.	Limiting all company-wide meetings to a minimum, including business-related meetings with customers/applicants.	♦	♦	♦	♦	♦	♦	♦	♦	♦
10.	Recommending that special care must be taken during contact with colleagues, limiting direct contact (e.g., handshakes), and paying special attention to hand hygiene.	♦	♦	♦	♦	♦	♦	♦	♦	♦
11.	Organising information and training sessions with a representative of the sanitary and epidemiological station.	♦		♦			♦			♦
12.	Taking continuous actions related to providing information about the threat with the use of all available means—OHS training boards, radio system, the Internet, posters, leaflets.	♦	♦	♦	♦	♦	♦	♦	♦	♦
13.	Providing workers with cotton masks for compulsory use when moving around passageways.	♦	♦	♦	♦	♦	♦	♦	♦	♦

Table 2. *Cont.*

No.	Actions Taken	LW Bogdanka SA	PGG SA	Węglokoks Kraj Sp. z o.o.	TAURON Wydobycie SA	JSW SA	SRK SA	ZG Bolesław SA	KGHM Polska Miedź SA	PG Silesia
14.	Modifying the terms and conditions of cooperation with external companies.	♦	♦	♦	♦	♦	♦	♦	♦	♦
15.	Implementing simplified procedures for purchasing dust masks, surgical masks, protective gloves, and disinfectants.	♦	♦	♦	♦	♦	♦	♦	♦	♦
16.	Measuring the temperature of all people entering the workplace and in means of public transport for workers with the use of remote thermometers and thermal cameras.	♦	♦	♦		♦	♦	♦	♦	♦
17.	Implementing changes to the working hours of underground workers in order to divide them into smaller groups.	♦	♦	♦	♦	♦	♦	♦	♦	♦
18.	Thinning groups of workers in lamp rooms, pitbottoms, and pitheads, in work division areas etc. by implementing one-way traffic, changing work schedules, specifying areas to wait in queues—keeping a safe distance.	♦	♦	♦	♦	♦	♦	♦	♦	♦
19.	Thinning groups of workers in cages of mining lifts by reducing the number of transported workers.	♦	♦	♦	♦	♦	♦	♦	♦	
20.	Installing additional protections in the form of a system of special partitions and provisional tunnels as well as making it mandatory to wear a mask while being transported.	♦		♦		♦	♦		♦	♦
21.	Making it mandatory to wear and use (cotton, surgical, dust) masks in the workplace and recommending that they are worn when commuting to and from the workplace as specified in general regulations.	♦	♦	♦	♦	♦	♦	♦	♦	♦
22.	Disinfecting equipment, devices, and workstations on a regular basis—unlimited access to disinfectants for every worker; disinfecting shaft cages and underground cars after every use by people; disinfecting handrails, handles etc. on a regular basis.	♦	♦	♦	♦	♦	♦	♦	♦	♦
23.	Installing additional underground hand washing stations.	♦	♦							
24.	Implementing a ban on taking snuff, eating seeds etc., which generate an additional risk of spreading the virus by droplet transmission.	♦	♦	♦		♦	♦			♦
25.	Shutting down touch-controlled equipment/devices if not necessary for mine operation (kiosks, vending machines).	♦		♦	♦	♦			♦	
26.	Reorganising the canteen—only takeaway meals.	♦	—	♦	♦		—		♦	
27.	Introducing remote work for workstations that can be operated remotely.	♦	♦	♦	♦	♦	♦	♦	♦	♦
28.	Providing special rooms for people who have shown symptoms during work and waiting for the decision of the State Sanitary Inspection on a further course of action.	♦	♦	♦	♦	♦	♦	♦	♦	♦
29.	Conducting screening tests among workers.		♦	♦		♦			♦	♦
30.	Launching a 24/7 psychological support service for employees.		♦	♦	♦	♦			♦	

Table 2. *Cont.*

No.	Actions Taken	LW Bogdanka SA	PGG SA	Węglokoks Kraj Sp. z o.o.	TAURON Wydobycie SA	JSW SA	SRK SA	ZG Bolesław SA	KGHM Polska Miedź SA	PG Silesia
31.	Suspending or limiting heading works.		♦	♦	♦		—			♦
32.	Suspending or limiting excavation.		♦	♦	♦		—			♦
33.	Installing decontamination chambers.			♦		♦				
34.	Revising the occupational hazard evaluation at workstations					♦	♦			
35.	Suspending the bonus for no absences due to sickness.	♦	—	—	—	—	—	—	♦	—
36.	Preparing and implementing Business Continuity Plans (BCPs).					♦				
37.	Implementing periodic OHS training in the form of e-learning.	♦								
38.	Suspending the obligation to conduct periodic check-ups of workers as specified in Article 12a of the Act of 31 March 2020.	♦								
39.	Introducing quarantine for incoming mail. Reorganising its reception so that direct contact between a mail department employee and external persons is limited.						♦			
40.	Implementing the possibility of conducting fast tests (at the cost of the company) for workers who may have had contact with people who contracted the virus.						♦			

Source: author's own elaboration based on the research carried out in mining companies.

Other actions were related to:

- Taking continuous action related to providing information about the threat with the use of all available means,
- Measuring the temperature of all people entering the workplace and in means of public transport for workers,
- Making it mandatory to wear and use protective masks in the workplace,
- Disinfecting rooms, equipment, devices and workstations on a regular basis, including the provision of wide access to disinfectants for workers.

In addition, special rooms for people suspected of contracting the virus and showing symptoms at work were established in all mining companies. Another common action was establishing crisis management teams (for the entire company and individual mines) that coordinated the implementation of anti-threat procedures and monitored the effects of their implementation. Other actions, listed in Table 2, were taken depending on the epidemic situation in a company. This particularly concerns conducting screening tests among workers and temporarily suspending or limiting work.

Figure 3 shows a diagram of classifying actions into groups concerning particular action areas based on the research carried out in mining companies.
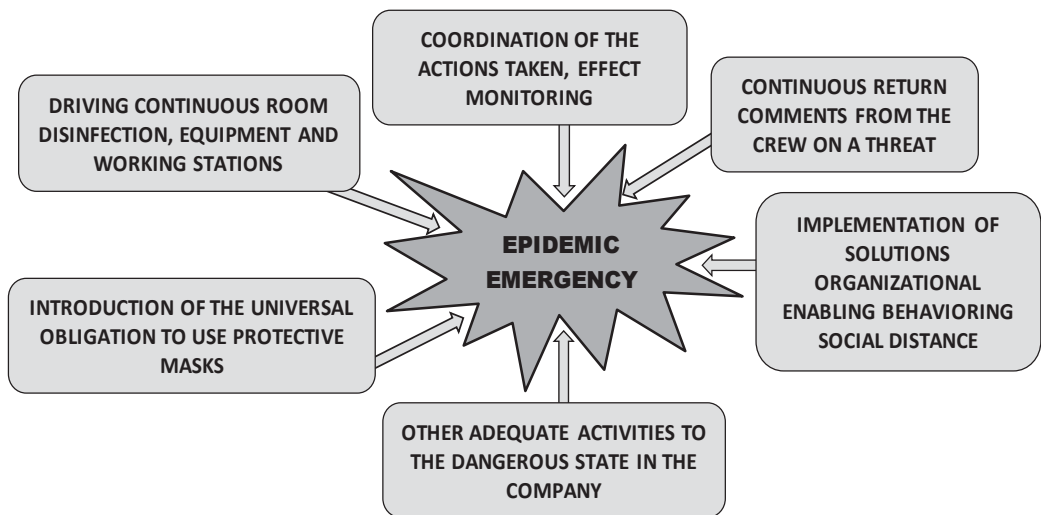
Figure 3. Actions taken to combat the epidemic threat in mines. Source: author's own elaboration based on the research carried out in mining companies.

5. Discussion

In all descriptions of actions prepared before, it was emphasised that the implemented anti-threat procedures had a positive effect and, despite initial considerable disruptions in the operation of individual mines, they helped to control crisis situations. In many cases, actions were taken "by intuition" in a manner that would, to the largest extent possible, satisfy the recommendations of epidemiological services for the society as a whole and manufacturing companies operating in sectors other than the mining industry. Their effectiveness makes it possible to formulate a thesis that in the absence of means that would combat the ongoing pandemic effectively, the six groups of various actions shown in Figure 3 may be considered a list of good practices used to fight the epidemic threat affecting the operation of companies. However, it is also important for the new procedures to be reflected in documents prepared in mines and plants belonging to the mining company. In particular, this applies to the "Safety Document" prepared according to the template included in the appendix to the Regulation of the Minister of Energy of 23 November 2016 [25]. This document should mainly include descriptions of:

○ Threats in a mining plant, how to identify and monitor them, and how to protect against them,
○ How to evaluate and document risks in workplaces and workstations,
○ How to inform workers of risks and prevent threats,
○ Provision of workplaces with collective protection measures and of employees with personal protective equipment as well as safety signs in use.

All of these points should include appropriate provisions on the epidemic threat and the established countermeasures. In addition, if the implemented procedures are in any way related to the applicable regulations or workstation instructions, these documents should also be modified accordingly.

There is one more observation based on the analysis of actions taken to combat the threat. Compared to other companies, the situation at LW Bogdanka SA is particularly interesting because it did not have a single case of COVID-19 for a long time. It seems that this is due to two main reasons. The first reason is the location of the mine—the Lubelskie Voivodeship—which has a considerably smaller population (approx. 2.1 million) compared to the Śląskie Voivodeship (approx. 4.5 million). In addition, the number of infections

in this voivodeship was considerably lower, less than 4200, while, at the end of the first decade of October, this number was almost 25,200 in the Śląskie Voivodeship. This is an advantage of some sort, fully utilised by the management of the mining company because the other reason is that actions were taken the earliest in this mine, while their scope was the most extensive and detailed.

6. Conclusions

According to numerous studies conducted all over the world on the fight against the threats posed by SARS-CoV-2, there is no chance of its natural extinction. Until an effective vaccine is developed, there will be no other way to slow down the spread of the pandemic than to limit contact between individuals. Therefore, the management of mining companies must adopt such an assumption when making decisions related to their operation.

First of all, it is necessary to take all measures to reduce the number of people in underground excavations. One of them includes a change to the organisation of work, which is commonly introduced and mainly involves an increase in the number of shifts combined with varying work starting hours. Still, in-depth technical and economical analyses may also be conducted in every mine concerning the possibility of:

1. Limiting the number of people working at the face of a mine,
2. Limiting the number of faces in terms of works related to driving both headings and excavations,
3. Shutting down certain excavations and basic facilities (e.g., shafts and foreshafts).

The principles and technologies for carrying out certain works often, among others, provide for employing the minimum number of people necessary for their safe operation. Therefore, the procedure aiming at a reduction in the number of people working at faces of a mine cannot involve reducing this number below the required minimum. However, in many cases, it is possible to apply modern technical solutions that allow for the number of workers to be reduced significantly. They include, for example:

○ The use of electro-hydraulic controllers for sections of powered roof supports carried out by only one operator located at the main gate,
○ The use of full visualisation and automation for controlling conveyors that transport the output,
○ The use of a container system for transporting materials—containers loaded on the surface can be transported directly to the face of a mine without the need of reloading them on main transport roads.

It is also very important to wear personal protective equipment, such as gloves and masks, and to disinfect rooms with such equipment, workstations and tools on a regular basis.

If there are other ways to prevent the epidemic threat in a given mining company and/or its mines, it is, of course, always necessary to use them. However, it is important for all activities to be taken in a coordinated manner, which should ensure their increased effectiveness.

Institutional Review Board Statement: Not applicable.

Informed Consent Statement: Not applicable.

Data Availability Statement: The data presented in this study are new and have not been previously published.

Conflicts of Interest: The authors declare no conflict of interest.

References

1. Regulation of the Minister of Health of 13 March 2020 on Declaring the State of Epidemic Emergency in the Republic of Poland, Dz. U./Journal of Laws/of 2020, Item 433. Available online: https://gov.pl/web (accessed on 1 April 2020).
2. Regulation of the Minister of Health of 20 March 2020 on Declaring the State of the Epidemic in the Republic of Poland, Dz. U. /Journal of Laws/of 2020, Item 491. Available online: https://gov.pl/web (accessed on 1 April 2020).
3. Regulation of the Minister of Health of 24 March 2020 Amending the Regulation on Declaring the State of the Epidemic in the Republic of Poland, Dz. U./Journal of Laws/of 2020, Item 522. Available online: https://gov.pl/web (accessed on 1 April 2020).
4. Dar, M.A.; Gladysz, B.; Buczacki, A. Impact of COVID19 on Operational Activities of Manufacturing Organizations—A Case Study and Industry 4.0-Based Survive-Stabilise-Sustainability (3S) Framework. *Energies* **2021**, *14*, 1900. [CrossRef]
5. Rapaccini, M.; Saccani, N.; Kowalkowski, C.; Paiola, M.; Adrodegari, F. Navigating Disruptive Crises through Service-LedGrowth: The Impact of COVID-19 on Italian Manufacturing Firms. *Ind. Mark. Manag.* **2020**, *88*, 225–237. [CrossRef]
6. Liu, F.; Wang, M.; Zheng, M. Effects of COVID-19 Lockdown on Global Air Quality and Health. *Sci. Total Environ.* **2021**, *755*, 142533. [CrossRef] [PubMed]
7. Ino, E.; Watanabe, K. The Impact of COVID-19 on the Global Supply Chain: A Discussion on Decentralization of the Supply Chain and Ensuring Interoperability. *J. Disaster Res.* **2021**, *16*, 56–60. [CrossRef]
8. Hauser, P.; Schönheit, D.; Scharf, H.; Anke, C.-P.; Möst, D. COVID-19's Impact on European Power Sectors: An Econometric Analysis. *Energies* **2021**, *14*, 1639. [CrossRef]
9. Wang, Q.; Zhang, Y.; Wu, L.; Zhou, H.; Yan, J.; Qi, J. Structural and Functional basis of SARS-CoV-2 Entry by Using Human ACE3. *Cell* **2020**, *181*, 894–904. [CrossRef] [PubMed]
10. WHO. Transmission of SARS-CoV-2: Implications for Infection Prevention Precautions. Scientific Brief. 2020. Available online: https://www.who.int/news-room/commentaries/detail/transmissionof-sars-cov-2-implications-for-infection-prevention-precautions (accessed on 1 March 2021).
11. Chan, J.F.-W.; Yuan, S.; Kok, K.-H.; To, K.K.-W.; Chu, H.; Yang, J. A familial cluster of pneumonia associated with the 2019 novel coronavirus indicating person-to-person transmission: A study of a family cluster. *Lancet* **2020**, *395*, 514–523. [CrossRef]
12. Liu, J.; Liao, X.; Qian, S.; Yuan, J.; Wang, F.; Liu, Y. Community Transmission of Severe Acute Respiratory Syndrome Coronavirus 2, Shenzhen, China. *Emerg. Infect. Dis. J.* **2020**, *26*, 1320. [CrossRef] [PubMed]
13. WHO. Modes of Transmission of Virus Causing COVID-19: Implications for IPC Precaution Recommendations. Scientific Brief. 29 March 2020. Available online: https://www.who.int/newsroom/commentaries/detail/modes-of-transmission-of-virus-causing-covid-19-implicationsfor-ipc-precaution-recommendations (accessed on 16 July 2020).
14. Kampf, G. Potential role of inanimate surfaces for the spread of coronaviruses and their inactivation with disinfectant agents. *Infect. Prev. Pract.* **2020**, *2*, 100044. [CrossRef] [PubMed]
15. Kampf, G.; Todt, S.; Pfaender, E.; Steinmann, P. Persistence of coronaviruses on inanimate surfaces and their inactivation with biocidal agents. *J. Hosp. Infect.* **2020**, *104*, 246–251. [CrossRef] [PubMed]
16. Carraturo, F.; Del Giudice, C.; Morelli, M.; Cerullo, V.; Libralato, G.; Galdiero, E.; Guida, M. Persistence of SARS-CoV-2 in the environment and COVID-19 transmission risk from environmental matrices and surfaces. *Environ. Pollut.* **2020**, *265*, 115010. [CrossRef] [PubMed]
17. Van Doremalen, N.; Bushmaker, T.; Morris, D.H.; Holbrook, M.; Gamble, A.; Wiliamson, B.N.; Tamin, A.; Harcout, J.; Thornburg, N.J.; Gerber, S.I.; et al. Aerosol and surface stability of SARS-CoV-2 as compared with SARS-CoV-1. *N. Engl. J. Med.* **2020**, *328*, 1564–1567. [CrossRef] [PubMed]
18. Kratzel, A.; Steiner, S. Temperature-dependent surface stability of SARS-CoV-2. *J. Infect.* **2020**, *81*, 452–482. [CrossRef] [PubMed]
19. Feng, Y.; Marchal, T.; Sperry, T.; Yi, H. Influence of wind and relative humidity on the social distancing effectiveness to prevent COVID-19 airborne transmission: A numerical study. *J. Aerosol Sci.* **2020**, *147*, 105585. [CrossRef]
20. Buxton, G. Spreadsheet Model of COVID-19 transmission: Evaporation and Dispersion of Respiratory Droplet. *SSRN Electron. J.* **2020**, *12*, 12861. [CrossRef]
21. Dubiński, J.; Turek, M.; Prusek, S. Key tasks of science in improving effectiveness of hard coal production in Poland. *Arch. Min. Sci.* **2017**, *62*, 3. [CrossRef]
22. Available online: https://www.gov.pl/web/coronawirus (accessed on 20 January 2021).
23. Schramm, W. *Notes on Case Studies of Instructional Media Projects*; Working Paper for the Stanford University; Californian Institute for Communication: Campbell, CA, USA, 1971.
24. Yin, R.K. *A Case Study in Scientific Research. Design and Methods*; Publishing House of the Jagiellonian University: Krakow, Poland, 2015.
25. Regulation of the Minister of Energy of 23 November 2016 on Detailed Requirements for Operation of Underground Mining Plants (Dz.U./Journal of Laws/, of 2017, Item 1118). Available online: https://gov.pl/web (accessed on 15 May 2020).

The European Education Initiative as a Mitigation Mechanism for Energy Transition

Natalia Kowalska [1], Ewelina Brodawka [2], Adam Smoliński [3] and Katarzyna Zarębska [2],*

[1] Faculty of Civil Engineering and Resource Management, AGH University of Science and Technology, Al. Mickiewicza 30, 30-059 Kraków, Poland
[2] Faculty of Energy and Fuels, AGH University of Science and Technology, Al. Mickiewicza 30, 30-059 Kraków, Poland
[3] Central Mining Institute, 40-166 Katowice, Poland
*   Correspondence: katarzyna.zarebska@agh.edu.pl; Tel.: +48-12-617-21-41

Abstract: The transformation of the European energy sector is becoming a priority for the European Union. This is indicated, for instance, in the European Union strategy known as the European Green Deal. According to the Green Deal, the area of 'research and innovation' is one which can counteract climate change. Universities can play a significant role in this by adopting a pedagogical approach aimed at mobilizing the spirit of innovation and entrepreneurship in young professionals. In addition to modifying curricula related to mining, energy, and environmental engineering, i.e., activities in recognized, traditional schemes, one prospective tool may be the involvement of students and PhD candidates in European initiatives such as the InnoEnergy PhD School (which is funded by the European Institute of Innovation and Technology). This paper aims to discuss the InnoEnergy PhD School programme as a possible instrument for mitigating the negative effects of energy transformation. The article analyzes the programme using a case study method, including surveys and open interviews. The paper draws attention to and highlights the role of human resources in the field of education and the stimulation of innovation, as well as the need to strengthen the business component in the education of PhD candidates.

Keywords: energy transformation; Green Deal; InnoEnergy; innovative education initiatives; European Institute of Innovation and Technology (EIT)

1. Introduction

The coal sector operates in 12 EU countries and 41 European regions (as of 2021) [1]. The European Commission, United Nations, and Climate Alliance, as well as others, have indicated the need to reorient carbon-intensive sociotechnical systems. In the 2030 Climate Target Plan [2], the European Commission proposed intensification of activities aimed at reducing greenhouse gases by at least 55% by 2030 compared to 1990 levels. This change in goals significantly differs from the previously adopted target of at least 40%. The new resolutions meet UN Sustainable Development Goal 13 and the European Green Deal (including the Fit for 55 package), and are in line with the Paris Agreement of 2015. The Paris Agreement emphasizes the need to limit global temperature increase to 1.5 °C [3]. Other EU legislation and strategies dealing with climate issues include:

- United Nations Framework Convention on Climate Change (UNFCCC) (2020) [1].
- EU Emissions Trading System (ETS) [4].
- Effort Sharing Regulation [5].
- European Climate Law [6].

EU member states are obliged to develop long-term national strategies aimed at implementing EU objectives and the provisions of the Paris Agreement at the national level. Strategies must be focused on the reduction of greenhouse gas emissions caused

by natural systems (including forest fires) and anthropogenic activities (including energy production) [7].

At the same time, attention must be paid to the COVID-19 crisis and the focus of policymakers on protecting lives. The global pandemic, which began in March 2020, is acting as a catalyst for long- and short-term changes and requires the empirical and theoretical attention of researchers [8]. The literature articulates the difficulties that need to be addressed. Post-pandemic challenges include job losses, declining revenues in certain sectors, and economic recessions, as well as sharing economy (SE) activities and other issues [9,10]. Financial losses associated with the COVID-19 crisis have been estimated at approximately 2.96 trillion US dollars in lost economic output [11], and Europe is experiencing a high level of inflation (6.2%, February 2022) [12]. Moreover, the crisis caused by the pandemic has been compounded by the Russian invasion of Ukraine. It is not clear what impact this geopolitical conflict will have on the pace of energy transition [13]. On the one hand, this event may cause a change in the energy policies of many countries and turn them more toward energy security than the goals of transitioning to green energy. However, it may require European policymakers to decide to support green technologies that will facilitate the decarbonization process and fit with the energy policy goals of the European Union [14]. It might reasonably combine the two approaches; an example is Germany, which in response to the current situation in the political arena has taken measures to accelerate the deadline for achieving full renewable energy from 2050 to 2035 [15]. However, this has not prevented them from deciding to renew the start-up of closed coal-fired power plants, which they explain by the need to secure gas reserves for winter by switching off gas-fired power plants and switching on coal-fired ones [16].

In general, divergence has been observed among member states in dealing with climate change [17]. Responses have included support schemes for renewable energies in addition to a lack of public acceptance and a fossil fuel lock-in, as well as inadequate National Energy and Climate Plans with collective targets in EU and UNFCCC policies [18]. The energy transition in Europe's mining regions poses many complications for the years between 2030 and 2050, and key among these is the reduction of greenhouse gas emissions [1]. In Europe, Estonia, Latvia, Lithuania, Belgium, Malta, Luxembourg, and Cyprus are carbon-free [19]. The countries that will face the biggest problems related to energy transformation are Poland, Bulgaria, the Czech Republic, and Romania [20,21]. Table 1 presents information on the direction and problems of the green transformation of the energy sector in selected countries. Decarbonizing national carbon-based economies is an ambitious and difficult undertaking and requires attention to local issues in developing economies to ensure global growth and common goals. The Joint Research Centre (JRC), in its study of opportunities and challenges in EU coal regions [22], stated that about 238,000 jobs may be lost as a result of the energy transition, and the operating horizons for coal-fired power plants in the EU indicate that two thirds are expected to have shut down by 2030. Moreover, indirect activities in the value chain of the coal industry, including power generation, equipment supply, research and development services, and others, provide thousands of additional jobs. The European Commission's platform for the European coal regions outlines that coal-fired power plants in the European Union and the United Kingdom account for 150 GW of total capacity, including 207 power plants and 53,000 direct job positions. There are 150 coal mines across 11 countries in Europe [20]. A particular difficulty is the so-called NUTS-2 region (one of the three levels according to the subdivisions of countries established by Eurostat), where 85% of the jobs related to hard or brown coal are concentrated [23]. Poland is in a unique situation; of the 53,000 jobs in the mining sector, as many as 13,000 of them involve workers from Poland [1].

Table 1. Selected information on the energy sector in different countries and the challenges involved (source: own elaboration, based on [19,24–27]).

Country	Main Source of Energy	Share of Coal in Electricity Generation	Share of RES	Declared Year to Move Away from Coal	Selected Problems of the Energy Sector and Energy Transformation
Czech Republic	Coal/Atomic	40%		2038	Nuclear power plant infrastructure to replace coal.
Poland	Hard coal	72%	17%		Pace of expansion and modernization of generation units is still insufficient; organizational structure of energy companies.
Romania	Coal and gas	17%	24%	2032	Infrastructure for RES sources.
Slovakia	Atomic	7%	17.48%	2023	Infrastructure for RES sources.
Spain	Oil and gas	2%	38%	2030	Infrastructure for renewable energy sources at 74% by 2030 and 100% in 2050;
Germany	Wind	24%	46.4%	2038	Synchronization of renewable sources with the grid transmission capacity power engineering; energy storage.

A McKinsey company study emphasized that Poland must intensify its decarbonization processes fourfold compared to the pace of the previous 30 years in order to achieve the goals of the EU and the Paris Agreement [28]. In 2021, a contract was signed to transform the coal mining sector [29]. This document outlines systemic solutions aimed at protecting the employees of mining plants while maintaining national energy security. The agreement includes, among other things, provisions for financing mechanisms for the hard coal sector and a guarantee of employment for workers and others. Moreover, the necessity is emphasized of additional investment outlay in the subsequent years projected at the level of EUR 10–13 billion per year, or alternatively 1–2% of GDP, for areas related to the decarbonization of the Polish economy. The challenges of decarbonization cover all sectors of the economy. This paper focuses on the mining industry, including the hard coal sector.

One of the ways to mitigate the forthcoming energy transition is to use a pedagogical approach aimed at mobilizing the innovative and entrepreneurial spirit of students, including PhD candidates. The literature emphasizes the rationale of directing young professionals to build innovative solutions in the field of energy [30–32]. One resource that will embody an assertive and equitable shift during the energy transformation may be represented by educational programmes such as the InnoEnergy PhD School (which has EIT funding) [33]. The InnoEnergy PhD School survey was completed in 2021 and the results form the content of this paper. The purpose is to discuss the InnoEnergy PhD School programme as a tool for mitigating the energy transition. The authors of this paper hypothesize that an appropriate pedagogical approach and suitable human resource training outside the traditional model can contribute to tangible benefits in the context of the economic transformations that European countries must face in the coming decades.

This article provides a basis for future analysis in the context of sustainable energy transition at the educational level. At the same time, it should be emphasized that the article also analyzes and considers the negative aspects of the energy transformation.

2. Materials and Methods

Qualitative methods were used in the presented paper. The case study method was adopted, incorporating surveys and open interviews (IDI—in-depth interview). These are typically used in social and environmental research focused on practice, including, among other sectors, education [34], health care, nursing, sociology, anthropology, psychology, management, and information systems [35]. The scope of the investigation undertaken in this study means that the use of this method allowed in-depth analysis of the selected project, policy, and programme, including its application in a real-life system [36].

Reference was made to a case study of a retrospective nature. Ethnographic research was carried out in the form of individual interviews. The challenges posed by the European Union in the context of the transition were characterized. As part of the paper, the issues of higher education in the coal mining industry in the context of transformation (the desk study method) were analysed. The InnoEnergy PhD School educational programme is discussed in terms of the results of the unit centred around the InnoEnergy Central European Office. The effects of implementing new business ideas in the socio-economic environment are presented. These are the results of the participation of young researchers in the InnoEnergy PhD School process, and offer a potential future opportunity to mitigate the energy transition to result in a transparent and fair transition. This paper's structure consists of several stages; the first identifies general challenges affecting the energy sector. General problems and strategic challenges related to the European energy transition are indicated. Furthermore, attention was paid to PhD students' education programmes oriented toward the energy sector. The research subject was defined as the EU InnoEnergy PhD School programme. Research methods and research tools were defined, and are described. Discussion addresses Poland's challenges in the context of energy transformation and the participation of Polish doctoral students in the InnoEnergy PhD School programme. The results of the research are presented. The results are discussed and conclusions drawn. Directions for further research are signposted. The stages of the research process are presented in Figure 1.
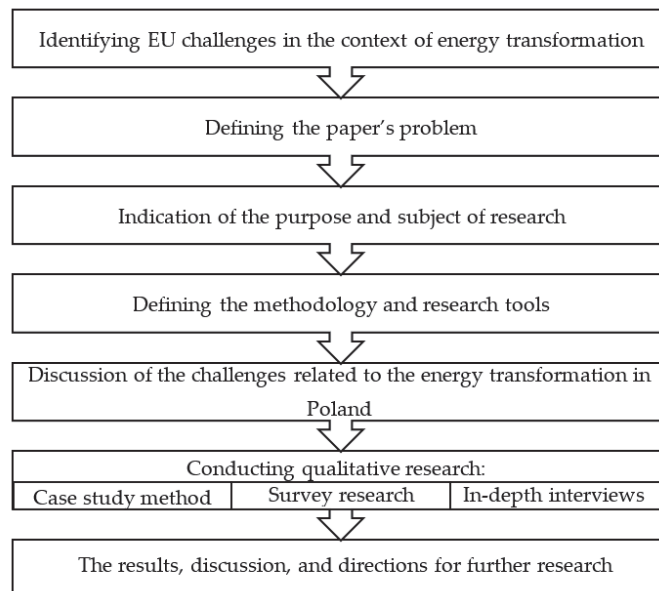

Figure 1. Stages of the research process (source: own elaboration).

3. The Role of Higher Education in the Energy Transition

Particularly important in this context is the aspect of innovation and commercialization in the education of doctoral students. An interesting and valuable perspective is presented in the research by Dooley et al. [37]. The results of the authors' research indicated that doctoral students wanted to increase their business and entrepreneurial skills and were convinced that educational modules could benefit them. At the same time, it is worth paying attention to studies by Pruett et al. [38] who put forward the thesis that the greatest predictor of the will to develop entrepreneurship depends on personal preferences and the subject's own conviction about their entrepreneurial abilities. The European University Association [39], in their paper on fostering creativity and innovation in doctoral education, cites the position that the best mechanism is to bring together doctoral students from various disciplines and encourage their dialogue. Examples of such platforms are summer schools, and specialized institutional and inter-institutional centres [39]. Examples of such centres include ESADE Business School, Grenoble Ecole de Management, etc.

The European Commission is placing increasing emphasis on addressing the topic of developing innovative knowledge and skills in mining activity. New mining projects related to critical raw materials are particularly important [40]. This is evidenced, for example, through the themes of Future Trends Innovation and Skills for Raw Materials during flagship industry events such as Raw Materials Week or the Raw Materials Summit. These events gather a wide range of European stakeholders to discuss policies and initiatives in the field of raw materials (EU Raw Materials Week 2021). Numerous educational projects are oriented around the social licence to operate (SLO), which is one of the major challenges facing the mining industry on the threshold of transition [41]. Examples of such projects include RM@School [42], AMIC [43], BetterGeoEdu [44], RawDTrip [45], TrainESEE [46], and others. In addition, the relevance of the creation of master projects in the context of the implementation of the development strategies of the European Union, and its initiatives related to the Green Deal and the energy transition, is emphasized by the RaVeN (Raw Materials Value Chain) project team [47].

According to the goals of the National Development Strategy, the conditions for the formation of attitudes through lifelong learning approaches will be improved over the next decade [48]. The McKinsey company, in the study 'Carbon-neutral Poland 2050' [28], point out that incentives are needed for universities to promote fields of education that are critical for low-carbon industry. This action fits into the concept of carbon-neutral education (CNE), in which a higher education institution (HEI) operates a dual strategy. First, the HEI aims to implement low-carbon practices in its activities, and second, to orient curricula and pedagogical approaches in order to teach students knowledge and skills relating to carbon-neutral practices [49]. The determinant of successful decarbonization is the modelling of change that results from the interaction of science with industry, government, and society. This approach helps to develop strategies that transcend traditional disciplinary boundaries to include political and social realities [50,51].

In addition to the dualistic CNE strategy outlined above, the concept of education for sustainable development (ESD) has become very popular [52,53], as coordinated by UNESCO [54]. Apart from promoting a more radical learning-centred social transformation in relation to sustainability in the education system, involving changes in the underlying epistemology of its culture, thinking, and practice, the need for discussion around areas such as climate change in the teaching and learning process in higher education has also been asserted [55]. Many studies have highlighted the importance of innovation in building a sustainable future [56]. The JRC has contributed in this area by researching the impact of the introduction and development of ICT (Information and Communications Technology) as a catalyst for teaching and learning innovation [57]. Many projects such as OpenEdu [58], DigCompEdu [59], and DigCompOrg [60] have shown advantages and disadvantages of the innovative use of digital technologies in education, for all parties involved, with a focus on higher education [61]. In addition, the JRC has helped to highlight the importance of raising digital competence throughout teaching and learning processes [62]. A combination

of institutional support and technological self-efficacy ensures the development of good educational practices. This approach translates into achieving a sustainable education system by linking ESD to the innovation stream [63]. An example of an initiative that fits into this concept is the Intercollegiate Climate Academy (MAK), which is implemented in cooperation with the AGH University of Science and Technology (AGH UST) in Krakow, the Warsaw School of Economics, and the University of Wroclaw (Poland). This is a consortium of postgraduate programmes designed to impart interdisciplinary knowledge in combination with the industry's professionalism [64].

4. Poland's Energy Challenge

Hard coal mining in Poland has been decreasing over the last 20 years [65]. In 2020, hard coal extraction amounted to 54.4 million Mg (Mg = 1 tonne; 1000 kg), which was more than 7 million Mg lower than in 2019. At the same time, it should be noted that Poland remains the production leader in the EU. On the international global scale, it ranks in the top 10 for global extraction, at 0.8%. Among Poland's 21 operational coal mines, 20 are located in the Upper Silesian Coal Basin. The other, Bogdanka S.A. Lubelski Wegiel, is located in the Lublin Coal Basin (Figure 2) in the east of the country [66].
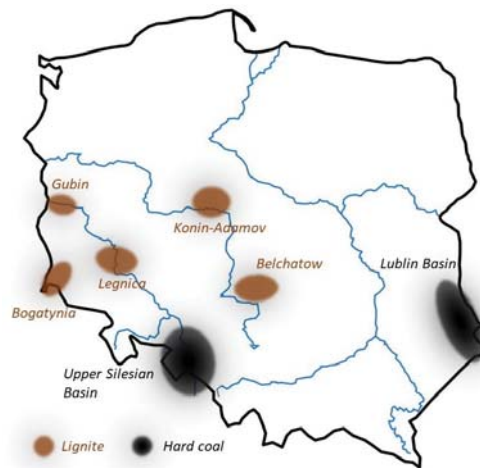

Figure 2. Coal regions in Poland (own elaboration, based on: https://euracoal.eu/, accessed on 2 September 2022).

A downward trend in output has also been observed for lignite. Until 2020, the raw material was extracted in five mines: Bełchatow, Turow, Adamow, Konin, and Sieniawa. The Adamow mine is currently being decommissioned. Poland, with a lignite output of approximately 47.3 million tons (data from 2020 [67]), ranks second in Europe.

The transmission system operator in Poland—the Polish Power Grid (PSE)—indicates that the structure of electricity generation (by power plant group according to fuel type) did not change drastically in 2018–2020 [68]. In 2020, coal-fired power plants continued to dominate generation (just over 70%), followed by renewable energy sources (RES), and an increasing share of wind power plants. Natural gas recorded the next highest growth rate over the three years in question (see Figure 3).
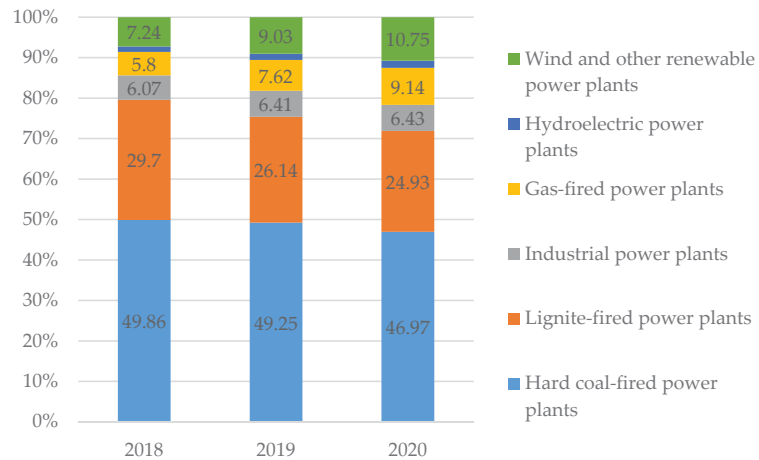
Figure 3. Electricity generation by power plants in Poland according to fuel type, 2018–2020 (source: own elaboration, based on: PSE data).

The origins of the changes in the structure of electricity production in Poland can be traced in this example in line with the strategy presented in the 'Energy Policy of Poland until 2040', which was adopted by the government in September 2020 (hereinafter EPP2040) [69]. The EPP2040 implementation indicators include reducing the share of coal used in electricity generation to 56% and increasing the share of RES to 23%. In addition to the numerical direction of changes in the Polish energy sector, the document presents a scenario framework for the future energy transition, based on three pillars:

1. Just transition. It establishes the 'transition of coal regions, reducing energy poverty and developing new branches of industry related to RES and nuclear power'.

2. Zero-emission energy system. This will be based on 'offshore wind energy, nuclear energy as well as local and civic power generation'.

3. Good air quality. This initiative by every citizen 'is one of the most noticeable signs of moving away from fossil fuels'. Clean air is guaranteed by 'investing in the district heating sector transition (system and individual), electrification of transport and promotion of passive and zero-emission houses using local energy sources'.

In the era of climate change, all these activities are aimed at ensuring Poland's energy self-sufficiency by using, among other things, domestic economic and raw material potential, as well as technological and personnel capacity [70]. Signposts for the direction of changes taking place in Poland include, among others, European Union regulations, which place great emphasis on sustainable economic development. According to the document 'Europe 2020—A strategy for smart, sustainable and inclusive growth', the priorities in this area are 'developing an economy based on knowledge and innovation', as well as 'promoting a more resource efficient, greener and more competitive economy' and 'fostering a high-employment economy delivering social and territorial cohesion' [71].

The education system, including technical and vocational schools as well as universities, is one of the elements of the Polish economy in which such shifts can be seen already to have had and will continue to have a visible impact. Linking science with industry, increasing the importance of innovation in the creation of new products and services, and increasing the environmental self-awareness of young people are the main points of change in higher education [72]. This article, in keeping with its premise, focuses on activities undertaken by universities in these areas. Expanding the didactic offer by reorganizing the old and creating new majors or specialties, such as 'Renewable Energy and Energy Management' or 'Revitalization of Degraded Areas' [73], are changes that can be observed at AGH UST, one of the three universities in Poland that provide education in mining [74].

This approach can meet the future challenges of the Polish mining sector. The preparation of doctoral dissertations may be carried out in different forms in Poland, e.g., as part of a doctoral school, through doctoral studies, or as an employee of a particular organization (the so-called 'implementation doctorate'). Dissertations on topics closely related to counteracting climate change may also be a part of the package of necessary, discussed changes. According to the points made in the work 'Research in EE and ESD in Portuguese Public Universities' [75], the production of doctoral theses is an important indicator of scientific and academic development within a discipline. The initiatives mentioned above are not the only ones being undertaken by Polish universities in order to meet the requirements posed by energy transformation. In addition to research conducted within universities [76], collaboration between universities and research institutions is another example of initiatives contributing to sustainable development goals, and adds value to society and the economy.

Several articles that are the results of cooperation between representatives of AGH UST (scientific staff and students) and the Central Mining Institute (GIG) include work on modern mining or its alternatives [77–82]. Participation in those educational projects co-financed by European institutions is an integral part of building a self-aware, innovation-oriented, business-connected, multicultural scientific community. An example of an educational initiative that addresses the challenges of energy transition and new business models in the energy sector is the InnoEnergy PhD School programme.

5. EIT InnoEnergy—Brief

Being a leader in cleaner energy production in the European Union is inextricably connected to the European Union's innovation efforts. According to the European Green Deal strategy, by 2050 Europe will become the first climate-neutral continent, largely due to research and innovation. Though modernization of the economy as well as society, the EU aims to help 'accelerate and navigate necessary changes', 'implement, demonstrate and remove risks', and 'engage citizens in social innovation' [83]. The Active Innovation paradigm [84] indicates that entrepreneurship and intrapreneurship, and thus use of the values of all those authorized to take action in the innovation process, have become a business imperative. The evolution of education—from traditional to environmentally oriented, encompassing social inclusion—means that 'future engineers' should be equipped with values and experiences that meet real societal challenges [85]. The European Institute of Innovation and Technology (EIT) has stated that the EU is facing an 'innovation crisis'. This is evidenced by the fact that Europe's share in global GDP decreased from 30% in 2006 to 22% in 2016 [86]. The response of the European Parliament and Council to global issues ranging from climate change to sustainable food production, etc., included the establishment of the EIT Innovation Community in 2008. It functions as an independent institute and brings together Europe's leading business, education, and research organizations. Together, they aim towards innovation solutions for Europe. The EIT consists of eight Innovation Communities (Table 2), including EIT InnoEnergy (marked in green).

Table 2. EIT Innovation Communities structure (source: own elaboration, based on: www.eit.europa.eu, accessed on 2 September 2022).

	EIT Climate-KIC
	EIT Digital
	EIT Food
EIT Innovation Communities	EIT Health
	EIT InnoEnergy
	EIT Manufacturing
	EIT Raw Materials
	EIT Urban Mobility

InnoEnergy's mission is: 'Accelerating sustainable energy innovations', connecting all actors from the knowledge triangle: industry, research, and education [87]. InnoEnergy invests in new technologies ranging from renewable energy sources to energy storage. The results of InnoEnergy's activities so far are presented in Table 3.

Table 3. EIT InnoEnergy results (source: own elaboration, based on: www.eit.europa.eu (accessed on 2 September 2022).

Investments	560 mln euro
Products	480
Sales amounting	5.3 mld euro
Alumni	1100
Community	500 key players 18 countries

EIT InnoEnergy strengthens the links between young researchers across Europe. One tool is the InnoEnergy PhD School programme, which is dedicated to PhD candidates. The main goal and motto of the InnoEnergy PhD School is to 'enable doctoral candidates to complement their research with essential entrepreneurial, innovation, business and personal skills'. The programme's emphasis on soft skills education, including teamworking and cross-cultural collaboration, should also be noted. The InnoEnergy PhD School is estimated to have over 260 alumni who understand the energy industry and have the skills and knowledge to deliver the industry's needs [88].

Due to the specific nature of the research, the PhD candidates work in eight critical thematic fields; clean coal and gas technologies, energy storage, energy efficiency, energy from chemical fuels, renewable energies, smart and efficient buildings and cities, smart electric grids, and nuclear instrumentation. The model of education consists of conducting research in the parent institution, where a doctoral thesis is prepared. The InnoEnergy PhD School provides complementary courses and training that should be carried out in entities cooperating with InnoEnergy. These are the flagship European universities and research centres.

The PhD candidates are required to participate in at least three courses from the group of core courses, and at least one from the pool of elective courses. A supplement to the education programme in addition to the courses is a fellowship in a foreign unit. Non-academic locations are recommended. This approach offers the opportunity to expand the student's experience and to strengthen cooperation within the so-called knowledge triangle (universities–business–research centres). The 'Innovation Doctorate' project proves the value of tightening cooperation within the knowledge triangle. PhD candidates working on innovative solutions as part of a doctoral dissertation, in cooperation with an industrial partner, can apply for funding for further studies and substantive support from the EIT. In addition, participants have the chance to transform their research into innovation by preparing an Innovation Project proposal. This is a research and development project that aims to develop a new technology or service that has the potential to become a commercial product, thus contributing to the energy transition.

Finally, the InnoEnergy PhD School is complemented by tutoring, mentoring, and coaching activities throughout the programme's life cycle. Figure 4 presents the InnoEnergy PhD School education model. This approach offers access to supplementation of basic research with key skills, including in the fields of management and innovation. Finally, networking is also an important topic. A three-day conference is organized annually in which all PhD candidates from the InnoEnergy PhD School participate. This provides opportunities to build potential cooperation, establish contacts (including within the business environment), and draw inspiration from each other [89]. Cooperation between PhD candidates and the mobility host is significant (AGH UST-SGPR.tech; AGH UST-Cepsis).
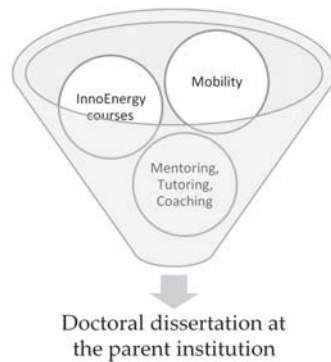
Figure 4. EIT InnoEnergy PhD education structure (source: own elaboration).

6. Results and Discussion

6.1. Polish Participants of the Programme

In 2018, 24 Polish PhD candidates participated in the InnoEnergy PhD School pro-gramme, 66.7% of whom were men. Throughout the life cycle of the programme, men dominated among the participants (see Figure 5). In 2018, eight doctoral students applied to the programme, of whom five were qualified. They were the last recruited PhD candidates to the programme from Poland. That year, one of the participants defended his PhD thesis and received an EIT certificate. An analogous interpretation of the data presented can be undertaken for future years based on Figure 6, which details the number of participants from 2018–2021.
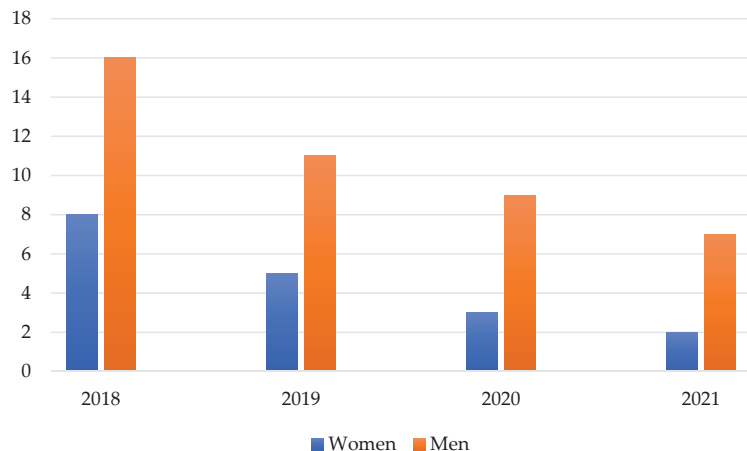

Figure 5. Gender of the participants.

In terms of research areas, the participants developed their scientific interests in the following topics:

- Clean coalfields (seven PhD candidates).
- Renewables (four PhD candidates).
- Smart grids (two PhD candidates).
- Energy efficiency (eight PhD candidates).
- Energy storage (two PhD candidates).
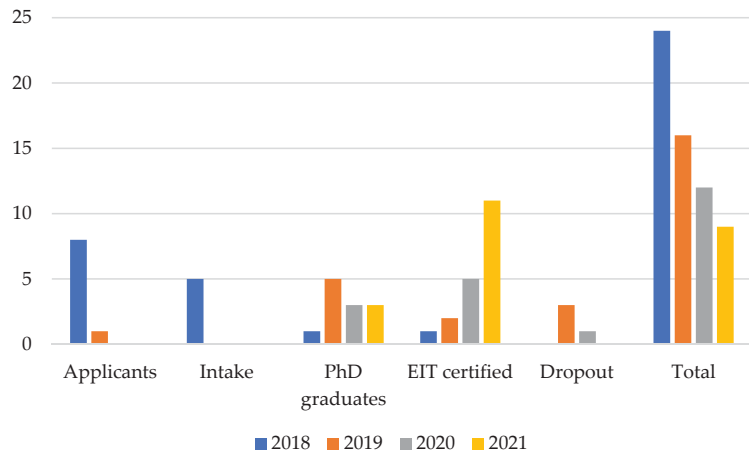- Chemical fuels (one PhD candidate).

Figure 6. Programme participants from 2018–2021.

6.2. The Results of the Research Analysis

The benefits and results to be gained from participation in the InnoEnergy PhD School programme include the acquisition of skills as well as business and decision-making competences enabling the transformation of basic research into projects applicable to the energy sector. One of the tools for verifying the progress of PhD candidates in these areas was a qualitative study conducted using a survey and an open-ended interview (IDI) technique. The survey was conducted annually by the PhD InnoEnergy Officers.

The study was divided into five areas: Section I: Scientific progress; section II: Capacity for innovation; section III: Personal professional plan; section IV: InnoEnergy PhD School activities; section V: General feedback and suggestions for the programme. The responses were varied in nature. The interviews were semi-structured and included the following:

- Beforehand preparation
- Opportunity to collect more in-depth information
- Allowing respondents time to open up about sensitive issues
- Providing qualitative data for joint models.

The following is a summary of the interviews conducted at the end of 2021. Nine active PhD candidates (two women and seven men, ranging in age from 29–38) participated in the interviews.

Section I: Scientific Progress

This section was the broadest section, consisting of four questions.

The first question was about the progress made in 2021. In general, for most students, the main progress in 2021 focused on finalizing their work, i.e., summarizing past studies (such as experimental and computational research) and developing scientific conclusions. Some candidates pointed out that the tremendous support from Knowledge Innovation Community InnoEnergy during those years had simplified the development of their PhDs, including the incorporation of a business approach into an extremely technical thesis.

The second question was 'Which academic competences have been reinforced for your research progress while undertaking InnoEnergy PhD School programme participation?' Among the academic competencies that were reinforced, the PhD candidates listed seeking funds and applying for grants, writing papers and reports, and making research logs and notes, as well as public speaking, teamwork, and networking. Most of them emphasized their improved English. A good example was one of the participants who conducts classes with ERASMUS+ students, who, due to InnoEnergy, feels confident teaching foreigners in English. Some candidates became oriented towards business and opportunities, and

opened up to others. Participants also become project managers or task managers by participating in projects, including European schemes (Horizon Europe, Cost, EIT).

The answers to the third question 'Could you give a highlight from the last year, that you are proud of?' were varied, among which may be distinguished those relating to the PhD itself. The PhD candidates were happy and proud that they were finishing their theses and of having completed the courses provided in the EIT InnoEnergy Programme. One mentioned that he participated in the Battle of Green Talent organized by EIT InnoEnergy and his start-up sent the first samples of its product to China, Switzerland, Germany, Poland, Australia, and Argentina. Another was proud of beginning to cooperate with a start-up from Poland. Some of them specified that they applied for financial support for projects. It is worth mentioning that one of the students received financial support of 1.3 million euro for a project of which she is the manager. Finally, one of the PhD candidates also emphasized that participation in InnoEnergy may not have resulted in the commercialization of research, but it certainly expanded their horizons and understanding of the need for a business approach in such work.

To the fourth question 'What was the main difficulty you met, whatever the nature of it?', there were also many answers on different levels, such as, for example, time management, overtasking, and personal challenges. Among those connected with undertaking a PhD, the candidates listed securing financial support (i.e., for new equipment and appliances) and accurately locating the findings of their PhD theses within the realities of the market at its current state. Only one person mentioned the COVID-19 restrictions and their impact on daily life.

Section II: Capacity for Innovation

In this section, PhD candidates sought to answer whether their work has a capacity for innovation, and what kind. All PhD candidates saw potential for innovation in their research or knowledge. Some of them have elaborated prototypes of their devices. Among them are a number who have already launched their start-up, and some who have developed a supply chain for individual components for prototypes but need to raise necessary funds. Others are performing research into increasing levels of technological readiness. The latter group identified areas in which their studies have innovative and business potential.

Section III: Personal Professional Plan

Most PhD candidates have specific goals for their future careers. This is related to the fact that some have jobs, and others want to continue their careers in academic and commercial industries connected to their PhD topics, and thus will be able to further their PhD research after their defence. Among those who have jobs, a number want to climb the career ladder, and others are thinking of opening their own businesses.

Section IV: InnoEnergy PhD School Activities

This section gathered information about the activities in which the PhD candidates participated in 2021, as well as their assessment of those activities. All PhD candidates completed all the provided courses in the EIT InnoEnergy Programme in 2020. In 2021, three of them participated in placements. For these PhD candidates, these were very fruitful. For one of them, the key aspect of this practice was to gain knowledge about running a business, which he succeeded in doing. For the second, the main goals were to verify the ideas of his thesis and to test his simulations in real-life industrial applications, and he also achieved them all. For the third, the experience provided him with the opportunity to build new relationships and increased his self-management skills (prioritization, time management, and focus).

Section V: General Feedback and Suggestions for the Programme

In general, all the feedback was positive. Some of the PhD candidates mentioned that InnoEnergy provided them with possibilities that they would not have access to in any other way, for example, interesting courses relevant to their topic and held professionally even in difficult pandemic circumstances. These activities taught them the business approach to research, which was very helpful when applying for financial support and has had a positive impact on their current as well as undoubtedly their future professional careers. Most of

them mentioned the placement as a unique experience which increased their competences significantly, and demonstrated that individuals can make a change if surrounded by passionate people and given the right tools. Many participants pointed out that their soft skills increased, and they developed interpersonally because this programme offered a great opportunity to network with industry leaders, scientific specialists, and other PhD candidates around the world. With a clear conscience, all the candidates recommended the InnoEnergy PhD School programme to anyone interested in studying at the border between science and business, as well as for those who are not afraid of challenges.

The survey presented shows that PhD candidates participating in the InnoEnergy PhD School programme recognize the key value of gaining expertise in conjunction with business education. Their understanding of the entrepreneurial spirit, and thus the need to commercialize their work, enables them as young innovators to advance their careers in ways that they did not foresee before joining the programme. They also appreciate the opportunities they have received through participation. These have included testing their solutions in real-world conditions and presenting their ideas to experienced business players. With the knowledge of how to turn research activities into concrete innovation, some have found their place in the business world. One PhD candidate founded his own start-up. Others, even if they have not created their own start-ups, are involved in commercial activities and continue their research work. At the same time, they have achieved an understanding of the importance of creating disruptive innovation in the age of energy transition. The soft skills noted by the PhD candidates, their development emphasized by the EIT throughout the programme, have been helpful in realizing the chosen directions of development. Collaboration between research and private companies has offered great opportunity in terms of knowledge transfer and development of cross-sector skills and competence. In many cases, after international experiences by PhD candidates, collaboration continues. This is also a great return for the network, as PhD candidates exchanging knowledge and experience have a significant impact on the financial stability of the European community [90].

Attention should also be given to PhD candidates who have remained at the university. Several of these have become project managers or task managers through participating in projects, or are passing on to students the knowledge they themselves have gained. In addition, all continue to develop the research they began during their PhD studies. It is also worth noting that the PhD candidates who are employed at the universities continue the mission of InnoEnergy. This means that they do not simply focus on teaching or traditional research work, but continue to seek opportunities and pathways for growth through participation in training, including soft skills. They participate in tutoring and mentor training and become leaders of small teams themselves. Participation in the programme has sparked PhD candidates' interest in the possibility of European scholarships, which they apply for with greater confidence that they will succeed on the international stage. They also seek national funds to conduct international staff exchanges and gain new experience, which results in joint research. The PhD InnoEnergy School has also strengthened cooperation between AGH University of Science and Technology faculties in Krakow. The result has been the formation of new working groups and the preparation of joint papers, and in the future perhaps also projects. This makes the approach to science more interdisciplinary and broadens horizons [90].

Finally, taking into account the challenges faced by Poland in the fields of mining and energy, the project also implements the strategic goals of other EIT networks, including Raw Materials, extending the reach of its impact. This primarily relates to two strategic goals of EIT Raw Materials, i.e., the designing of solutions and the closing of material loops. This means the project implements the agenda of building the diversity and strength of the InnoEnergy network across the value chain. Once a partnership has been established, incorporating a wide range of stakeholders, it integrates all the actors who rely on natural resources, including start-ups and local communities. The Consortium, representing ESEE

(east and southeast Europe) and RIS (Regional Innovation Scheme) countries, fills a gap related to the KTI (knowledge triangle integration) goals [90].

7. Conclusions

The European initiative presented in this article, implemented in cooperation with AGH University of Science and Technology in Krakow, among other institutions, is a practical example of a tool that supports education by enriching it with entrepreneurship, innovation, and business education (EIB) and that can help the future generation mitigate the effects of the energy transition. Through the implementation of courses, workshops and international mobilities, PhD candidates have been equipped with the right competencies to become experts and entrepreneurs. Programme participants find it easier to implement innovative solutions in their workplaces, start their own businesses, and transfer knowledge. This confirms the hypothesis that an appropriate pedagogical approach and personnel training outside the traditional model can contribute to tangible benefits in the context of the economic transformations that European countries will face in the coming decades. Universities are likely to play a key role in tackling climate change and will influence the attitudes of young people as they embark on their careers, so their role should not be limited to imparting knowledge, but should also equip them with the tools to tackle the problems on an immediate basis. Key to the future will be shaping the mindset of an innovator who is able to offer a powerful range of products and services that can be tailored to meet the most complex business needs.

It should be emphasized the research group was relatively small (see the Section 6.1), which may raise doubts as to the representativeness of the study. However, considering the total number of all survey participants and the participation of Polish PhD candidates, the results are satisfactory and may allow certain conclusions to be drawn and some analysis to be conducted.

This article is the first in a series on educational programs responding to the challenges related to the energy sector and its transformation. Further research will be aimed at verifying the legitimacy of investing in educational programs. The criteria of research interest will be business ideas that respond to real socio-economic problems in the energy sector and are of interest to key market players. In addition, it is planned to conduct a comparative analysis of the results of the InnoEnergy programme in other countries, including Portugal. Portugal is an example of a country that has stopped using coal to generate electricity, so it can be a model for countries like Poland, which is still determined by high-carbon economy.

The study does not in any way pretend to present a theoretical model of how higher education should face the climate crisis. Its task is to recognize the possibilities of using European initiatives in the field of education, and the benefits they bring; e.g., stimulating innovation through an appropriate pedagogical approach, or pointing to the need to strengthen the business imperative in doctoral education. The authors believe that supporting such educational initiatives in the future will provide a basis for changing curricula in higher education, and thus contribute to mitigating the effects of the energy transition. Furthermore, in the context of reinforcing the need for a transition to a green economy (i.e., a fundamental transformation towards more sustainable modes of production and consumption), this kind of initiative should be helpful, because it (i) promotes the development and adoption of innovative and sustainable technologies, (ii) offers information on the growing importance of global environmental challenges, and (iii) provides future decision-makers (in this case, PhD candidates) with knowledge about the business sector and so-called sustainability entrepreneurs who can play a part in bringing about the shift to a green economy.

References

1. Cała, M.; Szewczyk-Świątek, A.; Ostręga, A. Challenges of Coal Mining Regions and Municipalities in the Face of Energy Transition. *Energies* **2021**, *14*, 6674. [CrossRef]
2. Climate Target Plan. Available online: https://ec.europa.eu/clima/eu-action/european-green-deal/2030-climate-target-plan_en (accessed on 2 September 2022).
3. Paris Agreement. Available online: https://ec.europa.eu/clima/eu-action/international-action-climate-change/climate-negotiations/paris-agreement_en (accessed on 2 September 2022).
4. EU Emissions Trading System (EU ETS). Available online: https://ec.europa.eu/clima/eu-action/eu-emissions-trading-system-eu-ets_en (accessed on 2 September 2022).
5. The European Parliament and the Council of the European Union. Regulation (EU) 2018/842 of the European Parliament and of the Council of 30 May 2018 on Binding Annual Greenhouse Gas Emission Reductions by Member States from 2021 to 2030 Contributing to Climate Action to Meet Commitments Under the Paris Agreement and Official Journal of the European Union L156. 2018, Volume 61, pp. 26–42. Available online: https://eur-lex.europa.eu/legal-content/EN/TXT/PDF/?uri=CELEX:32018R0842&from=EN (accessed on 2 September 2022).
6. The European Parliament and the Council of the European Union. Regulation (EU) 2021/1119 of the European Parliament and of the Council of 30 June 2021 Establishing the Framework for Achieving Climate Neutrality and Amending Regulations (EC) No 401/2009 and (EU) 2018/1999 ('European Climate Law')," Official Journal of the European Union L243. 2021, Volume 64, pp. 1–19. Available online: https://eur-lex.europa.eu/legal-content/EN/TXT/PDF/?uri=CELEX:32021R1119&from=EN (accessed on 2 September 2022).
7. Fawzy, S.; Osman, A.I.; Doran, W.J.; Rooney, D.W. Strategies for mitigation of climate change: A review. *Environ. Chem. Lett.* **2020**, *18*, 2069–2094. [CrossRef]
8. Verma, S.; Gustafsson, A. Investigating the emerging COVID-19 research trends in the field of business and management: A bibliometric analysis approach. *J. Bus. Res.* **2020**, *118*, 253–261. [CrossRef] [PubMed]
9. Jackson, J.K.; Weiss, M.A.; Schwarzenberg, A.B.; Nelson, R.M.; Sutter, K.M.; Sutherland, M.D. *Global Economic Effects of Covid-19; Congressional Research Service*. 2020. Available online: https://sgp.fas.org/crs/row/R46270.pdf (accessed on 2 September 2022).
10. Roy, S. *Economic Impact of Covid-19 Pandemic*. 2020. Available online: https://www.researchgate.net/publication/343222400_ECONOMIC_IMPACT_OF_COVID-19_PANDEMIC (accessed on 2 September 2022).
11. Szmigiera. Impact of the Coronavirus Pandemic on the Global Economy—Statistics & Facts. 2022. Available online: https://www.statista.com/topics/6139/covid-19-impact-on-the-global-economy-/#topicHeader__wrapper (accessed on 2 September 2022).
12. Eurostat. PRC_HICP_MANR. 2022. Available online: https://ec.europa.eu/eurostat/databrowser/view/PRC_HICP_MANR_custom_79197/bookmark/table?lang=en&bookmarkId=c8a8c259-ee51-444c-9c4b-9e1d41397f63 (accessed on 2 September 2022).
13. Agaton, C.B. Will a Geopolitical Conflict Accelerate Energy Transition in Oil-Importing Countries? A Case Study of the Philippines from a Real Options Perspective. *Resources* **2022**, *11*, 59. [CrossRef]
14. Gatto, A. The energy futures we want: A research and policy agenda for energy transitions. *Energy Res. Soc. Sci.* **2022**, *89*, 102639. [CrossRef]
15. Żuk, P.; Żuk, P. National energy security or acceleration of transition? Energy policy after the war in Ukraine. *Joule* **2022**, *6*, 709–712. [CrossRef]
16. Tollefson, J. What the war in Ukraine means for energy, climate and food. *Nature* **2022**, *604*, 232–233. [CrossRef]
17. Eyl-Mazzega, M.-A.; Mathieu, C. The European Union and the Energy Transition. In *The Geopolitics of the Global Energy Transition*; Springer: Berlin/Heidelberg, Germany, 2020; pp. 27–46. [CrossRef]

18. Nikas, A.; Gambhir, A.; Trutnevyte, E.; Koasidis, K.; Lund, H.; Thellufsen, J.; Mayer, D.; Zachmann, G.; Miguel, L.; Ferreras-Alonso, N.; et al. Perspective of comprehensive and comprehensible multi-model energy and climate science in Europe. *Energy* **2020**, *215*, 119153. [CrossRef]

19. Ministry of State Assets (Poland). Transformacja Sektora Elektroenergetycznego w Polsce Wydzielenie Wytwórczych Aktywów Węglowych ze Spółek z Udziałem Skarbu Państwa; 2021. Available online: https://www.gov.pl/attachment/e0bda880-f23d-4992-8ee6-242c3ca9f34b (accessed on 2 September 2022).

20. Pakulska, T. Green Energy in Central and Eastern European (CEE) Countries: New Challenges on the Path to Sustainable Development. *Energies* **2021**, *14*, 884. [CrossRef]

21. Ćetković, S.; Buzogány, A. The Political Economy of EU Climate and Energy Policies in Central and Eastern Europe Revisited: Shifting Coalitions and Prospects for Clean Energy Transitions. *Politics Gov.* **2019**, *7*, 124–138. [CrossRef]

22. Alves Dias, P.; Kanellopoulos, K.; Medarac, H.; Kapetaki, Z.; Miranda-Barbosa, E.; Shortall, R.; Czako, V.; Telsnig, T.; Vazquez-Hernandez, C.; Lacal Arántegui, R.; et al. EU Coal Regions: Opportunities and Challenges Ahead; 2018. Available online: https://publications.jrc.ec.europa.eu/repository/handle/JRC112593 (accessed on 2 September 2022).

23. European Coal Regions. Available online: https://visitors-centre.jrc.ec.europa.eu/tools/coal-report/ (accessed on 2 September 2022).

24. Forum Energii. Energy Transition in Poland. 2022. Available online: https://forum-energii.eu/public/upload/articles/files/Energy%20transition%20in%20Poland.%202022%20Edition(2).pdf (accessed on 2 September 2022).

25. World Bank. Gross Domestic Product. Available online: https://www.worldbank.org/en/home (accessed on 10 October 2021).

26. Clean Energy Wire. Available online: https://www.cleanenergywire.org/ (accessed on 2 September 2022).

27. Statista—The Statistics Portal for Market Data, Market Research and Market Studies. Available online: https://www.statista.com/ (accessed on 2 September 2022).

28. Engel, H.; Purta, M.; Speelman, E.; Szarek, G.; van der Pluijm, P. Carbon-Neutral Poland 2050, Turning a Challenge into an Opportunity. 2020. Available online: https://www.mckinsey.com/~{}/media/McKinsey/Industries/Electric%20Power%20and%20Natural%20Gas/Our%20Insights/Carbon%20neutral%20Poland%202050%20Turning%20a%20challenge%20into%20an%20opportunity/Carbon-neutral-Poland-2050.pdf (accessed on 2 September 2022).

29. Ministry os State Assets (Poland). Umowa Społeczna Dotycząca Transformacji Sektora Górnictwa Węgla Kamiennego oraz Wybranych Procesów Transformacji Województwa Śląskiego. Available online: https://www.gov.pl/web/aktywa-panstwowe/umowa-spoleczna (accessed on 8 December 2021).

30. Nowiński, E. Transformacja energetyki a bezpieczeństwo energetyczne Polski. *Nowa Energ.* **2021**, *3*, 42–46.

31. Sukiennik, M.; Kowal, B.; Bąk, P. Identification of Market Gap as a Chance for Enterprise Development—Example of Polish Raw Materials Industry. *Energies* **2021**, *14*, 4678. [CrossRef]

32. Sukiennik, M.; Zybała, K.; Fuksa, D.; Kęsek, M. The Role of Universities in Sustainable Development and Circular Economy Strategies. *Energies* **2021**, *14*, 5365. [CrossRef]

33. EIT. Available online: https://european-union.europa.eu/institutions-law-budget/institutions-and-bodies/institutions-and-bodies-profiles/eit_en (accessed on 2 September 2022).

34. Suárez-Perales, I.; Valero-Gil, J.; la Hiz, D.I.L.-D.; Rivera-Torres, P.; Garcés-Ayerbe, C. Educating for the future: How higher education in environmental management affects pro-environmental behaviour. *J. Clean. Prod.* **2021**, *321*, 128972. [CrossRef]

35. Mohajan, H.K. Qualitative research methodology in social sciences and related subjects. *J. Econ. Dev. Environ. People* **2018**, *7*, 23–48. [CrossRef]

36. Sagadin, J.; Bertoncelj, L. *Razprave iz Pedagoške Metodologije*; Znanstveni inštitut Filozofske fakultete: Ljubljana, Slovenia, 1991.

37. Dooley, L.; Kenny, B. Research Collaboration and Commercialization. *Ind. High. Educ.* **2015**, *29*, 93–110. [CrossRef]

38. Pruett, M.; Shinnar, R.S.; Toney, B.; Llopis, F.; Fox, J. Explaining entrepreneurial intentions of university students: A cross-cultural study. *Int. J. Entrep. Behav. Res.* **2009**, *15*, 571–594. [CrossRef]

39. European Universities and Ministers of Higher Education. Doctoral Programmes in Europe's Universities: Achievements and Challenges. 2007. Available online: https://eua.eu/resources/publications/652:doctoral-programmes-in-europe-s-universities-achievements-and-challenges.html (accessed on 2 September 2022).

40. European Commission. Critical Raw Materials Resilience: Charting a Path towards Greater Security and Sustainability. 2020. Available online: https://eur-lex.europa.eu/legal-content/EN/TXT/PDF/?uri=CELEX:52020DC0474&from=EN (accessed on 10 May 2022).

41. Łacny, Z.; Ostręga, A. The impact of corporate social responsibility on social acceptance as a determinant of the sustainable mineral extraction—Polish case study. *Gospod. Surowcami Miner. -Miner. Resour. Manag.* **2021**, *37*, 161–178. [CrossRef]

42. Torreggiani, A.; Zanelli, A.; Degli Esposti, A.; Polo, E.; Dambruoso, P.; Lapinska-Viola, R.; Forsberg, K.; Benvenuti, E. How to Prepare Future Generations for the Challenges in the Raw Materials Sector. In *Rare Metal Technology*; Springer: Berlin/Heidelberg, Germany, 2021; pp. 277–287. [CrossRef]

43. Koivurova, T.; Lesser, P.; Kähkönen, J.; Pääkkölä, S.; Wallen, H. Social Licence to Operate in Lapland: Tools from the University of Lapland's SLO Research, Final Report for the AMIC Project. 2018. Available online: https://lauda.ulapland.fi/handle/10024/63894 (accessed on 10 May 2022).

44. Godfirnon, M.; Pirard, E.; Evrard, M.; Barnabé, P.; Shikika, A. BetterGeoEdu: European Project for Popularizing Science through Video Games. 2020. Available online: https://orbi.uliege.be/handle/2268/251387 (accessed on 10 May 2022).

45. EIT RawMaterials. "RawDTrip—A New Summer School about the Raw Materials VALUE Chain," in Abstract Book. Available online: https://eitrawmaterials.eu/rawdtrip-a-new-summer-school-about-the-raw-materials-value-chain/ (accessed on 2 September 2022).

46. Pomykała, R. "Wyzwania i potrzeby edukacyjne—Educational Challenges and Needs," in Trainesee Workshop. Book of Abstracts, Kraków. 2021, p. 6. Available online: Https://wilgz.agh.edu.pl/wp-content/uploads/2022/02/Book_of_abstracts.pdf (accessed on 2 September 2022).

47. Wiktor-Sułkowska, A.; Lorenc, S.; Kustra, A.; Kowalska, N. The RaVeN Project—An Example of University Education for the Green Deal. In Proceedings of the 2nd International Conference Strategies toward Green Deal Implementation—Water, Raw Materials & Energy, Online, 8–10 December 2021; Available online: https://greendeal2021.pl/wp-content/uploads/2022/01/Abstract-Book.pdf (accessed on 2 September 2022).

48. Rada Ministrów, Uchwała Nr 157 Rady Ministrów z dnia 25 września 2012 r. w sprawie przyjęcia Strategii Rozwoju Kraju 2020. 2012. Available online: http://g.ekspert.infor.pl/p/_dane/akty_pdf/MPO/2012/170/882.pdf#zoom=90 (accessed on 2 September 2022).

49. Baumber, A.; Luetz, J.M.; Metternicht, G. Carbon Neutral Education: Reducing Carbon Footprint and Expanding Carbon Brainprint. In *Quality Education*; Encyclopedia of the UN Sustainable Development Goals; Springer: Cham, Switzerland, 2020; pp. 55–67. [CrossRef]

50. Pade-Khene, C.; Luton, R.; Jordaan, T.; Hildbrand, S.; Proches, C.G.; Sitshaluza, A.; Dominy, J.; Ntshinga, W.; Moloto, N. Complexity of Stakeholder Interaction in Applied Research. *Ecol. Soc.* **2013**, *18*, 13. [CrossRef]

51. Miller, C.A.; Wyborn, C. Co-production in global sustainability: Histories and theories. *Environ. Sci. Policy* **2018**, *113*, 88–95. [CrossRef]

52. Filho, W.L.; Sima, M.; Sharifi, A.; Luetz, J.M.; Salvia, A.L.; Mifsud, M.; Olooto, F.M.; Djekic, I.; Anholon, R.; Rampasso, I.; et al. Handling climate change education at universities: An overview. *Environ. Sci. Eur.* **2021**, *33*, 1–19. [CrossRef]

53. Bautista-Puig, N.; Sanz-Casado, E. Sustainability practices in Spanish higher education institutions: An overview of status and implementation. *J. Clean. Prod.* **2021**, *295*, 126320. [CrossRef]

54. UNESCO. Education for Sustainable Development: A Roadmap. 2020. Available online: https://unesdoc.unesco.org/ark:/48223/pf0000374802 (accessed on 10 May 2022).

55. Reimers, F.M. The role of universities building an ecosystem of climate change education. In *Education and Climate Change*; Springer: Berlin/Heidelberg, Germany, 2020; pp. 1–44. [CrossRef]

56. Mulder, K. *Sustainable Development for Engineers, a Handbook and Resource Guide*; Routledge: London, UK, 2006.

57. Learning and Skills for the Digital Era. Available online: https://joint-research-centre.ec.europa.eu/scientific-activities-z/learning-and-skills-digital-era_en (accessed on 2 September 2022).

58. European Commission (Joint Research Centre); Inamorato dos Santos, A.; Punie, Y.; Muñoz, J.C. EUR 27938—Opening Up Education: A Support Framework for Higher Education Institutions. Publications Office. 2017. Available online: https://op.europa.eu/en/publication-detail/-/publication/c52b6cab-a82c-4e75-8420-d2431196d11d/language-en (accessed on 2 September 2022).

59. DigCompEdu. Available online: https://joint-research-centre.ec.europa.eu/digcompedu_en (accessed on 2 September 2022).

60. European Framework for Digitally Competent Educational Organisations—DigCompOrg. Available online: https://joint-research-centre.ec.europa.eu/european-framework-digitally-competent-educational-organisations-digcomporg_en (accessed on 2 September 2022).

61. European Commission (Joint Research Centre); Mora-Cantallops, M.; Inamorato dos Santos, A.; Villalonga-Gómez, C.; Lacalle Remigio, J.R.; Camarillo Casado, J.; Manuel Sota Eguzábal, J.; Velasco, J.R.; Ruiz Martínez, P.M. The Digital Competence of Academics in Spain: A Study Based on the European Frameworks DigCompEdu and OpenEdu. Publications Office of the European Union. 2022. Available online: https://op.europa.eu/en/publication-detail/-/publication/a99c9125-0251-11ed-acce-01aa75ed71a1/language-en (accessed on 2 September 2022).

62. European Commission (Joint Research Centre); Langer, L.; Rasmussen, M.; Conrads, J.; Winters, N.; Geniet, A. Digital Education Policies in Europe and Beyond: Key Design Principles for more Effective Policies. Publications Office. 2018. Available online: https://op.europa.eu/en/publication-detail/-/publication/2ae2c833-f1cb-11e7-9749-01aa75ed71a1/language-en (accessed on 2 September 2022).

63. Fourati-Jamoussi, F.; Dubois, M.; Chedru, M.; Belhenniche, G. Education for Sustainable Development and Innovation in Engineering School: Students' Perception. *Sustainability* **2021**, *13*, 6002. [CrossRef]

64. AGH, SGH i UWr tworzą Międzyuczelnianą Akademię Klimatu. Available online: https://www.agh.edu.pl/info/article/agh-sgh-i-uwr-tworza-miedzyuczelniana-akademie-klimatu/ (accessed on 2 September 2022).

65. Tajduś, A. "'QUO VADIS' Polish mining?" Przegląd Górniczy. 2021, Volume 77, No. 1–3. pp. 7–13. Available online: http://yadda.icm.edu.pl/baztech/element/bwmeta1.element.baztech-f92b25e5-ec7a-4659-aa00-137bbda37bd4?q=bwmeta1.element.baztech-3ca75745-cde4-428d-8024-c2637930b334;2&qt=CHILDREN-STATELESS (accessed on 2 September 2022).

66. *Annual Report (2020) on the State of Basic Natural and Technical Hazards in the Hard Coal Mining Industry*; Central Mining Institute (GIG): Katowice, Poland, 2021.

67. Polish Geological Institute-National Research Institute (PGI-NRI). The Balance of Mineral Resources Deposits in Poland as of 31.12.2020. Warszawa. 2021. Available online: http://geoportal.pgi.gov.pl/css/surowce/images/2020/bilans_2020.pdf (accessed on 10 May 2022).

68. Polish Power Grid (PSE). Available online: https://www.pse.pl/dane-systemowe/funkcjonowanie-kse/raporty-roczne-z-funkcjonowania-kse-za-rok/raporty-za-rok-2020 (accessed on 2 September 2022).

69. Ministry of Climate and Environment. Energy Policy of Poland until 2040 (EPP2040). 2021. Available online: https://www.gov.pl/web/climate/energy-policy-of-poland-until-2040-epp2040 (accessed on 2 September 2022).

70. Siwiec, D. Transformacja energetyczna w kontekście realizacji projektu strategii wodorowej w Polsce. *Nowa Energ.* **2021**, *4*, 38–40.

71. EUROPE 2020 A Strategy for Smart, Sustainable and Inclusive Growth; European Commission. 2010. Available online: https://ec.europa.eu/eu2020/pdf/COMPLET%20EN%20BARROSO%20%20%20007%20-%20Europe%202020%20-%20EN%20version.pdf (accessed on 2 September 2022).

72. Adach-Pawelus, K.; Gogolewska, A.; Górniak-Zimroz, J.; Kiełczawa, B.; Krupa-Kurzynowska, J.; Paszkowska, G.; Szyszka, D.; Worsa-Kozak, M.; Woźniak, J. A New Face of Mining Engineer—International Curricula to Sustainable Development and Green Deal (A Case Study of the Wrocław University of Science and Technology). *Sustainability* **2021**, *13*, 1393. [CrossRef]

73. Ostręga, A.; Łacny, Z.; Kowalska, N.; Preidl, K. Reclamation, redevelopment and revitalisation of post-mining areas—a review of the experience of the Mining and Geoengineering Faculty. *Przegląd Górniczy* **2019**, *75*, 11–20.

74. Adach-Pawelus, K.; Gogolewska, A.; Górniak-Zimroz, J.; Herbert, J.H.; Hidalgo, A.; Kiełczawa, B.; Krupa-Kurzynowska, J.; Lampinen, M.; Mamelkina, M.; Paszkowska, G.; et al. Towards Sustainable Mining in the Didactic Process—MEITIM Project as an Opportunity to Increase the Attractiveness of Mining Courses (A Case Study of Poland). *Sustainability* **2020**, *12*, 10138. [CrossRef]

75. Borges, F.; Benayas, J. Research in EE and ESD in Portuguese public universities. *Int. J. Sustain. High. Educ.* **2019**, *20*, 57–74. [CrossRef]

76. Czerw, K.; Krzyżanowski, A.; Baran, P.; Zarębska, K. Vapour Sorption on Coal: Influence of Polarity and Rank. *Energies* **2022**, *15*, 3065. [CrossRef]

77. Wodołażski, A.; Skiba, J.; Zarębska, K.; Polański, J.; Smolinski, A. CFD Modeling of the Catalyst Oil Slurry Hydrodynamics in a High Pressure and Temperature as Potential for Biomass Liquefaction. *Energies* **2020**, *13*, 5694. [CrossRef]

78. Gabruś, E.; Wojtacha-Rychter, K.; Aleksandrzak, T.; Smoliński, A.; Król, M. The feasibility of CO_2 emission reduction by adsorptive storage on Polish hard coals in the Upper Silesia Coal Basin: An experimental and modeling study of equilibrium, kinetics and thermodynamics. *Sci. Total Environ.* **2021**, *796*, 149064. [CrossRef] [PubMed]

79. Gazda-Grzywacz, M.; Burchart-Korol, D.; Smoliński, A.; Zarębska, K. Environmental protection—Greenhouse gas emissions from electricity production in Poland. *J. Phys. Conf. Ser.* **2019**, *1398*, 012004. [CrossRef]

80. Czerw, K.; Dudzińska, A.; Baran, P.; Zarębska, K. Sorption of carbon dioxide on the lithotypes of low rank coal. *Adsorption* **2019**, *25*, 965–972. [CrossRef]

81. Baran, P.; Zarębska, K.; Bukowska, M. Expansion of Hard Coal Accompanying the Sorption of Methane and Carbon Dioxide in Isothermal and Non-isothermal Processes. *Energy Fuels* **2015**, *29*, 1899–1904. [CrossRef]

82. Żyła, M.; Dudzińska, A.; Cygankiewicz, J. The Influence of Disintegration of Hard Coal Varieties of Different Metamorphism Grade on the Amount of Sorbed Ethane/Wpływ rozdrobnienia odmian węgla kamiennego o różnym stopniu metamorfizmu na ilości sorbowanego etanu. *Arch. Min. Sci.* **2013**, *58*, 449–463. [CrossRef]

83. European Commission. Research and Innovation for the European Green Deal. Available online: https://ec.europa.eu/info/research-and-innovation/strategy/strategy-2020-2024/environment-and-climate/european-green-deal_en (accessed on 2 September 2022).

84. Meissner, D.; Kotsemir, M. Conceptualizing the innovation process towards the 'active innovation paradigm'—Trends and outlook. *J. Innov. Entrep.* **2015**, *5*, 1–18. [CrossRef]

85. Högfeldt, A.K.; Papell, G.T.; Gumaelius, L.; Coral, J.S. Bridging engineering and sustainability through challenge driven education: A case study on InnoEnergy Masters of the European Institute of Innovation and Technology. In Proceedings of the 19th European Roundtable for Sustainable Consumption and Production (ERSCP 2019) Institute for Sustainability Science and Technology, Universitat Politècnica de Catalunya, Barcelona, Spain, 15–18 October 2019; Available online: https://upcommons.upc.edu/bitstream/handle/2117/176303/Proceedings+Abstract.pdf?sequence=1 (accessed on 2 September 2022).

86. European Institute of Innovation & Technology (EIT). Frequently Asked Questions (FAQs). Available online: https://eit.europa.eu/who-we-are/faq (accessed on 2 September 2022).

87. European Institute of Innovation & Technology (EIT). EIT InnoEnergy. Available online: https://eit.europa.eu/our-communities/eit-innoenergy (accessed on 2 September 2022).

88. European Institute of Innovation & Technology (EIT). Engineering Innovation A Sustainable Energy Future for Europe. Available online: https://www.innoenergy.com/media/4355/corp_brochure_online_april-2019.pdf (accessed on 2 September 2022).

89. European Institute of Innovation & Technology (EIT). EIT InnoEnergy—Accelerating Sustainable Energy Innovations. Available online: https://www.innoenergy.com/ (accessed on 2 September 2022).

90. Zarębska, K.; (AGH-UST, Krakow, Poland). InnoEnergy PhD School Officer Annual Report. Unpublished Materials. 2021.